University of California
Santa Barbara

Quantum decoherence of near-surface nitrogen-vacancy centers in diamond and implications for nanoscale imaging

A dissertation submitted in partial satisfaction
of the requirements for the degree

Doctor of Philosophy
in
Physics

by

Bryan Andrew Myers

Committee in charge:

Professor Ania C. Bleszynski Jayich, Chair
Professor Andrew Cleland
Professor Andreas Ludwig

September 2016

The Dissertation of Bryan Andrew Myers is approved.

Professor Andrew Cleland

Professor Andreas Ludwig

Professor Ania C. Bleszynski Jayich, Committee Chair

August 2016

Quantum decoherence of near-surface nitrogen-vacancy centers in diamond and implications for nanoscale imaging

by

Bryan Andrew Myers

For my family
present and future

Acknowledgements

My research in the Ph.D. has been supported by grants from government agencies that include AFOSR, DARPA, and NSF. The Catalyst AFM used in my first scanning magnetometry project was provided by Bruker Nano Surfaces. I also benefited from technical AFM discussions with local Bruker Nano Surfaces engineers Chanmin Su, Izhar Medalsy, and their development team. I owe much appreciation to the Department of Defense, AFOSR, and ASEE for granting and managing my NDSEG fellowship in 2012-2015 and I thank IBM for the generous fellowship support in my last year. I am also thankful to my dissertation committee members Professor Andrew Cleland and Professor Andreas Ludwig for their time in listening to my proposed research, for comments on ongoing research and the dissertation, and for discussion on post-graduate careers.

I am very grateful to Professor Ania Jayich for hiring me on as a researcher in her new group at UCSB. She introduced me to experimental research, and for that general fact I will always be immeasureably thankful. Every practical laboratory skill I now have, from laser optics to cleanroom techniques, I really owe to Ania's excellent guidance and resources. Ania has consistently been supportive of my professional growth as a scientist and encouraged me to attend enough conferences to present my work and meet others in the broad nanoscale physics field. She granted me freedom to pursue my ideas for experiments, and refocused my dephased approach when necessary. The number of hours and late nights Ania spent to make sure we had excellent grant support and equipment to pursue our research will remain unfathomable to me. It's been amazing to see so many of her early ideas come to realization in the lab; I still remember in 2011 Ania explaining to me the once-strange concepts of doing NV-strain Hahn echoes and cryogenic NV magnetometry. I will certainly look back well on Ania's enthusiasm in the lab, and her happy willingness to meet with and support students and postdocs, even on

a busy day. I wish the best for the continued success of the Jayich lab.

We started as a small group nearly six years ago, and I enjoyed working with the students who helped build up the room 4209 confocal microscope hardware and software: Paul Lauria, Matt Strader, Eric Miller, and Victor Spiro-Jaeger. Our group has grown rapidly, and I can only include brief words here. Preeti Ovartchaiyapong of our entering grad class became my early collaborator on homework sets, and then we both joined Ania's group where he has pioneered single-crystal diamond fabrication. I could always count on both Preeti and his wife Gift, now Dr. and Dr. plus son, for advice on process equipment in the cleanroom, and Preeti patiently performed the electron beam lithography exposures for our diamond nanopillar and silicon nanostructure samples. I admire the hard work of Dr. Laetitia Pascal, our group's first postdoctoral scholar, on magnetometry and diamond fab projects including our collaboration in the gadolinium scanning work. Claire McLellan has always been a diligent diamond CVD team member, and soon took the lead on our diamond purchases, polishing, and logistics. We have had ongoing collaboration in diamond processing for NVs and lots of CVD troubleshooting. I appreciate Claire's and Jens' work on designing the "coffeeside" optics setup that benefited many users and later evolved into our second scanning probe magnetometer. Kenny Lee and I first exchanged ideas at the ITAMP/B2 Institute Winter school 2013 at Biosphere 2. I have enjoyed many discussions with him on spin control sequences, debugging, and analysis for the ground-state strain project and onwards. I can't wait to see what he and Jeff do with NV-strain coupling next.

I have learned a lot from gifted experimentalist Dr. Matt Pelliccione, who patiently introduced me to low noise electrical measurements, pcb circuit design, and tuning forks. Our gadolinium project set the foundation for my last two years of work. I benefited from fabrication conversations with Alec Jenkins, who has worked hard on improving the diamond nanopillar fab process for scanning probes. I wish Dr. Donghun Lee well in his

hard-earned professorship at Korea University and have enjoyed his insights about the broader quantum hybrid systems field. I've had the pleasure of discussing several NMR, EPR, and optics topics with Dr. Tim Eichhorn, and, given more time, I think we could have collaborated on a cool NV NMR project. I thank Dr. Amila Ariyaratne, who has been an excellent teammate in the final year of my work on the near-surface NV relaxation and scanning probe project. Amila came up with the idea to start fabricating our own flat silicon AFM probes from silicon-on-insulator, a rewarding effort that has really expanded my knowledge of etch and lithography tools in a short time. Our morning versus night routines became quite complementary. As I write this summer, he and new recruit Dolev have rapidly made thoughtful progress in adding functionalities to the setup.

I have had the pleasure of working with several Master's students from Europe, Matthieu Dartiailh, Jens Boss, Danijela Markovic, and Thomas Chalopin on topics ranging from scanning magnetometry to dynamical decoupling and numerical simulations of NV-^{15}N dynamics. I thank the many undergraduates who have done projects with the group, especially Ananda Das and Ilan Rosen who worked closely with me on proton sensing, tip fabrication, and designing magnet stages. I also thank Sasha Zibrov and Bo Dwyer on their machining work and physics discussions on our UC San Diego trips.

I am indebted to Ken Ohno and Professor David Awschalom, who set up the diamond CVD growth machine at UCSB before I arrived. Ken trained me carefully on the CVD equipment and made sure I understood the maintenance procedures and formed good habits of status and sample logging. I enjoyed bouncing around ideas with Ken, Steve, and Claire in our sometimes weekly CVD journal clubs. Having the in-house isotopic ^{12}C diamond samples has been an essential ingredient to my NV coherence measurements. The collaborative delta-doping project with Ken, Joe Heremans, Lee Basset, and David Toyli was a vital period of getting the coherent spin control aspects of our first Jayich-lab setup working well, and that project motivated the rest of my research on near-surface

NVs. I have benefited from many excellent interactions with the talented people of the Awschalom group. Each of the members had a unique impact on my early experimental physics exposure or continuing grad research perspective that will not be forgotten: Brian Maertz, Bob Buckley, Greg Calusine, Chris Yale, Viva Horowitz, David Christle, Andrew Yeats, Paul Klimov, Benji Aleman, Paolo Andrich, Greg Fuchs, Abram Falk, Will Koehl, and Charlie de las Casas. I wish David's group continued excellence in Chicago.

I have benefited much from collaboration and fellowship support with the IBM Almaden team of Dan Rugar, John Mamin, Mark Sherwood, and Moonhee Kim. They are always working on groundbreaking ideas towards the goal of nano-MRI, and I appreciate our many discussions about near-surface NVs, detection of nuclei, spin physics, experimental equipment, and manuscripts.

The Martinis, Cleland, and Han groups were helpful with our effort in 2015 to set up one of the GHz DAC AWG boards for experimenting with optimally controlling NV centers beyond square pulses. For this effort, I thank Ryan, Peter, Chris, Yu, and particularly thank Dan Sank for his expert help on startup and workings of the code. Earlier on, I appreciated microwave waveguide and simulation tips from Jim and Amit.

While traveling to grant reviews, poster sessions, and conferences I met several people in the NV diamond field. A few of those who I talked to about scanning probes, NMR, diamond processing, or decoherence projects were Shimon Kolkowitz, Igor Lovchinsky, Slava Dobrovitski, Michael Flatté, Mike Grinolds, Marc Warner, Jean-Philippe Tetienne, Dmitry Budker, Andrey Jarmola, Linh Pham, Nir Bar-Gill, and Jens Boss. I also thank Shimon and Georg Kucsko for sending a nice mask pattern for omega striplines.

Of course I could not have done that traveling, or any research and diamond growth, without great administrative support through the California Nanosystems Institute and Department of Physics, all experts at what they do, and patient and kind. Lynne, Dan Daniels, Dan, and Dave in purchasing and travel, Holly at CNSI, graduate advisor

Jennifer, the attentive Broida and Elings building managers Mike and Bob, machine shop managers Guy and Jeff, and the unnamed many who constructed our 1219 Broida lab in 2011 and kept facilities running. Development engineer Peter Duda taught me about vacuum leak check systems and he set up bench interlocks systems for our new diamond-cleaning processes. Engineer Lee Sawyer has been great in making sure we got our parts shipped out, retrieved, and installed for maintenance when we had CVD vacuum issues in 2015 and has always been responsive in writing masks with quick turnaround time. I've also benefited from the Microscopy Facility in Elings Hall. Tom Mates has offered his expertise in running and analyzing SIMS and XPS measurements for our functionalization experiments. Mark Cornish made available the facility's micromanipulator, which has been an invaluable tool for preparing tips on tuning forks.

I used the UCSB Nanofabrication Facilities more and more frequently throughout my research, and I often reminded myself not to take for granted having such a complete cleanroom available on campus. The managers and development engineers and scientists who train, upgrade, maintain, and advise 24/7 are a great team. Brian Thibeault helped Amila and I brainstorm about the silicon tip and cantilever etching options for our AFM probes. I would particularly like to thank Aidan Hopkins for extra tutorials on running the EDX-SEM instrument, and especially to recognize engineer Don Freeborn for his awesome responsiveness and professionalism, as well as his kind friendship.

I thank Professor Craig Hawker for supporting our group's magnetometry projects, which includes a MRL seed grant. His students and postdocs Justin, Yingdong, Will, and Bernard have also been dedicated collaborators in devising and performing chemical functionalizations to silicon AFM tips for our ongoing imaging experiments, most of which I could not include in this dissertation, but our subgroup will continue to benefit from what we've learned. I also thank Professor Echegoyen and his student Danisha for providing rare and interesting Gd-containing samples for attaching to probes.

Finally, I want to acknowledge my family who has shaped who I am long before graduate school and provides me tremendous love and support. My parents David and Sharon, your wise words and kind actions always inspire encouragement. And thanks for cheerfully helping me move eight different places in the past decade of my education. Brandon, we've shown that the coherence time of an entangled state of two identical but far-separated Ph.D. students studying $|\text{CS}\rangle$ and $|\text{Physics}\rangle$ is quite long and inferred to be unmeasureable in our lifetime. Peter, roommates for the last four years, but always brothers, you reminded me daily of creative uses of math outside of physics. Rachael, every visit leaves me smiling, and your Einstein canvas painting has stared at me while I wrote my whole dissertation, though I might have forgotten to cite him in the bibliography. The years of my grad school experience have been enriched by Chem (Moureen) Kemei, my better half and friend, who has been with me every step of the Ph.D. since our conversations on crystal-field theory in Condensed Matter 223B. Your immense love, kindness, and encouragement and admirable example in generosity and scientific work inspires me each day. I thank God for guiding our path together in peace and joy, and I eagerly look forward to where we are going next. Job 12:8: *Speak to the earth and it shall teach you.*

Curriculum Vitæ

Bryan Andrew Myers

Education

2016	Ph.D. in Physics, University of California, Santa Barbara.
2013	M.A. in Physics, University of California, Santa Barbara.
2010	B.A. in Physics (High Honors), University of California, Berkeley.

Publications

11. **B. A. Myers**, A. Ariyaratne, A. C. Bleszynski Jayich, Double-quantum spin-relaxation limits to coherence of near-surface nitrogen-vacancy centers, (*Submitted*) (2016) arXiv: 1607.02553
10. S. Sangtawesin, C. A. McLellan, **B. A. Myers**, A. C. Bleszynski Jayich, D. D. Awschalom, J. R. Petta, Hyperfine-enhanced gyromagnetic ratio of a nuclear spin in diamond, New Journal of Physics **18** (8) (2016) 083016. [**doi**]
9. C.A. McLellan, **B. A. Myers**, S. Kraemer, K. Ohno, D. D. Awschalom, A. C. Bleszynski Jayich, Patterned formation of highly coherent nitrogen-vacancy centers using a focused electron irradiation technique, Nano Lett. **16** (4) (2016) pp 2450–2454. [**doi**]
8. S. Cui, A. Greenspon, K. Ohno, **B. A. Myers**, A. C. Bleszynski Jayich, D. D. Awschalom, E. Hu, Reduced plasma-induced damage to near-surface nitrogen-vacancy centers in diamond, Nano Lett. **15** (5) (2015) pp 2887–2891. [**doi**]
7. M. Pelliccione, **B. A. Myers**, L. M. A. Pascal, A. Das, and A. C. Bleszynski Jayich, Two-dimensional nanoscale imaging of gadolinium spins via scanning probe relaxometry with a single spin in diamond, *Phys. Rev. Applied* **2** (2014) 054014. [**doi**].
6. K. Ohno, F. J. Heremans, C. F. De las Casas, **B. A. Myers**, B. J. Aleman, A. C. Bleszynski Jayich, and D. D. Awschalom, Three-dimensional localization of spins in diamond using ^{12}C implantation, *Appl. Phys. Lett.* **105** (2014) 052406. [**doi**].
5. P. Ovartchaiyapong, K.W. Lee, **B. A. Myers**, A.C. Bleszynski Jayich, Dynamic strain-mediated coupling of a single diamond spin to a mechanical resonator, *Nat. Commun.* **5** (2014) 4429. [**doi**].
4. **B. A. Myers**, A. Das, M. C. Dartiailh, K. Ohno, D. D. Awschalom, and A. C. Bleszynski Jayich, Probing surface noise with depth-calibrated spins in diamond, *Phys. Rev. Lett.* **113** (2014) 027602. [**doi**].
3. P. Ovartchaiyapong, L. M. A. Pascal, **B. A. Myers**, P. Lauria, A. C. Bleszynski-Jayich, High quality factor single-crystal diamond mechanical resonators, *Appl. Phys. Lett.* **101** (2012) 163505. [**doi**].

2. K. Ohno, F. J. Heremans, L. C. Basset, **B. A. Myers**, D. M. Toyli, A. C. Bleszynski Jayich, C. J. Palmstrom, and D. D. Awschalom, Engineering shallow spins in diamond with nitrogen delta-doping, *Appl. Phys. Lett.* **101** (2012) 082413. [**doi**].

1. **B. Myers**, M. Bernardi, and J. C. Grossman, Three-dimensional photovoltaics, *Appl. Phys. Lett.* **96** (2010) 71902. [**doi**].

Abstract

Quantum decoherence of near-surface nitrogen-vacancy centers in diamond and implications for nanoscale imaging

by

Bryan Andrew Myers

Nitrogen-vacancy (NV) centers in diamond excel as room-temperature quantum sensors by virtue of their long-lived spin coherence and experimental addressability at the single-spin level. When isolated deep within bulk diamond, NVs' spin coherence times and relaxation times are limited to several milliseconds by internal nuclear and electronic spin baths and vibrations in the crystal structure. However, when NVs are placed just nanometers from the diamond surface, which is necessary for nanoscale imaging of external fields, NV spin properties are impacted by a host of new decoherence sources that must be understood and mitigated to optimize the utility of the NV as a magnetometer.

This dissertation addresses the questions: 1) What is the length scale over which near-surface NV spins experience decoherence due to the diamond surface? 2) What are the physical noise sources, and their frequency spectra, that cause surface-induced decoherence in NV centers? In addressing these questions, we also develop a NV on a scanning probe tip platform and use it to perform nanoscale imaging based on the NV spin-relaxation rate in the presence of magnetic and electric field fluctuations.

First, we develop a method of nitrogen delta-doping during single-crystal diamond growth to create near-surface NV centers localized at multiple few-nanometer layers. Through a technique of scanning probe magnetic resonance imaging, we measure the depths of these shallow NVs with nanoscale precision. We correlate these depths to spin coherence times measured with dynamical decoupling and model this depth dependence

with a combined model of surface-related and bulk magnetic noise.

We find that significant discrepancies between the maximum measured coherence time and its maximum theoretical limit – twice the spin relaxation time – necessitate further study of the relaxation rates of near-surface NV centers. We develop a method to measure relaxation rates between all three NV spin-triplet ground state levels and find that a double-quantum (DQ) spin relaxation channel is a major, and under some conditions dominant, contributor to the total spin decoherence rate. We demonstrate a surface-noise spectroscopy technique combining dephasing and DQ relaxation data to identify which parts of the derived noise spectral density are due to magnetic fields or electric fields. The susceptibility of the NV to electric field noise through DQ relaxation, as with other decoherence channels, is simultaneously a problem and a potential resource for sensing and imaging.

Finally we employ the near-surface NV as a scanning probe to perform nanoscale decoherence-based imaging of electromagnetic noise from various target samples. Using NV spin relaxation as a signal, we demonstrate two-dimensional imaging of magnetic noise from a few-thousand Gd^{3+} spin labels with 20-nm spatial resolution, limited by setup drift in ambient conditions over long time scales. We then make a number of magnetometer enhancements towards imaging at the level of single-spin sensitivity, including engineering diamond nanopillars, forming shallower NV centers, and improving scanning probe microscope stability. We apply the three-level relaxometry techniques to study both magnetic and electric field noise at the NV as a function of nanometer-scale distance from metallic surfaces. Surface-induced decoherence is a major challenge in a variety of qubit systems and hybrid qubit interfaces, and the shallow NV center in diamond is positioned to be a valuable scientific tool for studying these noise sources at nanometer, and even sub-nanometer, length scales with high precision.

Contents

List of Figures

Chapter 1

Introduction: Nanoscale imaging with a quantum spin sensor

The broad goal of this dissertation is to develop a quantum sensor platform for applications in room temperature quantitative magnetic and electric field imaging at nanometer length scales. An ideal sensor for achieving such spatial resolution would be a single atom or atom-like entity that operates even in ambient conditions while maintaining high sensitivity. It is now common in the physics lab to controllably address and read out few or single quantum objects, namely electronic and nuclear spins in quantum dots [1], trapped ions [2], and atom-like few-level systems trapped in crystals [3]. If such an "atom" can be positioned close enough – a few angstroms to nanometers – to a sensing target then the mutual interaction becomes so large that entanglement with and sensitivity to single spins may even be achieved [4, 5, 6]. Unlike a macroscopic or even microscopic magnetic probe [7], a one-electron-based sensor exerts minimal back-action on the sample under study, assuming that the electromagnetic fields or forces that control the sensor do not affect the sample. One long term goal of such a single-spin-based sensor is, for example, to image with chemical specificity the positions of single nuclei in the structures of

individual biomolecules [8].

Most known quantum spin systems do not measure up to the strict sensor requirements for these imaging applications, a list that begins with the DiVincenzo and Loss criteria for spin qubits [9]: identification of well-defined qubit levels, reliable state preparation, low decoherence, accurate and fast quantum gate operations, and strong quantum measurement. Beyond these, the quantum spin sensor must maintain its qubit properties in ambient conditions and be reliably produced in a host environment that permits bringing the spin within nanometers of the target sample. To date, these challenges are overcome effectively by only the electronic spin associated with a nitrogen-vacancy (NV) center in diamond, which can functionally be thought of as an atom trapped robustly within a solid crystal. Unlike most spins, the NV center's electronic spin can be optically polarized and read out [10], after which, magnetically induced rotations can be used to generate quantum coherence [11] that persists from 700 K [12] down to cryogenic temperatures [13, 14].

From the 1970s to 1990s, significant progress was made in research of optically detected magnetic resonance (ODMR) of defect centers in diamond, which was primarily performed with ensembles of nitrogen-containing defects such as NVs in bulk diamond [10, 15, 11, 16, 17]. The early studies gradually elucidated the spin triplet ground-state structure of the NV, its basic polarization mechanism, and its interactions with nuclear and electronic spin baths internal to the diamond [18]. These advances set the stage for the application of confocal microscopy to diamond samples containing low concentrations of NVs, enabling ODMR of single NVs inside bulk diamond in the late 1990s [3].

In the early 2000s, the individually addressable NV center was researched primarily as a potential resource for quantum information, precisely because it fulfills the five spin-qubit criteria quite well and, moreover, it promises long-preserved spin coherence for a quantum memory at room temperature [19, 20, 21, 22, 23]. Single-molecule ODMR of

other systems prompted a proposal of the general single-spin microscope in 2005 [24]. In 2008, the application of single NVs to nanoscale magnetic sensing and imaging was formally proposed [4, 5] and demonstrated [25, 26] by several groups, followed by magnetic imaging demonstrations with NV ensembles [27, 28]. The rich Hamiltonian of the NV ground state has also been recognized as a tool to sense electric fields [17, 29, 30], as well as temperature [31, 12] and strain [32, 33, 34]. Only within the last few years have very shallow – few-nm-deep – NV centers been engineered in nanodiamonds [25, 35, 36, 37], bulk single crystals [38, 39, 40, 41], and single-crystal thin films [42, 43, 40] to begin realizing nanoscale magnetic imaging of magnetism originating from samples outside of the diamond. This last property, that individually addressable NVs can be produced and remain functional near the solid-state surface, makes it truly exceptional in the field of other quantum sensors, such as atomic vapors [44], since nanometer spatial resolution is practically accessible.

What can an instrument based on a near-surface NV quantum sensor accomplish in imaging that is not feasible with existing tools? First, we compare its sensing and imaging capabilities to traditional electron paramagnetic resonance (EPR) [45] and nuclear magnetic resonance (NMR) [46], which are techniques used to elucidate the average structure of ensembles of nuclei and electronic spins in liquids and solids. In contrast to EPR and NMR, *single* NV center spins can be probed due to the capability of focused optical fields to readout the NV spin [11]. The spin state information from the individual quantum optical emitter can be transduced using single-photon detectors, such as silicon-based avalanche photodiodes [47], in place of weak rf and microwave inductive readout [48]. Furthermore, the NV spin is optically polarizable, so no large magnetic fields and cryogenic temperatures are necessary, as used for increasing NMR and EPR signals with thermodynamic spin polarization. State-of-the-art micro-coils, cryogenics, and dynamic nuclear polarization for NMR experiments have brought about orders of

magnitude gains in sensitivity [49, 50], but these enhancements are still far from reaching single-spin sensitivity on one molecule rather than an ensemble of identical molecules. Similarly, traditional magnetic resonance imaging (MRI) is usually restricted to voxel sizes larger than $\sim$ (10 μm)^3, or picoliters [51, 52]. In the case of a NV, its local environment (spins, strain, electric fields, temperature,...) can be probed through ODMR techniques. One can, for example, image the location of individual nearby spins in (few-nm)^3, or $< 10^{-10}$ picoliter, volumes by determining their distance- and angle-dependent coherent coupling strengths to the NV [53, 54, 55, 56].

Second, we compare the NV center to nanoscale scanning probe imaging techniques. More traditional nanoscale imaging tools, such as scanning tunneling microscopes (STM) [57] and atomic force microscopes (AFM) [58], have long ago achieved subnanometer and atomic spatial resolution [59, 60, 61], even leading to atomic scale AFM at ambient conditions [62], imaging chemical reactions of single molecules [63], and manipulation of magnetic atoms [64, 65] under highly controlled environments. By integrating the NV center itself into a scanning probe microscope (SPM) [4, 25, 38, 66, 36] for nanoscale positioning, the local sensitivity of a NV can be used for imaging a wide range of interesting samples from nanoscale magnetism in condensed matter [36, 66, 67, 68, 69] to extended spatial distributions of spins [70, 71, 72, 73, 74] and thermal conductivity [75]. The advantage of the scanning NV single-spin quantum sensor in the impressive backdrop of existing SPM techniques is to offer several types of versatility: a wide range in operating temperature and pressures [12, 68], sensitivity to electromagnetic frequencies of dc to microwave [36, 76, 77], quantum optical emission [78, 79], and the advantages of magnetic resonance like quantitative chemical selectivity [80, 73, 81], non-invasiveness, polarization transfer [82], and three-dimensional imaging with externally applied field gradients [70] or hyperfine gradients [55]. Furthermore, a single type of diamond-NV probe can, in principle, be used for simultaneous electric, magnetic, and thermal imaging. Magnetic

resonance imaging with a scanning NV has reached close to nanometer-cubed voxel sizes, which can be pushed to angstrom-level spatial resolution in three dimensions using strong magnetic field gradients [70]. Diamond is also compatible with biological systems, and NVs in nanodiamonds can be used as a non-photobleachining fluorescent markers, magnetic sensors, or temperature sensors in cells at ambient conditions [83]. The exquisite quantum and optical properties of the solid-state defect ensure that it will find several niches in the nanoscale metrology field. In brief, any spatially varying parameter that affects the NV's quantum spin state or optical emission is fair game to implement as a signal for imaging. However, this versatility also makes the NV susceptible to several sources of spin decoherence.

The central topic of this dissertation is quantum decoherence of the near-surface NV center electronic spin, first for fundamental understanding so that it might be mitigated, and second to use decoherence as a new resource for imaging of magnetic and electric field noise. To achieve nanoscale imaging, NV centers near the diamond surface are necessary, and over the last few years, there has been a big push to generate shallow NV centers. The recognition that the coherence properties of these shallow spins are severely degraded by the presence of the diamond surface [40, 43] has stimulated a broad effort to understand and mitigate this surface noise in nanodiamonds [84, 85] and single-crystal diamond [86, 87, 88, 89, 90, 91, 92]. Surface noise-induced dephasing and dissipation is an outstanding problem that limits many technologies, such as ions in microtraps [2, 93, 94], ultrasensitive cantilevers [95], and superconducting qubits [96, 97]. Here, we probe diamond surface noise via decoherence measurements of shallow NV spins. We follow closely the traditional magnetic resonance picture of dephasing, population relaxation, and dynamical decoupling [46, 98, 99, 100, 101], which has proved fruitful within the NV diamond community for unprecedented demonstrations in nanoscale spin sensing [53, 102, 103] and imaging [70, 74, 72] in ambient conditions.

We also extend the same NV decoherence measurement techniques to imaging and demonstrate the scanning NV spin-relaxation microscope, a flavor of the instrument proposed in [104]. We apply this tool to the study of incoherent fluctuations from spins and charges from material surfaces on the nanometer-scale. Surface-induced NV decoherence will also be a concern for future nanoscale imaging experiments that do not aim to use this spatially varying decoherence directly as the signal. The open questions of surface noise guide the outline of the present work.

First, the experimentally relevant properties of the NV center are reviewed in this chapter with a focus on control and decoherence of the ground state spin levels. Next, the components of the scanning NV diamond magnetometer instrument are described (Chapter 2). The following chapters describe the engineering of shallow NV sensors (Chapter 3), scanning probe imaging measurements of the NVs' nanoscale depths (Chapter 4), coherence and relaxation based characterization of diamond surface noise spectra that affect magnetic sensitivity (Chapters 4 and 5), and lastly, nanoscale scanning probe imaging experiments based on measuring the decoherence of a single NV center placed in nanoscale proximity to gadolinium electronic spins (Chapter 6) and various metallic surfaces (Chapter 7).

1.1 The nitrogen-vacancy center in diamond

A nitrogen-vacancy center is a point defect in the sp^3 carbon crystal of diamond and is composed of a substitutional nitrogen atom and an adjacent carbon vacancy oriented along a [111] axis (Fig. 1.1) [10]. The defect exists in at least two known charge states labelled NV^- and NV^0. The negatively charged state is the one most widely studied for applications in metrology, and henceforth the term "NV" will refer to NV^- in the chapters of this work. This NV's orbital electronic structure is occupied by six electrons,

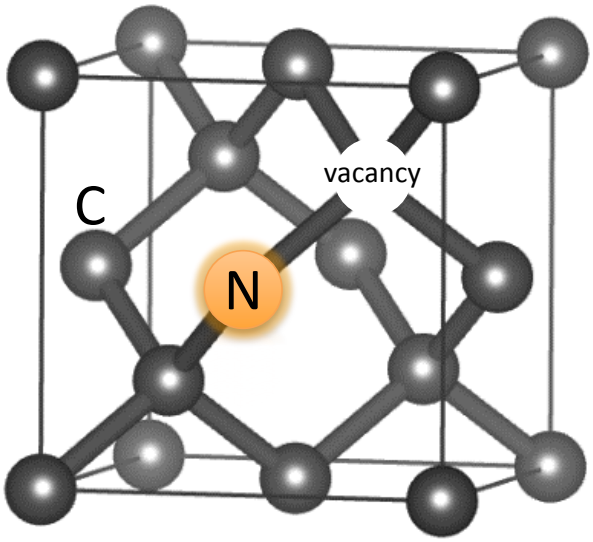

Figure 1.1: Schematic of the nitrogen-vacancy center in the diamond crystal structure. A N atom and a vacancy substitute for carbon atoms (gray), and the NV axis is oriented in the [111] direction. Six electrons are associated with the NV^- – two from the nitrogen, three from carbons, and one captured from the crystal.

as shown in Fig. 1.2 – three from the three adjacent carbon atoms, two from the nitrogen, and one extra from the diamond crystal – which gives the NV an electronic spin of $S = 1$. Although it is like a trapped atom in that its spin is well-isolated and immobile in the crystal, the crystal breaks the rotational symmetry that free atoms have. Specifically, the NV center's C_{3v} crystallographic symmetry about [111] gives a preferred direction of spin quantization and thus determines important features of its Hamiltonian [105]. The phenomenological form of the electronic Hamiltonian is captured in zero-field splitting parameters D_{gs} and E_{gs} in the language of EPR and crystal field theory applied to trigonal symmetry [45]: [1]

$$H_{gs}/\hbar = D_{gs}S_z^2 + E_{gs}\left(S_x^2 - S_y^2\right) + \gamma_{\mathrm{nv}}\mathbf{B}\cdot\mathbf{S} \tag{1.1}$$

[1]The $\mathbf{S}$ matrices here indicate spin rather than angular momentum and do not contain $\hbar$. Therefore D and E have units of angular frequency.

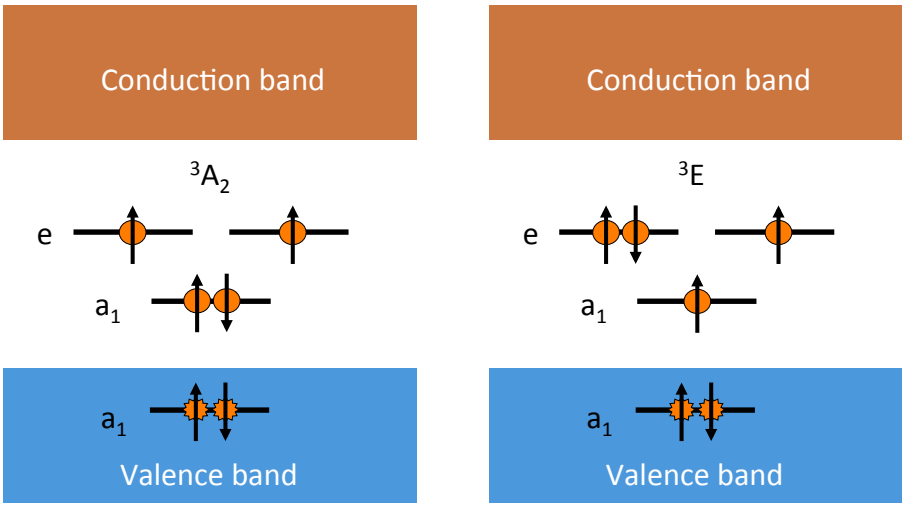

Figure 1.2: Accepted electronic occupation of orbitals in the six-electron configurations for the NV^- ground state triplet (left) and excited state triplet (right). Each configuration has two unpaired spins, giving the NV center a total spin of 1. The lowest-lying orbital is within in the valence band.

where constants dependent on total spin S in the first term have been omitted since we only consider the $S = 1$ ground state. In the Zeeman term, $\gamma_{\text{nv}} = g\mu_B/\hbar$ is the electron's gyromagnetic ratio, where g is approximately 2.0028 for the NV electron spin [10], μ_B is the Bohr magneton, and $\mathbf{B}$ is the magnetic field. The experimental implications of Eq. 1.1 and additional nitrogen nuclear spin terms are addressed in the next sections.

Several decades of research and debate have been devoted to discovering the electronic structure and relative energies of the NV center, and it is an ongoing area of inquiry. A detailed review article on the status of NV theory has recently been published [18], and several phononic and electronic features continue to be investigated for new sensing applications in temperature [106], strain [107], and others. The magnetic sensing applications in the following chapters rely on a few abstracted aspects of the presently accepted NV picture, with focus on spin states in the ground state.

Figure 1.3 shows the basic NV energy level structure. The ground state is a spin triplet ($^3A_2$) and an excited spin triplet (^3E) exists at an energy $\sim$ 1.945 eV. A fine

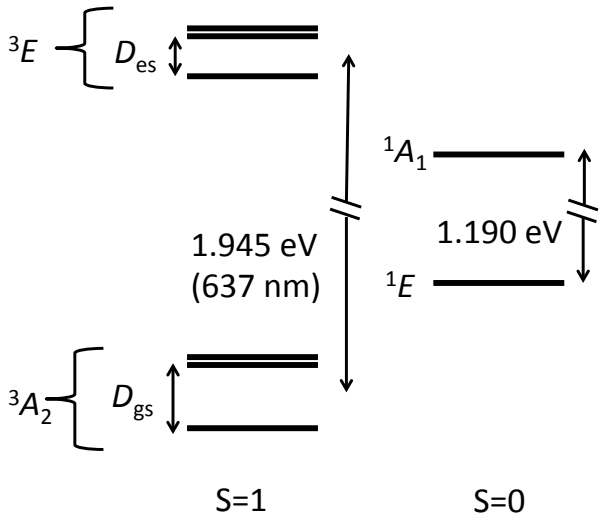

Figure 1.3: Basic electronic orbital and spin structure of the NV center in the negatively charged state. The ground state and optically-excited state are spin triplets ($S = 1$). $D_{gs}/\hbar$ and $D_{es}/\hbar$ are crystal zero-field splitting parameters of order 2.9 GHz and 1.4 GHz, respectively. Intersystem crossing between triplet and singlet levels is critical for the NV spin initialization and readout used in most magnetic sensing sequences. This dissertation focuses on spin coherence in the $^3A_2$ manifold.

orbital structure exists in the excited state at low temperature, which is paramount in applications with spin-photon entanglement [108, 109], spin-phonon-based cooling and strain sensing [110, 107], and all-optical NV control [111, 14]. However, at room temperature the levels are broadened and we consider a vibronic continuum [112] allowing for a spectrum of detectable radiation at wavelengths longer than the zero-phonon-line ~ 637 nm, detectable at the individual NV level with confocal microscopy [3, 113]. A pair of in-between singlet states ($^1A_1$ and ^1E) are often abstracted to a single level, the "singlet state," for a simplified operating picture of the standard mechanism of NV ODMR explained below.

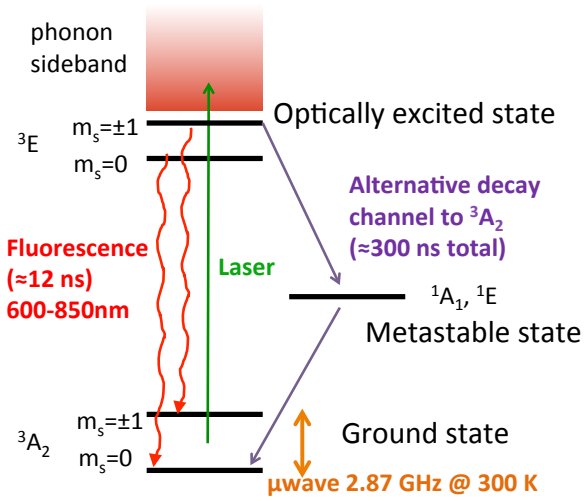

Figure 1.4: Schematic of NV level transitions at room temperature. The nonresonant laser excitation (green) and fluorescence (red) are both conserve spin within the triplet manifolds. The metastable state decay path (violet) occurs on a longer timescale and does not conserve the m_s spin quantum number. Together the cycling transition, intersystem crossings, and ground state microwave transitions enable optical spin polarization and readout of magnetic resonance.

1.2 Optically detected magnetic resonance

Interesting properties arise from the electronic and spin structure of NV centers that make them feasible as qubit-based sensors even at ambient temperature. We discuss here the properties that enable ODMR of single NVs. The primary transition energy of 1.945 eV is about 75× larger than the room temperature scale, and thus the spin population by default is completely in the ground state $^3A_2$. This spin population is fully mixed among the sublevels $m_s = 0, -1, 1$ because the longitudinal zero-field splitting D_{gs} is comparably small: 2.87 GHz, or equivalently $\sim$ 138 mK. In density matrix form the ground state equilibrium population is written $\rho = \frac{1}{3}I$, where I is the identity operator in the $\{|1\rangle, |0\rangle, |-1\rangle\}$ basis. However, under optical illumination, the singlet state mediates an alternative transition pathway between ground and excited triplets that enables both spin initialization and spin readout, as we discuss next.

1.2.1 Spin polarization

The most common approach to optical addressability is to use a non-resonant laser to populate the excited state, usually 532 nm as depicted in Figure 1.4, though a range of excitation wavelengths are possible [114]. After non-resonant optical excitation the NV undergoes rapid phonon-mediated decay to the excited state and then spontaneous emission to the ground state with spin-dependent lifetimes on the order of 12 ns [115]; importantly, the transition preserves the spin projection quantum number m_s. Red photoluminescence (PL) between about 650-800 nm can be collected from the phonon sideband emission. The salient point here is that about 50% of the decay rate from $m_s = \pm 1$ ^3E levels is non-radiative to $^1A_1$, while the non-radiative branching ratio for $m_s = 0$ is effectively zero.[2] The population shuttled to the singlet levels relaxes on a time scale of about 300 ns, preferably to the $m_s = 0$ ground state, so $m_s = \pm 1$ is not conserved. Thus, in practice continuous optical illumination for a few microseconds at sufficient power prepares an initialized $|m_s = 0\rangle$ state with typical efficiencies of $80-90\%$, as reported in [117, 118].

This level of spin polarization is quite remarkable at room temperature and zero applied magnetic field. From the canonical partition function for the three level system of energies $E_0 = 0$ and $E_{\pm 1} = \hbar D_{\mathrm{gs}}$, $Z = [1 + 2\exp(-\hbar D_{\mathrm{gs}}/k_B\theta)]$, the spin temperature [46] is just $\theta = 66$ mK given a spin polarization $P = 0.8 = 1/Z$. Furthermore, this polarization persists for a timescale of the NV's T_1, its spin relaxation time, which is typically of the order of several milliseconds [119]. During this time, quantum-state operations can be performed starting from the initial $|0\rangle$ state.

[2]Some details on the branching of ^3E to the singlet state are still under question, particularly with temperature changes [18, 116].

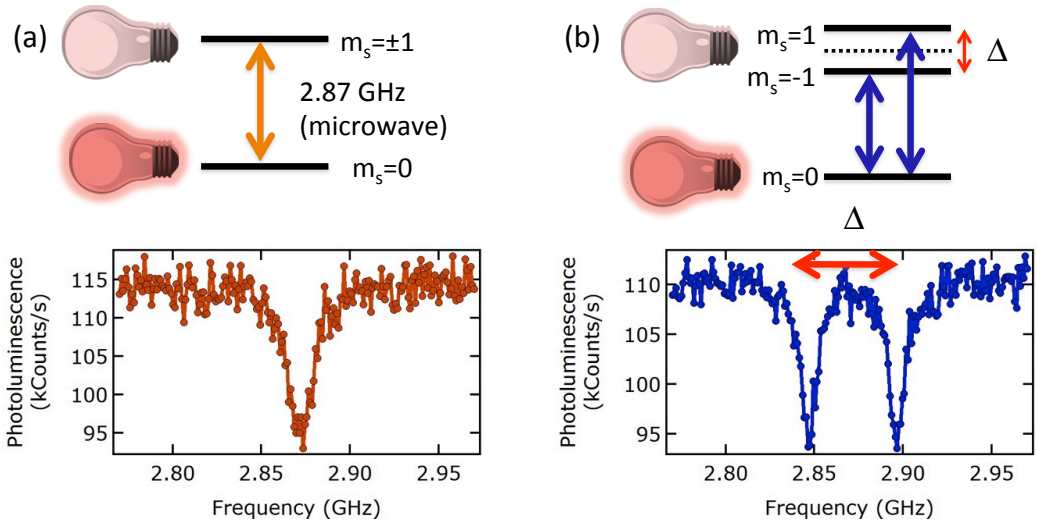

Figure 1.5: ODMR measurements under continuous microwave and optical illumination (CWESR) on a single NV. (a) The absence of an applied magnetic field results in spin eigenvalue degeneracy and a single microwave transition. The $m_s = 0$ state fluoresces brighter than do the $m_s = \pm 1$ states. (b) In a finite magnetic field the Zeeman splitting can be measured. Note that the PL contrast here less than 30% because in CWESR the ratio of optical to microwave power determines equilibrium cycling rates and therefore also determines the linewidth and contrast.

1.2.2 Spin-state readout and spin resonance

Via the same properties that enable spin polarization – optical excitation and the spin-selective two-path decay mechanism – the spin population can also be read out by collecting the NV's photoluminescence. Because the $|m_s = \pm 1\rangle$ states have a 50% chance of being shelved in the dark metastable singlet, the NV appears $30 - 35\%$ darker than in the $|m_s = 0\rangle$ state as there are fewer radiative emission events than for the NV in $|m_s = 0\rangle$.[3]

The optical spin polarization and readout capabilities are vital components of magnetic sensing with a NV at room temperature. The transverse component of the Zeeman term in Eq. 1.1 allows for driving of resonant microwave transitions between the $m_s = 0$

[3]The $30 - 35\%$ PL contrast as measured is reduced in the presence of more than one NV orientation in an addressed optical spot or due to other background luminescence.

and $m_s = \pm 1$ levels. By a combination of optical and microwave fields, the population of the NV spin can be first initialized and then arbitrarily rotated and read out [19]. A static magnetic field $\mathbf{B}$ applied along the NV $\hat{z}$ symmetry axis further splits the $m_s = \pm 1$ levels according to the electronic gyromagnetic ratio $\gamma_{\mathrm{nv}} \approx 2\pi \times 2.8$ MHz/G. Figure 1.5 shows data from a continuous-excitation ODMR measurement on a single NV in diamond. The NV center has a crystal-field splitting that defines the center of the transition frequencies, where $D \equiv D_{gs}$ has a value $2\pi \times 2.87$ GHz at 300 K. At $B_z \approx 0$ a single transition is observed due to eigenvalue degeneracy within the experimental linewidth δf. For finite $B_z \gg \delta f$ the two microwave transitions $\nu_{0,1}$ and $\nu_{0,-1}$ are well resolved. Analysis of the frequency splitting $\Delta \approx 2g\mu_B B_z$ serves as a simple form of dc magnetometry.

A nonzero perpendicular component $B_\perp$ of the static $\mathbf{B}$ will cause these levels to split non-linearly, as shown in the eigenvalue plot of Fig. 1.6. For $B_\perp \neq 0$, the eigenvectors of the system are mixed superpositions of the three spin states. Generally, the spin mixing results in a reduction of ODMR contrast because the bright $|0\rangle$ state is linearly combined with the dimmer $|\pm 1\rangle$ states to form new eigenstates [120, 121]. This contrast is one important consideration for precise alignment of the magnetic fields used in some of the experiments throughout the following chapters.

1.2.3 Control of the NV qutrit as a qubit

Under sufficiently large B_z, the three-level system can be treated effectively as a two-level system when considering coherent manipulation. The "qubit" subspace is either $\{|0\rangle, |-1\rangle\}$ or $\{|0\rangle, |1\rangle\}$, and the unaddressed microwave transition will be negligibly driven when $|\nu_{0,1} - \nu_{0,-1}| \gg \omega_r/2\pi$. ω_r is the Rabi frequency, and an applied microwave field $B_1 \cos(\omega_1 t + \phi_1)$ drives one of these resonant transitions when $\omega_1/2\pi \approx \nu_{0,\pm 1}$. The

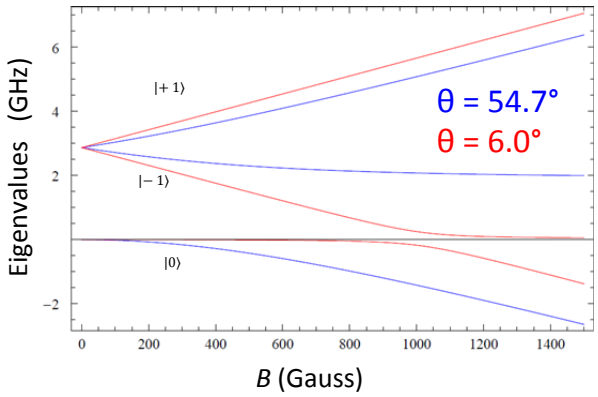

Figure 1.6: NV ground state spin eigenvalue spectrum versus magnitude of a static applied magnetic field. θ is the angle between the magnetic field direction and the NV axis. Two magnetic dipole-allowed transition energies per fixed B are given by the differences of the $|0\rangle$ eigenvalue with each of the $|\pm 1\rangle$ eigenvalues.

effective Hamiltonian for the two-level system is

$$H_0/\hbar = \frac{1}{2}\omega_0\sigma_z + \Omega_1 \cos\left(\omega_1 \mathrm{t} + \phi_1\right)\sigma_\mathrm{x} \tag{1.2}$$

where σ_i are Pauli matrices, $\omega_0 = 2\pi\nu_{0,1} = 2\pi\left(D + \gamma_\mathrm{nv}B_z\right)$, and $\Omega_1 = \gamma_\mathrm{nv}B_1$. A unitary matrix

$$U_1 = \begin{pmatrix} 1 & 0 \\ 0 & e^{-i\omega_1 t} \end{pmatrix} \tag{1.3}$$

describes the rotating frame of the driving field. Using $|\tilde{\psi}\rangle = U_1|\psi\rangle$ and $\langle\tilde{\psi}| = \langle\psi| U_1^\dagger$ in the Schrödinger equation $H_0|\psi\rangle = i\hbar\partial|\psi\rangle/\partial t$ gives the transformed Hamiltonian as

$$\tilde{H}_0 = i\hbar\frac{\partial U_1}{\partial t}U_1^\dagger + U_1 H_0 U_1^\dagger. \tag{1.4}$$

The detuning from resonance is defined as $\delta = \omega_1 - \omega_0$. The Hamiltonian in matrix form is

$$\tilde{H}_0/\hbar = \begin{pmatrix} 0 & \frac{\Omega_1}{2}\left(e^{2i\omega_1 t + i\phi_1} + e^{i\phi_1}\right) \\ \frac{\Omega_1}{2}\left(e^{-2i\omega_1 t - i\phi_1} + e^{-i\phi_1}\right) & \delta \end{pmatrix} \tag{1.5}$$

and suppressing fast-oscillating terms in the rotating wave approximation yields

$$\tilde{H}_0/\hbar = \begin{pmatrix} 0 & \frac{\Omega_1}{2}e^{i\phi_1} \\ \frac{\Omega_1}{2}e^{-i\phi_1} & \delta \end{pmatrix}. \tag{1.6}$$

The phase ϕ_1 of the driving field can be chosen as zero for typical experiments because the first microwave pulse defines the phase and the source is assumed perfectly phase coherent over one measurement shot. The Schrödinger equation applied to $|\tilde{\psi}(t)\rangle = c_0(t)\,\hat{e}_0 + c_1(t)\,\hat{e}_1$ then gives a set of second-order differential equations

$$\begin{aligned} i\dot{c}_0(t) &= \tfrac{\Omega_1}{2}c_1(t) \\ i\dot{c}_1(t) &= \tfrac{\Omega_1}{2}c_0(t) + \delta\dot{c}_1(t) \end{aligned} \tag{1.7}$$

that has imaginary roots $r_{1,2} = -i\delta/2 \pm i\left(\delta^2 + \Omega_1^2\right)^2/2$ and a solution

$$c_1(t) = A_1 e^{-i\delta t/2}\cos\left(\frac{t}{2}\sqrt{\delta^2+\Omega_1^2}\right) + A_2 e^{-i\delta t/2}\sin\left(\frac{t}{2}\sqrt{\delta^2+\Omega_1^2}\right). \tag{1.8}$$

Since the NV center can be optically pumped into $|0\rangle$ we take the spin population initial condition of $P_{|1\rangle} = |c_1(0)|^2 = 0$, and for all times t the population is constrained in this two-level subspace so $|c_0(t)|^2 + |c_1(t)|^2 = 1$. [4] Taking these constraints we solve for the coefficients, finding $A_1 = 0$ and $|A_2|^2 = \Omega_1^2/(\Omega_1^2 + \delta^2)$. The final result is the classical Rabi solution for general detuning of the driving field from resonance

[4] For simplicity here we neglect that optical polarization does not have perfect fidelity, as noted earlier, such that $\rho_{0,0}(t=0) < 1$ and so both $\rho_{-1,-1}(0)$ and $\rho_{1,1}(0)$ could be non-zero.

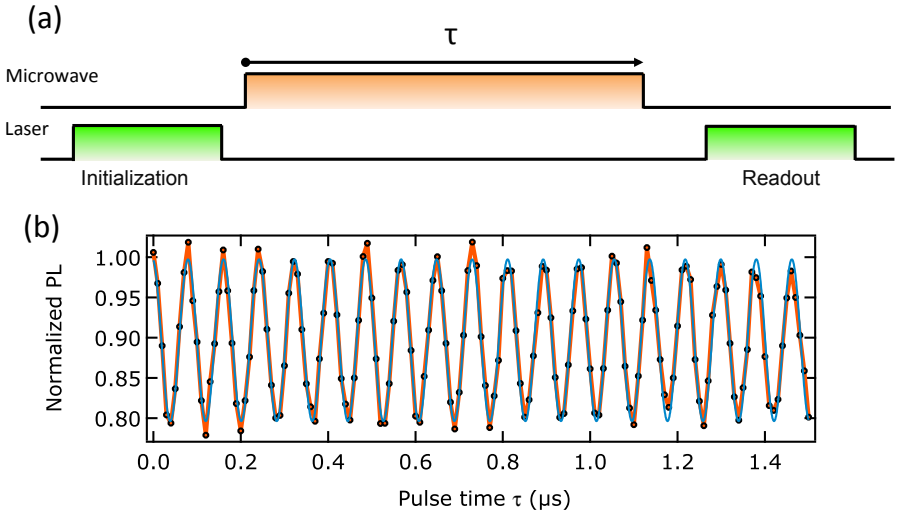

Figure 1.7: On-resonance Rabi driving of a single NV spin. (a) Pulse sequence: 532 nm laser pulse for optical pumping to $|0\rangle$, microwave pulse to rotate the spin, and population readout during the first portion of another laser pulse. The pulse time τ is swept to map out the population oscillations. (b) Plot of normalized PL as a function of τ for a single NV. Orange points are data and the blue curve is a fit to the Rabi model of Eqn. 1.9. The full contrast of the PL fringes could be mapped to $P_{|0\rangle} = [1, 0]$. The Rabi frequency is 12.3 MHz, giving $t_\pi \approx 40.7$ ns.

$$\begin{aligned} P_{|1\rangle}(t) &= \frac{\Omega 1^2}{\Omega_1^2+\delta^2} \sin^2\left(\frac{t}{2}\sqrt{\Omega_1^2+\delta^2}\right) \\ P_{|0\rangle}(t) &= \frac{\delta^2}{\Omega_1^2+\delta^2} + \frac{\Omega_1^2}{\Omega_1^2+\delta^2} \cos^2\left(\frac{t}{2}\sqrt{\Omega_1^2+\delta^2}\right) \end{aligned} \tag{1.9}$$

that demonstrates for $\delta \neq 0$ a reduction in population oscillation contrast and faster oscillation frequency. In summary, a transverse driving field of of frequency $\omega_1 \approx \omega_0$ will drive a population inversion at a rate that depends on the magnitude of the driving field B_1 since $\Omega_1 \propto B_1$. Figure 1.7 shows the pulse sequence and example data for $|0\rangle \leftrightarrow |-1\rangle$ Rabi driving of a single NV with ith $\delta = 0$. Starting in the $|0\rangle$ state after a green optical pulse, the first full population inversion occurs after a duration $t_\pi = \pi/\Omega_1$, termed a π-pulse. Starting in $|0\rangle$, a $\pi/2$-pulse will prepare the spin in a superposition $|\psi\rangle = (|0\rangle + i\,|1\rangle)/\sqrt{2}$, which is the starting point for various ac magnetometry pulse sequences where field-induced phase accumulation is transferred into a population that

can be optically read out.

In the following section, we discuss examples of NV magnetometry that use this superposition $(|0\rangle + i\,|1\rangle)/\sqrt{2}$. We introduce these examples within a discussion of decoherence because 1) the control sequences used to study electromagnetic noise via NV decoherence are the same as those for performing magnetometry, and 2) decoherence is a primary limitation to the field sensitivity of a quantum spin sensor. We follow the decoherence section with a discussion of magnetic sensitivity and imaging spatial resolution, which depend additionally on factors like photon collection signal-to-noise and separation between the NV and target sample.

1.3 Spin decoherence of single NV centers

Spin decoherence is important to the field sensitivity of NV centers because it corresponds to a loss of information about the fields being sensed. By decoherence we mean the decay in time of an off-diagonal element of the NV density matrix, $\rho_{ij}(t)$ with $i \neq j$ [9, 122]. This loss of a definite phase relationship between two spin states occurs by two different processes, dephasing and relaxation, which describe random spin rotations on the Bloch sphere about the z and x, y axes, respectively [46], in contrast to deterministic unitary phase and population rotations. These two processes are illustrated in Fig. 1.8. Although both dephasing and relaxation change the quantum state, they are different from the perspective of the Hamiltonian describing the NV spin eigenstates. Relaxation does not conserve energy while dephasing conserves energy because $[H, S_z] = 0$. Dephasing and relaxation are concepts that arose from magnetic resonance experiments, which we consider here to identify basic causes of each process and differences between traditional spin ensembles and single spins.

The first decoherence process, pure dephasing, occurs due to inhomogeneities in the

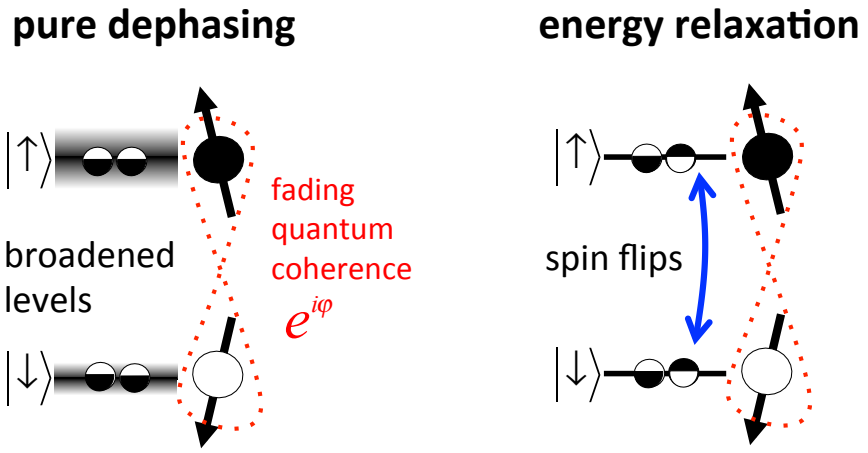

Figure 1.8: Illustration of dephasing and relaxation contributions to total decoherence rate. Dephasing is related to random energy shifts of the spin sublevels due to fluctuations in the environment, causing the spin to precess at different rates each time it is measured. Energy relaxation describes random quantum jumps between the spin sublevels due to thermalization with the crystal or electromagnetic noise at the splitting frequency. Both processes make the phase $e^{i\phi}$ random over sufficiently long free evolution times of the spin superposition.

environment that can be distributed in either space or time. In classical NMR and EPR, an ensemble s_i of addressed spins is inhomogeneous in space because any given spin will have a different coupling to its environment depending on random disorder in the crystal. Each s_i will precess at a rate f_i dependent on its local environment, and the distribution of environmental couplings dictates the lineshape [46]. In EPR specifically, inhomogeneous broadening can be caused, for example, by a spread in gyromagnetic factors due to local crystal imperfections or a distribution of hyperfine couplings due to random positions of surrounding nuclear spins [45]. If net magnetization perpendicular to the applied magnetic field, M_x or M_y, exists at some time, then the spread in spin precession frequencies f_i causes a loss in global spin coherence over time, leading to $M_x, M_y \to 0$. The larger the spread in f_i, the faster this dephasing occurs.

For a single spin, the concepts of inhomogeneous broadening and dephasing must be considered as as a time average rather than ensemble average. Time-averaged mea-

surements of the spin state of the NV are mandated by quantum mechanics: projective measurements are accompanied by quantum projection noise even in the case that all other experimental noise can be eliminated [44]. At measurement time t_0 there may be a well-defined magnetic field B_e at the NV due to nearby spins, but in a later measurement at $t = t_0 + \delta t$ this B_e may have changed, e.g., due to a nuclear spin flip. The result is a shifted NV resonance frequency and, over many measurement shots, a distribution of precession frequencies. In induction-readout EPR, the experimentalist can in principle track in real time the phase evolution of the ensemble through M_x as the spins' phases fan out amongst themselves. If one could track in real time the phase evolution of a single NV, and not disturb it in the process [123], then it would not perhaps be considered to be dephasing with anything, just evolving at a non-constant rate with changes in the environment. Yet, in practice the NV does dephase with itself upon looking at successive iterations of the disruptive projective measurement, since each shot yields a different accumulated phase from environment-induced spin precession. Thus, the inhomogeneities we consider here are primarily in time, rather than space.

The second cause of decoherence, spin relaxation, describes processes that change the energy of the spin system. Broadly, sources of relaxation are identified as direct pairwise spin flips, crystal vibrations at finite temperature, and incoherent magnetic and electric fields [46, 32]. Direct spin flips that exchange the m_s of two coupled spins, usually of similar Larmor frequencies, can be said to conserve total energy if the Hamiltonian of the coupled system is known: that is, the pairwise spin flip conserves the total magnetization, M_z, that is parallel to a large applied magnetic field. However, the M_x and M_y components are not restricted by energy conservation in a z-oriented magnetic field and so these transverse components can reduce to zero from spin flips [45], consituting decoherence. Spin relaxation that is due to crystal vibrations can be considered a thermalization process of inelastic scattering events: if the spin ensemble is polarized to a

particular S_z energy level such that the total spin temperature is lower than the crystal temperature, then the spins will depolarize over time, that is, total M_z reduces to return to a state in equilibrium with the crystal temperature [46, 32]. For an optically polarized single spin like the NV center, a discrete spin flip will occur at a random time during each successive measurement, so that in a total time average the polarization appears to be decaying with increasing time between initialization and readout. Electric and magnetic fields with zero or short-lived phase coherence, incoherent fields, also cause spin-flip transitions at random times after polarization. The rate of these spin flips will be proportional to the noise power spectral density of the fields at the Larmor precession frequency of the spin. Such fields can arise from random fluctuations of ensembles of spin or charge impurities in the crystal or from external sources in the laboratory, and the coherence and relaxation measurements shown in this dissertation are sufficiently modeled by considering classical fluctuating fields from multiple discrete sources rather than quantized fields.

Together, dephasing and relaxation destroy coherence at a total rate that is a sum of the two, summarized in the equation $1/T_2 = 1/T_d + 1/(2T_1)$. In the following sections, we discuss the time constants for dephasing (T_d), decoherence (T_2^*, T_2), and relaxation (T_1), what might cause them, and how to measure them for a NV. In the dynamical decoupling section, we show how decoherence can be mitigated through reduction of the dephasing rate. It is important to remember throughout that spin relaxation can be observed without a coherent superposition of spin eigenstates, but it still plays a role in loss of coherence that cannot be mitigated with dynamical decoupling.

1.4 Dephasing T_d contribution to decoherence: T_2^* and T_2

1.4.1 Definitions of T_d, T_2^*, and T_2

The inhomogeneous decoherence time T_2^* is defined as the free precession time τ after which the qubit superposition's coherence decays from 1 to $1/e$ on the interval $C(\tau) \in [0, 1]$. $C = 1$ indicates a definite phase relationship between the spin states and $C = 0$ indicates a random phase relationship between the spin states. By "free precession" we mean a period between initialization of the two-state superposition and phase readout during which no microwave or laser control pulses are applied to the system. The decoherence rate $1/T_2^*$ has contributions from both dephasing and spin relaxation, and $\Gamma_d = 1/T_d$ we define as the pure dephasing contribution to $1/T_2^*$. Both dephasing and relaxation processes affect the spin, and therefore the combined effect T_2^* is easier to measure directly than T_d. However, in practice $T_2^* \approx T_d$ because the pure dephasing rate is typically orders of magnitude faster than the relaxation rate $1/T_1$ during free precession, $\Gamma_d \gg 1/T_1$.[5]

Control pulses during the free precession period can reduce Γ_d to the point where $\Gamma_d \gg 1/T_1$ no longer holds. The homogeneous decoherene time T_2 is defined as the time for loss of coherence from $C = 1$ to $C = 1/e$ under the application of any control pulses during the total precession period. The simplest such case is a Hahn echo, where a free precession period is punctuated by a π pulse in the middle. The π pulse serves to mitigate the dephasing caused by fields changing much slower than the free precession periods. Thus, T_2 can be extended through reduction of the Γ_d contribution by carefully

[5]One example where T_1 may actually dominate T_2^* for a NV sensor is when external magnetic field noise reduces T_1 substantially, but this is a special case relevant to Chapter 6 where external Gd spins are sensed and image based on T_1.

timed control pulses, so that $T_2 \sim T_1$ is possible. We note that Γ_d in the case of T_2 is an overall average or effective dephasing rate, since dephasing and partial refocusing of the phase will occur between π control pulses. Even so, the constraints that relate decoherence, dephasing, and relaxation rates must all be satisfied to ensure a physically valid density matrix at all times between initialization of the superposition and its readout (see Chapter 5). We first describe the T_2^* measurement techniques from a perspective of pure dephasing ($T_2^* = T_d$), and then we return to T_2 and T_1.

1.4.2 Causes and measurement of T_2^*

In magnetometry of dc fields, T_2^* sets the NV's sensitivity. The sensing measurement looks for shifts in the NV's ESR line by probing changes in the ODMR PL, as illustrated in Fig. 1.9. Larger linewidths due to inhomogeneous broadening result in smaller PL changes, and hence lower sensitivity. Similarly, a longer T_2^* allows a longer free precession time before phase information about the sensed dc field is lost. Thus, smaller magnetic fields have time to measurably affect the NV phase before dephasing occurs. These sensitivity concepts are developed more formally in a later section on magnetic sensitivity. Here, we discuss first the relationship between inhomogeneous linewidth and dephasing time, their causes for NVs in diamond, and how each is measured.

The T_2^* of a NV center $\{|0\rangle, |-1\rangle\}$ or $\{|0\rangle, |1\rangle\}$ qubit is inversely proportional to the inhomogeneous linewidth of its resonance line. Each time the qubit phase is prepared, a change in the environmental fields leads to a different phase accumulated and read out. For a longer free precession time τ, these individual phase measurements of same τ become less correlated, and at long enough τ the net phase is random. For the same reason, in a frequency-sweep measurement of the qubit resonance, the measured resonance $\nu_{0,\pm1}$ will be slightly different on each sweep as the qubit energy is affected by changes

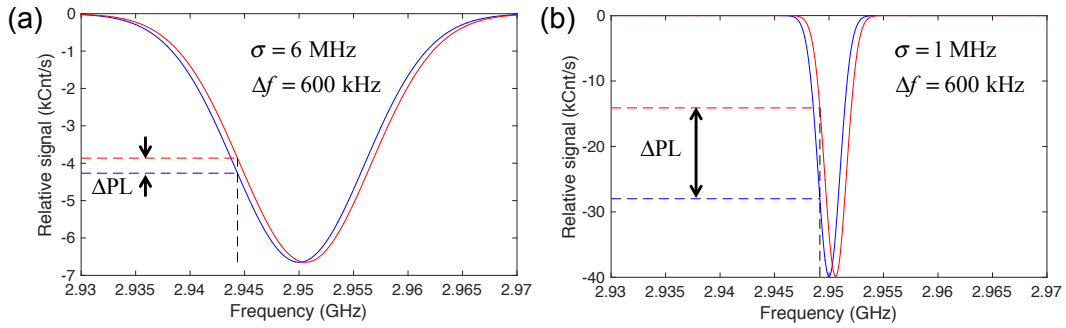

Figure 1.9: Dependence of sensitivity in dc magnetometry on NV linewidth. The plots show a Gaussian resonance line (blue) and the same line shifted by $\Delta f = 600$ kHz (red), as from a static magnetic field of $B_z \approx 0.214$ G. The Gaussian widths of the lines are $\sigma = 6$ MHz in (a) and $\sigma = 1$ MHz in (b). The fractional PL change per Δf shift is larger in (b) because the linewidth is narrower, and the absolute change ΔPL is larger because more spin population is centralized near the peak resonance value. For a resonance line broadened as a Gaussian, the inhomogeneous decoherence time is $T_2^* = \sqrt{2}/\sigma$ (see dynamical decoupling analysis).

in the environment. Thus, the same sources of inhomogeneous broadening also cause dephasing. The proportionality constant between $1/T_2^*$ and the linewidth depends on the type of noise bath dominating the shape of the resonance line. For example, in the section on dynamical decoupling below we show in Eq. 1.25 that a noise bath with normally distributed (Gaussian) amplitudes at each time step gives a result $T_2^* = \sqrt{2}/b$, where b is the standard deviation of the field amplitudes in units of frequency coupling.

Inhomogeneous broadening of a NV center buried deep in bulk diamond is predominantly caused by the fluctuating spins in its vicinity [124], namely those associated with ^{13}C and N atoms [22, 21, 125]. ^{13}C has a nuclear spin of $I = 1/2$ and natural abundance 1.1%, while ^{12}C has no net spin. Substitutional nitrogen also has an electron spin, the P1 center, that dominates NV inhomogeneous broadening in samples rich with nitrogen [126]. The nitrogen can be less densely concentrated than ^{13}C and still dominate decoherence because electrons have a higher gyromagnetic ratio than ^{13}C nuclei, a factor of $\sim$ 2600, and thus they produce a larger dipolar field. Our present work is on

NVs in diamond samples with enriched ^{12}C ($99.99 - 99.999\%$) and low nitrogen content (< 100 ppb), so the linewidth and corresponding T_2^* is likely limited by fluctuating magnetic fields from P1 centers and residual paramagnetic defects [127]. Other sources of inhomogeneous broadening are discussed at the end of the section.

To measure the inhomogeneous linewidth Γ from such fluctuating fields, a pulsed scheme termed "pulsed ESR" is employed to mitigate additional broadening from high optical and microwave power in a typical CW measurement [128]. Figures 1.10(b,c) show data for ODMR taken on NVs in a diamond film. The pulsed ESR sequence in Fig. 1.10(a) is the same Rabi driving shown in Fig. 1.7(a), where here the $\tau = t_\pi$ time is carefully chosen to give a full population inversion for very low microwave power during a laser-off period. Rather than sweeping τ, the frequency $\nu_{0,-1}$ is swept, and population inversion only occurs near resonance. The reduction of microwave power leads to a longer-duration pulse required to fully invert the spin, and thus the π pulse becomes narrow in the frequency domain, enabling high-resolution spectroscopy [129]. For $t_\pi \gtrsim T_2^*$, the pulse bandwidth is similar to Γ, which in Fig. 1.10(b,c) we find to be of the order 100 kHz. [6]

The relationship between the NV's resonance linewidth and its dephasing rate is seen most readily in a free induction decay (FID) measurement [130, 125] shown in Fig. 1.11(a). Here, after optical pumping to $|0\rangle$, a $\pi/2$ pulse prepares the state $|\psi\rangle = (|0\rangle + i\,|1\rangle)/\sqrt{2}$. The microwave frequency ω_1 is typically detuned a few MHz from the approximate NV resonance – as determined from CWESR – so that a phase accumulation

[6] These measurements of Γ also reveal strong hyperfine couplings of the NV with nearby spins, leading to the multiple resonance lines in Fig. 1.10(b,c). Nitrogen atoms are found in two common nuclear isotopes, ^{14}N and ^{15}N, with natural abundances of 99.6% and 0.4%, and these determine the frequency signatures observed in the linewidth measurements. Figures 1.10(d,e) show the hyperfine structure of the NV energy levels due to the ^{14}N ($I = 1$) or ^{15}N ($I = 1/2$) host nucleus. The ^{14}N has a non-zero electric quadrupole splitting P which is absent in the spin-1/2 ^{15}N nucleus.[7] The detection of these single nuclei constitutes a form of magnetometry, and NV phase oscillations due to these coherent interactions can be modeled precisely and are not branded as decoherence (see Appendix E).

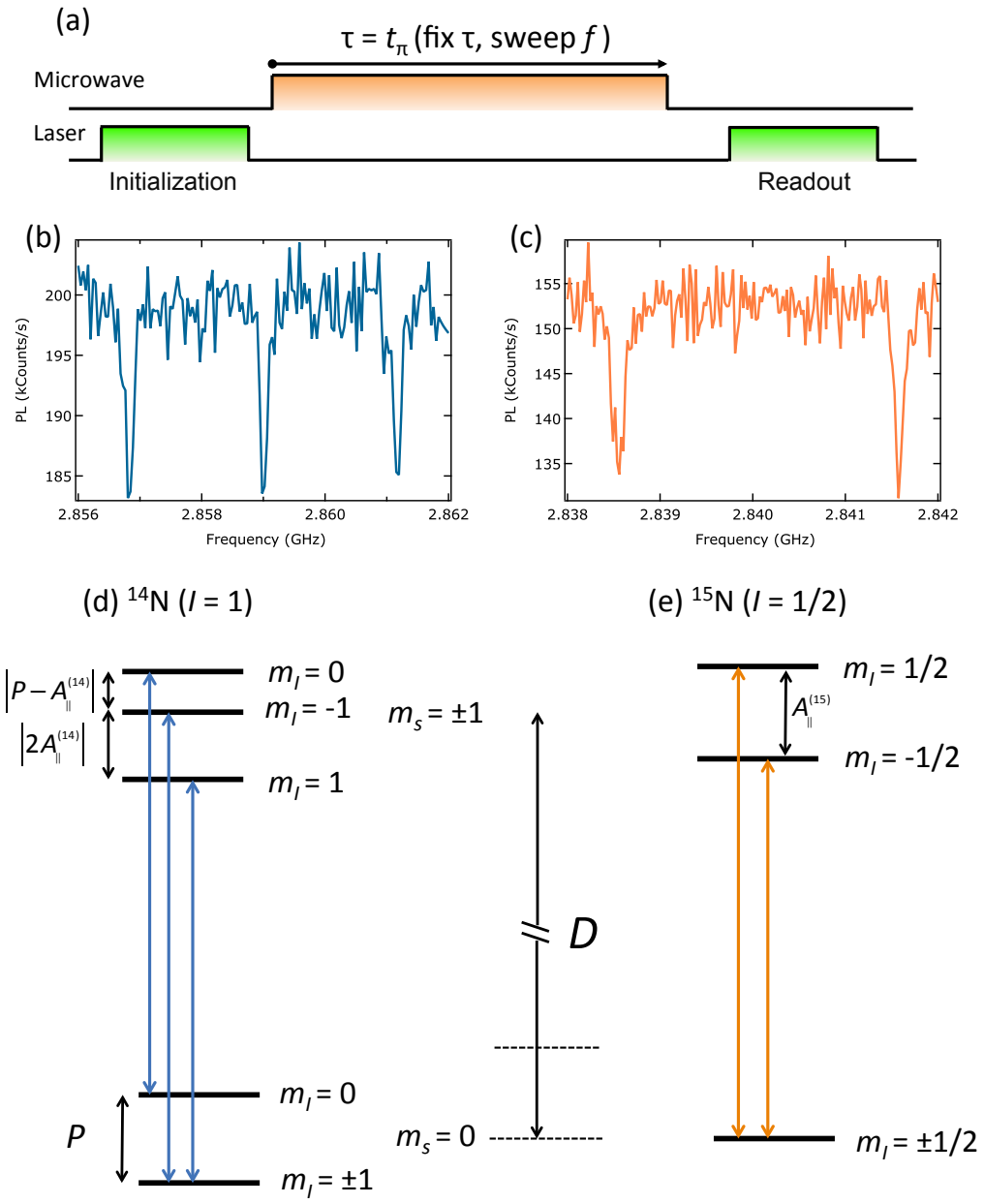

Figure 1.10: Pulsed ESR spectroscopy and hyperfine level structure of the ^{14}NV and ^{15}NV in the ground state triplet. (a) Pulsed ESR sequence to mitigate optical and RF power broadening. To obtain a non-power-broadened ESR line, the microwave power must be set low enough that the t_π time is long compared to T_2^*, but not so long that Rabi contrast is fully diminished. (b,c) Pulsed ESR spectroscopy of ^{14}NV and ^{15}NV resonances for NVs in a diamond film B001a. (d) The ^{14}NV has three transitions per $\Delta m_s = \pm 1$ transition, spaced by ≈ 2.1 MHz, where P is the quadrupolar splitting and $A_\parallel^{(14)}$ is the axial hyperfine coupling. (e) The ^{15}NV has two transitions per $\Delta m_s = \pm 1$ transition, and $A_\parallel^{(15)} \approx 3.1$ MHz.

in the succeeding time τ shows a beating oscillation at each frequency $\delta_i = \omega_1 - \omega_i$, where here ω_i is each sublevel due to a coupled nuclear spin.[8] The beating here gives a signal of nonzero frequency, which serves to resolve the overall envelope of coherence decay. The phase accumulation from a total field B is

$$\Delta\phi = \int_0^\tau B\,(t)\,dt \tag{1.10}$$

where the integration occurs over the free precession time between initialization of the coherence and phase readout.

Figure 1.11(b) is a plot of FID data for a ^{15}NV. For net phase $\Delta\phi = 0$, the final $\pi/2$ pulse transfers the NV to the $|-1\rangle$ state, giving minimum normalized PL. For $\Delta\phi = \pi$, the final state is $|0\rangle$, giving 1.0 normalized PL. A Fourier transform of the data is shown in Fig. 1.11(c) where two frequency peaks at $\delta_{1,2} \approx 1.5, 4.5$ MHz correspond to hyperfine levels of the electron due to the host ^{15}N. The peak splitting gives the hyperfine coupling parameter $A_\parallel^{(15)} = 3.05$ MHz. We can also see that without a detuning these linewidths would be centered at zero frequency and difficult to ascertain. The timescale of the decay rate of the FID data, when fit directly to $\exp\left(-t^2/T_2^{*2}\right)$, yields $T_2^* = 8.1(2)$ μs. The form of this stretched exponential decay factor is derived in a later section on dynamical decoupling from assumptions about the magnetic noise bath in the diamond. The FFT linewidth is obtained by fitting to a Gaussian peak function.[9] A consideration of the FFT of the $\exp\left(-t^2/T_2^{*2}\right)$ to $\exp\left(-(T_2^*\omega)^2/4\right)$ yields a relationship $T_2^* = \sqrt{2}/(\pi\sigma)$. By

[8]The free precession measurement also provides information about the average m_I state of the ^{15}N nucleus. The FFT data and CWESR data in Figs. 1.11(c,d) both display a difference in the area of the two hyperfine peaks of ratio 1.3. The area under these peaks corresponds to the relative probability of the ^{15}N to be spin up or down, indicating the nuclear spin is slightly polarized. In this case the mechanism is a magnetic field-dependent effect due to the optical pumping of the NV center when close to its excited-state level anti-crossing at $B_z \approx 514$ G [131]. This polarization mechanism is also useful as feedback in the alignment of the static applied field to the NV center axis (see Appendix F).

[9]Note that in the Igor program the Gaussian fit function's "width" parameter is $\sqrt{2}\sigma$ where σ is the standard deviation.

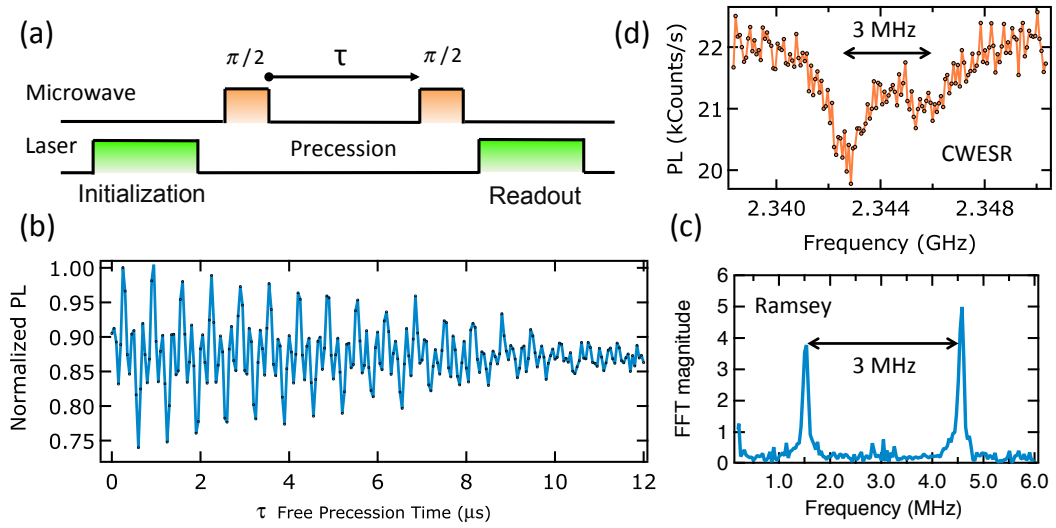

Figure 1.11: Free-induction decay measurement to determine T_2^* and hyperfine couplings in a 188 G applied field. (a) Ramsey sequence for NV ODMR. An initial superposition in the spin ground state is prepared and accumulates phase for a time τ. This phase is mapped into a population for optical readout. (b) Ramsey data for a single ^{15}NV showing a decay and multiple higher frequency components. (c) Fourier transform of the data in (b), revealing a N_{15} hyperfine splitting of 3.05 MHz and line standard deviation of 55 kHz and $T_2^* = 8.1$ μs, in agreement with fit to the decay in (b) (see main text). The 1.3× difference in peak area is an indication of partial field-dependent ^{15}N spin polarization, an effect confirmed in the CWESR data (d) for this NV.

fitting the FFT peaks to Gaussian functions $A\exp[-(f-f_0)^2/(2\sigma^2)]$, where $f = \omega/(2\pi)$, we confirm that $T_2^* = 8.1$ μs from the extracted fit parameter $\sigma \approx 55.2$ kHz. Note that this σ is different from the b amplitude standard deviation mentioned above because σ comes from fitting a FFT and b is from a direct frequency domain measurement using pulsed ESR. $T_2^* = \sqrt{2}/b = \sqrt{2}/(\pi\sigma)$, so $b = \pi\sigma$.

T_2^* for NVs in diamonds with very low concentrations of magnetic impurities can be more than 100 microseconds [42, 132], which is exceptionally long for an electronic spin in a solid state material. However, decoherence caused by fluctuating parameters in the laboratory, namely stray magnetic fields and temperature, can also limit T_2^*. For example, the zero-field splitting D changes with temperature as -74 kHz/K [31, 12], causing a

different phase to be measured at a fixed τ precession period [133, 134]. Therefore, to maintain a $T_2^* > 100$ μs, a temperature stability of better than ~ 100 mK is necessary over the timescale of the measurement, which is typically several minutes to an hour. Stray magnetic fields in the lab environment from stationary or moving materials near the diamond sample could also slowly change over time and shift the resonance proportional to γ_{nv}. To maintain a $T_2^* > 100$ μs requires a long-term ambient magnetic field stability of better than 0.5 μT, about two orders of magnitude smaller than Earth's magnetic field. In the next section, we discuss the elimination of dephasing that is due to slowly changing environmental parameters to give the homogeneous decoherence time T_2.

1.4.3 Causes and measurement of T_2

The sources of noise dominating T_2^* may fluctuate on a timescale much longer than a single measurement shot. These slow-noise effects that randomize NV phase can be eliminated using the Hahn echo sequence [46]. The echo technique, adapted to ODMR of the NV center [11, 19], is shown in Fig. 1.12. The initially prepared $(|0\rangle + i\,|1\rangle)/\sqrt{2}$ accumulates phase as in Eq. 1.10 for a precession time τ due to a $B(t)$ that we assume has an effectively static value B_s on the timescale of τ. A π pulse flips the spin state, such that in a succeeding precession time τ the spin accumulates precisely $-\Delta\phi$ due to B_s. The effect after a final $\pi/2$ pulse is to transfer the net phase angle accumulated to a population angle that is then read out optically in the S_z basis, so in the case of static $B(t)$ the spin is returned to $P_{|0\rangle} = 1$. The analytical signals for echo-type measurements are derived in the sections below on dynamical decoupling and magnetic sensitivity using a formalism of applying frequency filters to a noise spectrum.

Decoherence of single and ensemble NV centers due to the natural ^{13}C spin bath in diamond has been studied extensively over the last decade [22, 26, 135, 129, 136, 125, 130].

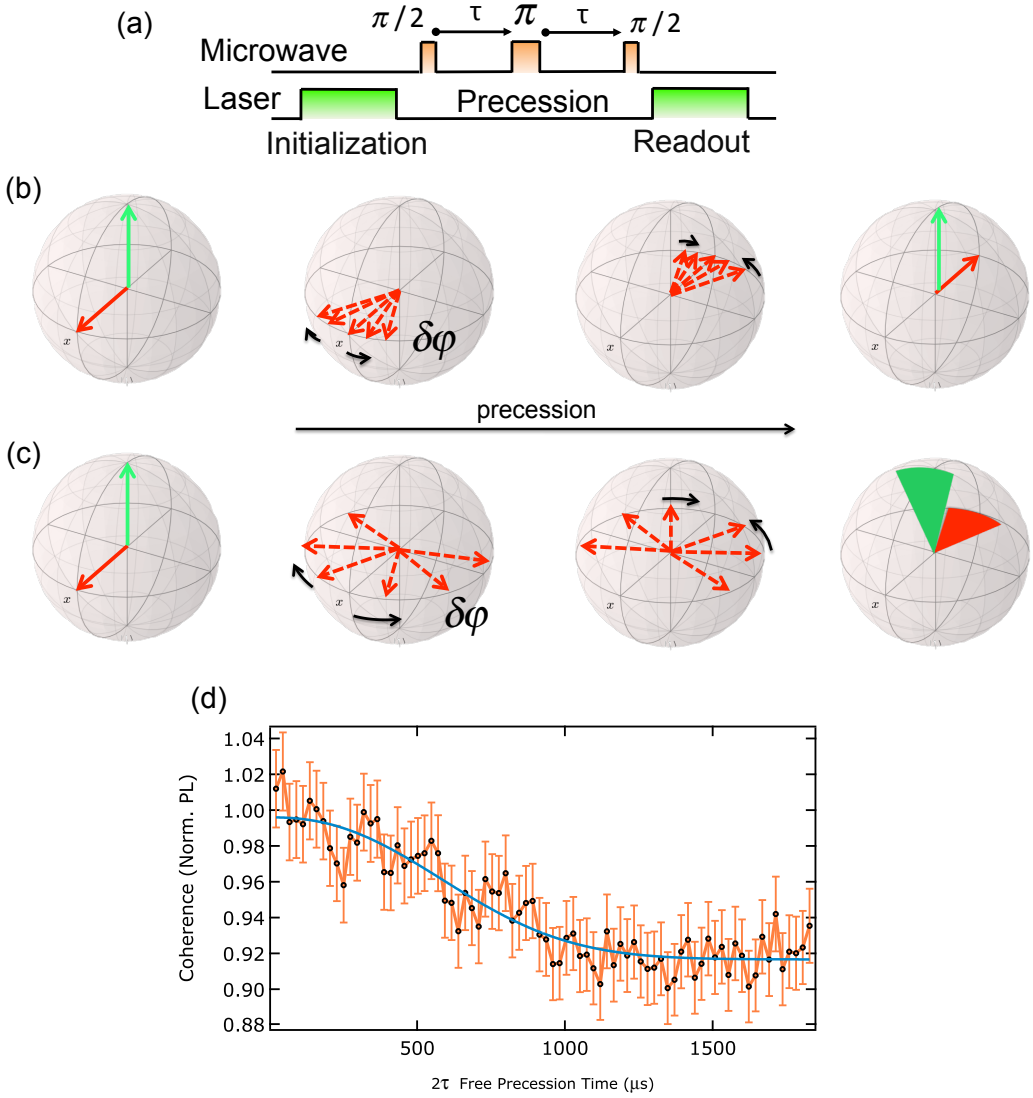

Figure 1.12: Measurement of coherence time T_2 in a single NV. (a) Hahn echo pulse sequence to initialize a spin superposition and measure loss of coherence as a function of total precession time 2τ. A π pulse reverses dephasing from magnetic fields that change much slower than a single pulse shot. (b) Bloch sphere representation of the spin state from left to right for short τ: i) initialized spin (green) and superposition (red), ii) fanning out of phase for different pulse sequence shots, iii) refocusing of phase after π pulse, and iv) rotating refocused phase back onto population axis for projective readout. (c) Same sequence as in (b) but for long τ, so the phase is not perfectly refocused and the final phase is randomly spread out (red wedge). Therefore the population readout is also spread out (green wedge) in the last frame. (d) Coherence measurement of a NV in a CVD diamond film, showing a long $T_2 = 740(40)$ μs. The PL at long 2τ is halfway between the $|0\rangle$ and $|1\rangle$ PL levels: $a_0/2 + a_1/2$.

The nuclear spin bath causes a nontrivial and nonmonotonic coherence decay envelope of the NV echo measurement that depends on the applied magnetic field mangitude and angle as well as the precise distribution of ^{13}C spins around a particular NV [137]. For a general applied $\mathbf{B}$ of a few 10s of G not particularly aligned to the NV axis, this bath limits T_2 to about 300 μs [138] because individual NV electron-nuclear interactions are more important to the overall bath precession dynamics.[10] With larger and well-aligned $\mathbf{B}$, theory and experiments show that T_2 may increase to 600-800 μs [137, 136].

T_2 is also inversely proportion to spin concentration in the crystal over certain ranges of concentration [139]. In 2009, it was demonstrated that by growing chemical vapor deposition (CVD) single-crystal diamond films with isotopically pure ^{12}C methane, the ^{13}C percentage was reduced from the natural 1.1% abundance to $\sim 0.3\%$, thereby making the average distance of the NV to ^{13}C farther away. Bulk NV centers were observed in these diamonds with T_2 enhanced up to 1.8 ms with a Hahn echo. Spin-lattice relaxation or residual ^{13}C couplings were hypothesized as the limits to T_2 at this timescale [132]. The diamonds studied in this dissertation were all grown by CVD with enriched ^{12}C of 99.99-99.999 % (see Chapter 3), so ^{13}C is not a primary contributor to bulk-induced NV decoherence.

In diamonds with a large concentration of substitutional nitrogen impurities, or reduced ^{13}C concentration, the NV coherence time is limited by electronic spins of paramagnetic $S = 1/2$ defects [140], such as the P1 center [21]. The cumulative magnetic field effects of a bath of P1 centers on NV decoherence can be described by a mean-field theory that parameterizes the noise spectrum with a correlation time τ_c and total NV-bath rms coupling b [100, 141], as we describe in Chapter 4.

[10] Coherence time as a single decay constant T_2 is not always appropriate under some distributions of ^{13}C spins and applied fields; see [137]. However, this case will not apply to the diamonds used our experiments as ^{13}C concentration is reduced.

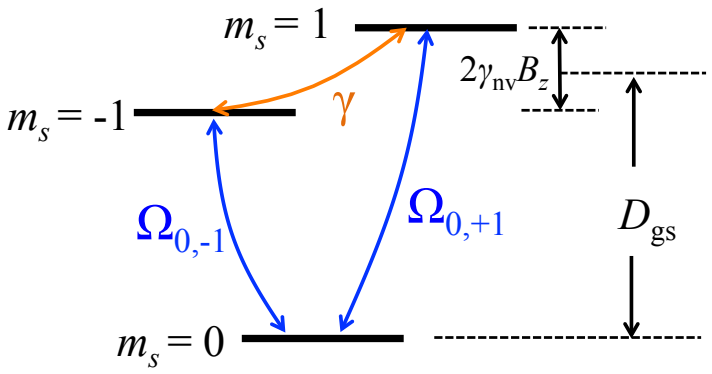

Figure 1.13: Relaxation rates in the NV spin ground state. The blue ($\Omega_{i,j}$ refer to $\Delta m_s = \pm 1$ transitions, and the orange ($\gamma_{+1,-1}$) indicate magnetic dipole forbidden $m_s = \pm 2$ transitions. These rates are determined by electromagnetic noise at the transition frequencies, as described in detail in Chapter 5.

1.5 Spin relaxation: T_1

Spin relaxation, unlike dephasing, does not conserve energy from the perspective of the individual spin system. Spin-flips between the different energy levels of a spin lead to decay of coherences, which is required to preserve the positivity of the spin's density matrix (i.e., non-negative eigenvalues, or populations) [122]. For the NV ground state, these flips are transitions between $m_s = 0, -1, +1$ states, as shown in Fig. 1.13 . We focus on the most common case that these $\{m_s\}$ are approximately the eigenstates of S_z, which is valid under conditions of parallel applied magnetic field sufficiently greater than perpendicular magnetic field, strain, and electric field.[11] The definition of spin relaxation time T_1 for the NV three-level system is an important concept in this dissertation. The relaxation rate $1/T_1$ as it contributes to the decoherence rate $1/T_2$ depends on the specific qubit sublevels that share the coherence, so in this work we focus on individual relaxation

[11]For single-crystal diamond with low strain, these conditions for S_z eigenstates are not difficult to obtain with better than 99.9% precision: a B_z of 4 G or greater and angle $\tan^{-1} B_\perp/B_\parallel$ smaller than a few 10s of degrees is sufficient. More often we use 10s to 100s of Gauss and alignment to within a couple degrees.

rates between sublevels, rather than exponential decay rates of spin polarization. Such a picture also lends more immediate insight into the noise sources affecting each transition.

1.5.1 Causes of NV spin relaxation

There are several potential causes of spin relaxation for NVs in diamond. First, spin transitions associated with interactions of the NV's electronic orbitals with phonons in the crystal [32] are presumed to ultimately limit the spin relaxation times between individual m_s sublevels to about 7-10 milliseconds at $T \sim 300$ K [142]. The dominant mechanisms at this temperature appear to be two-phonon Raman processes whereby a phonon is inelastically scattered, which leaves the spin in a different energy state and emits a phonon of different energy [143, 32, 119]. Second, the Zeeman term of the Hamiltonian in Eq. 1.1 shows that coherent $B_\perp$ fields cause spin transitions that change m_s by one quantum when the field oscillates near a NV resonance frequency $\omega_{0,\pm1} = D \pm \gamma_{\mathrm{nv}} B_z$, as for driving Rabi oscillations. Thus, magnetic noise with a sufficient spectral density at one or both of the single-quantum $\omega_{0,\pm1}$ transition frequencies (GHz-scale) also causes incoherent transitions. Cross-relaxation between the NV and other spins, such as from P1 centers, can reduce T_1 dramatically at matched resonance frequencies [119, 144, 145]. We do not consider cross-relaxation here because the samples we study have rather low concentrations of nitrogen and we do not tune the NV transitions into resonance with low-frequency nuclear spin resonances or resonances of $g \approx 2$ electrons, such as in P1 centers [145].

1.5.2 Measurement of spin relaxation rate

In our experiments, we consider single-quantum spin relaxation due to phonons and external magnetic fluctuations $\langle B_\perp^2 \rangle$, such as from fast-fluctuating spins. The relaxation

rates are

$$\Omega_{0,\pm1} = \Omega_{\text{ph}} + \Omega_{\langle B_\perp^2 \rangle}. \tag{1.11}$$

The $\Omega_{0,\pm1}$ from Eq. 1.11 refers specifically to the average rate at which a NV with its spin polarized into $|0\rangle$ will lose population, eventually reaching thermal equilibrium. At room temperature, this final density matrix is an equal mixture of the three $\{|m_s\rangle\}$, written with the identity matrix as $\rho = I_{3\times3}/3$. The transitions are bidirectional because the $\omega_{i,j}$ energies are all much smaller than $k_B T/h \approx 6$ THz, yielding no preference in state population. This thermal relaxation behavior is described by exponential solutions to the population rate equations

$$\begin{aligned}
\tfrac{d\rho_{00}}{dt} &= -(\Omega_{0,-1} + \Omega_{0,+1})\rho_{00}(t) + \Omega_{0,+1}\rho_{11}(t) + \Omega_{0,-1}\rho_{-1-1}(t) \\
\tfrac{d\rho_{11}}{dt} &= \Omega_{0,+1}\rho_{00}(t) - \Omega_{0,+1}\rho_{11}(t) \\
\tfrac{d\rho_{-1-1}}{dt} &= \Omega_{0,-1}\rho_{00}(t) - \Omega_{0,-1}\rho_{-1-1}(t)
\end{aligned} \tag{1.12}$$

where again the $\Omega_{i,j}$ are incoherent transition rates between $|i\rangle$ and $|j\rangle$, as shown in Fig. 1.13. The canonical T_1 measurement (Fig. 1.14) for NV centers can be carried out without microwave control, and it yields the single-quantum relaxation rates $\Omega_{0,\pm1}$ [119]. If $\Omega_{0,-1} = \Omega_{0,+1} \equiv \Omega$ – as is often the case, especially at low B_z where the two Larmor frequencies are similar – then the decay time of the data is $1/(3\Omega)$. In Chapter 6, we use this all-optical sequence to detect and image magnetic field noise from Gd^{3+} spins external to the diamond. As shown in Fig. 1.14, an additional final microwave pulse $\pi_{0,-1}$ resonant with the $\omega_{0,-1}$ transition can help normalize the measurement data by eliminating the final PL contrast through a subtraction and thus yield more accurate fits of Ω.

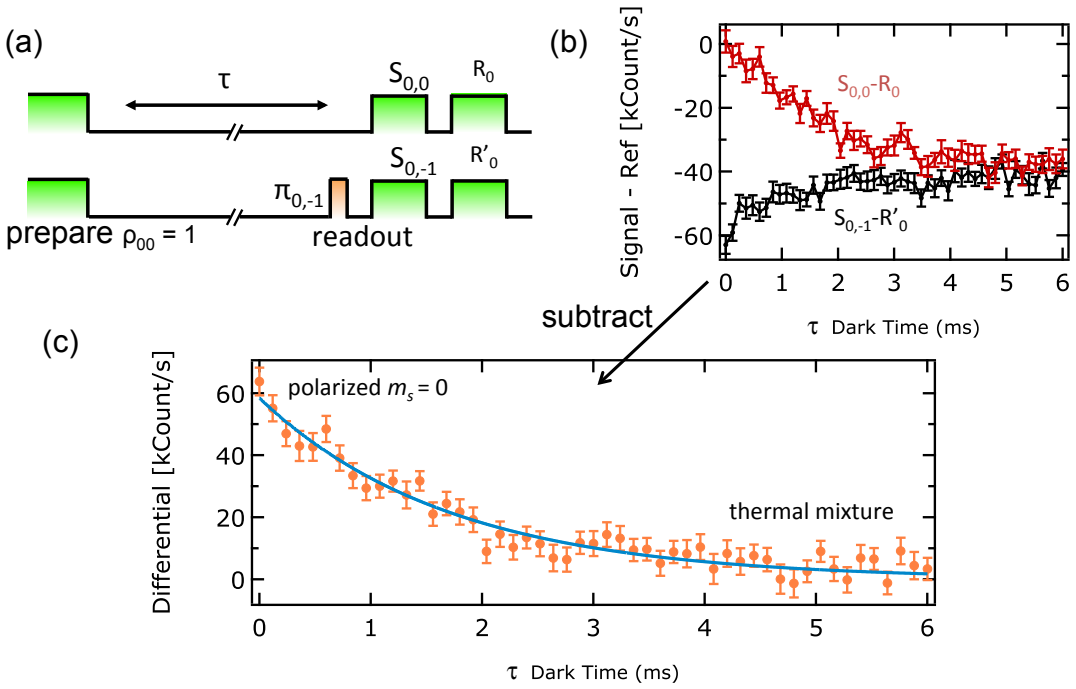

Figure 1.14: Spin relaxation time measurement for a single NV. (a) All-optical sequence (top) and similar sequence for optional normalization (bottom). The spin is initialized in each case into $\rho_{00} = 1$ and either ρ_{00} or ρ_{-1-1} is read out. The polarized spin population decays over a dark time τ. (b) Raw data for the two sequences in (a) in photon counts per second. Both curves decay to the PL level of $a_0/3 + 2a_1/3$ where the subscript refers to $|m_s|$, unlike the phase measurement result (e.g., Hahn echo) $a_0/2 + a_1/2$. (c) Normalized data (orange points) fit to $A\exp(-t/T_1^{(0)})$ (blue curve), yielding $T_1^{(0)} = 1.71(8)$ ms and contrast $A = 58(2)$ kCount/s. $T_1^{(0)}$ refers to the time constant for depolarization and does not fully describe the relaxation limit to T_2.

1.5.3 T_1 contribution to decoherence

While the $1/(3\Omega)$ time describes the depolarization process, it is not the only relaxation contribution to decoherence time T_2. An important part of this dissertation is the more-complete consideration of T_1, which is a topic of Chapter 5. A complete definition of T_1 must include the $\gamma \equiv \gamma_{+1,-1}$ relaxation rate in Fig. 1.13, which has not been widely considered in the literature for two reasons: 1) it is magnetic dipole forbidden and 2) it does not affect the straightforward measurement of depolarization of the $|0\rangle$ state. Furthermore, we show in Chapter 5 that γ plays an important role in the total spin relaxation and decoherence of near-surface NV centers due to electric field noise transverse to the NV axis. This rate actually becomes dominant over $\Omega_{i,j}$ in determining T_2 at low magnetic fields, especially for certain qubit subset levels of the three-level ground state, such as $\{|-1\rangle, |1\rangle\}$. This consideration enables us to show that that $T_2 > T_1$ can be achieved with dynamical decoupling on NV centers that are in proximity to the diamond surface. Even at high magnetic fields and for deep NVs, we find that γ is often 1-2 times larger than Ω and should be accounted for in the relaxation contribution to T_2.

1.6 Mitigating dephasing by dynamical decoupling

Dynamical decoupling techniques are drawn from the field of NMR and extend the Hahn echo. The motivation for their development was to prolong the phase coherence of a spin ensemble using periodic microwave control π pulses [146], whereby reducing the time between pulses desensitizes the spin to faster and faster fluctuating fields. Phase cycling of the successive π pulses [147, 148], which refers to alternating the Bloch direction about which coherent rotations are performed, can help mitigate pulse errors. For example, phase cycling in the sequences of Fig. 1.15 can help in more robust preservation of coherence for a single axis on the Bloch equator, as in CPMG [149], or arbitrary super-

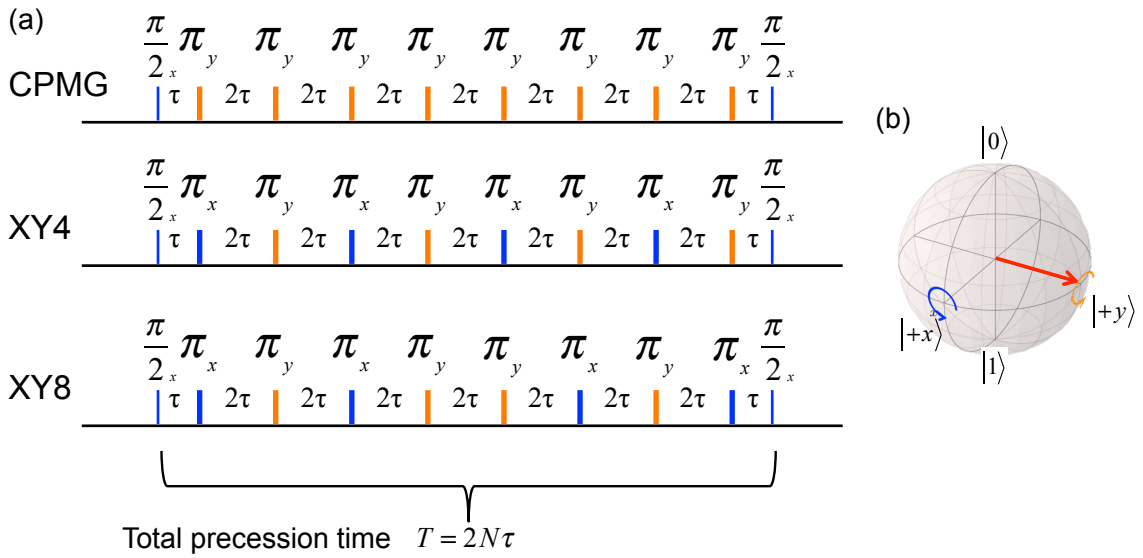

Figure 1.15: (a) Dynamical decoupling pulse sequences with the Car-Purcell periodic timing, here shown with $N = 8$ the number of π pulses and total precession time $T = 2N\tau$. All sequences begin with a $(\pi/2)_{\mp x}$ pulse to prepare state $|\pm y\rangle = (|0\rangle \pm i\,|1\rangle)/\sqrt{2}$. A CPMG must all π pulses of the same y phase as the initial NV state, here $|+y\rangle$. For CPMG, a chunk $\tau - \pi_y - 2\tau - \pi_y - \tau$ is repeated, where 2τ is the delay time between π_y pulses. CPMG with π_y preserves $|+y\rangle$ extremely well but causes errors if the $|\pm x\rangle = (|0\rangle \pm |1\rangle)/\sqrt{2}$ is prepared. XY4 cycles the phase between π pulses and XY8 only differs by mirroring the second four pulses of the sequence. XY4 and XY8 preserve either $|+x\rangle$ or $|+y\rangle$ due to the two-axis control, however, XY8 is significantly more effective (see Fig. 1.18). When modeled assuming zero pulse errors and infinitesimal pulse width, all three sequences have the same filter function derived in the text. (b) Bloch sphere representation of initial $|+y\rangle$ state (red arrow) and control pulses about the x (blue) and y (orange) axes.

positions using sequences like XY4 and XY8 [100, 150]. The basic dynamical decoupling schemes use only rectangular pulses with only four 90° phase intervals, which are technically simple to implement, though an active area of research is the careful tailoring of pulse shapes and timings to mitigate particular noise sources [151, 152]. In this work, we use square pulses with $\pm x$ and $\pm y$ phases in the three sequences shown in Fig. 1.15 to measure decoherence of NVs or sense fluctuating nuclear spins outside the diamond.

1.6.1 Derivation of dynamical decoupling filter functions

Applying dynamical decoupling sequences to the NV spin makes it a spectrometer of its local nanoscale environment with a filter function peak f_0 and bandwidth Δf specified by the number of pulses N and the time delays 2τ. In general, increasing N while keeping the total precession time T fixed will improve the quality factor $Q = f_0/\Delta f \propto N$ of the filter, making it approach the form of a delta function. This application will be developed in Chapters 4 and 5 for analyzing the frequency spectra of noise from the diamond surface.

In this section, we derive an expression that shows how the dephasing of a superposition spin state can be described as a convolution of the environmental noise spectrum with a filter function that is determined by the microwave pulse sequence. We will be concerned here with dephasing between $|0\rangle$ and $|-1\rangle$ due to magnetic fields, although the analysis can be straightforwardly extended to describe dephasing from electric fields parallel to the NV axis (see Chapter 5). The basic perturbing Hamiltonian comprises the Zeeman interaction in the NV ground state spin $|0\rangle, |-1\rangle$ qubit basis,

$$\mathcal{H}/\hbar = \hat{\eta}_z(t)\,\sigma_z \tag{1.13}$$

where $\hat{\eta}_q(t)$ is a fluctuating vector quantity at the NV spin. In the pure dephasing model with magnetic noise, the noise spectral density $\tilde{S}_q(\omega)$ is negligible for components $q = x, y$ that would cause spin relaxation near the qubit Larmor frequency. The classical noise variable $\hat{\eta}_z(t)$ is assumed to have a Gaussian distributed value at each time t with a standard deviation b, such that

$$\text{Prob}\left[\hat{\eta}_z(t) = \eta'\right] = \frac{1}{\sqrt{2\pi b^2}}\exp\left[-\frac{\eta'^2}{2b^2}\right] \tag{1.14}$$

The spin coherence is quantified as the time-evolved expectation value of the trans-

verse spin components, where at $t = 0$ the spin density matrix after an initial $\pi/2$ pulse is $\rho(0) = \frac{1}{2}(|0\rangle + i|-1\rangle)(\langle 0| - i\langle -1|)$. Applying the time-evolution operator to the spin density matrix and averaging over all noise trajectories reduces to the final result for the coherence $C(t)$ (or transverse magnetization) [99]

$$C(t) = \mathrm{Tr}(\sigma_+ \rho(t)) = \exp\left[-\int_{-\infty}^{\infty} d\omega \tilde{S}(\omega)\mathcal{F}(t,\omega)\right]. \tag{1.15}$$

where $\sigma_+ = \sigma_x + \sigma_y$ is the spin qubit raising operator. Here $\tilde{S}(\omega)$ is the Fourier transform of the noise correlation function $\langle \eta'(t)\eta'(t+T)\rangle$. A choice of pulse sequence $s(t)$, such as a series of equally spaced π pulses, gives a specific form of the filter function $\mathcal{F}(t,\omega)$. For this experiment we are interested primarily in the decay envelopes produced by Hahn echo $(\tau - \pi_x - \tau)$ and XY4

$$(\tau - \pi_x - 2\tau - \pi_y - 2\tau - \pi_x - 2\tau - \pi_y - \tau) \tag{1.16}$$

sequences. The alternating X and Y phases do not affect the analytical result assuming pulses perfect in duration and relative phase.

The N-pulse filter function can be computed with several different methods. We start here from the form of $\mathcal{F}(t,\omega)$ given in ref. [99] for general $s(t)$:

$$\mathcal{F}(t,\omega) = \int_0^t dt' s(t') \int_0^{t'} dt'' s(t'') \cos[\omega(t'-t'')] \tag{1.17}$$

The 4-pulse XY4 sequence reverses the sign of phase accumulation after each pulse

and has a total time 8τ, so

$$s\left(t''\right)=\begin{cases}+1 & \text{for} 0<t''<\tau\\ -1 & \text{for}\tau<t''<3\tau\\ +1 & \text{for}3\tau<t''<5\tau\\ -1 & \text{for}5\tau<t''<7\tau\\ +1 & \text{for}7\tau<t''<8\tau\end{cases} \tag{1.18}$$

The dt'' integral in intervals of t'' leads to

$$\mathcal{F}(8\tau,\omega)_{\mathrm{XY4}}=\int_0^{8\tau}dt's\left(t'\right)\begin{cases}X_0 & \text{for} 0<t''<\tau\\ A_{01}+X_1 & \text{for}\tau<t''<3\tau\\ A_{01}+A_{31}+X_3 & \text{for}3\tau<t''<5\tau\\ A_{01}+A_{31}+A_{35}+X_5 & \text{for}5\tau<t''<7\tau\\ A_{01}+A_{31}+A_{35}+A_{75}+X_7 & \text{for}7\tau<t''<8\tau\end{cases} \tag{1.19}$$

in terms of the four A_{jk} integrals

$$A_{jk}\left(t',\tau\right)=\int_{j\tau}^{k\tau}dt''\cos\left[\omega\left(t'-t''\right)\right]=\frac{\sin\left[\omega\left(t'-j\tau\right)\right]-\sin\left[\omega\left(t'-k\tau\right)\right]}{\omega} \tag{1.20}$$

and five X_m integrals

$$X_m\left(t',\tau\right)=\pm_{m=1,5}^{m=0,3,7}\int_{m\tau}^{t'}dt''\cos\left[\omega\left(t'-t''\right)\right]=\pm_{m=1,5}^{m=0,3,7}\frac{\sin\left[\omega\left(t'-m\tau\right)\right]}{\omega} \tag{1.21}$$

The final dt' integral in $\mathcal{F}\left(8\tau,\omega\right)$ is then performed over the respective intervals. The result is

$$\mathcal{F}(8\tau,\omega)_{\mathrm{XY4}}=\frac{128\left[\cos\left(\frac{3\omega\tau}{2}\right)+\cos\left(\frac{5\omega\tau}{2}\right)\right]^2\sin^6\left(\frac{\omega\tau}{2}\right)}{\omega^2}. \tag{1.22}$$

By a similar calculation the Hahn echo filter function is

$$\mathcal{F}(2\tau,\omega)_{\text{echo}} = \frac{8\sin^4\left(\frac{\omega\tau}{2}\right)}{\omega^2}, \tag{1.23}$$

and the Ramsey free induction decay filter function is

$$\mathcal{F}(2\tau,\omega)_{\text{FID}} = \frac{2\sin^2\left(\frac{\omega\tau}{2}\right)}{\omega^2}. \tag{1.24}$$

This FID filter function on a noise bath with a normally distributed amplitude at each time step gives a coherence envelope of

$$C(\tau) = e^{-\frac{1}{2}b^2\tau^2} = e^{-(\tau/T_2^*)^2} \tag{1.25}$$

where b^2 is the variance, so $T_2^* = \sqrt{2}/b$. The general filter function for a sequence with N pulses can be computed as

$$\mathcal{F}_N(T,\omega) = \frac{2\sin^2\left(\frac{\omega T}{2}\right)\left[1-\sec\left(\frac{\omega T}{2N}\right)\right]^2}{\omega^2} \tag{1.26}$$

where here $T = 2\tau N$ is the total free precession time during the sequence. These functions are sometimes written $F(\tau,\omega) = \omega^2\mathcal{F}(\tau,\omega)$ [98]. The filter functions are plotted in both log and linear scales in Figure 1.16 (Ramsey and echo) and Figure 1.17 (dynamical decoupling) to demonstrate three main points: 1) low-frequency noise is decoupled efficiently with Hahn echo in contrast to the Ramsey case, 2) that with sufficiently large N the sequence behaves similarly to a delta function filter, and 3) harmonics do exist at higher frequencies that must be considered to perform accurate dephasing spectroscopy.

The main peak of the filter function becomes more like a delta function at large N because the peak frequency increases linearly in N and the bandwidth narrows with longer

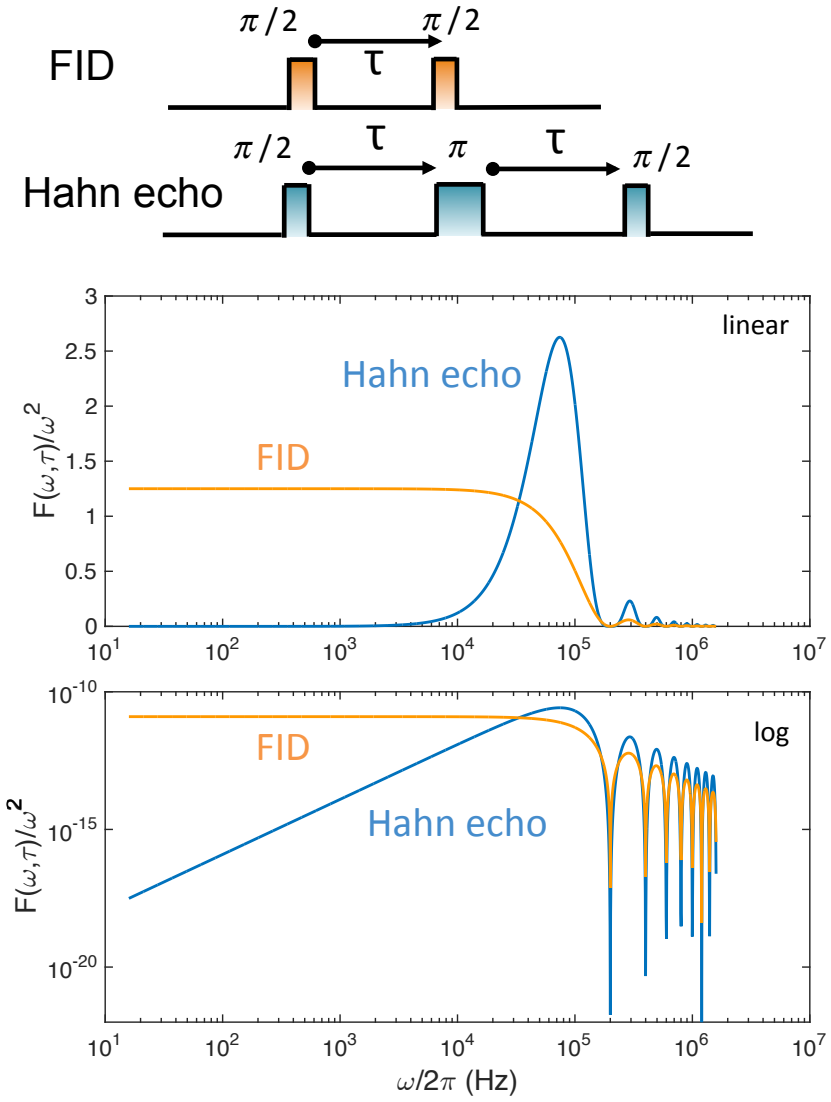

Figure 1.16: Plotted analytical filter functions for the pulse sequences of free induction decay and Hahn echo on linear (top, scaled by $\times 10^{11}$) and log (bottom) scales, showing which frequencies of fluctuating fields each control scheme makes the NV sensitive to. Here $\tau = 5$ μs, so $F(\omega, \tau)$ peaks at $1/(2\tau) = 100$ kHz for maximal net phase accumulation (note $F(\omega, \tau)/\omega^2$ is plotted as it appears in the time evolution operator). The FID leaves the NV susceptible to noise at dc to low frequencies, which the echo π pulse mitigates. Thus FID is useful for detecting slowly varying fields but yields fast spin dephasing rates. The functions share the same minima: the FID gives zero net phase, accumulation when $\omega/2\pi = \tau$ because equal positive and negative phase is accumulated, and the same holds for the echo with a full period (zero net phase) before and after the π pulse.

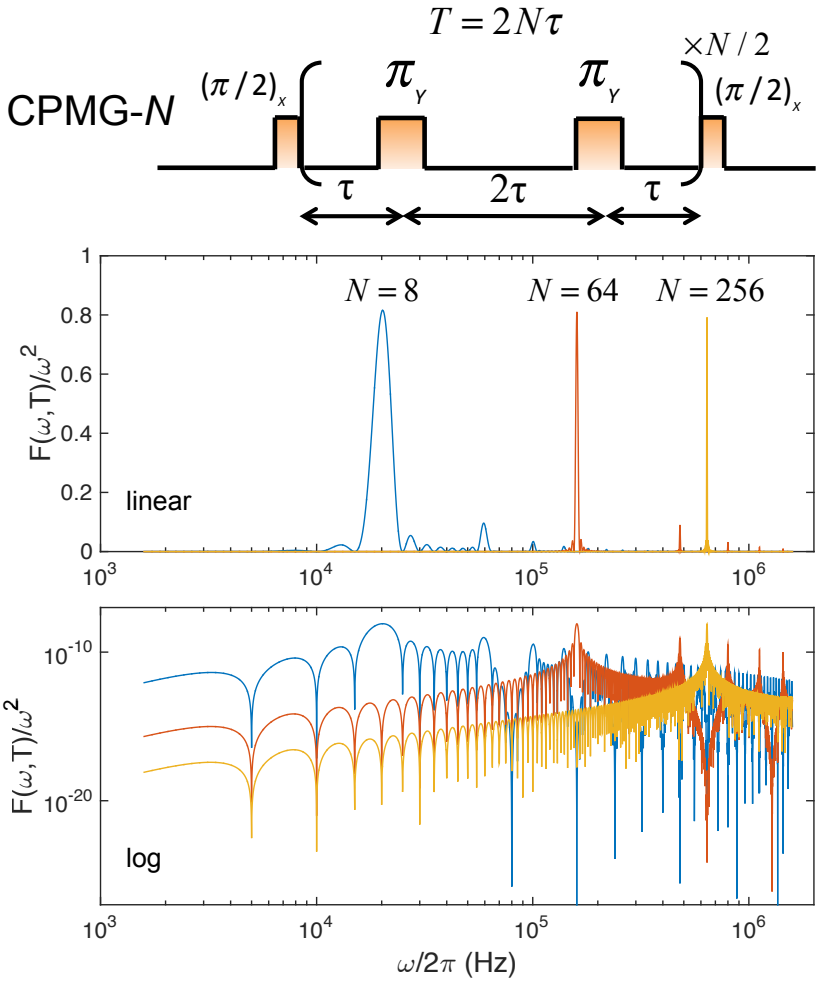

Figure 1.17: Pulse sequence filter function for CPMG-like periodic dynamical decoupling on linear (top, scaled by $\times 10^8$) and log (bottom) scales. N is the number of total π pulses, all of phase y for strict CPMG. Three filter functions are shown with different N, all with total precession time $T = 2\tau N = 200$ μs. As N increases, more pulses are fit in the time T, which increases the frequency as $f_0 = N/(2T)$ while keeping the bandwidth $\Delta f = 1/T$ constant, leading to a quality factor of $Q \approx N/2$. Spectroscopy is done by varying both N and T in measurements of phase coherence and deconvolution of the coherence curve with the known filter function.

total precession time $T = 2\tau N$ (Fig. 1.17). However, T cannot be increased indefinitely because the coherence time $T_2(N)$ is increased only sub-linearly with higher N due to the nature of the environmental electromagnetic noise in the diamond. Specifically, $T_2(N) = N^{\lambda}$ with $\lambda < 1$, and for NV centers $\lambda \leq 2/3$ is most often observed [100, 87], although $\lambda \sim 0.8$ has recently been reported [91].

1.6.2 Noise spectral density of the NV environment

Evaluating the coherence envelope in Eq. 1.15 and computing the theoretical dynamical decoupling efficiency λ requires an assumption of the noise spectral density $\tilde{S}(\omega)$. This calculation is shown analytically for small $N \leq 4$ and numerically for larger $N > 4$ in Chapter 4 in the context of analyzing noise sources located within the bulk and at the surface of diamond. Therein, we find experimentally, and support with theoretical calculation, that $\lambda = 2/3$ for deep bulk NVs and $\lambda < 2/3$ for near-surface NVs. A numerical deconvolution technique is used also in Chapter 5 to reconstruct $\tilde{S}(\omega)$ from NV spin coherence measurements.

In this dissertation we have focused on Carr-Purcell-Meiboom-Gill (CPMG) type periodic dynamical decoupling [147] sequences such as CPMG-N, XY4-N, and XY8-N because these sequences have been shown for NVs to be superior [100, 148] to non-periodic sequences like aperiodic Uhrig DD [153]. This difference in performance between periodic and non-periodic sequences stems from the distinction between noise spectra that have a soft or hard frequency cutoff. A soft cutoff refers to a spectrum that decays as a continuous function of frequency as f increases, such as $1/f$ or $1/f^2$, while a hard cutoff is an abrupt reduction to zero spectral density above a specific frequency. A soft cutoff is found to describe the NV's environment [148] for frequencies accessible by experimentally practical inter-pulse delays.

As discussed in Chapters 4 and 5, the coherence time T_2 can always be defined as the time in a monotonic coherence decay where $C(T)$ drops from 1 to $1/e$. However, the commonly used fit function of a stretched exponential $\exp[-(t/T_2)^n]$ for free n is one level of abstraction higher than the full form of the decay derived by considering the specific noise spectral density. That is, the analytical forms of the coherence fit functions derived in Chapter 4 do not have a single decay time constant, but rather have a complicated dependence on the parameters that describe the noise spectral density. Nevertheless, T_2 itself also contains valuable information about the noise spectrum and the contributions of decoherence from dephasing and relaxation processes, particularly if obtained as a function of N and compared to a correctly measured T_1. For example, a T_2 that remains constant with increasing N indicates dephasing due to white noise if $T_2 \ll T_1$. In contrast, $T_2 \propto N^{2/3}$ indicates a spectrum of the form $1/f^2$, such as in the spectral window above the soft cutoff frequency in a Lorentzian spectrum.

1.6.3 Control-pulse errors

Pulse errors can reduce coherence and their effects become especially relevant at large numbers of pulses. For rectangular pulses, these errors can arise from deviations in the microwave frequency, amplitude, or phase [154]. CPMG (Fig. 1.17) is generally quite robust for decoupling on a single axis because, for an initial $(\pi/2)_x$ pulse, the spin's phase never translates too far from the y axis during precession intervals [148]. This property makes it quite useful for demonstrating enhancement of $T_2 = T_2(N)$ for hundreds or thousands of pulses [149]. However, CPMG phase cycling is at a disadvantage for ac magnetometry schemes, where the goal is to achieve a large net phase accumulation from a tiny magnetic signal. In other words, for magnetometry the Bloch vector must leave the initial $|+y\rangle$ state, and CPMG accumulates significant errors unless the vector stays

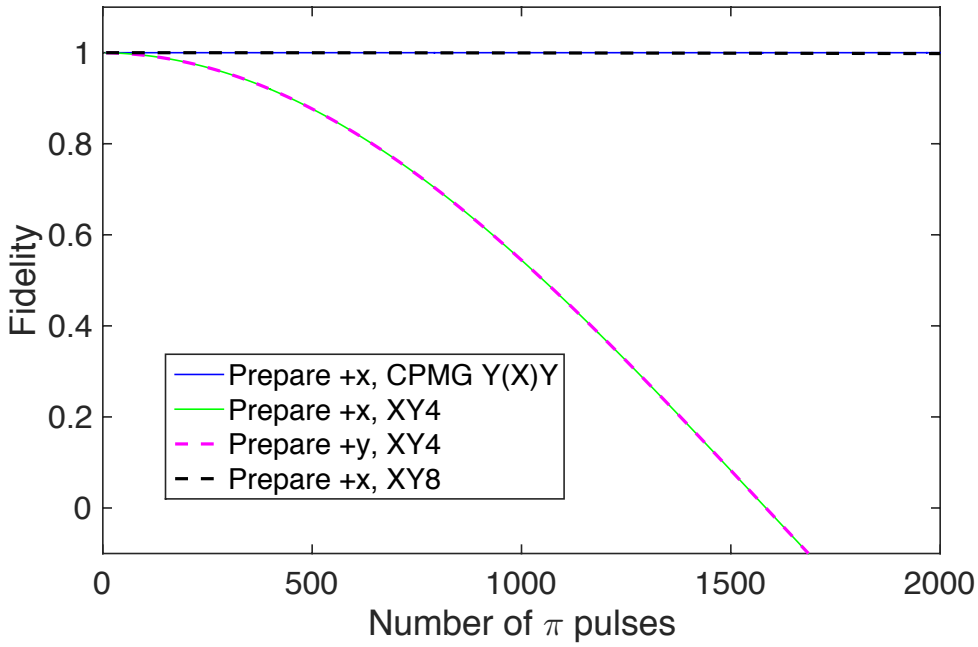

Figure 1.18: Simulated comparison of fidelities for phase-cycled dynamical decoupling sequences CPMG, XY4, and XY8 in the presence of pulse timing errors of 2%. The calculation is simply based on classical three-dimensional rotation matrices R_x, R_y, and R_z. First a vector is prepared along the $+x$ or $+y$ axis. During each precession period the R_z matrix applies a fixed phase rotation $\phi_z \ll \pi$. Each $\pi_x(\pi_y)$ pulse is computed with a $R_x(R_y)$ operation with a fixed pulse timing error of 2% from an ideal π-pulse duration. After the full sequence of N total π pulses, an inner product is made between the final vector and the initial $+x$ or $+y$ vector, and this "fidelity" is plotted. CPMG performed with π pulses about the initial vector axis ($+x$ here) has perfect fidelity, and XY8 for any prepared axis is only marginally inferior (0.9995 at $N = 1000$). XY4 preserves the state relatively poorly for more than 100 pulses. CPMG with π_y pulses on an initial $+x$ state (not shown) has extremely poor fidelity for any number of pulses (e.g, 0.88 at $N = 8$ and 0.06 at $N = 24$) because the rotations cause the vector to make wide swings about the sphere in a single direction, accumulating errors rapidly.

near the y axis. Therefore, XY sequences like XY8 are more often used for sensing of coherent magnetic fields, such as from ensembles of precessing ^{1}H nuclei [102, 155]. XY4 is robust for ac magnetometry for a very small N, but it achieves significantly worse fidelity than either CPMG or XY8. These basic conclusions about fidelity can even be drawn from applying to a vector successive classical rotation matrices about the x and y axes for pulses and z axis for precession intervals, as demonstrated in Fig. 1.18.

Recent work shows that even XY8 has serious drawbacks for coherent spin sensing because the pulses are not infinitesimal, thus producing spurious harmonics that make multiple nuclear species' signatures appear at unresolved frequencies [156]. Correlation spectroscopy sequences [157, 55, 158] are a current trend to overcome this problem and obtain narrower, T_1-limited, frequency resolution. We describe the possible implications of this dissertation on spin relaxation limits to correlation spectroscopy in the future directions of Chapter 7. Our main use for the sequences is to perform dephasing spectroscopy on broad incoherent noise spectra and enhance T_2, therefore CPMG and XY8 are both suitable techniques.

1.6.4 Summary of NV decoherence

The dephasing and spin relaxation rates each contribute to overall decoherence of a spin superposition, or decay of an off-diagonal element of the density matrix. Dephasing can be reduced by applying dynamical decoupling protocols that refocus the random phase accumulation that is due to slow noise sources. Conversely it can be used to make the NV highly sensitive to ac magnetic fields within a narrow bandwidth. However, spin relaxation cannot be reversed in the same way, and T_2 is limited to $2T_1$ [46, 122]. In Chapter 5, we present derivations and measurements of the full three-level relaxation times of near-surface NVs to analyze noise sources and provide a benchmark T_1 that

is relevant to any specific subset NV qubit superposition's ultimate T_2 limit. On the flipside, any of these dephasing and relaxation rates can be used as signals, each for specific purposes, in scanning probe NV-based decoherence imaging of samples producing electromagnetic noise.

1.7 Magnetic sensitivity and spatial resolution

Two critical figures of merit for a sensor of magnetic fields are its magnetic sensitivity and its spatial resolution. We first give conceptual definitions of these quantities and then derive more rigorous examples in the next section. Magnetic sensitivity η can be defined as the minimum detectable magnetic field δB as it scales with total measurement time, $\eta = \delta B\sqrt{t}$, and it is often quoted in units of $\mu\mathrm{T}/\sqrt{\mathrm{Hz}}$ [5]. Longer total and per-shot measurement times increase the signal-to-noise ratio (SNR) and therefore allow for smaller signals to be measured, specifically $\delta B \propto 1/\sqrt{tT}$. The total number of measurements is t/T, where T is the total precession time in one measurement. Therefore, η improves (gets smaller) as T becomes longer, at least to the point where decoherence begins to deteriorate the collected phase information ($T \gtrsim T_2$).

Next, we illustrate why SNR scales with total measurement time t. In ODMR the magnetic field effect on a NV center is transduced to an optical signal read out by a single-photon counter. This readout is susceptible to photon shot noise, which scales as $\sqrt{n}$ for n the total number of collected photons. If the average rate of emitted photons is p then the uncertainty in the total optical signal is $\sigma_S = \sqrt{n} = \sqrt{pt}$. Therefore, if the signal $S \propto t$ and the noise increases with $\sqrt{t}$ then the SNR only improves as $\sqrt{t}$ [5]. Even with the elimination of shot noise, quantum projection noise will yield an SNR $\propto \sqrt{t}$ [159], which is the uncertainty σ_0 in the state readout that uses a projection operator such as $P_0 = |0\rangle\langle 0|$. That is, $\sigma_0 = \sqrt{\langle P_0^2\rangle - \langle P_0\rangle^2} = \sqrt{\langle P_0\rangle - \langle P_0\rangle^2}$, which ranges between 0 and

0.5 depending on the population of the state measured. If w independent measurements are performed on the spin, then the total uncertainty is $\sigma_Q \approx \sqrt{\sum^N \sigma_0^2} = \sqrt{w\sigma_0}$. w increases linearly with the measurement time t, as does a small phase signal, so again the SNR increases only as $\sqrt{t}$.

While magnetic sensitivity η is an independent concept from the spatial resolution, the quantity SNR can be related to spatial resolution when the discrete source of magnetic fields is known, such as a spin or ferromagnetic particle. From the above discussion, we know that δB can be improved by measuring for a longer total time, interrogating the signal for longer per measurement, and collecting more photons per measurement. The minimum detectable number discrete sources δm, for example, is reduced with smaller δB, but δm decreases further by increasing the magnetic signal per source experienced by the NV. Thus, the required δB does not need to be as small to sense the same object. Because the magnitude of any interesting magnetic field invariably falls with the distance to its source, this increase in signal can be obtained by positioning the NV as close as possible to the target, which has the added benefit of increasing spatial resolution.

Spatial resolution is often less straightforward to define and the definition may depend on the type of sample being measured. Roughly it is the minimum distance between two features on the sample that can be resolved by the sensor. Likewise, it can be quantified as the area or volume of the sample that is responsible for a fraction X of the signal transduced by the sensor, where $X \approx 70\%$ is a typical cutoff. This definition is particularly useful for the imaging of an ensemble of target spins in a small volume as illustrated in Figure 1.19. Each spin s_i produces a classical dipolar magnetic field that falls off with its distance r_i to the NV, so the field along the NV axis is $B_i \propto 1/r_i^3$, neglecting here angular dependence for simplicity. Spins that are the closest to the NV, such as a few nanometers, will contribute more strongly to the total signal $B_{\text{tot}} = \sum_i B_i$ than spins that are far away. If a specific m spins contribute 70% of the signal and the

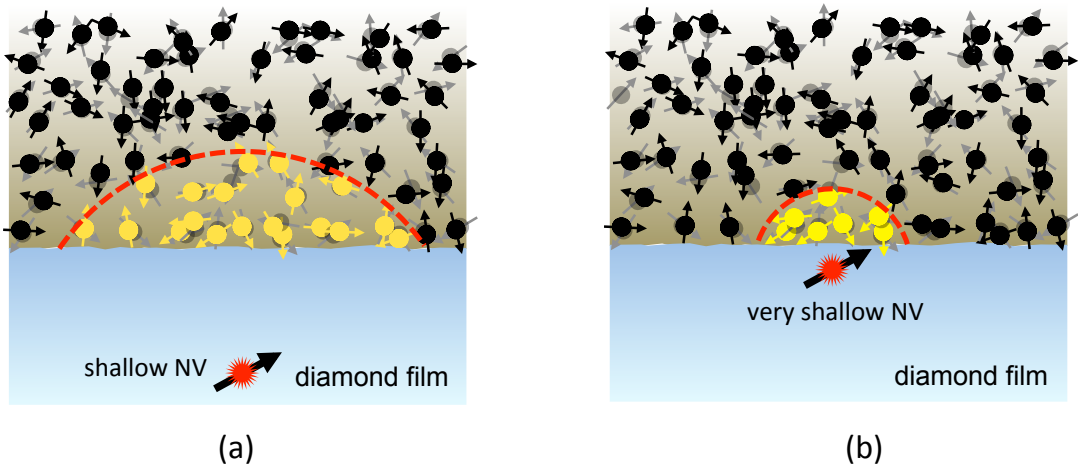

Figure 1.19: Illustration of spatial resolution for NV detecting ensemble spins in a target sample. (a) A NV within 10s of nanometers of the surface of diamond will experience a magnetic signal from an ensemble of spins placed on the surface, for example proton spins in an organic sample (brown region). The yellow-colored spins represent those that contribute strongest to the total magnetic signal detected by the NV, for example 70% of the total signal. This defines an effective spatial resolution because black-colored spins outside the dashed red boundary contribute relatively little signal. (b) An even shallower NV just a couple nanometers from the surface will detect a much larger total signal, and its sensitivity to just a few spins is greatly increased. Only a small volume of spins here contribute the majority of the magnetic signal, and therefore the effective spatial resolution is improved over the case shown in (a).

number density of spins is ρ_s, then the effective volume probed by the NV is $V \approx m/\rho_s$. If a fewer number of spins contribute the majority of the total signal then the effective volume probed becomes smaller.

From this discussion, it should be evident that the two quantities sensitivity and spatial resolution are inextricably linked in spin-sensing magnetometry because reducing the separation r between the sensing NV and the target spins can improve (i.e., reduce) both spin number sensitivity and spatial resolution. For this reason, to sense spins external to the diamond it is highly desirable to create NV centers a few nanometers from the diamond surface. This topic will be discussed in the next section and Chapter 3.

Below we derive in more detail the ac magnetic sensitivity of a NV to both phase-coherent and randomly fluctuating magnetic fields. This sensitivity is important for the sensing and imaging of electronic and nuclear spins, as we show later.

1.7.1 Sensitivity in detecting an ac magnetic field of fixed phase

First we consider the simplest case of the response of a NV to a square wave magnetic field of the form

$$B(t) = \begin{cases} B_0, & 0 < t < 1/(2\nu) \\ -B_0, & 1/(2\nu) < t < 1/\nu \end{cases} \tag{1.27}$$

that has perfect phase coherence. That is, the measurement is arranged so that B has the same phase at the beginning of each measurement shot. As discussed earlier, ac magnetic fields can be detected with a Hahn echo measurement with the $\pi/2 - \tau - \pi - \tau - \pi/2$ sequence timed such that $2\tau = 1/\nu$ so that $B(t)$ causes positive phase accumulation during both free precession periods. For this example, we alter the phase of the final $\pi/2$ pulse by 90° so that we have $(\pi/2)_x - \tau - (\pi)_x - \tau - (\pi/2)_y$. If a_0 and a_1 are the average number of photons collected from the $|0\rangle$ and $|1\rangle$ states, respectively, then the final $\pi/2$ pulse will project the phase to a population giving a signal between a_0 and a_1.

If $B_0 = 0$ then the phase is zero and the state remains on the x, y plane of the effective qubit Bloch sphere. The total number of photons collected after w repetitions of the measurement is

$$n(B_0 = 0) = \frac{1}{2} w (a_0 + a_1) \tag{1.28}$$

If the amplitude is now $B_0 > 0$ and the measurement is in phase with $B(t)$ with $2\tau = 1/\nu$ then the phase accumulated is over the total precession time is

$$\phi(\tau) = \frac{g\mu_B B_0}{\hbar} 2\tau \tag{1.29}$$

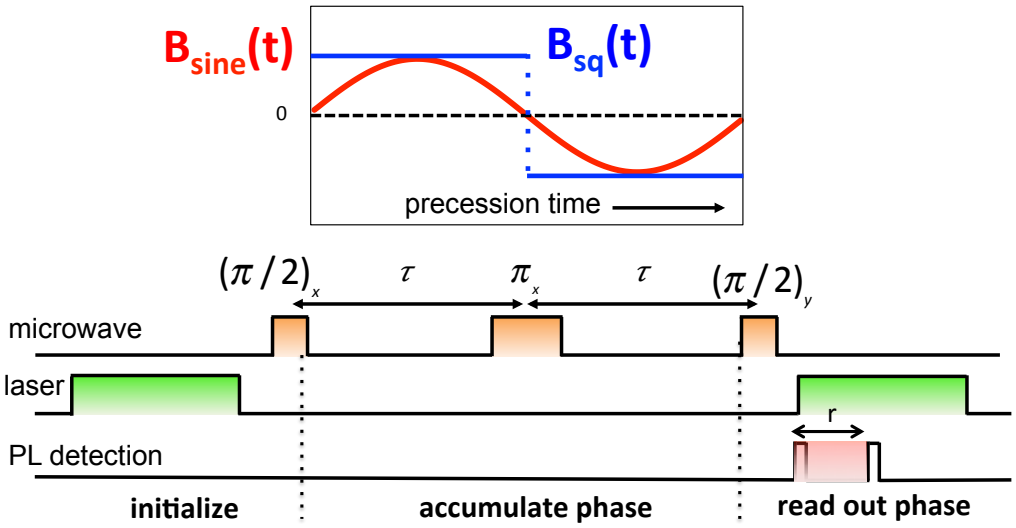

Figure 1.20: Magnetometry of ac fields via Hahn echo of a single NV. The NV is initialized into a superposition and its phase evolves during the precession time. When 2τ is matched the period of an oscillating magnetic field, here an in-phase square wave (blue) or sine wave (red), then maximal net phase accumulation occurs. Last, the collected phase is transferred to a population and read out. The PL readout here is typically $r = 350$ ns, after which the NV begins to polarize again. A $B_{\text{sine}}(t)$ could come from the precession of nuclear spins near the NV, though with unknown phase.

In this case, the final $(\pi/2)_y$ pulse causes the spin to raise out of the x, y plane of the Bloch sphere with the population angle $\theta = \phi(\tau)$. The total number of photons collected is

$$n(B_0 \neq 0) = \frac{1}{2} w \left[a_0 + a_1 + (a_0 - a_1) \sin\left(\frac{g\mu_B B_0}{\hbar} 2\tau \right) \right] D(\tau, T_2) \tag{1.30}$$

where we have included a coherence decay envelope $D(\tau, T_2) \in [0, 1]$. Here, we also see why the final $\pi/2$ pulse was chosen to have an opposite phase: the pulse causes the final population to follow a $\sin x$ function, which is linear in x for small x and therefore yields a larger signal than in a $\cos x$ case. In other words, the population, and thus PL, changes most rapidly with θ near the equator of the Bloch sphere. Let the signal be the difference

of the photon counts in Eqs. 1.28 and 1.30 so that

$$S\left(B_0\right) = n\left(B_0\right) - n\left(0\right) = \frac{1}{2} w \left[\left(a_0 - a_1\right) \sin\left(\frac{g\mu_B B_0}{\hbar} 2\tau\right)\right] D\left(\tau, T_2\right). \tag{1.31}$$

If the measurement noise is dominated by photon shot noise then

$$\sigma_n = \sqrt{n\left(B_0\right)} \approx \sqrt{n_0} = \sqrt{\frac{1}{2} w \left(a_0 + a_1\right)} \tag{1.32}$$

where the approximation assumes that B_0 is sufficiently small to give a small signal. The SNR is simply the ratio of Eqs. 1.31 and 1.32

$$\mathrm{SNR}\left(B_0\right) = \frac{S\left(B_0\right)}{\sigma_n} = \sqrt{\frac{w\left(a_0 - a_1\right)^2}{2\left(a_0 + a_1\right)}} \sin\left(\frac{g\mu_B B_0}{\hbar} 2\tau\right) D\left(\tau, T_2\right) \tag{1.33}$$

The minimum detectable B_0 is found when $\mathrm{SNR}\left(B_0\right) = 1$. We use the assumption that for small B_0 the accumulated phase is sufficiently small so that $\sin\phi \approx \phi$. Then

$$1 \approx \sqrt{\frac{w\left(a_0 - a_1\right)^2}{2\left(a_0 + a_1\right)}} \left(\frac{g\mu_B B_0^{\min}}{\hbar} 2\tau\right) D\left(\tau, T_2\right). \tag{1.34}$$

Solving for $B_0^{\min}$ and noting the total measurement time[12] is $T_\tau = 2\tau w$ gives the result

$$B_0^{\min} = \sqrt{\frac{2\left(a_0 + a_1\right)}{\left(a_0 - a_1\right)^2}} \left(\frac{\hbar}{g\mu_B \sqrt{2\tau T_\tau} D\left(\tau, T_2\right)}\right) \tag{1.35}$$

as the minimum detectable ac magnetic field amplitude in a total measurement time T_τ.

[12]This $T_\tau = 2\tau w$ is practically a minimum total measurement time, as it has excluded deadtime in the experimental measurement, such as initialization, metastble depopulation, and readout periods. However, it is a good approximation if the 2τ time is 10s or 100s of μs, since the deadtime can be less than 10 μs per shot.

Finally, the sensitivity is given by

$$\eta_{B,\text{square}} = B_0^{\min}\sqrt{T_\tau} = \sqrt{\frac{2\left(a_0+a_1\right)}{\left(a_0-a_1\right)^2}}\left(\frac{\hbar}{g\mu_B\sqrt{2\tau}D\left(\tau,T_2\right)}\right) \tag{1.36}$$

in typical units of $\mu\text{T}/\sqrt{\text{Hz}}$. We note that the final result Eq. 1.36 here does not depend on r, distance to the target, because it is strictly a magnetic sensitivity in $\mu\text{T}/\sqrt{\text{Hz}}$, with the field produced by an unspecified source. The goal is for sensitivity to be minimized, which Eq. 1.36 hints can be done by 1) increasing photon contrast $\sim (a_0 - a_1)$ of the two spin states, 2) maintaining coherence $D \sim 1$, 3) increasing the signal per shot with longer accumulation time 2τ, and 4) minimizing the total measurement time required by, for example, collecting more photons per shot. A typical photon count per shot may be $a_0 = 0.03$ and $a_1 = 0.02$, which after $w = 10^5$ measurements would lead to a photon shot noise of $\sigma_n = 50$ photons from Eq. 1.32. The pre-factor in Eq. 1.36 scales as $1/\sqrt{a_0}$, assuming $a_1 = ra_0$ for some contrast $r \in [0, 0.\bar{9}]$, which verifies that more photons per shot increases the sensitivity.

Assuming a sinusoidal magnetic field $B\left(t\right) = B_0 \sin\left(2\pi f t\right)$, rather than a square wave, gives a slightly reduced phase accumulation

$$\phi\left(\tau\right) = \frac{g\mu_B B_0}{\hbar}\int_0^\tau 2\left[\sin\left(\frac{2\pi}{2\tau}t\right)\right]dt = \frac{g\mu_B B_0}{\hbar}\frac{4\tau}{\pi} \tag{1.37}$$

that modifies the final sensitivity by a constant factor:

$$\eta_{B,\text{sine}} = B_0^{\min}\sqrt{T_\tau} = \sqrt{\frac{2\left(a_0+a_1\right)}{\left(a_0-a_1\right)^2}}\left(\frac{(\pi/2)\hbar}{g\mu_B\sqrt{2\tau}D\left(\tau,T_2\right)}\right) \tag{1.38}$$

1.7.2 Sensitivity in detecting a field of finite phase coherence

Next we consider the case of detecting an ensemble of nuclear spins that have a finite phase coherence time, that is, a potentially uncorrelated phase between measurement shots. The main idea for measuring small nuclear magnetic field signals is to extend the Hahn echo technique to a dynamical decoupling sequence to acquire more phase per shot by increasing T_2. For example, in this calculation we assume a volume of target spins is deposited on the diamond surface with number density ρ_{target}. The rms magnetic field from Larmor precession is detected by a single NV using a CPMG-like periodic pulse sequence with two-axis phase cycling that is appropriate for net NV phase accumulation.[13]

In the measurement to detect a field of random phase, the NVs phase accumulation is equally likely to be negative or positive. Therefore, to obtain a non-zero average signal the axis of the final $\pi/2$ rotation is always the same as the axis of initial $\pi/2$ rotation, the opposite of the case shown earlier in Fig. 1.20. That is, if the initial state after a $(\pi/2)_x$ pulse were $|+y\rangle = (|0\rangle + i\,|1\rangle)/\sqrt{2}$, then the accumulation of a tiny phase signal in either direction would leave the NV state quite close to $|+y\rangle$. Therefore, if one were to apply a $(\pi/2)_y$, then the read out population would just be 0.5 on average over many shots, giving no signal. A final $(\pi/2)_x$ pulse instead treats the two phase signals $\pm|\delta\phi|$ as equal populations for projective readout.

The target spins will have a finite coherence time T_c for Larmor precession, so that the correlation function is $\left\langle \tilde{B}\,(t)\,\tilde{B}\,(t')\right\rangle = B_{\text{rms}}^2 \exp\left(-\left|t-t'\right|/T_c\right)\cos\left(\omega_0\,(t-t')\right)$. We take τ here to be the total phase accumulation time of the NV per shot, so an echo sequence is $\tau/2-\pi-\tau/2$ and 4-pulse XY4 is $(\tau/8-\pi-\tau/8)_4$. The variance of the total

[13] We still consider zero-time pulses with no pulse errors in the calculation, so the phase cycling of π pulses here has no theoretical effect in the equations.

accumulated phase given NV gyromagnetic ratio γ is

$$\left\langle (\Delta\Phi)^2 \right\rangle_1 = \left\langle \gamma^2 \left[\int_0^{\tau/2} dt\tilde{B}(t) - \int_{\tau/2}^{\tau} dt\tilde{B}(t) \right]^2 \right\rangle \tag{1.39}$$

$$\left\langle (\Delta\Phi)^2 \right\rangle_4 = \left\langle \gamma^2 \left[\int_0^{\tau/8} dt\tilde{B}(t) - \int_{\tau/8}^{3\tau/8} dt\tilde{B}(t) + \int_{3\tau/8}^{5\tau/8} dt\tilde{B}(t) - \int_{5\tau/8}^{7\tau/8} dt\tilde{B}(t) + \int_{7\tau/8}^{\tau} dt\tilde{B}(t) \right]^2 \right\rangle \tag{1.40}$$

for echo and XY4, respectively. The alternating signs coincide with the π pulse timing. For XY4-N with any even number of pulses N, each double integral term has the form

$$c_{mn}c'_{kl} = \gamma^2 \int_{\frac{m\tau}{2N}}^{\frac{n\tau}{2N}} \int_{\frac{k\tau}{2N}}^{\frac{l\tau}{2N}} dtdt' \exp(-|t-t'|)\cos(\omega_0(t-t')) \tag{1.41}$$

where one of two cases applies for each term: (A) $n > m \geq k > l$ or (B) $(n = l) > (m = k)$. Applying Eq. 1.41 to the 1 and 4 pulse cases gives

$$\left\langle (\Delta\Phi)^2 \right\rangle_1 = c_{01}^2 - 2c_{12}c'_{01} + c_{12}^2 \tag{1.42}$$

$$\begin{aligned} \left\langle (\Delta\Phi)^2 \right\rangle_4 = {} & c_{01}^2 - 2c_{13}c'_{01} + c_{13}^2 + 2c_{35}c'_{01} - 2c_{35}c'_{13} + c_{35}^2 - 2c_{57}c'_{01} + 2c_{57}c'_{13} \\ & - 2c_{57}c'_{35} + c_{57}^2 + 2c_{78}c'_{01} - 2c_{78}c'_{13} + 2c_{78}c'_{35} - 2c_{78}c'_{57} + c_{78}^2 \end{aligned} \tag{1.43}$$

where the (B) cases are shortened to c_{nm}^2. The first integral (dt') of each (B) term is best computed by splitting up into two terms integrated on $t' \in \left[\frac{k\tau}{2N}, t\right]$ and $t' \in \left[t, \frac{l\tau}{2N}\right]$ due to the absolute value in the correlation function. In the (A) terms $t \geq t'$ always holds.

We make the assumption that the sensing interval τ is chosen to match the π pulse inter-delay to half the Larmor period. This is fairly general because experimentally we

can tune ω_0 by adjusting the externally applied field. Therefore $\omega_0 = 2\pi/\tau$ for echo and $\omega_0 = 4\pi/\tau$ for XY4. By making this substitution and computing the integrals in Eqs. 1.42 and 1.43, the results for the NV phase accumulation with finite field correlation time T_c are

$$\left\langle (\Delta\Phi)^2 \right\rangle_N = \gamma^2 B_{\mathrm{rms}}^2 \tau^2 h_N(\tau, T_c) \tag{1.44}$$

For $N = 1$ and $N = 4$ the h factor is

$$h_1(\tau, T_c) = \frac{2T_c}{\left(4\pi^2 T_c^2 + \tau^2\right)^2}[12\pi^2 T_c^3 + 4\pi^2 T_c^3 e^{-\tau/T_c} + 16\pi^2 T_c^3 e^{-\tau/2T_c} + 4\pi^2 T_c^2 \tau - 3T_c\tau^2 + T_c\tau^2 e^{-\tau/T_c} - 4T_c\tau^2 e^{-\tau/2T_c} + \tau^3] \tag{1.45}$$

$$h_4(\tau, T_c) = \frac{2T_c}{\left(16\pi^2 T_c^2 + \tau^2\right)^2}[\pi^2 T_c^3 \left(144 - 16e^{-\tau/T_c} + 64e^{-3\tau/4T_c} + 128e^{-\tau/2T_c} + 192e^{-\tau/4T_c}\right) - 32\pi T_c^2 \tau \left(e^{-7\tau/8T_c} + e^{-5\tau/8T_c} + e^{-3\tau/8T_c} + e^{-\tau/8T_c} - \pi/2\right) + T_c\tau^2 \left(-9 + e^{-\tau/T_c} - 4e^{-3\tau/4T_c} - 8e^{-\tau/2T_c} - 12e^{-\tau/4T_c}\right) + \tau^3]. \tag{1.46}$$

If we were to take $T_c \gg \tau$ (correlation time much longer than a measurement shot) in Eqs. 1.45 and 1.46 then the variance in phase accumulation, Eq. 1.44, reduces to

$$\left\langle (\Delta\Phi)^2 \right\rangle_1 = \gamma^2 B_{\mathrm{rms}}^2 \frac{4\tau^2}{\pi^2} \tag{1.47}$$

$$\left\langle (\Delta\Phi)^2 \right\rangle_4 = \gamma^2 B_{\mathrm{rms}}^2 \frac{4\tau^2}{\pi^2}. \tag{1.48}$$

With the first and last $\pi/2$ pulses around the same axis for a variance measurement, the state is returned fully to $|-1\rangle$ (or $|0\rangle$ for negative pulse) in the absence of any signal field, $B_{\mathrm{rms}} = 0$. Let the average number of photons collected per shot be a_0 for the

$|0\rangle$ state and ra_0 for the $|-1\rangle$ state. We can choose to measure with both $\pm\pi/2$ pulses over two consecutive shots to double the PL contrast while doubling the measurement time, so it does not alter the sensitivity, in principle. With the usual coherence decay D_N depending on the number of pulses N, these two types of measurements shots give photon counts of

$$\alpha_0 = \frac{a_0\left(1+r\right)}{2} + \frac{a_0\left(1-r\right)}{2} D_N\left(\tau, T_2, n\right) \tag{1.49}$$

$$\alpha_1 = \frac{a_0\left(1+r\right)}{2} - \frac{a_0\left(1-r\right)}{2} D_N\left(\tau, T_2, n\right). \tag{1.50}$$

τ is the total precession time per shot as in the results Eqs. 1.44-1.48.

Combining those results, the total signal in the presence of the target spin field B_{rms} is

$$S_N\left(B_{\mathrm{rms}}\right) \approx w\left(\alpha_0+\alpha_1\right) + w\left(\alpha_0-\alpha_1\right)\left(1 - \frac{\gamma^2 B_{\mathrm{rms}}^2 \tau^2}{2} h_N\left(\tau, T_c\right)\right) \tag{1.51}$$

where we have assumed a small $\left\langle \left(\Delta\Phi\right)^2 \right\rangle_N$ since we are interested in the limits of phase detection. The factor w is the number of measurement shots. If for clarity we disregard initialization, readout, and dead times, then the total measurement time is $T_{\mathrm{meas}} = w\tau$. Subtracting off background PL level, the signal-to-noise ratio assuming photon shot noise limited sensitivity is

$$\mathrm{SNR} = \frac{\left|S_N\left(B_{\mathrm{rms}}\right) - S_N\left(0\right)\right|}{\sqrt{\left|S_N\left(B_{\mathrm{rms}}\right) - S_N\left(0\right)\right|}} = \sqrt{\left|S_N\left(B_{\mathrm{rms}}\right) - S_N\left(0\right)\right|}. \tag{1.52}$$

Setting SNR = 1 gives the minimum detectable rms field B_{min}. We multiply by $\sqrt{T_{\mathrm{meas}}}$ to compute a magnetic field sensitivity

$$\eta_b = B_{\mathrm{min}}\sqrt{w\tau} = \frac{1}{\gamma}\left[\frac{2}{\tau_{\mathrm{op}} a_0\left(1-r\right)\exp\left[-\left(\tau_{\mathrm{op}}/T_{2,N}\right)^n\right] h_N\left(\tau_{\mathrm{op}}, T_c\right)}\right]^{1/2}. \tag{1.53}$$

Here $\tau_{\mathrm{op}} = n^{-1/n} T_{2,N}$ is the "optimal" sensing time obtained by maximizing the denominator factor $\sqrt{\tau}\exp\left[-(\tau_{\mathrm{op}}/T_{2,N})^n\right]$. In principle, this optimization can be done in terms of the correlation time T_c by including the complicated h_N factor.

To extend this analysis to arbitrary N pulses, the computationally difficult step for arbitrary T_c is finding $h_N(\tau, T_c)$. For long $T_c \gg \tau$, however, the increased number of π pulses simply enables phase accumulation proportional to N since the signal is essentially constant over one pulse sequence cycle. Therefore, if the N-pulse enhanced $T_{2,\mathrm{N}}$ and n exponent are known, then one can estimate the sensitivity straightforwardly. For a large enough number of pulses, $T_{2,\mathrm{N}}$ may become so long that it is similar to the nuclear spin coherence time T_c and the full form of h_N is then relevant. N-pulse sensitivity analyses have been shown in refs. [3,10] for (1) coherent and (2) phase incoherent lab-supplied fluctuating fields (for a case where essentially correlation time is much longer than (1) measurement time or (2) shot time τ).

As a concrete example for a shallow NV measured in Chapter 4, we compute the result of Eq. 1.53 for experimental parameters obtained from a 12.4 nm deep NV: $N = 256$, $T_{2,\mathrm{N}}$= 480 μs, $n = 1.4$, $a_0 = 0.035$, $r = 0.7$, and assuming $T_c \gg \tau$ (again note in this section τ is the total precession time). This a_0 refers to a count rate of 100 kPhotons/s in a 350 ns readout window. These parameters yield $\eta_B = 9.4\ \mathrm{nTHz}^{-1/2}$, where the optimum free precession sensing time is $\tau_{\mathrm{op}} \approx 377\ \mu$s, which is suitable to detect a field oscillating with $f = N/(2\tau_{\mathrm{op}}) \approx 340$ kHz. This is an easily accessible nuclear Larmor frequency, for example, achievable by tuning the externally applied magnetic field; $B_0 \approx 80$ G would be required for proton spins. Chapter 4 discusses this proton sensing DD further as a technique for finding the distance of a NV to the diamond surface using XY8-N.

1.7.3 Sensing and imaging with spin relaxation

The above examples discuss sensing of an ac field that is at least phase coherent over part of a measurement shot, and the frequencies accessible to sensing by dynamical decoupling are of the order of 10s of kHz to a few MHz as determined by typical T_2 times and inter-pulse delays. However, fluctuating fields at higher frequencies matched to the NV transition energies, such as 10s of MHz to several GHz, can be sensed by the effect on spin relaxation rates between the NV sublevels. The sensitivity of this technique depends on many of the same factors, such as photon collection efficiency and the PL contrast. A main difference is that a longer shot time, or $\tau \sim T_1$, does not increase the time that a signal accumulates since no phase is measured. However, longer T_1 does improve SNR since the spin population contrast is large if the intrinsic NV $T_{1,\mathrm{int}}$ is much longer than the $T_{1,\mathrm{sig}}$ in the presence of the noise. The optimal sensing time tends to be of the order $\tau_{\mathrm{op}} \sim T_{1,\mathrm{sig}}$, since this value maximizes PL contrast without increasing the time per shot too significantly. In chapters 5-7 we develop this technique for noise spectroscopy and imaging.

1.8 Conclusions

We have motivated the use of a single near-surface NV center in diamond as a room-temperature quantum sensor of ac and dc magnetic fields and electromagnetic noise for sensing and imaging with nanoscale spatial resolution. We have reviewed the enabling capabilities of NV centers at room temperature, including individual addressability, optical spin polarization and readout, coherent spin control, and long spin coherence and relaxation times. The same qualities that are desired for a good qubit are much the same as those needed for a quantum sensor. The rich Hamiltonian of the NV center makes it a potential sensor of magnetic fields, electric fields, strain, and temperature. With these

versatile capabilities for sensing comes the double-edged sword of decoherence, however, as the NV is susceptible to a host of noise sources. By placing NVs extremely close to the surface, for sensing nanoscale entities outside the diamond, the NV experiences, in addition, surface-related noise sources that we study in the remainder of this dissertation.

In the next chapter, the components of the scanning NV diamond magnetometer instrument are described (Chapter 2). The following chapters describe the engineering of shallow NV sensors (Chapter 3), scanning probe imaging measurements of the NVs' nanoscale depths (Chapter 4), coherence and relaxation based characterization of diamond surface noise spectra that affect magnetic sensitivity (Chapters 4 and 5), and lastly, nanoscale scanning probe imaging experiments based on measuring the decoherence of a single NV center placed in nanoscale proximity to gadolinium electronic spins (Chapter 6) and various metallic surfaces (Chapter 7).

Chapter 2

Experimental setups: scanning NV magnetometers

The experimental setups for each of the scanning-NV magnetometry measurements in this dissertation have a few key components allowing for ODMR characterization, spin control pulse sequences, and nanoscale spatial positioning of the NV with respect to a target sample. A homebuilt confocal fluorescence microscope (CFM) with microwave electronics was used to optically locate single NV spins in diamond, initialize and read out their spin state, and coherently manipulate the spin. An atomic force microscope (AFM) was combined with each CFM for NV-based scanning probe microscopy of magnetic fields and electromagnetic fluctuations.

Two scanning probe magnetometers were constructed for the experiments, both operating in ambient conditions. The primary technical differences are compared in Fig. 2.1:"Magnetometer A" uses an optical-based silicon cantilever detection in a commercial AFM and "Magnetometer B" uses electrical detection of a quartz cantilever as a custom AFM. Magnetometer A is in lab Broida 4209 and was used for the experiments of Chapter 4, and additionally in the $^{13}C/^{12}C/^{13}C$ measurements of Chapter 3. Magnetometer

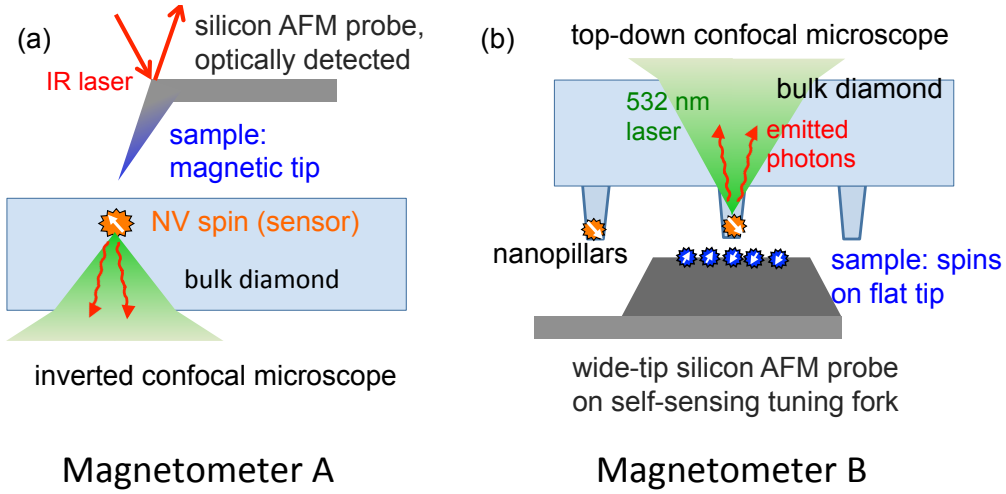

Figure 2.1: Schematics of scanning-NV magnetometers A and B. Both setups are combined scanning-laser confocal microscopes with an atomic force microscope (AFM). Both setups have the optics and AFM addressing the diamond from opposite sides, with the AFM on the side with near-surface NVs. Differences include the orientation of top-down or bottom-up AFM and the use of optically detected cantilever in (a) and a self-sensing piezoelectric tuning fork in (b).

B is in the east side of lab Broida 1219 and was used for the experiments in Chapters 5, 6, and 7.

In the present chapter, we first introduce the general concept of confocal microscopy and then describe the parameters that are important for imaging NV centers. We also list the limitations of confocal microscopy that preclude its use for imaging the nanometer-scale depth of NV centers in diamond. We then introduce atomic force microscopy and describe the useful features of this technique to NV-based nanoscale electromagnetic imaging. In the last sections, we describe the implementation and control of the combined CFM and AFM experiments.

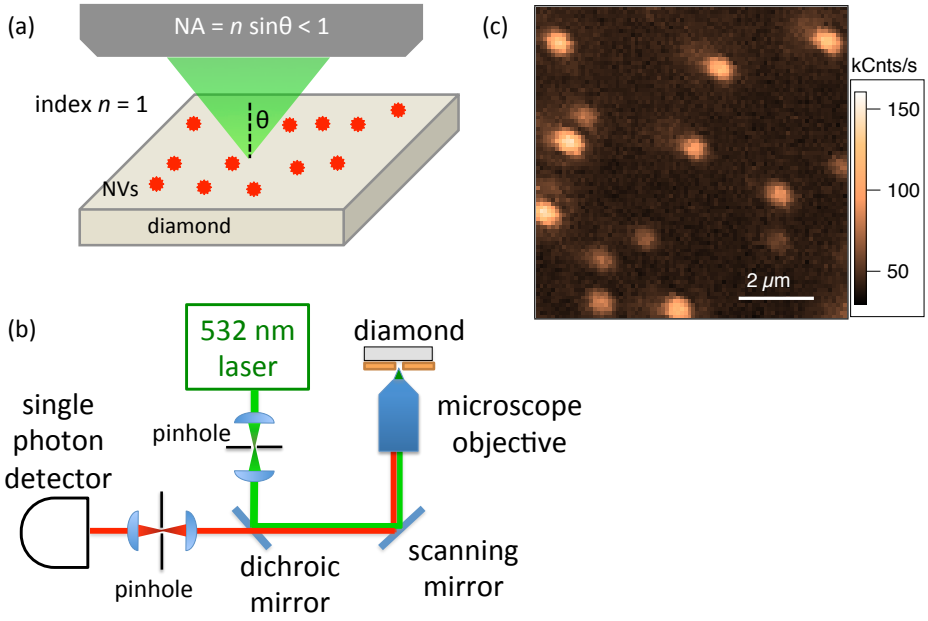

Figure 2.2: Confocal microscopy for optically addressing single NVs. (a) Cartoon of a microscope objective focusing a green laser onto the surface of a diamond chip. NV centers emit red fluorescence when illuminated. The numerical aperture (NA) indicates the angle of collection in a given immersion medium, here air. (b) Basic schematic of the confocal microscope for optically imaging single NV centers. The pinholes reject diverging light so that a thin optical slice is imaged with minimal out-of-plane illumination and background fluorescence. Scanning mirrors guide the focused spot to acquire an image pixel-by-pixel. A dichroic mirror transmits collected red photons to a detector. (c) Scanning confocal fluorescence image of several single near-surface NV centers. Image acquisition of this scan size typically requires 20-120 seconds for 6400 pixels, depending on desired signal-to-noise ratio and laser power.

2.1 Laser scanning confocal microscope

2.1.1 Spatial resolution in optical microscopy

Confocal microscopy was developed over the last several decades to address specific limitations of conventional light microscopes for imaging the fluorescence of biological specimens [160]. A key advance made possible by the confocal microscope is the capability to image sub-micron depth slices of a specimen through simple manipulation of optical components, that is, minimally invasive optical sectioning of a thick sample (thickness microns to millimeters). Thus, the advantage of a confocal microscope is its narrow axial resolution, which will allow us to image single NV centers over the background light from surrounding sample. In any basic optical microscope, the objective lens that collects light from the sample under study is the most critical component that determines the spatial resolution and signal-to-background of the acquired image. An objective's numerical aperture (NA) is given by

$$\mathrm{NA} = n \sin\theta \tag{2.1}$$

where n is the index of refraction of the medium outside the lens (usually $n \approx 1$ for air or $n \approx 1.5$ for oil) and θ is the maximum angle of light accepted by the lens from a source at its focal point, as depicted in Fig. 2.2(a). Therefore, an objective with larger NA can collect a greater fraction of the fluorescence from an emitter, such as a single NV center, and thereby potentially enable higher photon collection rates, better signal-to-noise, and improved spatial resolution, as explained below.

The primary technical and operational differences of a laser-scanning confocal microscope in comparison to a conventional light microscope are 1) the introduction of a pinhole in both the illumination (or excitation) and detection (or collection) paths and 2) the acquisition of an image pixel by pixel by scanning the illumination and collection

spots concurrently. Figure 2.2(b) shows a basic schematic of the confocal microscope. In ideal confocality ("having the same focus point") the illumination and detection point spread functions, $\mathrm{PSF}_{\mathrm{ill}}(x, y, z)$ and $\mathrm{PSF}_{\mathrm{det}}(x, y, z)$, are determined by two point sources and take a comet-like rotationally symmetric shape. The PSFs can be thought of as the probability for a photon to "hit" a volume unit of the sample ($\mathrm{PSF}_{\mathrm{ill}}$) and for a photon to be detected ($\mathrm{PSF}_{\mathrm{ill}}$). In practice these points are generated by focusing the illumination and detected light each through apertures of diameter on the order of the optical diffraction-limited spot size.

Expressions for the lateral resolution of a microscope, or extent of the lateral PSF, have the general form

$$\phi_r = \frac{k\lambda}{\mathrm{NA}} \tag{2.2}$$

where λ is the illumination wavelength for confocal microscopy and NA is the objective lens numerical aperture. k is a number of order 1 used to quantify a criterion for defining a theoretical resolution or used to describe a practical achieved resolution. Eq. 2.2 may be used to refer to a spot diameter or a radius for the minimum distance between a diffraction minimum and maximum. For our purposes a useful reference is the Airy unit diameter $1\mathrm{A.U.} = 1.22\lambda/\mathrm{NA}$ for the diffraction-limited spot size of a uniform beam illuminating the back aperture of the objective lens. For excitation light of $\lambda = 532$ nm and $\mathrm{NA} = 0.95$, the Airy diameter result is $\phi_r \approx 680$ nm, so the minimum resolvable distance between two points is about $\phi_r/2 = 340$ nm. In practice the minimum resolvable distance could be made smaller with image processing. For example, if the lateral PSF for a single point is known from measurement then a deconvolution procedure could be use to deduce the positions of the constituent objects each having the same PSF individually [160]. However, nonideal illumination beamshapes, imperfections in the optical path components and various resulting aberrations, as discussed below, can conversely cause a

significant enlargement of the PSF compared to the ideal case. In summary, the confocal microscope's lateral resolution is not typically any different from that of a conventional microscope, with the minor exception in the wavelength λ used in Eq. 2.2 for each case.

The real advantage of a confocal microscope comes from discrimination in the axial direction. For axial resolution of a general microscope, the distance of the intensity peak to first diffraction minimum gives a radius

$$z_{\min} = \frac{2n\lambda}{\mathrm{NA}^2} \tag{2.3}$$

where n is the index of refraction of the lens immersion liquid [160]. The optical depth of field is

$$\phi_z = \frac{1}{4}\left(z^+_{\min} - z^-_{\min}\right) = \frac{1}{2}z_{\min} = \frac{n\lambda}{\mathrm{NA}^2} = 1\mathrm{R.U.} \tag{2.4}$$

where R.U. stands for Rayleigh unit. In a conventional microscope, stray fluorescence and background light from other z planes will effectively increase the depth of field beyond Eq. 2.4. However, the addition of a confocal detection pinhole can improve the contrast to meet the ϕ_z limit in Eq. 2.4, which is why for a confocal microscope Eq. 2.4 is often called the axial resolution [160, 161, 162]. Hence, the optical slice thickness can be quantified in R.U. Confocal microscopy does not increase the lateral resolution beyond conventional microscopy unless the pinhole is quite small compared to 1 A.U. [160], which is not the optimal case of interest for imaging NVs.

2.1.2 Confocal design considerations for imaging individual NV defects

The purpose of the confocal microscope for addressing individual spin defects in a crystal is to reject background photoluminescence and other stray light originating from

z-slice planes outside of the desired imaging plane. Therefore the signal to noise ratio (or contrast) may be increased and z scan imaging also becomes possible. The first demonstration of applying confocal microscopy to resolve single NV centers was reported in 1997 [3]. Because NVs can be formed with lateral NV-NV displacements of microns from one another, lateral resolution is only a central concern for single-NV studies when the NV density is sufficiently large [163, 164] or for ensemble NV magnetometry with diffraction-limited spatial resolution [5, 165, 27, 28].

We focus here on a few interrelated design considerations to optimize the performance of a confocal microscope for the NV imaging application. These points are not necessarily in order of importance.

1. **Pinhole diameter:** The diameter of the collection pinhole, D_{ph}, should be chosen to obtain an optimal balance between rejection of background light from other fluorescent planes in the sample (decrease diameter) and maintaining a large enough fraction of the signal from the desired emitter (increase diameter). One rule of thumb is to choose the pinhole diameter to be at least 30% larger than the spot size focused onto the pinhole. This specification comfortably allows the first diffraction peak to pass through the clear aperture with some practical tolerance for axial or transverse misalignment of the focused spot on the pinhole. We next explain the reasoning for this choice of diameter.

   In theory, D_{ph} should be roughly equal to the size of the Airy spot (1 Airy unit = 1 A.U.) formed by the lens focusing the fluorescence onto this pinhole. We aim towards a larger diameter D_{ph} since background from deeper fluorescent emitters is less of a concern than it might be for imaging a truly three-dimensional specimen. We primarily measure diamond samples where the NVs are concentrated, by design, within 200 nm of the surface; at deeper positions there is a very low density of NVs

at perhaps less than 1 per 10×10 μm^2.

For $D_{\mathrm{ph}} > 1$ A.U., the depth discrimination is mainly based upon geometric-optical confocality. The PSF of the detection optics is generally larger because emitted photoluminescence wavelengths $\lambda_{\mathrm{pl}} > \lambda_{\mathrm{ill}}$. Hypothetically, as D_{ph} decreases then $\mathrm{PSF}_{\mathrm{det}}$ approaches $\mathrm{PSF}_{\mathrm{ill}}$ from above until the limit $\mathrm{PSF}_{\mathrm{det}} \approx \mathrm{PSF}_{\mathrm{ill}}$ at $D_{\mathrm{ph}} \approx 0.25$ A.U., and at that point depth discrimination is determined by wave-optical confocality [161]. We will be concerned only with the geometric confocality case ($D_{\mathrm{ph}} > 1$ A.U.) to detect as much NV PL as possible.

The following expression quantifies the modification of the detected optical slice thickness, or axial resolution full width at half maximum (FWHM), according to the diameter of the detection pinhole [161]:

$$\mathrm{FWHM}_{\mathrm{axial}} = \left[\left(\frac{0.88\lambda_{\mathrm{pl}}}{n - \sqrt{n^2 - \mathrm{NA}^2}} \right)^2 + \left(\sqrt{2} \frac{n D_{\mathrm{ph}}}{\mathrm{NA}} \right)^2 \right]^{1/2} \tag{2.5}$$

with all parameters as defined before. Equation 2.5 is valid when $D_{\mathrm{ph}} > 1$ A.U. so that geometric confocality, the second term, is dominant. The wave-optical term is constant for given objective parameters n and NA, and it depends on the photoluminescence emission wavelength λ_{pl}, as in a conventional microscope. A plot of Eq. 2.5 is shown in Fig. 2.3 for an experimentally relevant range of D_{ph}.

The physical spatial filter used as the pinhole can either be a simple free-space aperture or a single-mode fiber. Fibers in principle have larger losses from imperfect coupling, about $70 - 80\%$ transmission, but they are also much simpler to use for alignment of the confocal microscope. For example, an excitation fiber can decouple the optics alignment of the excitation path from the rest of the setup so that modular changes can be made more efficiently, such as changing out the laser

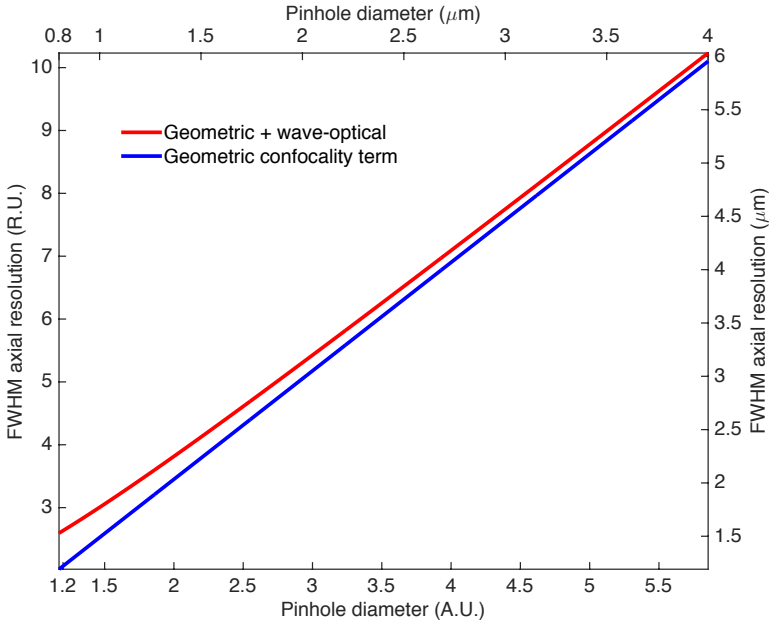

Figure 2.3: Calculation of the axial resolution of a confocal microscope according to Eq. 2.5, plotted against the diameter of the detection pinhole D_{ph}. The Airy units and Rayleigh units were computed with an excitation wavelength 532 nm, and the wave-optical contribution was computed with a PL wavelength $\lambda_{\mathrm{pl}} = 750$ nm. The parameters are for an air objective UPLSAPO40X2 from Olympus with NA= 0.95 and $n \approx 1$. Geometric optics of the confocal pinhole contributes most to the optical slice thickness at pinhole diameters $D_{\mathrm{ph}} > 1$ A.U. used for the NV experiments. The actual pinhole diameter will be larger by the factor of magnification from lenses between the objective and pinhole, which for a simple laser-scanning CFM layout is ordered as objective, tube lens, scan lens, pinhole-focusing lens.

source.

2. **Objective lens**: The microscope objective must be chosen carefully to suit the application. Parameters to consider include numerical aperture (NA), chromatic aberration correction, flatness of field, air versus oil immersion, back aperture size, and transmission spectrum. In addition, the spherical aberration correction, working distance, and coverslip correction collar specification should be well suited to a particular diamond thickness if imaging through microns to > 100 μm of diamond. To image single NVs, we desire an NA greater than ~ 0.7. This number should be

chosen as close to 1 as possible, the limit for a dry objective, to achieve adequate collection efficiency from NVs. An objective with larger NA generally has a smaller working distance. An example of a NV application where a longer working distance of millimeters may be necessary is in a diamond scanning probe [66, 36, 71] where the AFM probe must fit between the lens and the sample, or in the case of an objective outside a cryostat window [68]. However, for the magnetometers in this dissertation work we primarily imaged through a bulk diamond from the opposite side as the AFM, and we chose the highest NA for air (0.95) or oil immersion (1.49). These arrangements are shown in the later sections of this chapter.

Chromatic aberrations occur in any real lens because the index of refraction is a function of wavelength. For our CFM, we excite with 532 nm and collect photons above 630 nm, which makes chromatic aberration a particular concern for confocality in the axial direction. An achromatic objective contains lens doublets or triplets with a set of specific curvatures, n values, and thickness are designed to make the focal planes of disparate colors coincide. Apochromats have corrections to achieve multiple coinciding wavelengths at the focus point. The need to collect a wide band of NV PL between 650-800 nm means it is helpful to have apochromatic correction. Objectives with "plan" correction also ensure a relatively flat imaging field over 10s of microns. Although NVs are point emitters, this flat imaging plane is still very useful for ease of use and various calibration purposes, including for AFM scanning distance calibration and alignment.

The **transmission spectrum** of the objective should also extend far enough into the near-IR to collect more of the NV phonon sideband PL. Generally above 80% is available over these wavelengths.

When looking through any substantial **thickness of diamond** (more than ~ 10

microns of the high-refractive-index material), one must consider spherical aberrations that become more severe with increased focusing depth below the surface of incidence. This consideration is relevant to both of our magnetometers, in which we focus and collect light from the CFM through 20-150 μm so that the AFM is free to approach the NV-containing surface side. We must consider the objective parameters for each diamond thickness individually. The NA, working distance, coverslip correction collar, and immersion medium are all important considerations for matching the objective to a particular diamond plate thickness and the related method of mounting the diamond.

For a large NA, the paraxial approximation is not valid to describe focusing into diamond and this problem should be addressed by wave-optical calculations. Figure 2.4 shows an example of a series of wave-optics simulations in Matlab using the integral method for focusing a collimated beam into a diamond slab for different types of objectives [166, 167, 168]. As the objective lens moves closer to the diamond, the focusing depth increases and the spherical aberrations are seen as a lengthening tail of intensity deeper than the main peak. This aberration effectively spreads out the PSF axially and reduces intensity. By comparing results for NAs of 0.65 to 0.95, it is suggested that the extra marginal "rays" at higher NA cause this tail to be more pronounced. However, as long as the main peak remains discriminated then the effect on resolution for a confocal microscope is not as severe as for a conventional microscope because the detection pinhole can reject much of the tail. The trade-off of using a higher NA is that more of the signal occurs outside this peak so the total signal suffers, whereas in a conventional microscope the effect is blurring of the image. Increasing the size of the pinhole too far beyond $D_{\mathrm{ph}} \approx 1$ A.U. will make the CFM more like a conventional microscope in the sense that the

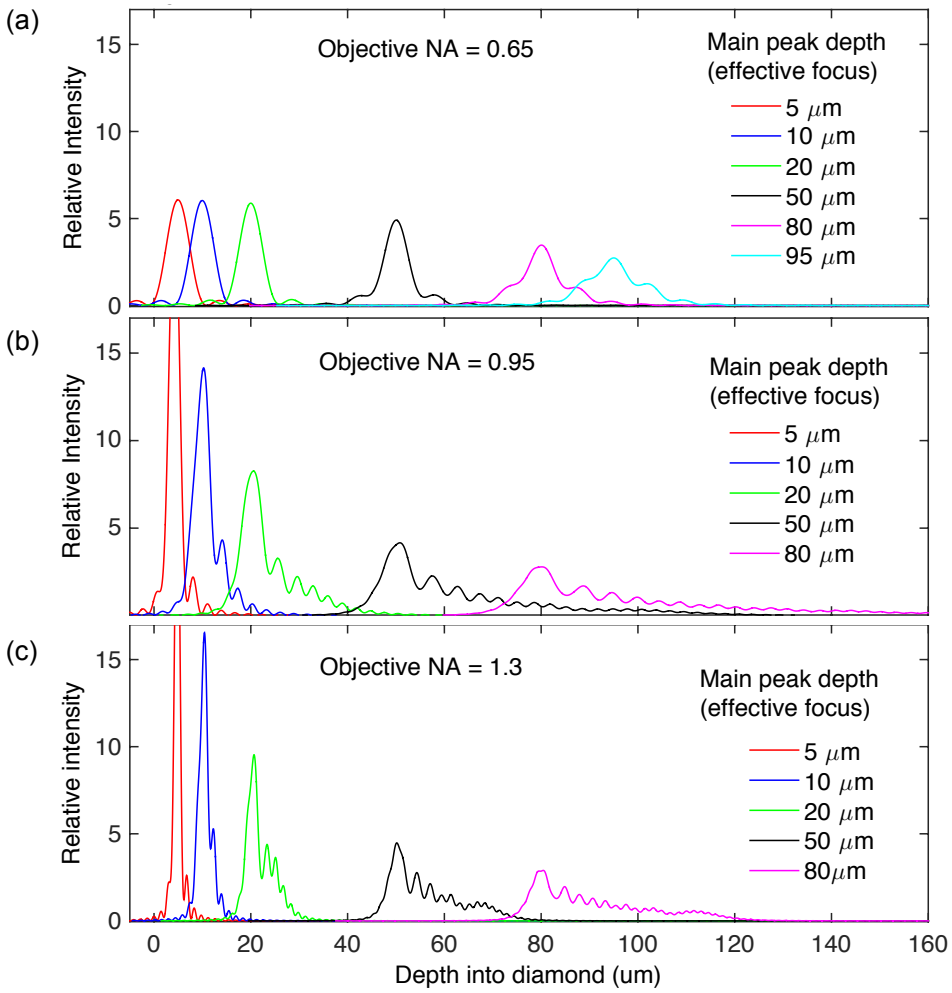

Figure 2.4: Numerical wave-optical calculations of the aberrations resulting from focusing collimated light into diamond. Plotted is the axial intensity PSF of 532-nm light in the diamond at $(x = 0, y = 0, z)$ for objective NAs of 0.65 (a), 0.95 (b), and with oil immersion 1.3 (c). For larger NA (b,c) the axial tail is longer, but with the addition of a confocal detection pinhole the main peak can be isolated. The calculations were performed numerically in Matlab, following the wave-optical integral methods in references [166, 167, 168] for focusing into dielectric slabs.

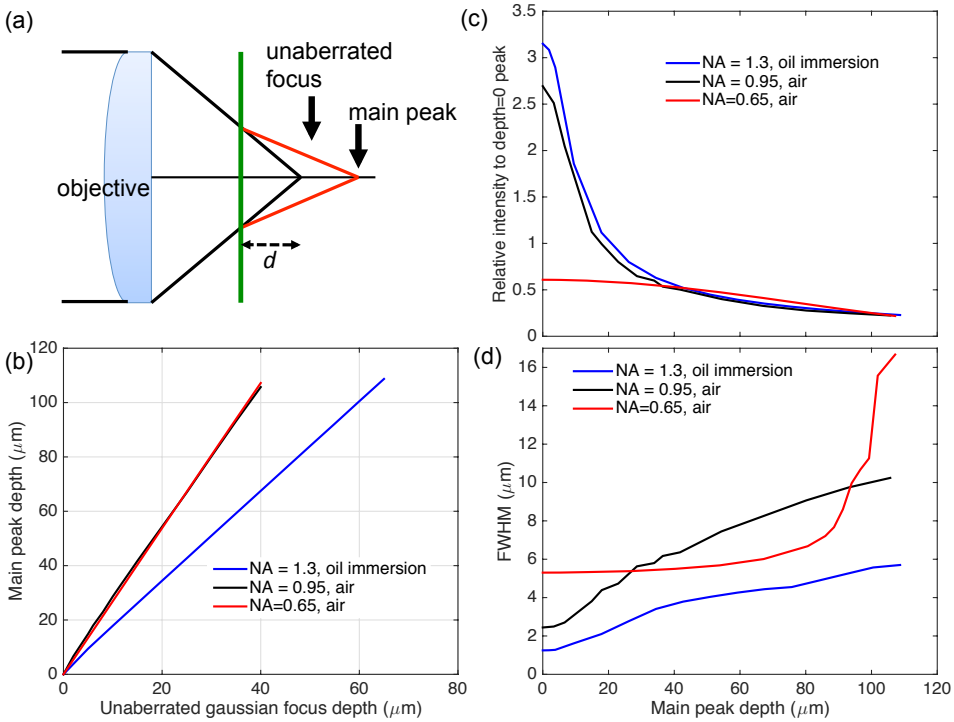

Figure 2.5: Summary of the main-peak characteristics of the wave-optical calculations shown in Fig. 2.4. (a) Schematic of focusing into a diamond slab, where the main intensity peak is shifted deeper than d. (b) Focus shift as a function of objective z translation. (c) Intensity and (d) axial FWHM of the main peak versus the z position of the peak below the surface.

tail-like aberrations begin to affect the axial resolution [162].

Figure 2.5 summarizes the upshots of Fig. 2.4 calculations. For air objectives, the main intensity peak is shifted approximately $2.6 - 2.7\times$ further into diamond than the unabberated focus peak (that is, the focus position in air). For a smaller index change from oil (1.5) to diamond (2.4), the focus shift is about $1.7\times$. The intensity and axial FWHM of the main intensity peaks are shown in Figs. 2.5(c,d). The main conclusions are 1) that higher NA focuses more excitation power in the main peak as long as the focusing is not many 10s of microns into diamond and 2) that the axial FWHM is also narrower for higher NA and in oil as long as focusing is not too deep. These results show, for example, that an oil immersion objective with high NA can look through even 40 μm of diamond and still maintain an axial FWHM of a few microns. We chose an oil immersion lens of NA = 1.49 for looking through diamonds of thicknesses 20-40 μm using Magnetometer A, as discussed in a section below.

The **coverslip correction collar** of an objective is also very useful for imaging through diamond. Typically this correction collar is meant to be set to the thickness of the glass ($n \approx 1.5$) between the objective and sample under study, for example 0.17 mm. This collar adjustment shifts internal lenses such that the imaging resolution, cylindrical symmetry, and perhaps confocality of the focused spot is optimized. For Magnetometer B, the use of this collar in an air objective (Olympus UPLSAPO40X2) was vital to achieving excellent signal-to-noise of the collected NV PL while imaging through about 150 μm of diamond. The correction collar was set to approximately 0.11 mm and adjusted as needed for variations in diamond sample thicknesses.

3. **Beam diameter**: The back aperture diameter of the objective is important for

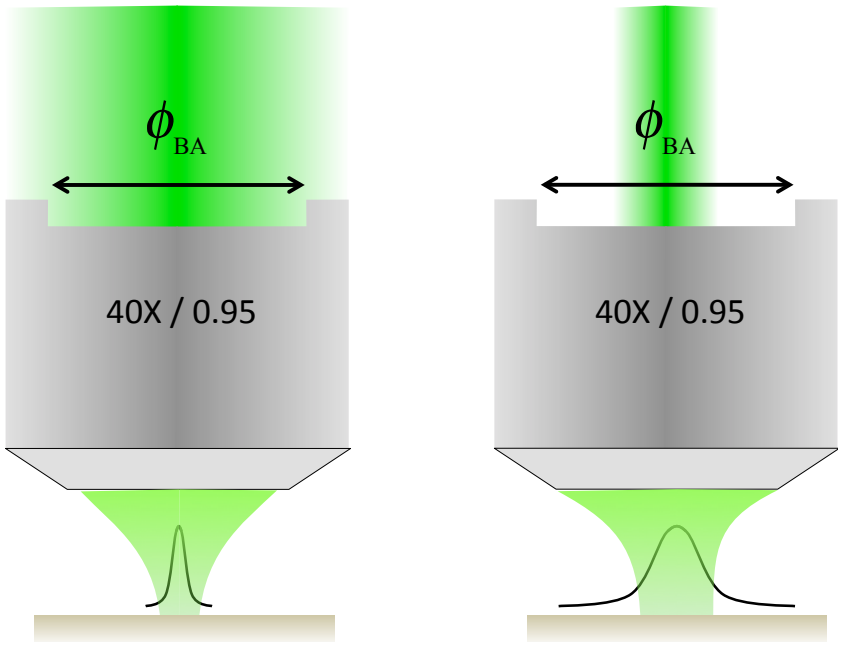

Figure 2.6: Cartoon of filling the objective back aperture with illumination beam. The back aperture diameter ϕ_{BA} is specified in Eq. 2.6, based on vendor-specified magnification and NA. As shown in calculations summarized in Fig. 2.7, overfilling the back aperture with the illumination beam (left) gives the best lateral and axial resolution, while underfilling (right) gives poorer resolution.

two main reasons. 1) It defines the red emission beam size and therefore determines the optimal diameter D_{ph} of the collection pinhole. 2) Optimized lateral and axial resolutions for NV imaging can be achieved if the green illumination beam fills the back aperture of the objective appropriately. In analogy to choice of pinhole size, the filling fraction of the back aperture with the illumination beam has a trade-off. Most importantly, if the collimated incoming beam is too small then spot focused by the objective is large and resolution suffers. However, if the incoming beam is too wide then the illumination is not an efficient use of optical power since a large portion of the Gaussian beam is then clipped by the aperture. In other words, the ideal Airy disk result for uniform illumination is neither practical nor necessary. We first discuss calculation of the back aperature size and then compute effects of the filling fraction.

Modern microscope objectives contain a complex array of lenses, though they are designed to operate in some ways like a single thin lens, highly corrected for aberrations. The back aperture diameter can be measured simply with a metric ruler, however, for choosing an objective, a simple design formula also relates the back aperture diameter to the magnification of the objective when paired with the manufacturer's standard tube lens focal length:

$$\phi_{\mathrm{BA}} = 2\mathrm{NA} f_{\mathrm{obj}} = 2\mathrm{NA}\frac{f_{\mathrm{tube,v}}}{M_{\mathrm{v}}} \tag{2.6}$$

where the effective objective focal length f_{obj} is not typically specified by the vendor. The tube lens length $f_{\mathrm{tube,v}}$ and magnification M_{v} are specified by the vendor; for Olympus $f_{\mathrm{tube,v}} = 180$ mm and for Nikon $f_{\mathrm{tube,v}} = 200$ mm. Typical M_{v} values for high-NA objectives are 40×, 60×, and 100×. These M_{v} result in effective focal lengths $f_{\mathrm{obj}} = 1.8$, 3.0, or 4.5 mm for Olympus, and typical apertures $\phi_{\mathrm{BA}} \approx 4 - 9$

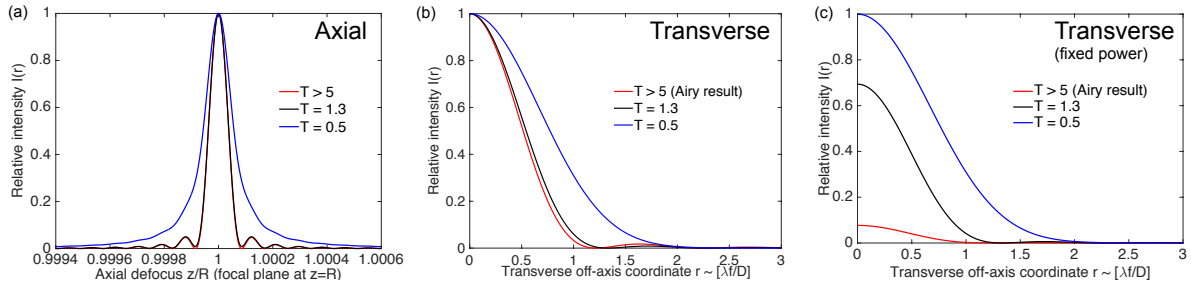

Figure 2.7: Calculation of microscope resolution for different objective back aperture illumination spot sizes relative to the aperture size. The truncation factor is $T = w/a$ where w is the Gaussian illumination beam radius and a is the objective back aperture radius. (a) Axial resolution improves for $T \gtrsim 1$ and there is little improvement for a more uniform beam. (b) Transverse resolution shows the same qualitative trend versus T. (c) Same as in (b) but for constant power in the illumination spot for the three cases, showing that the disadvantage of a very broad and uniform illumination (e.g., $T \sim 5$) is the truncation of most of the input power. For clarity these calculations are for focusing in air, so they do not include aberrations from diamond.

mm. The tube lens used in the custom laser-scanning CFM does not have to be matched to the tube length specified by the manufacturer, although of course ϕ_{BA} itself is fixed from the design formula Eq. 2.6. We used different $f_{\mathrm{tube}} \neq f_{\mathrm{tube,v}}$ in our CFMs due to distance requirements, which primarily just changes the effective magnification $M \neq M_{\mathrm{v}}$. An illustration of the tube lens arrangement with the objective is shown in Fig. 2.8.

Figure 2.7 shows examples of calculations relating the width of a Gaussian beam to the focused spot linewidth in the transverse and axial directions. The truncation factor $T = w/a$ is the ratio of the beam waist diameter to aperture diameter. These calculations show that the resolution greatly improves as T increases from 0.5 to 1, however, the linewidth only moderately improves beyond that point. Therefore, for laser power efficiency it is practical to only slightly overfill the back aperture, for example $T \approx 1.3$ [169, 170].

4. **Laser source:** The excitation laser for the room-temperature confocal imaging of

NVs has less stringent requirements than for most quantum-optical control techniques for atoms because here we do not use optics for actual Rabi nutations. However, there are a few helpful specifications. Laser wavelength, although used as non-resonant excitation, has been found to affect the NV negative charge state and fluorescence contrast is optimized for a wavelengths of about 510-540 nm [114]. We use $\lambda = 532$ nm, which is widely available in diode-pumped solid-state lasers, and recently, diode lasers at 520 nm and 532 nm have become available. For home-built CFM optics setups, it is convenient to have 50-200 mW of power available to tolerate fiber, lens, and mirror losses and allow some power tuning range, though the initial power must be attenuated enough as not to damage the acousto-optical modulator (AOM). Typical power is 0.5-2 mW into the objective back aperture for NV saturation and much less (~ 10 μW) can be used if the diamond is nanostructured to enhance the collection efficiency [78, 171]. Although a single longitudinal mode and narrow-frequency laser line is not necessary, having the laser output a single non-elliptical transverse Gaussian mode is helpful for imaging though it can also be cleaned up by coupling into a well-matched single-mode fiber in the excitation path. Finally, specification of low amplitude noise (rms $< 1\%$) helps towards the goal of shot-noise limited detection of NV PL.

5. **Other design considerations for NV imaging:** Other components include dichroic mirrors, lens antireflection coatings, and mirrors that must all be chosen to maximize transmission of NV PL through the collection path and rejection of background light. For example, coated dielectric mirrors are generally better for maximized reflection of red light than silver mirrors. APDs need to have low dark counts ($\lesssim 100$ count/s) and be sensitive in the NV's emission range at wavelengths above the zero-phonon line (ZPL) 637 nm.

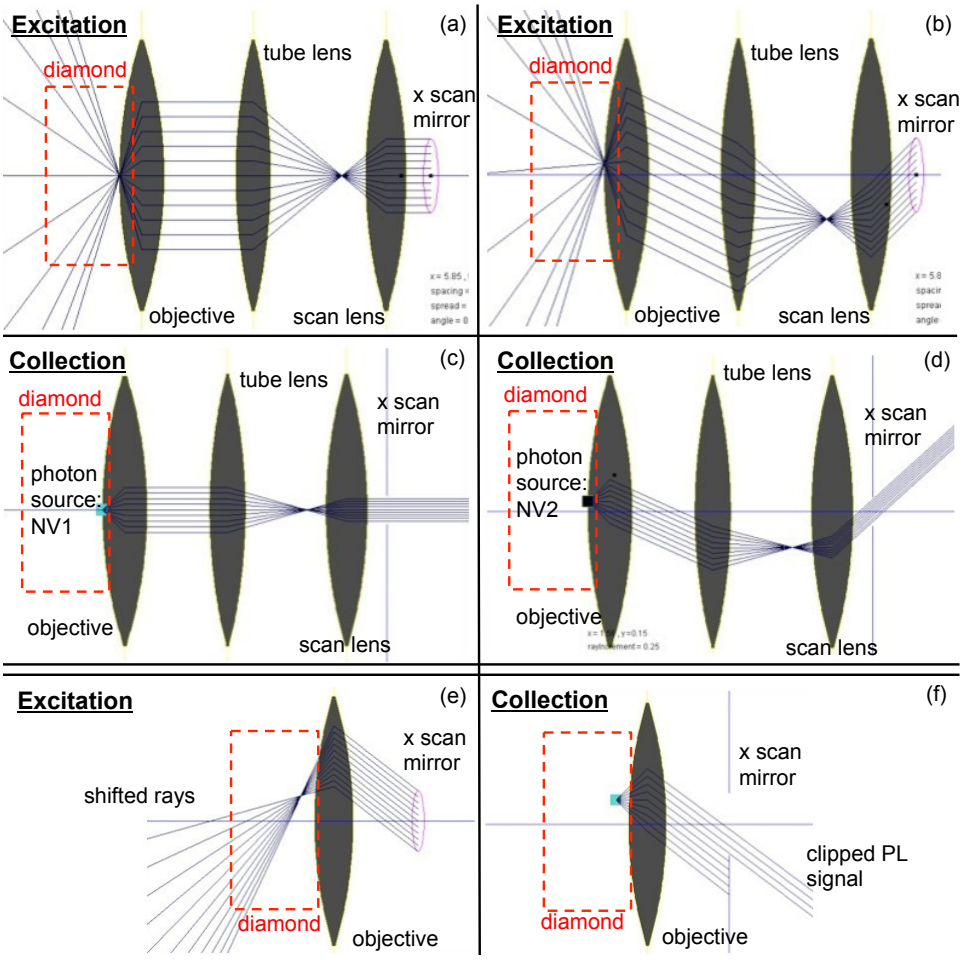

Figure 2.8: Lens optics of the lateral scanning of the imaging point for confocal microscopy. The red-dashed box is for reference of the sample position and effects of the diamond index are not included here. (a,b) Collimated excitation laser from right to left with normal incidence (a) and a scan mirror angle offset (b). The distance between the scan and tube lenses is ideally the sum of the focal lengths $f_s + f_t$, and the spot between them scans in the shared focal plane as the scanning mirror rotates. The left-side focal point of the tube lens should coincide with the back aperture of the objective lens, here simulated by another shared focal plane. This alignment allows the beam to pivot at the back aperture and not become clipped, as well as provide symmetric spatial illumination of the sample pixel regardless of scan offset. The micron-scale scan distance at the sample depends on the magnification ratio f_t/f_{obj}. (c,d) From left to right the optical path of isotropically emitted light from a point source like a NV emitter in the sample for an emitter on the optical axis (c) and off the optical axis (d). The fluorescence light ideally follows the same path as the excitation beam. (e,f) Non-ideal setup with one lens translates rather than pivots the beam at the objective back aperture, causing non-symmetric illumination and clipping. Simulations produced with Optics Bench online applet [172].

2.1.3 Noise in the confocal microscope

The signal we desire to measure in our experiments is the spin state of the NV after a given sensing time, wherein $|m_s = 0\rangle$ or $|m_s = \pm 1\rangle$ is determined by a high or low photon count rate, respectively. The noise in the confocal microscope that is most important to the signal-to-noise (SNR) of these spin state measurements concerns variations the collection rate of photons from the sample and background, and it arises from many sources. Sources of noise on the Hz timescale can include fluctuations of the excitation laser power, time variations in the coupling into single-mode fibers, vibrations between optical components, and stray background light from the room, sample, or other NVs. In laser-power operation at NV saturation, it is not straightforward how laser intensity fluctuations affect the SNR because the background noise level can change while the NV might emit an unchanged average rate of photons. Slower drifts in optical alignment or laser power could also cause the PL signal to change, though in practice these can be mitigated or normalized out of the measurement. For example, in pulsed measurements a typical shot time is 100s of microseconds and during this time a signal and reference of the NV in two spin states is taken to normalize PL readout. We have found empirically for pulsed measurements that the PL signal is very nearly limited by shot noise of the collected emitter signal. The procedures to determine measurement detection noise are discussed further in Appendix C.

The average excited-state lifetime of a NV polarized in $m_s = 0$ is about 12 ns [115]. Therefore, if the excitation laser intensity is high enough that the transition is saturated then the NV emits PL on the order of 80 Mphotons/s. The amount collected light in practice for a diamond slab is of the order $1 - 3\%$ that register as digital counts at the detector, and often a laser power well below the PL-saturation level is used in magnetometry for various reasons, so 100 kCnt/s is a typical count rate. The biggest

reduction to collection efficiency is due to the finite collection angle of a single objective; only a fraction of the emission light can possibly be collected. For example, assuming an isotropic emitter and NA=0.95 this is 34% collection based on the solid angle of a cone: $\%\mathrm{PL} = \Omega/4\pi = 0.5\left(1 - \cos\left(\sin^{-1}\mathrm{NA}\right)\right)$. Other reductions in this signal include loss due to internal reflection in diamond, transmission loss through the objective $(80-90\%)$ and other optical components ($\sim 99\%$ per lens or mirror), and finite quantum efficiency of the detector $(50-60\%)$. The 100 kCnt/s from the NV in a bulk film can be improved by an order of magnitude by reducing reflective losses within diamond using various etch-fabricated diamond structures or on-diamond antennas [173, 78, 174, 175]. At present, the etched diamond nanopillar is the photon collection enhancement method most readily applicable to scanning probe AFM magnetometry.

The photon count rates and differences of count rates that we measure are 2-4 orders of magnitude larger than the dark counts of the avalanche photodiode (APD), which are usually 50-500 Cnts/s. Therefore, the sensor noise n_s on the detector is negligible in our analysis of practical signal-to-noise ratio. Quantum efficiency Q_E, however, does reduce the signal and noise so that for a number of photons n_p incident on the detector $\mathrm{SNR} = Q_E n_p/\sqrt{Q_E n_p}$. Q_E is approximately $60-70\%$ over the range of NV phonon-sideband wavelengths measured.

2.1.4 Limitations in confocal microscopy for nanometer-scale imaging

The optical depth of field, or axial slice thickness, of the confocal microscope given parameters of NA= 0.95, $n = 1$, and $\lambda = 532$ nm is at best about 600 nm based on Eq. 2.4. This is sufficient to determine differences in NV distance to the surface on the micron scale. However, as introduced in Chapter 1, the spatial resolution and magnetic

sensitivity of the single-NV sensor falls off rapidly with distance: nanometer-scale spatial resolution and sensitivity to a small number of spins external to the diamond requires the NV to be just nanometers from the diamond surface. To study the dependence of the NV spin properties and its sensing ability as a function of distance from the surface then we must use a super-resolution technique beyond confocal microscopy. For this purpose we employ a scanning probe ODMR technique and the results of this method are presented in Chapter 4. The technique is based on atomic force microscopy, which is the topic of the next section.

2.2 Atomic force microscope

Atomic force microscopes (AFM), and more generally scanning probe microscopes (SPM), comprise a versatile class of tools for probing surfaces — and subsurfaces — with nanoscale spatial resolution. The first basic use of these tools was to map the height profile of a sample [58], and that capability remains today an integral part of more sophisticated interleaved measurements, such as magnetic force microscopy (MFM) [7]. It is perhaps counterintuitive that a bulky microscopic tip that measures mechanical forces can achieve atomic-scale resolution [61] like an STM, yet non-contact AFM enables now imaging of individual bonds in a single molecule [63, 126]. We use the AFM to control the distance of the NV-containing diamond to the surface of a target sample and to position it laterally with nanometer precision for magnetic and electric field imaging.

2.2.1 Principles and modes of AFM

An atomic force microscope measures the forces between a sample material surface and a micron-millimeter-scale mechanical cantilever with a sharp nano-sized tip attached, as illustrated in Fig. 2.9. This cantilever-tip system is translated in three-dimensions

using precise piezoelectric scanners, where the sample surface is roughly in the x, y plane and the z piezo allows careful approach of the tip to the surface. For standard topographic imaging, as the distance z_c between the tip and the surface is varied, the cantilever experiences a spatially varying force $F(z) = -\partial V/\partial z$ due to a combination of attractive and repulsive tip-sample interactions, summing to a potential energy V. The traditional detection method uses an optical lever as depicted in Fig. 2.9(a): a laser is focused onto the end of a piezoelectrically driven cantilever, and the reflected light is incident on a split photodiode. The signal on the photodiode can be used to readout a cantilever deflection in contact AFM modes or a change in cantilever vibration amplitude in dynamic modes. For contact mode, as the tip is pressed into the sample, the cantilever bends and reflects the light towards the top or bottom half of the photodiode, and the difference of the intensity gives a static deflection signal. Because the distance between the cantilever apex and the detector is orders of magnitude larger than the deflection amplitude, this optical lever can sensitively detect small changes in force. When the cantilever is then translated in the x, y plane along the sample surface, the deflection signal can be read out to image the topography in two dimensions.

We have described a non-feedback deflection type of contact mode imaging. However, normal AFM operation uses a continuous proportional-integral feedback loop to move the tip closer or farther from the surface. Many AFM modes exist for tracking the height of a surface. Broadly, these are divided into contact and dynamic modes. In contact AFM, the compliant cantilever, usually silicon-nitride, has a low < 1 N/m spring constant allowing it to deflect a large amount under short-range repulsive forces, thus enabling a large optical lever signal. Here, the deflection setpoint is the error signal in a feedback loop to adjust the tip-sample separation. The advantage of this AFM mode is simplicity for imaging relatively flat, hard surfaces. In this thesis work, contact mode AFM is used to measure diamond surface morphology and roughness after various processing steps.

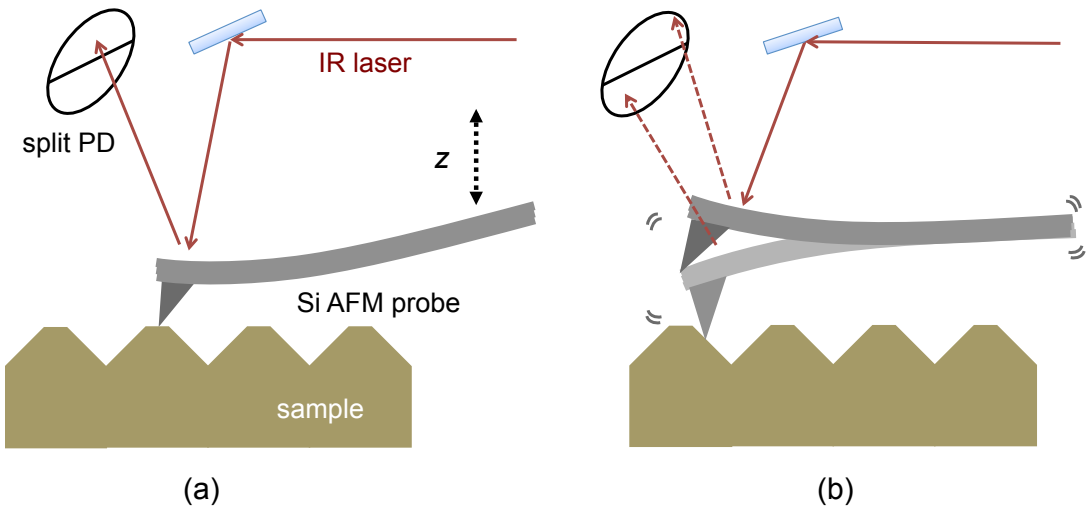

Figure 2.9: Illustration of atomic force microscopy (AFM) based on an optical lever. A laser is reflected from a silicon cantilever into a split photodiode (PD) detector. Deflection of the cantilever due to forces between its sharp tip and a sample surface causes the reflected laser to primarily hit the top or bottom of the PD. This signal gives a measure of static deflection in contact mode (a), and in a resonantly driven cantilever (b) lock-in detection gives a change in amplitude, frequency, or phase. The error between a setpoint deflection or amplitude and the measured signal, for example, can be used as input for a feedback loop that controls the z position of the cantilever with nanometric resolution to keep the tip-sample force constant. Drawing not to scale: cantilever lengths are ~ 200 μm while the optical path length is several cm.

However, we do not use contact mode for magnetometry primarily because contact-mode scanning is more damaging than non-contact scanning. In addition, undesirable snap-to-contact (or snap-in) due to strong attractive forces can easily occur in floppy cantilevers, which makes maintaining a tip-sample separation on the order of nanometers impossible. Using high-stiffness probes in dynamic mode can mitigate the snap-in issue.

Dynamic AFM (Fig. 2.9(b)) comes in many varieties that rely upon resonant excitation and response of the probe cantilever. The oscillation amplitude, frequency, or phase can be used as error signals in a feedback loop to adjust the tip-sample separation z_c, and different types of forces can be measured including magnetic forces. We focus on amplitude modulation AFM (AM-AFM) for scanning magnetometry, which is suitable for simple operation in ambient conditions at slow scan rates since the Q is lower than in vacuum, thus allowing a faster response time. In this mode, the cantilever is driven on or near its resonance frequency, and the amplitude is used as the sole feedback parameter. As the tip approaches below 100 nm of the surface, short-range Van der Waals attractive forces cause a change in the shape of the resonance curve. Consequently, the amplitude changes, usually becoming lower than the free driven amplitude [176]. The analysis of the tip motion in AM-AFM is complicated and non-linear due to the non-constant force gradient as a function of z_c. Theoretical analysis of the problem shows that there are generally two solutions for the amplitude, and either or both may be most stable for small changes in driving amplitude and tip-sample separation. Generally, solution A is non-contact where the tip never feels appreciable contact forces and solution B is intermittent contact, or tapping mode, where the fraction of time per period in contact with the surface increases as z_c is reduced, thus reducing the amplitude. We use the tapping mode, B.

Other detection methods exist for dynamic-mode imaging beyond the optical lever and micro-cantilever. Another approach is to use a macroscopic quartz tuning fork os-

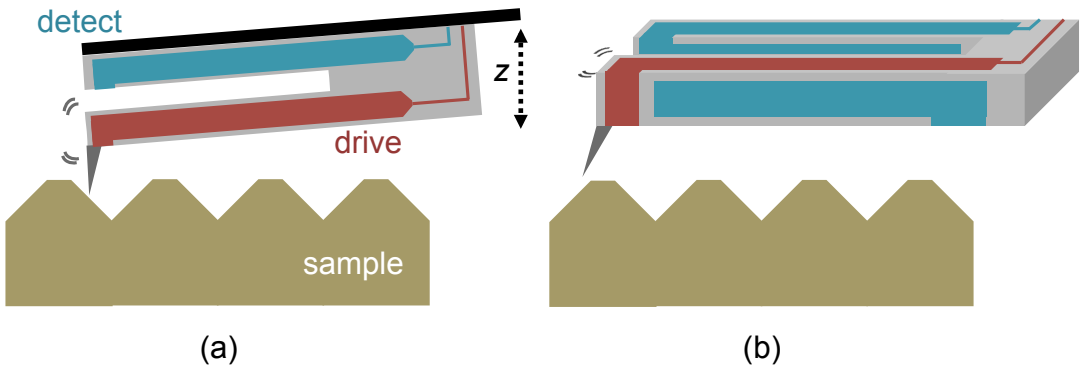

Figure 2.10: Illustration of AFM using a self-sensing quartz tuning fork in (a) intermittent tapping mode with oscillation normal to the sample surface and (b) shear-force mode with oscillation parallel to the surface. In both cases, the tuning fork is electrically driven (red lead) at the mechanical resonance frequency ($f \approx 32$ kHz) and an independent lead (blue) is used for current readout; one tip-attached tine is mechanically free in both, while the other tine is fixed to a piezo x, y, z scanner. Either detection of amplitude or frequency modulation can be used for feedback to control the z height of the tip above the sample.

cillator [177], which is advantageous for scanning-NV magnetometry because no extra optics are necessary. Such probes are called "self-sensing" because they are electrically driven at a resonance that corresponds to the mechanical shape of the device, and they can then be electrically read out via current from an independent metal lead on the device. Beyond elimination of an optical system, the quartz tuning fork detection has the benefit of an extremely high spring constant of order 10^4 N/m, which more effectively prevents undesirable snap-in of the tip to the sample. By comparison, typical tapping mode Si cantilevers have spring constants of 0.1-100 N/m. The macroscopic tuning fork is also a versatile platform because any number of different commercial tips or diamond scanning probes can be glued on while keeping the spring constant and resonance frequency relatively unchanged. However, while mass production of silicon cantilever probes is achieved routinely with wafer-scale lithographic fabrication methods, the assembly of a tip on a tuning fork cannot yet be mass-produced in the same way.

The tuning-fork sensor can be operated in intermittent tapping contact mode (Fig.

2.10(a)) or in shear-force mode (Fig. 2.10(b)) [61]. Shear-force mode is often used in high vacuum for non-contact imaging at atomic-scale resolution. In shear-force mode, it has been reported that one must be more careful to mount and operate the tip with parameters that ensure it comes within nanometers of the sample surface [178, 66]. One advantage of the alternative of tapping mode is that it is easier to determine that the amplitude is changing due to actual intermittent tip contact with the sample, and this is the primary method we employ for our scanning probe Magnetometer B in ambient conditions.

2.2.2 Spatial resolution of AFM

The spatial resolution of dynamic AFM is different in height z compared to in x and y. Subnanometer resolution in height is readily accessible because the feedback loop makes continuous small changes to the piezo voltage due to minute changes in the oscillation amplitude. In contrast, lateral resolution depends on many other factors, such as AFM tip size, shape of sample features, piezo creep, and thermal tip-sample drifts over longer measurements. Therefore, typical lateral resolutions are a few nanometers to 10s of nanometers. The cartoon in Fig. 2.11(a) illustrates the convolution of a tip's shape with the contours of a sample with sharp sidewalls, demonstrating the limited lateral spatial resolution, despite excellent determination in the measurement of the trench depth. If the vertical:horizontal aspect ratio of a trench is too high in comparison with a broader tip shape, however, then the depth can be underestimated as shown in Fig. 2.11(b).

2.2.3 Scanning probe microscopy with a NV quantum sensor

In the present work, we use an AFM for the general purpose of bringing a magnetic sample of interest near a shallow NV spin sensor in diamond with nanoscale three-

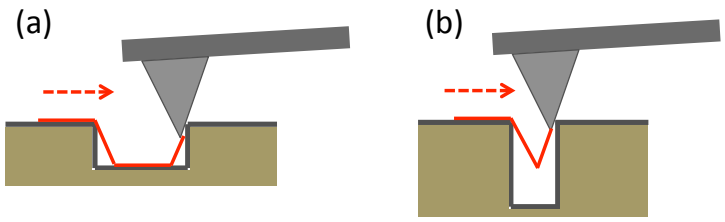

Figure 2.11: Illustration of an AFM probe scanning in a lateral direction (red dashed arrow) to show a limitation to lateral resolution. (a) The tip is broader than the 90° sample sidewalls, so the tip shape is convolved (red line trace) with the feature while the total height difference is still accurately imaged. (b) The feature's vertical aspect ratio is large, so a broad tip cannot access the bottom of the trench, which underestimates the height difference and limits lateral resolution.

dimensional spatial control. Detection of the mechanical force between the diamond and sample is used as a tool to reliably position the NV nanometers from the sample surface; however, force does not serve as the signal for magnetic imaging. The magnetic sample could range from a strongly ferromagnetic micron-scale MFM tip to a sample of dilute or single spins. As the NV-containing diamond is raster scanned in nanoscale proximity to the sample, we collect fluorescence photons from the NV under the influence of continuous-wave or pulsed microwave and optical fields. Depending on the control sequence, this fluorescence signal yields spatial-dependent information about the static or fluctuating magnetic fields from the sample. A schematic of two NV-based scanning probe modes is shown in Fig. 2.12, for sample-on-tip or NV-on-tip geometries. Each has its advantages and challenges, which we partially list in Table 2.1, though what qualifies as a challenge is subjective to some degree and reflects the present state of the art. The NV-on-tip can more easily be used to image to general large-area magnetic samples of interest because the sample is not restricted to being fabricated on a small scanning-tip platform. However, fabrication of the all-diamond AFM probe is more intensive and allows a yield of fewer NVs to choose from. The sample-on-tip geometry is more limited in the types of samples that can be studied (they must be prepared on the tip), how-

ever, it is simpler on the diamond materials processing side and a higher yield of shallow NVs are typically available on the same diamond chip to use as potential sensors. The sample-on-tip or nanodiamond-on-tip geometry is more readily combined with the standard optical-lever AFM as it uses common Si probes with a custom tip, though any of the diamond scanning modes can be performed via the tuning-fork system with the Si or diamond probe glued to one tine.

For the experiments throughout this thesis, we exclusively use the sample-on-tip mode with different variations. In Chapter 4, we use a sharp ferromagnetic tip to apply magnetic field gradients on the order of 1 G/nm for the magnetic resonance imaging of relative nanoscale depths between shallow NVs. In Chapters 6 and 7, the sample on the tip is a source of magnetic field noise, either fluctuating electronic spins or fluctuating currents in a metal; we use silicon probes with both sharp tips (radius < 50 nm) and custom-fabricated plateau tips (diameter $1 - 3$ μm). The diamond itself may be flat, as in the experiments of Chapters 4 and 6. Alternatively, it may also be fabricated into an array of nanoscale diamond tips, as in the experiments in Chapter 7 and Fig. 2.12(b). This diamond-sensor array somewhat blends the sample-on-tip and all-diamond NV-on-tip AFM modes but retains the advantages of a full bulk diamond, such as simpler fabrication and higher NV sensor yield per area of the diamond chip.

2.2.4 Spatial resolution of a scanning NV microscope

The concept of spatial resolution is more nuanced for NV-based scanning probe magnetometry in comparison to the discussion above on topographic AFM spatial resolution, because the signal being probed depends on the magnetism of the sample and also on the topography. We have introduced in Chapter 1 some of the ways in which spatial resolution can be defined for imaging an ensemble of spins or a static magnetic field and

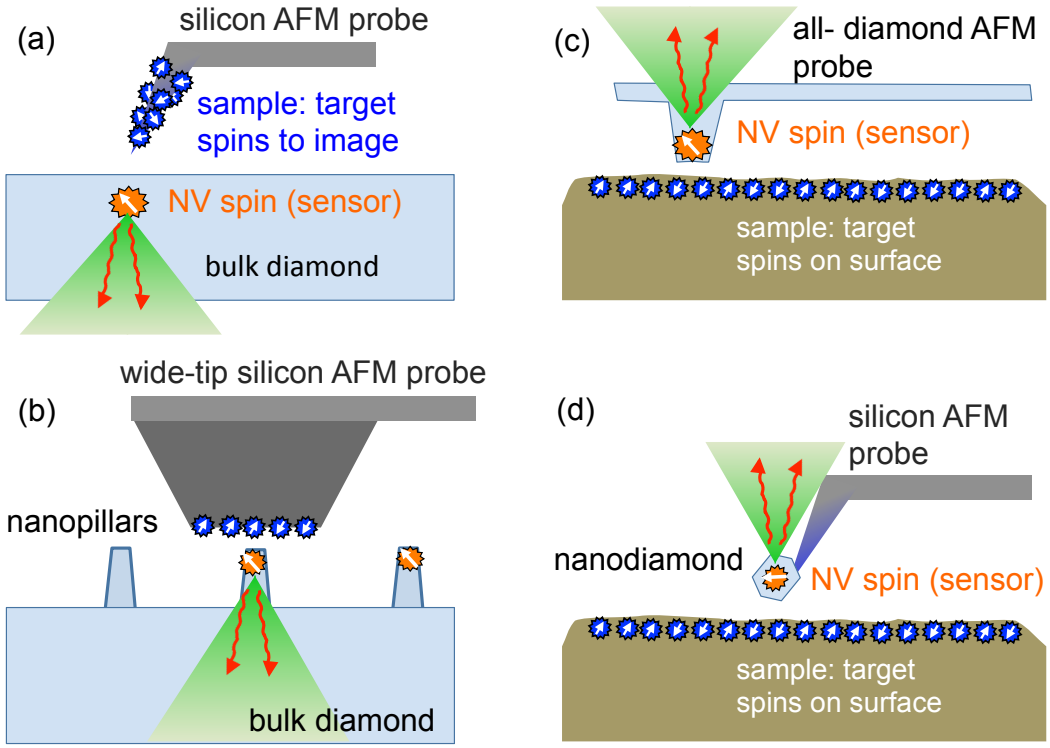

Figure 2.12: Illustration of scanning probe magnetometry modes using a single NV center in diamond, categorized as sample-on-tip (a,b) and a NV-on-tip (b,d). Methods (a) and (b) are used in this thesis, the latter which combines some advantages of the sample-on-tip (a) and all-diamond NV-on-tip (c).

	Advantages	Challenges
(a) sample-on-tip	many candidate NVs per area; no diamond fab; single-crystal diamond	lower photon collection; very limited sample types
(b) sample-on -wide-tip	many candidate NVs per area; flat probe for imaging; high nanopillar collection efficiency; single-crystal diamond	limited sample types; tip-to-tip tilt correction; preparing custom tips
(c) all-diamond probe	study large-area samples high nanopillar collection efficiency; single-crystal diamond; robust to tip damage	intensive diamond fab; lower-NA optics; lower yield of NVs
(d) nanodiamond -on-tip	study large-area samples simple nanodiamond attachment; good collection efficiency; excellent demonstrations in dc B-field imaging	worse NV optical and spin properties; NV orientation "random"; more diamond surface area exposing NV; less control of NV distance to sample

Table 2.1: Comparison and complementarity of relaxation and dephasing for classical-noise spectroscopy with NV centers.

how this resolution is linked with magnetic sensitivity. A key concept in either case is the magnetic field gradient in each direction, either $\partial B/\partial x_i$ for a static field or $\partial\langle B^2\rangle_{\mathrm{rms}}/\partial x_i$ for a fluctuating field. This gradient is important because, for whichever CW or pulsed ODMR method is used, NV PL has some minimal detectable change for any change in B or $\langle B^2\rangle_{\mathrm{rms}}$ with position. Therefore, it is universally useful in NV magnetometry to bring the NV as close to the magnetic field source as possible before conflicting material-related effects come into play. Such effects may include large off-axis magnetic fields that quench NV PL contrast [36, 66] or instability of the NV charge state if it is too close to the diamond surface as in tiny nanodiamonds [35].

The first step to improving the scanning probe NV spatial resolution is to near-deterministically place a NV just nanometers below the diamond surface, which is the topic of Chapter 3. Second, the magnetic sample geometry or diamond geometry must

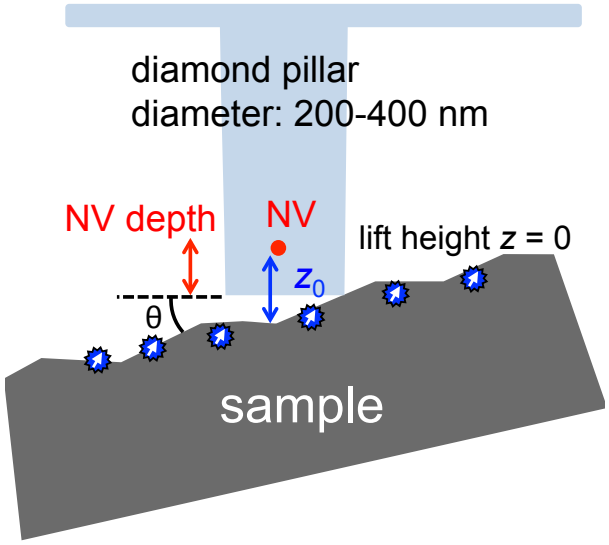

Figure 2.13: Spatial resolution of diamond magnetometer with tip-sample tilt. The NV-containing pillar has width of a few hundred nanometrs, which limits how close the diamond surface, and NV, can get to the sample in the presence of surface roughness or tilt. A smaller z_0 typically implies a smaller volume of sample imaged and hence, better spatial resolution.

be nanostructured so that the diamond and sample surfaces can practically come into direct contact. This geometry requirement is relatively straightforward if the magnetic sample is a regular nanoscale AFM tip, as in the magnetic force microscopy probes used in experiments of Chapter 4. However, if the magnetic sample has further spatial extent on the order of 100s of nanometers to microns, then the relative tilt of the two surfaces becomes important to bring the NV as close as possible to the sample (see Figs. 2.13 and 7.13). Furthermore, a diamond nanopillar as an AFM tip is typically made large, at least 200-400 nm in diameter, to preserve the NV properties, so any nanometer-scale topographic features on the sample could cause height differences in a scan. Because the broad diamond tip is convolved with these features, the height variations cause the magnetic field experienced by the NV to change even if the NV itself is not directly above the topographic feature. We address these experimental challenges in the scanning probe experiments of Chapter 7.

2.3 Scanning magnetometer A for NV depth imaging

The confocal microscope of Magnetometer A was designed in an inverted-objective layout to be combined with a commercial AFM system, a Bruker BioScope Catalyst.

2.3.1 Optical setup

The optics table schematic for the inverted CFM is shown in Fig. 2.14. The objective is a total internal reflection (TIRF) APON 60XOTIRF from Olympus, although it is used here for its high NA with regular backside collimated illumination. This oil immersion lens has an NA of 1.49. A thin diamond sample ($10 - 40$ μm) was placed NV side up on a glass coverslip of thickness 170 μm with a small volume Olympus Type F immersion oil in between the coverslip and diamond as well as between the objective and coverslip.[1] More recent improvements to the setup to limit vibrations and extend the thickness of diamond samples up to 150 μm are given in Appendix B. Microwaves were applied to the diamond via a two-port or shorted one-port coplanar Ti/Au waveguide microfabricated onto the glass coverslip. Figure 2.15 gives the parameters for lenses, mirrors, and other optical components.

The excitation beam is prepared as follows: The 532-nm excitation laser (Elforlight) passes through an electronic filter wheel containing absorptive neutral density (ND) filters and a manual filter wheel containing complementary ND filters. The beam is focused on an acousto-optical modulator (Isomet 1250C or IntraAction ATM200 AOM) driven by an AOM driver (Isomet 525C-1) and then recollimated. All beam-expanding telescopes in the CFM used convex lenses. The beam is guided into a single mode fiber (Thorlabs

[1] This oil also provides a temporary bond that is simple to separate and can be cleaned off by swabbing the diamond and glass independently with acetone and IPA solvents.

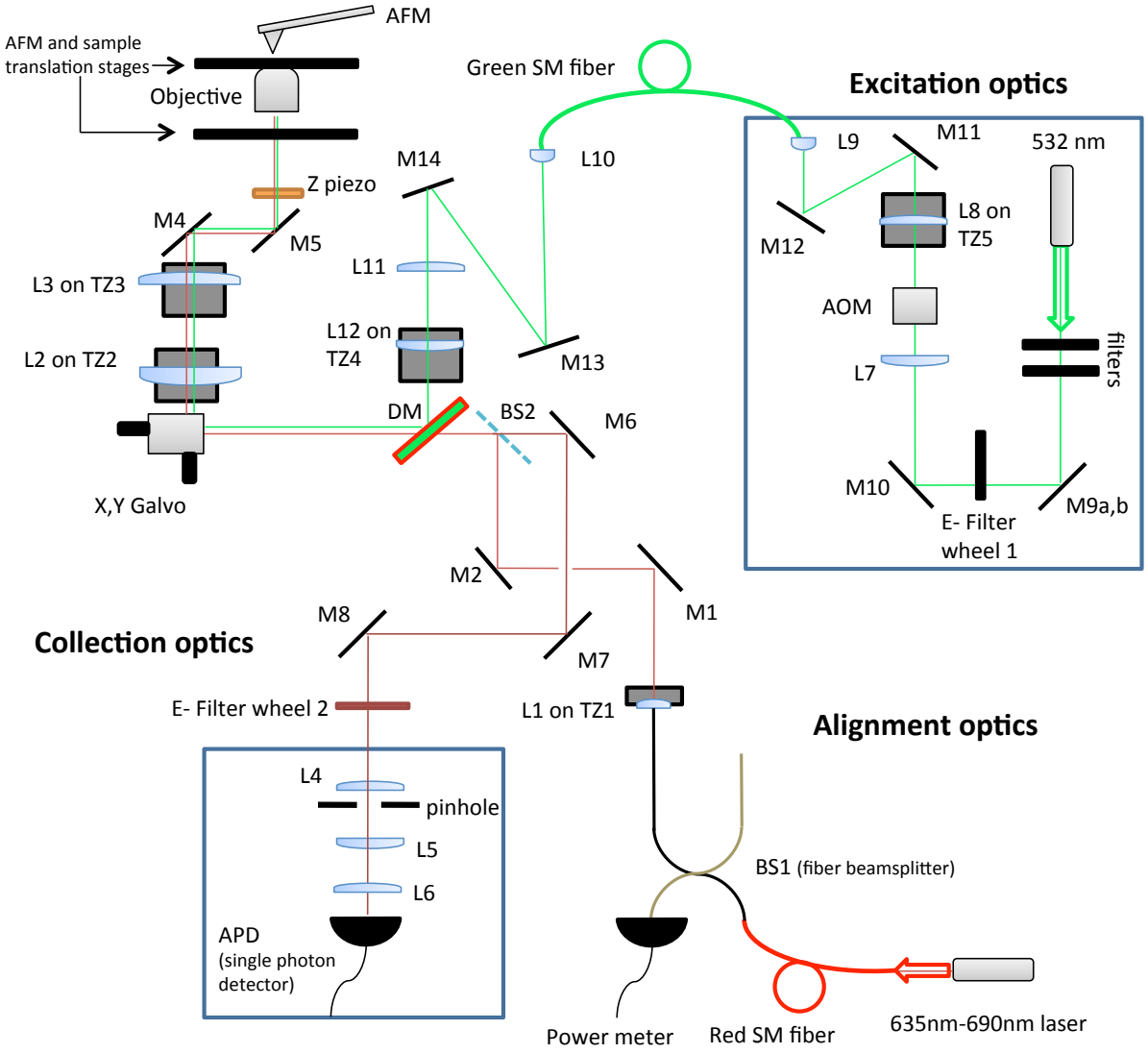

Figure 2.14: Schematic of the laser scanning inverted confocal microscope of Magnetometer A for the magnetic depth imaging and coherence experiment. Mirror M5 to the objective is a vertical path, and otherwise the optical path is parallel to the table. Fine x, y laser scanning is provided by two galvo mirrors and fine z focus is provided by objective translation on a piezo. Details about the labeled components are given in Figure 2.15.

Lenses	Description	Purpose	Vendor	Part no.
objective	NA = 1.49, Ø = 8.94 mm, oil immer.	Excite NV and wide-angle PL collection	Olympus	APONTIRF60x
L1	11 mm asphere, B-coated	Collimate red alignment laser	Thorlabs	A397TM-B
L2	75 mm achromat, B-coated	M=4 scanning telescope, “scan lens”	Thorlabs	AC508-75-B
L3	300 mm achromat, B-coated	M=4 scanning telescope, “tube lens”	Thorlabs	AC508-300-B
L4	50 mm achromat, B-coated	Focus NV PL into confocal pinhole	Thorlabs	AC254-050-B
L5	100 mm achromat, B-coated	Re-collimate NV PL after pinhole	Thorlabs	AC254-100-B
L6	100 mm achromat, B-coated	Focus NV PL into the APD		
L7	150 mm plano-convex, A-coated	Focus 532 nm laser into AOM	Thorlabs	LA1433-A
L8	125 mm plano-convex, A-coated	Re-collimate 532 nm laser after AOM	Thorlabs	LA1986-A
L9	7.5 mm asphere, A-coated (fiber port)	Couple 532 nm into excitation fiber	Thorlabs	PAF-X-7-A
L10	7.5 mm asphere, A-coated (fiber port)	Re-collimate 532 nm after fiber	Thorlabs	PAF-X-7-A
L11	30 mm plano-convex, A-coated	M=2 green telescope	Thorlabs	LA1805-A
L12	60 mm plano-convex, B-coated	M=2 green telescope	Thorlabs	LA1134-B

Mirrors/filters	Description	Purpose	Vendor	Part no.
BS1	Fiber beamsplitter	Collect returning red light: test confocal	Thorlabs	FC632-50B-FC
M1, M2	1” silver mirrors	Align red laser alignment path	Thorlabs	PF10-03-P01
BS2	R45%:T55% pellicle beamsplitter	Alignment only; remove during imaging	Thorlabs	BP145B1
DM	Dichroic mirror, OD 4	Transmit NV PL, reflect 532 nm excitation	Semrock	Di01-R532-25
X,Y Galvo	Scanning mirrors	Scan beam along the diamond plane	Thorlabs	GVSM002
M4, M5	2” dielectric mirrors	Direct laser and NV PL to/from sample	Thorlabs	BB2-E02
M6, M7, M8	1” dielectric mirrors; Polaris mounts	Direct and align beam to collection path	Thorlabs	BB1-E02
E-filter COM4	Longpass filter, OD 6, PC-controlled	Reject wavelengths < 600 nm	Semrock	BLP01-594R-25
Pinhole	Ø20-30 µm pinhole	Reject out-of-focus light from sample	Thorlabs	P20S, P30S
E-filter COM3	Interference filters, PC-controlled	Variable attenuation of 532 nm laser	Thorlabs	FW102C
M9, M10	1” silver mirrors	Align 532 nm laser into AOM	Thorlabs	PF10-03-P01
M11, M12	1” silver mirrors	Align 532 nm laser into SM fiber	Thorlabs	PF10-03-P01
M13, M14	1” silver mirrors	Align 532 nm laser to overlap red path	Thorlabs	PF10-03-P01

Figure 2.15: Table of optics lens, mirror, and filter components for the confocal microscope of Magnetometer A in the most recent configuration.

460HP) to act as a spatial filter and isolate the alignment of the AOM system from the rest of the CFM.

The laser exiting the fiber is recollimated and guided to a dichroic mirror (see Fig. 2.15 for optical part numbers) to reflect the green light. Next a pair of galvo scan mirrors reflect the beam into the scan and tube lens pair. The scanned beam is directed vertically into the back aperture of the objective. PL from the sample returns along the same optical path and the red component is transmitted through the dichroic to be directed to the detection telescope. The first lens focuses the PL onto the detection pinhole (Thorlabs) on an x, y translation mount (Thorlabs ST1XY-D). The final two lenses resize and focus the beam onto the avalanche photodiode (APD) photon detector (Perkin Elmer SPCM-AQR-14).

2.3.2 CFM control ,microwaves, and pulse timing

Magnetometer A is controlled using custom software written in Matlab. The primary function of the program and GUI is to communicate with the data acquisition and DAC board (NI PXIe-6363 referred to generally as "DAQ") and electronics for pulse sequencing. Two DAQ analog outputs pass voltages to the galvo scanning mirrors and a third voltage controls the objective piezo (MCL F100S) position over a 100-μm range for fine focus and z image scans. These scan voltages are clock-synchronized on the DAQ with a counter task to bin photon counts and form a PL image in 1-3 dimensions. The clock internally triggers this counter. A second counter input is set up for external triggering by a digital line. The APD output, in the form of square voltage pulses, is split (Minicircuits ZSC-2-1-75+) and input to both counters.

As discussed in Chapter 1, the NV's orbital ground state is a spin triplet with a zero-field splitting of $D_{\mathrm{gs}} = 2.87$ GHz at room temperature. The energy levels can be split

by a Zeeman magnetic field and these $|0\rangle \leftrightarrow |\pm 1\rangle$ transitions addressed with resonant microwaves to rotate the spin. For pulse sequences a SpinCore PulseBlasterESR-PRO 500 MHz card is used to generate multiple TTL digital outputs (3.3 V high) on a single clock. Bit1 is assigned to the AOM driver for digital modulation of the laser beam. Bit2 is assigned to the trigger of the second counter input, which is configured to advance the count buffer, or sample, on each up edge. Bit3 is assigned to gate the microwave switch, and Bit4 is reserved for a second in-series microwave switch or other temporary purposes. Bit5 through Bit8 are assigned to control the IQ modulation of the microwave carrier. The Bit1 and Bit3 lines passed through a SpinCore TTL Line Driver to ensure sufficient total current over 50Ω loads under any channel on/off combinations. This additional current was particularly helpful for gating the switch correctly, which affected the quality of spin rotations. See Appendix G for further details on pulse sequence timing.

Figure 2.16 is a diagram of the pulsed ODMR experiment with each component that is triggered by the PulseBlaster. A simple microwave exciter circuit was designed for driving NV spin rotations. This begins with generation of the carrier frequency ($f = D \pm g\mu_B B/h$) by a signal generator (SRS SG384). The output is modulated by a fast SPST switch (CMC CMCS0947A-C2 with S0016 option). This output is attenuated by 6 dB for ensuring a safe input to the microwave amplifier (Minicircuits ZHL-16W-43+). The amplified signal passes through a circulator (NARDA 4923) and dc block to a coplanar waveguide (CPW) fabricated on a glass coverslip.

CWESR measurements to identify the NV ground state transition frequencies were performed by triggering a list of frequencies to sweep on the SG384 while continuously collecting PL photon counts with the laser AOM on. The frequency sweep and count buffer increment are done with a software trigger in this case, which is sufficient because the dwell time per frequency point is set to be long, 10s of milliseconds.

Pulsed ODMR measurements were performed with only external hardware triggers

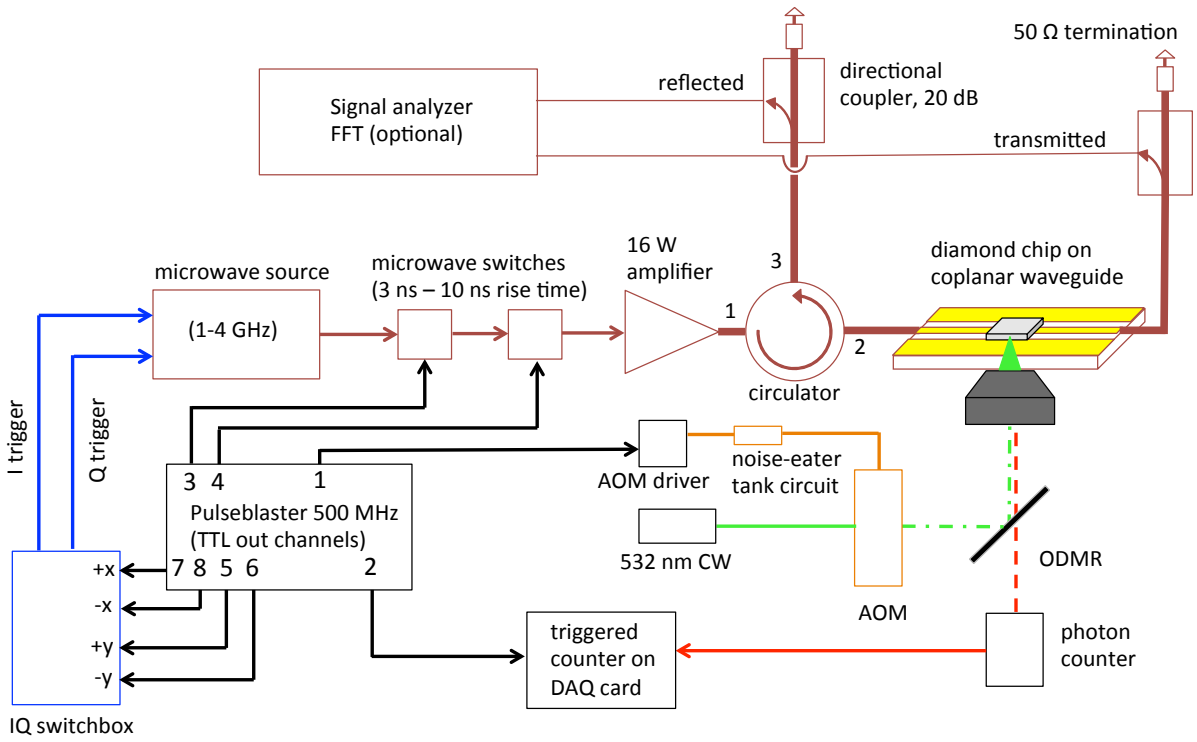

Figure 2.16: Diagram of the microwave circuit and pulse timing for ODMR experiments that use a single microwave tone for spin rotations. The PulseBlaster card outputs digital pulses (1-8) to control the laser acousto-optic modulator (1), photon count binning (2), microwave switches (3,4), and IQ modulation switches (5-8). The microwave circuit is in dark red, digital timing lines are in black, IQ control is in blue, rf for the AOM is in orange, the laser path is in green, and the collected NV PL is in red.

from the PulseBlaster outputs. The structure of the typical pulse sequences was described in Chapter 1. The AOM Bit1 is first pulsed on for a time of $3 - 10$ μs for optical initialization of the NV spin in $|m_s = 0\rangle$. The details of time delays between the bit channels are discussed in Appendix G including a calibration procedure for the "AOM delay", that is the timing offset required between the AOM and readout bits. The initialization is followed by a dark time where a specific set of microwave switch Bit3 pulses are done to manipulate the NV spin. Next, the AOM is turned on concurrently with a short 50-ns pulse on Bit2 to trigger the DAQ counter with an up edge to begin a new count buffer. After the readout time, typically 350 ns, another Bit2 up edge triggers the beginning of a new count buffer. A reference readout follows the same procedure for Bit2. For a pulse sequence with one signal $S(\tau)$ and one reference $R(\tau)$, every fourth buffer starting from buffer1 contributes to $S(\tau)$ and every fourth buffer starting from buffer3 contributes to $R(\tau)$. The other half of the count buffers are "garbage" in that they are filled during non-readout periods but these are still monitored for anomalies.

The dynamical decoupling pulse sequences introduced in Chapter 1 require phase cycling of the pulse-modulated microwave carrier with four discrete 90° values of $+x, -x, +y, -y$. The SG384 generator takes two external IQ modulation inputs (I and Q) of up to $\pm$500 mV for the full modulation range. We designed an IQ switchbox to take TTL inputs to produce a positive (Bit5) or negative (Bit6) $\sim$ 500-mV output for the Q input of the SG384 and likewise used Bit7 and Bit8 for $\pm$500 mV for the I input. These four IQ bits were switched some time "q" before and after the microwave switch pulse to ensure the phase was fully changed.

2.3.3 AFM setup for Magnetometer A

The preceding sections described all the components needed to do NV spin coherence and relaxation measurements and magnetometry on fixed-position samples, for example external spins placed on the diamond surface. The AFM was added to perform 3D nanoscale magnetic imaging in a sample-on-tip configuration. The Bruker BioScope Catalyst AFM contains a sample-scanning x, y stage on which we scan a bulk diamond sample. The AFM head controls the coarse and fine z positioning of the AFM tip for approach and scanning. Figure 2.17(a) shows a photograph of the combined inverted CFM and AFM sample stage. During AFM imaging this tower section of the setup was enclosed in a box of lead-lined panels with acoustic-damping foam (Fig. 2.17(b)) to further minimize stray light, temperature drift, and air currents. A close-up photo of the AFM head and sample region is shown in Fig. 2.17(c). An infrared laser in the head is directed by a small mirror to the AFM cantilever from which it then reflects into a quadrant photodiode (QPD) to read out the dc deflection and on-resonance lock-in amplitude. The diamond sample sits on a shorting path of a Ti/Au CPW on a glass coverslip. A flexible microwave cable is soldered to the CPW to deliver the pulsed microwaves. This PCB-SMP connector was required to be small and well positioned so as not to block the IR beam path into the QPD, as inferred from Fig. 2.17(c).

Figure 2.17(d) is a top-down micrograph of the system when a magnetic AFM cantilever and its tip are aligned to an optically addressed NV residing in a clear window of the CPW. The procedure for alignment the 532-nm laser spot, NV, and AFM tip to a given x, y position is illustrated in Chapter 4. We summarize here the degrees of freedom: the objective x, y position is mechanically fixed, but the laser spot can scan three-dimensionally over the diamond. The entire AFM baseplate is mounted on a bread-board on top of a x, y translation stage (Newport 406). This manually moves the AFM

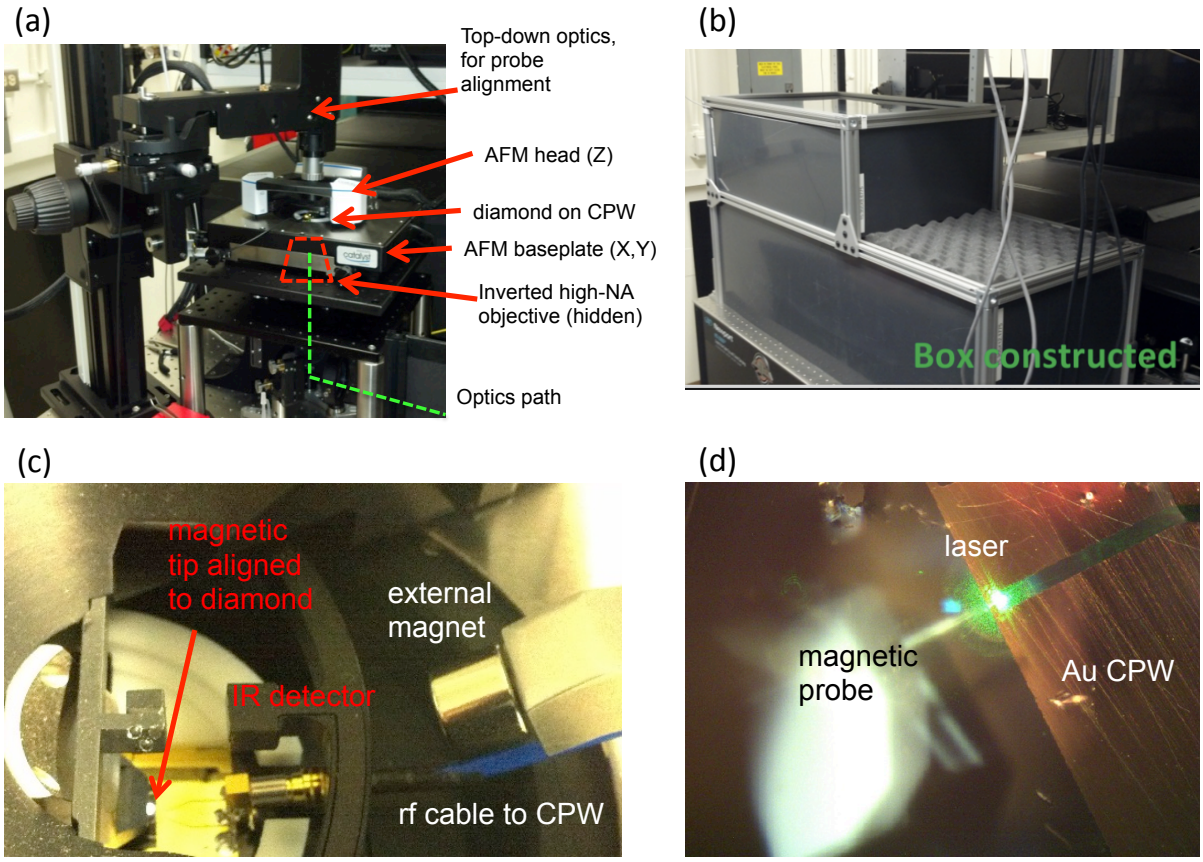

Figure 2.17: Photographs of Magnetometer A setup on an optical table for NV scanning magnetometry. (a) AFM, sample area, and optical imaging region of the confocal microscope. The diamond sample is scanned in x and y while the AFM head controls z positioning of the magnetic tip. (b) Fully assembled isolation box around structure shown in (a) for acoustic damping, blocking air currents, and mitigating temperature drifts. (c) Up-close AFM head region showing AFM infrared detection optics and rf waveguide circuit for NV spin rotations. (d) Micrograph using top-down optics showing magnetic probe cantilever aligned to a metal-clear gap on the gold waveguide-on-glass where the confocal microscope laser is focused on the diamond surface. Microscope oil is between the waveguide and diamond.

baseplate (i.e., diamond sample) and AFM head (i.e., tip) together relative to the objective. The AFM baseplate coarse x, y motor positioners translate the diamond sample relative to both the objective and tip.

Because the diamond-on-CPW is scanned relative to the objective and tip, then during a magnetometry image acquisition the laser must scan to "follow" the changing position of the NV to keep excitation rate and PL constant. AFM scan sizes were typically larger than the lateral resolution of the CFM. NV following requires quantitative calibration of the AFM scanner's linear translation and scan angle to the CFM laser scanning. In summary, calibration involves fine-tuning the CFM's galvo μm/V in x and y to match the scanner displacement as well as transforming all AFM scan coordinates by the offset angle θ_{scan} before executing a scan. In other words, the AFM scan distance was used as the linear ruler and the two CFM scan mirrors defined the x and y directions.

The Catalyst AFM was interfaced with the Matlab confocal microscope software via a Distributed Component Object Model (DCOM) connection on the local network (see Appendix B). The "Nanoman" nanolithography functions from Bruker were used to control the tip z position, sample x, y, feedback settings, and stage position of the AFM through DCOM. Figure 2.18 is a basic schematic of the AFM electronics and network connection to the CFM.

The combined CFM and AFM was sufficiently stable against mechanical vibrations to resolve sub-nanometer height features. This is demonstrated for example by Fig. 2.19, which shows a contact-mode topographic image of a diamond film surface acquired with the system loaded with a standard silicon nitride probe (Bruker SNL). The atomic-scale steps of the step-flow diamond growth mode are clearly visible and no comparable noise amplitude is present in the image. For the NV magnetometry measurements in Chapter 4 tapping mode was preferred to preserve the integrity of the AFM tip over many successive

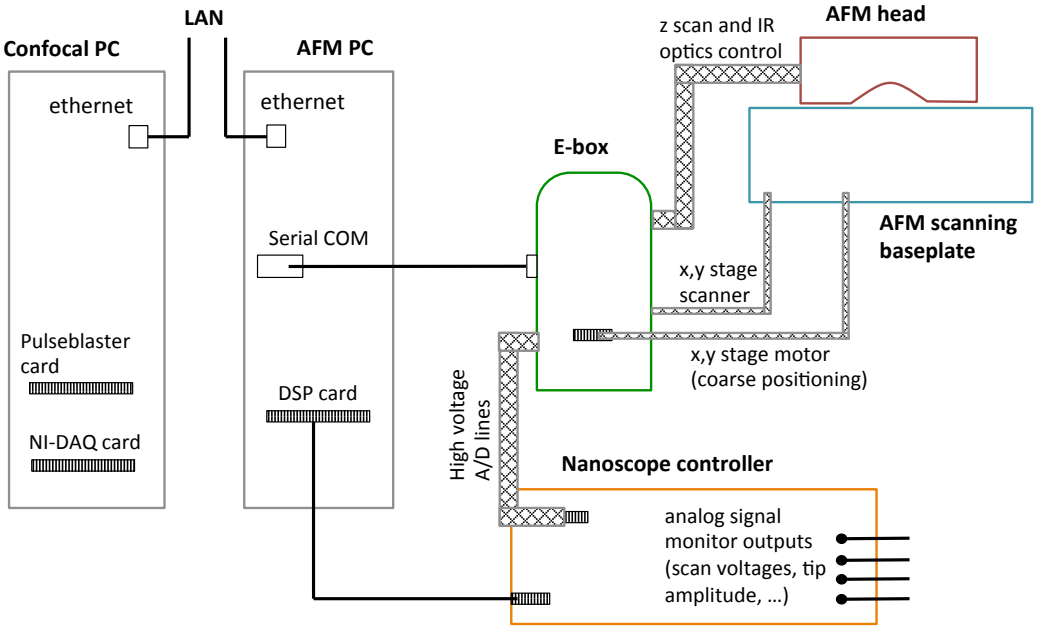

Figure 2.18: Schematic of optical-based AFM scanning electronics for Magnetometer A. The AFM PC, E-box, Nanoscope controller, and AFM baseplate and head are part of the Bruker Catalyst system. For synchronization with ODMR for NV magnetometry the AFM positioning commands are controlled from the custom confocal microscope Matlab software on "Confocal PC" through a lab network connection using Microsoft Distributed Component Object Model (DCOM).

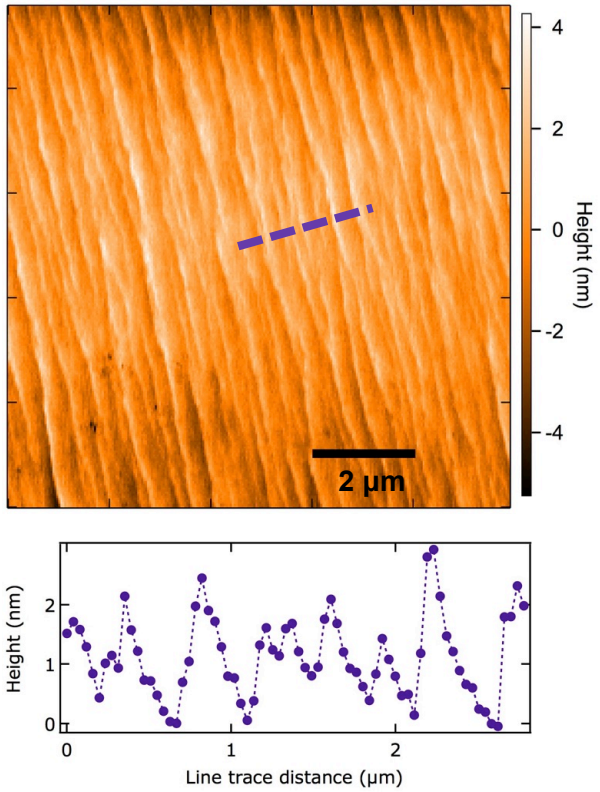

Figure 2.19: Topographic AFM image of a CVD-grown [001] diamond surface using contact mode with a sharp SiN AFM tip on Magnetometer A. The scan reveals a atomic-scale steps on a flat surface and demonstrates the stability of the combined AFM-CFM setup. The lower panel shows a line cut at the dashed purple line. The growth-formed steps proceed in the [110] crystal direction as discussed in Chapter 3.

scan measurements.

2.4 Scanning magnetometer B for electromagnetic noise imaging

We now describe the components of Magnetometer B, which was designed for imaging electromagnetic fields in a sample-on-tip geometry because custom and versatile samples on tips can be engineered and easily integrated. In general, it can be used for various imaging modes, such as dc static magnetic fields [66, 36], electromagnetic noise (the focus

in this dissertation), or coherent electronic and nuclear spins [179, 72, 73]. In comparison to the commercial AFM of Magnetometer A, the custom tuning-fork-based AFM for Magnetometer B was designed to minimize the optics involved in the experiment and thereby open up the region around the probe for easier access of microwave lines, a permanent magnet, and other components. The all-electrical detection eliminates background infrared light and the need for extra alignment steps. In addition, it is convenient to be able to scan the tip in all three dimensions while keeping the diamond fixed, eliminating the need to calibrate the CFM laser scan axes to the AFM stage scan axes to have the laser spot follow the NV during a scan. Finally, while a commercial AFM and its software are not designed for the needs of scanning-NV magnetometry, the Magnetometer B system is easier to use and more versatile because the AFM hardware and software is homebuilt.

2.4.1 Optical setup

The confocal microscope schematic for Magnetometer B is shown in Fig. 2.20 and the optics parts list is given in Fig. 2.21. The optical layout is nearly the same as the one for Magnetometer A (Fig. 2.14) with a primary difference being the use of a single-mode red collection fiber in place of a free space pinhole. Besides simplifying alignment, the fiber is easily swapped with a fiber beamsplitter to perform Hanbury Brown and Twiss measurements of intensity correlation to identify single NV emitters. Like Magnetometer A, the relative arrangement of the optics and AFM from opposite sides of the diamond allows for close access of a high-NA objective, though here the objective comes from the top and the AFM from the bottom.

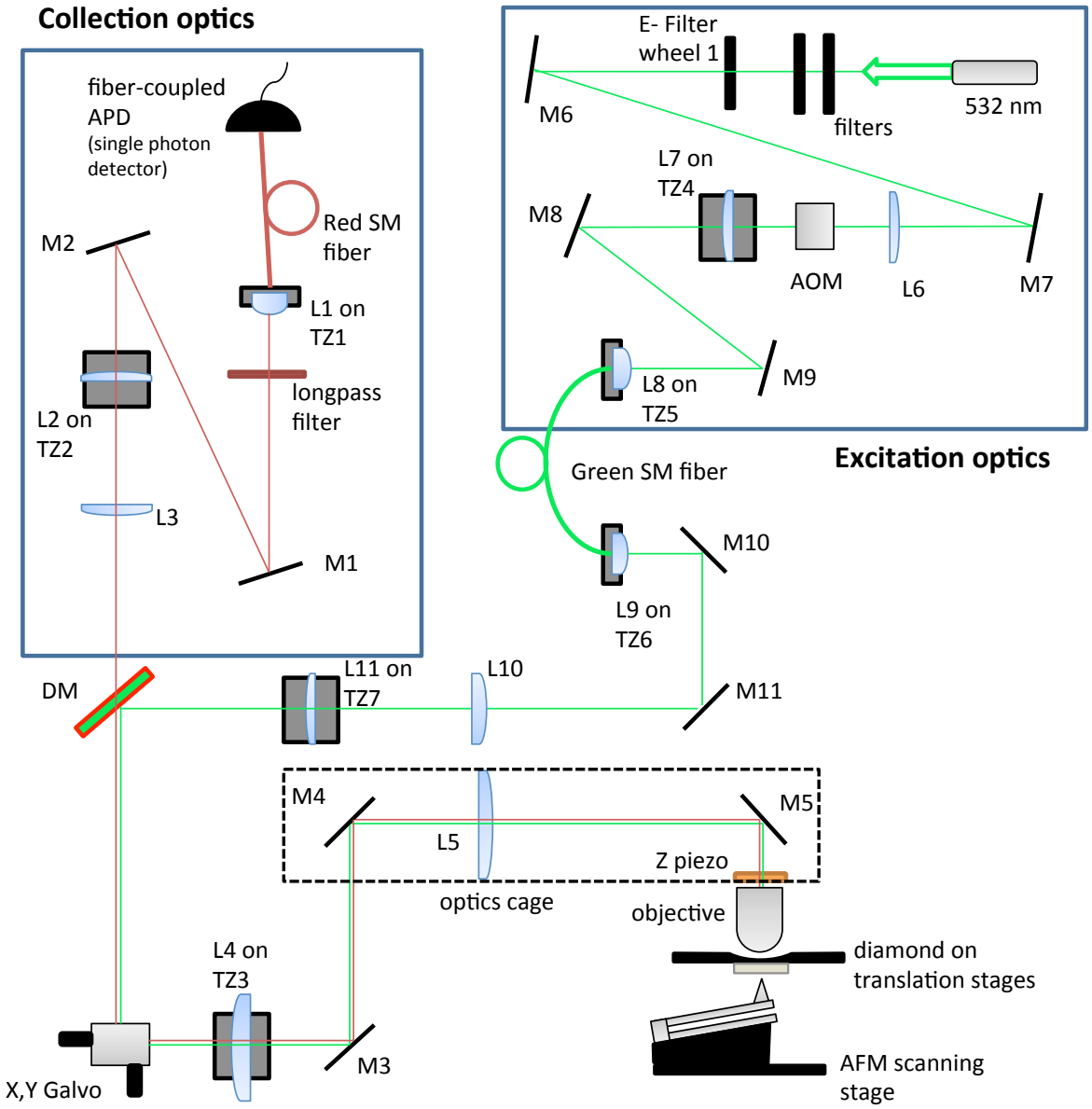

Figure 2.20: Schematic of the laser-scanning confocal microscope of Magnetometer B for electromagnetic noise imaging and decoherence experiments. Mirror M3 to M4 is a vertical path to an optics cage and M5 to the objective is a second vertical path, and otherwise the optical path is parallel to the table. Fine x, y laser scanning is provided by two galvo mirrors and fine z focus is provided by objective translation on a piezo. Details about the labeled components are given in Figure 2.21.

Lenses	Description	Purpose	Vendor	Part no.
objective	NA = 0.95, Ø = 8.55 mm, air	Excite NV and wide-angle PL collection	Olympus	UPLSAPO40X2
L1	11 mm asphere, B-coated	Focus red PL into fiber for detection	Thorlabs	A397TM-B
L2	100 mm achromat, B-coated	M=0.5 collection telescope	Thorlabs	AC254-100-B
L3	200 mm achromat, B-coated	M=0.5 collection telescope	Thorlabs	AC508-200-B
L4	150 mm achromat, B-coated	M=2.0 scan telescope, “scan lens”	Thorlabs	AC508-150-B
L5	300 mm achromat, B-coated	M=2.0 scan telescope, “tube lens”	Thorlabs	AC508-300-B
L6	125 mm plano-convex, A-coated	M=1.6 telescope, focus laser into AOM	Thorlabs	LA1986-A
L7	200 mm plano-convex, A-coated	M=1.6 telescope, re-collimate after AOM	Thorlabs	LA1708-A
L8	8 mm ashpere, A-coated	Focus 532-nm laser into excitation fiber	Thorlabs	C240TME-A
L9	11 mm asphere, A-coated	Re-collimate 532-nm laser after fiber	Thorlabs	A220TM-A
L10	50 mm plano-convex, A-coated	M=2.0 green telescope	Thorlabs	LA1131-A
L11	30 mm plano-convex, A-coated	M=2.0 green telescope	Thorlabs	LA1509-A

Mirrors/ filters/misc	Description	Purpose	Vendor	Part no.
M1, M2	2” and 1” dielectric mirrors	Direct collected PL into red fiber	Thorlabs	BB2-E02, BB1-E02
DM	Dichroic mirror, OD 4	Transmit NV PL, reflect 532 nm excitation	Semrock	Di01-R532-25x36
X,Y Galvo	Scanning mirrors	Scan beam along the diamond plane	Thorlabs	GVS012 (10 mm)
M3, 45,	2” dielectric mirrors	Direct laser and NV PL to/from objective	Thorlabs	BB2-E02
M6, 7, 8, 9	1” silver mirrors; Polaris mounts	Direct laser through AOM and green fiber	Thorlabs	PF10-03-P01
E-filter 1	Interference filters, PC-controlled	Variable attenuation of 532-nm laser	Semrock	FW102C
Red fiber	single-mode 633-780 nm	Reject out-of-focus light from sample	Thorlabs	SM600
Green fiber	single-mode 450-600 nm	Reject out-of-focus excitation light	Thorlabs	SM460HP
M10, 11	1” silver mirrors	Direct excitation laser to dichroic mirror	Thorlabs	PF10-03-P01
TZ1, 5, 6	Z-axis cage translation mount, 2 mm	Fine focusing of fiber-coupling lenses	Thorlabs	SM1Z
TZ2, 3, 4, 7	translation stage, 1”	Adjust telescope lens-lens distance	Thorlabs	PT1
Longpass	Long wavelength filter > 600 nm	Cut out collection light outside NV PL band	Semrock	BLP01-594R-25

Figure 2.21: Table of optics lens, mirror, and filter components for the confocal microscope of Magnetometer B in the most recent configuration.

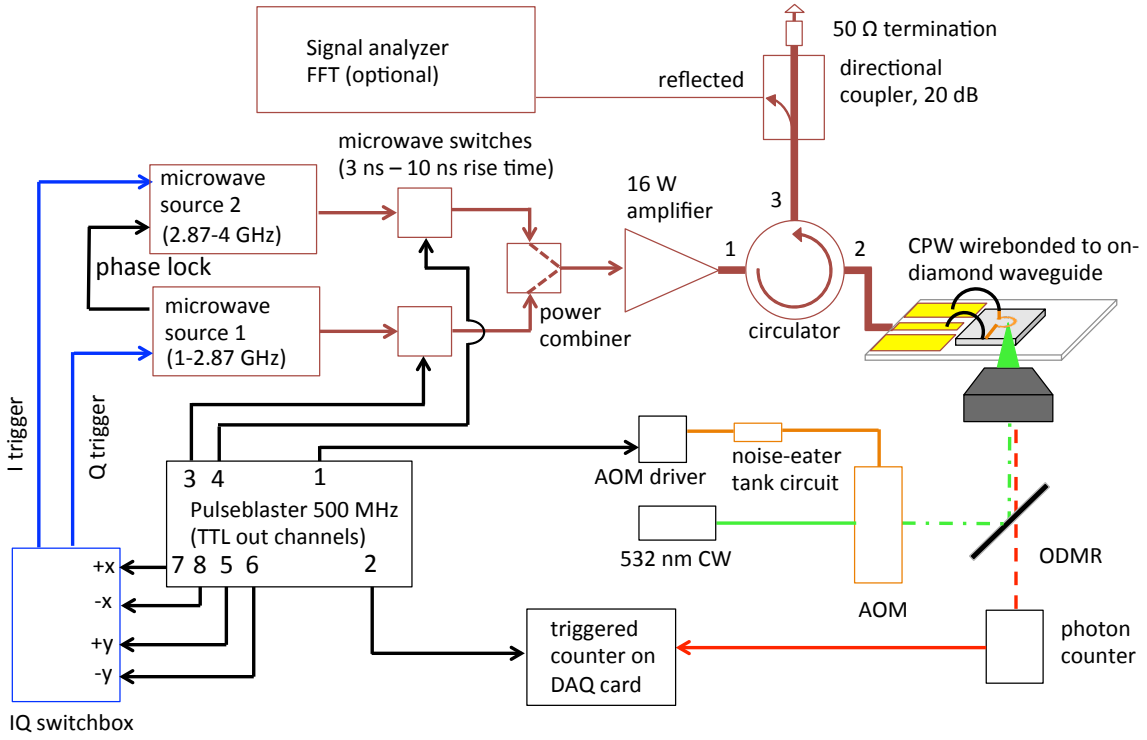

Figure 2.22: Diagram of the microwave circuit and pulse timing for ODMR experiments that use dual microwave tones for $|0\rangle \leftrightarrow |-1\rangle$ and $|0\rangle \leftrightarrow |1\rangle$ spin rotations. The setup is mostly the same as in Fig. 2.16. In addition, there are two frequency-locked signal generators with individual switches, and these signals are combined before amplification. IQ control gives added isolation between on and off states. The diagram also shows the shorted waveguide patterned on diamond and wirebonded to a larger CPW.

2.4.2 CFM control, microwaves, and pulse timing

The CFM and pulse sequence timing of Magnetometer B are controlled identically as in Magnetometer A. We include here a modified illustration of Fig. 2.16 to show changes to the microwave circuit that enable us to use two microwave tones to drive simultaneously the $|m_s = 0\rangle \leftrightarrow |m_s = 1\rangle$ and $|m_s = 0\rangle \leftrightarrow |m_s = -1\rangle$ transitions in one pulse sequence shot. These signals are combined, amplified, and then sent to the diamond sample. The two-tone pulse sequences are for measuring all three relaxation rates of the NV center's spin-triplet ground state, which we demonstrate in Chapter 5 to identify and study a previously unobserved source of decoherence related to the diamond surface.

2.4.3 Combined AFM and optical setup

Photographs in Figure 2.23 overview the diamond sample stage region of the setup where the CFM and AFM both access the NV centers. The tube lens and mirrors are mounted in a rigid cage system that reflects the excitation beam into the objective, which is mounted to a fine piezo focus positioner (MCL Nano) and a coarse manual translation stage (Thorlabs LT1) with 2" of range. This long range is helpful for mounting the diamond sample and AFM tip with the objective safely retracted. In Figs. 2.23(b) and 2.24(a) the system is shown with the optics and AFM fully aligned to and engaged to a single NV center.

Magnetic materials were minimized close to the diamond sample, as shown in Fig. 2.24(b). The diamond was glued to a thin titanium foil sheet ($t < 50$ μm) drilled with a 1-mm hole in the center for optical access through the backside of the diamond. The sheet is fastened to an aluminum mounting plate with four brass screws. This plate is attached to a three-axis piezo motor stage assembly (Micronix PPS-10, x, y, z: $12, 12, 18$ mm of travel) for independent positioning of the diamond NVs relative to the AFM tip and optics. The diamond positioning stage and tip scanning stage are both mounted to a coarse x, y positioning stage (Newport 406). This shared stage was adjusted first to align the tip to the center of the objective's laser scan field of view, which also moves the diamond sample. After the tip is aligned to the optics, the diamond sample is inserted and its piezo motors translated for positioning the desired NV to the center of the field of view. A detailed procedure of AFM-to-optical alignment is included in Appendix B. Figures 2.24(b) and (c) also show the CPW-on-pcb that delivers microwaves to the diamond and a close-up photo of a diamond (B031) with lithographically patterned wires wirebonded to this larger CPW. Also visible here is the 1-mm hole for optical access from the backside of the diamond. Figure 2.25 shows four pictures of the mounting of a tuning

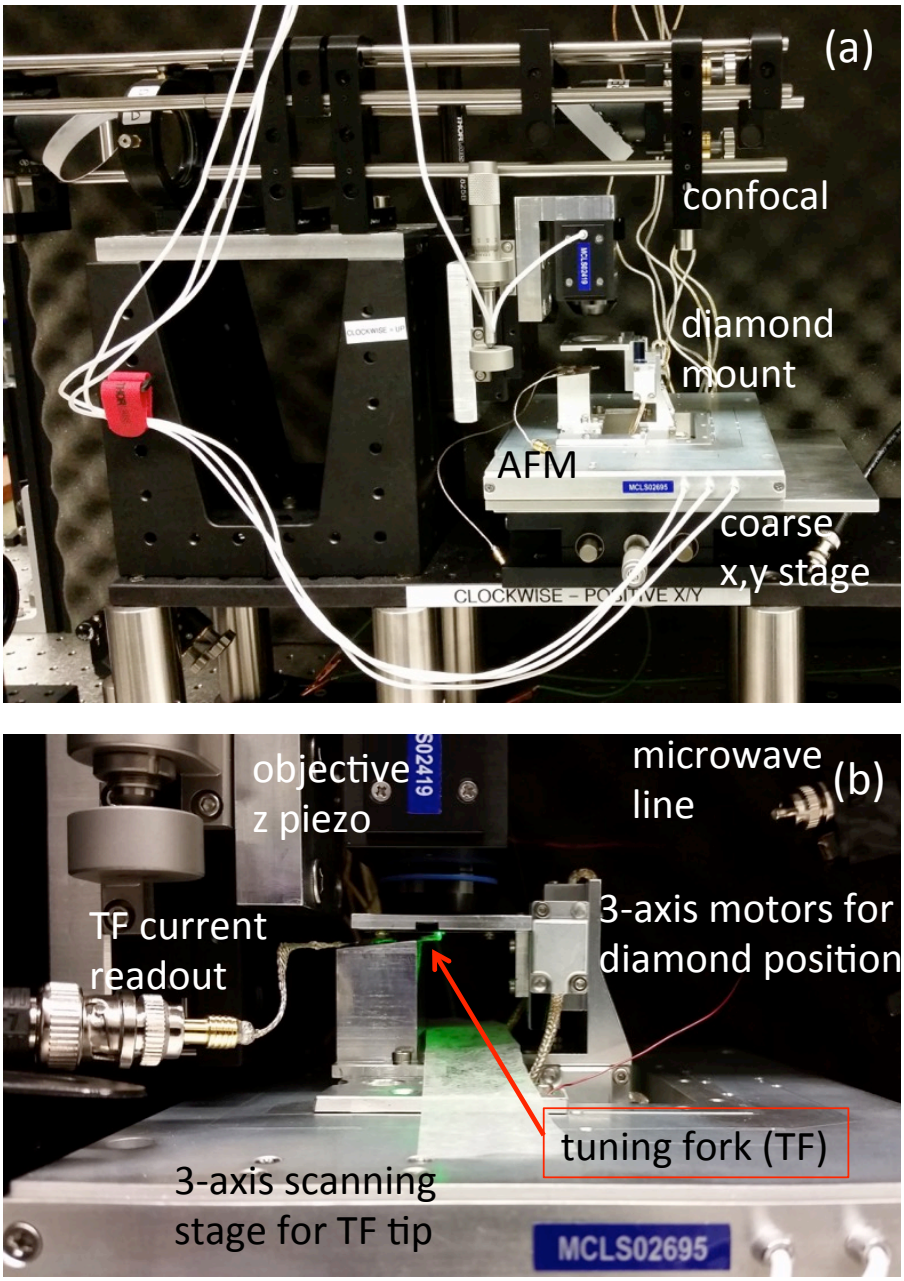

Figure 2.23: Photographs of Magnetometer B setup on an optical table for NV scanning magnetometry. (a) Sample area of the setup in an enclosure box, showing the top-down confocal microscope above the diamond mount and the inverted tuning–fork-based AFM at the bottom. The objective and tip are both far from the diamond sample. (b) Close-up photo of the system when the AFM is engaged and the confocal microscope's 532-nm laser is focused on the diamond. The TF is angled at 5° relative to the scan axis. In the top right is an MCX connector for the microwave line.

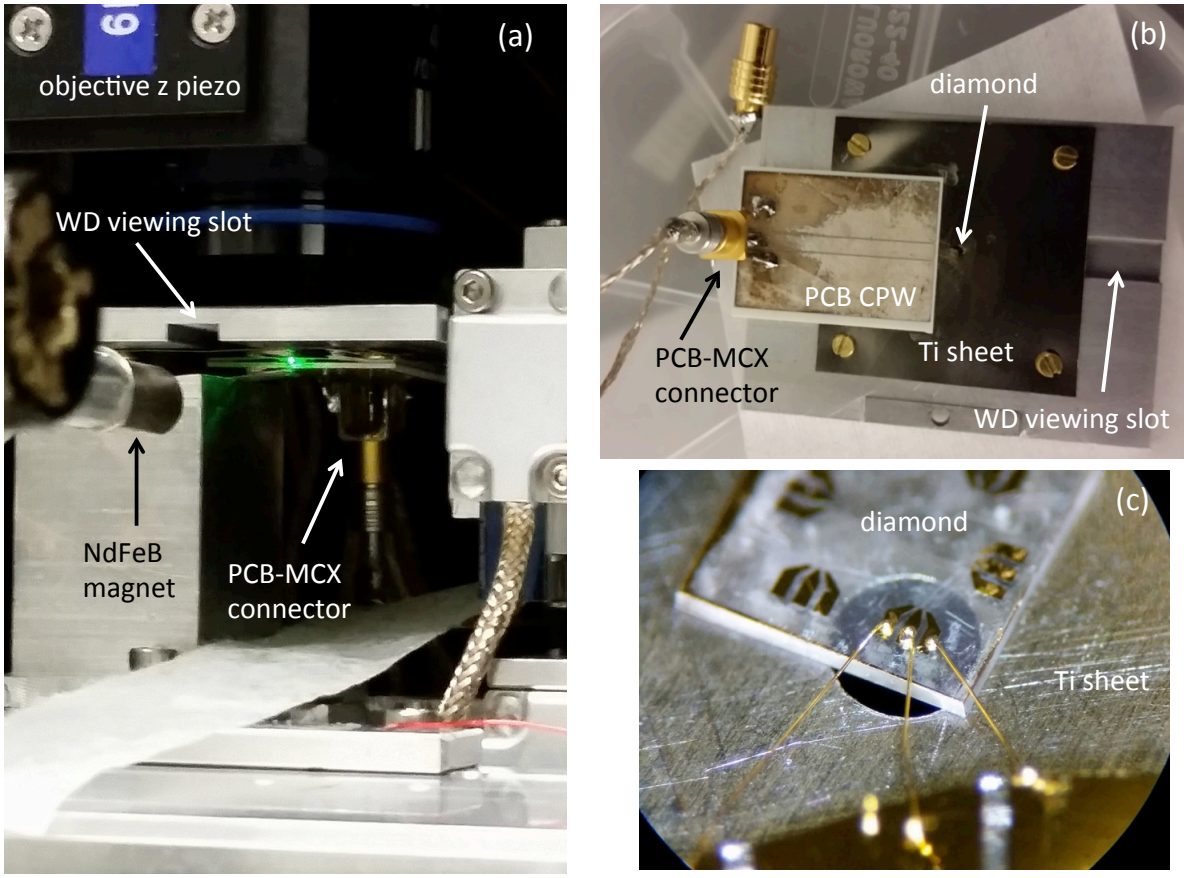

Figure 2.24: (a) Magnetometer B with aligned and engaged AFM and optics for scanning ODMR measurements on a single NV. A retractable permanent magnet applies a static bias field aligned along one NV axis orientation. A PCB waveguide delivers microwaves to the diamond chip. The WD viewing slot is for monitoring the objective working distance, which is WD $\lesssim 0.18$ mm from the Ti sheet. (b) Aluminum mount for the diamond sample. The diamond is glued to a 50-μm-thin Ti foil sheet and its on-chip waveguide is wirebonded to a larger PCB waveguide for applying microwaves. An MCX connector is soldered to the PCB waveguide and connected to a floppy stranded wire to prevent transmission of vibrations to the AFM. (c) Micrograph of a 2 mm$\times$ 2 mm$\times$ 0.15-mm diamond chip (B031) from the face accessed by the AFM tip. The diamond is over a 1-mm hole in the Ti sheet and wirebonds connect to a shorted on-chip CPW.

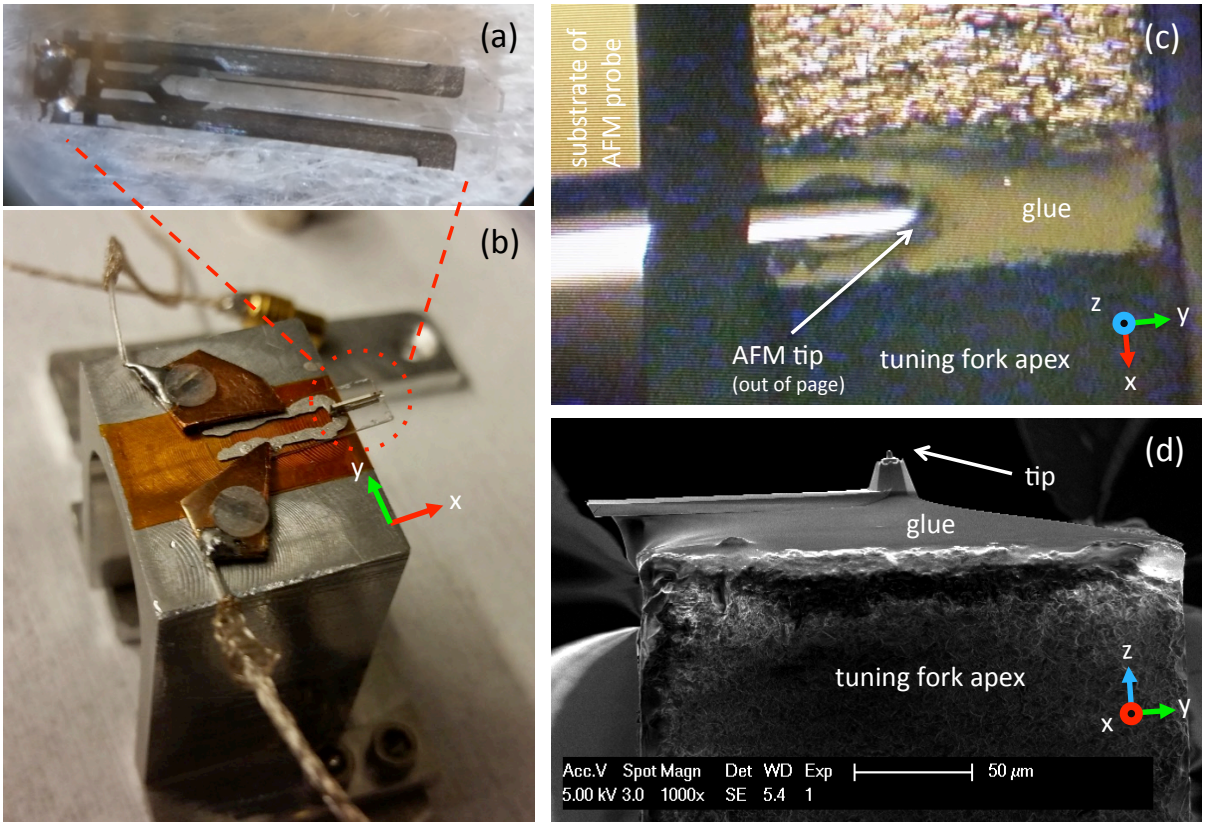

Figure 2.25: Photos of tuning-fork-based AFM probe for magnetometer B. (a) Example of a 32-kHz quartz tuning fork (TF), with two electrical leads, used for the AFM's force detection. (b) The TF is glued to a sapphire chip in vertical tapping–mode orientation and the assembly is clamped to conducting leads for on-resonance excitation and current readout. An AFM tip is glued to the apex (far $+x$ direction) of the TF's free tine, as seen under a microscope. (c) Top-down micrograph of standard silicon AFM cantilever and tip glued to the apex of the TF tine. (d) Scanning electron micrograph from the front looking down the tine ($-x$ direction).

fork AFM probe from the centimeter scale of mounting the tuning fork to the micron scale of a silicon tip glued to one tine of the tuning fork. The procedures for micro-fabricating custom plateau-topped silicon tips and gluing them to tuning forks is outlined in Chapter 7. In the next section of this chapter, we discuss the principle of amplitude modulation AFM using a tuning-fork-based system, and then we describe our implementation and electronics for the NV scanning magnetometer.

2.4.4 Scanning probe with a quartz tuning fork

Like the silicon micro-cantilever AFM, a tuning-fork AFM also uses a sharp tip attached to a resonator to "feel" the topography of a surface, but major differences arise in the detection method and mechanical properties. Although tuning forks in general are mechanical resonators, a TF made of quartz can also be modeled electrically due to its piezoelectricity. The piezoelectric effect is the accumulation of charge or voltage due to a mechanical stress of the material, and reversibly, an applied voltage causes deformation of the material. Piezoelectric materials also enable the sub-nanometer precision of scanning stages for most AFMs regardless of the type of probe used. Because of this property, the quartz TF's mechanical resonance is usually modeled with an electrical RLC circuit analog. Here R, L, and C are the effective resistive, inductive, and capacitive parameters corresponding to damping, inertia, and elastic potential of the mechanical TF resonator. The TF also has actual electrical parameters R_e, L_e, and C_e. The two isolated metal leads snaking around the tines give the TF a large electrical DC resistance of $R_e > 1$ GΩ. The inductance L_e is negligible, but the "shunt capacitance", C_e, is significant enough to alter the behavior of the TF resonance from the ideal RLC-like behavior.

The resonance of the RLC circuit corresponds to the mechanical resonance as $\omega_0 = 1/\sqrt{LC} = \sqrt{k/m}$. We can relate the current signal to the applied drive voltage by

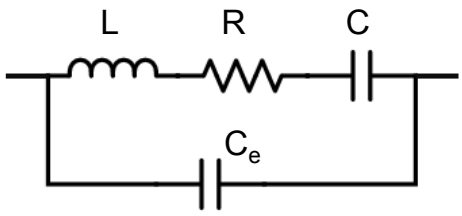

Figure 2.26: Equivalent electrical RLC circuit for tuning-fork mechanical resonator. The three top elements are electrical analogs for the mechanical dissipation (R), mass (L), and spring constant ($1/C$). The parallel shunt capacitance C_e is an actual electrical contribution due to both the geometry of the TF and the cable for current readout.

computing the impedance of the circuit in Fig. 2.26 with $j = \sqrt{-1}$

$$\begin{aligned} \frac{1}{Z} = \frac{1}{Z_{\text{mech}}} + \frac{1}{Z_{\text{elec}}} &= \frac{1}{R + j\omega L + \frac{1}{j\omega C}} + j\omega C_e \\ &= \frac{\omega^2 C^2 R + j\omega C\left(1 - \omega^2 LC\right)}{\omega^2 C^2 R^2 + \left(1 - \omega^2 LC\right)^2} + j\omega C_e \end{aligned} \tag{2.7}$$

and applying a voltage drive $v(t) = v_0 e^{j\omega t}$ so that the current is

$$\begin{aligned} i\left(t\right) = \frac{v\left(t\right)}{Z} &= \frac{\omega^2 C^2 R + j\omega C\left(1 - \omega^2 LC\right)}{\omega^2 C^2 R^2 + \left(1 - \omega^2 LC\right)^2} v_0 e^{j\omega t} + j\omega C_e v_0 e^{j\omega t} \\ &= i_0\left(\omega\right)\cos\left(\omega t + \phi\left(\omega\right)\right) + i_e\left(\omega\right)\sin\left(\omega t\right) \end{aligned} \tag{2.8}$$

The first term in Eq. 2.8 is current due to the tuning fork piezoelectric effect alone, and it has both real (in phase) and imaginary (out of phase) components. The phase angle of the current response for this term is

$$\phi\left(\omega\right) = \tan^{-1}\left(\frac{1 - \omega^2 LC}{\omega RC}\right) \tag{2.9}$$

such that $i(t)$ is completely in phase with the drive $v(t)$ when $\omega = \omega_0 = (LC)^{-1/2}$. The imaginary shunt capacitance term in Eq. 2.8, however, is 90° out of phase with the drive

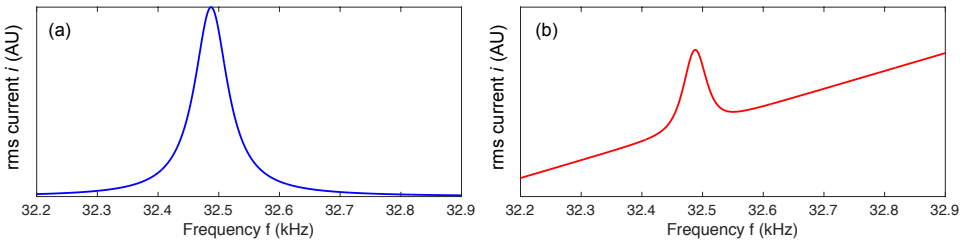

Figure 2.27: Calculation of rms current response, Eq. 2.10, of tuning fork to a driving voltage using a simple RLC electrical model of the mechanical resonance. Parameters used are $R = 1$ MΩ, $L = 2.4$ kΩ, and $C = 10$ fF, giving resonance frequency $f_0 = 32.487$ kHz and $Q = 490$. (a) Ideal current response where the shunt capacitance C_e is zeroed. (b) Non-ideal response for when this capacitance is large, $C_e = 30$ μF.

when $\omega = \omega_0$. The rms current is calculated from Eq. 2.8 as

$$\begin{aligned} i_{\text{rms}}(\omega) &= \lim_{T\to\infty} \sqrt{\frac{1}{T}\int_0^T |i(t)|^2\, dt} \\ &= \frac{v_0}{z_0(\omega)} \sqrt{\omega^4 C^4 R^2 + \omega^2 \left[C\left(1-\omega^2 LC\right) + z_0(\omega)\, C_e\right]^2} \end{aligned} \tag{2.10}$$

where $z_0(\omega) = \omega^2 C^2 R^2 + (1-\omega^2 LC)^2$. For the purpose, of the AM-AFM this C_e is important because it can distort the rms current amplitude response curve of the tuning fork or completely dominate over the resonance signal if it is too large. In Fig. 2.27 we plot Eq. 2.10 for example RLC parameters in the cases of a negligible C_e and large C_e.

We operate the TF only in the "qPlus" mode [60], where one of the tuning fork tines is mechanically fixed so that it is more like a quartz cantilever than a tuning fork. Therefore, a single spring and mass attached to a much larger mass becomes an adequate mechanical description. This qPlus configuration was invented for non-contact AFM because in the original two-prong TF configuration the inevitable asymmetry between the prongs when one contacts a surface can cause the quality factor Q to collapse [61]. In our case, the goal is not strict non-contact AFM, but we benefit from the TF's self-sensing that doesn't require optical detection and its very high stiffness that prevents snap-in of the tip to the sample surface. The spring constant k is large even compared

to the interatomic carbon bond effective spring constant in diamond, which is $k_d \approx 1020$ N/m [61].

The type of tuning forks that we use as force sensors have tine dimensions of length $L = 3$ mm, width $W = 300$ μm, and thickness $T = 400$ μm. The unloaded resonant frequency of the TF's single clamped beam is $f_0 = 32.768$ kHz. The spring constant for the beam structure's bending mode is $k_{\mathrm{TF}} \approx EWT^3/(4L^3) \approx 14000$ N/m, where $E \approx 79$ GPa/strain for quartz [60]. This k_{TF} is an approximation because the tip is an added mass and also is not glued directly at the edge of the TF tine, and moreover each TF has geometric and elastic variations, but the main point is that k_{TF} is orders of magnitude larger than for a silicon micro-cantilever. We do not require precise knowledge for the force constant for our application, however, we use these parameters to estimate the tapping amplitude of the quartz cantilever.

The large k_{TF} of the TF cantilever is helpful in allowing stable small-amplitude operation even when the tip is interacting with a surface, which we want to use to keep the NV near the sample continuously. For effective mass m of the eigenmode, frequency is given by $f = \left[k_{\mathrm{TF}}/m\right]^{1/2}/(2\pi)$, and this value shifts with the addition of tip-sample forces to $f + \Delta f = \left[(k_{\mathrm{TF}} + k_{ts})/m\right]^{1/2}/(2\pi)$. For large amplitudes of oscillation (e.g. 10s of nanometers) the k_{ts} changes significantly over the oscillation period so a mean $\langle k_{ts} \rangle$ is more appropriate to describe $f + \Delta f$. Then $\langle k_{ts} \rangle$ may be small since most of the cycle the tip is not close to contacting the surface. However, for small amplitudes of oscillation on the order of a nanometer the tip is never too far from the surface and $\langle k_{ts} \rangle$ can become very large. If we reasonably assume the tip contacts a diamond surface with a $k_{ts} \lesssim k_d$, then the tuning fork k_{TF} is still an order of magnitude larger than k_{ts}. Therefore $\Delta f/f \ll 1$ so stable oscillation is easier to achieve [61] compared to an attempt of small-amplitude operation with a silicon microfabricated cantilever.

There exist several semi-empirical methods to determine the amplitude of the TF

oscillation. We show here a method that relies on straightforward measurements of electromechanical properties of the TF [180]. We assume for the calculation that one of the two tines is free to vibrate at its $n = 1$ eigenmode and the other is fixed; $k = k_{n=1}$ and $\omega \equiv \omega_{n=1}$. First, the spring constant is computed from dimensional and elastic properties as in the equation above for $k = k_{\mathrm{TF}}$. The elastic energy stored in the free tine is $\xi_m = ka_0^2/2$ for a sinusoidal motion at the end of the tine $a(t) = a_0 \cos(\omega t)$. During each oscillation period, the fraction of ξ_m lost is quantified by the Q-factor, so that the energy loss per unit time is

$$\left(\frac{d\xi_m}{dt}\right)_{\mathrm{loss}} = -\frac{\omega k a_0^2}{2Q}. \tag{2.11}$$

The TF is electrically driven so that mechanical energy is pumped into the oscillator at a rate

$$\left(\frac{d\xi_m}{dt}\right)_{\mathrm{drive}} = v_{\mathrm{rms}} i_{\mathrm{rms}} \tag{2.12}$$

where v_{rms} and i_{rms} are the voltage and current from the lock-in output to drive the TF. Note that this v_{rms} describes the drive signal, which has a bandwidth much narrower than the TF response. Equating Eqs. 2.11 and 2.12 gives the amplitude result

$$a_{0,\mathrm{rms}} = \sqrt{\frac{2Q v_{\mathrm{rms}} i_{\mathrm{rms}}}{2\pi f k}} \tag{2.13}$$

where the factor of 2 in the numerator again comes from considering one free prong and $f = \omega/2\pi$ is the resonant frequency of the TF at which the sinusoidal drive is tuned. To determine Q and f, we sweep the drive frequency at constant v_{rms} and fit the response peak with a Lorentzian. Typical values of the loaded TF exposed to air are $Q = 300 - 2000$ and $f = 32 - 33$ kHz. The i_{rms} is computed by assuming the rms current of the drive (i_{rms}) and detection ($i_{\mathrm{meas,rms}}$) leads are equal. We measure the output current via a current amplifier with a gain of $G = 5 \times 10^7$ V/A, so that the current is

$i_{\text{rms}} \approx i_{\text{meas,rms}} = G v_{\text{meas,rms}}$; $v_{\text{meas,rms}}$ is the rms voltage output of the amplifier measured at the lock-in. Our target peak-to-peak amplitude $a_{p-p} = 2\sqrt{2} a_{0,\text{rms}}$ is about 1-3 nm so that the tip always remains close to the surface when the drive and height feedback are on. This 1-nanometer amplitude is typically achieved for $v_{\text{drive}} = v_{\text{rms}}\sqrt{2} \approx 1$ mV for the parameters listed above. The possible limitations of this elastic-energy method are that a small finite resistance in the leads attached to the tuning fork will dissipate some energy and lead to computation of a slightly underestimated tapping amplitude. Thus, Eq. 2.13 might be considered a lower bound on the amplitude.

An alternative method to determine the tapping amplitude is based on the thermal Brownian motion of the tuning fork. This is easier with the vacuum can still on the tuning fork since the Q should be higher. The amplitude curve of the undriven tuning fork is measured at its resonance frequency f, which is the same amplified current-to-voltage measurement as above. The integral under this voltage peak can then be compared to the expected rms Brownian motion

$$x_{0,\text{rms}} = \sqrt{k_B T / k} \tag{2.14}$$

where k is again the spring constant, T is the ambient temperature, and k_B is the Boltzmann constant. For $k = 14000$ N/m this gives $x_{0,\text{rms}} \approx 0.54$ pm or peak-to-peak $x_{0,p-p} \approx 1.5$ pm. Once the pm-per-V conversion between the area under the undriven curve $v_{0,\text{rms}}$ and theoretical $x_{0,\text{rms}}$ is known, then one can drive the tuning fork without the vacuum can and use the same unit conversion to obtain x_{rms} from v_{rms}. The Q will decrease under ambient conditions, but the integrated area under the resonance curve should remain the same. k will vary slightly for different "identical" tuning forks due to production variations, but the order of magnitude conversion ratio is sufficient for our purposes.

Third, the tapping amplitude can be directly measured if the sample z piezo is calibrated for distance per volt. As the oscillating cantilever approaches the surface with a large tapping amplitude its amplitude will begin to go down roughly linearly with the distance because the tip will contact the surface before its full downward motion. For example a cantilever tapping with an unknown peak free amplitude a_p and output current i_{rms} will output only $i_{\mathrm{rms}}/2$ when its center of motion is within $a_p/2$ of the surface because the tapping trajectory is becomes constrained due to the enormous repulsive force of the surface. This experiment is performed by moving the z stage toward the tip until, for example, $i_{\mathrm{rms}}/2$ is observed and the stage displacement $\Delta z = a_p/2$. the result is a conversion factor from the observed output i_{rms} to physical amplitude a_p. This method is best done with a larger drive and tapping amplitude on the order of 10s of nanometers for a clear effect. However, too large a reduction in amplitude can also cause damage to the tip.

We use amplitude modulation AFM (AM-AFM) for operation of the qPlus sensor because a stable feedback loop is simpler to implement than in frequency modulation AFM (FM-AFM), the latter of which requires an additional phase-locked loop (PLL). In the ambient conditions of our scanning experiments, the Q is lower than in vacuum so the frequency sensitivity is reduced anyway. Changes in amplitude in AFM-AFM are slow due to ring-down time, for example, $Q = 1000$ and $f_0 = 32$ kHz gives a ring down time of $\tau = Q/(f\pi) \approx 10$ ms. However, this is sufficient for NV magnetometry experiments, which require a long dwell time per pixel on the order of 100s of milliseconds for static field imaging to minutes for decoherence imaging. The AFM-AFM mode does place a speed limit on fast topographic scanning, although in our case the low bandwidth ($\sim 10 - 100$ Hz) of the scanner piezo stage (MCL LP-100) is is more limiting to the feedback response. If the Q were too much higher, such as 10000-50000, then the AFM-

AFM mode may become less feasible.[2]

2.4.5 AFM control electronics

The control electronics for the AFM of Magnetometer B are centered on a commercial box (Zurich Instruments HF2LI 50 MHz) containing a lock-in amplifier, PI feedback loops, and an internal frequency reference. In addition, we use homebuilt electronics boards ("AFM box") to condition the various voltage signals in the experiment, including the elimination of group loops. The overall control scheme is illustrated in Fig. 2.28. Typically AM-AFM is performed by setting the frequency f of the lock-in drive v_{drive} a little lower than f_0 so that when the frequency shifts higher due to repulsive tip-sample forces then the amplitude changes rapidly on the steep part of the response curve. However, we have also found that driving at $f = f_0$ allows for a sensitive reduction in the amplitude signal, which we attribute to the Q of the quartz cantilever reducing with smaller tip-sample separation. The excitation output is sent for conditioning by the AFM box and used to drive one of the metal leads of the TF. The output current from the other TF lead serves as the self-sensing signal, which is read out as a voltage. We use a commercial current-to-voltage amplifier (Femto LCA-100K-50M) with a transimpedance gain of 5×10^7 V/A, bandwidth DC to 100 kHz that covers f_0, and equivalent input noise current 30 fA/$\sqrt{\text{Hz}}$. For the 1-mV-peak drive voltage, peak currents at from the TF are typically 0.1-1 nA (depending on Q) as measured by the lock-in. The cable between this TF lead and the current amplifier must be made as short as possible because cable capacitance negatively affects the noise in the measurement [61]. In addition, the TF's shunt capacitance and the cable capacitance are compensated by a potentiometer adjustment ("cap zero out"). The calibration of this compensation is done by sweeping

[2]In a more recent upgrade to the setup in 2016, we have added a high-bandwidth z scanner so that faster topographic imaging for drift analysis is enabled.

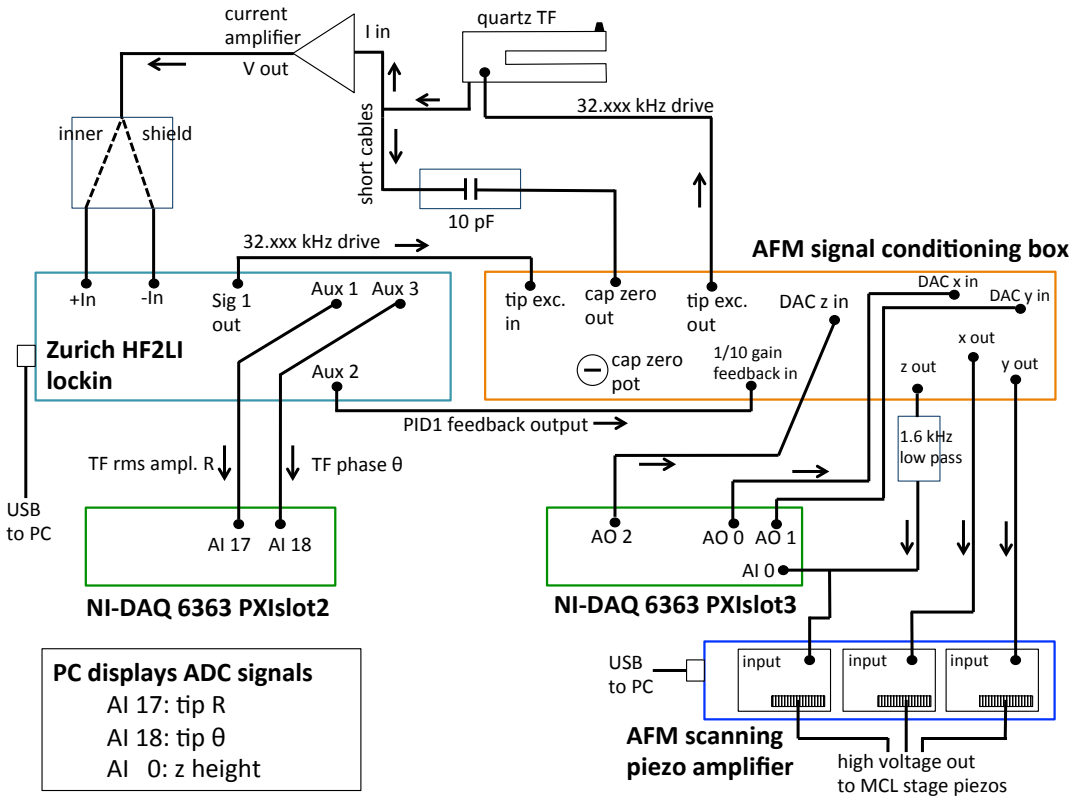

Figure 2.28: Schematic of tuning-fork AFM scanning electronics for Magnetometer B. The setup controls excitation and current-to-voltage readout $\left(Re^{i\theta}\right)$ of the AFM tuning fork, low-noise conditioning of the analog x, y, z scanning voltages, analog and digital offsets of scan voltages, and a feedback loop for the z voltage based on AFM amplitude as the error signal.

f of the drive across the resonance and observing the current response via the voltage sent to the lock-in input. The capacitance is compensated until the resonance curve is symmetric, which practically can be achieved by fixing the drive far off resonance and minimizing the current signal. The amplitude and phase of the readout are also sent to analog inputs (AI17, AI18) of a NI-DAQ to monitor them continuously in the custom AFM control software.

The second aspect of the control electronics involves the height feedback and scanning. The feedback loop uses a PI circuit in the HF2LI, where the error signal is the difference between the lock-in amplitude (TF current) and a setpoint voltage. The output voltage

of the PI loop is sent to the AFM box where it is divided by 10 and summed with an offset z voltage from the NI-DAQ ("DAC z in"). The output z voltage is sent to the piezo amplifier (MCL 3-axis Nano-Drive) analog input, which scales 0-10 V input into a high-voltage signal to displace the z piezo (MCL Nano-LP100) over a range 0-100 μm. Similarly, analog voltages for x, y scanning are generated at the NI-DAQ, conditioned by the AFM box, and sent to the piezo amplifier for each respective axis with 100 microns of range. These three axes also have digital offsets applied via software commands so that the stage is always operated away from bounds of its range even when the analog inputs to the amplifier are zero. During a topographic x, y scan the total z voltage is also read into the NI-DAQ (AI0) to serve as the height signal, where $H = 10\mu$m/V.

The control routine for the TF's attached tip to approach the sample, usually a single-crystal diamond surface, must be responsive and tuned to avoid damage to the tip on contact. We use a three step procedure to account for the low bandwidth of the massive z scanner stage. First the DAC z voltage is set low to 10-μm displacement of the z stage. The PI loop is enabled with a setpoint of 90-94% the free amplitude and corresponding integral gain I such that the speed of approach is about 100 nm/s. This feedback ensures that if the tip does reach the sample then the change in amplitude will quickly halt the approach via the feedback loop. The DAC z offset voltage steps up in 10-μm increments each time that the PI output ramps up to its set range of 10 μm and returns to 0 (feedback off). Once the total z scanner displacement reaches 90 μm, close to the limit, the DAC z offset returns to the bottom of the range. At this point the diamond sample is stepped toward the tip in a conservative 60-μm increment with a closed-loop piezo motor (Micronix PPS-10). The cycle repeats until the PI feedback stops ramping the output voltage, which occurs when the tip-sample forces reduce the amplitude to the setpoint and the error signal becomes zero.

Typical parameters used for the lock-in and PI feedback on the HF2LI panel are

differential input, AC coupled, 200-Hz filter 3-dB-bandwidth, 225 samples/s, continuous triggering readout, $1-2$-mV peak drive (depending on Q), -300-V/Vrms P gain, -40-V/Vrms/s I gain, $92-94\%$ rms amplitude setpoint, and 0-V default output for disabled feedback. The setpoint and I gain can be adjusted for effective topographic imaging or ideal approach/retract speed to prevent tip damage. A setpoint that is too similar to the free amplitude (e.g., 99%), while gentle, leads to unbalanced feedback behavior: it may not produce a large enough error signal during approach while changing too rapidly on retraction.

2.4.6 AFM vibration measurement

Vibrations of the AFM tip relative to the mounted diamond sample are important to consider because the magnetic signal at a NV sensor from a sample on the tip varies rapidly with nanometer-scale variations in NV-tip separation. To quantify the total rms vibrations of the Magnetometer B setup with the TF-based AFM, we first engaged a sharp silicon tip-on-TF to the sample, as in Fig. 2.23(b), by the approach method described above. Once the tip is in stable tapping-mode feedback with the diamond surface, we set the DAC to output a sinusoidal signal (e.g., 1-mV $\equiv$ 10-nm peak, 5 Hz) to the z axis of the 3-axis scanning stage. The height signal in feedback, that is the output of the PI loop, is acquired for several seconds. The Fourier transform of this signal gives a peak at 5 Hz over a noise floor, where units are amplitude in $\mathrm{V}/\sqrt{\mathrm{Hz}}$. We repeat the same measurement without the 5-Hz drive. We integrate the area under this peak, from it the noise floor under the peak, and compare the known piezo displacement (10-nm peak) to the measured voltage for a ratio r. We use r to convert the undriven measurement to a power spectrum of displacement. Integrating up to 500 Hz gives the spectrum plotted in Fig. 2.29, where we have taken a square-root to give the cumulative rms vibration from

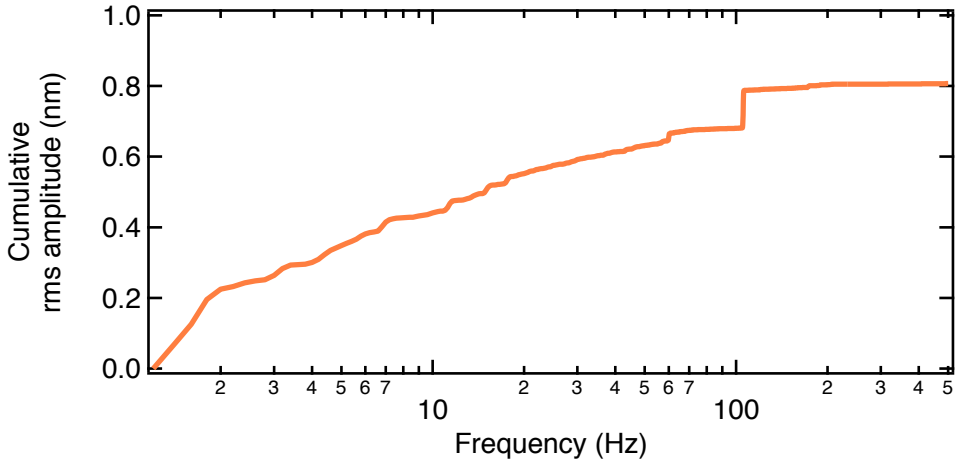

Figure 2.29: Sample-tip vibration spectrum for AFM of Magnetometer B, where the y axis is total rms summed from low to high frequency. The jump at 105 Hz is due to internal feedback for position stabilization in the x, y, z scan stage. The measurement procedure is described in the main text.

dc to frequency f. The jump at 105 Hz in Fig. 2.29 is due to an closed-loop control of the x, y, z scanning stage that is internal to the commercial amplifier and unfortunately could not be tuned over a wide bandwidth range. Nevertheless, these results show that up to 60 Hz the rms vibration level is only 0.64 nm and beyond 105 Hz is 0.81 nm. Thus, over short times scales the variation in NV-sample distance due to uncontrolled vibrations is smaller than the size of the driven tuning fork oscillation at the typical drive voltage 1 mV.

Chapter 3

Engineering near-surface nitrogen-vacancy centers in diamond

We demonstrate nanometer-scale precision in depth control of nitrogen-vacancy centers created near the surface of diamond using a nitrogen delta-doping technique during chemical vapor deposition diamond growth. The delta-doped NV centers in these synthetic diamond films display coherence times of $T_2 > 100$ μs despite nanoscale distance to the diamond surface. This delta-doping technique enables surface-proximate NVs for nanoscale magnetic imaging, such as of external target spins, and integration of the NVs into hybrid quantum systems. Furthermore, the ultrapure quality of the diamond films grown with isotopic carbon-12 enrichment allows the spin-decoherence-inducing effects of the surface to be distinguished from bulk effects, which is explored in subsequent chapters.

[1]Three figures and accompanying discussions in this chapter have been adapted from reference [43]: K. Ohno, F. J. Heremans, L. C. Basset, B. A. Myers, D. M. Toyli, A. C. Bleszynski Jayich, C. J. Palmstrom, and D. D. Awschalom, Engineering shallow spins in diamond with nitrogen delta-doping, *Appl. Phys. Lett.* **101** (2012) 082413

3.1 Introduction

The nanoscale spatial resolution and single-spin sensitivity afforded by the diamond nitrogen-vacancy magnetometer rely upon bringing the sensing NV spin as close as practically possible to the sample under study. Apart from sensing magnetic fields from spins within the diamond itself, this reduction of sensor-target separation requires the NV center to be formed just nanometers from the diamond surface. Near-surface NVs do not occur naturally in sufficient abundance, so it is necessary to employ some means of creating depth-localized spins.

The conventional method to create shallow NVs has been implantation of the diamond with few-keV nitrogen ions [181, 182, 40]. This process also produces vacancies within the ion range, and annealing the diamond causes the vacancies to migrate and combine with a fixed substitutional nitrogen atom. These synthetically formed NVs can be distinguished from naturally occurring ones through nuclear spin labeling with the less-abundant nitrogen-15 isotope [181]. Advantages of N implantation include the tunability of NV depth and concentration by ion energy and fluence and the capability to laterally localize the spins by implanting through nanofabricated apertures [182] or by focusing the incident ion beam [40].

Despite the benefits of implantation, studies of both deep and shallow (depth $\lesssim 50$ nm) implanted NV centers show that the coherence time of NVs vary over a wide range of a few microseconds to 10s of microseconds [182]. This reduction in coherence time, in comparison to T_2 of 100s of microseconds in bulk naturally occurring NVs [136], is thought to be due to surface effects and the variance due to undesired vacancy-related paramagnetic defects that form and persist during implantation and annealing at certain temperatures [183]. These defects have more recently been studied in detail by correlating ensemble EPR measurements with implanted NV coherence times in the same diamond

[127]. In addition, the depth localization of nitrogen implantation suffers from increased depth variation [38] with increased incident energy as well as ion channeling that is sensitive to angle [184]. The issue of low yield of stable NV centers with long coherence times is a challenge for applications from ensemble-NV magnetometry to single-NV scanning probe imaging.

The drawbacks of nitrogen implantation motivated work at UCSB to develop an alternative method to form shallow NV centers with the dual goals of maintaining consistently long coherence times and localizing the NVs to a few-nanometer-thin slice. This chapter first describes single-crystal epitaxial diamond growth using plasma-enhanced chemical vapor deposition (PE-CVD). We then describe the *in situ* nitrogen delta-doping technique developed to form near-surface depth-localized NVs. Finally, we summarize the results of depth localization and spin coherence properties for NVs created by delta-doping, for which complete details can be found in [43]. These engineered diamond materials motivated both parts of this dissertation: 1) investigation into the nature of decoherence sources that affect near-surface NVs, and 2) practical application of near-surface NVs to nanoscale imaging.

3.2 Thin-film diamond growth

Structurally, the solid forms of carbon include graphite with sp^2 bonding and diamond with sp^3 bonding. Graphite is thermodynamically stable at ambient temperature and pressure, although diamond exists as a metastable phase once formed [185]. Diamond can be preferentially formed under non-standard pressure and temperature conditions, and most well known is high-pressure high-temperature (HPHT) synthesis [185]. We focus on growth of single-crystal diamond via low-pressure CVD, which has become a heavily researched method due to capabilities for precise control of growth parameters and dop-

ing as well as promise for advanced semiconducting and heat management properties for electronic devices [185]. For NV-based sensing, single-crystal diamond is preferred over polycrystalline or nanocrystalline diamond materials because grain and crystal boundaries can lead to increased decoherence [35, 186, 187], the NV orientations are not random in SC material, and the SC surface morphology can be atomically smooth over a large area. However, SC diamond films are typically grown with homoepitaxy, which requires nucleation on a diamond substrate, though heteroepitaxial diamond growth on various substrates like silicon(100) is an active area of research [188].

3.2.1 Homoepitaxial step-flow CVD growth

In the homoepitaxial PE-CVD process, hydrogen radicals from a sustained H_2 plasma selectively etch sp^2 carbon while a gas such as methane provides carbon radicals for sp^3 growth. To potentially incorporate nitrogen atoms at layers with a well-defined depth to nanometer precision, a growth mode is desired that generates an atomically smooth surface. In step-flow growth [189], carbon atoms leave the plasma and contact the surface, a step terrace, and the atoms diffuse along the terrace until stopping at a step edge (see Fig. 3.1). The physical conditions favorable for this process can be described phenomenologically with three parameters: carbon deposition rate j, step terrace length L, and diffusivity D. If the speed of a carbon adatom diffusing on the terrace, v_{adatom}, is too slow compared to the rate of step edge growth, v_{step}, then accumulation of non-step nucleation centers can occur.

The step edges advance at a rate $v_{\text{step}} = jL$, where j is in units of monolayers/s. That is, if j is a known rate, then each step of monolayer thickness only needs to advance length L in the time it takes for a monolayer to be deposited. If only one step existed on the substrate, then its length L would be very long and the step would have to

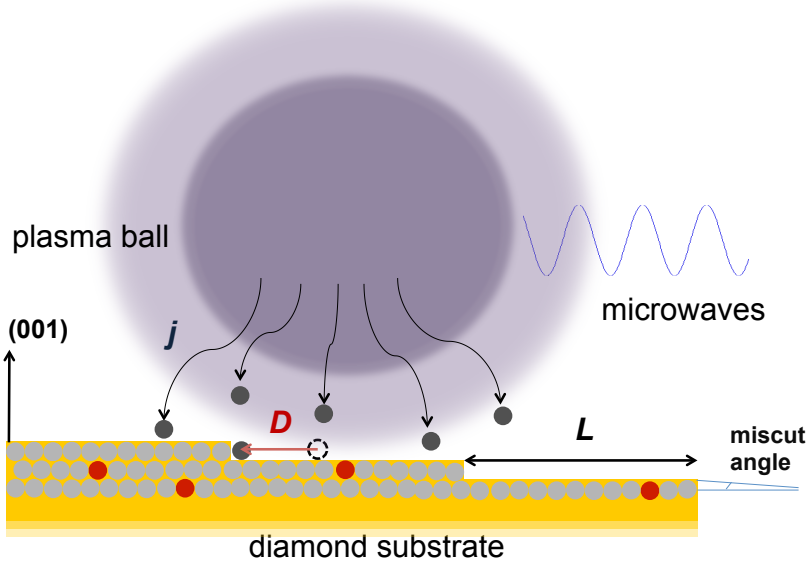

Figure 3.1: Cartoon of the diamond epitaxial growth process under conditions for nano-precise step flow growth. Black disks are carbon-containing radicals from a plasma, gray disks are sp^3-bonded carbon atoms in the diamond, and red disks are incorporated nitrogen atoms. For step flow growth, the diffusion length D must be sufficiently long compared to the step length L determined by initial miscut angle. The deposition rate j must also be slow enough that excess carbon does not aggregate on the surface before reaching a step edge.

advance quickly to achieve the rate j. Adatoms diffuse at a rate $v_{\text{adatom}} \approx D/L$ because a two-dimensional step terrace means an adatom will diffuse a mean-square distance $\langle r^2 \rangle = 4Dt$, where t is the time. Using this expression and $L \approx \sqrt{\langle r^2 \rangle} = 2\sqrt{Dt}$ the rate to move over the entire edge is $v_{\text{adatom}} \approx L/t \propto D/L$. The condition for step-flow growth, $v_{\text{step}} < v_{\text{adatom}}$, yields [190]

$$\frac{jL^2}{D} < 1. \tag{3.1}$$

If the deposition rate j is too large, then carbon atoms will attach to the step terraces and aggregate before each can fill a step edge. Hydrogen-plasma-based etching of non-diamond growth at the surface during step-flow growth is also essential to preserve the atomic step structure [189], and our procedure includes 15 min of no methane for preparation of the surface. The methane concentration is a major contribution to j, and we use a relatively low $[CH_4]/[H_2] = 0.025\%$ [190].

If L is too long compared to the diffusivity value, then adatoms cannot travel the length of the step terrace quickly enough to reach the step edge before aggregating with other deposited adatoms. The miscut angle determines L, as shown schematically in Fig. 3.1. A large miscut angle does not yield a surface of atomic steps to begin with, and a near-zero miscut angle makes L too large so that adatoms cannot reach a step edge. Thus the polishing of the substrate to a moderate miscut angle, of order 1°, is critical to preserving the step-flow mode and also affects growth rate [191]. Unfortunately, neither the miscut angle nor the precise crystallographic direction of the terraced slope (the "phase") are specified by the diamond vendor, which we believe contributes to sample-to-sample variations in growth rate and incorporation rate of nitrogen. These two angles should be considered in future work.

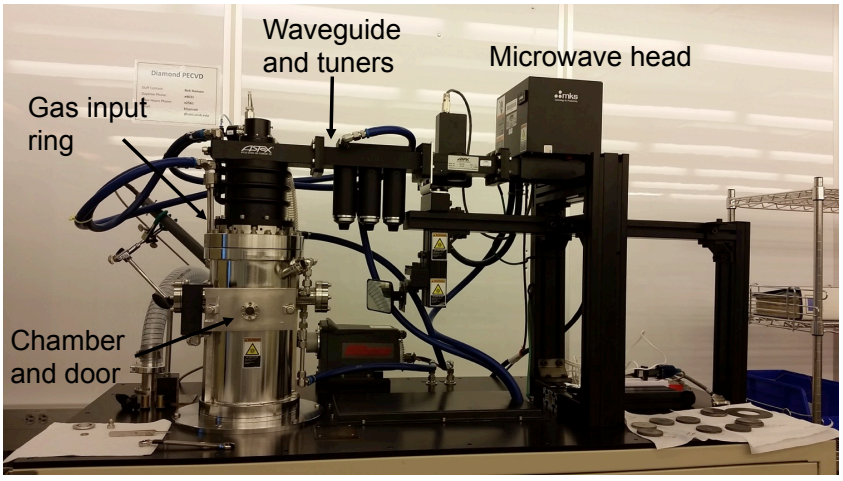

Figure 3.2: Photograph of the SEKI diamond chemical vapor deposition (CVD) system at UCSB used for growing single-crystal diamond films to form NV centers. The microwave head provides up to 1.5 kW of power to sustain a CVD plasma in the chamber. Input gasses for the process are hydrogen, methane, and nitrogen.

3.2.2 Growth substrate and parameters

The diamond films for this work were grown in a SEKI Technotron AX6300 PE-CVD system with a 1.5 kW microwave source, shown in Fig. 3.2. The controlled inputs to the growth chamber are gasses, microwaves, and heat. Individual mass flow controllers (MFCs) are used to regulate each gas, H_2 and CH_4, and these are combined in a gas manifold and introduced into the chamber. Microwaves at 2.45 GHz are directed from the source through a tuned waveguide and launched through a quartz window into the chamber, causing the gas mixture to become a sustained plasma at a certain range of pressure and flow conditions. A vacuum dry pump and throttle valve continuously control the moderate ($\sim$ 25 Torr) chamber pressure. For growth, a substrate temperature of 800 °C is maintained via heating of the molybdenum chuck that contains the starting diamond substrate.

The initial single-crystal (SC) diamond substrates used for all growths in this work are purchased from *Element Six* (E6): electronic grade plates of dimensions 2×2 mm$^2 \times 0.5$

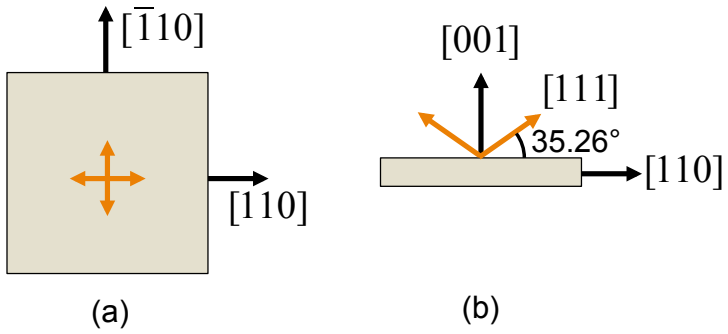

Figure 3.3: Schematic of crystallographic directions in [001]-oriented single-crystal diamond plates. (a) Top-down view of the diamond plate, where edges extend in the [110] directions. The projections of NV axes onto the surface plane are shown in orange. Atomic step edges in epitaxial growth also run along the [110] directions. (b) Side-view, showing one pair of NV axes along the [111] directions, which are in the plane of the page.

mm. The surface normal is in the [001] direction with edge normals in [110] directions (see Fig. 3.3), such that the four NV orientations, projected onto the surface, point towards the four edges. The substrate nominal nitrogen impurity level is < 5 ppb. Given the number density of diamond, 176.2×10^{27} m^{-3}, this impurity level translates to a mean N-N nearest neighbor distance of $R \gtrsim 60$ nm. Rough morphology of E6-purchased samples due to mechanical polishing, which prevents the atomic step growth of homoepitaxial diamond [191], is mitigated via additional polishing by *Syntek* to a rms roughness of $\sim 200 - 600$ pm, as confirmed by AFM topography.[1] Figure 3.4 shows an AFM topographic image of an electronic grade CVD diamond substrate after polishing, which exhibits a surface roughness of < 0.2 nm and step-flow terraces running in the [110] direction. The original substrate miscut angle θ_{mis} is nominally preserved by this polishing step, though we do not routinely measure it. Some 500-μm-thick substrates were additionally sliced in two pieces and thinned from the non-polished backside to $\sim 140 - 160$ μm prior to growth. The cutting and thinning may also be done post growth, for example samples B001 and B002 are of thickness ~ 30 μm, however, the risk

[1]Samples polished by *Syntek* tended to have lower roughness than those polished by *Applied Diamond*.

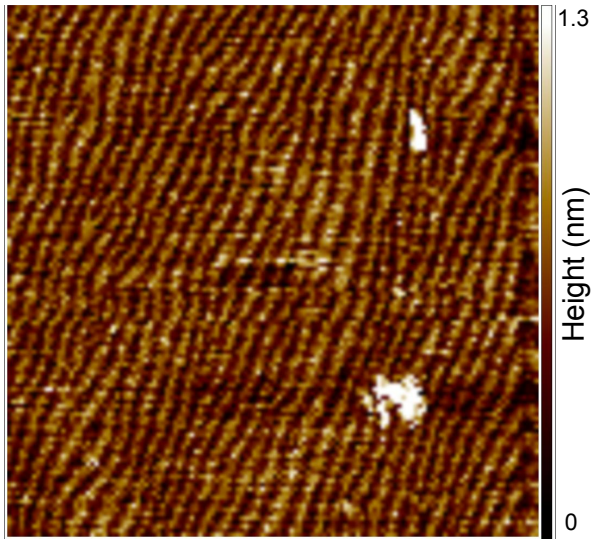

Figure 3.4: AFM topographic image of diamond step terraces on a polished (001) electronic grade substrate before in-house CVD growth. The step regions over this 3×3-μm^2 area run in the [110] directions and have a rms surface roughness of 140 pm. After CVD growth and near-surface NV formation, this sample (AD-150-05, B033) was used for the NV spin relaxation and coherence measurements of Chapter 5.

of damage or loss of sample during polishing makes pre-thinning a preferable procedure. For example, we have grown N delta-doped diamond films on starting substrates polished as thin as 20 μm. All substrates were cleaned to remove contaminants using a boiling acid mixture (ratio 2:3 NO_3:H_2SO_4, 130 °C, 30 min) and rinsed in DI water immediately prior to insertion into the growth chamber [190]. Remaining dust, visible under a microscope, was removed by swabbing the diamond while immersed in acetone and then isopropanol, followed by drying with N_2.

Several diamond growth experiments, described in Chapter 3 of [190], were done to tune the chamber conditions for optimal H_2 etching and step-flow growth on (001) diamond. The finalized parameters are listed in Table 3.1. This process results in a growth rate of 8.2 ± 3.2 nm/h as estimated from Secondary Ion Mass Spectrometry measurements of nitrogen content using a high-nitrogen starting substrate [43, 190]. One reason for variations in growth rate among samples used in computing this estimate

Parameter	Value
Pressure	25 Torr
H_2 flow	400 sccm
CH_4 flow	0.1 sccm
Microwave power	750 W
Temperature	800 °C
H_2 etch time	15 min

Table 3.1: PE-CVD growth parameters optimized for the step-flow growth mode used in the nitrogen delta-doping process. H_2 etching occurs throughout growth but is started first without methane once the temperature ramps to 800 °C.

could be small differences in θ_{mis}, which has been seen to have an effect on growth rate in step-flow growth (Ch. 3 in [185]). Characterization and precise control of the substrate miscut angle may be a helpful future direction of research for improving growth for NV creation.

3.3 Nitrogen delta-doping for near-surface NVs

3.3.1 Process summary

We describe here a growth process to form near-surface NV centers and characterize their spin coherence T_2 times for applications to sensing and imaging of spins external to the diamond. The slow growth rate of $\sim$ 0.1 nm/min provided by the parameters in Table 3.1 allows us to precisely toggle the input of nitrogen gas to form a $\sim$ 2-nm-thin layer of nitrogen-rich CVD diamond. Residual gas analysis of nitrogen in the CVD chamber shows that nitrogen is evacuated to the $1/e$ level within one minute after delta-doping (see supplement of [43]). The basic sample growth structure is shown in Fig. 3.5(a). We grow isotopically pure (99.99-99.999% ^{12}C) SCD on the (001) substrate for 4 h ($\sim$ 32 nm). We then abruptly turn on flow of N_2 gas into the chamber (10-30 sccm in this initial work) and turn it off after a few nanometers of additional growth, typically

15 min ($\sim$ 2 nm). A final cap layer of variable thickness is grown on the delta-doped layer to define a nominal distance of the NVs to the final diamond surface. Vacancies were formed post-growth by irradiating the sample with 2-MeV electrons at a dose of $5 \times 10^{14}\text{cm}^{-2}$. The diamond was annealed in H_2/Ar gas at 850 °C for 2 h to form the NV centers. Ambient air cannot be used for annealing at this temperature since (001) diamond is rapidly oxidized [192]. Last, the diamond is immersed in an acid mixture of 1:1:1 H_2SO_4:HNO_3:HCl_4 at above 200 °C for at least 30 min, which stabilizes the negatively charged NV state via oxygen-related surface termination [193, 194]. Recently in our group, we have begun performing oxygen anneals at 450 °C, 0.1 sccm O_2, for 2 hours to further remove graphitized carbon and oxygen terminate the diamond [88]. Figure 2.19 shows AFM topography of terrace steps on sample B002 after the nitrogen delta-doping growth and NV formation. Identification of formed NV centers was done in a confocal microscope setup, such as described in Chapter 2 (Magnetometer A without AFM).

3.3.2 Identifying delta-doped NVs

For the delta-doping step, we use $^{15}N_2$ precursor gas (> 98% atomic purity) to provide a signature to distinguish delta-doped ^{15}NVs from ^{14}NVs [181]. The ^{14}NVs may originate from nitrogen already in the substrate that is converted to an NV before or after electron irradiation and annealing. The natural abundance of $^{14}N_2$ is 99.6%, leading to odds of 1:249 to find a naturally occurring ^{15}NV among a samples of NVs. In Fig. 3.5 we show a confocal microscope image taken on sample B001, which contains delta-doped nitrogen layers in a total grown diamond film thickness of about 160 nm. The fluorescent spots that are identified as ^{15}NVs are circled orange and these outnumber the identified ^{14}NVs, circled blue. We use CW ODMR measurements at low microwave and laser power to

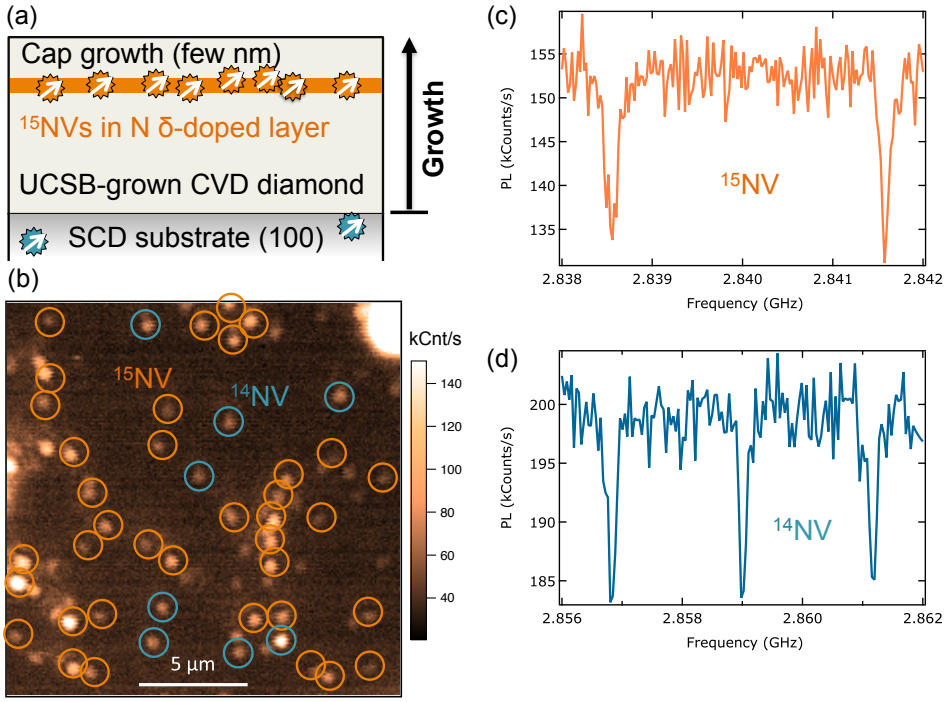

Figure 3.5: (a) Schematic of a nitrogen delta-doped CVD diamond grown on a single-crystal diamond (100) substrate. The ^{15}N-doped layer contains many ^{15}NVs (orange) and the substrate contains a small density of naturally abundant ^{14}NVs (blue). (b) Confocal image focused at the surface of the diamond film where many fluorescent spots can be identified as either ^{15}NV (orange circles) or ^{14}NV (blue circles) using ODMR. ^{15}N only has a natural abundance of (^{15}N:^{14}N)=1:249, yet is found here at a ratio 37:8, which confirms that the majority of these spots are delta-doped NVs. (c) Pulsed ODMR spectrum of a ^{15}NV showing the signature of two hyperfine transitions split by $\sim$ 3.1 MHz. (d) Pulsed ODMR spectrum of a substrate ^{14}N showing the signature of three hyperfine transitions spaced by $\sim$ 2.2 MHz.

determine the hyperfine signature of the NVs, as shown in Figs. 3.5(c,d).

3.3.3 Depth confinement of NVs

We investigated the degree of depth confinement of delta-doped NVs by growing a diamond film with a ^{13}C-^{12}C-^{13}C isotopic structure, where N delta-doping was done in the center of the 15-nm-thick ^{12}C layer. Therefore, delta-doped NVs that are confined to the nominal 2-nm-thin nitrogen layer are expected to show little to no coupling to the two surrounding semi-infinite carbon-13 nuclear spin baths. SIMS data on the ^{13}C content of the film is shown in Fig. 3.6(a), overlaid with positions of the substrate and N layer. In an applied field of magnitude B_0, the ^{13}C bath spins precess at a rate close to the Larmor frequency $f_c = B_0 \times 1.071$ kHz/G, where the precession rates of individual nuclei differ slightly due to weak intra-bath couplings and a range of weak hyperfine couplings to the NV spin [22]. To probe the nuclear spin bath, we use the Hahn echo sequence $(\pi/2 - \tau - \pi - \tau - \pi/2)$, which generates a $(|m_s = 0\rangle + |m_s = -1\rangle)/\sqrt{2}$ NV spin state with a relative phase that is sensitive to the effective ac magnetic field from the ^{13}C bath. At the applied field of 136 G, the contributions of the hyperfine couplings to the NV spin are relatively small, and the net result on the echo signal appears the same as from detecting a classical ac field oscillating at f_c. For example, when $\tau = 2n/f_c$, for integer n, the NV accumulates maximum net phase, and a collapse is observed in the echo signal. ^{14}NVs in the substrate show this collapse and revival behavior, as in Fig. 3.6(b), due to the 1.1% natural abundance of ^{13}C.

In contrast, ^{15}NVs confined near the center of the ^{12}C layer exhibit only electron spin echo envelope modulation (ESEEM) due to the coupled dynamics of the host ^{15}N nuclear spin, as in Fig. 3.6(c): to first-order, ESEEM manifests in Hahn echo as NV phase oscillations at frequency $f_1 \approx 3.1$ MHz and modulations at $f_0 \approx 14 \times 4.316$ MHz/T$\times B_\perp$,

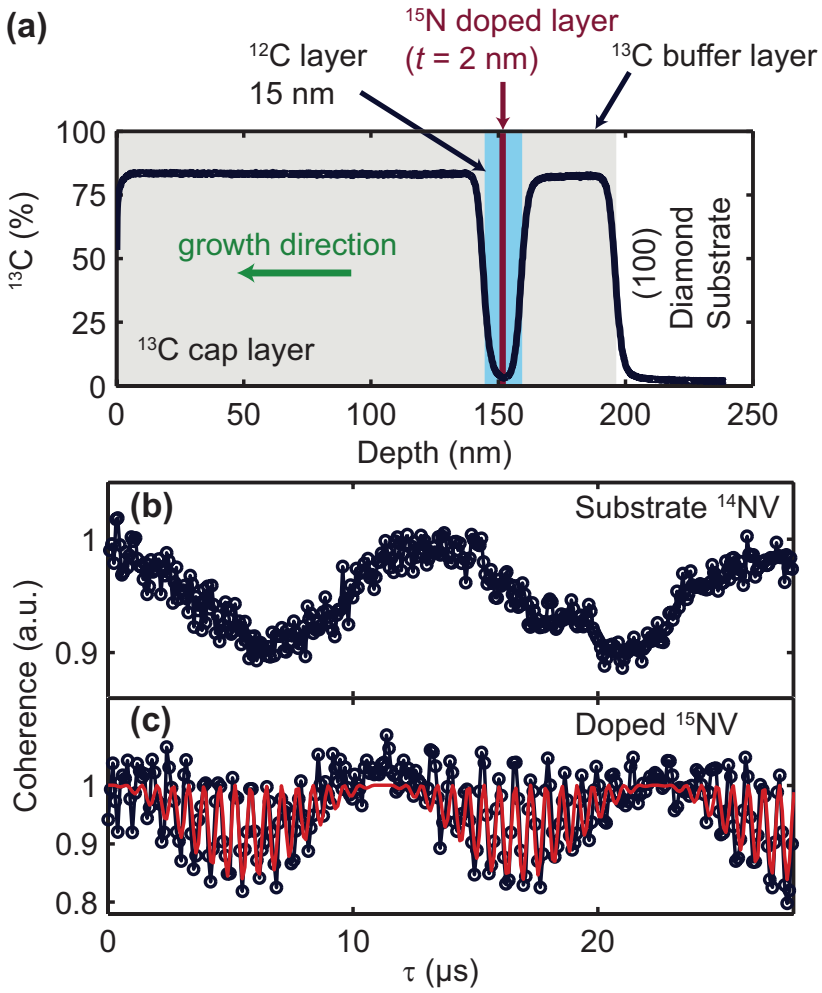

Figure 3.6: Nanoscale localization of delta-doped NVs between two ^{13}C nuclear spin baths in an isotopically structured CVD diamond. (a) SIMS measurement of the layered ^{13}C-^{12}C-^{13}C isotopic diamond structure; the data in black shows atomic percentage of ^{13}C and the red line marks the inferred location of delta-doped nitrogen based on the ^{15}N gas timing. (b) Hahn echo of a ^{14}NV in the diamond substrate, showing clear collapse and revival at the Larmor frequency of the ^{13}C spin bath. (c) Hahn echo of a ^{15}NV in the delta-doped layer, exhibiting no ^{13}C-induced collapse and revival, indicating that the NV is localized well within the 15-nm ^{12}C layer. The red curve is a fit to the ^{15}NV ESEEM model discussed in the text. Figure reprinted from reference *Appl. Phys. Lett.* **101** (2012) 082413 [43].

where $B_\perp$ is the off-axis magnetic field ($B_0 = \sqrt{B_z^2 + B_\perp^2}$). In an applied magnetic field perfectly aligned to the NV axis the ^{13}C collapse signal would still be visible, but the ^{15}N ESEEM signal would be fully suppressed. The ^{15}N ESEEM signal dependence on applied field magnitude and direction is derived theoretically in Appendix E for Hahn echo and XY4 control sequences, and in the present discussion we only focus on the distinction of whether NVs exhibit the ^{13}C coupling signal. Figure 3.7 shows two doped ^{15}NVs that have coupling to the ^{13}C spin bath, identified by a combination of collapses and ESEEM. Each has an additional strong hyperfine coupling to a proximal ^{13}C spin, and the full model captures the dynamics well (see Appendix E).

We performed the Hahn echo for 29 NV centers in the ^{13}C-^{12}C-^{13}C sample, and found only six to exhibit the signature of coupling to the ^{13}C bath. In summary, we determined 2.4 nm to be the minimum distance an NV must be from the enriched 80%-abundance ^{13}C bath to show echo oscillations within the experimental uncertainty. The results indicate a depth dispersion of $\sigma \approx 4$ nm for NVs formed by delta-doping. The full statistical analysis of these measurements are detailed in the supplemental information of [43]. The N delta-doping technique can therefore be used to confine NVs to specific distances from the diamond surface with a spread that can be significantly smaller than the depth value, here $d \approx 150$ nm according to the ^{12}C position in Fig. 3.6(a).

3.3.4 Coherence time measurements

In Chapter 1 we have discussed the importance of long spin coherence time for improved magnetic sensitivity of the NV center for detecting ac magnetic fields, as from nuclear spins. Because the sensitivity to a single magnetic moment scales as $r^3/\sqrt{T_2}$, the depth of an NV remains the more critical parameter to enable detection and imaging of individual spins. Nevertheless, long spin coherence must be maintained for NVs. Figure

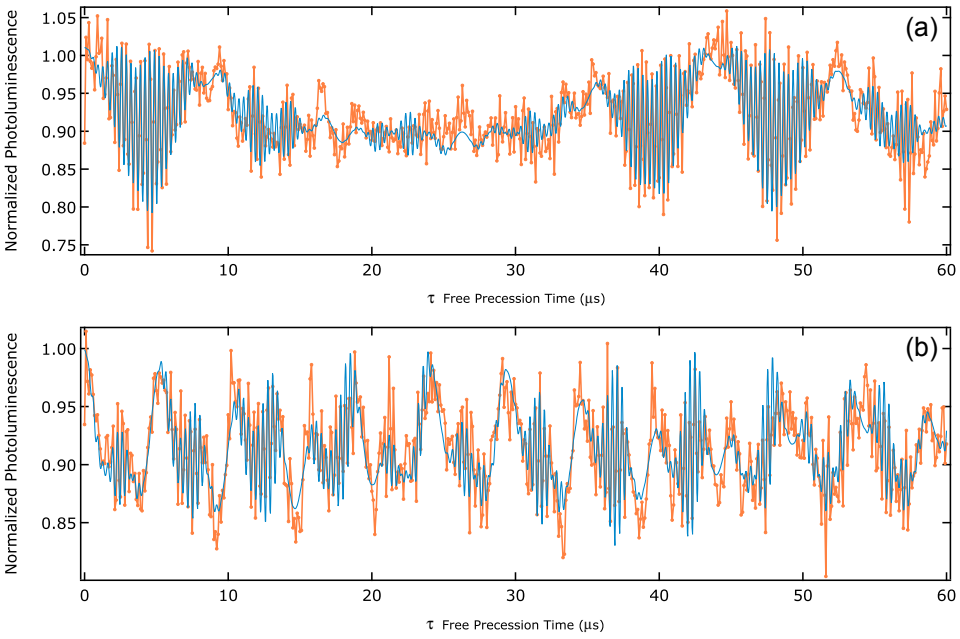

Figure 3.7: Hahn echo signals of two delta-doped NVs with nitrogen-15 ESEEM and coupling to carbon-13 bath, plotted against the precession time τ between pulses. Orange points are the data, and the model fit is in blue. (a) NVA at $B_0 = 21.8$ G and $B_\perp = 19.48$ G, computed from ^{13}C bath revivals at $f_c = 1/\tau_r = 23$ kHz, and ESEEM at $f_0 = 114$ kHz, respectively. (b) NVB at $B_0 = 154$ G and $B_\perp = 34.7$ G, computed from ^{13}C bath revivals at $f_c = 165$ kHz, and ESEEM at $f_0 = 203$ kHz, respectively. Both (a) and (b) show an additional strong hyperfine coupling to a proximal ^{13}C at rates $f_p = 419$ kHz and $f_p = 376$ kHz. The fastest oscillations are due to parallel hyperfine coupling of $f_1 \sim 3$ MHz to the host ^{15}N (See Appendix E).

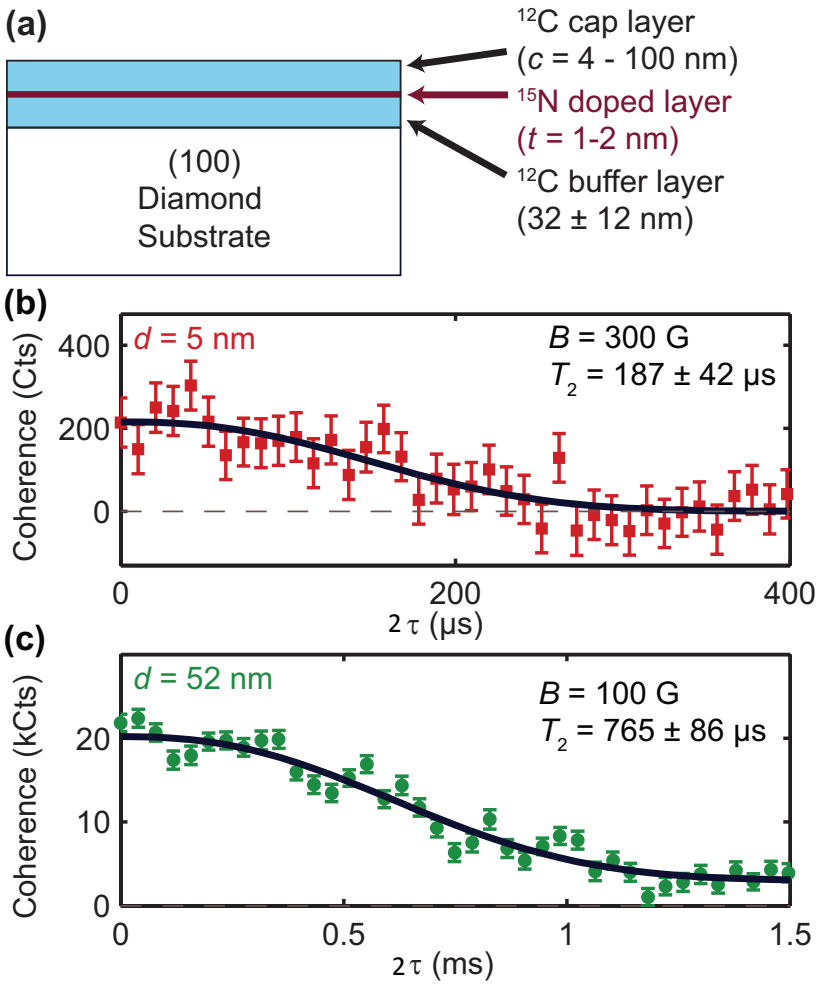

Figure 3.8: (a) Schematic of CVD diamond films grown with ^{15}N delta doping and isotopic ^{12}C source gas. The capping layer thickness c was varied to form NVs at specific depths $d \approx c + 1$ nm. (b,c) Hahn echo measurements of doped NV centers in the $d = 5$ nm (b) and $d = 52$ nm samples. The black curves are fits of the form $y_0 + A \exp\left[-(2\tau/T_2)^n\right]$, and uncertainties in T_2 are given at 95% confidence. Figure reprinted from reference *Appl. Phys. Lett.* **101** (2012) 082413 [43].

3.8(a) shows the basic N delta-doping diamond film structure with a variable cap thickness layer to define a nominal depth based on the growth rate. The same Hahn echo sequence was used, out to longer total precession time 2τ, to find the coherence times of doped NVs in these structures. For a cap thickness of $\sim$ 50 nm (4-h growth above N layer), doped NVs were identified with $T_2 > 700$ μs (Fig. 3.8(c)). Because the film was grown with enriched $^{12}CH_4$, this coherence time is more likely limited by interaction with a nitrogen electron spin bath (P1 centers). NVs in ^{12}C-enriched diamond with an ultra-low level of spin-containing impurities can some T_2 times as long as $\sim$ 2 ms [132]. It is likely then that the delta-doping process introduces a higher nitrogen content than in the background substrate, which has a specification of < 5 ppb nitrogen. In Chapter 4 we discuss quantitatively the nitrogen content of the film based on the coherence times of these relatively deep doped NV centers at depths of $50 - 160$ nm.

Figure 3.8(b) shows a Hahn echo decay data set for a delta-doped NV in a film with cap layer of just $\sim$ 4 nm (30-min growth above N layer). The extracted $T_2 = 187$ μs is shorter than for NVs in the thicker sample, however, this $T_2 > 100$ μs is considerably longer than those formed by nitrogen implantation at comparable or even larger depths [182, 66]. Assuming the depth of this NV is 5 nm, which we do not directly verify here, the magnetic sensitivity is significantly improved over the 52-nm-deep NV. The exact sensitivity comparison is dependent on ac bandwidth and photon collection as discussed earlier in Chapter 1. Nevertheless, for a simple comparison of the ratios $r^3/\sqrt{T_2}$, the 5-nm-deep NV can detect a 550$\times$ smaller magnetic moment in the same measurement time, which is of the same order as the magnetic field from a proton compared to and electron at equal distance.

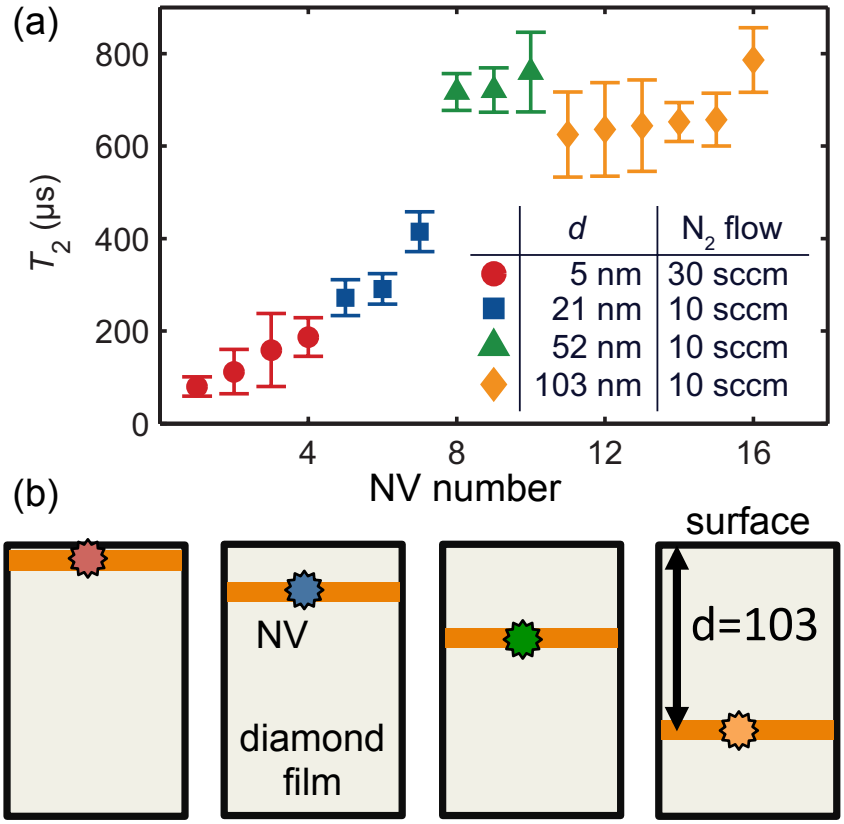

Figure 3.9: (a) Hahn echo T_2 measurements summarized for 16 delta-doped NV centers in four diamonds with different capping layer thicknesses. Each marker labels one NV. The NV number ordering plotted is in direction of increasing T_2, but this does not directly imply a known depth difference within a given sample. (b) Schematic of grown diamond films with NVs at different nominal average depths d specified in (a). Figure (a) adapted from reference *Appl. Phys. Lett.* **101** (2012) 082413 [43].

3.3.5 Evidence of surface-induced decoherence

To gain further insight into the trend of T_2 with NV depth, we grew delta-doped diamond films of different cap thicknesses (Fig. 3.9(b)) and compared the spin coherence times of a few NVs within each. Fig. 3.9(a) summarizes the results, where each color symbol refers to NVs in the corresponding film of Fig. 3.9(b). The ordering along the NV axis is sorted by lowest to highest T_2 times per sample. We emphasize two general findings. First, the coherence times in each particular sample are quite consistent, with none showing NVs with significantly shorter (e.g., few microsecond) T_2's. Second, the samples with nominal depths of $d = 21$ nm (blue squares) and $d = 5$ nm (red circles) show the largest variation in T_2 times, and T_2 tends to be shorter on average for the shallower-NV samples. This observation suggests a strong dependence of coherence time on NV distance to the surface, particularly below 50 nm, and therefore hints at a source of surface-related noise. The surface-induced decoherence, at sufficiently short distances, may dominate over bulk sources of NV decoherence like nitrogen electronic spins.

3.4 Conclusions

We have demonstrated an *in-situ* N doping method to form NV centers via epitaxial diamond growth in combination with isotopically pure carbon-12 precursor gas to limit decoherence from ^{13}C spins. We showed, via electronic-nuclear spin coupling measurements in a ^{13}C/^{12}C/^{13}C structure, that the N delta-doped layer is localized to within a dispersion of about ± 4 nm. Delta-doped NV centers within 10s of nanometers of the diamond surface, as estimated by growth rate, exhibited coherence times of $T_2 > 100$ μs. These coherence times are consistent across several NVs in each sample that has a nominal depth of the delta-doping layer, and the shorter coherence times observed for NVs in shallower growth layers (5-20 nm) suggest surface effects on the decoherence

rate. These initial results and the surface-related questions motivated the experiments in the remainder of this dissertation. In Chapters 4 and 5, we explore the depth dependence, frequency dependence, and origin of faster decoherence in near-surface NVs. Surface-proximate delta-doped or implanted NVs in these grown diamond films also enable magnetic imaging of external spins, as we demonstrate in Chapter 6, and imaging of electromagnetic noise from metals, as in Chapter 7.

Both N implantation and N delta-doping are viable methods to form the spin sensors for magnetometry applications, and in fact the wide availability and long-studied tunability of N implantation has made it, as of 2016, remain the method most often used for nanoscale NMR demonstrations [155, 81, 195, 196]. Combined with vacuum and oxygen annealing techniques to mitigate implantation damage and surface effects [183, 88, 127, 196], implanted NVs can potentially have coherence times as long as those found in delta-doped films, though no systematic yield comparison has been done to date. NV-target distance is the most significant variable in magnetic sensitivity, in comparison to coherence time, so research focus has been on ultra-shallow NVs first (depth 2-5 nanometers), and coherence second. In addition to depth-localization, delta-doped NVs have the advantage of NV-to-NV consistency in coherence times without special or extensive annealing techniques, as evidenced in this chapter and Chapter 4. The delta-doping technique of NV creation is a younger technology with much room for further research.

One of the important knobs on the delta-doping technique is the capability to separate, in both process type and spatial position, the nitrogen incorporation and vacancy creation. This degree of freedom allows optimization of the NV concentration and vacancy-related damage in the crystal. Thus, variation in the method of vacancy creation has constituted much of the ongoing delta-doping research. High-energy electron irradiation has been used in the above-described work, but these electrons penetrate the whole

diamond and thus do not localize vacancies well, for example producing some background NVs in the non-film substrate [43]. ^{12}C implantation has recently been used to tune the NV density and to localize both vacancies and NVs when combined with carefully timed annealing steps [163]. Irradiation with a low-energy focused electron beam, such as in a transmission electron microscope, has also been used to localize NV creation in three dimensions while preserving millisecond-long coherence times of delta-doped NVs [164]. We have also found that nitrogen incorporation is not noticeably affected by nitrogen flow rates between 0.1-30 sccm in the CVD delta-doping process [164, 163], so 0.1 sccm is used for preserving the isotopic gas supply. Helium implantation [197] is another route for creating vacancies near or at the N delta-doped layer [198], and combination with low-damage etching processes can further tune the final NV depth and localization volume [199, 200, 198, 91]. Shallow delta-doped NV centers may also be formed during the growth process itself, without separate crystal-damaging vacancy creation, by using different gas ratios, temperatures, or post-growth surface treatments [201, 202, 203]. Low-energy (few keV) electron irradiation methods also suggest mechanisms of NV creation that don't necessarily rely on thermal annealing [204]. Altogether, the nitrogen incorporation modes provided by delta-doping CVD growth provide an important material framework for fundamental studies into how NV centers are formed, especially those close to the diamond surface.

Chapter 4

Probing surface noise with depth-calibrated nitrogen-vacancy centers

Sensitive nanoscale magnetic resonance imaging (MRI) of target spins using nitrogen-vacancy (NV) centers in diamond will require a quantitative understanding of dominant noise at the surface. We probed this noise by applying dynamical decoupling to shallow NVs at calibrated depths. Results support a model of NV dephasing by a surface bath of electronic spins having a correlation rate of 200 kHz, much faster than that of the bulk N spin bath.[1] Our method of combining nitrogen delta-doping growth and nanoscale depth imaging paves a way for studying spin noise present in diverse material surfaces.

[0]The contents of this chapter have substantially appeared in reference [87]: B. A. Myers, A. Das, M. C. Dartiailh, K. Ohno, D. D. Awschalom, A. C. Bleszynski Jayich, Probing surface noise with depth-calibrated spins in diamond *Phys. Rev. Lett.* **113** 027602 (2014)

[1]Although the depth dependence of the noise is consistent with a surface of fluctuating magnetic dipoles, it can also be consistent with fluctuating electric dipoles. We observed this point later and it is discussed in Chapter 5, where we introduce a method to selectively probe electric fields.

4.1 Introduction

The negatively charged nitrogen-vacancy (NV) center in diamond is a robust quantum sensor of magnetic fields [25, 4, 26, 5]. Although an individual NV has the capability to detect small numbers of electronic [179, 39, 41] and nuclear spins external to diamond [205, 102, 206], its widespread application in spin imaging has been limited by the ability to form shallow NVs that retain spin coherence near the surface. Shallow spins with long coherence time, T_2, are important because quantum phase accumulation between two electronic spin states of the NV provides signal transduction, and hence the minimum detectable magnetic dipole moment scales as $\delta\mu \propto r^3/\sqrt{T_2}$, with r the NV-target spin distance [26, 5]. At odds with this figure of merit is strong evidence that the diamond crystal surface adversely affects T_2, reducing it from ~ 2 ms for bulk NVs [132, 127] to less than 10 μs for few-nm deep NVs [39, 183, 66, 40, 43], but the origin of this decoherence is an outstanding question. In this chapter, we consider a model of surface spin induced decoherence, a theory which has emerged from experiments on other systems [97, 207] where long coherence is a requirement, such as in superconducting circuits [208, 96] and spin qubits in silicon [209]. We show that an electronic surface spin model is quantitatively supported for NVs in diamond. The key step we present is to link NV coherence with precise, independently measured NV depth data, as enabled by recent advancements in depth-controlled NV center creation and nanometer-scale magnetic imaging.

Recently, Ohno et al. demonstrated shallow, coherent NVs using delta-doping of nitrogen during chemical vapor deposition (CVD) of single-crystal diamond (SCD) [43], as described in Chapter 3. This crystal growth technique both permits nm-scale depth confinement and minimizes crystal damage incurred during nitrogen ion implantation [183, 40, 182], the conventional method of generating shallow NVs. The long T_2 of these doped NVs has enabled detection of a nanoscale volume of actively manipulated

external protons [206]. The consistent NV quality in delta-doped SCD makes depth measurements a suitable probe of surface physics, not masked by effects of other process-induced crystal variations. Therefore we used this promising material in the reported work: we exploit depth-calibrated NVs to understand how the surface contributes to decoherence and provide a way to mitigate surface noise for enhanced external spin sensing. Using dynamical decoupling (DD) with periodic spacing of π pulses for coherence analysis [100], we varied the number of pulses to deduce the noise spectral contributions from the surface and bulk environments as a function of depth. We show that using shorter inter-pulse spacing can progressively increase efficiency in decoupling from rapid magnetic fluctuations at the surface.

4.2 Methods summary

4.2.1 Experimental setup: Magnetometer A

Experiments were done at room temperature and ambient conditions. The experimental setup consists of an enclosed home-built confocal microscope combined with a commercial atomic force microscope that scans the sample in x and y. The details of this setup (Magnetometer A) are explained in Chapter 2. For spin coherence and relaxation measurements, the NV $|m_s = \pm 1\rangle$ sublevels are split with a rare earth magnet, providing $\sim$200 Gauss and aligned within a few degrees of the NV axis.

The entire glass-waveguide-diamond sample is clamped to the x, y scanning baseplate of the AFM. The AFM head, containing a $z-$axis piezo and coarse approach motor, is placed on the scanning stage so that the AFM tip addresses the side of the diamond containing shallow NVs. The head uses a 850 nm laser and quadrant diode for detection of the cantilever deflection and lockin amplitude. The unreflected part of the laser light

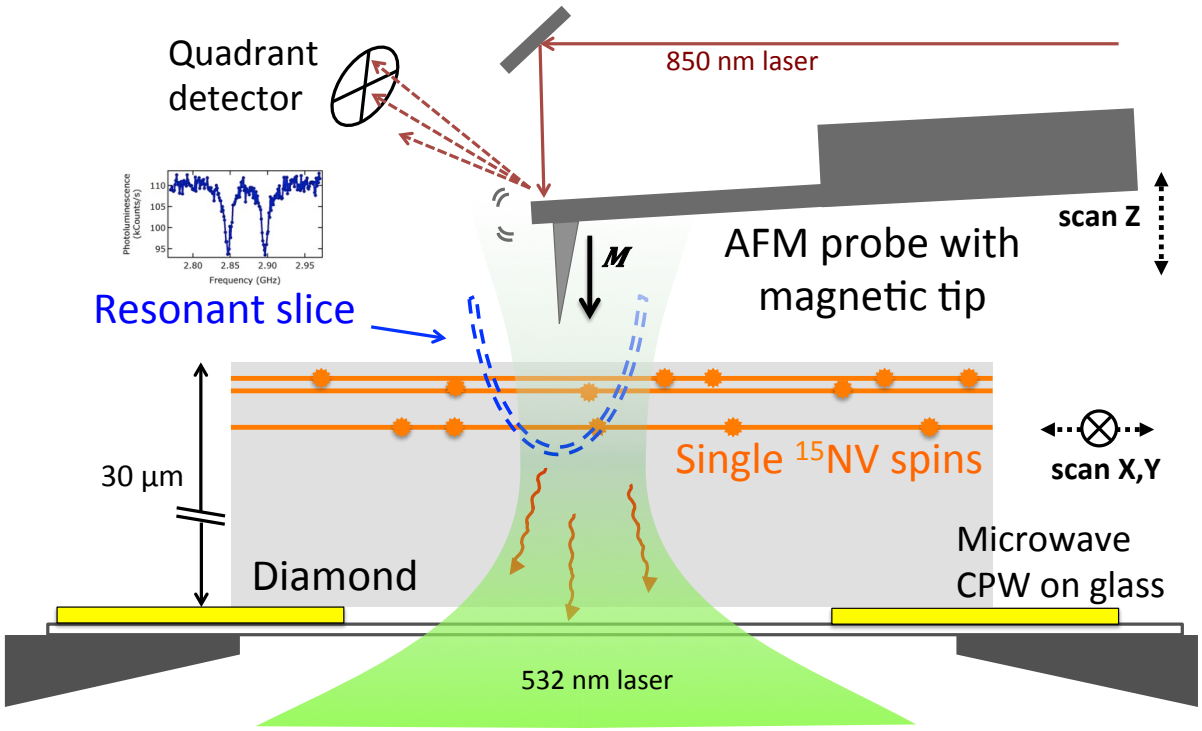

Figure 4.1: Schematic of the delta-doped diamond sample as probed by the inverted confocal microscope and magnetic force microscope tip. A resonant slice is a nano-thin locus of points in space where the magnetic tip shifts the NV resonance line to the fixed microwave frequency applied through a CPW. For nanoscale depth imaging the sample is scanned in the x, y plane and the tip is scanned by a piezo in z.

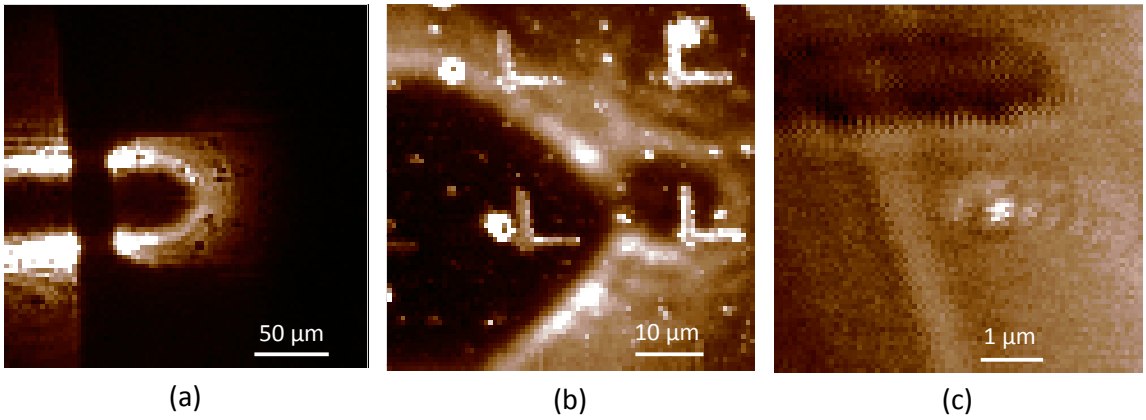

Figure 4.2: Laser scanning confocal microscope images of alignment of AFM tip to NVs in diamond film. (a) Longpass filter (594+ nm) image of cantilever illuminated with infrared AFM detection light with its apex aligned inside the CPW gap. Assuming the objective is at the reader's perspective looking into the page the layers are glass, gold CPW (dark borders), diamond, cantilever, IR source. (b) Longpass filter image showing the cantilever apex IR-shadowing the NVs and "L"-shaped metal markers on diamond. The AFM tip is not seen here but set back by 7-10 μm from the apex. (c) Broadband-filter image to block NV PL and highlight reflected green laser light from the AFM tip, seen here as a bright spot and fringes near one of the "L"-shaped markers.

can leak past the cantilever and enter the confocal objective, which causes undesirable background for the NV signal. When the cantilever is fully engaged with the diamond it IR-shadows the part where the tip is aligned, as shown in Fig. 4.2. For NV depth measurements, magnetic force microscopy AFM cantilevers (Bruker MESP-HM and MESP) are used to generate a scanning magnetic field with gradients of $0.1 - 1$ G/nm at the NV for magnetic resonance imaging. These probes can be operated in tapping or contact mode; the former allows avoidance of tip damage over long engage time intervals so that height measurements are consistent between the set of studied NVs. Magnetic fluctuations internal to these high moment probes can decohere NV centers, so all spin coherence and relaxation measurements were done in the absence of the AFM scan head.

4.2.2 N delta-doped diamond

We prepared shallow NVs — all within 160 nm of the surface — in three depth-confined layers of isotopically pure ^{15}N ($> 98\%$) within an isotopically purified ^{12}C (99.999%) CVD-grown film, shown schematically in Fig. 4.3(a). We fabricated Ti/Au markers on the surface for locating NVs repeatably. The details of the processing of sample B001a processing are in Appendix A. NVs are laterally several microns from each other and the metal markers.

4.3 NV depth measurements

4.3.1 Scanning probe nano-MRI

All experiments were performed within a single grown diamond film, thereby eliminating sample-to-sample surface variations. Nanometer scale changes in an NVs depth are critical to both its magnetic sensitivity and spatial resolution; thus we require an independent method to discriminate NVs depths beyond the diffraction-limited resolution afforded by standard confocal microscopy [3]. NV-based detection of nuclear spins prepared on the surface can infer an absolute NV depth, though analysis requires an assumed spin magnetic field model and the measurement is time intensive and inaccessible for all but the highest quality NVs sufficiently close to the surface [102, 206]. Here we employed a magnetic field gradient assisted optically detected electron spin resonance (ODESR) imaging technique that resolves NV depth differences with nanometer resolution [25, 38] over a wide depth range of several 100 nm. Moreover, no assumed model is necessary to extract relative NV depths. Absolute depths were inferred by linking this technique with a model of NV coupling to surface spins.

The optically detected magnetic resonance images in two dimensions y and z (tip

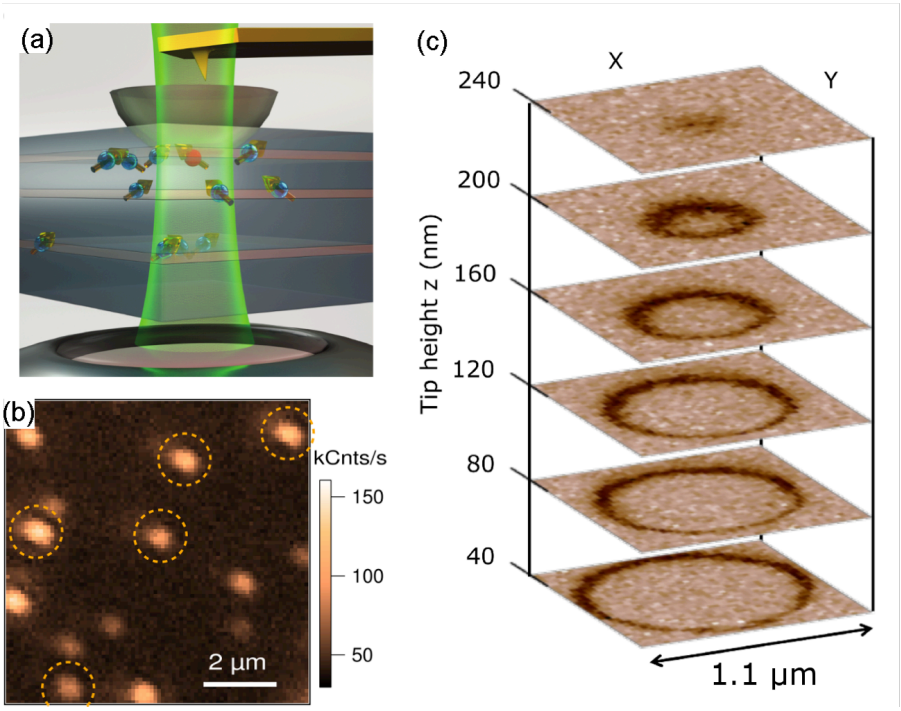

Figure 4.3: (a) Schematic of a CVD-grown diamond film with three nitrogen delta–doped layers (orange) that contain nitrogen-vacancy (NV) spins at nanoscale separations. A 532 nm laser is focused onto NVs via an inverted confocal microscope giving a diffraction-limited depth of field. To achieve nanoscale depth discrimination between NVs, a scanning magnetic tip and microwave field form a resonance slice. Colored red is an NV that intersects this slice. (b) Confocal image showing individual NVs. Circled spots are a few of the investigated ^{15}NVs of identical crystallographic orientation. (c) Optically detected ESR images recorded as a function of the magnetic tip position over a single NV. Dark rings mark reduced fluorescence when the ESR slice crosses the NV.

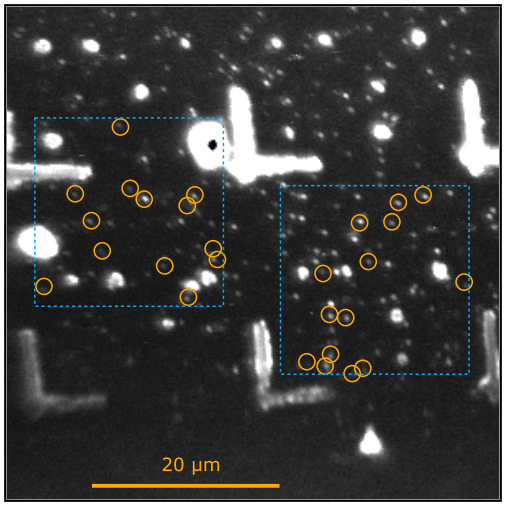

Figure 4.4: Confocal scanning laser microscope image (532 nm excitation) of the diamond sample containing three nitrogen delta-doped layers. The two blue dotted boxes illustrate the two 20 × 20 m areas that were investigated for depth and coherence measurements. The 27 doped ^{15}NVs of the studied orientation are bright spots circled in orange, which encompass all of the NVs that have a specific one out of the four NV crystal orientations. The brighter crosses and dots are part of a coordinate system deposited on to the surface.

height versus horizontal scan line) were collected for all doped ^{15}NVs of a single orientation that resided within a 20×40 μm^2 region of the diamond film. The external static magnetic field, $B_{dc} = 6.5$ mT, was aligned to within a few degrees of the NV axis. A confocal microscope image of this area is shown in Fig. 4.4, where the doped NV centers of the single measured orientation are circled. Of these 27 we measured the spin properties of all the shallow ones (< 60 nm depth). We measured only a sampling of the deep NVs because their properties were found to have little variation and shallow NVs are the focus of the study.

Within the film of nitrogen delta-doped layers (Fig. 4.3(a)) we differentiate doped ^{15}NVs from bulk, naturally occurring ^{14}NVs through confocal fluorescence (Fig. 4.3(b)) and ODESR spectroscopy (Fig. 3.5) of the ^{15}N hyperfine sublevels [43, 181]. All data pre-

sented in this chapter are on ^{15}NVs, which are referred to as NVs. To image NV depths, the magnetic AFM tip is scanned over the diamond surface at constant height, producing a bowl-shaped scanning ESR slice near the NVs (Fig. 4.3(a)). This slice corresponds to the locus of points in space where the magnetic field along a specified NV axis is constant and brings the NV $|m_s = 0\rangle \leftrightarrow |m_s = -1\rangle$ transition, $\nu_{\mathrm{NV}} = 2.87$ GHz$-\gamma_{\mathrm{NV}}\,(B_{\mathrm{dc}} + B_{\mathrm{tip}})$, into resonance with a microwave field ν_{rf}, where γ_{NV} is the NV gyromagnetic ratio and B_{dc} and B_{tip} are the externally applied and tip magnetic fields. When an NV intersects the slice, its fluorescence decreases due to its spin-dependent coupling into a long-lived metastable state. In this way, a single NV images the resonant slice, as shown in Figs. 4.3(c) and 4.8, where the dark contours correspond to the (x, y, z) tip positions for which $\nu_{\mathrm{NV}} \approx \nu_{\mathrm{rf}}$.

4.3.2 Alignment of x, y resonance slices

The relative NV depth measurements were carried out over a continuous time period of < 40 hours to minimize changes to tip magnetization or shape. This period began when the MFM probe was engaged to the surface of the diamond after alignment to the confocal area in Fig. 4.4. The probe tip was aligned above the first NV by monitoring the shift in its ESR frequency as well as by optically imaging the tip using 532 nm reflections with removal of the collection longpass filter. An initial resonance slice (x, y) image, shown in Figs. 4.6(a-c), was recorded by continuously exciting the NV with the laser and microwaves; the microwaves were detuned from the "tip-absent" resonance by 160 MHz and were switched with a 0.5 duty cycle (Fig. 4.5) to collect both signal and reference images, as in Figs. 4.6(a,b). During magnetic imaging the tapping mode feedback was always turned off after locating the surface and then the tip was scanned at a fixed Z piezo position, rather than following topography. This height was periodically

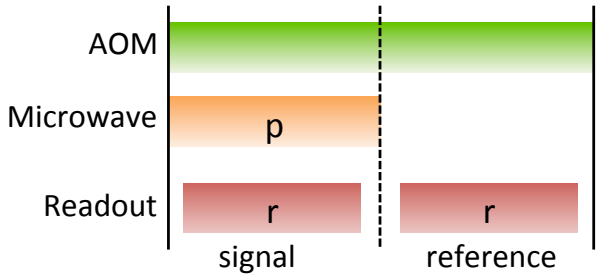

Figure 4.5: Pulse sequence for nanoscale depth imaging. The first half of the sequence measures the CWESR signal of the NV at a fixed microwave frequency, and the second half is for normalization of the PL signal. The cycle time was chosen long enough to minimize the fraction of switching time between readouts: $p = 50$ μs is the microwave-on time, and $r = 39.5$ μs is the readout time.

refreshed from a common lateral position by returning to feedback mode at the center of the (x, y) scan area. The purpose of the initial (x, y) image is to locate the x position to fix the scanner at for performing a (y, z) scan that intersects the apex of the full three-dimensional resonance slice. This position was found by fitting the (x, y) image to a circle. Its radius also provides a way to determine an appropriate z range for the tip height to image the apex of the resonance slice in a (y, z) scan.

4.3.3 Extracting relative depth from y, z slices

We obtained relative depth between any two NVs by registering their (y, z) resonance slice images (Fig. 4.8) and extracting the vertical offset. The relative depth for a given NV was computed from its mean offset from every other NV, and the standard error of the mean for each NV depth ranged 1-2 nm. The procedure for collecting (y, z) slice images, Figs. 4.6(d-f), is the same as for (x, y) images except the cantilever was put into feedback mode to refresh the tip height at the end of each fixed$-z$ scan line. Images were 40×40 for acquisition time of about 40 minutes and the pixel size is 46.15 nm in y and 7.69 nm in z. In principle, if the magnetic tip were actually to change its shape or magnetization over longer acquisition times than used here, then the measured relative

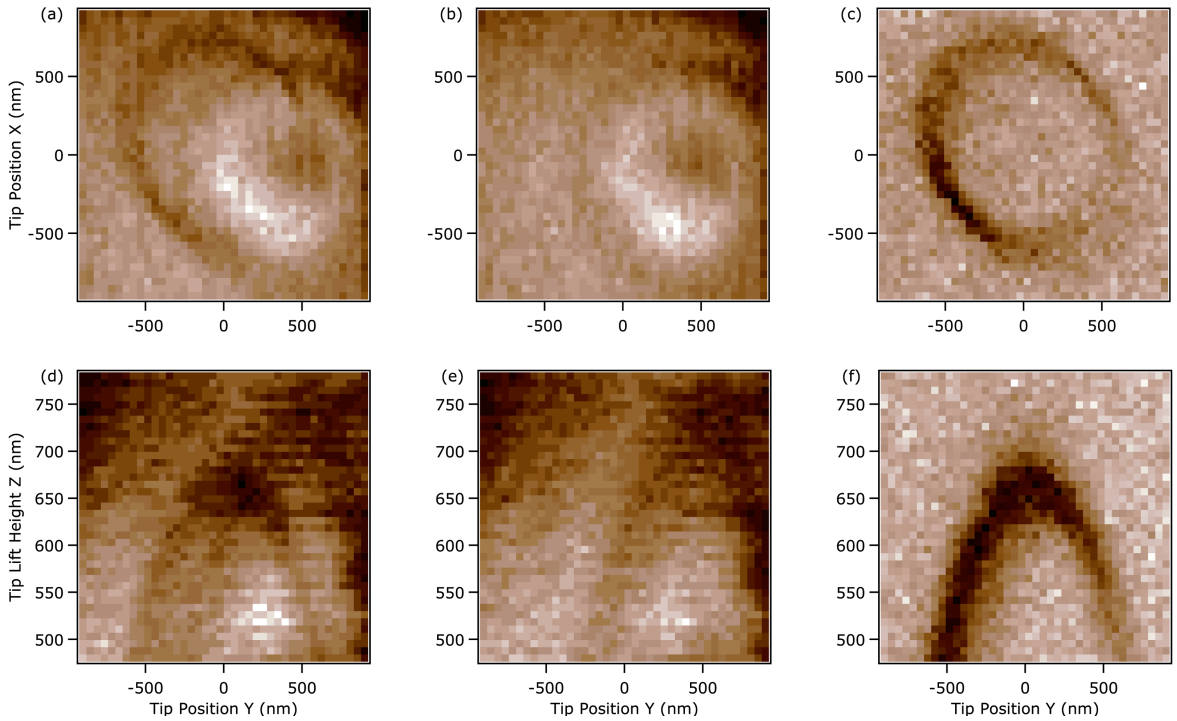

Figure 4.6: Set of magnetic resonance images for one of the studied doped NVs. (a,b,c) Signal, reference, and normalized images for a (x, y) scan at fixed tip height $z = 460$ nm. For each pixel, the signal image is taken with the microwaves on and the reference with microwaves off. The signal/reference image in (c) eliminates photoluminescence quenching and other PL variations not due to the magnetic resonance. (d-f) Signal, reference, and normalized (y, z) scans for the same NV along the $x = +50.3$ nm scan line.

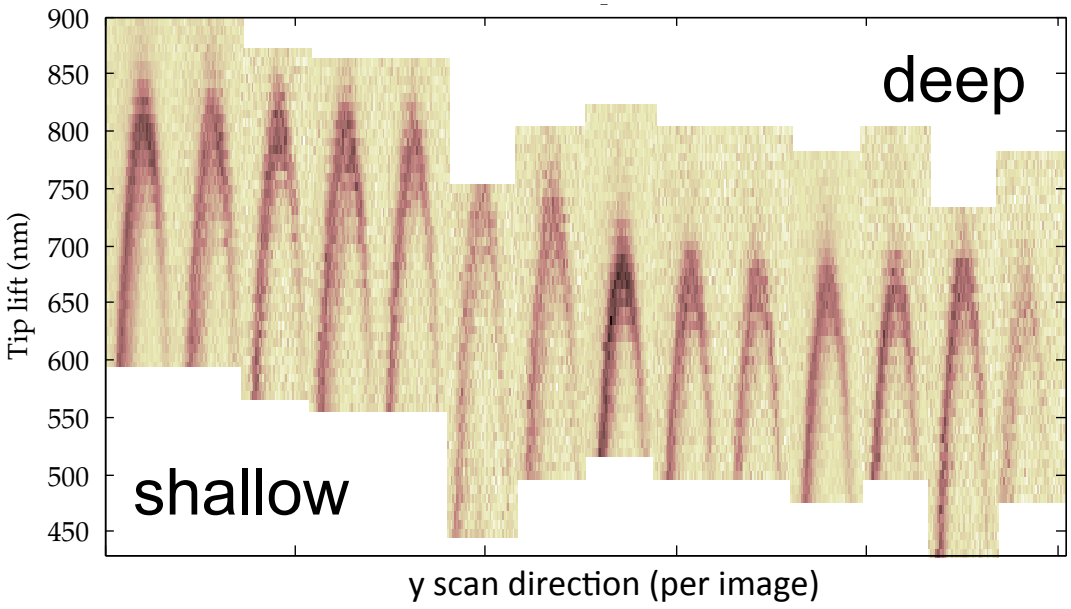

Figure 4.7: Resonance slice images for 14 NVs sorted by depth from shallow (left) to deep (right). The sorting is done by an algorithm that compares each slice image to every other in the set and provides a ranking and detph result based on the extracted vertical offsets.

depths within a subset of NVs measured adjacent in time could be compared to another subset through a single or few pairwise depth comparisons, thereby linking all NV depth data.[2]

The full set of data for 14 NVs is shown in Fig. 4.7 sorted from shallowest to deepest with the image registration algorithm. Details about the registration algorithm and error analysis are in Appendix C.

[2]Data cropping [38] is not necessary with our single-contour data sets (*i.e.,* NVs are laterally separated), so the procedure of alignment and imaging is easily automated for multiple NVs.

4.4 Surface-induced decoherence

4.4.1 NV spin coherence versus depth

Figure 4.9 is a plot of the Hahn echo coherence envelopes for NVs at four distinct depths, showing T_2 decreases with proximity to the surface. The coherence decay envelope of an NV depends on the nature of the environmental spin bath, described by its noise spectral density $\tilde{S}(\omega)$, and the measurement microwave pulse sequence, which applies a filter function to $\tilde{S}(\omega)$. To further isolate the surface-specific contribution we applied higher order DD, specifically XY4, to reduce the inter-pulse spacing τ for a given total precession time T and thereby decouple the NV from fluctuating fields at frequencies $f < 1/\tau$. Hence, comparing NV coherence subject to different pulse sequences reveals the bath dynamics [210]. The data for $T_{2,\mathrm{echo}}$ and $T_{2,\mathrm{XY4}}$ versus depth are plotted in Fig. 4.10 for 13 NVs; the zero depth mark is at an estimated absolute position discussed later. Both $T_{2,\mathrm{echo}}$ and $T_{2,\mathrm{XY4}}$ increased nearly monotonically with depth and are suppressed most drastically for depths < 25 nm. Importantly, the coherence enhancement $T_{2,\mathrm{XY4}}/T_{2,\mathrm{echo}}$ declined from a value of $\sim$2.52 deep in the film to as low as 1.2 for a shallow NV (lower panel of Fig. 4.10). This reduced decoupling efficiency of NVs near the surface suggests a depth-dependent change in the nature of the dominant spin bath from that of a homogeneous bulk bath to a faster fluctuating configuration of surface spins whose effects are not decoupled at longer precession times. Figure 4.10 also shows that the longitudinal spin relaxation time T_1 decreases for shallow NVs over a similar depth scale as the T_2 decrease, though T_1 was generally an order of magnitude larger than $T_{2,\mathrm{echo}}$. Therefore, T_1 processes did not dominate spin decoherence.

What we refer to as "T_1" through this chapter is an all-optical measurement referring to the time constant for an NV polarized into the $|0\rangle$ state by the green laser to relax to a fully mixed state. We suggest at the end of this chapter that this definition is inadequate,

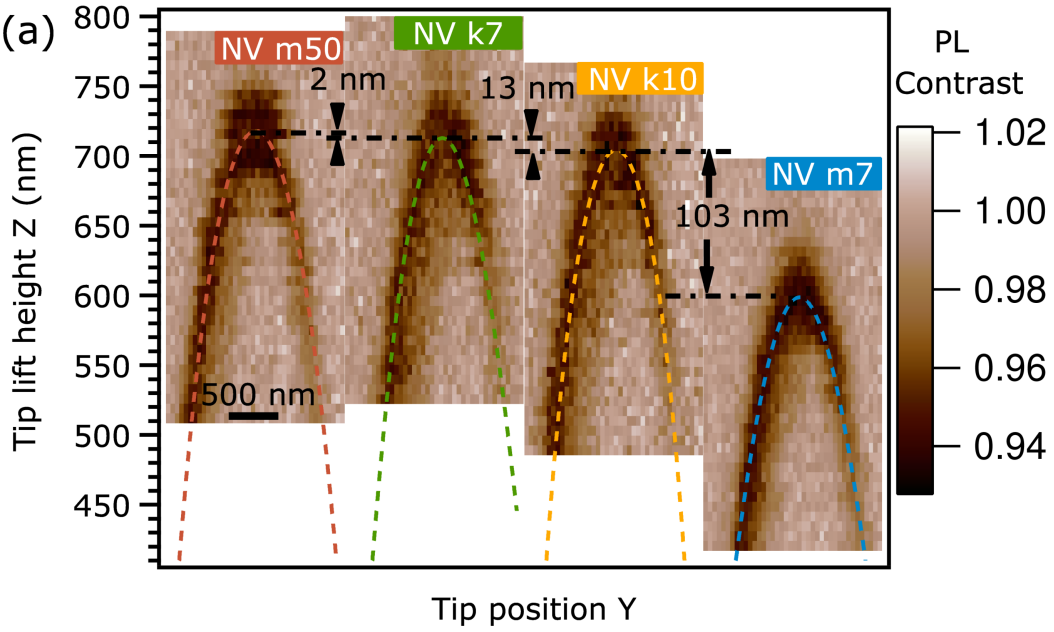

Figure 4.8: ESR slice photoluminescence (PL) contrast images in a lateral-height plane (yz) measured for four NVs of identical orientation. Relative depths were extracted via image registration, and dashed curves are polynomial fits as guides to the eye.

especially for shallow NVs, and more precise definition of T_1 is a main focus of Chapter 5.

4.4.2 Theory: two-bath noise model of dephasing

To explain the degradation of NV coherence near the surface, we assumed a noise model of pure spin dephasing because only small number of pulses N are used so that the condition $T_2 \ll T_1$ is maintained. Based on the saturation of T_2 in Fig. 4.10 and the isotopically pure $^{12}CH_4$ growth precursor [43], we expected that the dephasing of NVs deep in the film was dominated by interactions with a bulk-like spin bath of nitrogen P1 centers. Such magnetic noise is well described by a mean field theory [100] with the Ornstein-Uhlenbeck process [211], which phenomenologically has a Lorentzian spectral density centered at zero frequency. It is a natural ansatz to take the total noise spectral

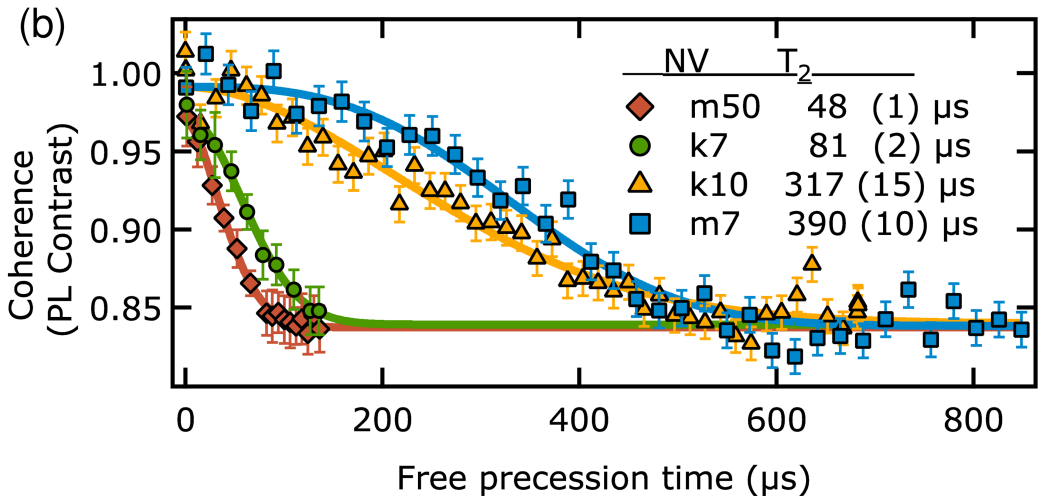

Figure 4.9: Hahn echo coherence data (markers) with shot noise-limited error bars and fits (lines) for the four NVs in (a).

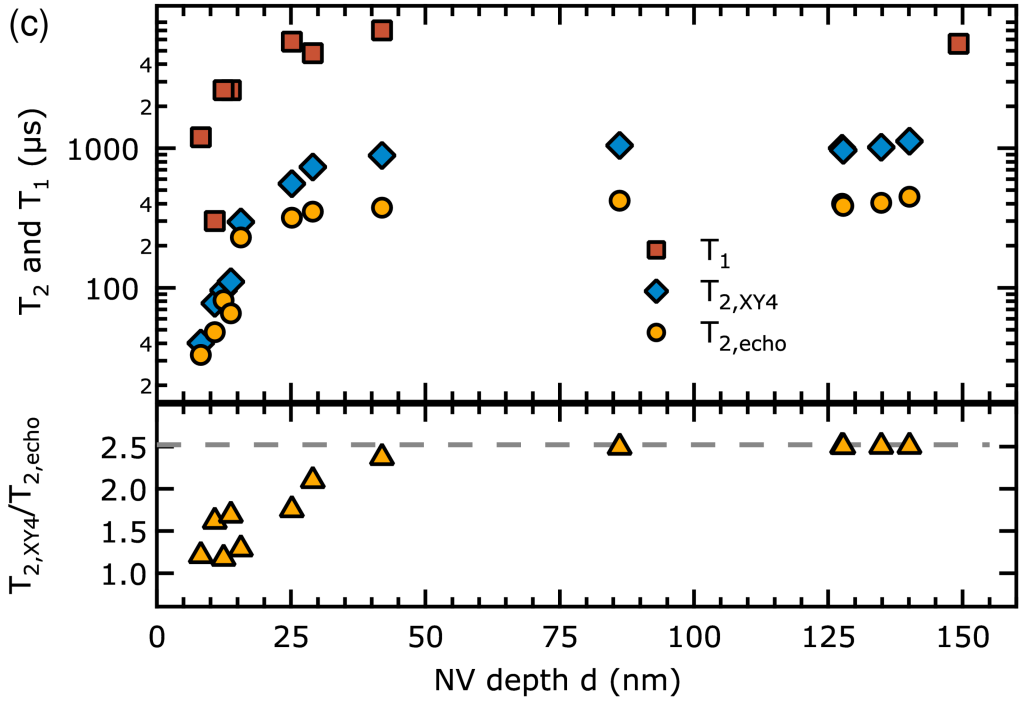

Figure 4.10: Coherence times ($T_{2,\mathrm{echo}}$ and $T_{2,\mathrm{XY4}}$) and relaxation times (T_1) versus NV depth, showing strong suppression of coherence near the surface. The lower panel shows $T_{2,\mathrm{XY4}}/T_{2,\mathrm{echo}} = N^{\lambda}$ is reduced with decreased depth, indicating that dynamical decoupling with $N = 4$ pulses is less efficient for shallower NVs. The dashed line $\lambda = 2/3$ is expected for NV dephasing by a slow bulk nitrogen spin bath.

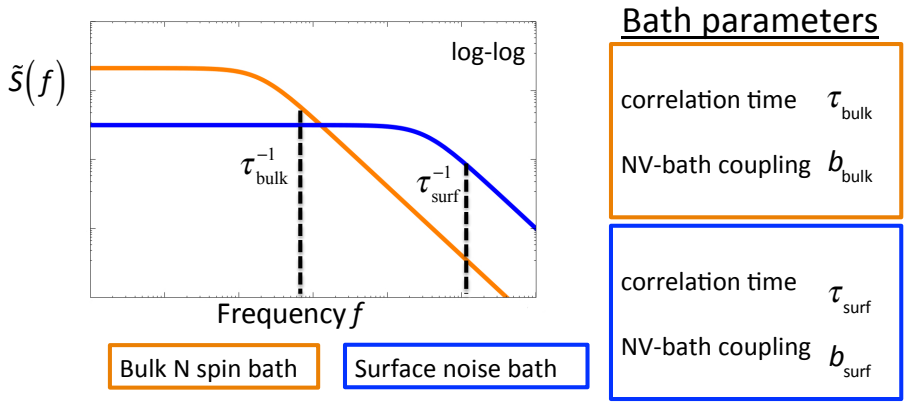

Figure 4.11: Schematic plot of the two-bath noise spectrum model for coherence fitting. The total noise spectrum in the model is the sum of contributions from a bulk spin bath (orange) and a surface noise bath (blue). The model is parameterized by two cutoff frequencies, τ_{bulk}^{-1} and τ_{surf}^{-1}, and two total couplings b_{bulk} and b_{surf}. The b couplings are the total integrated area under each curve, of which $\sim 90\%$ is contributed from noise at frequencies below the cutoffs.

density for an NV to be a two-Lorentzian sum (Fig. 4.11) with contributions from the bulk and surface

$$\tilde{S}_{\text{bulk}}(\omega) + \tilde{S}_{\text{surf}}(\omega) = \frac{b_{\text{bulk}}^2}{\pi} \frac{\tau_{\text{bulk}}}{1+\omega^2\tau_{\text{bulk}}^2} + \frac{b_{\text{surf}}^2}{\pi} \frac{\tau_{\text{surf}}}{1+\omega^2\tau_{\text{surf}}^2} \tag{4.1}$$

where b_{bulk}, b_{surf} are the NV-noise bath coupling frequencies and τ_{bulk}, τ_{surf} are the baths' autocorrelation times.

The fit functions for coherence decay envelopes in Hahn echo and Carr-Purcell-like [147] N-pulse sequences were considered using a mean field model to incorporate noise from the environment [99]. The mean field assumption has been shown to be valid for NV spin interaction with bulk electron spin baths [141] where the back action on the spin bath is neglected. The derivations in this section start from the discussion of dynamical decoupling filter functions presented in Chater 1, in particular Eq. 1.15.

Evaluating the coherence envelope in Eq. 1.15 requires an assumption of the noise spectral density $\tilde{S}(\omega)$. Dynamical decoupling studies on NVs in bulk, subject to a P1

center spin bath, show that a Lorentzian noise spectral density

$$\tilde{S}(\omega) = \frac{b^2\tau_c}{\pi}\frac{1}{1+\omega^2\tau_c^2} \tag{4.2}$$

is an accurate description of the mean field at the central NV spin [100], so it is a reasonable perspective from which to begin evaluating the surface noise. This type of $\tilde{S}(\omega)$ arises from a stationary exponential noise correlation function $\langle \eta'(0)\,\eta'(t)\rangle = b^2 \exp(-|t|/\tau_c)$ [99]. The coherence envelope is

$$|\langle\langle \sigma_+(8\tau)\rangle\rangle|_{\mathrm{XY4}} = \exp\left[-\frac{128b^2\tau_c}{\pi}\int\limits_{-\infty}^{\infty} d\omega \frac{\left[\cos\left(\frac{3\omega\tau}{2}\right)+\cos\left(\frac{5\omega\tau}{2}\right)\right]^2 \sin^6\left(\frac{\omega\tau}{2}\right)}{\omega^2\left(\omega^2\tau_c^2+1\right)}\right]. \tag{4.3}$$

The integral is computed by expanding the numerator of the integrand into its frequency components. This expansion is

$$\begin{aligned}\frac{1}{256}[&-18+4e^{-i\omega\tau}+4e^{i\omega\tau}+12e^{-2i\omega\tau}+12e^{2i\omega\tau}-4e^{-3i\omega\tau}-4e^{3i\omega\tau}-8e^{-4i\omega\tau}-8e^{4i\omega\tau}\\ &+4e^{-5i\omega\tau}+4e^{5i\omega\tau}+4e^{-6i\omega\tau}+4e^{6i\omega\tau}-4e^{-7i\omega\tau}-4e^{7i\omega\tau}+e^{-8i\omega\tau}+e^{8i\omega\tau}].\end{aligned} \tag{4.4}$$

The constituent integrals now have the form

$$I_{n,\pm} = a_n \int\limits_{-\infty}^{\infty} dz \frac{e^{\pm inz\tau}}{\tau_c^2 z^2 (z+i/\tau_c)(z-i/\tau_c)}. \tag{4.5}$$

The residues of the integrand are $\left(-\frac{i}{2}\tau_c e^{\pm n\tau/\tau_c}, +\frac{i}{2}\tau_c e^{\mp n\tau/\tau_c}, \pm in\tau\right)$ for the zeros $z_0 = (-i/\tau_c, +i/\tau_c, 0)$. Using the sum of residues, $I_{n,+}$ ($I_{n,-}$) can be computed as the principal part of the integral around a contour of the upper (lower) half of the complex plane. The

final result for the coherence envelope in the XY4 measurement is

$$|\langle\langle\sigma_+(8\tau)\rangle\rangle|_{\mathrm{XY4}} = \exp[-b^2\tau_c^2(8\tau/\tau_c + 4e^{-\tau/\tau_c} + 12e^{-2\tau/\tau_c} - 4e^{-3\tau/\tau_c} - 8e^{-4\tau/\tau_c} + 4e^{-5\tau/\tau_c} + 4e^{-6\tau/\tau_c} - 4e^{-7\tau/\tau_c} + e^{-8\tau/\tau_c} - 9)]. \quad (4.6)$$

For the Hahn echo, using Eqs. 1.15, 1.24, and 4.2 gives the coherence envelope

$$|\langle\langle\sigma_+(2\tau)\rangle\rangle|_{\mathrm{echo}} = \exp\left[-b^2\tau_c^2\left(2\tau/\tau_c + 4e^{-\tau/\tau_c} - e^{-2\tau/\tau_c} - 3\right)\right]. \quad (4.7)$$

These envelope functions are general for all cases of the noise parameters b and τ_c. In the case of an electron spin bath that changes its noise amplitude slowly compared to the interaction rate with the central NV ($\tau_c \gg 1/b$) [100], the exponential decay arguments reduce to the lowest order term. Letting $T \equiv 8\tau_{\mathrm{XY4}} = 2\tau_{\mathrm{echo}}$ be the total free precession time then

$$|\langle\langle\sigma_+(T)\rangle\rangle|_{\mathrm{echo}} = \exp\left[-\frac{1}{12}\frac{b^2}{\tau_c}T^3\right] \quad (4.8)$$

$$|\langle\langle\sigma_+(T)\rangle\rangle|_{\mathrm{XY4}} = \exp\left[-\frac{1}{192}\frac{b^2}{\tau_c}T^3\right]. \quad (4.9)$$

These expressions can each be simplified in terms of a single decay constant and predict a coherence time enhancement of $T_{2,\mathrm{XY4}}/T_{2,\mathrm{echo}} = (192/12)^{1/3} \approx 2.52$. This ratio is precisely the enhancement verified in our measurements of NVs deeper than about 50 nm (Fig. 4.10, bottom panel), which is evidence that the dominant source of dephasing for NVs deep in the delta-doped CVD film is the nitrogen spin bath.

In this $\tau_c \gg 1/b$ limit, the echo and XY4 coherence envelopes are not sufficient to extract unique values of b_{bulk} and τ_{bulk} because only the ratio $b_{\mathrm{bulk}}^2/\tau_{\mathrm{bulk}}$ appears in each function. Therefore, we verified the appropriate choice of b_{bulk} by performing pulsed

ESR spectroscopy with minimized microwave power to prevent power broadening. An example linewidth for a deep NV was 28.4 kHz (Fig. 4.12), and the computed average for the Gaussian $\sigma = b_{\rm bulk}$ over five deep NVs was 13.0 kHz. Simulations by Wang et. al. [140] predict a linear scaling of decoherence rates with nitrogen spin concentration $\rho_{\rm bulk}$ when the nitrogen bath dominates NV decoherence. Their reported relations are $1/T_2 = \left(5 \times 10^{-2}\right) \rho_{\rm bulk}$ MHz/ppm and $\Gamma_2^* = b_{\rm bulk}/\sqrt{2} = 0.19\rho_{\rm bulk}$ MHz/ppm, where $\rho_{\rm bulk}$ is in ppm nitrogen in diamond. Using our average values $b_{\rm bulk} = 13.04$ kHz and $T_2^{\rm echo} = 412.7$ μs over five NVs, we find in both cases that $\rho_{\rm bulk} = 48.5$ ppb $= 8.6 \times 10^{15}$ N/cm^3, corresponding to mean spin-spin separations of ~ 30 nm. This result in excellent agreement with N densities measured with Secondary Ion Mass Spectrometry (SIMS) data on N doped CVD diamond films [43]: SIMS findings ranged 8.0 to 31 $\times 10^{15}$ N/cm^3 for doping flow rates of 10 sccm to 50 sccm. Our results provide strong support for the limitation of deep ($d > 60$ nm) doped NV coherence in these films by a nitrogen spin bath.

The pulsed ESR measurement is not necessary for the shallower NVs because exponential arguments of the C_1 and C_4 coherence functions are linearly independent in terms of $b_{\rm surf}$ and $\tau_{\rm surf}$. The shallower NVs are less susceptible to the benefits of multiple pulse measurements, where $T_{2,\rm XY4}/T_{2,\rm echo}$ was in some cases not much larger than 1 (Fig. 4.10, bottom panel). If the Lorentzian noise bath assumption is to be followed to describe the surface-induced dephasing, then $\tau_{\rm surf} < 1/b_{\rm surf}$. That is, the noise amplitude from the bath changes faster than the bath coupling rate to the NV, so shorter intervals between π pulses would be needed to filter out the noise. The full forms Eqs. 4.6 and 4.7 are required to describe the decay envelopes in this case that T_2 is of the same order of magnitude as $\tau_{\rm surf}$, which occurs once $b_{\rm surf}$ becomes large enough compared to bulk noise.

The coherence envelopes were fully described by the product of two exponential decay functions that comes from adding the $\tilde{S}(\omega)$ functions for the surface and bulk noise.

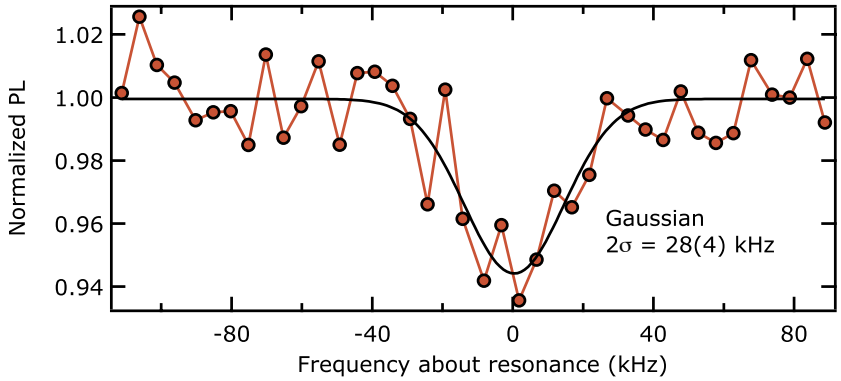

Figure 4.12: Optically detected pulsed ESR spectroscopy on the $m_s = 1$ NV sublevel (here 2.3429 GHz) of a 135-nm-deep NV; plotted are photoluminescence measurements (red points) and fit to a Gaussian (black). The width 2σ is 28(4) kHz, which gives a value for the coupling to the nitrogen spin bath $b = 14(2)$ kHz. The Rabi frequency used for the π pulse in this measurement was ~ 7 kHz. This coupling value is acquired independently of the dynamical decoupling measurements because for deep NVs, where $\tau_{\text{bulk}} \gg 1/b_{\text{bulk}}$, echo and bulk XY4 together do not provide sufficient information to extract coupling b_{bulk} and correlation time τ_{bulk} independently. Data acquisition time was minimized to mitigate broadening due to long-term effects, such as temperature drift.

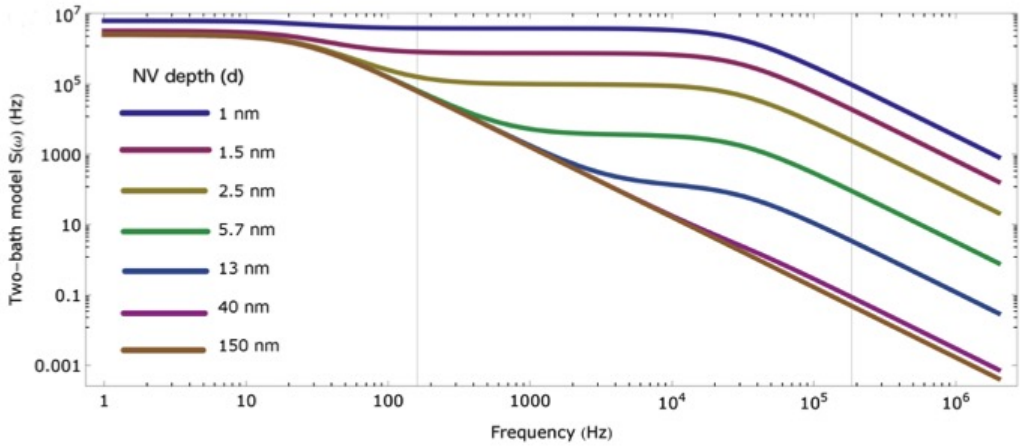

Figure 4.13: Examples of calculated noise spectral density, for various NV depths given the fit to a spin-bath model with two contributions: bulk and surface electronic spins. The high-frequency cutoff here is $1/\tau_{\text{surf}} = 190$ kHz from the surface spins, and this contributions $\tilde{S}(\omega)$ amplitude b_{surf} increases near the surface. The low-frequency cutoff is due to the bulk nitrogen spin bath. The effect of the surface bath on the total sum appears negligible around 40 nm and deeper, since b_{surf} becomes orders of magnitude smaller.

Subscripts "s" and "b" are used below for "surface" and "bulk." Assuming these are both Lorentzian and the deep bath correlation time τ_{bulk} is long, as shown in the section above, gives for the echo

$$C_1 = |\langle\langle \sigma_+ (2\tau)\rangle\rangle|_{\text{echo}} = \exp\left[-b_s^2(d)\,\tau_s^2\left(2\tau/\tau_s + 4e^{-\tau/\tau_s} - e^{-2\tau/\tau_s} - 3\right) - \frac{b_b^2(d)\,\tau_b^2}{12}\left(\frac{2\tau}{\tau_b}\right)^3\right]. \quad (4.10)$$

The XY4 result is

$$C_4 = |\langle\langle \sigma_+ (8\tau)\rangle\rangle|_{XY4} = \exp[-b_s^2(d)\,\tau_s^2(8\tau/\tau_s + 4e^{-\tau/\tau_s} + 12e^{-2\tau/\tau_s} - 4e^{-3\tau/\tau_s} - 8e^{-4\tau/\tau_s} + 4e^{-5\tau/\tau_s} + 4e^{-6\tau/\tau_s} - 4e^{-7\tau/\tau_s} + e^{-8\tau/\tau_s} - 9) - \frac{b_b^2(d)\,\tau_b^2}{192}\left(\frac{8\tau}{\tau_b}\right)^3]. \quad (4.11)$$

The functions for the surface and deep bath couplings to the NV are both considered to be dependent on depth, as described in the next section.

4.4.3 Results: fitting the two-bath noise model

In summary, the dephasing theory predicts a reduced coherence C_N after total NV precession time T:

$$C_N(T, b, \tau_c) = \exp\left[-\int_{-\infty}^{\infty} d\omega \tilde{S}(\omega)\,\mathcal{F}_N(T, \omega)\right] \quad (4.12)$$

where $\mathcal{F}_N(T, \omega)$ is a filter function for the specific N-pulse measurement. We simultaneously fit Hahn echo and XY4 coherence decay data to C_1 (Hahn) and C_4 (XY4) and extracted parameters b_{bulk}, b_{surf}, τ_{bulk}, and τ_{surf}. Examples of the linked fitting shallow and deep NVs are shown in Figs. 4.14 and 4.15. The converging values for b_{surf} and τ_{surf} were extracted from each fit and plotted versus NV depth, as shown in Fig. 4.16(a).

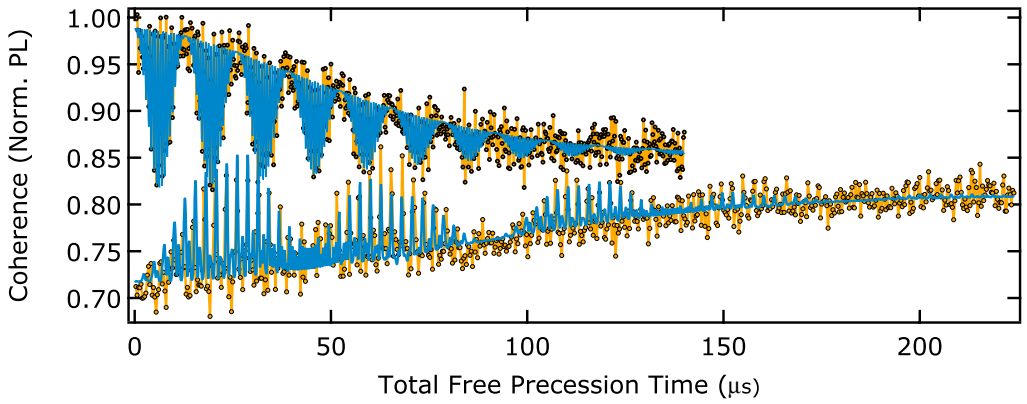

Figure 4.14: Simultaneous fitting (blue) of the coherence decay data (orange points) using Hahn echo (upper) and XY4 (lower) measurement sequences on a 14-nm-deep NV labeled m61. The extracted NV-noise coupling b_{surf} and noise correlation time τ_{surf} are 51 kHz and 10 μs, respectively. In this "fast-bath" regime of $1/\tau_{\text{surf}} > b_{\text{surf}} \sim 1/T_2$ the coherence envelopes are not described by a single time constant T_2 , as seen in Eqs. 4.6 and 4.7. However, we can also fit to $y_0 = A \exp\left[-(T/T_2)^n\right]$ and directly find coherence times 66(3) μs and 111(3) μs, and the exponents n are 1.7 and 2.3. The ratio $T_{2,\text{XY4}}/T_{2,\text{echo}} = N^{\lambda}$ yields a coherence enhancement exponent $\lambda = 0.38$ for $N = 4$ pulses.

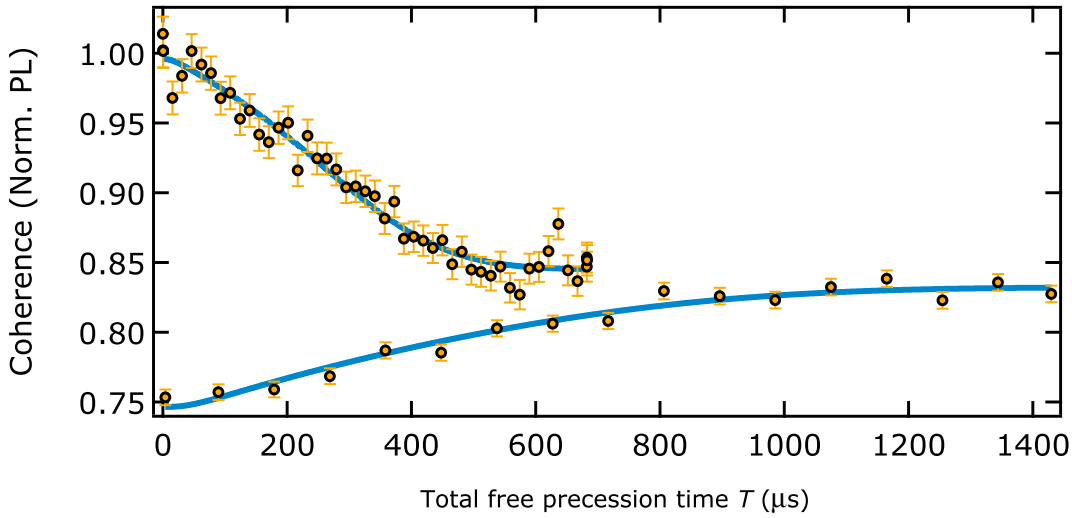

Figure 4.15: Simultaneous fitting of the coherence decay data using Hahn echo (orange) and XY4 (blue) measurement sequences on a 25-nm-deep NV labeled k10. The fit yields τ_{surf} and b_{surf} parameters for the two-bath model. The data points are taken at the nodes of the ESEEM measurement where the coherence returns to its maximal value. (This is different from the method in measurements shown below for larger number of pi pulses, N, where the ESEEM oscillations were actually physically eliminated by precisely aligning the external magnetic field.)

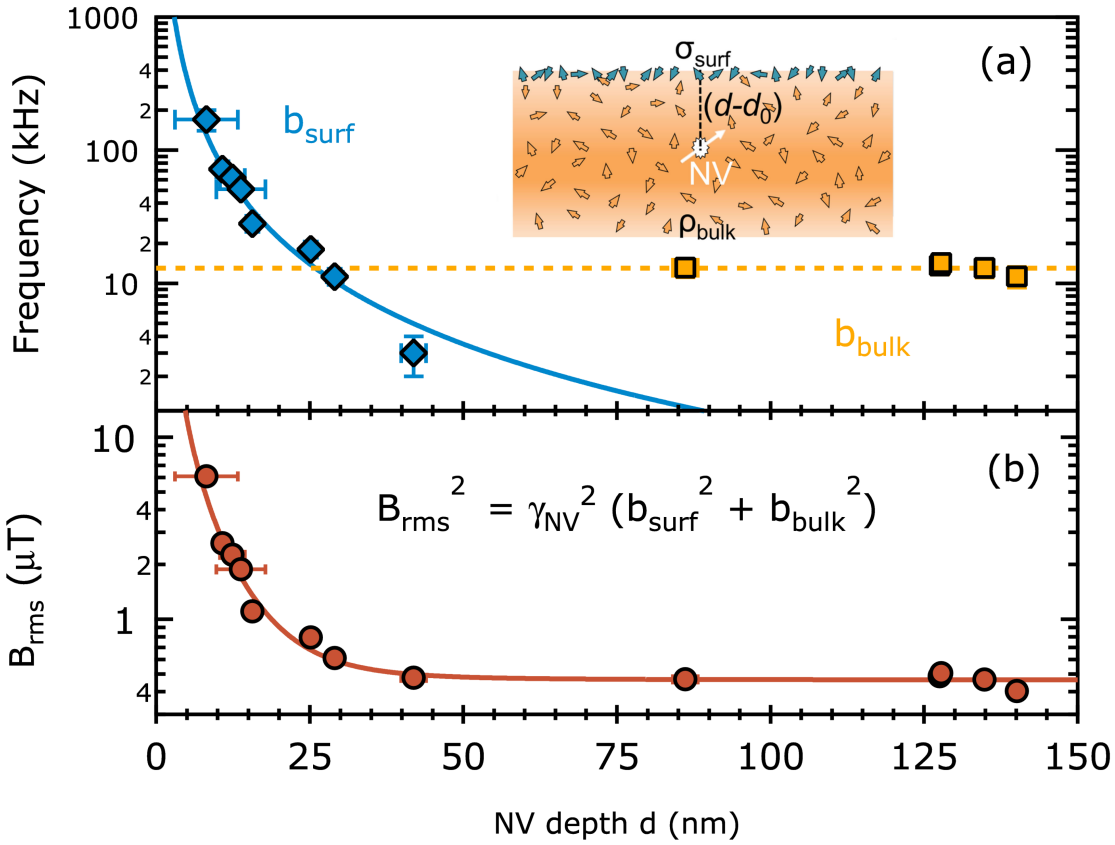

Figure 4.16: (a) Depth dependence of NVs coupling frequency to the surface (blue diamonds) and bulk (orange squares) noise baths as extracted by fitting coherence decay data to a two-bath dephasing model (see inset schematic). Horizontal error bars on data points denote relative depth errors from the MRI registration. The solid blue curve is a fit to a 2D electronic spin bath model. The fit gives a surface spin density $\sigma_{\text{surf}} = 0.04$ nm^{-2} and absolute NV depths (shallowest 8.2 nm). (b) Total rms magnetic field of the two spin baths. The solid line is a fit to the two-bath model.

For deep NVs ($d \gtrsim 60$ nm), we found that b_{surf} is small so that $\tilde{S}_{\text{surf}}(\omega)$ is negligible, and we determined parameters $b_{\text{bulk}} \approx 13$ kHz and $\tau_{\text{bulk}} \approx 830.2$ μs. The $T_{2,\text{XY4}}/T_{2,\text{echo}}$ values of these NVs are consistent with N^{λ}, where $\lambda = 2/3$ is expected for a "slow bath" of fluctuating nitrogen spins [100]. This theory predicts from the measured b_{bulk} a nitrogen density of $\rho_{\text{bulk}} = 8.6 \times 10^{15}$ cm^{-3} (48.5 ppb), also consistent with our mean $T_{2,\text{echo}}$= 410 μs (as discussed above) and Secondary Ion Mass Spectrometry data on nitrogen concentration in the delta-doped films [43].

For spins closer to the surface, we fit the coherence envelopes to the full two-bath model of Eq. 4.12, fixing b_{bulk} and τ_{bulk} to the values found for deep spins. We found a depth-dependent b_{surf} ranging $3 - 170$ kHz and a depth-independent $\tau_{\text{surf}} = 5(3)$ μs, corresponding to a faster bath than in the bulk and explaining why $T_{2,\text{XY4}}/T_{2,\text{echo}}$, and hence λ, was significantly reduced with NV proximity to the surface. The lack of depth dependence in τ_{surf} is consistent with τ_{surf} being internal to the bath. The depth dependence of b_{surf} is well described by a 2D layer of surface $g = 2$ spins, and furthermore, the model yields an absolute NV depth. By integrating over a uniform surface distribution σ_{surf} of fluctuating $S = 1/2$ dipoles, we find the total mean square field along the NV axis. The derivation of this model follows.

The coupling rate of the proposed surface spins to an NV is given by $b_{\text{surf}}(d) = \gamma_{NV} B_{\text{rms}}$. The dipolar magnetic field from a single external spin is

$$\mathbf{B}_i = \left(\frac{\mu_0}{4\pi r_i^3}\right)\left[3\left(\mathbf{m}_i \cdot \hat{r}_i\right)\hat{r}_i - \mathbf{m}_i\right], \tag{4.13}$$

where the position vector to the spin is $\mathbf{r}_i = r_i \hat{r}_i$ from the central NV. For a fluctuating field which causes NV spin dephasing we are primarily concerned with the component of Eq. 4.13 along the NV axis, $\hat{n}$. We will compute the field from three orthogonal components of the external spin moment $\mathbf{m}$ where each component in general fluctuates with a different noise power spectrum. We choose one component parallel to the externally applied field along $\hat{n}$, so $\hat{m}_{\parallel} = \hat{n} = \frac{1}{\sqrt{3}}(1,1,1)$, defined in the coordinate system of Fig. 4.17(a). The orthogonal components are $\hat{m}_{\perp,A} = \frac{1}{\sqrt{2}}(1,-1,0)$ and $\hat{m}_{\perp,B} = \frac{1}{\sqrt{6}}(1,1,-2)$.

The position vector of the surface spin is $\hat{r} = \frac{1}{\sqrt{s^2+d^2}}(s\cos\varphi, s\sin\varphi, d)$ where we have suppressed subscripts i for the spin. The field contribution along the NV axis is $B_n = \left(\frac{\mu_0}{4\pi r^3}\right)\left[3\left(\mathbf{m}\cdot\hat{r}\right)\hat{r}\cdot\hat{n} - \mathbf{m}\cdot\hat{n}\right]$ where $\mathbf{m}$ is any of the moment components. The three

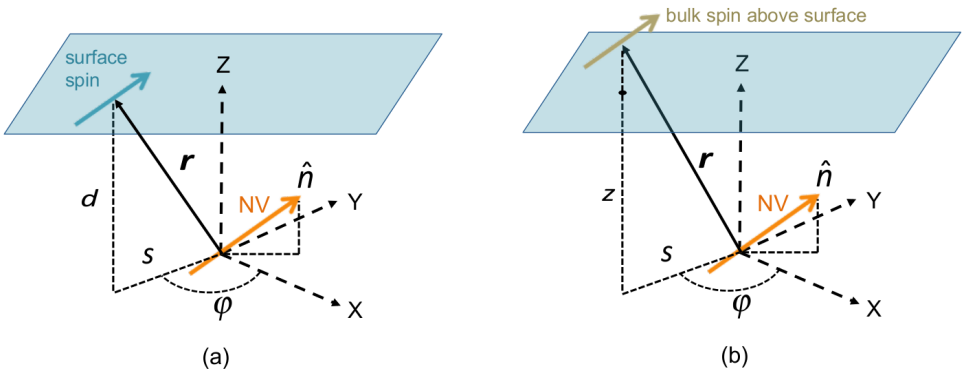

Figure 4.17: Geometry of a central NV spin with its orientation along the [111] axis in the X, Y, Z coordinate system defined with the [001] Z axis normal to the diamond surface. (a) Surface spin location in cylindrical coordinates $(s, , d)$ to compute its contribution to the total rms magnetic field along the NV axis. (b) Similar consideration for the field from a nitrogen bath spin inside the diamond or proton bath spin outside the diamond at $(s, , z)$.

magnetic fields are

$$\begin{aligned} B_n^{\perp,A} &= \frac{\mu_0 m_e}{4\pi(s^2+d^2)^{3/2}}\left[\frac{3s}{\sqrt{6}(s^2+d^2)}\left(\cos\varphi - \sin\varphi\right)\left(s\cos\varphi + s\sin\varphi + d\right)\right] \\ B_n^{\perp,B} &= \frac{\mu_0 m_e}{4\pi(s^2+d^2)^{3/2}}\left[\frac{1}{\sqrt{2}(s^2+d^2)}\left(s\cos\varphi + s\sin\varphi - 2d\right)\left(s\cos\varphi + s\sin\varphi + d\right)\right] \\ B_n{}^{\parallel} &= \frac{\mu_0 m_e}{4\pi(s^2+d^2)^{3/2}}\left[\frac{1}{(s^2+d^2)}\left(s\cos\varphi + s\sin\varphi + d\right)^2 - 1\right] \end{aligned} \tag{4.14}$$

The RMS magnetic field from this one spin, along the NV axis, is then given by $B^2_{n,\mathrm{rms}} = \left[\left(B_n{}^A\right)^2 + \left(B_n{}^B\right)^2 + \left(B_n{}^{\parallel}\right)^2\right]/3$. We are interested in the RMS magnetic field [205] from a uniform surface of electronic spins. Considering a uniformly distributed monolayer where the spin-spin intra-bath distance is less than NV depth d, the sum over all field contributions is approximated as an integral over the mean square field from each spin,

$$\left[B^2_{n,\mathrm{rms}}(d)\right]_{\mathrm{total}} = \sigma_{\mathrm{surf}} \int_0^{\infty} sds \int_0^{2\pi} d\phi \left[B^2_{n,\mathrm{rms}}(s,\varphi,d)\right]. \tag{4.15}$$

Combined with the evaluation of the magnetic moment,

$$\left\langle \mathbf{m}_e^2 \right\rangle = 3\Big(\frac{g\mu_B}{\hbar}S\Big)^2 = \frac{3(g\mu_B)^2}{4}, \tag{4.16}$$

the final result is

$$\left[B_{n,\mathrm{rms}}^2(d)\right]_{\mathrm{total}} = \Big(\frac{g\mu_B\mu_0}{4\pi}\Big)^2 \frac{\pi}{4}\frac{\sigma_{\mathrm{surf}}}{d^4} \approx \left(1.644\mathrm{mTnm}^3\right)^2 \frac{\sigma_{\mathrm{surf}}}{d^4} \tag{4.17}$$

We have used all three magnetic moment components in this derivation because both longitudinal and transverse parts will have a fluctuation related to the T_1 relaxation time of the electronic surface spins, and the transverse part also depends on the spin precession frequency ($\sim \gamma_e \times 200$ Gauss) and phase coherence time. For effects on NV dephasing, we are interested in the presumably slower longitudinal moment fluctuations. The noise power from the $m_\perp$ fluctuation at the electron Larmor frequency ($f_L > 500$ MHz at 200 Gauss applied field) will have a significantly smaller effect on the NV coherence envelope.

The correlation time of the surface spin bath, τ_{surf}, corresponds to the T_1 energy relaxation time of the spins. A possible relaxation mechanism is dipole-dipole interactions between electronic spins in the 2D bath. Based on σ_{surf}, we compute the intra-bath dipolar coupling for $S = 1/2$ spins, giving a correlation time $f_{\mathrm{dip}} \approx 5$ MHz. This is larger than our $1/\tau_{\mathrm{surf}} = (200 \pm 120)$ kHz, however, numerical simulations on bulk nitrogen spin baths have shown that the actual correlation time $1/\tau_c$ can be smaller than f_{dip} by an order of magnitude [100]. τ_{surf} may also be set by a different mechanism than dipole-dipole coupling, which is a topic for future consideration.

To fit surface-NV coupling data to this model, we directly use the following fit function

by evaluating the constants in Eq. 4.17 and dividing by the NV gyromagnetic ratio:

$$b_{\mathrm{surf,fit}}\,(\mathrm{d})\,[\mathrm{kHz}] = \frac{10^3}{(d-d_0)^2}\sqrt{(2118.37\mathrm{nm}^6/\mu\mathrm{s}^2)\,\sigma_{\mathrm{surf}}} \tag{4.18}$$

with σ_{surf} in nm^{-2} and depths in nm. d_0 is the absolute zero depth, free to vary in the fit, while the measured relative NV depths d have an arbitrary zero point prior to the fit. All depth axes within this chapter are plotted as the absolute depth acquired from the fit.

In summary, the surface spin model yields a coupling rate

$$b_{\mathrm{rms}}^2 = b_{\mathrm{surf}}^2\,(d)\,/\gamma_{\mathrm{NV}}^2 = \left(\frac{g\mu_0\mu_B}{4\pi}\right)^2 \frac{\pi}{4}\frac{\sigma_{\mathrm{surf}}}{(d-d_0)} \tag{4.19}$$

where d is the relative NV depth (arbitrary zero) and d_0 is an offset to find absolute depth. A fit of Eq. 4.19 to the b_{surf} data points in Fig. 4.16(a) predicts absolute depths $(d-d_0)$ of the shallowest two NVs at 8.2 nm and 10.8 nm, consistent with the growth rate; the fit error in d_0 is ± 0.5 nm, and henceforth d denotes absolute depth. We find a surface spin density $\sigma_{\mathrm{surf}} = 0.04(2)$ spins/nm^2, corresponding to a $r_0 \approx 2.3(7)$ nm mean spin separation. The non-discrete surface spin model is justified because $d \geq r_0$ for all NVs studied here. The depth dependence $b_{\mathrm{surf}} = 1/d^2$ is in good agreement with the b_{surf} data, and by fitting to $b_{\mathrm{surf}}\,(d) \propto 1/\,(d-d_0)^{\alpha}$ we find a best goodness-of-fit for $\alpha = 1.8 \pm 0.2$. We emphasize the importance of measuring a broad depth range of NVs in constraining this exponent. Figure 4.16(b) joins the shallow and bulk noise models in a plot of integrated noise power $b^2 = b_{\mathrm{bulk}}^2 + b_{\mathrm{surf}}^2$, as expressed in magnetic field units as $B^2 = b^2/\gamma_{\mathrm{NV}}^2$. The sharp increase in B^2 reflects the decrease in spin coherence times at $d < 25$ nm in Fig. 4.10, and therefore 25 nm is approximately the depth at which rapidly fluctuating surface spins, rather than the slow P1 spin bath, begin to dominate

NV decoherence.

4.5 NV depth measurements by proton sensing

As a cross-check of absolute depth offset d_0, we performed proton sensing on NVs of fitted depths 10.8 nm, 12.4 nm, and 13.8 nm by placing immersion oil on the diamond and using XY8-N detection to time the NV phase accumulation periods to the Larmor precession frequency of the protons in the oil (see Refs. [102, 206, 212]). In summary, fitting our proton sensing data corroborates the 10-14 nm depth range spanned by the three NVs, as detailed below. The depth ordering of the NVs, however, is not consistent with the depths imaged directly with nano-MRI, raising the question of which NV's depth to fix for d_0; hence we do not use proton sensing measurements to fix d_0. The strength of the proton analysis is its nanoscale precision in absolute depth, rather than relative depth, under the model assumption that the sample's proton sample density is truly quantified and uniform at the diamond surface. The technique is limited in practice to NVs within less than 20 nanometers of the surface [89] because these NVs experience a large enough magnetic field from the protons. The DD technique is a fundamentally important tool for coherent spin sensing, and the following proton example is readily extended to other nuclei or general samples of interest.

4.5.1 Model of magnetic field from protons on the diamond

We first calculate the magnetic field from a semi-infinite block of protons on the surface of diamond. This field is assumed to be classical, that is, we do not consider back-action of the NV on the relatively far-separated and dense ensemble of proton spins. No one spin is strongly coupled to the NV, in contrast to the case of the NV's host nitrogen nuclear spin in Appendix E. The detection scheme here is passive, rather

than active [206], in that the protons are not coherently manipulated by rf radiation and hence there is no double-resonance. For this reason, the NV is sensitive to the frequencies characteristic of fluctuations in the target spins perpendicular moments $m_\perp$. For a proton we have

$$\left\langle m_z^2 \right\rangle = \mu_{\mathrm{p}}^2, \tag{4.20}$$

$$\left\langle m_\perp^2 \right\rangle = \left\langle m_x^2 \right\rangle + \left\langle m_y^2 \right\rangle = 2\mu_{\mathrm{p}}^2. \tag{4.21}$$

The rms field at the NV of depth d from a single proton spin a distance $\Delta z = z - d$ above the surface will depend only on the magnetic moments transverse to the applied field along the NV axis, so $\hat{m}_{\perp,A} = \frac{1}{\sqrt{2}}(1,-1,0)$ and $\hat{m}_{\perp,B} = \frac{1}{\sqrt{6}}(1,1,-2)$. The direction of the proton spin position vector is $\hat{r} = \frac{1}{\sqrt{s^2+z^2}}(s\cos\varphi, s\sin\varphi, z)$ as in Fig. 4.17(b). The magnetic fields from these transverse moments along the NV axis $\hat{n}$ are

$$\begin{aligned} B_{\mathrm{p}}^{\perp,A} &= \tfrac{\mu_0 m_{\mathrm{p}}}{4\pi(s^2+z^2)^{3/2}} \left[\tfrac{3s}{\sqrt{6}(s^2+z^2)} \left(\cos\varphi - \sin\varphi\right)\left(s\cos\varphi + s\sin\varphi + z\right) \right] \\ B_{\mathrm{p}}^{\perp,B} &= \tfrac{\mu_0 m_{\mathrm{p}}}{4\pi(s^2+z^2)^{3/2}} \left[\tfrac{1}{\sqrt{2}(s^2+z^2)} \left(s\cos\varphi + s\sin\varphi - 2z\right)\left(s\cos\varphi + s\sin\varphi + z\right) \right] \end{aligned} \tag{4.22}$$

where we use the subscript "p" to differentiate from the electronic surface spins model. The rms magnetic field, along the NV axis, from this one spin precessing about the applied field is then $B_{\mathrm{p,rms}}^2 = \left[\left(B_{\mathrm{p}}{}^A\right)^2 + \left(B_{\mathrm{p}}{}^B\right)^2 \right]/2$. By integrating over a uniform density ρ_{target} of such proton spins in a block above the diamond surface one obtains the total rms magnetic field as

$$\left\langle B_{\mathrm{p,rms}}^2(d) \right\rangle = \rho_{\mathrm{target}} \int_d^\infty dz \int_0^\infty s\,ds \int_0^{2\pi} d\phi \left[B_{\mathrm{p,rms}}^2(s,\varphi,z) \right] \tag{4.23}$$

Together with Eq. 4.21 and $\mu_p = 1.4106 \times 10^{-26}$J/T, the final result is

$$\left\langle B^2_{\mathrm{p,rms}}(d) \right\rangle = \frac{\mu_0^2 \mu_{\mathrm{p}}^2}{(4\pi)^2} \frac{5\pi}{24} \frac{\rho_{\mathrm{target}}}{d^3} \approx \left(1.141 \mu \mathrm{Tnm}^3\right)^2 \frac{\rho_{\mathrm{target}}}{d^3} \tag{4.24}$$

A typical proton spin density is $\rho_{\mathrm{target}} \sim 6 \times 10^{28}$ m^{-3}. For the NV of depth 12.4 nm the result is $\sqrt{\left\langle B^2_{p,\mathrm{rms}} \right\rangle} = 202$ nT. This increases to 376 nT for an 8.2 nm deep NV. Eq. 4.24 is used in the following section for proton sensing depth measurements.

4.5.2 XY8 sensing protocol and results

For the depth measurements, immersion oil (Olympus Type-FF) was deposited between the delta-doped diamond film surface and a glass coverslip to provide the ^{1}H nuclei external to the diamond. The XY8-N sequence [102]

$$(\tau - \pi_x - 2\tau - \pi_y - 2\tau - \pi_x - 2\tau - \pi_y - 2\tau - \pi_y - 2\tau - \pi_x - 2\tau - \pi_y - 2\tau - \pi_x - \tau) \tag{4.25}$$

was used because it can robustly preserve an arbitrary state on the Bloch sphere, rather than one transverse magnetization direction, during phase accumulation magnetometry [100]. The applied magnetic field was aligned to $< 1^\circ$ of the NV axis to suppress the ESEEM from the interaction between the shallow doped NVs electronic spin and ^{15}N nuclear spin, as discussed earlier. The magnitude of the field was 142 G – 172 G in the experiments, giving proton Larmor frequencies of $f_{\mathrm{L}} = (4.258\mathrm{kHz/G})B = 605$ kHz – 732 kHz. The proton spin precession can be detected via the collapse of the echo signal near $4\tau = 1/f_{\mathrm{L}}$. Sequences with 96 and 128 pulses were used to accumulate sufficient phase from the small proton bath field.

As shown in previous works [205, 102, 206], this measurement can provide a value of the absolute distance from the NV to the diamond surface. One can infer from the

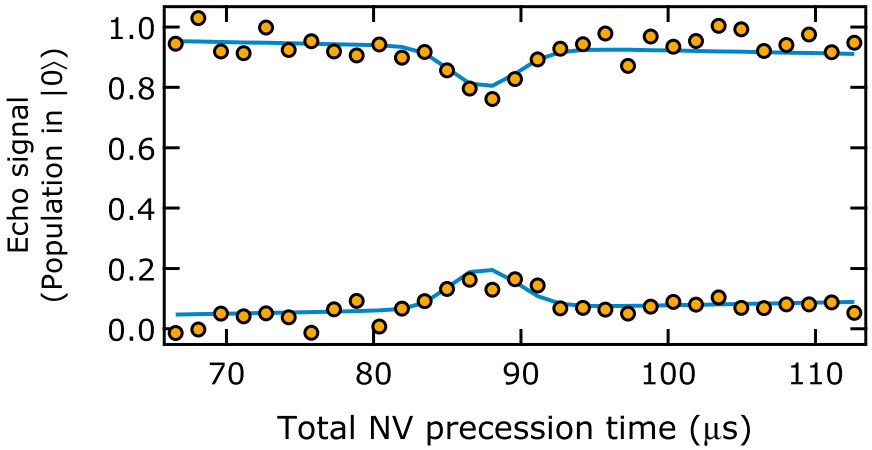

Figure 4.18: XY8-128 data (orange circles) and numerical fit (blue line) for an NV found by MRI relative depth data and the surface spin fit data to be at depth 12 ± 2 nm. Population error bars are smaller than the symbols. The fit of the proton signal gives a NV depth of $d_p = 14 \pm 2$ nm and spectrum width of $\sigma = 17 \pm 2$ kHz. The applied field was 172 Gauss, which gives the collapse feature at total evolution time $T_p = N/(2B\gamma_p) \approx 87.4$ μs . We estimated the proton sensing depth uncertainty 2 nm by comparing proton data taken on this same NV at different fields, numbers of pulses, and number of time data points.

strength and shape of the echo collapse signal the magnitude of the rms magnetic field required to cause this collapse. Given a known density of ^{1}H nuclei in the oil, the NV depth can be inferred by computing that rms magnetic field from the effectively semi-infinite proton spin bath on the surface.

To simulate the proton signal, we have used the spin coherence approach with the DD filter functions described earlier, except we have assumed the noise spectral density to be a Gaussian of width $\sigma_{\rm p}$ centered at $f_{\rm L}$, so

$$S_{\rm p}(\omega, d, \sigma_{\rm p}) = \frac{\left\langle B^2_{\rm p,rms}(d)\right\rangle}{\sqrt{2\pi\sigma^2_{\rm p}}} {\rm Exp}\left[-\frac{(\omega - 2\pi f_{\rm L})^2}{2\sigma^2_{\rm p}}\right] \tag{4.26}$$

where $\left\langle B^2_{\rm p,rms}\right\rangle$ is given by Eq. 4.24. The filter function for XY8-N is Eq. 1.26 with a total evolution time $T = 2\tau N$. The filter function assumes an infinitesimal π-pulse time, so in practice we account for the finite π-pulse time τ_π to scale the time axis of the data

to match the simulation axis. We acquired the data with a $\pm\pi/2$ pulse at the end of the sequence to obtain two signals. The simulated signal in terms of population of the $m_s = 0$ state is

$$S_{\pm}(T) = \frac{1}{2}\left(1 \mp \mathrm{Exp}\left[-\left(\frac{g\mu_B}{\hbar}\right)^2 \int_{\omega_1}^{\omega_2} d\omega S_p\left(\omega, d, \sigma_p\right) \frac{2\sin^2\left(\frac{\omega T}{2}\right)\left[1-\sec\left(\frac{\omega T}{2N}\right)\right]^2}{\omega^2}\right] \mathrm{Exp}\left[-\frac{T^n}{T_2^n}\right]\right) \tag{4.27}$$

Numerical integration limits ω_1 and ω_2 were chosen to ensure convergence. We performed a least squares fit of Eq. 4.27 simultaneously to the $\pm\pi/2$ data with free parameters d and σ_{p}. Coherence decay parameters T_2 and n were independently measured with the same XY8-N sequence and nevertheless varying these did not significantly affect the proton fit results.

4.6 Limits of T_2 for near-surface NVs

4.6.1 Enhancing T_2 via dynamical decoupling

To mitigate surface noise and investigate the validity of our two-bath model, we used higher-order DD. We focus here on shallow spins, specifically NV k7 ($d = 12.4$ nm), since they are critical for nanoscale magnetometry. For $N \geq 8$, XY8-N was chosen for its relevance to those applications. Using the general N-pulse filter function Eq. 1.26 within Eq. 4.12 with the same two-Lorentzian $\tilde{S}(\omega)$ gives the coherence envelope for perfect pulses. We numerically integrate over ω for fixed τ_{surf} and b_{surf} with N set to 2 through 320. Fig. 4.19(a) shows the results of the calculation and fit to a stretched exponential function to estimate a single decay constant $T_{2,\mathrm{N}}$. Fig. 4.19(b) shows this experimental

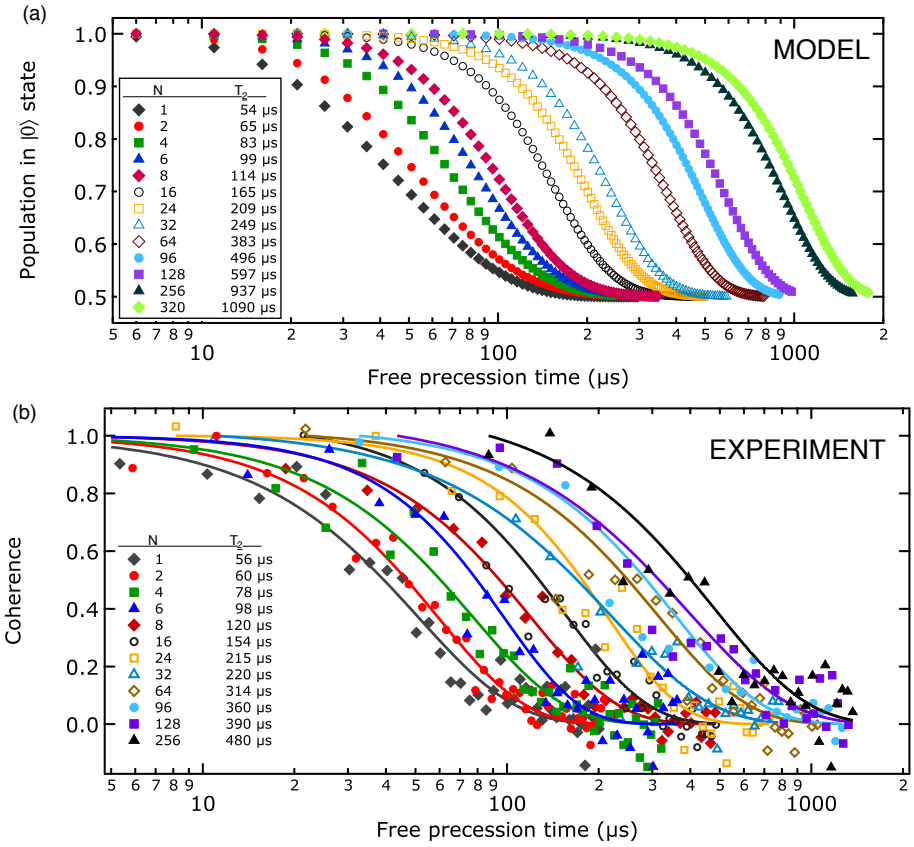

Figure 4.19: Numerically calculated (a) and experimental (b) coherence decay envelopes for the 12.4-nm-deep NV, as summarized in Fig. 4.21. Each symbol type refers to the NVs coherence for a number of pulses N. Calculated plots in (a) assume that the overall noise is the two-bath model with the same $b_{\text{surf}} = 71$ kHz and $\tau_{\text{surf}} = 5$ μs found from the analytical fits to echo and CPMG-4 data. The points are fit to a stretched exponential (solid lines) with free exponent to find a value for T_2. These results show that the two-Lorentzian noise model reproduces the increase in T_2 and the dynamical decoupling efficiency λ for values of N up to about 64. "Coherence" $[0, 1]$ and "Population in $|0\rangle$ state" $[0.5, 1]$ are equivalent as defined here.

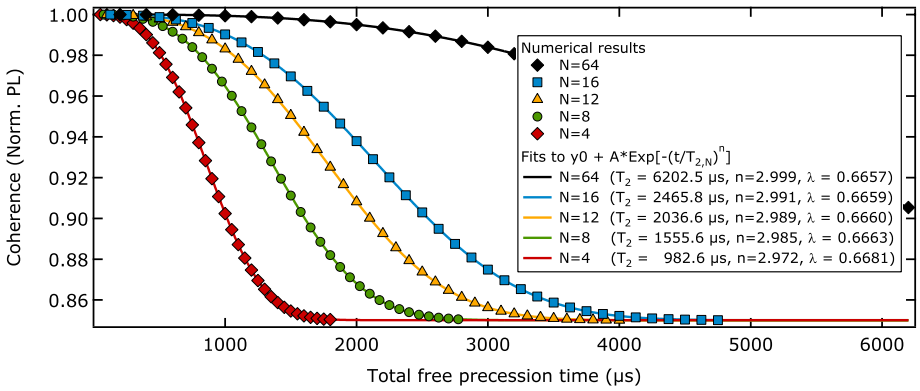

Figure 4.20: Numerically calculated coherence decay envelopes for a typical deep NV, assuming a Lorentzian spectrum with $b_{\text{bulk}} = 13$ kHz and $\tau_{\text{bulk}} = 830.2$ μs. These data points were fit to a stretched exponential shown in the legend. $\lambda = 2/3$ remains an excellent description as N is increased, and $n \approx 3$. The analytical theory in the $\tau_{\text{bulk}} \gg 1/b_{\text{bulk}}$ limit, shown in Eqs. 4.8 and 4.9, predicts $n = 3$ exactly. The specific bulk parameters from experiment therefore fit this limit very closely. The origin of the $< 1\%$ change in λ and n between these numerically calculated curves may arise from τ_{bulk} being only 10 times larger than b_{bulk}. This deviation would be imperceptible in the experiment given the SNR. We also note that the relaxation time here is taken to be much larger and in practice will limit $T_{2,\text{N}}$ at large N.

coherence data up through $N = 256$. The model supports the experimentally observed increased efficiency of dynamical decoupling on shallow NVs as more pulses are applied. For $N = 256$ pulses we measure a $T_2 > 450$ μs, corresponding to a magnetic sensitivity of < 10 nT/Hz$^{-1/2}$, as computed for the example in Chapter 1 using Eq. 1.53. Figure 4.20 is a similar calculation performed for the bulk bath parameters assuming $b_{\text{surf}} = 0$ for a deep NV, showing that the dynamical decoupling efficiency easily reaches 2/3. The reason for this λ difference between shallow and deep NVs is discussed in more detail in Chapter 5. In summary, the noise spectrum limiting the bulk-NV coherence time is slow, so the filter function at all precession time points lies on the $1/f^2$ part of the Lorentzian spectrum. For shallow NVs the Lorentzian correlation times are short enough that the noise looks relatively white at some filter frequencies lower than or near $1/\tau_{\text{surf}}$, so using more pulses — making the NV most sensitive to higher frequencies – does not reduce the noise as rapidly as $1/f^2$.

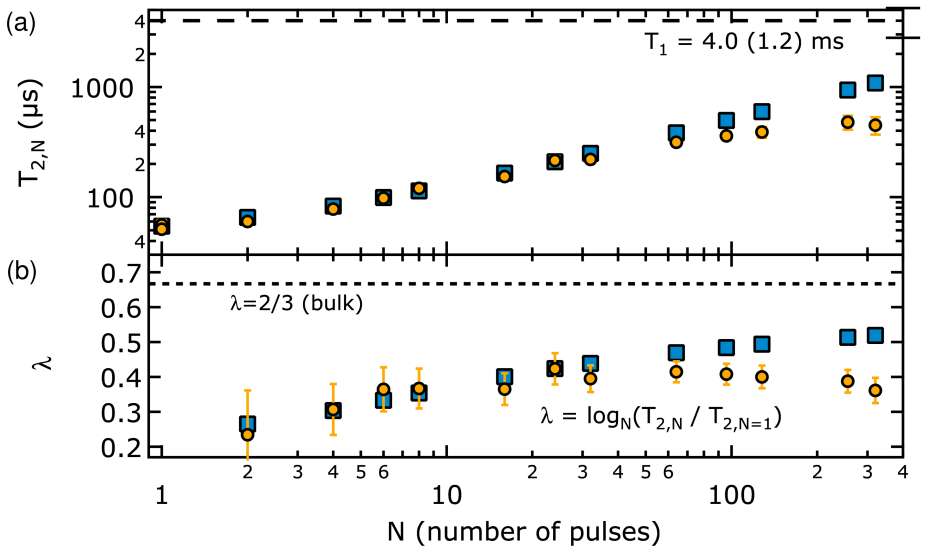

Figure 4.21: The effect of the number of dynamical decoupling pulses N on coherence of a 12.4 nm deep NV. (a) T_2 measured using CPMG-N ($N < 8$) and XY8-N (orange circles) and numerical calculations (blue squares) based on the dephasing due to surface and bulk spin baths. The model parameters are $b_{\text{surf}} = 71(4)$ kHz and $\tau_{\text{surf}} = 5(1)$ μs, based on fits to the echo and CPMG-4 data. $T_{2,N}$ error bars ($\delta T_{2,N}$) are coherence fit parameter standard deviations, and the dashed line indicates the measured T_1. (b) Plotted is the decoupling efficiency λ, which relates each $T_{2,N}$ to $T_{2,N=1}$. Error bars are propagated from $\delta T_{2,1}$ and each $\delta T_{2,N}$. The dotted line indicates the measured value of 2/3 for bulk NVs. The model and data exhibit excellent agreement through $N = 24$.

4.6.2 Saturation of T_2 versus number of π pulses

Figure 4.21 summarizes the shallow-NV dependence of T_2 and decoupling efficiency λ on the number of Car-Purcell-Meiboom-Gill (CPMG) and XY8 pulses up to $N = 320$. Plotted are the measured data (orange circles) and the calculated, two-bath model prediction (blue squares). These points are in good quantitative agreement up through $N = 24$, demonstrating that the model captures the low frequency noise spectrum well. The increase in λ with N is in contrast with a constant $\lambda_{\text{bulk}} = 2/3$ due to bulk spin noise. As N increases beyond 24, λ reaches $\sim$0.42 and then begins to decrease. This behavior is accompanied by a saturating coherence time of $T_{2,N=256} = 480\,(70)$ μs. The fact that λ saturates at a value below λ_{bulk} and does so for an N smaller than the

point where $T_{2,N}$ stops increasing could be explained by a second surface related noise with a correlation time shorter than 5 μs. This observation is consistent with a recent investigation of diamond surface noise that probed T_1 and $T_{1\rho}$ of NVs and reported $\tau_{\text{surf}} = 0.28\,(3)$ ns assuming a single Lorentzian spectrum [86]. We emphasize, however, that the non-exponential shape and relatively large decoupling efficiency of our coherence data are not explained with this sole GHz correlation rate Lorentzian. We also note that the same study attributed the noise to a surface spin density 0.01-0.1 spins/nm^2 [86], consistent with our value of σ_{surf}, suggesting that both noise sources may arise from the same electronic spin bath. We found that cleaning the sample with solvents prior to these measurements resulted in slightly altered coherence times from those presented in Figs. 4.34.16, which could be attributed to redistribution of surface spins. Specifically, $T_{2,\text{echo}}(T_{2,\text{XY4}})$ changed from 81(96) to 56(78)s for this NV (though other shallow NVs showed increased $T_{2,\text{echo}}$).

4.6.3 Predicted variance in T_2 for very shallow NVs

It is expected that as the NV becomes shallower, the discreteness of the surface spins, spaced by a few nm, will begin to be important. That is, the variance of the field, over many configurations, should increase with decreased depth. We simulated the total rms magnetic field from the surface spins as a function of depth by summing over the individual square dipole fields under many configurations of randomly placed surface spins at the average density $\sigma_{\text{surf}} = 0.04/$ nm^2 extracted above. In Fig. 4.22 we plot the mean surface spin field at NV depths $d \geq 2$ nm, with error bars of standard deviation, and the fractional deviation (standard deviation/mean). The fractional deviation for an 8 nm deep NV is $\pm 17\%$ about the mean field of 5.14 μT, and for a 2 nm deep NV the field is 82 $\mu\text{T} \pm 58\%$.

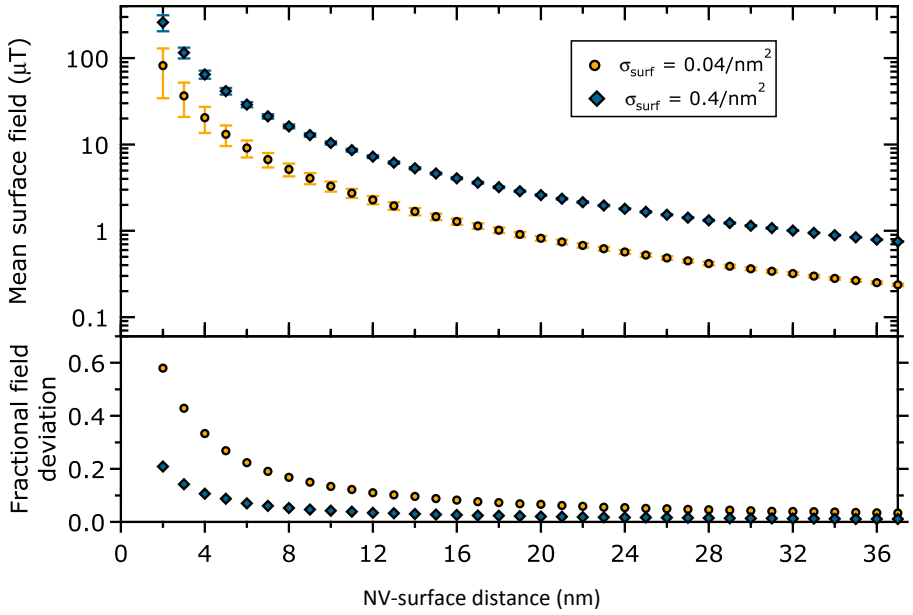

Figure 4.22: (Top panel) Surface spin field versus depth computed as a sum of discrete fluctuating dipoles. The square root of the average square field $B_{\text{mean}} = \sqrt{\langle B^2 \rangle}$ over 5000 different spin placement configurations is plotted at each depth. The surface spins were distributed in a 150×150 nm^2 planar area with a fixed average number density. The error bars indicate $\pm$ the standard deviation δB computed from the 5000 spin configurations. NVs at a very shallow depth will be more sensitive to the few nearest neighbor surface spin positions, and the large error bars for the 2-nm depth verify this hypothesis. Both sets of data points, since they are mean field values, fit best to a $1/d^{\alpha}$ function with $\alpha = 2$, consistent with the integrated uniform surface result. (Lower panel) $\delta B / B_{\text{mean}}$ versus NV depth. The experimentally extracted spin density of 0.04/nm^2 (orange circles) shows a larger fractional spread at a given depth than for the same calculation with 0.4/nm^2 (blue diamonds) because a denser set of spins "looks" more uniform from a given depth.

There is not a general equation giving a single time constant T_2 as a function of the couplings and correlation times, except where the bulk bath dominates, as shown in Eq. 4.8. In that limit we have $T_2 \propto b_{\text{bulk}}^{-2/3}$, and propagation of the field deviation to the standard deviation in the coherence time is then $\Delta T_2 = \frac{2}{3}\frac{\Delta b_{\text{bulk}}}{b_{\text{bulk}}} T_2$. That is, ΔT_2 is still proportional to the fractional deviation in the surface spin field, but is only 2/3 of that value. Physically, ΔT_2 means the standard deviation in spin coherence times that would be expected if many NVs were measured deep in the film, each seeing a slightly different configuration of nitrogen spins. For the shallow spin case it may be expected by extension approximately that $T_2 = b_{\text{surf}}^{-\gamma} \times \left(\frac{A}{\tau_{\text{surf}}}\right)^{\gamma-1}$ for some $A, \gamma > 0$ that will change with depth. This equation assumes that for very shallow NVs the T_2 depends only on the surface bath, and the expected standard deviation is then $\Delta T_2 \approx \gamma \frac{\Delta b_{\text{bulk}}}{b_{\text{bulk}}} T_2$. In summary, we will expect that T_2, for predicted ranges of surface spin density, will vary at least on the order of 10% for NVs at depths < 10 nm even if the depth of multiple NVs is identical. This expected spread in coherence times could be a useful signature in future depth-calibrated NV based studies of discrete spin effects, such as local clustering.

4.7 Conclusions

We have presented a detailed study of decoherence of shallow NVs in a nitrogen delta-doped diamond film. The surface noise is well modeled by a 2D electronic spin layer with sub-MHz dynamics, as evidenced by the depth dependence of coherence enhancement and total noise power probed by NVs at independently measured depths. We have shown that the decohering effects of fluctuating surface and bulk spins in nitrogen delta-doped diamond are mitigated via dynamical decoupling with appropriately chosen inter-pulse timing, which has significant impact for nano-MRI and coherent spin coupling applications. The extracted $\sigma_{\text{surf}} = 0.04\,(2)$ spins/nm^2 is comparable to the densities

found in experiments on metallic and insulating films [207]; this apparently universal phenomenon further emphasizes the need to identify the nature of these spins and the mechanism of the bath fluctuations. The scanning magnetic gradient concept used here has recently facilitated high resolution NV based MRI of dark spins [70], making NVs an excellent sub-nm spectroscopic probe of this spin noise apparent in a variety of crystal surfaces.

Remaining questions about the diamond surface can be addressed using our method of shallow NV creation via growth combined with nanoscale depth imaging. Firstly, depth-calibrated studies of shallower NVs (< 5 nm) may reveal wide variations in T_2 from discrete surface spin effects or spin clustering. Secondly, using delta-doping to form a dark nitrogen spin layer isolated from the diamond surface — $d > 60$ nm based on our findings — could provide a controlled test bed to study 2D spin bath effects on an NV outside the layer. Thirdly, under our present applied magnetic field we expect that NV coupling to electric and strain fields is of second order [29] although experiments at $B_{\|} \approx 0$ could probe these effects near the surface. Lastly, we have presented a two-level dephasing model, but the incompletely understood T_1 processes between the $S = 1$ NV sublevels ultimately limit DD as a sensing protocol [142]. T_1 measurements of bulk [119] and shallow [86] NVs at lower temperatures suggest thermally activated relaxation rates of surface spins, and a future depth-calibrated study of both T_1 and T_2 at variable temperature could clarify the mechanism behind surface spin fluctuations or point to other sources of decoherence. Work on this subject of near-surface NV decoherence is continuing in the community [89], and in the next chapter we address in detail the coherence time limits due to spin relaxation.

To date, it is not certain whether the coherent $g \approx 2$ spins commonly detected near diamond surfaces with double electron-electron resonance (DEER) [41, 70, 55, 90] are the same spins responsible for surface-induced NV decoherence. These DEER signals are

typically modeled as due to the dipolar field from fluctuating electrons with T_{1e} times of 1-20 μs, which may be consistent with the 200-kHz correlation rate we observe for surface noise. However, it has more recently been found that the low-frequency surface noise causing dephasing can be suppressed by a dielectric on the diamond, while the DEER spin signal is unaffected [88]. To add further insight and help tie together the electric and magnetic noise findings reported through 2014-2015, in the next chapter we use double-quantum spin relaxation measurements to probe non-magnetic noise and find evidence for an electric-field origin of this dephasing due to a low-frequency surface noise spectrum.

Chapter 5

Double-quantum spin-relaxation limits to coherence of near-surface nitrogen-vacancy centers

We probe the relaxation dynamics of the full three-level spin system of near-surface nitrogen-vacancy (NV) centers in diamond to define a T_1 relaxation time that helps resolve the $T_2 \leq 2T_1$ coherence limit of the NV's subset qubit superpositions. We find that double-quantum spin relaxation via electric field noise dominates T_1 of near-surface NVs at low applied magnetic fields. Furthermore, we differentiate $1/f^\alpha$ spectra of electric and magnetic field noise using a novel noise-spectroscopy technique, with broad applications in probing surface-induced decoherence at material interfaces.

[1]The contents of this chapter have substantially appeared in reference [92]: B. A. Myers, A. Ariyaratne, A. C. Bleszynski Jayich, Double-quantum spin-relaxation limits to coherence of near-surface nitrogen-vacancy centers, arXiv:1607.02553 (2016).

5.1 Introduction

Nitrogen-vacancy (NV) centers in diamond excel as room-temperature quantum sensors and quantum bits, where long-lived spin coherence and population are critical to an NV's functionality in these roles. In particular, the coherent control of near-surface NVs has been used to detect few to single electronic spins [179] and nuclear spins [155, 55, 81] and to perform nanoscale magnetic resonance imaging [179, 70, 72, 73]. The placement of these NVs just nanometers from the diamond surface is vital to strongly couple to external degrees of freedom [213] and achieve nanoscale spatial resolution in imaging [5]. However, our understanding of surface-related noise and its effect on coherence is an incomplete puzzle that remains a grand challenge [40, 86, 87, 89, 90, 91] for NV-based sensing. In a broader context, identifying surface noise on the nanoscale is useful to the study of a variety of quantum technologies, such as trapped ions [93, 94], mechanical resonators [95], and superconducting circuits [96, 97], whose performance is limited by pervasive surface-related decoherence and dissipation.

The NV spin levels that display long coherence reside in the orbital ground state, a three-level spin $S = 1$ system [18]. Any two of the levels may constitute a qubit for coherent quantum sensing, and although the sensor's functionality resides in the coherence of the qubit [26, 214], this functionality is compromised by the coupling of all three levels to the environment. For a two-level system, coherence time T_2 is known to be ultimately limited by spin relaxation time T_1 as $T_2 \leq 2T_1$ [46, 101], and much attention has been paid to this theoretical T_1 limit for NVs [149, 187]. However, for NVs in bulk diamond a saturating $T_2 = 0.53(2)T_1$ has been reported [149], and for shallow NVs, those within ~ 25 nm of the surface, the discrepancy is more striking with $T_2 \lesssim 0.1T_1$ [87, 89]. These prior results suggest a decoherence channel that has not been accounted for.

The NV qutrit is rendered a powerful and versatile sensor by the different frequency

scales and selection rules of its spin transitions. And for precisely the same reasons – the double-edged sword of sensitivity – the NV is also highly susceptible to environmental noise of various origins. The NV has both single-quantum (SQ, $\Delta m_s = \pm 1$) and double-quantum (DQ, $\Delta m_s = \pm 2$) transitions [215] tunable in the MHz to GHz frequency range, as shown in Fig. 5.1(a). This full capacity of probing noise has not yet been utilized, in particular concerning the direct relaxation rate between the $m_s = \pm 1$ states of the qutrit, which we will refer to as DQ relaxometry. Here, we measure both SQ and DQ relaxation rates of the three-level system and find that shallow NVs exhibit particularly fast DQ relaxation, accounting for decoherence that has not been directly observed before. We then use multipulse dynamical decoupling to show that T_2 of the $m_s = 0, -1$ qubit can exceed a properly defined T_1, where DQ relaxation dominates this limit at low magnetic fields ($\lesssim 40$ G). Furthermore, because the DQ relaxation channel is a magnetic-dipole-forbidden transition, it can be used to selectively probe electric fields [216] and strain [33, 217, 34]. We combine spectroscopic DQ relaxometry with standard SQ dephasing spectroscopy [13, 87, 89] to quantitatively map the spectral character of noise sources responsible for decoherence of near-surface NVs, and this technique enables us to distinguish electric and magnetic contributions to the noise spectrum.

5.2 Double-quantum spin relaxometry

5.2.1 Sources of dephasing and relaxation

The ground-state spin Hamiltonian [32, 29] of the NV center indicates how magnetic, electric, and strain fields contribute to dephasing and spin relaxation, with the

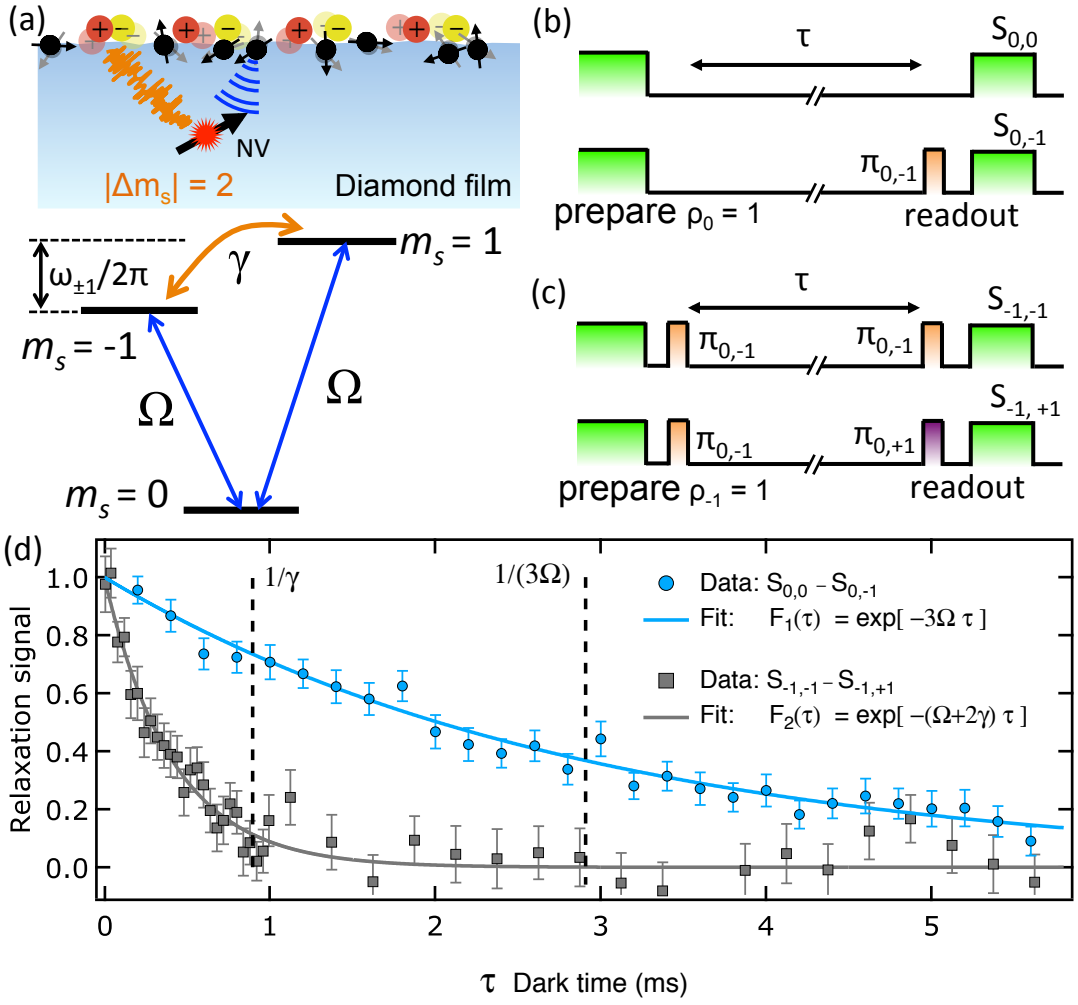

Figure 5.1: (a) Surface-noise spectroscopy with the triplet ground state of a shallow NV center. The double-quantum (DQ) relaxation channel (orange, γ) is sensitive to electric field noise, and the single-quantum (SQ) channel (blue, Ω) is sensitive to magnetic field noise. An applied dc magnetic field tunes the DQ transition frequency $\omega_{\pm1}/2\pi$. (b,c) Measurement sequences to extract the relaxation rates Ω and γ. The spin is initialized into (b) $|0\rangle$ or (c) $|-1\rangle$ by a green laser pulse and, for $|-1\rangle$, a microwave $\pi_{0,-1}$ pulse. After a dark time τ, any of the three spin state populations ρ_j can be read out by a choice of $\pi_{0,\pm1}$ pulse before photoluminescence detection, giving signal $S_{i,j}$. (d) Population decay data with three-level relaxation model fits as solid lines.

corresponding energy level diagram shown in Fig. 5.1(a).

$$H_{\mathrm{NV}} = \left(hD_{\mathrm{gs}} + d_{\parallel}\Pi_{\parallel}\right) S_z^2 + g\mu_B \mathbf{B}\cdot\mathbf{S} - \frac{d_{\perp}\Pi_{\perp}}{2}\left(S_+^2 + S_-^2\right) \tag{5.1}$$

where $\mathbf{S}$ is the spin-1 operator, h is Planck's constant, $g\mu_B/h = 2.8$ MHz/G is the gyromagnetic ratio, $D_{\mathrm{gs}} = 2.87$ GHz is the crystal-field splitting, $d_{\parallel}/h = 0.35$ Hz·cm/V and $d_{\perp}/h = 17$ Hz·cm/V are the components of the NV's electric dipole moment parallel and perpendicular to its symmetry axis [17], and $\Pi_{\parallel}$ and $\Pi_{\perp}$ are the corresponding total effective electric field components [32, 29]. $\mathbf{\Pi} = (\mathbf{E} + \boldsymbol{\sigma})$ contains electric field $\mathbf{E}$ and scaled strain $\boldsymbol{\sigma}$ terms. We attribute the $\mathbf{\Pi}$ noise identified in our experimental results with $\mathbf{E}$ electric fields, as discussed throughout the supplemental section 5.7.

The spin raising and lowering operators in the last term of Eq. 5.1 couple the $m_s = \pm 1$ states and thus serve as a route for electric noise-induced DQ spin relaxation with a rate γ (Fig. 5.1(a)). For the $\{|0\rangle, |-1\rangle\}$ qubit, the $d_{\parallel}E_{\parallel}$ term describes electric-field-induced energy shifts [29, 90] that contribute to the dephasing rate $\Gamma_d^{(-10)}$. The second (Zeeman) term accounts for magnetic fields that cause additional dephasing [5, 100, 87] and SQ relaxation [85, 86, 71, 218, 145] between $|0\rangle$ and $|\pm 1\rangle$ with rates $\Omega_{0,\pm 1}$ ($\Omega_{0,+1} = \Omega_{0,-1} \equiv \Omega$, as we verified experimentally in 5.7.2). The energy splitting between the $|\pm 1\rangle$ levels, $\hbar\omega_{\pm 1} = 2g\mu_B B_z$, is tunable via a dc magnetic field B_z, enabling us to probe the noise spectral density that affects γ [219]. We consider the regime where dc strain, dc electric field, and dc transverse magnetic field are small compared to the applied B_z, so the eigenstates are approximately $\{|0\rangle, |-1\rangle, |1\rangle\}$ of the S_z operator [29].[1] Temperature changes can also lead to dephasing through D_{gs} [133], though we neglect them here as

[1]The three eigenstates of the S_z operator $|S = 1, m_s\rangle \equiv |m_s\rangle$ with $m_s = 0, \pm 1$ are alternately written in terms of the single-electron spin-1/2 states as $|0\rangle = (|\uparrow\rangle|\downarrow\rangle + |\downarrow\rangle|\uparrow\rangle)/\sqrt{2}$, $|1\rangle = |\uparrow\rangle|\uparrow\rangle$, and $|-1\rangle = |\downarrow\rangle|\downarrow\rangle$. In this form, the term single-quantum diretly refers to a single electron spin flip, and the double-quantum refers to both electrons flipping simultaneously, $|\uparrow\uparrow\rangle \leftrightarrow |\downarrow\downarrow\rangle$. Therefore, state $|0\rangle$ is immune to double-quantum spin relaxation due to indistinguishability of the two electrons.

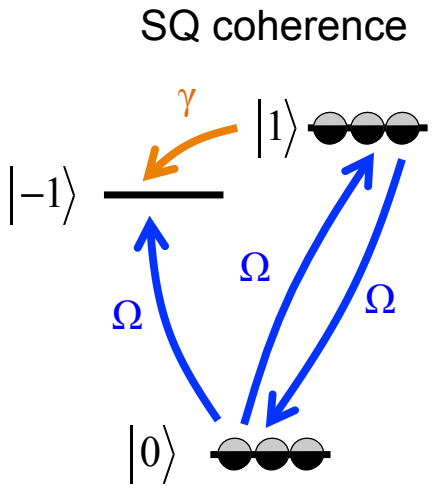

Figure 5.2: Diagram of the NV ground state spin triplet with two-state single-quantum coherence at finite magnetic field along the z axis. Quantum coherence is illustrated here between the two levels occupied with black and white discs. In the single-quantum (SQ) coherence there are three Ω relaxation events possible (blue arrows) and one γ relaxation event (orange arrow) to leak population out of the superposition state.

our measurements are insensitive to slow (sub-kHz) fluctuations.

5.2.2 DQ relaxation contribution to T_2

For the NV qutrit in Fig. 5.1(a), the total T_1 relaxation time that limits T_2 of the qubit is built from the relaxation rates between the three $|m_s\rangle$ spin states, as illustrated in Fig. 5.2. However, the most prevalent definition of T_1 in the NV literature [119, 13, 85, 220, 86, 87, 89, 187], which we label here $T_1^{(0)}$, considers only Ω and implicitly assumes $\gamma = 0$. $T_1^{(0)}$ is the time constant for an NV prepared in density matrix $\rho = |0\rangle\langle 0|$ to depolarize into a fully-mixed state $\rho = I_{3\times 3}/3$. Therefore, $T_1 = T_1^{(0)}$ describes a specific depolarization process but does not apply to loss of coherence. To understand what limits T_2 of the $\{|0\rangle, |-1\rangle\}$ qubit the correct definition should be

$$\frac{1}{T_1} = \frac{1}{T_1^{(0)}} + \gamma = 3\Omega + \gamma. \tag{5.2}$$

SQ coherence ρ_{-10} initialized between the $|0\rangle$ and $|-1\rangle$ states will decay at a total rate $1/T_2$ due to the sum of pure dephasing $\Gamma_d^{(-10)}$ and spin relaxation rates [122], so that in the zero-dephasing limit $T_2^{\mathrm{SQmax}} = 2T_1 = 2\left(3\Omega + \gamma\right)^{-1}$ (see 5.7.3). Hence, to evaluate the revised decoherence limit $T_2 \leq 2T_1$ we used SQ and DQ relaxometry to extract Ω and γ.

5.2.3 Measurement of three-level relaxation rates

The experimental setup consists of a homebuilt, room-temperature confocal microscope with a 532-nm excitation laser and single-photon counters to collect sideband photoluminescence (PL) [3]. A single-crystal diamond film was epitaxially grown using isotopically purified methane (99.99% ^{12}C) to minimize NV decoherence due to ^{13}C nuclear spins [132]. The sample contains NVs at a mean depth of 7 nm, formed via 4-keV nitrogen implantation [181, 40] (see Appendix A for details). A microwave stripline was used for coherent $|0\rangle \leftrightarrow |\pm 1\rangle$ spin rotations, namely spin inversion $\pi_{0,\pm 1}$ pulses [19].

The rates Ω and γ can be experimentally determined by measuring the decay of each diagonal element of the density matrix through pulsed optically detected magnetic resonance [119]. The population dynamics of the $\{|m_s\rangle\}$ are given by three differential equations with the solutions [220, 85] (see 5.7.1)

$$\rho_0\left(\tau\right) = \frac{1}{3} + \left(\rho_0\left(0\right) - \frac{1}{3}\right) e^{-3\Omega\tau} \tag{5.3}$$

$$\rho_{\mp 1}\left(\tau\right) = \frac{1}{3} \mp \frac{1}{2}\Delta\rho\left(0\right) e^{-(\Omega+2\gamma)\tau} - \frac{1}{2}\left(\rho_0\left(0\right) - \frac{1}{3}\right) e^{-3\Omega\tau} \tag{5.4}$$

where τ is the time between initialization and readout, ρ_{m_s} are the $|m_s\rangle$ state populations, and the initial conditions are $\rho_0\left(0\right)$ and $\Delta\rho\left(0\right) = \left[\rho_{+1}\left(0\right) - \rho_{-1}\left(0\right)\right]$.

We performed two sets of pulse sequences (Fig. 5.1(b,c)) that directly probe the spin

populations under initial conditions $\rho_i(0) = 1$. The final $\pi_{0,j}$ pulse before PL readout determines which population $\rho_j(\tau)$ is probed, yielding a relaxation signal $S_{i,j}(\tau)$. Figure 5.1(b) shows a standard method to measure $T_1^{(0)} = (3\Omega)^{-1}$ [119], and applying this sequence to Eqs. 5.3 and 5.4 gives a fit function (see D.1 for details)

$$F_1(\tau) = S_{0,0}(\tau) - S_{0,-1}(\tau) = re^{-3\Omega\tau} \tag{5.5}$$

where parameter r is PL contrast. The second set of sequences (Fig. 5.1(c)) initialize $\Delta\rho(0) \neq 0$ and measure $\rho_{\mp1}(\tau)$, and data is fit to

$$F_2(\tau) = S_{-1,-1}(\tau) - S_{-1,+1}(\tau) = re^{-(\Omega+2\gamma)\tau}. \tag{5.6}$$

Figure 5.1(d) shows data for shallow NV A1 fitted to Eqs. 5.5 (blue circles data) and 5.6 (gray squares data), revealing a slow SQ rate $\Omega = 0.115(4)$ kHz and faster DQ rate $\gamma = 1.11(5)$ kHz. Hence the traditional relaxation time $T_1^{(0)} = 2.90(3)$ ms overestimates by $4\times$ the full $T_1 = 0.69(7)$ ms from Eq. 5.2, due to significant DQ relaxation.

5.3 Enhancement of $T_2 > T_1$ for near-surface NVs

The complete T_1 enables evaluation of the limit $T_2 \leq 2T_1$, for which we reduced $\Gamma_d^{(-10)}$ via dynamical decoupling. Figure 5.3 shows Hahn echo and CPMG-N measurements for two shallow NVs, where N is the number of π_y pulses [147]. The coherence time $T_2 = T_2(N)$ is extracted from a stretched-exponential fit $\exp[-(T/T_2)^n]$ to data $C(T)$, where T is total precession time. Figure 5.3(a) shows that for sufficiently large $N = 512$, and at $\omega_{\pm1}/2\pi = 37.1$ MHz, T_2 saturates at $1.2(3)T_1$, in clear contrast to the incomplete comparison $T_2 = 0.14(1)T_1^{(0)}$ (see 5.7.6 for additional plots and data summary). This demonstration of $T_2 \gtrsim T_1$ for shallow NVs also exceeds the ratio previously reported

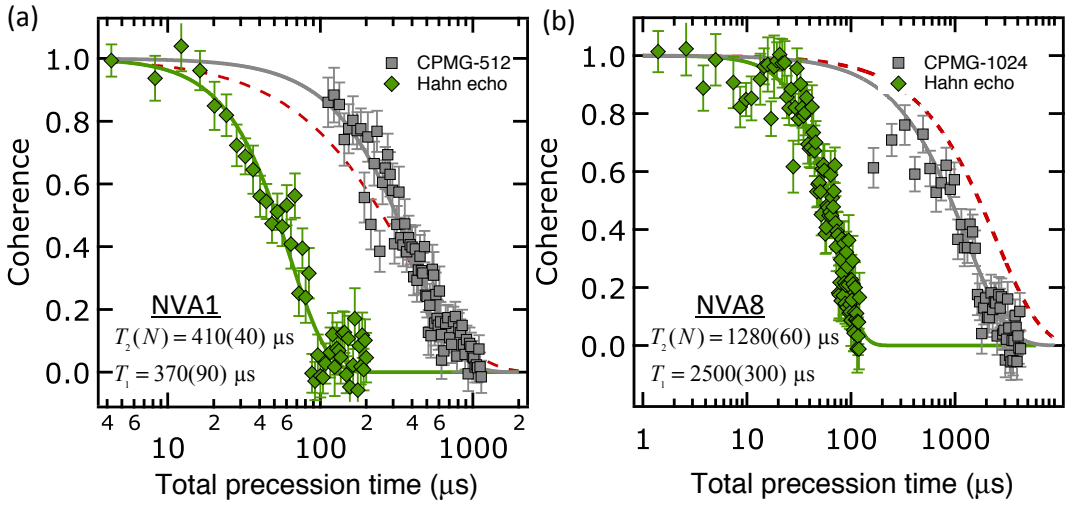

Figure 5.3: Enhancement of SQ coherence time using CPMG-N for shallow NVs under conditions of (a) large γ at $\omega_{\pm 1}/2\pi = 37.1$ MHz and (b) small γ at $\omega_{\pm 1}/2\pi = 1376$ MHz. Data shown are Hahn echo (green diamonds) and CPMG-N (gray squares) where N is the number of π pulses, and solid lines are fits to $\exp\left[-(T/T_2)^n\right]$. Dashed red lines are reference plots of $\exp\left(-T/T_1\right)$ using the measured $T_1 = (3\Omega + \gamma)^{-1}$.

for bulk NVs, $T_2 \approx 0.53(2)T_1^{(0)}$ [149]. At a much larger $\omega_{\pm 1}/2\pi = 1376$ MHz (Fig. 5.3(b)), $T_2(N = 1024)$ saturates at only $0.52(7)T_1$, while T_2 and T_1 both increase. The explanation for these changes at higher $\omega_{\pm 1}$ lies in the frequency dependence of γ, as we discuss next.

Figure 5.4(a) shows a strong dependence of γ on frequency $f = \omega_{\pm 1}/2\pi$ for shallow NVs, with two implications: 1) T_1 greatly decreases at lower magnetic fields, in contrast to $T_1^{(0)}$, and 2) double-quantum relaxation spectroscopy gives new insights about noise sources affecting γ. As B_z tunes $\omega_{\pm 1}/2\pi$ from 1612 MHz to 20 MHz, γ increases by up to an order of magnitude, showing a $1/f^\alpha + \gamma_\infty$ type of dependence with $\alpha = 1 - 2$. We observe the $1/f^\alpha$ part only for shallow NVs, and thus we identify its origin as surface-related electric field noise (see 5.7.5 for supporting data). We attribute γ_∞ relaxation to bulk effects [142]. In contrast to γ, we find Ω to be independent of magnetic field over the studied range of $B_z \approx 4 - 290$ G (see supporting Fig. 5.15). The ratio γ/Ω plotted in Fig. 5.4(b) demonstrates that the DQ relaxation contributes substantially to

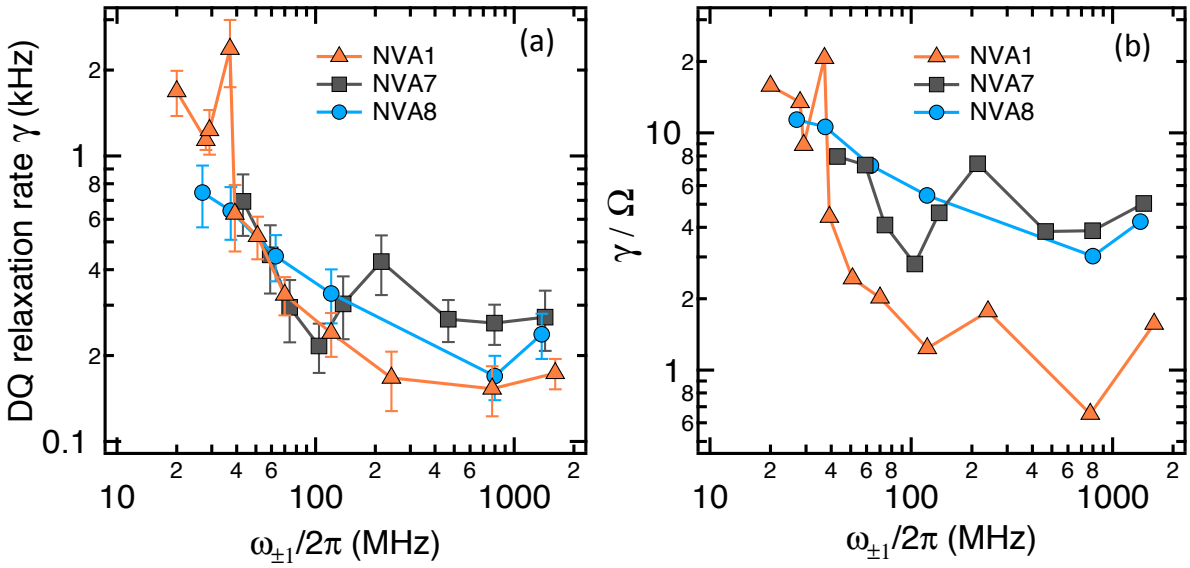

Figure 5.4: (a) Measured DQ relaxation rates γ for three shallow NV centers versus DQ frequency splitting $f = \omega_{\pm 1}/2\pi$. Each symbol type refers to one NV. The $1/f^{\alpha}$-type dependence is attributed to surface-related electric field noise and saturation at large $\omega_{\pm 1}$ is attributed to bulk effects. (b) Ratio γ/Ω plotted for the same NVs as in (a).

the total decoherence rate; $\gamma/\Omega \gg 1$ at low B_z and $\gamma/\Omega \gtrsim 1$ even at higher B_z. The suppression of shallow-NV decoherence via the DQ channel at large $\omega_{\pm 1}$ gives a practical reason for magnetometry experiments to operate at $B_z > 100$ G, and it also explains our observation in Fig. 5.3: relaxation slows down as $\omega_{\pm 1}$ increases, and dephasing takes over as the dominant decoherence channel. $\Gamma_d^{(-10)}$ cannot be eliminated completely because experimental limitations to π pulse duration and spacing restrict the maximum CPMG filter frequency $f_{\max}$ to a few MHz. The noise spectrum that causes dephasing, although decaying in frequency, has a finite value at $f_{\max}$, which explains why we do not reach $T_2 = 2T_1$ even for large γ (short T_1). The T_2/T_1 ratio is reduced at small γ because higher N is required to make $\Gamma_d^{(-10)} \ll 1/T_1$.

5.4 Relaxation and dephasing spectroscopy of surface noise

5.4.1 Overview of method and results

Finally, we identify the spectra of surface electric and magnetic field noise over a broad frequency range by employing a combination of SQ dephasing spectroscopy [98, 99, 101, 13, 89, 90] and DQ relaxometry. These complementary techniques are summarized in Table 5.1. SQ dephasing spectra $S_{\mathrm{cpmg}}(f)$ and DQ relaxation spectra $S_{\gamma}(f)$, in units of coupling power $\mathrm{Hz}^2/\mathrm{Hz}$, were generated from measurements like those presented in Figs. 5.3 and 5.4, respectively. The two spectral densities each have distinct noise origins (Table 5.1), and hence "coupling power" has different meanings for dephasing and relaxation. Therefore, to directly compare $S_{\mathrm{cpmg}}(f)$ and $S_{\gamma}(f)$ we scale each from a coupling rate to a shared effective transverse electric field noise power spectrum:

$$S_{E_{\perp}}^{\mathrm{cpmg}}(f) = 2\frac{S_{\mathrm{cpmg}}(f)}{d_{\parallel}^2/h^2}; S_{E_{\perp}}^{\gamma}(f) = \frac{S_{\gamma}(f)}{d_{\perp}^2/h^2}. \tag{5.7}$$

Equation 5.7 enables us to jointly model the dephasing and relaxation spectra (see 5.4.2 – 5.4.4 for analysis details), and the results are shown in Fig. 5.5, where the left axis of each plot is coupling power and the right axis is transverse electric noise power. To fit the $S_{E_{\perp}}^{\mathrm{cpmg}}(f)$ and $S_{E_{\perp}}^{\gamma}(f)$ data we assume a stationary Gauss-Markov process for electric and magnetic field sources [99]. A double Lorentzian is the sum of two such processes with different total noise power and frequency cutoffs. The fit results show that the electric Lorentzian (blue dash-dot line) has a lower-frequency cutoff than the magnetic noise (red dashed line): for NVA1 $\tau_e \approx 1$ μs and $\tau_m \approx 100$ ns. For NVA8, $\tau_m \approx 400$ ns and its electric noise curve actually fits best as $1/f^{\alpha}$ with $\alpha = 1.5$. This $\alpha < 2$ frequency

	DQ relaxation spectroscopy	**SQ dephasing spectroscopy**
Measurement	Relaxation between $m_s = \pm 1$ populations	CPMG multipulse on NV superposition
Filter frequency tuning	Applied B_z: $\omega_{\pm 1}/2\pi \approx 2g\mu_B B_z/h$	Number N and spacing T/N of π pulses
Primary noise probed	$\Pi_\perp$ (electric/strain) at f = [10 MHz - few GHz]	B_z and $\Pi_\parallel$ (magnetic/electric/strain) at f = [10 kHz - few MHz]
Coupling power [Hz^2/Hz]	$S(\omega_{\pm 1}) = \gamma$	$S(\omega = \pi N/T) \approx -\pi \ln C(T)/T$
Assumption for validity	$g\mu_B B_z/h \gg \Pi_\perp d_\perp/h$ $\implies$ eigenstates $\lvert m_s \rangle$	$B_z \gtrsim 100$ G $\implies$ small γ: $T_2(N) \ll T_1$

Table 5.1: Comparison and complementarity of double-quantum relaxation and single-quantum-qubit dephasing for classical-noise spectroscopy with NV centers.

dependence can be constructed from a sum of many discrete Lorentzians with a range of correlation times, as postulated for noise from charge traps [221] or fluctuating electric dipoles [93].

Our spectroscopy results help tie together prior work [86, 87, 89, 90] on decoherence of near-surface NVs, which primarily focused on magnetic noise. Kim *et. al.* [90] gave evidence for shallow-NV dephasing via $1/f$-like $E_\parallel$ electric field noise by showing that 1) dephasing noise is reduced when a high-dielectric-constant liquid is placed on the diamond surface, and 2) coherences of SQ and DQ qubits exhibit a ratio that cannot be explained by purely magnetic noise. Our addition of DQ relaxometry to the surface-noise-spectroscopy toolbox enables us to differentiate magnetic and electric noise sources, and importantly, our two-bath model identifies the lower-frequency noise component to be electric, in contrast to previous experiments [87, 89]. Together with previous depth-resolved work that identified a $1/d^{3.6(4)}$ dependence of $S_{\text{cpmg}}(f)$ [87, 89], we suggest that electric field noise from fluctuating electric dipole moments, such as modeled on metal electrodes in ion traps [93, 94], could explain the observed results. Furthermore, we note that the magnitudes of our observed $S_{E_\perp}(f)$ are quantitatively consistent with

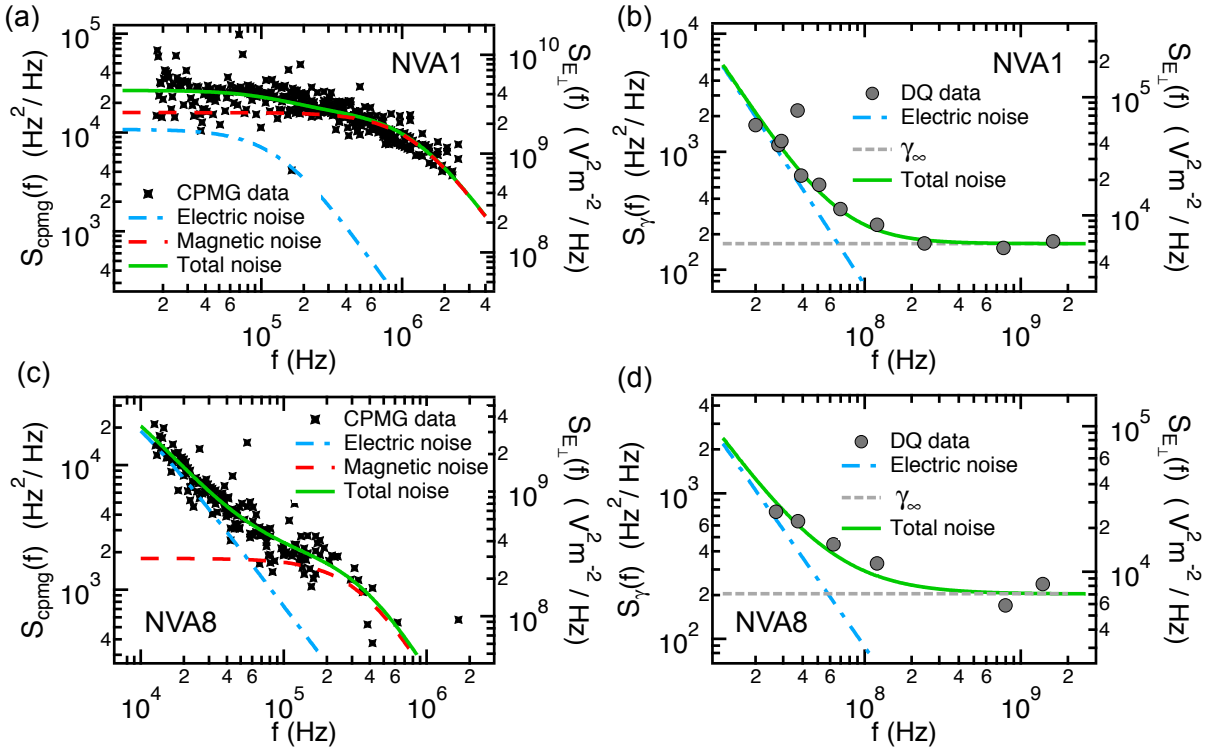

Figure 5.5: Measured noise spectra in terms of coupling power ($\mathrm{Hz}^2/\mathrm{Hz}$) and transverse electric field power ($\mathrm{V}^2\mathrm{m}^{-2}/\mathrm{Hz}$) for shallow NVs A1 (a,b) and A8 (c,d) using dephasing spectroscopy (left plots) and DQ relaxation spectroscopy (right plots). Each NV data set is jointly fit to a noise model (green solid line) of three parts: $1/f^{\alpha}$-like electric fields (blue dash-dot line), magnetic fields (red dashed line), and a minimum relaxation rate γ_{∞} due to bulk effects (horizontal dashed line).

those reported in experiments on ion-trap heating rates [222] (see 5.5.1 for calculation). Looking forward, the DQ relaxation technique can be readily combined with single-NV scanning probe microscopy [104, 71, 223] to investigate the microscopic origins of noise from various surfaces.

5.4.2 Dephasing spectroscopy with dynamical decoupling

We outline here a numerical method for deconvolution of the multipulse coherence data from the CPMG-N filter functions. A single stretched exponential with coherence time $T_2(N)$ to fit decoherence data is only an approximation in the presence of finite-frequency electromagnetic fluctuations along the z axis; that is the pure-dephasing contribution to coherence $C_{\mathrm{SQ}}(t)$ is generally non-exponential and depends on the frequency spectrum of these fluctuations [99, 13, 89]. The coherence defined on the interval $[0, 1]$ for total free precession time T is given by [98, 99]

$$C(T) = \exp\left[-\chi(T)\right]. \tag{5.8}$$

where the functional depends on the noise spectrum $\tilde{S}(\omega)$

$$\chi(T) = \frac{1}{\pi}\int_0^\infty d\omega \tilde{S}(\omega)\frac{F_N(\omega T)}{\omega^2}. \tag{5.9}$$

The total time T that we plot on the x axis for all coherence data is $T = 2\tau_{\max}N + N\tau_\pi$ because 2τ is the delay between π-pulses of duration τ_π. The N-pulse filter function is

$$F_N(\omega T) = 8\sin^4\left(\frac{\omega T}{4N}\right)\frac{\sin^2\left(\frac{\omega T}{2}\right)}{\cos^2\left(\frac{\omega T}{2N}\right)}, \tag{5.10}$$

which has a peak maximum at $\omega = \pi N/T$.

The problem is to extract $\tilde{S}(\omega)$ given the known filter function and coherence data.

This is a challenging task in general because there are a finite number of $C(T)$ points. Moreover the contributions to this noise spectrum at a given ω_i depend on unknown values of $\tilde{S}(\omega)$ at other frequencies due to convolution with F_N, which has a finite peak linewidth and harmonics.

An approximate method is to begin at the high frequency values of $\tilde{S}(\omega)$ by looking at $C(T_i)$ for the shortest T_i points. Particularly for large N the filter function is sharply peaked and can be approximated as a delta function in the form $F_N(\omega T)/\omega^2 = T_i\delta(\omega-\omega_i)$. Therefore, $\chi(T) \approx T_i\tilde{S}(\omega_i)/\pi$ at this point $\omega_i = \pi N/T_i$ and the noise spectral density by this method is

$$\tilde{S}_\delta(\omega_i) = \pi\frac{\chi(T_i)}{T_i} \tag{5.11}$$

This approximation $\tilde{S}_\delta(\omega_i)$ can first be computed for all T_i points in the data set as a first pass.

Assuming that the noise spectrum falls off as some power law of frequency, then the higher frequency ($\omega > \omega_i$) unknown parts of the spectrum won't contribute as largely to the full $\tilde{S}(\omega_i)$ as the $\tilde{S}_\delta(\omega_i)$ term will. We also assume that all harmonics in $F_N(\omega T)$ are at higher frequencies than the peak frequency ω_i. More completely, the coherence signal could be described as

$$\chi(T_i) \approx \frac{1}{\pi}\left[\int_0^{\omega_i-\epsilon} + \int_{\omega_i-\epsilon}^{\omega_i+\epsilon} + \int_{\omega_i+\epsilon}^{\infty}\right] d\omega\tilde{S}(\omega)\frac{F_N(\omega T_i)}{\omega^2}, \tag{5.12}$$

for $\epsilon \to 0$. The first term we take as negligible since, especially for larger N, $F_N(\omega T_i)$ has a small value and no harmonics for $\omega < \omega_i$. The second term can be approximated as the delta function result in Eq. 5.11. The final term is treated more carefully to subtract

out the effect of higher frequency contributions to each $\tilde{S}(\omega_i)$, giving

$$\chi(T_i) \approx \frac{1}{\pi}\tilde{S}(\omega_i)\, T_i + \frac{1}{\pi}\int_{\omega_i}^{\infty} \tilde{S}(\omega)\, \frac{F_N(\omega T_i)}{\omega^2}. \tag{5.13}$$

This can be solved to find $\tilde{S}(\omega_i)$ as

$$\tilde{S}(\omega_i) \approx \frac{\pi}{T_i}\chi(T_i) - \frac{1}{T_i}\int_{\omega_i}^{\infty} \tilde{S}(\omega)\, \frac{F_N(\omega T_i)}{\omega^2} \tag{5.14}$$

where again $\omega_i = \pi N/T_i$. The calculation of the noise spectrum assumes that $\tilde{S}(\omega)$ falls off as an arbitrary power law in ω and the steps are

1) Scale data to coherence $\in [0,1]$ using PL references of $|0\rangle$ and $|-1\rangle$ from a differential measurement. Exclude any data points $C(T)$ that are saturated near either 1 or 0 coherence as these do not contain useful spectral information.

2) For all $i = 1...n$ compute $\chi(T_i) = -\ln[\mathrm{C(T_i)}]$.

3) For all $i = 1...n$ compute the frequencies ω_i and the first term of Eq. 5.14.

4) Starting from $\omega_{i=1}$ as the highest frequency data point recursively compute the second term in Eq. 5.14 by a numerical integration. This was done by first interpolating the $\tilde{S}(\omega)$ result of previous steps over an upsampling rate of $R \propto N$ to accommodate for the narrowing of the harmonics with larger N. The reason for this interpolation is that if a higher harmonic of $F_N(\omega T_i)$ coincides with an ω_j (where all $\omega_j > \omega_i$) then its width will be much smaller than the value of $\Delta\omega = \omega_j - \omega_{j+1}$ and result in a greatly overestimated value of the subtraction term. In other words, the interpolation point spacing should be fine enough to "resolve" the sharp features of the filter function. For each ω_i of the $i = 1....Rn$ this subtraction term uses the full analytical form of F_N in Eq. 5.10 in the numerical integration. The

routine was performed on each CPMG-N data set in isolation, so there are several data points at particular frequencies. The highest-frequency points of each set were discarded in the final plot as they were only used for interpolation and subsequent subtraction since the spectrum to the right of them was fully unknown.

We also emphasize that the method of spectroscopic deconvolution of the coherence signal using a multipulse filter function [13, 89, 90] becomes incorrect when $T_2 \sim T_1$ because no longer is the assumption valid that low-frequency pure-dephasing noise determines the shape of the CPMG data curve $C(T)$. The valid use of this dynamical decoupling deconvolution requires that the decay in $C(T)$ data is due solely to dephasing effects because the derivation of Eq. 5.9 relies upon the assumption that the transverse noise terms, those that cause relaxation, can be set to zero [99]. It is possible that neglecting to consider the full T_1, which is always shorter than $T_1^{(0)}$, could lead one to assume dephasing deconvolution is valid when it would not be. Therefore, to judge this method's range of applicability it is important to measure the full T_1 from both γ and Ω. This is the reason we employ the technique only at high magnetic fields ($B_z \gtrsim 100$ G) where $T_1^{(-1,+1)}$ is sufficiently long compared to T_2 for at least some useful range of N. For example, at large N the τ-points used for low-frequency $S(f)$ points are particularly susceptible to influence from relaxation, and the data's high-frequency components will look like a "wall" of white noise that is not an accurate reflection of dephasing effects. For this reason, in our deconvolution results we place more confidence in the low- to mid-frequency parts of the CPMG spectrum where we found electric fields to contribute most significantly, as the higher-frequency Lorentzian may tend to be overestimated due to the onset of relaxation effects. A more-complete non-analytical model of surface-induced decoherence that incorporates relaxation should be developed to provide further insight.

The corollary to this relaxation effect, however, is that if one is studying how T_2

increases with N beginning with small N and the $T_2(N)$ appears to saturate this does not necessarily mean that relaxation timescales are yet significant. Rather this apparent saturation could be a frequency window of actual white-like dephasing noise that is followed by a decay in the noise spectrum where $T_2(N)$ rises once more pulses are used. The simplest example is the flat low-frequency part of a Lorentzian spectrum that would be accessed by small N. This slow start in the "decoupling efficiency" at small N can for example be seen in the experiment and modeling of the $\lambda = \log_N [T_2(N)/T_2(N=1)]$ parameter plotted in Fig. 4.21 of our prior study on dynamical decoupling of shallow NVs (also Fig. 4 of [87]).

A possible future experiment may be to employ "DQ swap" multipulse techniques discussed in [224] at large magnetic fields (100s of Gauss) to demonstrate a dephasing spectroscopy using the DQ qubit coherence. DQ swap sequences are more challenging to execute without accumulation of pulse errors than SQ dephasing CPMG sequences because two calibrated microwave tones are required. However, such DQ coherence data is insensitive to $E_\parallel$, so a deconvolution should yield a magnetic noise spectrum.

5.4.3 Spectroscopy with double-quantum relaxometry

We derive the relationship between the DQ relaxation rate γ and the electric field noise spectrum transverse to the NV axis. The result is analogous to the case of a S_x spin-1/2 operator for a qubit [219], however the noise operator connecting the $|1\rangle$ and $|-1\rangle$ is the $S_\pm^2$ spin-1 operator, so we overview the calculation to find the correct multiplicative factors relating γ to the power spectral density of electric field noise.

The relevant Hamiltonian for the $|1\rangle$ and $|-1\rangle$ sub-basis in energy units is only the Zeeman term since DS_z^2 gives equal energy for the $|\pm 1\rangle$ states:

$$H_0 = g\mu_B B_z S_z \tag{5.15}$$

where S_z is still the standard $S = 1$ spin operator, and this Hamiltonian yields the expected energy difference $\hbar\omega_{\pm1} = 2g\mu_B B_z$. From the full ground state spin Hamiltonian stated earlier, the time-dependent perturbation for the transverse electric field noise is

$$V(t) = \frac{-d_\perp E_\perp(t)}{2}\left[e^{-i\phi(t)}S_+^2 + e^{i\phi(t)}S_-^2\right] \tag{5.16}$$

where $\phi(t) = \tan^{-1} E_y(t)/E_x(t)$, $S_\pm = S_x \pm iS_y$ are the $S = 1$ raising and lowering operators, and $d_\perp$ is the transverse electric dipole coupling of the NV. The time-dependent parts will be specified later and here are general.

As in a DQ relaxation measurement we assume the initial state is $|\psi(0)\rangle = |-1\rangle$ after a green-laser pulse and π_{-1} pulse. We can assume that $\gamma \gg \Omega$ such that all the population in $|0\rangle$ remains zero, though this is only valid at small $\omega_{\pm1}$. Even so, the S_+^2 term in the Hamiltonian is the only one that gives nonzero first-order coupling of the $|1\rangle$ and $|-1\rangle$ states, and second-order magnetic terms are suppressed in their contribution to γ (see later supplement section on DQ magnetic driving). If $\Omega \sim \gamma$ then first-order magnetic terms (S_x, S_y) do contribute to the $|1\rangle$ state amplitude, but only directly through the Ω rate. Therefore, since our goal is to compute γ and we focus on the S_+^2 term only, then the final derivative in the following steps (on Eq. 5.21) can be identified directly with γ, even at large $\omega_{\pm1}$. Then first-order time-dependent perturbation theory in the interaction picture yields an amplitude for the $|1\rangle$ state

$$\alpha_1 = 0 - \frac{i}{\hbar}\int_0^t d\tau \langle 1|\left(\frac{-d_\perp}{2}E_\perp(\tau)\, e^{-i\phi(\tau)}S_+^2(\tau)\right)|-1\rangle \tag{5.17}$$

where the $\langle 1|\, S_-^2(\tau)\,|-1\rangle$ term has vanished, as justified below. The time-dependent quadratic raising operator in the interaction picture is given by

$$S_+^2(\tau) = e^{ig\mu_B B_z S_z \tau/\hbar}\left(S_+^2\right)e^{-ig\mu_B B_z S_z \tau/\hbar} = S_+^2 e^{i\omega_{\pm1}\tau} \tag{5.18}$$

which simplifies in the same way as in a σ_x perturbation operator in a two-level system case. With $\langle 1| S_+^2 |-1\rangle = 2$ the we find the amplitude is

$$\alpha_1 = \frac{id_\perp}{\hbar} \int_0^t d\tau E_\perp(\tau) e^{-i\phi(\tau)} e^{i\omega_{\pm 1}\tau} \tag{5.19}$$

The population of the $|1\rangle$ state in time is

$$\rho_1(t) = |\alpha_1|^2 = \left(\frac{d_\perp}{\hbar}\right)^2 \int_0^t \int_0^t d\tau_1 d\tau_2 E_\perp(\tau_1) E_\perp(\tau_2) e^{-i(\phi(\tau_2)-\phi(\tau_1))} e^{-i\omega_{\pm 1}(\tau_1-\tau_2)} \tag{5.20}$$

As in the case for a spin-1/2 coupling operator [219] a change of variables can be done with $\tau = \tau_1 - \tau_2$ and $T = (\tau_1 + \tau_2)/2$. The integration limits on the new $\int d\tau$ integral can be taken to $\pm\infty$ in the case that we only look at timescales such that $t \gg \tau_c$ [219], where τ_c is the correlation time of the noise. This is a valid assumption because the noise sources we find from analyzing CPMG and DQ relaxation data have correlation times of 100 ns to a few microseconds. To measure γ we use dark times (after initialization into $|-1\rangle$) of several to tens of microseconds to milliseconds, so $t \gg \tau_c$. We suppose a stationary noise process that gives translation invariance in time, and we are interested in the average population for many iterations of the $E_\perp(t) e^{i\phi(t)}$ noise trajectory since we execute 10s of thousands of pulse sequence shots to measure the populations. Under these assumptions the average population of the $|1\rangle$ state becomes

$$\bar{\rho}_1(t) = t \left(\frac{d_\perp}{h}\right)^2 S_{E_\perp}(-\omega_{\pm 1}) \tag{5.21}$$

where the noise spectral density for the perpendicular electric field has been identified as

$$S_{E_\perp}(\omega) = \int_{-\infty}^{\infty} d\tau e^{i\omega\tau} \left\langle E_\perp(\tau) e^{i\phi(\tau)} E_\perp(0) e^{-i\phi(0)} \right\rangle \tag{5.22}$$

The noise-induced transition rate from the initial $|-1\rangle$ to final $|1\rangle$ is the time derivative of Eq. 5.21 which gives the final result in units of Hz

$$\gamma = \left(\frac{d_\perp}{h}\right)^2 S_{E_\perp}\left(-\omega_{\pm 1}\right) \equiv S_\gamma\left(-\omega_{\pm 1}\right) \tag{5.23}$$

where the latter definition shows equivalence between the γ data and a coupling noise power spectral density $S_\gamma(\omega)$ of units $\mathrm{Hz}^2/\mathrm{Hz}$ or simply Hz. Therefore the DQ relaxation rate depends only on the transverse coupling and the noise power spectral density at the frequency splitting of the $|\pm 1\rangle$ levels. Because we consider the electric field trajectory as a classical random variable, the spectrum is the same on the positive and negative frequency side $S_{E_\perp}\left(-\omega_{\pm 1}\right) = S_{E_\perp}\left(\omega_{\pm 1}\right)$ [219].

The more-complete consideration of three different $\omega_{\pm 1}$ resonances due to the NV-^{14}N hyperfine interaction can be treated in the same way, except the initial population is 1/3 in each of the three $m_I = 0, \pm 1$ nuclear spin states (assuming zero polarization of the nuclear spin at low magnetic field). The NV electronic transitions between $m_s = \pm 1$ are spread out over three lines due to the hyperfine interaction with the host ^{14}N nuclear spin. For relaxation spectroscopy using these DQ transitions then the filter function is effectively $\approx 2A_{\|\|} \approx 4.4$ MHz wide [18]. Because the smallest frequency we probe is noise at $\omega_{\pm 1}/2\pi \sim 20$ MHz, the convolution effect becomes more important at these low frequencies, particularly as γ changes fastest in that region. However, the filter function is still 1-4 orders of magnitude narrower than the frequencies 20-1612 MHz probed. With the starting factor of 1/3 assuming no nuclear polarization, three delta-function-like resonances would give a relaxation rate

$$\gamma\left(^{14}\mathrm{N}\right) = \frac{1}{3}\left(\frac{d_\perp}{2}\right)^2 \left[S_{E_\perp}\left(-\omega_{\pm 1}\right) + S_{E_\perp}\left(-\omega_{\pm 1} + A_\|\right) + S_{E_\perp}\left(-\omega_{\pm 1} - A_\|\right)\right] \tag{5.24}$$

In principle such a deconvolution could be more effective if one probes $\gamma(\omega)$ at steps of $\Delta\omega = A_{\parallel}$ so that the contributions of neighboring points can be measured and known for subtraction (without interpolation) to find the spectrum S at a single frequency point. We do not attempt this deconvolution because the main conclusions of our paper do not rely upon this detail: 1) that $S_{\gamma}(\omega)$ increases at low frequencies and 2) that S_{γ} can be combined with dephasing data to learn about the spectral contributions of electric field noise. If the deconvolution were done we would expect that the lower-ω contribution of the three terms in Eq. 5.24 would contribute slightly more than the others since the noise is of $1/f^{\alpha}$ type, so this would have a net effect of reducing the actual $S_{\gamma}(\omega)$ at low ω. If anything this makes the noise decay appear more gradual, further supporting the identification of the electric noise as the lower-frequency-cutoff noise affecting dephasing.

The quantity $c(\tau) \equiv \left\langle E_{\perp}(\tau)\, e^{i\phi(\tau)} E_{\perp}(0)\, e^{-i\phi(0)} \right\rangle$ in Eq. 5.22 is the classical correlation function of the transverse electric field fluctuations. The phase gives the radial direction of the transverse field on the plane normal to the NV z axis, $\tan\phi = E_y/E_x$. Therefore, the function can also be written

$$S(\tau) = \langle [E_x(\tau) + iE_y(\tau)]\,[E_x(0) - iE_y(0)] \rangle \tag{5.25}$$

which has two autocorrelation terms and two x, y cross-correlation terms. There are certainly non-zero correlations between E_x and E_y from, for example, a surface distribution of electric dipoles fluctuating simply because the two transverse components E_x and E_y are ultimately generated from the same set of dipoles that have a specific configuration of orientations at time τ. However, because we have assumed time-translation invariance the terms are equivalent, that is $\langle E_x(\tau)\, E_y(0) \rangle = \langle E_x(0)\, E_y(\tau) \rangle$. Therefore the cross-terms cancel out because they have opposite signs in the full correlation function Eq. 5.25.

The result is that the x and y transverse components of the field relative to the NV axis are treated as if they are uncorrelated from one another. For a simple stationary Gauss-Markov process, where the mean and variance do not depend on past history, the correlation function looks like

$$S(\tau) = \langle E_\perp^2 \rangle e^{-|\tau|/\tau_c} \tag{5.26}$$

where $\langle E_\perp^2 \rangle = \langle E_x^2 \rangle + \langle E_y^2 \rangle$, again with x and y here defined perpendicular to the NV axis as throughout this section. The inverse Fourier transform of this function gives a Lorentzian power spectral density [99]

$$S_{E_\perp}(\omega) = \int_{-\infty}^{\infty} \langle E_\perp^2 \rangle e^{-|\tau|/\tau_c} e^{i\omega t} dt = \frac{\langle E_\perp^2 \rangle \tau_e}{\pi (1 + \omega^2 \tau_e^2)} \tag{5.27}$$

which appears like white noise for $\omega\tau_e \ll 1$, that is, for frequencies far below the cut-off. This function returns the total electric field noise power when integrated over all frequencies

$$\int_{-\infty}^{\infty} \frac{\langle E_\perp^2 \rangle \tau_e d\omega}{\pi (1 + \omega^2 \tau_e^2)} = \int_{-\infty}^{\infty} \frac{\langle E_\perp^2 \rangle \tau_e 2\pi df}{\pi (1 + (2\pi f)^2 \tau_e^2)} = \langle E_\perp^2 \rangle \tag{5.28}$$

5.4.4 Modeling the combined γ and CPMG data

The relaxation and dephasing noise spectra obtained from the above data analysis methods are each due to distinct noise sources and either transverse (relaxation) or parallel (dephasing) fields, relative to the NV axis. Therefore, the y axes of the extracted noise spectra are not equivalent in the two cases, even though the units of $\mathrm{Hz}^2/\mathrm{Hz}$ are the same. To compare them directly, we scale each to find an effective $E_\perp$ electric field noise spectrum; in other words we multiply the dephasing data by a geometric factor and NV-field coupling to reflect the $E_\perp$ fields that would be associated with $E_\parallel$ fields that

actually cause first-order dephasing. Part of this scaled spectrum is not due to electric fields, rather there is a magnetic component, which is the reason for the term "effective". With this electric field noise spectrum for relaxation and dephasing we can then plot the two on the same y axis and fit to a joint model of electric and magnetic field noise, as we next explain in detail. At the end, we scale the model parameters back to coupling units to present the data in main text Fig. 5.5.

We extracted an effective $E_\perp$ noise spectrum (units $\mathrm{V^2{\cdot}m^{-2}/Hz}$) from each dephasing spectroscopy and DQ relaxometry data set in the following scaling

$$S_{E_\perp}^{\mathrm{cpmg}}(f) = 2\frac{S_{\mathrm{cpmg}}(f)}{d_\parallel^2/h^2}, S_{E_\perp}^{\gamma}(f) = \frac{S_\gamma(f)}{d_\perp^2/h^2} \tag{5.29}$$

where the factor of 2 in the CPMG expression comes from considering the NV orientation in a surface electric field model of $\langle E_\parallel^2\rangle$ and $\langle E_\perp^2\rangle$. The geometry is described in the sections below about electric field noise sources.

We describe the details of the fitting procedure shown in Fig. 5.5 of the main text. The fit function for the combined data set has three terms written as

$$S(f) = \frac{\tau_e\langle E_{\perp,e}^2\rangle}{\pi\left[1+(2\pi f\tau_e)^\alpha\right]} + \frac{\gamma_\infty}{(d_\perp/h)^2} + \frac{\tau_m\langle E_{\perp,m}^2\rangle}{\pi\left[1+(2\pi f\tau_m)^2\right]}\frac{1}{1+\exp\left[q\left(f-10^7\mathrm{Hz}\right)\right]} \tag{5.30}$$

where the five fit parameters are γ_∞, $\langle E_{\perp,e}^2\rangle$, τ_e, $\langle E_{\perp,m}^2\rangle$, and τ_m. Table 5.2 summarizes the fit parameter results converted into NV-noise coupling units for comparison to previous work on CPMG-based spectroscopy [87, 89].

A sixth parameter exponent α in the first term would typically be equal to 2 for a Lorentzian, however, we let it vary and resulting fits gave $1 < \alpha < 2$. At high frequencies where $2\pi f\tau_e \gg 1$ this quantity in the denominator dominates and looks like the canonical A/f^α noise. We kept the 1 from the pure-Lorentzian form in the denominator to allow

NV	$\omega_{\pm1}/2\pi$	$\sqrt{\langle E^2_{\perp,e}\rangle}$ (b_e)	τ_e	$\gamma_\infty/\left(d_\perp/h\right)^2(\gamma_\infty)$	$\sqrt{\langle E^2_{\perp,m}\rangle}$ (b_m)	τ_m	E-noise exp. α
NVA1	784 MHz	6.9×10^7 V/m (170 kHz)	1.2 μs	5800 $\mathrm{V^2m^{-2}/Hz}$ (0.17 kHz)	25×10^7 V/m (620 kHz)	130 ns	2
NVA1	1612 MHz	6.9×10^7 V/m (170 kHz)	1.0 μs	5800 $\mathrm{V^2m^{-2}/Hz}$ (0.17 kHz)	25×10^7 V/m (620 kHz)	140 ns	2.1
NVA8	1431 MHz	3.4×10^7 V/m (85 kHz)	32 μs	7000 $\mathrm{V^2m^{-2}/Hz}$ (0.20 kHz)	4.6×10^7 V/m (110 kHz)	440 ns	1.5
NVA7	797 MHz	2.6×10^7 V/m (65 kHz)	8.1 μs	8600 $\mathrm{V^2m^{-2}/Hz}$ (0.25 kHz)	6.5×10^7 V/m (160 kHz)	360 ns	1.6

Table 5.2: Summary of fit results to combined dephasing and DQ relaxation noise spectra using the simple double-Lorentzian model where the $b_e = \sqrt{\langle E^2_{\perp,e}\rangle}\sqrt{1/2}\left(d_\parallel/h\right)$ is the total NV coupling rate, for dephasing, to the "electric" Lorentzian noise. τ_e is the correlation time of this noise source. $b_m = \sqrt{\langle E^2_{\perp,m}\rangle}\sqrt{1/2}\left(d_\parallel/h\right)$ and τ_m are the corresponding parameters for the "magnetic" noise source that is relevant only to dephasing. γ_∞ is the saturation level of the DQ relaxation rate at high frequency. The $\omega_{\pm1}/2\pi$ stated in this table refers to the value at which the CPMG spectroscopy measurements were done, which was always in the limit that $\gamma \to \gamma_\infty$. The electric field noise exponent α in the last column refers to the $1/f^\alpha$ component of the blue dashed curves in the fitted spectra. We find α is between 1 and 2 as would be expected for a sum of many Lorentzians, for example in the case of electric dipoles with various correlation times even for a single type of adatom on the diamond surface. The NVA1 measurements repeated at two large $\omega_{\pm1}$ shown yielded a spectrum fit to the same parameter values within the significant figures.

for the concept of a total sum of many constituent Lorentzians in the total electric noise spectrum, which has frequency regimes of effective $\alpha \sim 0$, $1 < \alpha < 2$, and $\alpha = 2$. This is the exponent shown in the end column of Table 5.2.

The sigmoid function in Eq. 5.30 (q arbitrarily large for step function) that multiplies the second Lorentzian is simply to give a cutoff frequency (here 10 MHz) above which the Lorentzian has zero effect; that is magnetic noise affects the CPMG dephasing data but not the γ relaxation data. This is similar to calculating a joint fit with two separate functions that have shared parameters, where the CPMG data is fit to the full form of Eq. 5.30 and the relaxation data is fit only to the two terms.

In Fig. 5.6 we plot spectrum data and fits for the two NVs that show higher electric field noise at low frequencies, NVA7 (a) and NVA8 (b), the latter shown in Fig. 5.5(b).

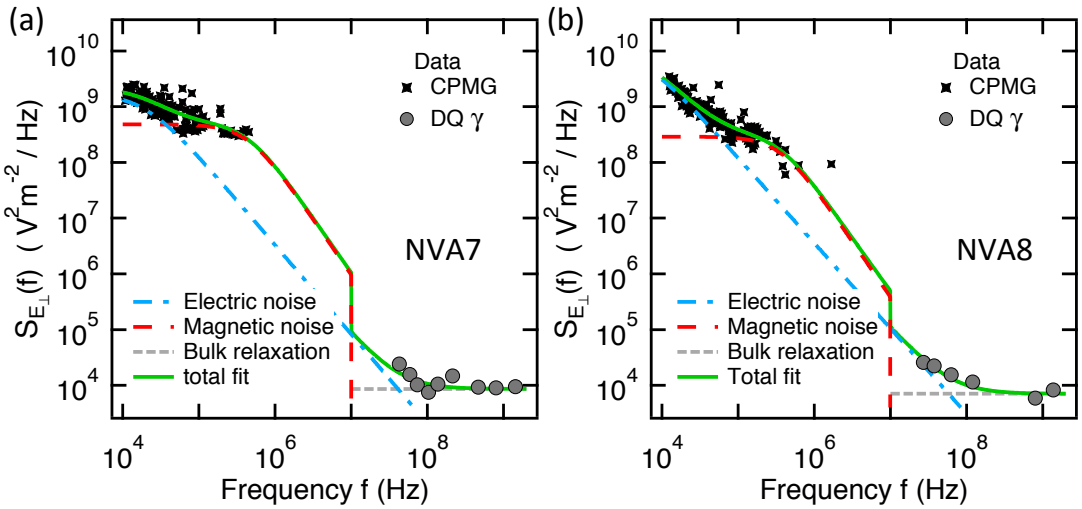

Figure 5.6: Transverse electric field noise spectra fits for NVA7 (a) and NVA8 (b), showing the deduced contributions from electric, magnetic, and bulk noise sources for dephasing and DQ relaxation. For both NVs the electric field component fit well to a $1/f^\alpha$ function with $\alpha \approx 1.5{-}1.6$. Such an exponent $1 < \alpha < 2$ can can arise from a sum of many Lorentzian power spectra with a distribution of different correlation times, for example from charge traps or electric dipoles. The power spectrum parameters are listed in Table 5.2 for both electric field and coupling units.

The parameters of the fits are included in Table 5.2, and the final scaling to dephasing and relaxation coupling is plotted in Fig. 5.7 using the inverse procedure of Eq. 5.29. One could alternatively write two separate fit functions for the dephasing and DQ relaxation data and fit their parameters jointly, however, the method of the effective transverse field is helpful to display the data as one complete noise spectrum.

In Fig. 5.8 we plot effective transverse electric field noise spectra data and fits for the NVA1 at two different applied magnetic fields. Figure 5.9 shows the same data sets for final scaling back to dephasing and relaxation coupling units. This comparison shows that there is negligible dependence on the magnetic field between 140 G and 290 G because the model fit parameters are nearly identical in the two $\omega_{\pm1}$ cases. We avoided performing dephasing spectroscopy at low magnetic fields since γ becomes large at small $\omega_{\pm1}$.

Finally, we predict based on our model of dephasing and relaxation that there is quite

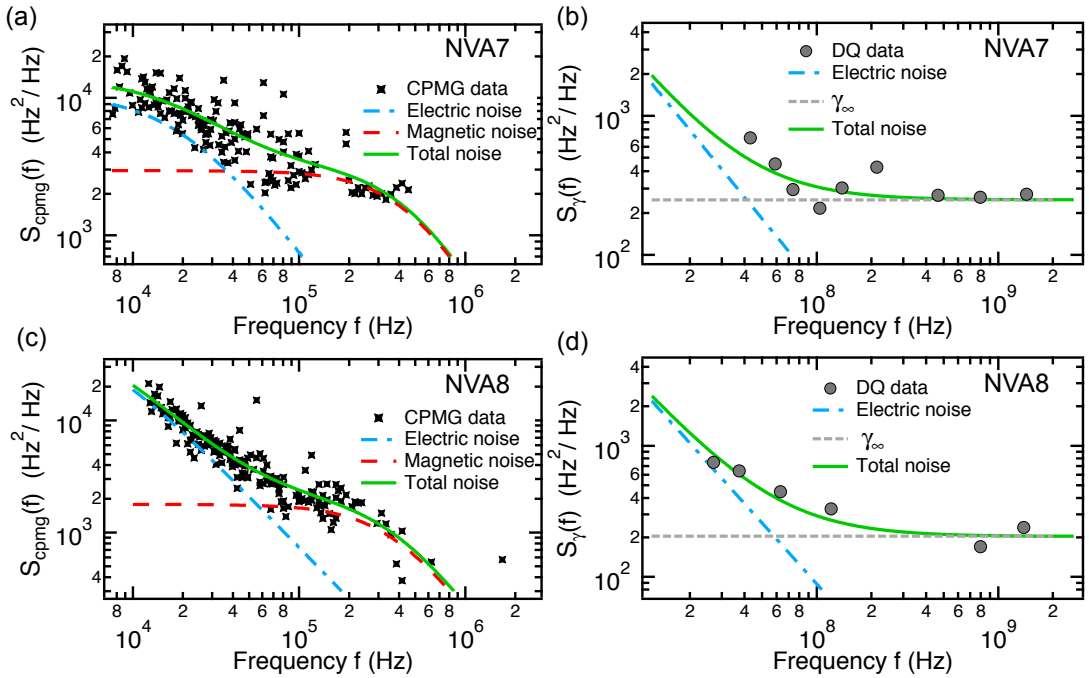

Figure 5.7: Coupling noise power spectra fits for NVA7 (a,b) and NVA8 (c,d), showing the deduced contributions from electric, magnetic, and bulk noise sources for dephasing and DQ relaxation. The power spectrum parameters are listed in Table 5.2 for both electric field and coupling units.

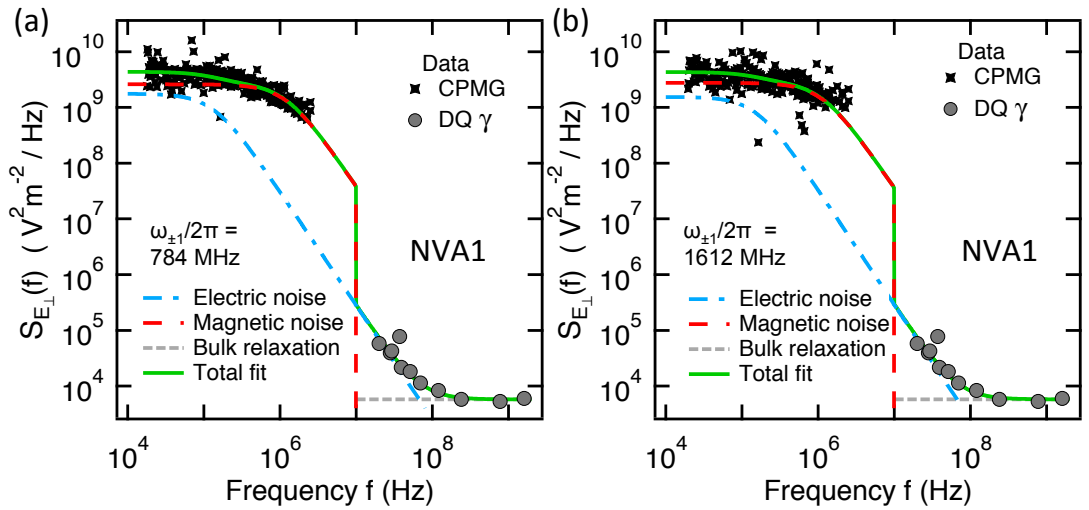

Figure 5.8: Transverse electric field noise spectra fits for NVA1 at $\omega_{\pm1}/2\pi = 784$ MHz (a) and $\omega_{\pm1}/2\pi = 1612$ MHz (b), showing that for sufficiently large applied magnetic fields the extracted dephasing spectra are described well by the same noise model parameters as shown in Table 5.2.

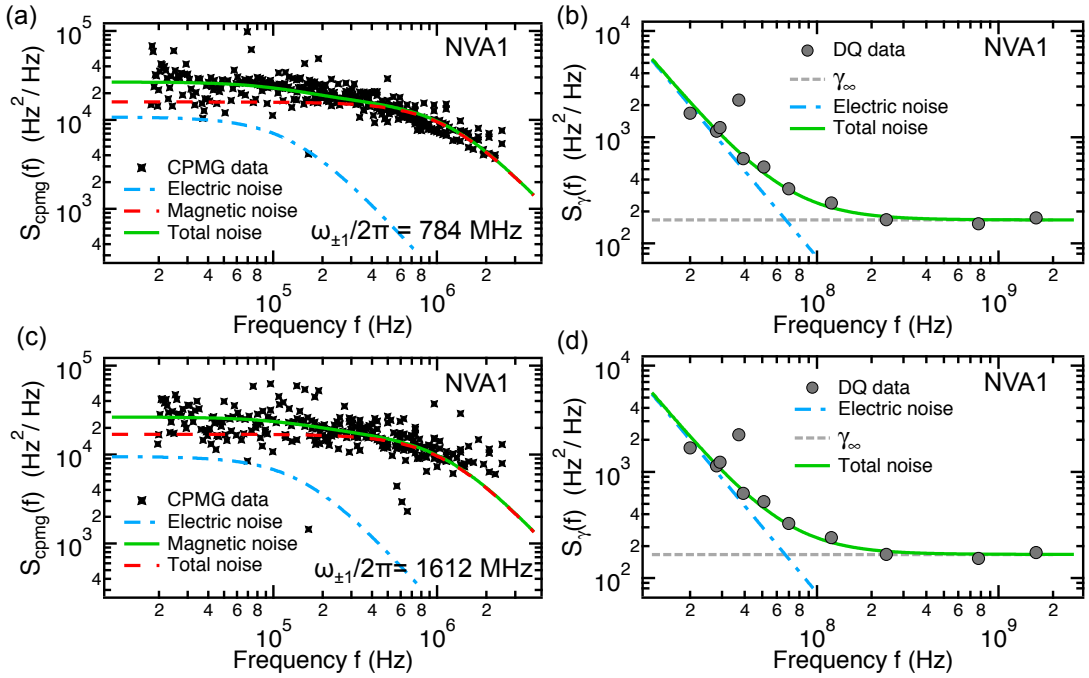

Figure 5.9: Coupling noise power data and fits for NVA1 at $\omega_{\pm1}/2\pi = 784$ MHz (a,b) and $\omega_{\pm1}/2\pi = 1612$ MHz (c,d), showing that for sufficiently large applied magnetic fields the extracted dephasing spectra are described well by the same noise model parameters (within fitting uncertainty) as shown in Table 5.2. The data in (b) and (d) are the same for this comparison, since DQ measurements are taken by tuning $\omega_{\pm1}$, but the fit results of electric noise (blue dash-dot line) and total noise (green solid line) are independently generated since the dephasing data are distinct in (a) and (c).

possibly no fundamental reason that the T_2 cannot be increased to beyond T_1, even at high fields where dephasing is dominant, because the noise spectrum continues to fall above the MHz regime. It is evident from the combined data that there is not significant white electric or phononic noise level due to the surface otherwise γ would be limited to a faster value than observed. Using present hardware, even increasing the number of pulses N past a certain point will help very little due to the limited pulse delay resolution, phase cycling rate, and finite pulse time. In other words, as N is increased in our example we probed a maximum CPMG frequency of $f_{\max} \gtrsim 2$ MHz on the noise spectrum. Once N is large enough to reach $f_{\max}$ then the portion of the accessible spectrum becomes shorter from the low-frequency side as N is increased, thus limiting the ability to even accurately measure the T_2 with CPMG.

5.5 Physical interpretations of surface noise results

We find that our spectroscopy results are most consistent with electric field noise, which is also bolstered by comparison to work on NV dephasing in [90] and our measurements of NVs near metal surfaces in Chapter 7. In this section, we outline simple models of depth dependence for fluctuating electric fields from electric dipoles and electric charges on the surface and comment on the notion of surface-strain noise.

5.5.1 Model of fluctuating surface electric dipoles

We derive a model of the power spectral density of fluctuating electric fields at the NV center based on the assumption of electric dipoles on the surface. First we derive the electric field at the NV of depth z for a single dipole at some distance d from the surface and then take the case $d \to 0$.

We suppose an interface with surface normal $\hat{z}$ between air and diamond with per-

mittivities ϵ_0 and $\epsilon_d\epsilon_0$, respectively. From the image-dipole method of calculating the potential of an electric dipole composted of charges q and $-q$ near a dielectric interface, we obtain a potential inside the ϵ_d region ($z < 0$) of

$$\Phi^{(z)}(\mathbf{r}) = \frac{p}{4\pi\epsilon_0}\left(\frac{2}{1+\epsilon_d}\right)\frac{z}{\left(x^2+y^2+z^z\right)^{3/2}} \tag{5.31}$$

for a dipole oriented parallel to the surface normal, $\mathbf{p} = p\hat{z}$. For the case of a dipole oriented perpendicular to the surface normal we obtain

$$\Phi^{(x)}(\mathbf{r}) = \frac{p}{4\pi\epsilon_0}\left(\frac{2}{1+\epsilon_d}\right)\frac{x}{\left(x^2+y^2+z^z\right)^{3/2}} \tag{5.32}$$

Let $E_0 \equiv \frac{p}{4\pi\epsilon_0}\left(\frac{2}{1+\epsilon_d}\right)$. We find the mean-square electric field from a fluctuating dipole sampling all directions by considering the x, y, z contributions to the electric field from each component p_x, p_y, p_z, a total of nine components:

$$\begin{aligned}
E_x^{(p_z)} &= \frac{\partial\Phi^{(z)}}{\partial x} = -E_0\frac{3xz}{(x^2+y^2+z^2)^{5/2}} \\
E_y^{(p_z)} &= \frac{\partial\Phi^{(z)}}{\partial y} = -E_0\frac{3yz}{(x^2+y^2+z^2)^{5/2}} \\
E_z^{(p_z)} &= \frac{\partial\Phi^{(z)}}{\partial z} = E_0\frac{x^2+y^2-2z^2}{(x^2+y^2+z^2)^{5/2}} \\
E_x^{(p_x)} &= \frac{\partial\Phi^{(x)}}{\partial x} = E_0\frac{-2x^2+y^2+z^2}{(x^2+y^2+z^2)^{5/2}} \\
E_y^{(p_x)} &= \frac{\partial\Phi^{(x)}}{\partial y} = -E_0\frac{3xy}{(x^2+y^2+z^2)^{5/2}} \\
E_z^{(p_x)} &= \frac{\partial\Phi^{(x)}}{\partial z} = -E_0\frac{3xz}{(x^2+y^2+z^2)^{5/2}}
\end{aligned} \tag{5.33}$$

where the components $E_i^{(p_y)}$ are identical to the $E_i^{(p_x)}$ with x replaced by y since the orientation of the dipole perpendicular to the surface normal is arbitrary.

The x, y, x coordinates are defined relative to the surface, and the NV is crystallographically aligned at an angle of $\theta_{\mathrm{NV}} \approx 54.74°$ to the surface normal. We take the NV to lie in the xz plane, and the goal is to compute the mean-square electric fields $\langle E_\perp^2 \rangle$

and $\left\langle E_{\parallel}^2 \right\rangle$ that appear in the NV Hamiltonian Eq. 1. These fields for the single electric dipole are given by

$$\left\langle E_{\perp}^2 \right\rangle_{\text{dipole}} = \left\langle E_x^2 \right\rangle \cos^2\theta_{\text{NV}} + \left\langle E_z^2 \right\rangle \sin^2\theta_{\text{NV}} + \left\langle E_y^2 \right\rangle \tag{5.34}$$

$$\left\langle E_{\parallel}^2 \right\rangle_{\text{dipole}} = \left\langle E_x^2 \right\rangle \sin^2\theta_{\text{NV}} + \left\langle E_z^2 \right\rangle \cos^2\theta_{\text{NV}} \tag{5.35}$$

Each $\langle E_i^2 \rangle$ with $i = x, y, z$ is computed from the mean-square sum of the three components in Eq. 5.33. This sum introduces a factor of $1/6$ from taking the rms per each fluctuating p_i component and the total mean, for example

$$\left\langle E_x^2 \right\rangle = \left[\left(E_x^{(p_x)}/\sqrt{2} \right)^2 + \left(E_x^{(p_y)}/\sqrt{2} \right)^2 + \left(E_x^{(p_z)}/\sqrt{2} \right)^2 \right] /3. \tag{5.36}$$

For the parallel and perpendicular mean-square fields from a uniform sheet of fluctuating electric dipoles, the terms of Eqs. 5.34 and 5.35 are computed from an integral over the surface area such that a small number of dipoles in a given area is $dN = \sigma_p r dr d\phi$ where σ_p is the areal number density of dipoles and ϕ, $r = x^2 + y^2$ are polar coordinates. For example in non-reduced form

$$\left\langle E_x^2 \right\rangle_{\text{surf}} = \frac{\sigma_E E_0^2}{6} \int_0^{2\pi} \int_0^{\infty} r dr d\phi \left[\left(\frac{3rz\cos\phi}{\left(r^2+z^2\right)^{5/2}} \right)^2 + \left(\frac{-2r^2\cos^2\phi + r^2\sin^2\phi + z^2}{\left(r^2+z^2\right)^{5/2}} \right)^2 + \left(\frac{-2r^2\sin^2\phi + r^2\cos^2\phi + z^2}{\left(r^2+z^2\right)^{5/2}} \right)^2 \right] \tag{5.37}$$

The final results for surface-induced electric fields at the NV of depth z are

$$\left\langle E_{\perp}^2 \right\rangle_{\text{surf}} = \left(\frac{p}{4\pi\epsilon_0} \right)^2 \left(\frac{2}{1+\epsilon_d} \right)^2 \frac{3\pi}{8} \frac{\sigma_p}{z^4} \tag{5.38}$$

$$\left\langle E_{\parallel}^{2}\right\rangle_{\mathrm{surf}}=\left(\frac{p}{4\pi\epsilon_{0}}\right)^{2}\left(\frac{2}{1+\epsilon_{d}}\right)^{2}\frac{3\pi}{16}\frac{\sigma_{p}}{z^{4}} \tag{5.39}$$

The ratio of $\langle E_{\perp}^{2}\rangle_{\mathrm{surf}}/\langle E_{\parallel}^{2}\rangle_{\mathrm{surf}}=2$ between these two results is a direct result of the orientation of the NV described in Eqs. 5.34 and 5.35 and is the reason we scale the noise spectral density for the CPMG data with 2 in Eq. 5.29. In fact this ratio $\langle E_{\perp}^{2}\rangle_{\mathrm{surf}}/\langle E_{\parallel}^{2}\rangle_{\mathrm{surf}}=2$ does not change if the particular surface electric field model has an altered ratio of $\langle E_{z}^{2}\rangle_{\mathrm{surf}}/\langle E_{x}^{2}\rangle_{\mathrm{surf}}$ and $\langle E_{x}^{2}\rangle_{\mathrm{surf}}=\langle E_{y}^{2}\rangle_{\mathrm{surf}}$; the second equality would be the case for a fairly uniform surface noise source. This invariant ratio is a consequence of the NV angle given by $\cos^{-1}(\theta_{\mathrm{NV}})=\sqrt{1/3}$, or $\theta_{\mathrm{NV}}\approx 54.74^{\circ}$. That is, from Eqs. 5.34 and 5.35 the ratio

$$\left\langle E_{\perp}^{2}\right\rangle/\left\langle E_{\parallel}^{2}\right\rangle=\frac{(\cos^{2}\theta+1)+k\sin^{2}\theta}{\sin^{2}\theta+k\cos^{2}\theta} \tag{5.40}$$

becomes equal to 2 for any $k=\langle E_{z}^{2}\rangle/\langle E_{x}^{2}\rangle$ if $\theta=\theta_{\mathrm{NV}}$ and if on average $\left\langle E_{y}^{2}\right\rangle=\langle E_{x}^{2}\rangle$.

Because the electric field power spectral densities are proportional to $\langle E_{\perp}^{2}\rangle_{\mathrm{surf}}$ (or $\langle E_{\parallel}^{2}\rangle_{\mathrm{surf}}$), they will have the depth dependence of $1/z^{4}$. Surface-induced anomalous heating of trapped ions due to non-Johnson-noise-related electric fields from electrode surfaces has been an important subject of study for several decades. At least two theories predict the distance dependence of noise power to be $1/z^{4}$, though they differ in the dependence on frequency. A model (A) of adatoms diffusing on the surface predicts $S\sim 1/f^{3/2}$ and a phonon-induced electric dipole fluctuator model (B) predicts a transition from white noise, to $1/f$, to $1/f^{2}$ as would occur from a sum of many Lorentzians with different cutoff frequencies [94]. The differences between those models and the present diamond situation are 1) The nearly atomic-scale distances we consider are much smaller, nanometers rather than 10s to 100s of micrometers, and 2) The NV is actually inside the dielectric material rather than in vacuum above a surface, so in model (B) it could potentially feel the phononic noise directly in addition to feeling electric field noise. We do not attempt

to distinguish between these two models since even model (B) would exhibit $\sim 1/f^{3/2}$ in some regimes due to the transition region from flat to $1/f^2$. The averaging we have done in summing up the components of these fields accounts for the various orientations of the dipole $\mathbf{p}$ that are sampled as it fluctuates measurement-to-measurement. These fluctuations will have a power spectrum $S_p(f)$ that in general depends on the type of adatom species, its trapping potential on the surface, and its vibronic spectrum as a function of temperature [93]. Since each possible vibronic transition may have different frequency cutoffs then there may be a sum of Lorentzian-like components in the total noise spectral density. For simplicity we assume the single-Lorentzian case and a typical molecular dipole magnitude of 2 Debye in order to compute an order of magnitude for the possible surface areal density of dipoles. We fit this power spectrum model to the combined CPMG and γ data assuming an NV depth of 7 nm consistent with the N implantation parameters and known T_2's from prior work [87, 89]. To produce the $\sqrt{\langle E_\perp^2 \rangle_{\text{surf}}} \sim 10^7$ V/m observed in the spectra, the extracted σ_p is orders of magnitude larger than would be physically possible. This either means that the magnitude of p at the surface must be much greater than 1 D or that the surface electric dipole model is not an accurate description of the surface electric field noise. In contrast to $\sim$ 1-D electric dipoles, only a small number of elementary electric charges are required to produce such a $\sim 10^7$ V/m magnitude of electric field at nanometric distances. A simple uniform charge sheet model, as studied in the next section, has an incorrect depth dependence of $S(f) \propto 1/z^2$, however accounting for discrete charges and only short-range NV-charge interactions can make the depth dependence look like $\alpha = 3 - 4$. It is also likely that for NVs within nanometers of electric dipole phenomena that quadrupolar fluctuations [225] may become important as well, and these terms will fall off more rapidly with depth.

We compare our electric field noise spectral density to those extracted from experiments on motional heating rates of trapped ions due to the trap's metal electrodes. For

an ion-electrode distance of 75 μm and trap frequency 1 MHz, experiments at room temperature report $S_{E_\perp}^{\text{ion}} \approx 2 \times 10^{-11}$ V^{2}m^{-2}/Hz [222]. We compare our value of $S_{E_\perp}(f = 1$ MHz$) \approx 3.5 \times 10^6$ V^{2}m^{-2}/Hz for NVA8 (Fig. 5.5(c)) by scaling $S_{E_\perp}(f)$ to account for the $\sim$ 7-nm NV-surface separation and diamond dielectric half-space, and we obtain $S_{E_\perp}(f) \approx 3 \times 10^{-10}$ V^{2}m^{-2}/Hz. This estimate is of similar magnitude as the $S_{E_\perp}^{\text{ion}}$ that is often attributed to "patch potential" electric fields. We note finally that, while ion trap studies suggest a wide range of $S_{E_\perp}^{\text{ion}}$ values experimentally and theoretically [226, 227, 93], the $1/d^4$ model appears widely accepted for various possible models [94]. Our comparison here is important not only to point out the possible universality of surface-related electric field noise, but also to suggest that the magnitudes seen in non-diamond surfaces are of the order that can be probed using the demonstrated sensitivity of the NV scanning probe.

5.5.2 Model of fluctuating surface charges

Perhaps the simplest surface-based model of electric field noise is due to a uniform density of charge traps that periodically become occupied or unoccupied. In the McWhorter charge trap model for surfaces [221] the $1/f$ noise regime arises due to a sum of many trap relaxation phenomena with a uniform distribution of frequencies $\lambda \in [\lambda_1, \lambda_2]$ and $\lambda_1 \ll f \ll \lambda_2$. In the regime that $f \gg \lambda_2 \gg \lambda_1$ the spectrum resembles a $\sim 1/f^2$ Lorentzian, and therefore the crossover in noise may occur in the transition regime of $f \sim \lambda_2$.

We consider a simplistic model of a "sheet" of surface charge traps that cause a fluctuating electric field at the NV at depth z. Although a static infinite sheet of charge shows no distance dependence of the electric field, the total mean square fluctuations of the constituent charges will have a distance dependence. Using the method of image

charges at a dielectric-air interface, the electric potential inside the diamond ($z > 0$) at NV position r, z due to a charge q at distance d from the interface is

$$\Phi\left(z>0\right)=\frac{1}{4\pi\epsilon_0\epsilon_d}\frac{q}{\sqrt{r^2+(d+z)^2}}+\frac{q}{4\pi\epsilon_0\epsilon_d}\left(\frac{\epsilon_d-1}{\epsilon_d+1}\right)\frac{1}{\sqrt{r^2+(d+z)^2}} \tag{5.41}$$

where $\epsilon_d = 5.7$ is the relative permittivity of diamond and $r^2 = x^2 + y^2$. For a charge $q = -e$ on the surface $d \to 0$ the three electric field components $E_{x_i} = d\Phi/dx_i$ are

$$E_{x_i}\left(r,z\right)=A_0\frac{x_i}{\left(r^2+z^2\right)^{3/2}}e \tag{5.42}$$

where $A_0 = \frac{1}{4\pi\epsilon_0}\frac{2}{1+\epsilon_d}$. We take the NV center axis to be in the xz plane an angle θ_{NV} from the z-axis normal as in the electric dipole noise calculation. Also like the dipole calculation, the contributions of mean square fluctuations on the perpendicular and parallel NV axes are given by Eqs. 5.34 and 5.35, now for charges

$$\left\langle E_\perp^2\right\rangle_{\mathrm{charge}}=\left\langle E_x^2\right\rangle\cos^2\theta_{\mathrm{NV}}+\left\langle E_z^2\right\rangle\sin^2\theta_{\mathrm{NV}}+\left\langle E_y^2\right\rangle \tag{5.43}$$

$$\left\langle E_\parallel^2\right\rangle_{\mathrm{charge}}=\left\langle E_x^2\right\rangle\sin^2\theta_{\mathrm{NV}}+\left\langle E_z^2\right\rangle\cos^2\theta_{\mathrm{NV}}. \tag{5.44}$$

The calculation of the mean-square electric field for a charge trap could be computed by considering that a charge trap is either occupied by an electron with electric field given by Eq. 5.42, or it is unoccupied with field $E_{x_i} = 0$. This assumption for rms gives $\langle E_x^2\rangle = E_x^2/3$.

If a uniform sheet of surface charge is assumed then the number of charges in a small area is $dN = \sigma_e r dr d\phi$ for surface charge number density σ_e, and the surface area integrals

$(r \to \infty)$ yield

$$\left\langle E_x^2 \right\rangle_{\text{surf}} = \left\langle E_y^2 \right\rangle_{\text{surf}} = \frac{\pi A_0^2 e^2 \sigma_e}{12 z^2} \tag{5.45}$$

$$\left\langle E_z^2 \right\rangle_{\text{surf}} = \frac{\pi A_0^2 e^2 \sigma_e}{6 z^2} \tag{5.46}$$

Combining these results with Eqs. 5.43 and 5.44 gives the results relevant to the axes in the NV Hamiltonian

$$\left\langle E_\perp^2 \right\rangle_{\text{surf}} = \frac{1}{(4\pi\epsilon_0)^2} \left(\frac{2}{1+\epsilon_d} \right)^2 \frac{2\pi e^2 \sigma_e}{9 z^2} \tag{5.47}$$

$$\left\langle E_\parallel^2 \right\rangle_{\text{surf}} = \frac{1}{(4\pi\epsilon_0)^2} \left(\frac{2}{1+\epsilon_d} \right)^2 \frac{\pi e^2 \sigma_e}{9 z^2} \tag{5.48}$$

which again is consistent with $\left\langle E_\perp^2 \right\rangle_{\text{surf}} / \left\langle E_\parallel^2 \right\rangle_{\text{surf}} = 2$ due to the magic NV angle. For an example of $\left\langle E_\perp^2 \right\rangle_{\text{surf}} = (7 \times 10^7 \text{ V/m})^2$ and assuming $z = 7$ nm for the NV depth this yields a surface charge density $\sigma_e \approx 1.9 \text{ nm}^{-2}$.

If the surface integral is not taken out to $r \to \infty$, but rather some nanometric distance on the order of the NV depth, then $\left\langle E_\perp^2 \right\rangle_{\text{surf}} \propto 1/z^\alpha$ with $\alpha \sim 2-4$. This could arise for example due to electric-field screening effects at the nontrivial semiconductor interface [228]. In such a case, surface charges could potentially account for the $1/z^{3.6(4)}$ dependence of the surface noise power observed in prior studies of coherence versus NV depth [87, 89].

The depth dependence of the Lorentzian that has a higher frequency cutoff, which we now suggest to be the magnetic noise, also needs further depth-correlated study, though [89] results have pointed to a roughly $S(f) \propto 1/z^{1.8}$ behavior. Rosskopf et. al. have studied high-frequency magnetic noise through $T_1^{(0)}$ and $T_{1,\rho}$ measurements, finding a

much shorter $\tau_e = 0.2$ ns [86], though depth dependence must still be characterized. We have discussed in a section above that this noise with ultra-short correlation time can explain faster Ω near the surface but not dephasing due to the necessarily low noise power at low frequencies. As there is a gap in frequency space in the characterization of magnetic noise, it may be that there is a broad distribution of magnetic noise correlation times from 100s of nanoseconds to less than 1 nanosecond.

5.5.3 Surface-related strain noise

In the prior discussions, we have identified the source of shallow-NV DQ relaxation as surface-related electric field noise. Here we consider the possibility of surface-modified phonon noise in in the place of surface electric field noise as the cause of faster DQ relaxation for small $\omega_{\pm 1}$. This case is more difficult to analyze because the strain coupling coefficients, while measured in the literature, are more complicated if fully considered in the tensor formalism [32, 107]. Although stress and strain are tensors, the NV susceptibility to strain is adequately described by the transverse and parallel terms in the Hamiltonian of the main text, Eq. 5.1, where here we write the strain terms separately

$$H_{\mathrm{NV}} = \left(hD_{\mathrm{gs}} + d_{\parallel}E_{\parallel} + \tilde{d}_{\parallel}\xi_{\parallel}\right) S_z^2 + g\mu_B \mathbf{B}\cdot\mathbf{S} - \left(\frac{d_{\perp}E_{\perp}}{2} + \frac{\tilde{d}_{\perp}\xi_{\perp}}{2}\right)\left(S_+^2 + S_-^2\right) \quad (5.49)$$

with strain coupling parameters $\tilde{d}_{\parallel}/h \approx 13$ GHz/strain and $\tilde{d}_{\perp}/h \approx 22$ GHz/strain [34]. The coupling ratio $\tilde{d}_{\perp}/\tilde{d}_{\parallel} \approx 1.7$ is much smaller than that of the electric field coupling parameters, $d_{\perp}/d_{\parallel} \approx 49$. Therefore, when we alternatively scale the dephasing and DQ spectroscopy data of coupling power spectral densities by these strain couplings the two spectra have a different relative separation compared with those for the pure-electric case

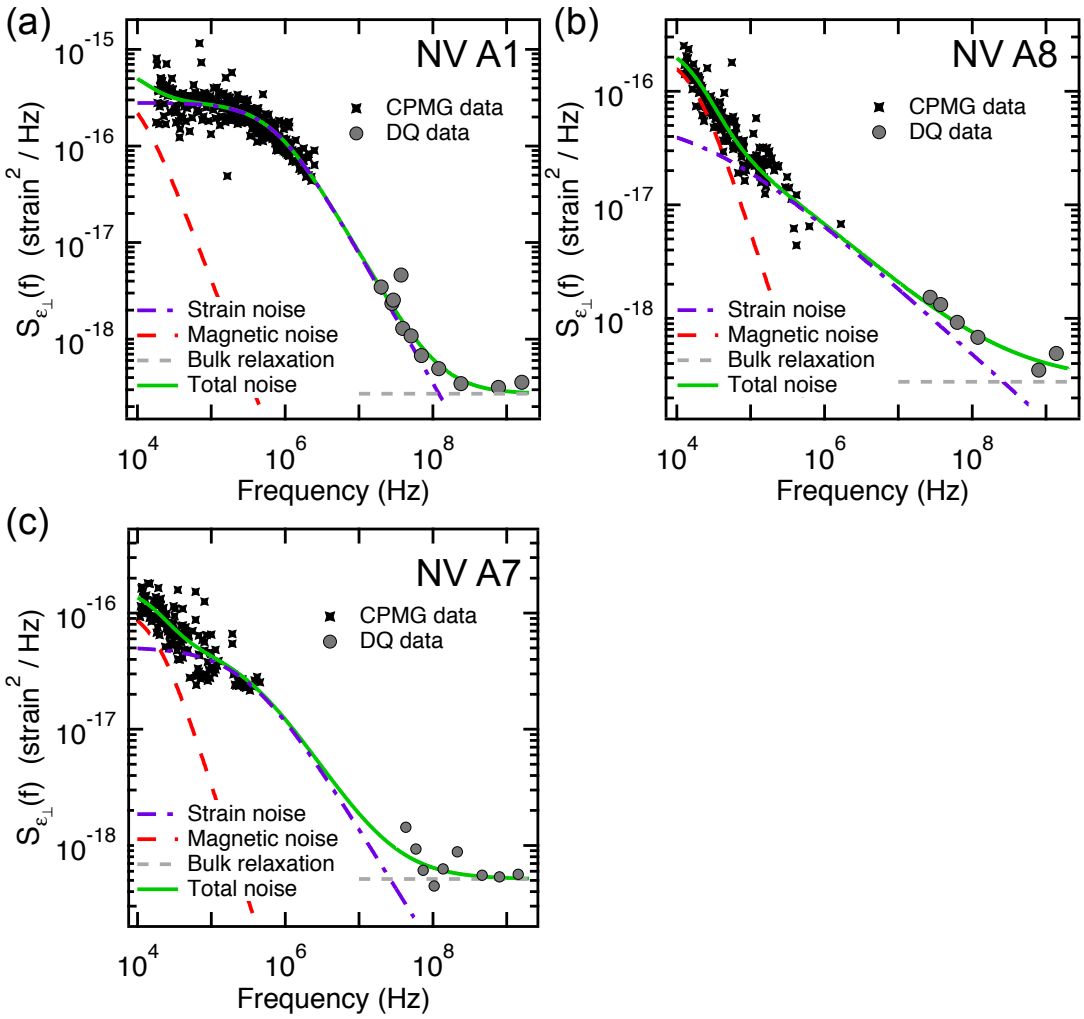

Figure 5.10: Noise spectra modeling for NVs A1, A8, and A7 with strain assumption rather than electric field. Strain coupling constants are more comparable, yielding a different relationship between the SQ dephasing and DQ relaxation spectra. The qualitative result, different from the electric case, is that strain noise is predicted as the higher frequency contribution and the remaining low frequency part is then magnetic. The exponents of the strain curves (purple dash-dot) are smaller, $\alpha = 1.4, 0.6, 1.0$ for A1, A8, and A7, respectively. This constraint means that the quality of the strain fit to the DQ data is lower in comparison to the electric case.

in main text Fig. 5.5. We make the scaling

$$S_{\varepsilon_\perp}^{\mathrm{cpmg}}(f) = 2\frac{S_{\mathrm{cpmg}}(f)}{\tilde{d}_\parallel^2/h^2}; S_{\varepsilon_\perp}^{\gamma}(f) = \frac{S_\gamma(f)}{\tilde{d}_\perp^2/h^2}. \tag{5.50}$$

from $\mathrm{Hz}^2/\mathrm{Hz}$ units to $(\mathrm{strain})^2/\mathrm{Hz}$. Also the factor of 2 in Eq. 5.50 has been borrowed from the simpler electric field case in Eq. 5.29, however, we do not know the form of surface-related strain fields (e.g., from defects, terminating atoms and dimers, etc...), so the relation between $\varepsilon_\parallel$ and $\varepsilon_\perp$ is likely off by at least a constant of order 1. In Fig. 5.10 we plot the analyses of dephasing and DQ relaxation spectra with the same data as for the electric field case but now with the strain coupling re-scaling.

The most obvious qualitative result for the three NVs studied is that strain noise (purple dash-dot line), that which affects both spectroscopy data sets, is now the high frequency component of the double Lorentzian, while the magnetic component (red dashed line) is then assigned to the low frequency part. Second, the exponents of the strain noise curve are smaller than for the electric case, $\alpha = 1.4, 0.6, 1.0$ for A1, A8, and A7, respectively, which are farther from resembling Lorentzian spectra. In fact, the DQ data is less well fit for these exponents constrained to small values, which makes a case for electric fields as a more likely explanation. For example, in Fig. 5.10(a) the total noise curve (green line) noticeable overestimates all of the data points around 10^8 Hz in comparison to the electric case in Fig. 5.8(a).

Another number to consider from the strain spectra model is the total amount of rms strain, or area under the strain noise curve $\sqrt{\langle \varepsilon_\perp^2 \rangle}$. This value is 6×10^{-5} strain, 5×10^{-6} strain, and 2×10^{-5} strain for NVs A1, A8, and A7, respectively. One question is whether this level of total dynamic strain is physically reasonable for NVs approximately 7 nanometers or farther from the diamond surface.

As we discuss in the overview of results above, the dephasing studies of ref. [90] using

dielectric liquids on diamond also point strongly to a source of electric field noise at the diamond surface, and the existence of parallel electric fields deduced in that work necessarily imply the existence of transverse electric fields at the same NVs. This apparent electric noise is reported in [90] to persist over a variety of surface treatments, including successive steps of oxygen annealing and boiling in perchloric, nitric, and sulfuric acids; therefore, it is likely that it exists as well in our diamond films prepared from similar starting material and same CVD growth parameters. Because terminating atoms of the surface have resonant modes that can cause strain in the top layers of diamond [229], albeit mostly THz modes, it is perhaps plausible that the applied viscous liquids serve to change the frequency spectrum of the surface phonons. However, liquids with the higher dielectric constants, such as D-glycerol, showed greater enhancement of coherence T_2 times [90], making electric screening a more likely explanation. Furthermore, our recent scanning probe measurements with other external surfaces brought within nanometers of the diamond suggest that the noise affecting γ may be mitigated, which is more consistent with the electric field hypothesis than with a strain hypothesis. These surface-noise measurements of NVs near metals are described in Chapter 7.

5.6 Conclusions

In conclusion, we have highlighted the importance of considering the coupling between all three levels of the NV ground state for understanding NV decoherence, especially for near-surface NVs. We find the double-quantum (DQ) spin relaxation rate γ to be a major, and even dominant, contributor to the limit of qubit coherence time T_2. We have also used shallow NVs to perform combined dephasing and DQ relaxation spectroscopies of diamond surfaces and furthermore demonstrated a method to distinguish electric and magnetic field noise. To gain more insight into diamond-surface-related electric field

noise, several experiments could be revisited with γ measured in tandem with T_2. Since γ should be even larger for ultra-shallow NVs at depths of 2-5 nanometers [155, 230, 196], one could sensitively probe the effects of, for example, annealing and thermal oxidation [88, 91], plasma etching [199, 200], surface termination [231, 201, 203], chemical treatments [196], temperature [86, 119], photoinduced space charge [232], and variations in the work function [233]. The DQ relaxometry technique we have presented will also be a useful asset for understanding the coupling of general spin $S > 1/2$ solid-state defects to interfaces in hybrid systems.

5.7 Additional information

5.7.1 Population rate equations for equal SQ rates

For $k_bT \gg \hbar\omega_{i,j}$ the relaxation is bidirectional, *i.e.* $\Omega_{i,j} = \Omega_{j,i}$, as depicted by the double-headed arrows between levels in Fig. 5.1(a). The equality of $\Omega_+ = \Omega_-$ is found in several measurements in past work where $T_1^{(0)}$appears relatively constant with tuning of the applied magnetic field over 100s of Gauss [119, 234] in the absence of cross-relaxation. Our CVD-grown diamond samples have a relatively low concentration of P1 centers and NV centers such that cross-relaxation is not observed. In some other cases, like NV coupling to ferromagnetic materials [218], this equality does not always hold for all applied fields. In this section we look at this simple case discussed in the main text. The rate of population change $d\rho_{00}/dt$ of state $|0\rangle$ is a sum of rates into and out of the state each weighted by the current populations. Therefore, abbreviating ρ_{ii} as ρ_i, the

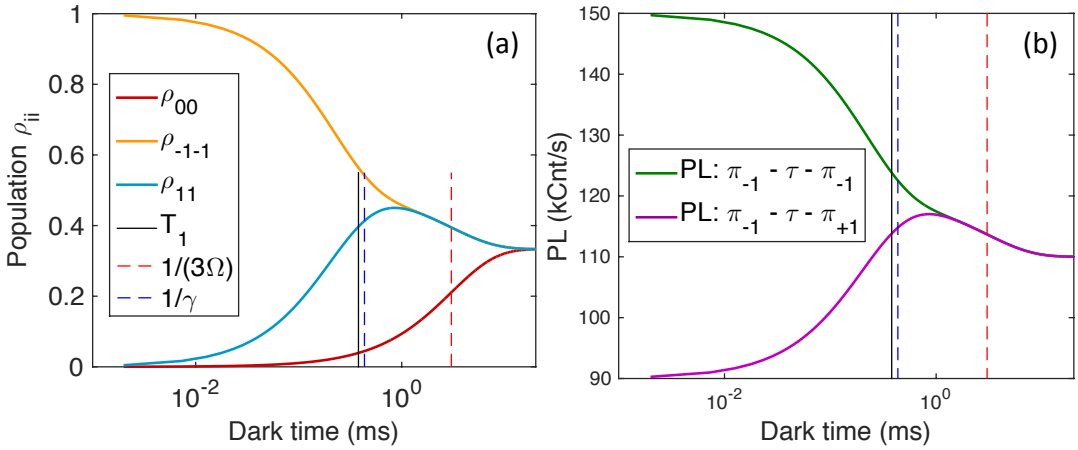

Figure 5.11: (a) Calculated NV ground state spin level populations as a function of time between initialization and readout. The case shown is for the parameters $\gamma = 2.3$ kHz and $\Omega = 0.11$ with initial state $\rho(0) = |-1\rangle\langle -1|$. The dashed vertical lines shown in the legend mark time constants of relaxation relevant to SQ decoherence, and the solid vertical line indicates $T_1 = 1/(\gamma + 3\Omega)$. (b) Calculated PL from these populations given typical PL rates $a_0 = 150$ kCnt/s and $a_1 = 0.6a_0$. The green line shows the measurement with two $\pi_{-1,0}$ pulses. The purple line is the result for a final $\pi_{+1,0}$ pulse. This results in effectively measuring the population of the initially-empty $|1\rangle$ state, seen as a non-monotonic change of PL that peaks between $1/\gamma$ and $1/(3\Omega)$. The difference of these two PL curves gives the single-exponential signal F_2.

system of equations is

$$\frac{d}{dt}\begin{pmatrix}\rho_0\\ \rho_{-1}\\ \rho_1\end{pmatrix} = \begin{pmatrix}-2\Omega & \Omega & \Omega\\ \Omega & -\Omega-\gamma & \gamma\\ \Omega & \gamma & -\Omega-\gamma\end{pmatrix}\begin{pmatrix}\rho_0\\ \rho_{-1}\\ \rho_1\end{pmatrix} \tag{5.51}$$

as compared to the more commonly treated situation in NV center literature [149, 234] of $\gamma = 0$

$$\frac{d}{dt}\begin{pmatrix}\rho_0\\ \rho_{-1}\\ \rho_1\end{pmatrix} = \begin{pmatrix}-2\Omega & \Omega & \Omega\\ \Omega & -\Omega & 0\\ \Omega & 0 & -\Omega\end{pmatrix}\begin{pmatrix}\rho_0\\ \rho_{-1}\\ \rho_1\end{pmatrix} \tag{5.52}$$

We plot in Figure 5.11(a) the calculated populations for the case that $\gamma/\Omega \gg 1$,

specifically using values for γ and Ω similar to those of NVA1 shown in Fig. 5.3 and an initial density matrix of $\rho(0) = |-1\rangle\langle -1|$ as would be the case initially before the dark time for a measurement of γ. For this case the ρ_{00} population changes little initially but population rapidly leaks from ρ_{-1-1} to ρ_{11} until the two equilibrate. Figure 5.11(b) shows the PL calculated from these populations given two different types of π pulses at the end before readout, to effectively either measure the population of the $|-1\rangle$ or $|1\rangle$ states. The purple line in particular shows the non-monotonic curve of PL that would result due to a change of sign in one of the two exponential terms using a final $\pi_{0,+1}$ pulse, leading to a competition between two decay processes. Note the PL curves in Fig. 5.11(b) though are not yet normalized with the subtraction procedure in the data analysis, though the curves demonstrate the direct correspondence between PL and populations of the $|m_s\rangle$ states.

5.7.2 Population rate equations for unequal SQ rates

In the more general case the transition rates between the $S = 1$ ground state levels are $\Omega_+ \neq \Omega_- \neq \gamma$, where we use the abbreviation $\Omega_\pm \equiv \Omega_{\pm 1}$ in this section. The system of differential equations is

$$\frac{d}{dt}\begin{pmatrix}\rho_0\\ \rho_{-1}\\ \rho_1\end{pmatrix} = \begin{pmatrix}-\Omega_+ - \Omega_- & \Omega_- & \Omega_+\\ \Omega_- & -\Omega_- - \gamma & \gamma\\ \Omega_+ & \gamma & -\Omega_+ - \gamma\end{pmatrix}\begin{pmatrix}\rho_0\\ \rho_{-1}\\ \rho_1\end{pmatrix} \tag{5.53}$$

Substituting for ρ_1 (where $\rho_1 = 1 - \rho_0 - \rho_{-1}$) in the equations of ρ_0 and ρ_{-1} leads to the differential equation system

$$\frac{d}{dt}\begin{pmatrix}\rho_0\\ \rho_{-1}\end{pmatrix} = \begin{pmatrix}-\Omega_- - 2\Omega_+ & -\Omega_+ + \Omega_-\\ \Omega_- - \gamma & -\Omega_- - 2\gamma\end{pmatrix}\begin{pmatrix}\rho_0\\ \rho_{-1}\end{pmatrix} + \begin{pmatrix}\Omega_+\\ \gamma\end{pmatrix} \tag{5.54}$$

The solution to the above equation could be found by first considering the first-order homogeneous equation:

$$\frac{d}{dt}\begin{pmatrix}\rho_0\\ \rho_{-1}\end{pmatrix} = \begin{pmatrix}-\Omega_- - 2\Omega_+ & -\Omega_+ + \Omega_-\\ \Omega_- - \gamma & -\Omega_- - 2\gamma\end{pmatrix}\begin{pmatrix}\rho_0\\ \rho_{-1}\end{pmatrix} \tag{5.55}$$

Solving the eigenvalue equation

$$\begin{vmatrix}-\Omega_- - 2\Omega_+ - \lambda & -\Omega_+ + \Omega_-\\ \Omega_- - \gamma & -\Omega_- - 2\gamma - \lambda\end{vmatrix} = 0 \tag{5.56}$$

gives the two eigenvalues as

$$\lambda_\pm = -(\Omega_- + \Omega_+ + \gamma) \pm \sqrt{\Omega_+^2 + \Omega_-^2 + \gamma^2 - \Omega_+\gamma - \Omega_-\gamma - \Omega_-\Omega_+} \tag{5.57}$$

and the corresponding solution to the homogeneous differential equation is

$$c_1 e^{\lambda_+ t}\begin{pmatrix}1\\ \frac{\Omega_- - \gamma}{\Omega_- + 2\gamma + \lambda_+}\end{pmatrix} + c_2 e^{\lambda_- t}\begin{pmatrix}1\\ \frac{\Omega_- - \gamma}{\Omega_- + 2\gamma + \lambda_-}\end{pmatrix} \tag{5.58}$$

Here c_1 and c_2 are constants to be evaluated based on the initial conditions. The particular solution of the inhomogeneous differential could be found by setting the populations ρ_0 and ρ_{-1} as constants and the result is that $\rho_0 = \rho_{-1} = 1/3$. Therefore the combined solution for equation 5.54 is

$$\begin{pmatrix}\rho_0\\ \rho_{-1}\end{pmatrix} = c_1 e^{\lambda_+ t}\begin{pmatrix}1\\ \frac{\Omega_- - \gamma}{\Omega_- + 2\gamma + \lambda_+}\end{pmatrix} + c_2 e^{\lambda_- t}\begin{pmatrix}1\\ \frac{\Omega_- - \gamma}{\Omega_- + 2\gamma + \lambda_-}\end{pmatrix} + \frac{1}{3}\begin{pmatrix}1\\ 1\end{pmatrix} \tag{5.59}$$

The population in the +1 state, ρ_1, can be obtained with the expression $\rho_1 = 1-\rho_0-\rho_{-1}$. Thus,

$$\rho_1 = \frac{1}{3} - c_1 e^{\lambda_+ t}(2\Omega_- + \gamma + \lambda_+) - c_2 e^{\lambda_- t}(2\Omega_- + \gamma + \lambda_-) \tag{5.60}$$

The validity of the assumption that $\Omega_- = \Omega_+$ was verified using an NV spin state relaxation experiment where an NV initially polarized to the $\rho = |0\rangle\langle 0|$ state and read out with the F_1 sequence for normalization. The constants c_1 and c_2 could be determined based on that fact that at time $\tau = 0$, the populations should correspond to $\rho_0(t=0) = 1$ and $\rho_{\pm 1}(t=0) = 0$. These conditions lead to

$$c_1 = -\frac{3\Omega_- + \lambda_-}{3(\Omega_- - \gamma)(\lambda_- - \lambda_+)} \tag{5.61}$$

and

$$c_2 = \frac{3\Omega_- + \lambda_+}{3(\Omega_- - \gamma)(\lambda_- - \lambda_+)} \tag{5.62}$$

The difference between the NV PL vs τ curves when the π pulse at the end of the dark time is tuned to the $|1\rangle$ state ($\pi_{0,+1}$) or the $|-1\rangle$ state ($\pi_{0,-1}$) can be used to probe whether $\Omega_- = \Omega_+$. The subtracted PL signal from such a pulse sequence is given by

$$\mathrm{PL}_{\pi_{0,+1}-\pi_{0,-1}} = -\frac{r(3\Omega_- + \lambda_+)(3\Omega_- + \lambda_-)}{3(\Omega_- - \gamma)(\lambda_+ - \lambda_-)}[e^{\lambda_+ t} - e^{\lambda_- t}] \tag{5.63}$$

where r is the contrast between the 0 state and ± 1 states. In the equation for the PL difference between the two pulse sequences (equation 5.63), the term $3\Omega_- + \lambda_-$ goes to zero in the event $\Omega_- = \Omega_+$ bringing the PL difference to zero.

We compared measurements using the F_1 sequence with a $\pi_{0,+1}$ or $\pi_{0,-1}$ and found

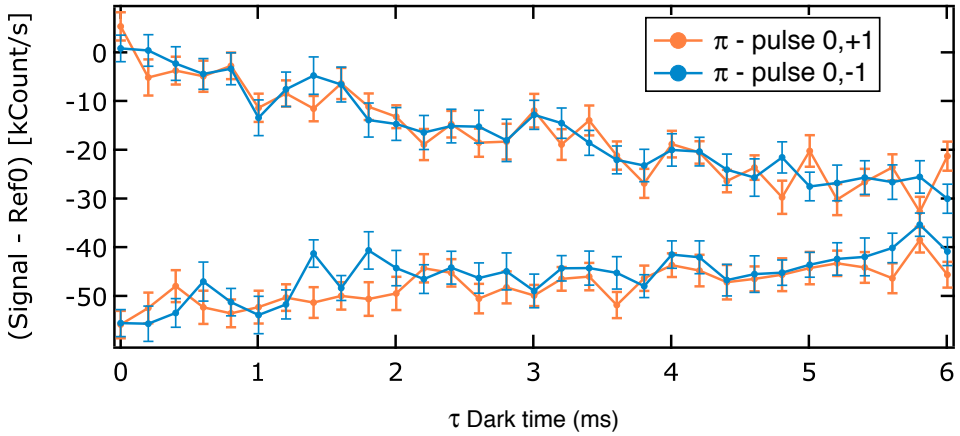

Figure 5.12: Comparison of the F_1 results for NVA1 using π pulses resonant with the $\omega_{+1,0}$ transition (orange) and the $\omega_{-1,0}$ transition (blue). The curves overlap and fit to the same relaxation rate, therefore we conclude that it is a good assumption to set $\Omega \equiv \Omega_+ = \Omega_-$ to simplify the γ analyses in this work.

the $\Omega_+ = \Omega_-$ in even the larger $\omega_{\pm 1}$ regimes where $\omega_{1,0} \gg \omega_{-1,0}$. The results are plotted in Fig. 5.12 for NVA1 at $\omega_{\pm 1}$= 800 MHz, a splitting large enough between $\omega_{+1,0}$ and $\omega_{-1,0}$ that some difference might be expected but was not observed. Subtracting the blue and orange curves gives zero on average as predicted by Eq. 5.63. Therefore, we use the simpler population dynamics model for relaxation measurements using one fitting parameter Ω for the $|\Delta m_s| = 1$ relaxation rates.

5.7.3 Limits to T_2 in $S = 1$ ground state

With the relaxation rates between the three sublevels measured using the sequences presented in Fig. 5.1 and Fig. D.1, we can compute the fundamental limits to T_2 in the case of no dephasing. By $(T_2)^{-1}$ here we mean the total decay rate of the off-diagonal coherence term in the density matrix, ρ_{0-1}. An intuitive way to look at the T_1 quantities for the three-level NV ground state superpositions is in terms of the constituent relaxation rates, so $1/T_1^{\mathrm{SQ}} = 3\Omega + \gamma$ and $1/T_1^{\mathrm{DQ}} = 2\Omega + 2\gamma$. That is, once a coherence is initialized it can decohere due to a quantum jump via any one of four channels, as illustrated in

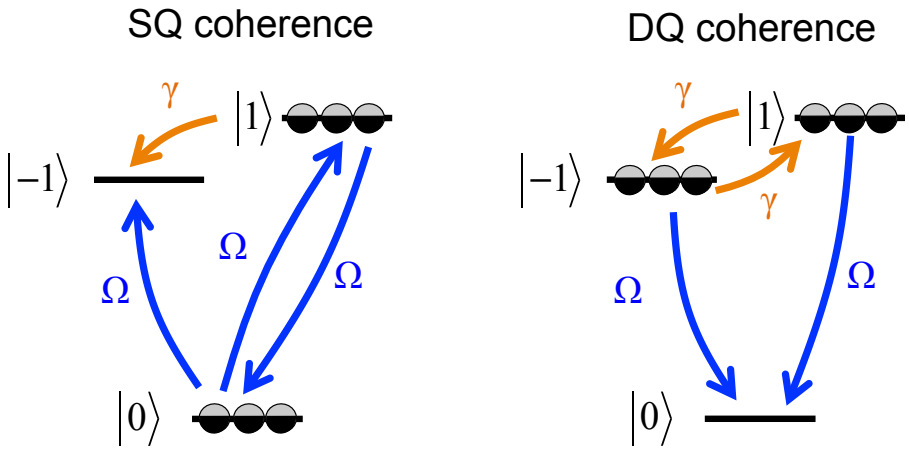

Figure 5.13: Diagrams of the NV ground state spin triplet with two-state coherences at finite magnetic field along the z axis. Quantum coherence is illustrated here between the two levels occupied with black and white discs. In the single-quantum (SQ) coherence there are three Ω relaxation events possible (blue arrows) and one γ relaxation event (orange arrow) to leak population out of the superposition state. In the double-quantum (DQ) coherence case there are two relaxation events possible of each type. The total $1/T_1$ relaxation rate in each case is the sum of these four rates.

Fig. 5.13. The physical properties of the density matrix ρ and its time evolution require the coherences (off-diagonal elements) to decay under specific constraints relating the dephasing and relaxation rates (Eqs. 20 and 41 in ref. [122]). We assume first that we perform a standard Hahn echo on the superposition of $|0\rangle$ and $|-1\rangle$. Let $\Gamma_d^{(ab)}$ denote the pure dephasing rate between $|a\rangle$ and $|b\rangle$. The pure dephasing rate we are interested in $\Gamma_2^{(-10)}$ must follow the constraints required for a three-level system

$$\Gamma_d^{(-10)} = \Gamma_2^{(-10)} - \frac{\Omega + \Omega + \Omega + \gamma}{2} \tag{5.64}$$

where we identify the total decoherence rate $\Gamma_2^{(-10)} = \Gamma_2 = 1/T_2$ that we measure in a N-pulse single-quantum coherence sequence. The dephasing rate $\Gamma_d^{(-10)}$ cannot be negative, therefore the zero-dephasing limit of Γ_2 is

$$\Gamma_2 = \frac{3\Omega + \gamma}{2}. \tag{5.65}$$

Thus, a ratio $\gamma/\Omega > 3$ means that SQ coherence is limited more by γ than Ω, which is what we observe at $\omega_{\pm 1}/2\pi \lesssim 100$ MHz (Fig. 5.4(b)). We identify $T_1^{(0)}$ as $T_1^{(0)} = 1/(3\Omega)$. This gives the final result

$$T_2 \leq T_2^{\mathrm{SQmax}} = \frac{2}{3\Omega + \gamma} = 2\left(\frac{1}{T_1^{(0)}} + \frac{1}{T_1^{(+1,-1)}}\right)^{-1}. \tag{5.66}$$

Table 5.3 lists the measured Ω, γ, $T_1^{(-1,+1)} = 1/\gamma$, $T_1^{(0)}$, and CPMG-N T_2 along with the theoretical upper bound T_2^{SQmax}. In our experiments at best the NV T_2 reached just over half of this maximum: $T_2 \gtrsim 0.5\ T_2^{\mathrm{SQmax}} = T_1$. From the spectral analysis we can infer that the existence of finite-frequency noise, even if decaying with frequency, will keep the dephasing term non-zero even for very large N. We infer that technical challenges, a combination of pulse errors and finite π-pulse times $t \sim \tau$, are responsible for the inability to space ideal pulses close enough together to completely eliminate dephasing from high-frequency noise. For the high-field case shown in Fig. 5.3(b) of the main text we found the $T_2(N)$ to begin saturating around $N = 1024$ pulses. For NVA7, applying $N = 2048$ appeared to cause a reduction in $T_2(N)$, and it appears that the main limitations to increasing it further were technical in combination with inherent surface noise sources.

We also consider the case of a DQ coherence where a superposition of $|1\rangle$ and $|-1\rangle$ is prepared, as has been relevant in experiments to enhance sensitivity to nuclear spins [90, 224]. In this case we are interested in the total decay rate $\Gamma_2^{(-11)}$ of the ρ_{-11} term and so

$$\Gamma_d^{(-11)} = \Gamma_2^{(-11)} - \frac{\Omega + \gamma + \Omega + \gamma}{2}, \tag{5.67}$$

which leads to a symmetric result in the contributions of the relaxation rates. The

resulting zero-dephasing limit to the DQ coherence time $T_2^{\mathrm{DQ}} = 1/\Gamma_2^{(-11)}$ is

$$T_2^{\mathrm{DQ}} \leq T_2^{\mathrm{DQmax}} = \frac{2}{2\Omega + 2\gamma} = 2\left(\frac{2}{3T_1^{(0)}} + \frac{2}{T_1^{(+1,-1)}}\right)^{-1} \tag{5.68}$$

where here we retain the definitions of $T_1^{(0)} = (3\Omega)^{-1}$ and $T_1^{(-1,+1)} = (\gamma)^{-1}$ that were stated for the SQ coherence case. Thus, a ratio $\gamma/\Omega > 1$ means that DQ coherence is limited more by γ than Ω.

The ratio of DQ and SQ coherence time limits $T_2^{\mathrm{DQmax}}/T_2^{\mathrm{SQmax}}$ can be written in terms of γ and Ω.

$$T_2^{\mathrm{DQmax}}/T_2^{\mathrm{SQmax}} = \frac{\gamma + 3\Omega}{2\gamma + 2\Omega} \tag{5.69}$$

We plot this quantity as a function of γ/Ω in Fig. 5.14, and we find that $T_2^{\mathrm{DQmax}}/T_2^{\mathrm{SQmax}} < 1$ when $\gamma > \Omega$ and $T_2^{\mathrm{DQmax}}/T_2^{\mathrm{SQmax}} > 1$ when $\gamma < \Omega$. This is an intuitively simple result that implies that the DQ relaxation channel will limit the coherence of the DQ coherences more than it limits the SQ coherences. For example, in the case of the NV we measured with $\gamma = 8(2)$ kHz and $\Omega = 0.31(2)$ kHz, the result is $T_2^{\mathrm{DQmax}}/T_2^{\mathrm{SQmax}} \approx 0.5$. When $\gamma/\Omega = 1$, the decoherence rate limits are equal in the two cases because effectively the three levels are all on the same footing, in a phenomenological way, despite having different spin projections. In a multipulse experiment that aims to measure both T_2^{DQ} and T_2^{SQ}, the ratio $T_2^{\mathrm{DQ}}/T_2^{\mathrm{SQ}}$ may not match the theoretical $T_2^{\mathrm{DQmax}}/T_2^{\mathrm{SQmax}}$ because the dephasing will be different for SQ and DQ coherences. For example, the pure DQ dephasing rate is more sensitive to magnetic B_z noise, but insensitive to electric E_z noise [29, 90].

The definition of $T_1^{(-1,+1)} = (\gamma)^{-1}$ is based is based on the SQ coherence case because that quantity appears in Eq. 5.66 for SQ coherence time limits. However, looking at Eq. 5.68 one could also define time constant from the view of DQ coherence: $(2\gamma)^{-1}$ captures

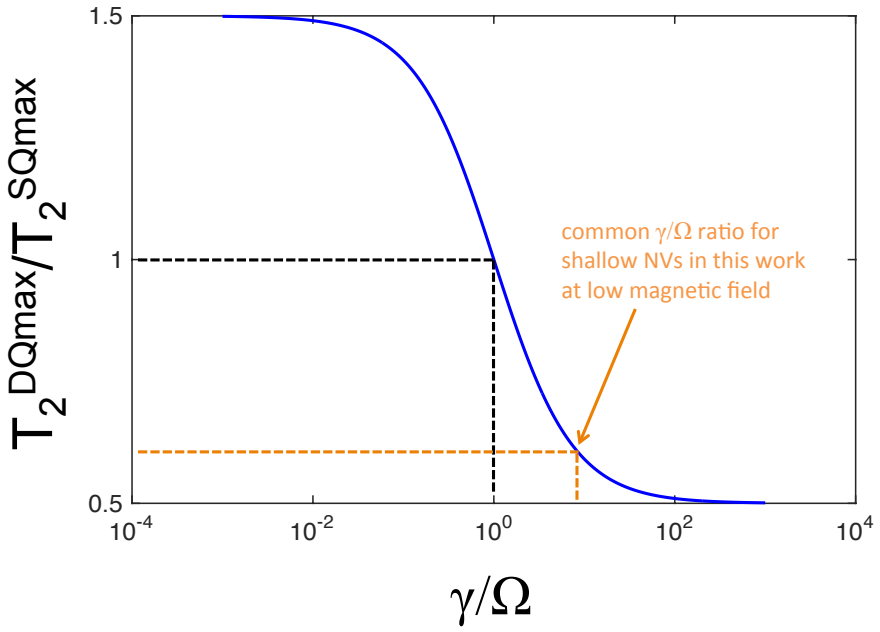

Figure 5.14: Ratio Eq. 5.69 of theoretical T_2 limits (i.e., zero dephasing) for the double-quantum to single-quantum cases, $T_2^{\mathrm{DQmax}}/T_2^{\mathrm{SQmax}}$ as a function of the SQ and DQ relaxation rates Ω and γ, respectively. This ratio can vary from 0.5 to 1.5 depending on which relaxation channel is dominant. The case most relevant to the main text experiments is $\gamma/\Omega > 1$ (bottom left quadrant of image) where DQ coherences are expected to be more limited by relaxation compared to SQ coherences.

the bidirectional chance of relaxation between the $|\pm1\rangle$ states when in superposition. This definition does not change the overall limit T_2^{DQmax}. If we define these time constants with respect to the coherences they most affect then $T_1^{(0,\mathrm{SQ})} \equiv T_1^{(0)} = (3\Omega)^{-1}$ and $T_1^{(\pm1,\mathrm{DQ})} \equiv \frac{1}{2}T_1^{(+1,-1)} = (2\gamma)^{-1}$. Using these definitions then Eqs. 5.66 and 5.68 can be written as

$$T_2 \leq T_2^{\mathrm{SQmax}} = \frac{2}{3\Omega+\gamma} = 2\left(\frac{1}{T_1^{(0,\mathrm{SQ})}} + \frac{1}{2}\frac{1}{T_1^{(\pm1,\mathrm{DQ})}}\right)^{-1} \tag{5.70}$$

and

$$T_2^{\mathrm{DQ}} \leq T_2^{\mathrm{DQmax}} = \frac{2}{2\Omega+2\gamma} = 2\left(\frac{2}{3}\frac{1}{T_1^{(0,\mathrm{SQ})}} + \frac{1}{T_1^{(\pm1,\mathrm{DQ})}}\right)^{-1}. \tag{5.71}$$

Eqs. 5.70 and 5.71 perhaps more equitably show the influence of each of these time constants on SQ versus DQ coherences.

Pulse sequences employing dual-frequency "DQ swap" pulses [224] could be useful tools for studying the γ transition rate as well. Even in the present work focused on SQ coherence times, we consider the possibility that at low applied B_z our $\pi_{0,-1}$-pulses also create small coherences within the $|+1\rangle$ and $|-1\rangle$ subspace due to a small Rabi detuning of 10s of MHz. The ratio of DQ to SQ coherence times is ≈ 0.5 for $\gamma \gg \Omega$, and therefore any unintentional DQ coherences formed by Rabi driving at at low magnetic fields would decay at a faster rate, if limited by relaxation, than would the intentional SQ coherences. Furthermore, in the absence of nuclear-bath-related anomalous decoherence effects [130] (as we use ^{12}C-enriched diamond films) the DQ coherences also generally dephase $2-4\times$ faster from magnetic noise [224, 90]. This DQ-to-SQ maximum coherence time ratio that we derive is a prediction that could be evaluated in future experiments in the context of Ω and γ measurements.

Although prior work on NV dephasing at finite B_z shows that the DQ spin coherence time is not affected to first order by electric fields [90] (since it shifts the $|\pm1\rangle$ energy

levels equally), we predict from the above analysis that electric fields in fact should greatly influence the DQ spin decoherence rate through the DQ relaxation channel. Also, near $B_z = 0$ the spin eigenstates become DQ superpositions of $|m_s = \pm 1\rangle$, and one may find a crossover between dominance of dephasing [29, 235] and DQ relaxation from electric fields.

5.7.4 Single-quantum relaxation data, Ω

Figure 5.15 is a plot of the single-quantum relaxation rates of the data shown in Fig. 5.4. The Ω data show a generally flat behavior with the $\omega_{\pm 1}$ splitting and the magnitudes even at large $\omega_{\pm 1}$ are typically smaller than the γ data. The flat behavior is likely due to the fractionally small change in $\omega_{0,-1}$, which is approximately given by $\omega_{0,-1} = 2\pi D_{\mathrm{gs}} - \omega_{\pm 1}/2$. The surface magnetic noise spectrum affecting Ω is either flat or negligible over this frequency range of about 2060 MHz - 2860 MHz. We determined that the magnitude of the magnetic noise spectra we measured with dephasing spectroscopy is too small to affect Ω if it continues to fall off as $1/f^2$, reaching NV-magnetic coupling strengths of around 1 Hz or less. Therefore, as noted in an earlier study [86], the $T_1^{(0)}$ for near-surface NVs may be limited by a magnetic noise source with a cutoff at much higher frequencies on the order of gigahertz.

Of the NVs studied in most detail (A1, A7, A8) NVA1 showed the fastest SQ relaxation and larger variation in Ω (up to a factor of 2). This is interesting because our dephasing and relaxation spectroscopy showed that NVA1 had a higher level of what we identified as magnetic noise (red dashed Lorentzian curve in Fig. 5.5(a)). We have already stated that this same magnetic noise that is responsible for dephasing cannot also affect Ω given the single correlation time because $S(\omega)$ becomes too small at $\omega = \omega_{0,-1}$. However, our and others' prior studies suggest that both $T_1^{(0)}$ [87, 86] and T_2 [87, 89]

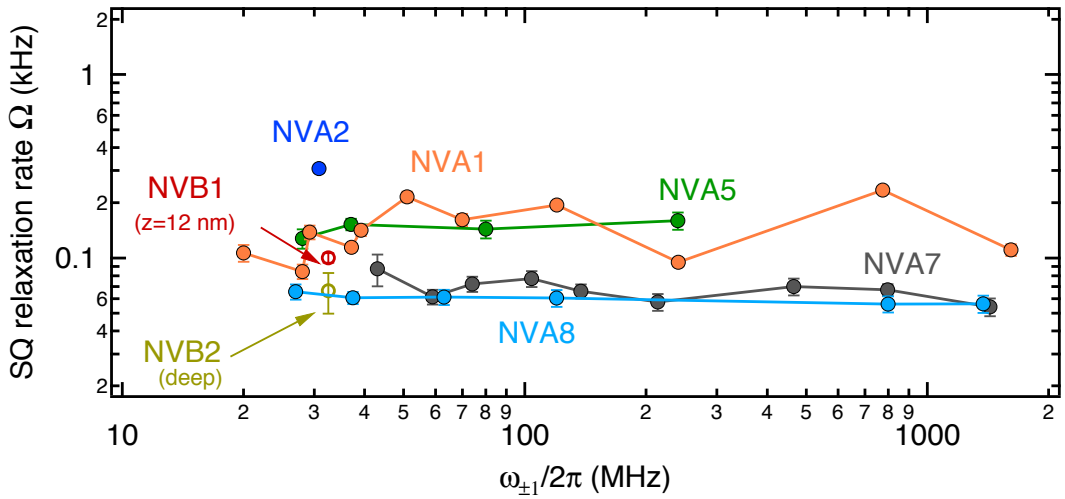

Figure 5.15: Single-quantum relaxation rate Ω measured as a function of the $|-1\rangle \leftrightarrow |1\rangle$ transition frequency $\omega_{\pm 1}$ plotted for several NV centers in samples A and B. The data is used to compute the γ/Ω ratios plotted in Fig. 5.4(b). Ω shows no dependence on the $\omega_{\pm 1}$ splitting; over this range the $\omega_{0,-1}/2\pi$ transition frequency, which determines the magnetic noise Ω is sensitive to, varies over only a small fractional range of about 2060 MHz - 2860 MHz.

have surface-distance dependence and perhaps there are at least two different regimes for surface-related magnetic noise correlation rates, a $\sim 0.1 - 1$ μs rate and a much faster sub-nanosecond. We discuss more about future experiments to address this in a later section on spin-locking and $T_{1\rho}$.

5.7.5 Relaxation for shallow versus deep NVs

Figure 5.16 shows F_1 (blue circles) and F_3 (orange triangles) relaxation signals for two nitrogen delta-doped NVs in sample B, NVB1 at depth 12 nm and NVB2 at 150 nm; depths were independently measured using magnetic resonance depth imaging and checked with surface-proton spectroscopy, as we previously reported [87]. In the case of deep NVB2 we found $\gamma/\Omega = 1.7$, while for NVB1 we measured $\gamma/\Omega = 4.5$. In sample A the main-text conclusion of surface noise origin of the γ relaxation is also supported by the observation that NVA5 showed a relatively small γ at $\omega_{\pm 1}$= 37 MHz in conjunction

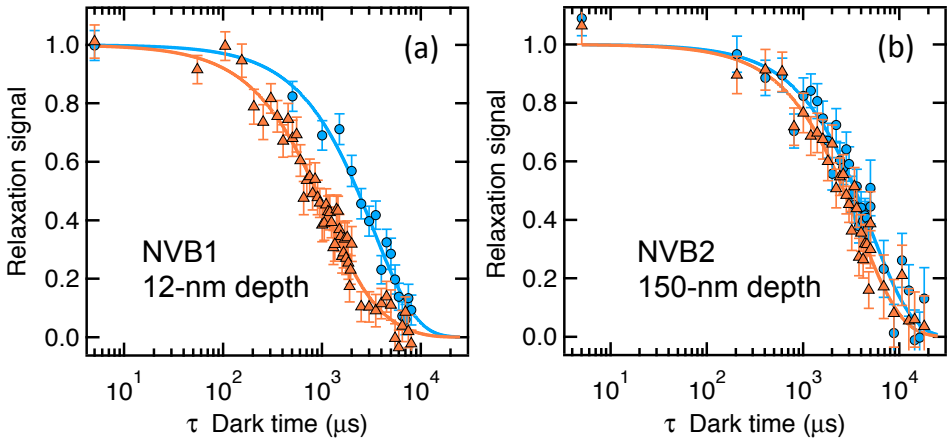

Figure 5.16: Comparison of the relaxation rate measurements at $\omega_{\pm 1}/2\pi = 32.5$ MHz for a shallow NV (a) and deeper NV (b) both in a ^{15}N delta-doped film Sample B. In the 12-nm-deep NV the double-quantum relaxation sequence data (orange triangles) decays faster than does the single-quantum data (blue circles), giving $\gamma = 0.45(4)$ kHz compared to $\Omega = 0.10(1)$ kHz. In the deeper NVB2 the extracted rate is $\gamma = 0.11(2)$ kHz, which is more comparable to $\Omega = 0.066(8)$ kHz. The larger γ rate for NVs at few-nanometer depths is evidence for an effect of surface-related electric field noise at frequency $\omega_{\pm 1}$.

with its identification as a deep NV; it's Hahn echo showed coupling to a ^{13}C spin bath outside the ^{12}C film and a relatively long Hahn echo $T_2 = 147(6)$ μs [43, 87]. Other NVs in sample A, identified as shallow, did not exhibit ^{13}C oscillations in the echo data and had shorter bare Hahn echo $T_2 < 100$ μs.

In the discussion of Fig. 5.4 of the main text we introduce the form of γ dependence on frequency $f = \omega_{\pm 1}/2\pi$ as $\gamma(f) = 1/f^{\alpha} + \gamma_{\infty}$. Our claim that γ_{∞} is primarily due to bulk effects is based on examining the mean γ_{∞} value for NVs identified as shallow (A1, A7, A8) and those identified as deep (A5, B2). For the shallow NVs $\langle\gamma_{\infty}\rangle = 0.21(4)$ and for the deep NVs $\langle\gamma_{\infty}\rangle = 0.14(5)$. These values are comparable enough that bulk effects likely contribute to most of the frequency-independent γ_{∞} rate for shallow NVs. The question of whether γ_{∞} is caused by spin-lattice relaxation, electric field noise internal to the diamond, or both is an open question, and a study of γ dependence on both temperature and f may be helpful.

5.7.6 Additional data comparing T_2 and T_1

In Fig. 5.17 we show supplemental data to the main text Fig. 5.3 on comparing CPMG-based T_2 enhancement to the T_1 computed from γ and Ω for four NV centers, two taken at small $\omega_{\pm1}$ (a,b) and two taken at large $\omega_{\pm1}$ (c,d).

In sample A, we have focused measurements on NVs that showed a consistent Ω over time. Some NV centers in the nanopillars exhibited Ω values that increased or decreased by up to an order of magnitude and sometimes between two values measurement to measurement. For these shown in Fig. 5.18 we judged that it was not reliable to continue to measure pairs of γ and Ω versus $\omega_{\pm1}$ for a larger range of values. NVA6 for example had a particularly unstable Ω value (not all data points shown) that tended to decrease over time. In fact, the total T_1 for NVA6 was so short that we were able to decouple its echo $T_2 = 24(1)$ μs up to $T_2\,(N = 512) = 216(70)$ at $\omega_{\pm1}$= 57.1 MHz. This $T_2\,(N)$ approaches 90% of $T_2^{\mathrm{SQmax}} = 242$ μs since the relaxation of both SQ and DQ channels was fast, where $T_1^{(0)} = 250$ μs. Relaxation and CPMG data for this NVA6 are shown in Fig. 5.19.

5.7.7 Implications for $T_{1\rho}$ and continuous dynamical decoupling

Future measurements comparing continuous-DD $T_{1,\rho}$ to the more complete definition of T_1 could shed light on the dephasing limitations we find at high applied magnetic field. The consideration of the γ relaxation channel has not been considered in prior work on SQ and rotating-frame relaxation of shallow NV centers [86]. The transition matrix used for analyzing spin-locking $T_{1,\rho}$ measurements [86] has treated these as zero-valued matrix elements though they will depend on γ, and at small $\omega_{\pm1}$ or very shallow NVs it may dominate the observed rotating-frame decay. Future $T_{1,\rho}$ experiments tuning both the Rabi frequency and $\omega_{\pm1}$ could help continue to elucidate relative contributions

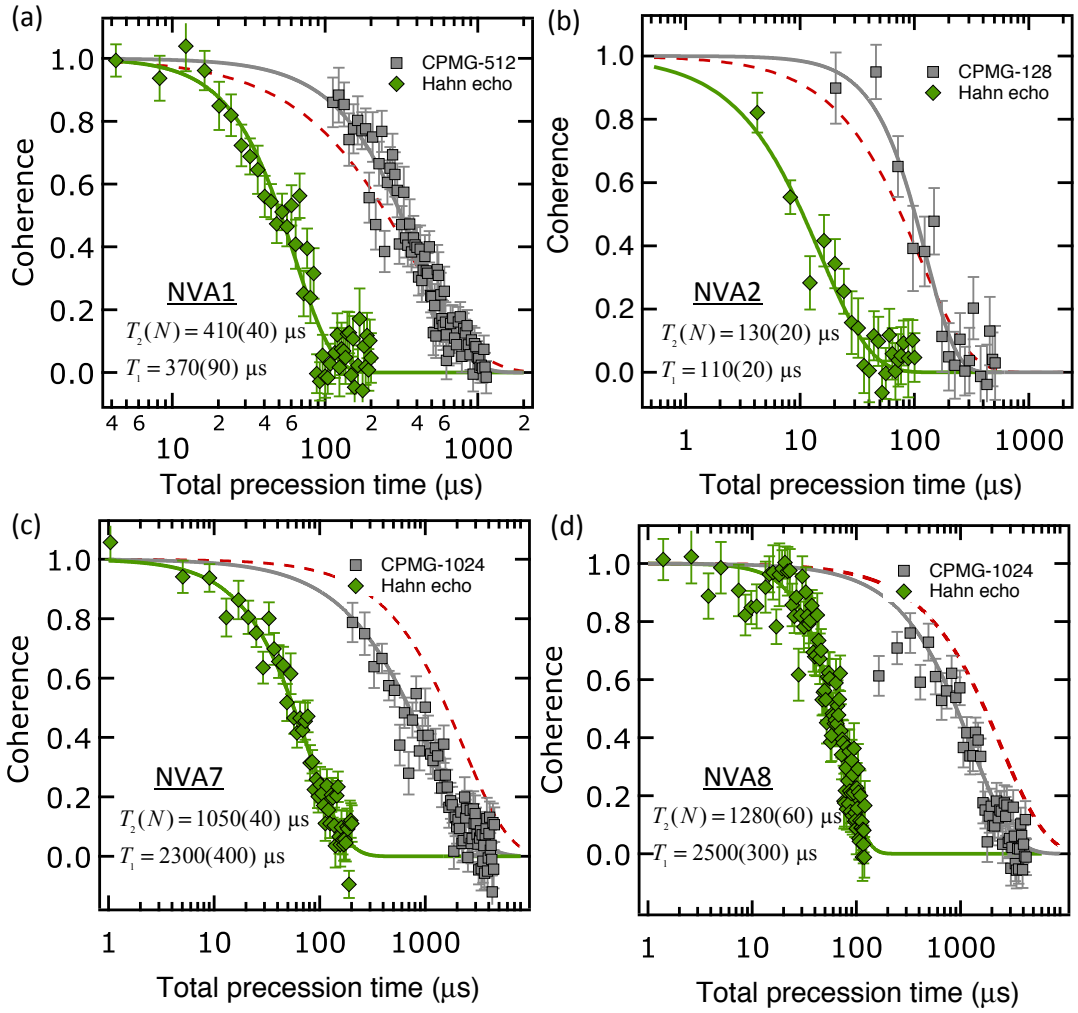

Figure 5.17: Enhancement of single-quantum coherence time using CPMG-N for shallow implanted NVs under conditions of (a,b) large γ at small $\omega_{\pm 1}$ and (c,d) small γ at large $\omega_{\pm 1}$. Data shown are Hahn echo (green diamonds) and CPMG-N (gray squares) where N is the total number of π pulses, and solid lines are fits to $\exp\left[-(T/T_2)^n\right]$ with free exponent n. Dashed red lines are reference plots of $\exp\left(-T/T_1\right)$ using the $T_1 = (3\Omega + \gamma)^{-1}$. (a) NVA1 with splitting $\omega_{\pm 1}/2\pi = 37.1$ MHz, where the CPMG-512 yields a $T_2(512) = 1.2T_1$. (b) NVA2 with $\omega_{\pm 1}/2\pi = 30.6$ MHz, where CPMG-128 yields $T_2(128) = 1.2T_1$. (c) NVA7 with $\omega_{\pm 1}/2\pi = 1431$ MHz where the CPMG-1024 yields $T_2(1024) = 0.45T_1$. (d) NVA8 with $\omega_{\pm 1}/2\pi = 1376$ MHz where the CPMG-1024 yields $T_2(1024) = 0.52T_1$.

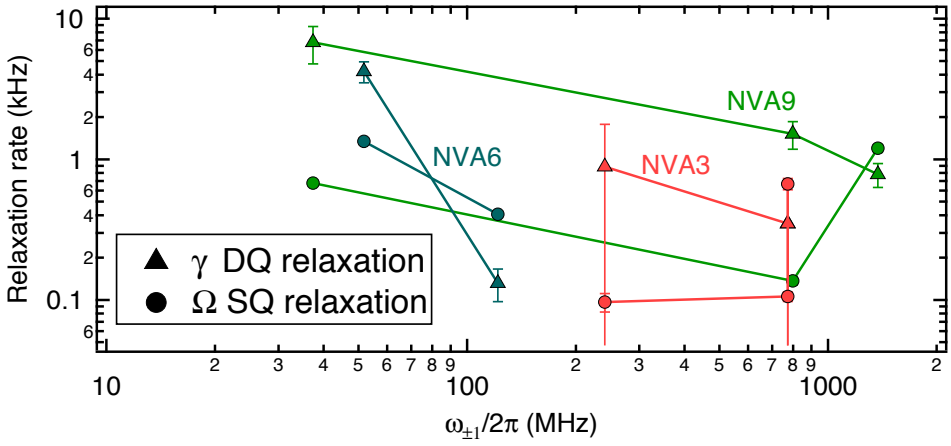

Figure 5.18: SQ and DQ relaxation rates Ω and γ for NVs that showed unstable Ω over hourly time periods of multiple measurements. For example, NVA3 (red circles) exhibited Ω that changed from one measurement to the next even at the same $\omega_{\pm1}$ value. In general, however, γ still appeared to increase at lower $\omega_{\pm1}$ values, most noticeably in NVA9. NVA9 is likely quite near to the surface because it shows a relatively short Hahn echo coherence time $T_2 = 9.5(9)$ μs.

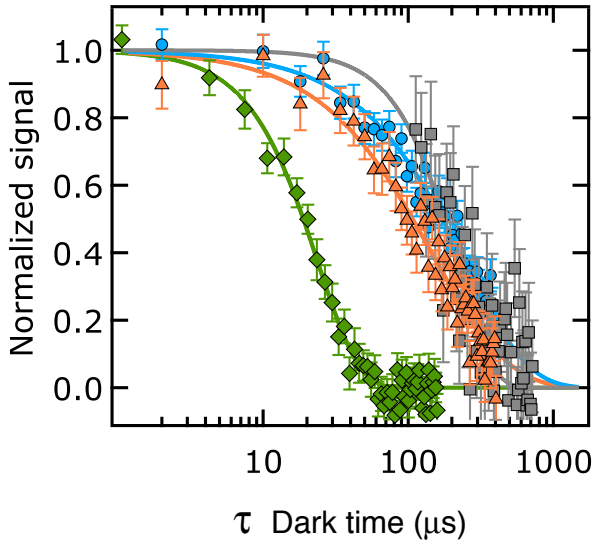

Figure 5.19: An example of an NV that showed an unstable and increasing Ω SQ relaxation rate over time. Relaxation data at $\omega_{\pm1}/2\pi = 57.1$ MHz is shown for signals F_1 (blue circles) and F_3 (orange triangles) in comparison to $T_2 = 24(1)$ μs with Hahn echo (green diamonds) and $T_2\,(N) = 220(70)$ μs with CPMG-N (gray squares) for $N = 512$ pulses. Total $T_1 = 120(10)$ μs is so short that $T_{2,N}$ could be extended to about 90% of $T_2^{\mathrm{SQmax}} = 240(20)$ μs, which is made evident in this plot, although note this comparison is only for qualitative reference as coherence and relaxation curves should not be directly compared.

of magnetic and electric noise in the 1 MHz - 30 MHz regime. Likewise surface electric fields may play an even more important role in continuous dynamical decoupling using coherent electrical or mechanical driving in the $|\pm 1\rangle$ manifold [236].

NV	$f_{\pm1}$ [MHz]	Ω [kHz]	γ [kHz]	$1/(3\Omega)$ [ms]	$1/\gamma$ [ms]	T_1 [ms]	$T_2(N)$ [ms]	T_2^{SQmax} $=2T_1$[ms]	T_2/T_2^{SQmax} (%)
NVA1	20	0.11(1)	1.7(3)	3.1(3)	0.6(1)	0.50(8)	NA	1.0(2)	NA
NVA1	28	0.084(8)	1.14(9)	4.0(4)	0.88(7)	0.72(5)	NA	1.44(9)	NA
NVA1	29.2	0.14(1)	1.2(2)	2.4(2)	0.8(1)	0.61(8)	NA	1.2(2)	NA
NVA1	37.1	0.115(4)	2.4(6)	2.9(1)	0.4(1)	0.37(9)	0.41(4)	0.7(2)	60(20)
NVA1	39.2	0.142(10)	0.6(2)	2.4(2)	1.6(6)	1.0(2)	NA	1.9(3)	NA
NVA1	51	0.22(1)	0.52(9)	1.55(7)	1.9(3)	0.85(7)	NA	1.7(1)	NA
NVA1	69.9	0.16(1)	0.33(5)	2.1(1)	3.1(5)	1.23(9)	NA	2.5(2)	NA
NVA1	120	0.194(9)	0.24(4)	1.72(8)	4.2(7)	1.22(7)	NA	2.4(1)	NA
NVA1	240.6	0.095(5)	0.17(4)	3.5(2)	6(1)	2.2(2)	NA	4.4(4)	NA
NVA1	774.5	0.235(9)	0.15(3)	1.42(5)	7(1)	1.17(6)	NA	2.3(1)	NA
NVA1	1612	0.111(8)	0.17(2)	3.0(2)	5.8(7)	2.0(1)	NA	4.0(3)	NA
NVB1	32.5	0.100(6)	0.45(4)	3.3(2)	2.2(2)	1.32(7)	NA	2.6(1)	NA
NVB2*	32.5	0.066(8)	0.11(2)	5.0(6)	9(2)	3.2(3)	NA	6.5(6)	NA
NVA2	30.8	0.31(2)	8(2)	1.08(7)	0.12(3)	0.11(2)	0.13(2)	0.21(4)	60(10)
NVA5*	28	0.13(2)	0.17(2)	2.6(4)	6.0(7)	1.8(2)	NA	3.6(3)	NA
NVA5*	37	0.15(1)	0.23(4)	2.2(1)	4.4(8)	1.5(1)	NA	2.9(2)	NA
NVA5*	80	0.14(2)	0.13(2)	2.3(3)	8(1)	1.8(2)	NA	3.6(3)	NA
NVA5*	240	0.16(2)	0.19(6)	2.1(3)	5(2)	1.5(2)	NA	3.0(4)	NA
NVA7	43	0.09(2)	0.7(2)	3.8(8)	1.4(4)	1.0(2)	NA	2.1(4)	NA
NVA7	59	0.062(6)	0.5(1)	5.4(5)	2.2(4)	1.6(3)	NA	3.1(6)	NA
NVA7	73.97	0.072(7)	0.30(7)	4.6(5)	3.4(8)	2.0(3)	NA	3.9(6)	NA
NVA7	104	0.077(8)	0.22(4)	4.3(4)	4.6(8)	2.2(2)	NA	4.5(5)	NA
NVA7	137.7	0.066(6)	0.30(8)	5.1(5)	3.3(9)	2.0(3)	NA	4.0(6)	NA
NVA7	214	0.058(6)	0.4(1)	5.8(6)	2.3(6)	1.7(3)	NA	3.3(6)	NA
NVA7	465.7	0.070(7)	0.27(5)	4.8(5)	3.7(7)	2.1(2)	NA	4.2(4)	NA
NVA7	797	0.067(5)	0.26(4)	5.0(4)	3.8(6)	2.2(2)	NA	4.3(4)	NA
NVA7	1431	0.054(6)	0.27(6)	6.2(7)	3.7(8)	2.3(4)	1.05(4)	4.6(7)	23(4)
NVA8	26.95	0.066(6)	0.7(2)	5.1(5)	1.3(4)	1.1(2)	NA	2.1(4)	NA
NVA8	37.4	0.061(5)	0.6(1)	5.5(4)	1.6(3)	1.2(2)	NA	2.4(4)	NA
NVA8	63	0.061(6)	0.45(8)	5.4(5)	2.2(4)	1.6(2)	NA	3.2(4)	NA
NVA8	119.85	0.061(6)	0.33(7)	5.5(5)	3.0(6)	2.0(3)	NA	3.9(6)	NA
NVA8	798.4	0.056(6)	0.17(3)	5.9(6)	6(1)	3.0(3)	NA	5.9(6)	NA
NVA8	1375.9	0.056(6)	0.24(4)	5.9(6)	4.2(7)	2.5(3)	1.28(6)	4.9(6)	26(3)

Table 5.3: Measured relaxation rates Ω, γ, and maximum coherence time $T_2(N)$ for the NVs in this work. The NV names with a * are deep NVs and do not show an increasing γ at low $f_{\pm1} = \omega_{\pm1}/2\pi$. The second column from the right shows the computed maximum expected spin coherence time from Eq. 5.66, and the rightmost column shows the ratio of experimental to theoretical maximum results. Standard errors from fitting routines are given parentheses for the least significant digit. "NA" refers to $\omega_{\pm1}$ values at which the maximum T_2 was not measured. The large difference between $1/(3\Omega)$ and the full T_1, in all cases, emphasizes the significant effect of γ on the relevant relaxation rate.

Chapter 6

Two-dimensional nanoscale imaging of gadolinium spins via scanning probe relaxometry with a single spin in diamond

Spin-labeling of molecules with paramagnetic ions is an important approach for determining molecular structure, however, current ensemble techniques lack the sensitivity to detect few isolated spins. In this chapter, we demonstrate two-dimensional nanoscale imaging of paramagnetic gadolinium compounds using scanning relaxometry of a single nitrogen vacancy (NV) center in diamond. Gadopentetate dimeglumine attached to an atomic force microscope tip is controllably interacted with and detected by the NV center, by virtue of the fact that the NV exhibits fast relaxation in the fluctuating mag-

[1]The contents of this chapter have substantially appeared in reference [71]: M. Pelliccione, B. A. Myers, L. M. A. Pascal, A. Das, and A. C. Bleszynski Jayich, Two-dimensional nanoscale imaging of gadolinium spins via scanning probe relaxometry with a single spin in diamond, *Phys. Rev. Applied* **2** (2014) 054014 (2014)

netic field generated by electron spin flips in the gadolinium. Using this technique, we demonstrate a reduction in the $T_1^{(0)}$ relaxation time of the NV center by over two orders of magnitude, probed with a spatial resolution of 20 nm. Here $T_1^{(0)}$ has been defined in Chapter 5 as the time constant for the NV spin prepared in $|m_s = 0\rangle$ to depolarize into a mixture of its three spin sublevels, whereas "T_1" is reserved to describe the complete relaxation time that limits NV coherence. Our result exhibits the viability of the technique for imaging individual spins attached to complex nanostructures or biomolecules, along with studying the magnetic dynamics of isolated spins.

6.1 Introduction

Mapping the structure of biomolecules including proteins and nucleic acids is of significant importance, as the functionality of a biomolecule is directly related to its structure [237]. For decades, paramagnetic compounds such as the gadolinium-based complex Gd-DTPA have been studied for their effect of reducing proton (T_{1n}) spin-lattice relaxation times [238], making them widely used as nuclear magnetic resonance imaging (MRI) contrast agents [239, 240, 241]. However, with conventional MRI techniques, the spatial resolution of contrast imaging is typically limited to the micron scale [242, 243, 244]. High-field electron paramagnetic resonance (EPR) has made possible nanometer-scale distance measurements between magnetically-interacting Gd^{3+} spins tagged to proteins [245, 246], but these approaches rely on a large ensemble of labeled molecules to obtain a measureable signal. A nanoscale scanning probe technique would enable non-averaged distance measurements on individual spin-labeled molecules, as well as an investigation of the magnetic dynamics of an isolated spin system. In this chapter, we demonstrate nanoscale imaging of Gd compounds using scanning relaxometry of a single nitrogen-vacancy (NV) center in diamond. The NV is an atomic-scale defect whose electronic

spin, at ambient temperatures, exhibits several millisecond long longitudinal relaxation times, and can be optically polarized and interrogated on the single defect level [247]. Together with its excellent photostability, biocompatibility, and noninvasiveness [103, 248], these properties make the NV a viable sensor for detecting and imaging individual spins in biological environments [214] and studying their fluctuation dynamics [104, 249].

Gadolinium (Gd^{3+}) ions are particularly interesting spin systems, as they have a large unpaired electron spin of $S = 7/2$ and fast spin dynamics in the GHz frequency range. These properties make Gd compounds particularly effective as MRI contrast agents [250], as the relaxation time of protons in water is reduced in the presence of Gd. Analogously, the significant level of Gd spin noise at the frequency of the NV zero-field splitting (2.87 GHz) reduces the NV spin relaxation time $T_1^{(0)}$, depending on the proximity and concentration of Gd [220, 85]. This susceptibility has inspired the technique of NV relaxometry to detect Gd spins. Few to single Gd spin sensitivities have been reported using single NV centers in nanodiamonds surrounded by a lipid bilayer [103] as well as with Gd compounds bonded to bulk diamond [195]. Relaxometry with NV centers has also enabled the detection of ferromagnetic proteins in ambient conditions [251, 252]. In addition, $T_1^{(0)}$-based imaging of Gd-tagged cellular structures has been demonstrated using ensembles of NV centers with a spatial resolution of 500 nm [220], where the resolution is limited by the use of wide-field optical detection.

For molecular scale imaging, improvements in the spatial resolution and sensitivity of relaxometry measurements are necessary. This goal can be achieved by using NV-based scanning probe techniques. Scanning probes have already enabled nanoscale magnetic imaging using a variety of detection schemes; including static stray field imaging [66, 36, 253, 254], double electron-electron resonance (DEER) [179], and proton magnetic resonance imaging [73, 72]. Relaxometry has the advantage of directly sensing electron spins, which have a magnetic moment nearly three orders of magnitude larger than pro-

tons spins sensed in NMR. In addition, relaxometry allows for the measurement of spins with T_{1e} times too short for DEER detection. Thus far, scanning $T_1^{(0)}$, or more generally T_1, relaxometry imaging has remained a challenge due to the requirement of stable, shallow NV centers with long T_1 times, coupled with the lengthy data acquisition times and associated scanning probe drift during the measurement. In this work, we overcome these challenges and perform two-dimensional NV relaxation imaging of a nanoscale volume of Gd electronic spins attached to an atomic force microscope (AFM) tip with 20-nm resolution. Furthermore, we show that with reasonable improvements this technique is capable of the sensitivity required to image a single isolated Gd spin.

6.2 NV spin depolarization due to magnetic fluctuations

The detection scheme for NV relaxometry in this chapter is all-optical; the NV center is polarized into the $|m_s = 0\rangle$ state of the ground state triplet with a non-resonant green laser pulse, and read out via spin-dependent photoluminescence during a subsequent laser pulse a time τ later, [11] as depicted in Fig. 6.6(a). During the dark time τ, the NV polarization relaxes to an equilibrium mixed state of $|0\rangle$, $|+1\rangle$ and $|-1\rangle$ with a characteristic time of $T_1^{(0)}$. In the presence of Gd a distance r from the NV, the NV $T_1^{(0)}$ is reduced according to the expression

$$\left(T_1^{(0)}\right)^{-1} = \left(T_{1,\text{int}}^{(0)}\right)^{-1} + \Gamma_{\text{Gd}}(r), \tag{6.1}$$

where $\left(T_{1,\text{int}}^{(0)}\right)^{-1}$ is the intrinsic NV relaxation rate in the absence of Gd and $\Gamma_{\text{Gd}}(r) = 3\Omega_{\text{Gd}}$ is the additional relaxation rate due to Gd. The NV is relaxed by magnetic fields perpendicular to its symmetry axis that appear static in the rotating frame, or equiv-

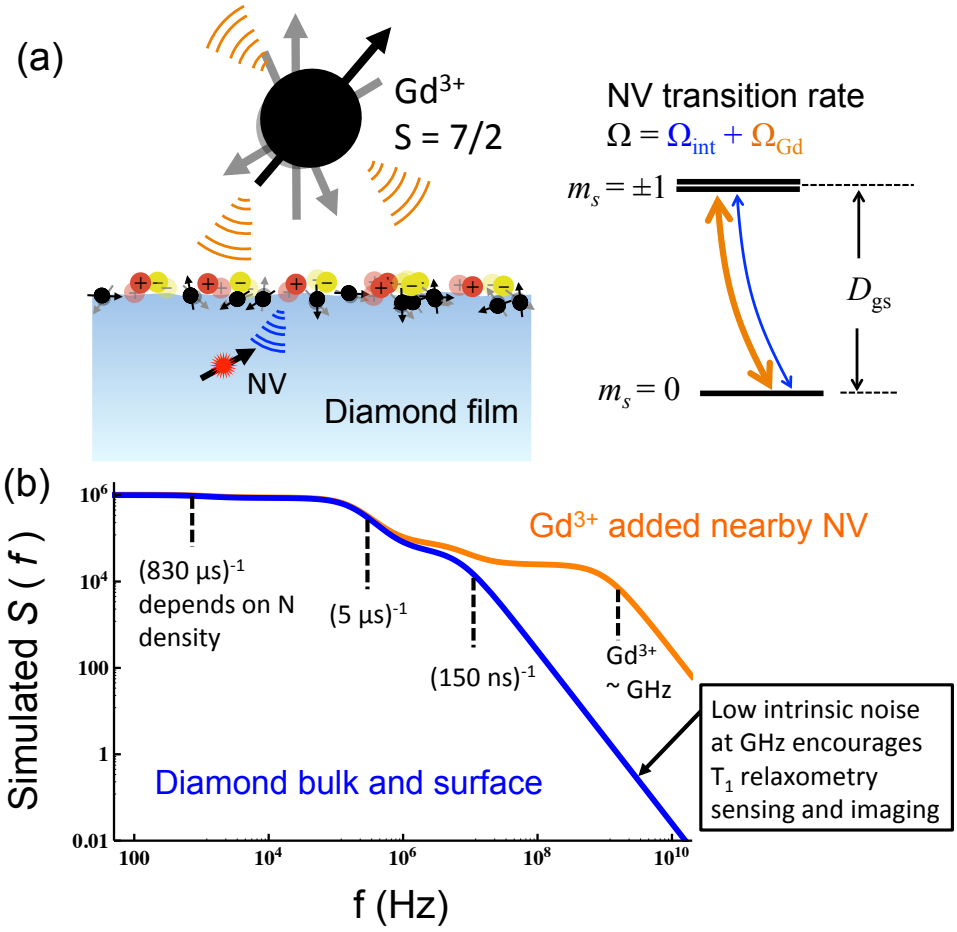

Figure 6.1: (a) Rapid spin relaxation of a Gd^{3+} electronic spin, near the diamond, causes magnetic fluctuations at an NV center close to the diamond surface. (b) Rough example of a simulated noise spectrum to demonstrate why Gd fluctuations can cause such a large effect on NV single-quantum spin relaxation. The blue curve is the noise spectral density due to summed bulk noise from P1 centers and two surface noise sources as determined by measurements in Chapter 4 and [87, 89, 86]. Since the NV Larmor frequency is typically tuned to $\sim D_{\mathrm{gs}}$ near zero applied magnetic field, the intrinsic NV depolarization time, $T_{1,\mathrm{int}}^{(0)}$, is long because the total noise contributions decay above MHz frequencies. The orange curve is the total noise spectral density including the effect of the Gd spin on the NV. Gd is expected to produce fluctuations with a high-frequency correlation time in the GHz regime, and therefore its noise power rises over the small presence of GHz-scale fluctuations from the noise sources considered in the blue curve.

alently, those that oscillate at the Larmor frequency $\omega_{\mathrm{NV}}/(2\pi) \approx 2.87$ GHz in the lab frame. Gadolinium has a magnetic noise spectral density that is broadened into the GHz range [220], and hence for sufficiently small r and sufficiently long $T_{1,\mathrm{int}}^{(0)}$, Γ_{Gd} can be of the same order or larger than $\left(T_{1,\mathrm{int}}^{(0)}\right)^{-1}$, leading to a detectable change in the NV $T_1^{(0)}$.

A large $\Gamma_{\mathrm{Gd}}(r)$ signal is expected because Gd is expected to have a noise correlation time of the order of nanoseconds or faster, which is of the same order as the NV Larmor frequency ~ 2.87 GHz. The exact Gd correlation time is not well known for Gd applied to the diamond or tip. For our simulations in this chapter, we make an estimate of $\tau_c \sim 0.4$ ns based on prior EPR literature [241]. Figure 6.1 shows a schematic and example noise spectrum demonstrating why the depolarization signal of the NV near Gd can be so large. Other surface noise sources, as studied in the previous chapters, have decaying noise power at frequencies larger than a few MHz, which is why $T_{1,\mathrm{int}}^{(0)}$ is long even for quite shallow NVs.

The spectrum shown in Fig. 6.1(b) is a semi-quantitative estimate to demonstrate the concept of Gd detectability by NV relaxometry, and the spectrum is not particular to only relaxation measurements since magnetic fluctuations occur in the NV z axis as well. Concerning dephasing, since the Gd spin correlation time is so short, its broad distribution of noise power leads to a low presence of Gd-induced noise at kHz frequencies that would dominate the dephasing rate $1/T_d$, and by extension T_2. Thus, Gd should have a significantly lesser effect on the dephasing contribution to T_2 [220] than it does on $T_1^{(0)}$, even if many dynamical decoupling pulses are used to push the dephasing filter function up to a few MHz.

Of course, if $T_1^{(0)}$ were reduced by orders of magnitude by Gd-induced noise, then direct NV spin relaxation may actually end up dominating its T_2. The dephasing rate can also increase but will be difficult to untangle from the relaxation rate in a T_2 measurement, especially when the timescales become very short, as we see in the next section.

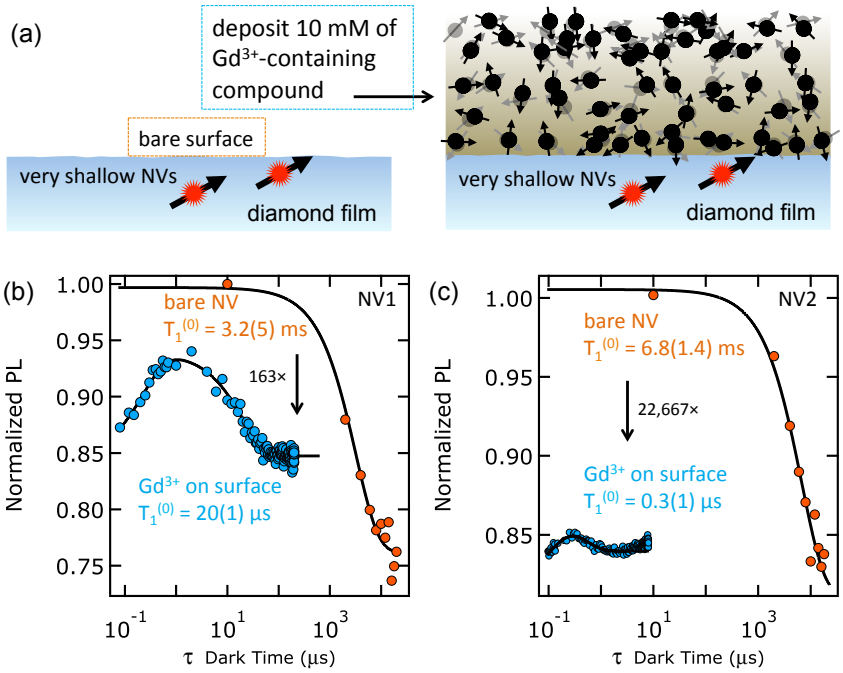

Figure 6.2: NV relaxometry of gadolinium spins placed on the diamond surface. (a) Cartoon of the experiment with a bare as-cleaned diamond surface (left) and the same surface deposited with 10 mM of Magnevist. (b,c) Relaxation data for NV1 and NV2 before (orange) and after (blue) depositing Gd spins. Both experience several orders of magnitude decrease in $T_1^{(0)}$. The fits to data are a biexponential accounting for both spin relaxation and depopulation of the metastable state $T_m = 240(30)$ ns and 130(50), respectively. All uncertainties are one standard error from the fit.

6.3 NV relaxometry of Gd spins on the diamond surface

We first performed a simple non-scanning relaxometry experiment to determine the maximum reduction in $T_1^{(0)}$ that could be expected from a given concentration of Gd spins placed extremely close to the NVs. Figure 6.2 shows the experiment to measure $T_1^{(0)}$ of very shallow delta-doped NV centers (D237a: nominal depth 3 nm by growth rate). The intrinsic relaxation times of the two NVs studied in this film were both of the order 3-6 milliseconds as fit by a single exponential $\mathrm{PL}(\tau) = \mathrm{y_0} + \mathrm{C}\exp\left[-\tau/\mathrm{T}_{1,\mathrm{int}}^{(0)}\right]$ with offset y_0 and contrast C. We deposited a solution containing a compound Magnevist that

contains a chelated Gd solution (Gadopentetate dimeglumine in water: Magnevist) at a rather high concentration of 10 millimolar. The solution was set to evaporate and the diamond was placed in the confocal microscope of Magnetometer A. The relaxation rates of both NVs increased by several orders of magnitude, so much that the optical pumping process begins to compete with the spin relaxation. Optically excited population that relaxes from the orbital $m_s = -1$ state must take the spin non-conserving route through the metastable singlet states, which typically requires a few-hundred nanoseconds before decaying into the ground $m_s = 0$ state. Therefore, we fit these data (blue circles in Figs. 6.2(a,b) to a biexponential [85] where one process populates the $|0\rangle$ state population at a rate $1/T_{\mathrm{m}}$ and the other process depletes the $|0\rangle$ state population at a rate $1/T_1^{(0)}$:

$$\mathrm{PL}(\tau) = \mathrm{y}_0 + \mathrm{C}_1 \exp\left[-\tau/\mathrm{T}_1^{(0)}\right] - \mathrm{C}_{\mathrm{m}} \exp\left[-\tau/\mathrm{T}_{\mathrm{m}}\right] \tag{6.2}$$

where C_1 and C_{m} are contrast fit parameters similar in magnitude. It is clear, particularly for NV2, that the magnetic noise from Gd has an enormous effect on the spin relaxation rate. The $T_1^{(0)}$ reduced from a bare value 6.8(1.4) ms to 300(100) ns, over four orders of magnitude, such that the spin relaxation depletes the $|0\rangle$ state as quickly as it is populated by the metastable state once the initialization laser pulse is turned off. NV1 and NV2 are both ^{15}NVs, so they are both highly likely to reside in the shallow nitrogen delta-doped layer. Furthermore, the NVs are separated laterally by just a few microns, so the reason for their large difference in final $T_1^{(0)}$ values (20 μs versus 300 ns) is quite likely to be a difference of a few nanometers in depth instead of variations in Gd concentration. We found in Chapter 4 that nitrogen delta-doping has some spread of a few nanometers for a single delta-doped layer and moreover, that depth on the nanometer scale critically determines the magnitude of surface noise felt by the near-surface NV. It is interesting, however, that both NVs had quite long $T_{1,\mathrm{int}}^{(0)}$ values given their expected 3-nm depths

in comparison to Chapter 4 data in Fig. 4.10 that shows reduction of $T_{1,\mathrm{int}}^{(0)}$ as depth decreases. In fact the "shallower" NV2 here had a longer $1/T_1^{(0)}$.

These simple diamond-surface relaxometry measurements highlight a few key points that direct the scanning probe experiments. First, it is possible to reduce the relaxation time by 2-4 orders of magnitude with 10mM of Magnevist if the $T_{1,\mathrm{int}}^{(0)}$ is milliseconds. This large change is a promising benchmark for obtaining an acceptable PL signal-to-noise ratio in a point-by-point imaging experiment. Second, if $T_1^{(0)}$ becomes 10s of microseconds or shorter then the contrast also begins to reduce due to metastable state depopulation being "too slow" to completely keep up with the spin relaxation. This contrast change is a challenge if one attempts a fixed-τ imaging measurement as discussed later because $T_1^{(0)}$ is more difficult to quantify from a single point if contrast (*i.e.,* maximum polarization difference) also reduces in addition to the depolarization rate increasing. As we show, we overcome this contrast challenge by measuring at several short τ points to obtain an image of $T_1^{(0)}$. Third, when using pulsed ESR measurements to detect an incoherent noise signal, as with T_1 changes, one must be careful to understand whether the effect actually arises due to the expected target sample phenomena or another noise source. For example, in the case above we cannot conclusively say, without further independent depth measurements, whether the difference in final $1/T_1^{(0)}$ of the two NVs is due to nanometer-scale variations in Gd density near the NV or due to differences in NV depth. Nevertheless, by virtue of the 2.87-GHz zero-field splitting of the NV, the all-optical relaxometry technique provides sensitivity of the NV to fast GHz-scale electronic-spin fluctuations that are undetectable by methods of coherent phase accumulation.

6.4 Scanning NV relaxometry

6.4.1 Determination of a candidate NV sensor

For the scanning probe magnetic noise-imaging experiments described in the next section, we desired to have an estimate of the NV depth to the nanometer scale,. Therefore, we again performed relative-depth calibration using the methods developed in Chapter 4. The diamond film used in this work, named B001c, was grown with the nitrogen delta-doping method of Chapter 3, and details are in Appendix A.

Magnetometer A was used for the depth imaging measurement shown schematically in Fig. 6.3(a). Delta-doped ^{15}NVs of one common crystallographic orientation were selected so that the resonance slices would have identical shapes. The shallowest NV centers used in the present work are $8-10$ nm below the diamond surface, as determined by prior work on magnetic resonance depth imaging [87], and typical measured $T_{1,\mathrm{int}}^{(0)}$ times are about $1-4$ ms at room temperature. The procedure for the magnetic depth imaging was the same as used for the previous depth measurements shown in Chapter 4. In this second data set, analysis and data visualization was simplified by imaging (y, z) resonances slices with a consistent z range from NV to NV. Two z ranges were used, a shallow or deep one, a choice that depended on the diameter of the (x, y) resonance ring used for the alignment procedure summarized in Fig. 6.3(b). The set of three images per NV was repeated for 12 ^{15}NVs over a continuous time of 25 hours.

Figure 6.3(c) shows the resonance slice images for the investigated ^{15}NVs in B001c, sorted from shallowest to deepest by relative depth image registration calculations. The shallowest NVs were assigned a likely absolute depth based on previous findings shown for B001a in Chapter 4. For B001c, no T_2 measurements or proton sensing experiments were done, so this assignment of absolute depth is purely a guide implied by the B001a results, and the error margin of absolute depth is $\sim \pm 2$ nm. This number is important

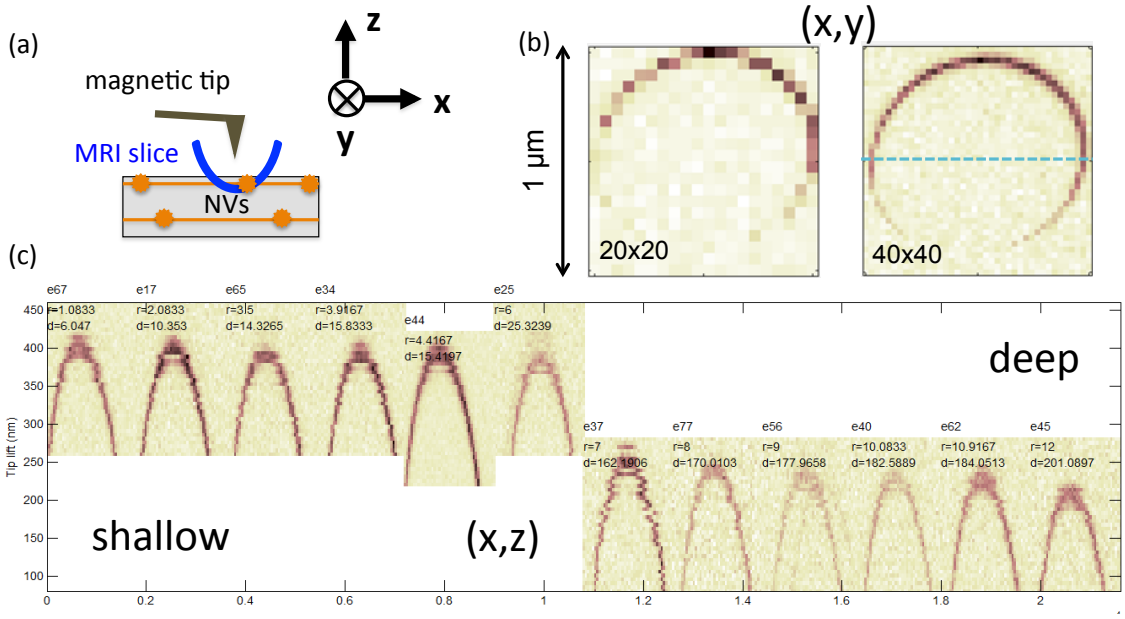

Figure 6.3: Nano-MRI depth imaging of NVs in sample B001c for selecting a near–surface sensor. (a) Simplified schematic of the experiment shown in Chapter 4, where a sharp magnetic tip images the relative depths of NVs in the diamond via a magnetic field gradient that shifts the NV into resonance with a fixed-frequency microwave field, lowering its emitted PL. (b) Rough x, y alignment scan (left) and finer scan while in tapping feedback of the sample. The scans are 1×1 μm^2 in size. The resonance slice ring is fit to a circle and a line cut made through the center along the x axis. The x-axis cut was chosen because the image is harder to resolve along the y axis as the highest gradient occurs at the bottom ($-y$). (c) A x, z scan is done along the line cut for 12 NVs. The images here are registered to every other image and sorted left to right by shallowest to deepest ranking r. The technique measures relative depths, so d is the estimated depth using a likely absolute depth offset based on absolute results from Chapter 4. Imperfections are seen in some image pixels, but the image registration algorithm compares the entire images, so relative depths are more precise than a by-eye comparison might indicate.

mainly for simulating the expected magnetic signal from Gd^{3+} spins at the position of the NV. We selected the shallowest few NV centers to use as individual sensors in the scanning probe Gd imaging experiments described below.

6.4.2 Experimental setup: Magnetometer B

As depicted schematically in Fig. 6.4, the scanning probe setup Magnetometer B combines a top-down tuning fork-based AFM, a top-down confocal microscope, and bulk diamond containing NV centers near the surface.[1] The custom AFM probe is constructed from a tuning fork with a tapered glass fiber glued to one tine and the other tine fixed to the mass of the setup. Figure 6.4(a) describes the attachment of a commercial silicon tip to the probe. Gadolinium is attached to the silicon AFM tip by submerging the cantilever in a Gd solution (Magnevist, concentration 30 mM) for several minutes. Experiments are performed at ambient conditions and in the absence of an applied static magnetic field. During the measurement, the AFM is operated in tapping mode with a tapping amplitude of 1 nm RMS. Figure 6.4(b) shows a photon-count image taken as a single NV is scanned under a fixed silicon tip. Again, the confocal spot is also galvo-positioned to follow the NV. The signal of this imaging technique does not depend on the presence of Gd at the tip, rather we believe it occurs due to a change of the dielectric environment near the shallow NV due to the presence of the silicon, which changes the pattern of emission. The image serves as a method to quickly assess lateral drift in the system during a longer image acquisition for Gd spin detection, as described in the next sections. The topography height image itself (not shown) is flat on the nanometer scale since the

[1]This all-top-down approach was the first configuration style of Magnetometer B, which is not described in Chapter 2, and it was used only for these Gd imaging experiments. Differences from the more recent setup include a lower-NA objective, since the AFM tip must fit between the sample and objective, and, as indicated in Fig. 6.4, this geometry causes partial occlusion of the NV with the tip. In addition, the diamond here is on the three-axis AFM scanning stage (MCL LP-100) while the tip is fixed during imaging. Therefore, as with Magnetometer A operation, the laser galvo mirrors must scan to follow the single NV as the diamond scans under the fixed tip.

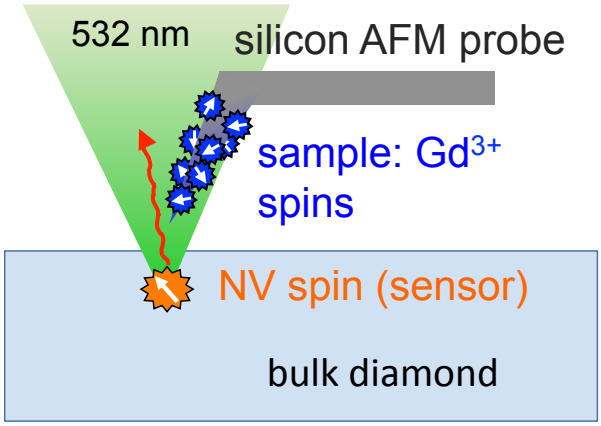

Figure 6.4: Schematic of the scanning relaxometry measurement. A silicon AFM tip is coated with Gd compounds (Magnevist) and scanned near a shallow nitrogen vacancy center in single-crystal diamond. A confocal microscope excites and polarizes the NV spin with a laser power of 437 μW, and detects red photoluminescence to read out the NV spin polarization. This configuration allows for sensing a change in NV spin relaxation rate due to nearby Gd.

diamond was grown in step-flow mode and was not subsequently etched.

6.4.3 Imaging Gd spins via NV relaxometry

We first show that positioning the Gd-coated tip in nanoscale proximity to a shallow NV center can reproducibly change its relaxation time. Figure 6.6(b) shows the $T_1^{(0)}$ relaxation curves for a single NV at two tip positions; centered above the NV center (blue) and 5 μm laterally displaced from the NV (orange). At a tip-NV separation of 5 μm, the tip is sufficiently far away such that $T_1^{(0)} = T_{1,\text{int}}^{(0)}$. By positioning the tip within tens of nanometers of the NV, we observe an almost three orders of magnitude reduction in $T_1^{(0)}$, from 4.4 ms to 8.8 μs. This measurement can be cycled with consistent results, which provides verification that the surface is not becoming contaminated with Gd, and that the tip retains its integrity; both are critical requirements for faithful imaging. In addition we repeated the experiment several times with sharp and blunt bare-silicon AFM tips and no change in $T_1^{(0)}$ was observed (see also Chapter 7).

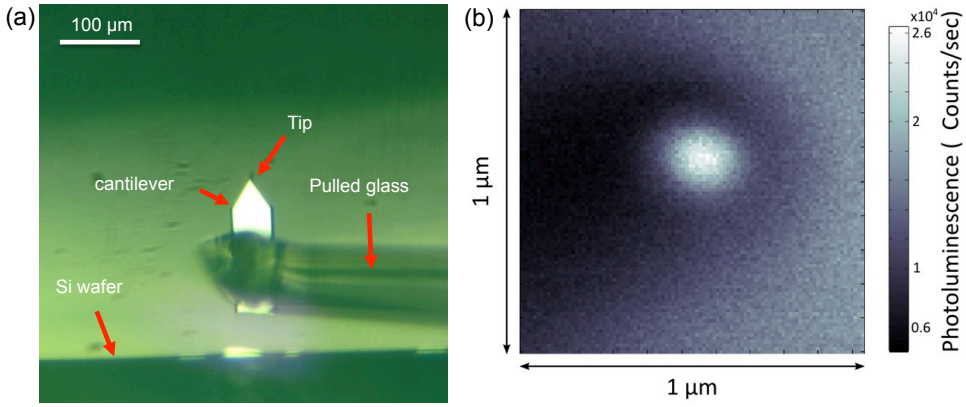

Figure 6.5: (a) Top-down micrograph of the tip attachment process. A pulled glass fiber, glued on one end to a tuning fork (not shown), is dipped in glue and then micromanipulated on to the cantilever of a commercial silicon AFM probe. Once the glue cures, the cantilever is broken off and the assembly is transferred to the NV magnetometer. (b) Topographic scan result showing the NV PL channel as an NV scans under the fixed tip. The tip occludes the optical path in some regions (dark) while close to directly over the NV there is a near-field enhancement effect of the silicon tip on PL. This type of subdiffraction image is acquired much faster than a spin relaxometry image (few minutes rather than hours), so it is repeated before every pixel of the relaxometry image to assess and correct the lateral tip-NV drift.

The measurement of the full relaxation curve shown in Fig. 6.6(b) can take many hours, limited mainly by photon shot noise, which is impractical for imaging experiments. Data acquisition time is of heightened importance for two- or three-dimensional imaging, as the number of data points scales rapidly as the spatial resolution is increased. Furthermore, it is difficult to keep the tip-NV separation stable in ambient conditions with traditional AFM techniques over these time scales, due mainly to thermal drift. To reduce data acquisition time and mitigate measurement errors induced by thermal drift, we sample only a small subset of τ points on the curve in Fig. 6.6(b) when imaging. The set of τ points we use is judiciously chosen to maximize the signal-to-noise ratio (SNR). It is straightforward to show that the SNR is maximized for a fixed τ approximately equal to $T_1^{(0)}$. However, when performing scanning measurements, $T_1^{(0)}$ can vary across the sample by many orders of magnitude, and hence different τ values optimize the SNR at different positions in the scan.

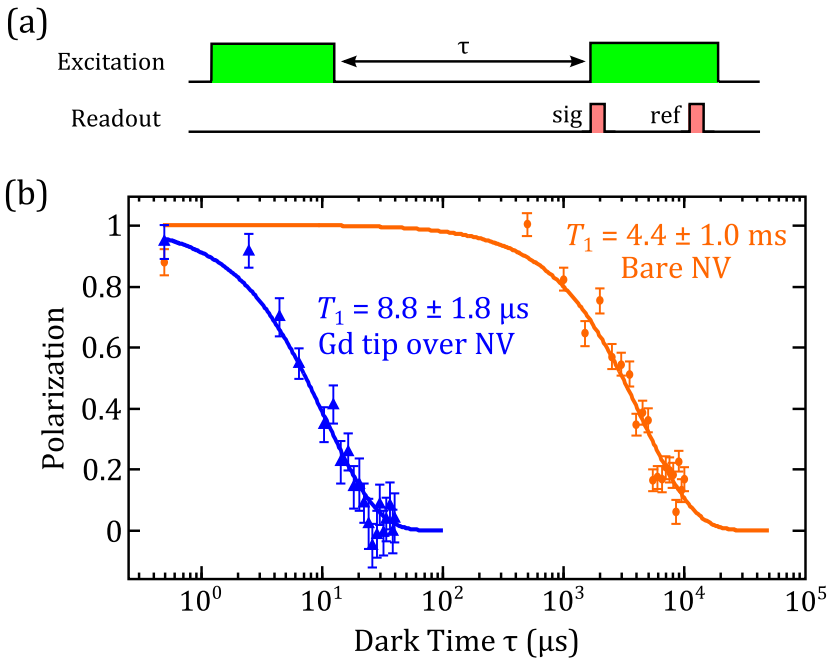

Figure 6.6: (a) Pulse sequence used to measure the $T_1^{(0)}$ relaxation time, where the dark time τ is varied. Each signal pulse has a duration of 350 ns, and is followed by a reference pulse after a delay of 2.5 μs. The dark time τ does not include a 500 ns dark time after the initialization pulse, which allows for full depopulation of the metastable state. (b) Measurement of spin relaxation of a single NV center with the Gd-coated AFM tip positioned over the NV center (blue triangles) and moved 5 μm away (orange circles). The vertical axis is plotted in terms of NV polarization, with a polarization of 1 referring to the NV in the $|0\rangle$ state, and a polarization of 0 referring to the NV in an equilibrium mixed state of $|0\rangle$, $|+1\rangle$ and $|-1\rangle$. The data is best fit to an exponential decay (solid lines) with a single decay constant $T_1^{(0)}$.

A two-dimensional map of the NV $T_1^{(0)}$ versus tip position is presented in Fig. 6.7. There is a clear and highly localized reduction in $T_1^{(0)}$ near the center of the scan that indicates the location of closest approach between the Gd-coated tip and the NV center. As expected, the $T_1^{(0)}$ increases as the tip-NV separation is increased until the original $T_{1,\text{int}}^{(0)}$ of the NV center is observed along the periphery of the scan area. The observation of $T_{1,\text{int}}^{(0)}$ is important because it indicates that there is no significant Gd contamination on the diamond surface during the scan. To mitigate thermal drift, observed to be approximately 1 nm/min, after each pixel an image registration algorithm [255] was used to realign the tip with the NV center. The alignment image was provided by the near field optical profile of the NV photoluminescence (PL) in the presence of the tip, which allowed for a reproducible alignment with a maximum error of 10 nm.

The image in Fig. 6.7 is compiled from a set of measurements with τ = [4, 8, 40, 80, 400, 800] μs, which span the range of $T_1^{(0)}$ times accessible in the scan area. To generate a $T_1^{(0)}$ image from the fixed τ measurements, a fit to an exponential decay is performed for the data taken at each fixed τ. The $T_1^{(0)}$ times extracted from the six fixed τ measurements are then averaged, weighted by the error in their respective fit, to arrive at a final $T_1^{(0)}$ time that is plotted in the image. The $T_1^{(0)}$ exponential fit is complicated by the dependence of the measured PL on tip position, due to a combination of shadowing and near field effects from the tip, and a reduced PL when $T_1^{(0)}$ becomes comparable to the sub-μs metastable state relaxation time [85]. Therefore, at each tip position the steady-state PL reference under laser excitation is measured and included in the $T_1^{(0)}$ fit.

Figure 6.8(a) shows a one-dimensional line cut of a single $\tau = 8$ μs measurement in Fig. 6.8 taken through the location of the NV center. In order to maximize the SNR when the tip is near the NV, we chose this fixed τ value to be around 8.8 μs, the expected $T_1^{(0)}$ when the tip is near the NV from Fig. 6.6(b). Plotted on the vertical axis is the percentage change in PL at each tip position. This change, defined as [PL(sig)/PL(ref) $-$ 1] and

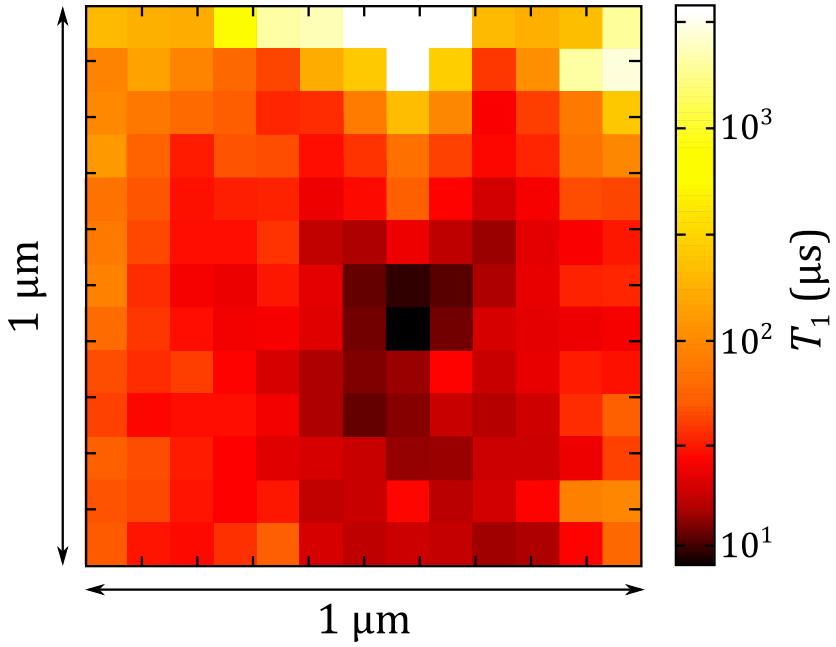

Figure 6.7: Two-dimensional map of the $T_1^{(0)}$ relaxation time of the NV center versus Gd-coated tip position. The $T_1^{(0)}$ times were inferred from fixed τ measurements with $\tau = (4, 8, 40, 80, 400, 800)$ μs at each pixel. The distinct reduction in $T_1^{(0)}$ in the center of the image indicates the closest approach of the tip to the NV. The spatial resolution of the scan (75 nm per pixel) was chosen to limit the measurement time, a higher resolution line cut of the data is shown in Figure 6.6.

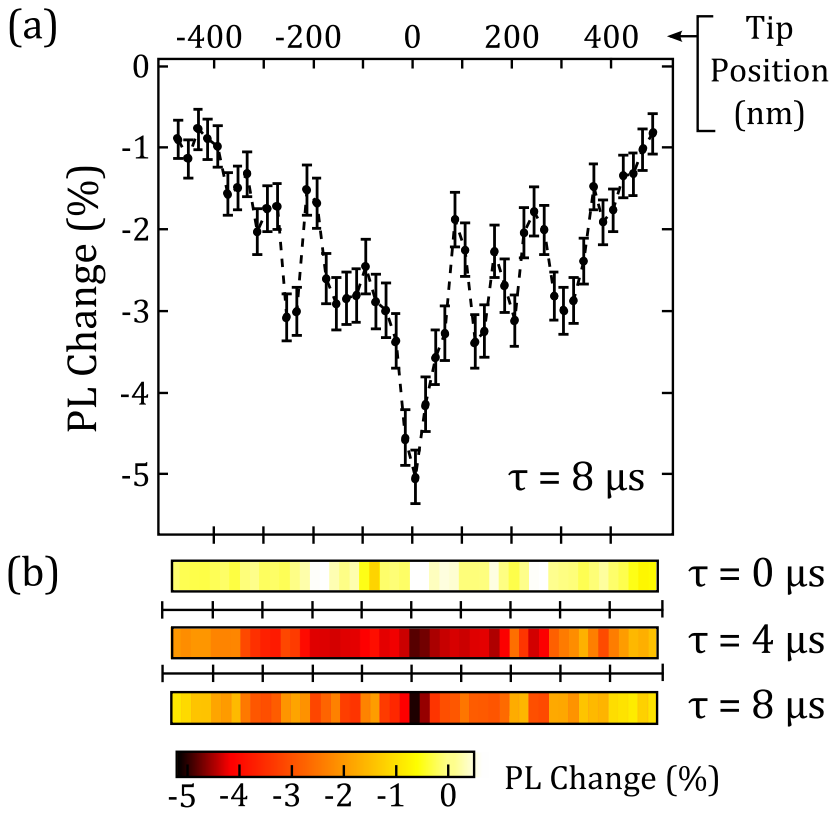

Figure 6.8: (a) One-dimensional line cut of the data in Fig. 6.7, showing the measured PL change for a fixed dark time $\tau = 8$ μs. The error bars are computed from two consecutive line scans with nearest-neighbor averaging, and are attributed to photon shot noise and tip drift. (b) Line scans for $\tau = (0, 4, 8)$ μs. There is no discernable contrast at $\tau = 0$ μs, but at longer τ there is a clear reduction in $T_1^{(0)}$ at the center of the line scan that depends sharply on tip position. The total data acquisition time at each tip position was 6 minutes.

heretofore referred to as contrast, is equal to zero if the NV is polarized in the $|0\rangle$ state, and becomes negative as the NV evolves into an unpolarized state. The one-dimensional color plots in Fig. 6.8(b) show how the fixed τ contrast changes with choice of τ. At $\tau = 0$ μs, the state of the NV is polarized at all tip positions, resulting in little contrast across the entire scan. Increasing τ to 4 μs begins to reveal contrast in the center of the line scan where the NV $T_1^{(0)}$ is the shortest, while the contrast remains near zero at the extremes of the line scan where $T_1^{(0)}$ is the longest. The contrast at the center of the line scan is further enhanced at $\tau = 8$ μs, where $T_1^{(0)} \approx \tau$.

6.5 Analysis of imaging results

Figure 6.9 plots $T_1^{(0)}$ as a function of tip position zoomed in to a 300-nm-wide region in the center of Fig. 6.8. In this case, $T_1^{(0)}$ is extracted from a fit to the $\tau = (4, 8)$ μs data shown in Fig. 6.8, as these fixed τ points provide the best estimate for $T_1^{(0)}$ in this range. The data show an approximately 50-nm-wide feature and importantly, from the slope of the feature edges, a spatial resolution estimated to be 20 nm. This spatial resolution is set by the 20-nm scan step size, which was chosen to be slightly larger than the combined effect of $\sim$ 10-nm AFM drift and $\sim$ 10-nm repeatability of the image registration algorithm used per point. Pushing to higher spatial resolution will require first an improvement in the AFM drift during the measurement, and eventually shallower NV centers.

6.5.1 Simulation of magnetic signal from Gd spins

The 50-nm-wide plateau of reduced $T_1^{(0)}$ in the center of Fig. 6.9 represents a region of the tip with locally enhanced Gd concentration over a background, the densities of which can be estimated from a simulation shown in the red trace. The discrete model

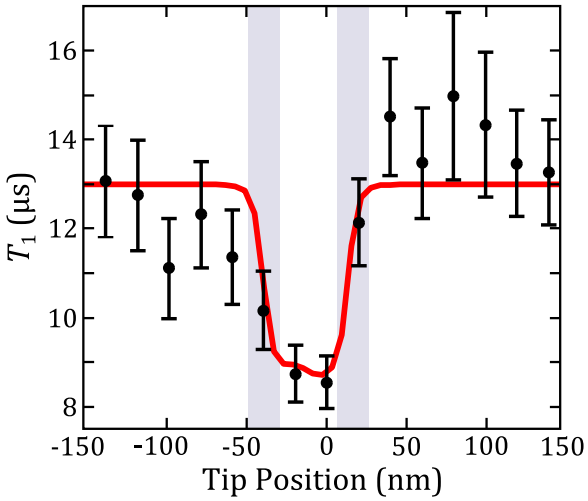

Figure 6.9: Extracted $T_1^{(0)}$ times from the data presented in Fig. 6.8. A spatial resolution of 20 nm is deduced from the change in $T_1^{(0)}$ versus tip position in comparison to the magnitude of the vertical error bars. The shaded blue regions are 20-nm-wide as a guide to the eye. The data is modeled by a simulation that computes, as a function of scan position, the magnetic field from a finite 50 nm × 50 nm surface of Gd. The result (red solid line) indicates a Gd density of 10.7 spins/nm^2 for an NV depth of 10 nm.

for our simulation places a two-dimensional layer of Gd ions on a plane and computes the magnetic field the NV would experience from the ensemble of Gd spins at each scan position [103]. Assuming the Gd samples all $\{|m_s\rangle\}$ in the $S = 7/2$ Hilbert space in a thermal mixture with equal spin populations, we compute the mean square perpendicular magnetic field the NV experiences from each Gd spin, $\left\langle [\mathbf{B}_\perp(\mathbf{r})]^2 \right\rangle$. In this expression, $\langle \ldots \rangle$ denotes a mean square average over the $\{|m_s\rangle\}$ subspace taken by a trace over the density matrix of the mixed state. The magnetic field from a single Gd spin is given by

$$\mathbf{B}(\mathbf{r}) = \frac{\mu_0}{4\pi} \frac{g_{\mathrm{Gd}} \mu_B}{|\mathbf{r}|^3} \left[\mathbf{S} - \frac{3\mathbf{r}(\mathbf{r} \cdot \mathbf{S})}{|\mathbf{r}|^2} \right], \tag{6.3}$$

where $\mathbf{S}$ is the Gd electron spin vector, $g_{\mathrm{Gd}} = 2$ is the Gd electron g-factor, and μ_B is the Bohr magneton. The NV relaxation rate due to the fluctuating field of a single Gd spin at position $\mathbf{r}$ is modeled by an Ornstein-Uhlenbeck process, (see Chapter 4 for similar

spin noise analysis), and is given by

$$\Gamma_{\mathrm{Gd}}(\mathbf{r}) = 3\Omega_{\mathrm{Gd}}(\mathbf{r}) = \frac{3\tau_c\gamma_{\mathrm{NV}}^2}{1+\omega_{\mathrm{NV}}^2\tau_c^2}\left\langle[\mathbf{B}_\perp(\mathbf{r})]^2\right\rangle, \tag{6.4}$$

where $\gamma_{\mathrm{NV}} = 2\pi \times 28$ GHz/T is the NV electron spin gyromagnetic ratio, and τ_c is the effective correlation time of the Gd noise spectrum, taken to be 0.36 ns [256]. The factor of 3 in Eq. 6.4 is from the existence of two transitions $|0\rangle \leftrightarrow |\pm1\rangle$ that occur at equal rates $\Omega_{\mathrm{Gd}}(\mathbf{r})$ for the small applied magnetic field of order few Gauss (see discussion of population relaxation rates defining $T_1^{(0)}$ in Chapter 5). With a 10-nm-deep NV, the simulation result in Fig. 6.9 predicts a background concentration of 7.2 ± 0.2 spins/nm^2, with an additional 3.5 ± 0.2 spins/nm^2 in a 50 $\times$ 50-nm region of the tip, which reduces $T_1^{(0)}$ from 13 μs to 8.8 μs at the center of the line scan. At the tip position that yields the shortest $T_1^{(0)}$, the simulation predicts that 70% of the measured $T_1^{(0)}$ reduction is a result of the magnetic field generated by 2320 ± 30 Gd spins.

6.5.2 Spatial resolution and sensitivity

We now turn to a more detailed discussion of spatial resolution and sensitivity, which are intimately related in this experiment. In particular, we focus on the goal of imaging a single Gd spin. Thermal AFM tip drift during the measurement can have dramatic effects, as is evidenced by the simulation results shown in Fig. 6.10. Plotted are one-dimensional $T_1^{(0)}$ images simulated with different magnitudes of tip drift for a single Gd target spin, a 3 nm deep NV center and $T_{1,\mathrm{int}}^{(0)} = 1$ ms. To calculate these results, first the dependence of $T_1^{(0)}$ on tip position is calculated in the absence of drift, shown as the red trace with the largest dip in Fig. 6.10. When drift is encountered experimentally, the result will be a sampling of many tip positions during the measurement, which serves to blur out the effect of the Gd spin. This can be modeled by taking a sampling of

$T_1^{(0)}$ times around each tip position, with a spatial width equal to the magnitude of the drift during the acquisition time for each measurement point. We can then sum the exponential decay curves of each $T_1^{(0)}$ time in the sampling area to represent the curve that would be measured experimentally. Although this curve is a sum of exponential decays with different time constants, we can do a least squares fit to a single exponential decay with one time constant to obtain an averaged $T_1^{(0)}$ response. Carrying out this procedure for different drift magnitudes of $(5, 10, 20)$ nm shows a stark reduction in the predicted $T_1^{(0)}$ response as drift is increased, evident on a log scale. Notably, the shortest measured $T_1^{(0)}$ time decreases from 145 μs with 20 nm of drift to 0.50 μs with no drift. Using the current experimental parameters of a 10-nm-deep NV, $T_{1,\text{int}}^{(0)} = 4.4$ ms, 10 nm of drift per measurement point, and 70 kCounts/second of photon counts from the NV center, we can use the simulation results to predict a single spin sensitivity that accounts for thermal drift. Under these conditions with a single Gd spin, one predicts a minimum $T_1^{(0)}$ time of 715 μs, and a SNR of 1 to be reached in 30 seconds of averaging time.

To reach the goal of imaging single Gd spins we address several areas for improvement, namely shallower NV centers, reduced thermal drift, and improved photon collection. Using shallower NV centers would provide a much larger signal, since $\Gamma_{\text{Gd}}(r) \sim r^{-6}$ for a single Gd spin. Thermal drift, estimated to be about 1 nm/min in this work, can be reduced by using active drift compensation at the expense of measurement complexity, which has been shown to improve drift to 5 pm/min in ambient conditions [257]. Operating at cryogenic temperatures can also reduce drift significantly, but also at the expense of measurement complexity and incompatibility with biological systems. Photon shot noise can be improved by increasing the number of counts from the NV center. In the current geometry, the AFM tip and objective are on the same side of the diamond sample, which leads to partial shadowing of the NV center by the AFM tip. Using a geometry where the objective and AFM tip are on opposite sides of the sample [87] would

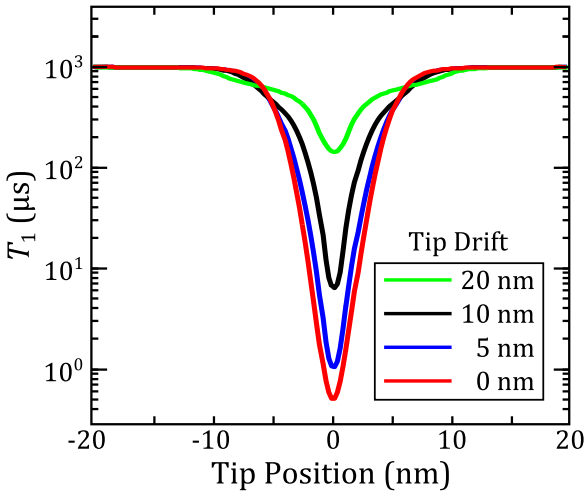

Figure 6.10: Simulated $T_1^{(0)}$ response to a single Gd spin for a 3 nm deep NV center with $T_{1,\text{int}}^{(0)} = 1$ ms, accounting for various magnitudes of tip drift during the measurement. The minimum $T_1^{(0)}$ time observed depends strongly on the size of the drift, increasing from 0.50 μs with no drift to $(1.04, 6.36, 145)$ μs with $(5, 10, 20)$ nm of drift, respectively.

improve the NV count rate, as well as allow for the use of an oil immersion objective with a large numerical aperture. Alternatively, collection efficiency can be dramatically improved by structuring the diamond with nanopillars, in particular by using an NV diamond nanopillar as the scanning probe [66, 179], though presently NV spin properties in such nanostructures are poor compared to those in bulk diamond.

We now estimate the sensitivity to a single Gd spin for optimized conditions of reduced drift, higher photon counts, and shallower NV centers based on the discussions above. Using a 3 nm deep NV, $T_{1,\text{int}}^{(0)} = 1$ ms to account for shorter $T_1^{(0)}$ times typically seen in shallower NV centers [87], 1 nm of drift per measurement point, and 120 kCounts/second from the NV center, one predicts a minimum $T_1^{(0)}$ time of 0.55 μs, and a SNR of 1 to be reached in 10 ms of averaging time. We note that these improvements are realistic: $2-3$ nm deep NV centers have already been demonstrated as external nuclear spin sensors [155, 81], and oil immersion objectives readily achieve such photon count rates.

6.6 Conclusions

Using the spin relaxation rate of a single NV center in diamond as a resource, we demonstrated two-dimensional scanning probe imaging of Gd spin labels attached to a sharp tip. We achieve a spatial resolution of 20 nanometers, limited primarily by drift of the scanning setup in ambient conditions and the precision to which we are able to correct for this drift. We estimate that the majority of the imaging signal arises from fewer than 3000 Gd spins. This result is the first demonstration of the feasibility of scanning relaxometry with NV centers, and our current and projected sensitivity calculations provide a roadmap for controllably detecting individual Gd electron spins with scanning probe microscopy. Potential improvements include improving signal-to-noise, through shallower NVs and diamond nanopillars, and spatially isolating target spin labels via chemical engineering of the sample. Furthermore, decoherence channels beyond the single-quantum spin flip may be used simultaneously to access other types and frequencies of noise, and these techniques can be extended to the nanoscale study of noise from various material surfaces.

Chapter 7

Towards single-spin imaging via scanning NV relaxometry

7.1 Introduction

In Chapter 6 we demonstrated relaxation imaging of Gd^{3+} electronic spins in a scanning probe experiment where the NV sensor is near the surface of a bulk and the Gd is on a sharp atomic force microscopy tip approached to the diamond. The signal imaged was due to a few-thousand Gd spins and the spatial resolution was 20 nm. This magnetic noise imaging technique can be enhanced considerably to reach the goal of single-spin sensitivity with nanometer spatial resolution and can also be extended to image different types of noise. The end goals of sensitivity and spatial resolution often go hand-in-hand because bringing the NV closer to target spins greatly increases the sensed magnetic field from a smaller and smaller volume of the target. Presented here are improvements we have made to the diamond materials, scanning probe configuration and stability, target sample preparation, and pulse sequences to enhance the sensitivity, spatial resolution, and versatility of the scanning probe magnetometer. We also emphasize that our top-down

approach of making diamond nanopillars with shallow NVs having few-millisecond-long spin relaxation times is critical to the sensitivity of these measurements of decoherence imaging because alternative sphere-like nanodiamonds house NVs with poor relaxation times of 1-100 μs [85, 103], likely due to higher proximal surface area.

First, we overview the changes to the scanning magnetometer from Chapter 6 to do wide-field-of-view nanoscale imaging and improve photon collection, temperature stability, drift, and tip-sample tilt. Second, we show the fabrication of nanoscale diamond pillars on CVD-grown diamond films containing NVs for enhancing the collection efficiency of the NV photoluminescence signal and enabling imaging of spatially extended samples. Third, we describe the fabrication of custom silicon scanning probes that have a wide flat tip for placing target samples to image via the diamond nanopillar sensors, including nanoscale magnetic structures, molecules, and thin films. Fourth, we show photoluminescence quenching and dc magnetic field imaging results over a wide field of view with nanometer-scale spatial resolution using this setup.

Finally, we present an experiment that advances the versatility of the NV decoherence imaging technique of Chapter 6 by using both the single-quantum relaxation and double-quantum relaxation pulse sequences developed in Chapter 5. These sequences allow probing of not just magnetic but electric field noise, which is present above many material surfaces, and we apply the full three-level relaxometry to image the distance dependence of electromagnetic noise from metallic surfaces. We find evidence that the spin relaxation time can actually be increased for NVs nanometers from metal with low electrical conductivity, and by extension the maximum relaxation-limited coherence time also increases. The scanning-NV metal relaxometry experiment also serves as a testbed for determining how close the NV sensor can get to the target sample, given practical challenges like tip-sample tilt, which will be helpful for the more ambitious target of sensitivity to single electronic spins in quantum decoherence imaging.

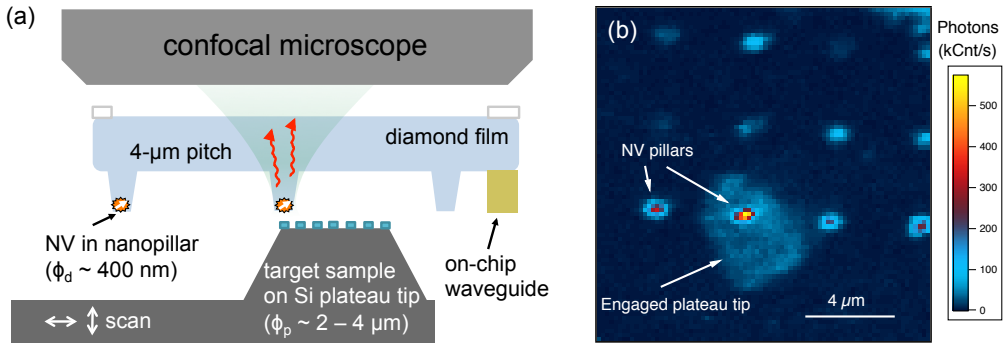

Figure 7.1: (a) Cartoon (not to scale) of the sample-on-tip magnetometry experiment with shallow NVs in diamond nanopillars. The pillars' lateral pitch is wider than the scanning tip's diameter so that the sample contacts a single pillar. (b) Confocal microscope image of an array of NV nanopillars on diamond sample B033, showing a relatively large plateau tip that is tapping (via tuning fork) on a single nanopillar.

7.2 Experimental setup

7.2.1 Scanning probe configuration

As shown earlier in the schematics of Fig. 2.12, there several choices for an AFM-based scanning NV magnetometer configuration. These are divided broadly into sample-on-probe and NV-on-probe, where "probe" is here taken to mean the smaller of the two objects that sits on a oscillating AFM cantilever. Here, we take the hybrid approach (Fig. 2.12(b)) of using a NV in a diamond tip and a scanning sample on a wide flat probe. That is, instead of fabricating a bulk diamond cantilever [66] or using a standalone nanodiamond [36], we pattern an array of a few thousand pillars on the bulk diamond chip. The advantage is that we can keep a single diamond sample in the scanning magnetometer setup with many potential NV sensors to choose from, and secondly, there are also fewer fabrication steps that may potentially affect the NV quality. The challenge is that the sample to be imaged must be prepared on a tip roughly narrower than the pitch of the diamond nanopillars (few microns) so that it only contacts one diamond nanopillar at a time. Thus, in this configuration we have the ability to compare several NV sensors

in situ directly on the same sample to be imaged, rather than testing an array of diamond sensor candidates with non-imaging measurements before the diamond-on-AFM is prepared and the sample is brought in. The sample-on-probe is also an appropriate choice for the ultimate goal of imaging single spins in a small ensemble of molecules since the sample does not need to extend over several microns. We simultaneously retain the diamond-nanopillar advantage of higher photon collection efficiency [78] and thus high sensitivity.

To build this setup configuration, the scanning probe magnetometer described in Chapter 6 was modified so that the optics and scanning probe addressed the NVs from opposite sides of the diamond, more in line with the design of Magnetometer A in Chapter 4. The recent photographs are shown in the Magnetometer B section of Chapter 2. This change avoids shadowing of the collection optics by any probe tip structures, and it allows for backside photon collection from diamond nanopillars, which is more efficient as dipole emission is preferentially guided through the diamond.

Figure 7.1(a) shows a schematic cartoon of the optics, diamond, and scanning stage arrangement. The dry objective is an Olympus UPLSAPO 40X2 with an NA of 0.95, working distance 180 μm, and a coverslip correction collar. The diamond chip is approximately 150 μm thick, and the objective collar is adjusted to roughly 0.12 to optimize the photon counts and three-dimensional resolution of confocal imaging through the backside [258]. The 2×2 mm^2 diamond is glued with UV curing adhesive to a sheet of Ti foil with a 1 mm hole. Care must be taken in gluing such that any gap between the diamond back surface and Ti is does not preclude the short-WD objective from imaging the front surface. The sample mount is fixed to a three-axis stepper motor system to translate the sample millimeters relative to both the objective and the scanning probe. Both the three-axis sample stage and independent nano-scanning stage are fixed to a manual two-axis platform to perform coarse alignment relative to the objective. Figure 7.1(b) shows

a confocal image of an array of NV-containing nanopillars and a plateau tip engaged on one of the pillars.

7.2.2 Diamond nanopillars with NVs as sensors

We fabricated NV-containing nanopillars on the surface of bulk diamond films for sample-on-probe scanning NV magnetometry. These pillars are designed in a way as to fulfill multiple goals: 1) guide emitted NV fluorescence at a smaller collection angle so that a higher fraction of the emitted photons reach the microscope objective, 2) preserve NV spin properties, and 3) act as a nanoscale AFM-like tip to reduce the separation between the NV and an extended (i.e., non-tip-like) sample that may have nanometer-scale surface roughness. These three are somewhat competing requirements because, for example, an ultra-sharp diamond tip of diameter $\phi_d < 100$ nm would be less likely to preserve NV spin properties or optical stability based on prior reports on small nanodiamonds [35, 85] and our findings on surface noise in previous chapters. Similarly, to yield a high fraction of pillars containing a single NV center one must plan the NV density in relation to the pillar diameter; a smaller diameter requires a higher areal density of NVs to maintain the same probability of the pillar containing a single NV, and when NV density gets too high spin properties suffer due to coupling to nitrogen P1 center spins or other vacancy defects [165, 140, 127]. A tested range of diameters in the NV literature is at least in the range 200-500 nm [78, 66, 171].

We made two diamond samples to test a similar range of nanopillar diameters, one with $\phi_d \approx 250$ nm (sample B031) and the other with $\phi_d \approx 400$ nm (sample B033). The procedure begins with a isotopically pure ^{12}C diamond film grown epitaxially on a 2×2-mm^2 single-crystal diamond plate. The growth process is described in Chapters 3 and 4, though here we do not use nitrogen doping during growth. Instead we use nitrogen

implantation with a low incident energy of 2.5 keV (B031) and 4 keV (B033) to form NV centers at a desired concentration at average depths 4.4 ± 1.5 and 6.6 ± 2.6 nm. These estimates were obtained from Stopping Range of Ions in Matter (SRIM) calculations. An overview of the nanopillar fabrication procedure follows:

1. Use standard metal deposition and contact lithography to etch Ti/Au microwave waveguides onto the diamond surface. These CPWs are for stable microwave spin control lines that do not obstruct the AFM access.

2. Securely adhere the diamond NV-side-up to a clean silicon chip by pressing it onto a layer of fresh resist on the silicon followed by baking on a hotplate.

3. Spin PMGI and PMMA for preparing a metal liftoff process for an etch mask.

4. Expose a grid of dots on the diamond using electron-beam lithography, and develop the PMMA and PMGI.

5. Evaporate 90 nm of Ti as the etch mask.

6. Do lift-off of the mask, leaving disks of Ti on the diamond.

7. Dry etch to the desired pillar height using O_2 or O_2/CH_4 ICP/RIE.

8. Inspect NVs in pillars by confocal microscopy and ODMR. The height can also be measured by SEM.

9. Remove the Ti etch mask completely by etching in Ti etchant or BHF.

10. Inspect flatness of pillars by SEM to ensure the Ti cap is removed.

SEM images of the first set of finished pillars containing NV centers are shown in Figs. 7.2 and for sample B031; note, the images were taken before removing the Ti mask that

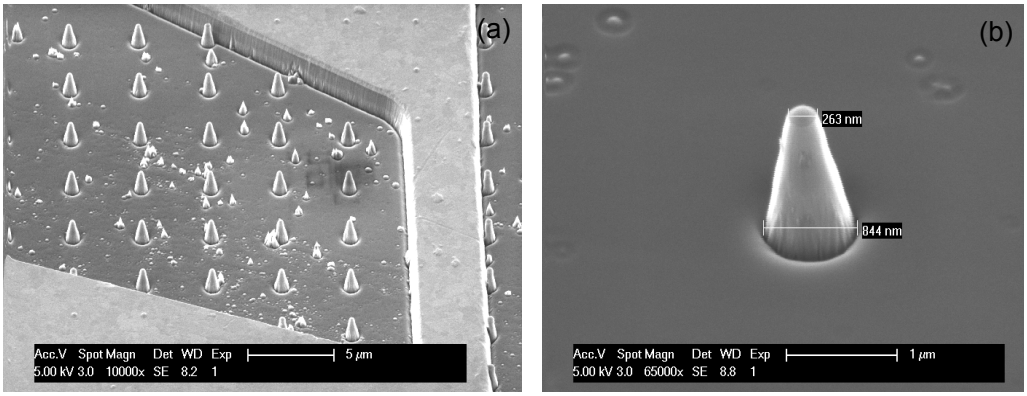

Figure 7.2: Scanning electron micrographs of narrow-diameter nanopillars etched on diamond sample B031. The heights are about 1.5 μm. The array shown in (a) have a pitch of 4 μm and are surrounded by a Ti/Au shorted CPW for microwave-driven spin rotations. (b) A close-up image of a single nanopillar. NVs in these pillars showed relatively short T_1 times of 50 μs to 400 μs after the diamond etching process.

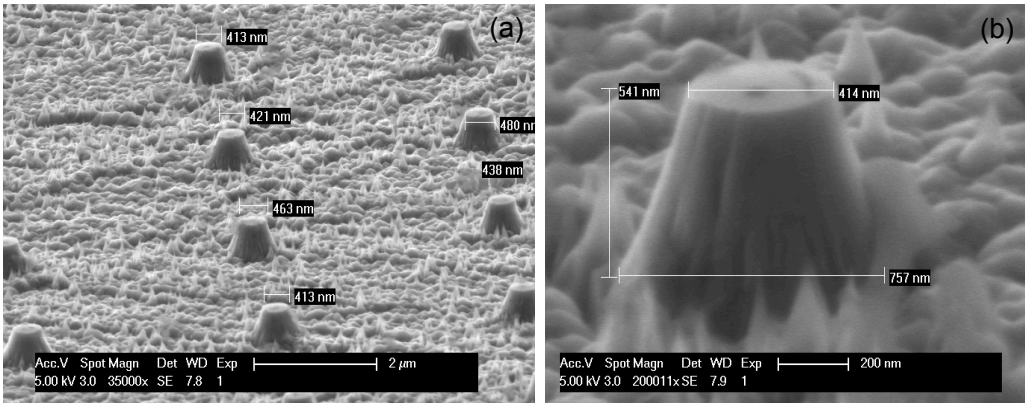

Figure 7.3: SEM images of broad-diameter nanopillars etched on diamond sample B033. The heights are less than 1 μm. The array shown in (a) has a pitch of 4 μm, and a close-up image is shown in (b). The shorter height is preferred for faster topographic AFM imaging since the z position does not need to change as rapidly as the tip scans in x, y, in comparison to pillars in Fig. 7.2. NVs in these pillars had long T_1 times of 1-5 ms, but it is not certain whether this improvement over B031 is due more to the nitrogen implantation depth or the diamond etching process.

makes the pillar top appear dome-shaped. The pillar diameters were about 260 nm at the top diamond surface. Etching of B031 was done with O_2/CF_4, and the field around the pillar is mostly smooth. Using Hanbury-Brown and Twiss measurements, as described in Appendix A, we can identify a sufficient number of pillars with quantum emission characteristic of a single NV center. At saturation excitation power, which was about 4 mW at the back aperture of the objective, we observe single-NV pillars with 600-1000 kCounts/s. We refer to prior detailed nanopillar studies [78, 171] for more information about typical yields and count rates for NV-containing nanopillars.

Here, we are most concerned with how the pillars preserve the NV spin properties, so that they can be used for scanning relaxometry imaging. In sample B031, we observed NV depolarization times $T_1^{(0)}$ of 1-2 milliseconds before the diamond pillar processing. We expect these tended not to be more than 3 milliseconds because the implanted NVs at energy 2.5 keV are quite shallow on average, about 4 nm. In Fig. 4.10 of Chapter 4, we showed evidence that $T_1^{(0)}$ decreases from as high as 7 ms in the bulk to around 1 ms for NVs doped at shallower depths. Nevertheless, B031 had relaxation times not much degraded from bulk values.

However, after diamond pillars were etched in B031, the typical $T_1^{(0)}$ times ranged from 50 μs to 250 μs, as shown in the histogram of measurements in Fig. 7.4.[1] The laser power is reduced to 30-60 μW for spin relaxation measurements to prevent laser-induced repolarization or other unknown effects to the surface at high laser power, which can be made lower than in in our prior scanning measurements without nanopillars [71]. We observed no improvement of the histograms in grids of these pillars at areas of the sample surface. These typical relaxation times did not improve after annealing in pure oxygen for 2 h at 450° C. Thus, we concluded that the pillar etching or other process step had

[1] Although spin relaxation measurements are generally slow due to the long delay times and low photon counts, the combination of excellent photon count rates from the pillars and the shorter relaxation times of the NVs enabled us to measure NVs in as many as 40 pillars in 1-2 days.

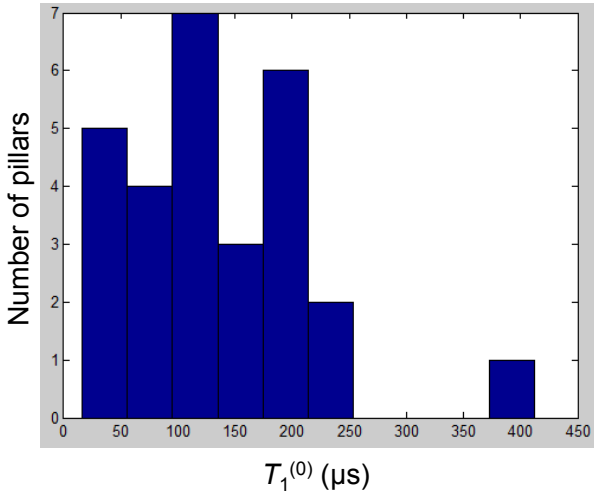

Figure 7.4: Histogram of spin depolarization times $T_1^{(0)}$ for NVs in 250-nm-diameter nanopillars on sample B031. The median is an order of magnitude smaller than the millisecond-long $T_1^{(0)}$ times measured in the sample before etching pillars. The particular fabrication process is concluded to have not preserved the spin properties, though the precise reason is not known.

degraded the spin properties, and we sought to improve the process in another trial. According to our estimates of sensitivity to single Gd spins simulated in Chapter 6, we concluded that these relaxation times would be a hindrance to observing the Gd in the presence of drift.

We made four changes to the process steps to maximize the chances of obtaining NVs with better spin properties, where the general aim was to minimize the chance of having NVs close to a region that might be damaged or contaminated by process steps: 1) produce NVs a a few nanometers farther from the surface with 4.0-keV nitrogen implantation, 2) make larger-diameter pillars of 400 nm, 3) etch for a shorter total time, and 4) use only O_2 gas for etching. Fig. 7.3 shows SEM images of diamond nanopillars in sample B033, where the typical diameter is close to 400 nm, and the height is about 500 nm. Fig. 7.5 shows bright-field and confocal microscope images of the diamond surface. We also obtained single NVs in these pillars with saturation collection rate exceeding 400 kCounts/s at 4 mW at the objective back aperture. Again, we perform spin relaxation

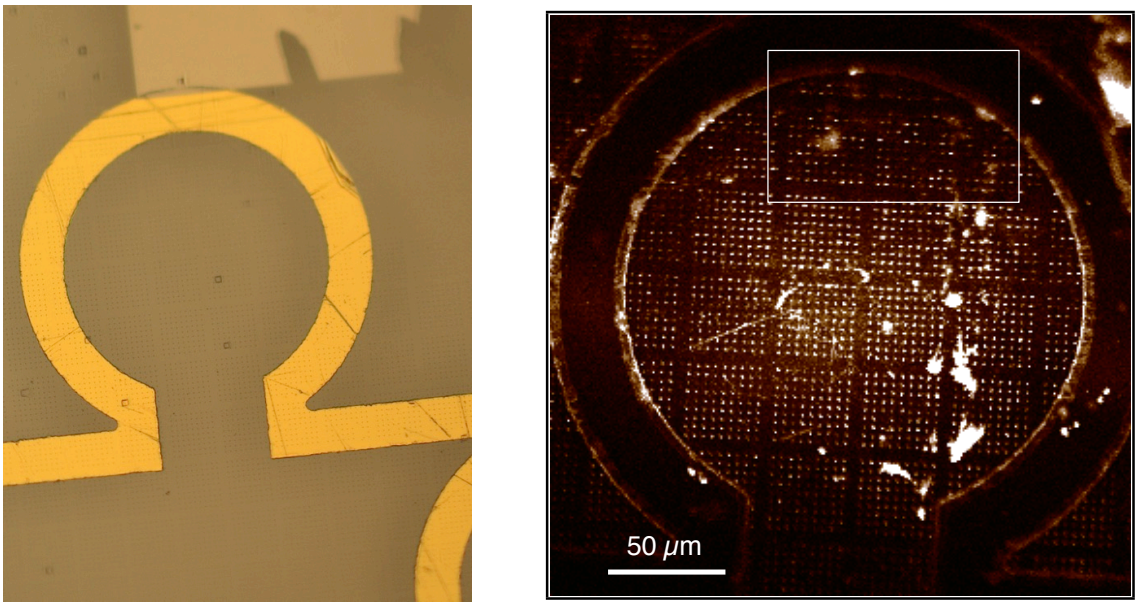

Figure 7.5: (a) Top-down brightfield image showing an Ω-shaped Ti/Au waveguide on the diamond film B033. The 9×9 grids of nanopillar spots are formed with E-beam lithography on PMGI/PMMA and here have been fully developed for deposition of a Ti etch mask to etch the nanopillars. (b) Confocal PL image of the NVs in diamond nanopillars. The large size of waveguide structure helps to keep widebonds away from the AFM scanning tip. We look at NVs near the top of the waveguide (white box) to ensure Rabi frequencies of up to 12 MHz without significant heating that can disrupt the AFM feedback. Spots in the middle appear brighter due to confocal effects, so to measure a particular NV pillar we translate it to 0,0 via a piezo motor stage.

measurements at laser power below 100 μW at the back aperture.

The NVs in nanopillars of sample B033 exhibited $T_1^{(0)}$ times that were of the same 2- to 4-ms timescale as those measured before pillar fabrication. These are the pillars used for relaxation measurements in Chapter 5 as well, so all measurements reported therein are examples of this point. Without further processing trials, we cannot verify the dominant reason for these improved spin properties in B033 over B031. It seems unlikely that the faster relaxation rates in B031 are mainly due to NV depth because it is likely we would have found at least one slightly or significantly deeper implanted NV that showed preserved long $T_1^{(0)}$, but they were no higher than about 500 μs. It seems

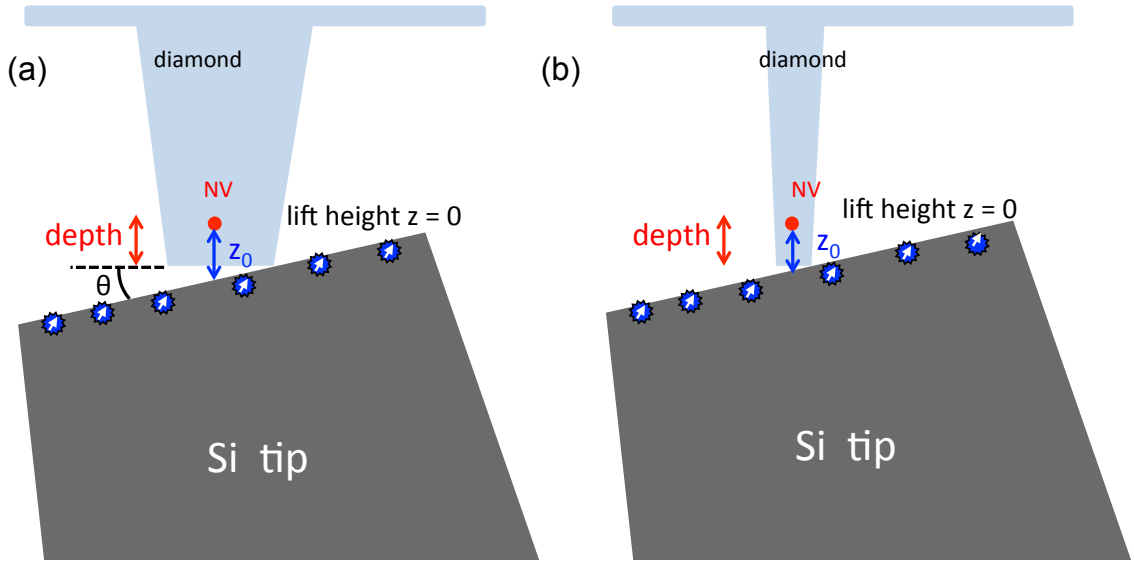

Figure 7.6: Cartoon of diamond-sample tilt in scanning probe imaging for diamond nanopillars of (a) larger diameter ϕ and (b) smaller diameter. The total NV-target separation is given by the sum of NV depth and geometrical offset z_0. For an NV in the center of each pillar and same depth d, z_0 is smaller for case (b), giving a larger electric or magnetic signal to sense. That is, for tilt angle θ then $\tan(\theta) = [2(z_0 - d)/\phi]$. However, pillar diameter cannot be reduced too small without a high probabilty of reducing the NV spin properties. Therefore, tilt control is critical to ensure even a larger diameter pillar can allow the NV to approach close to the sample on the Si tip.

more likely that process-induced vacancies or other defects [127, 199] near the NV could cause an increase in magnetic noise that would increase the single-quantum relaxation rate.

The larger-diameter pillars of B033 in practice make it more likely that the NV will be farther from a target sample when sample-diamond tilt is present, simply due to geometrical reasons shown schematically in Fig. 7.6. Therefore, we developed multiple techniques to control for tilt both in sample probe prepartion and finer adjustments within the scanning magnetometer itself. These methods are discussed in more detail in the next section.

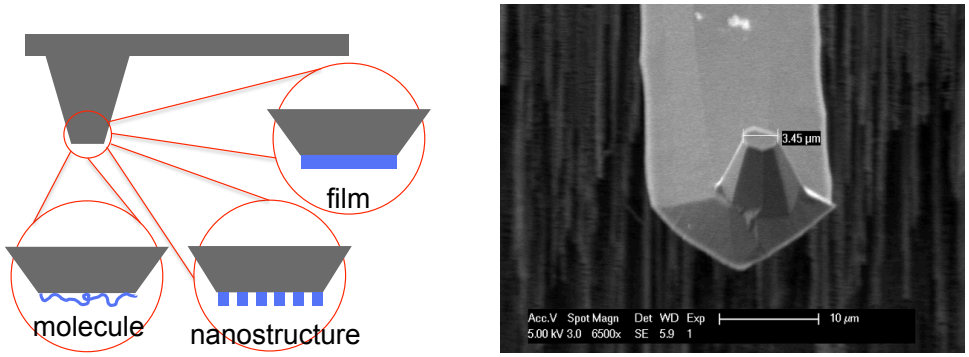

Figure 7.7: (a) Cartoon of a silicon AFM probe with a plateau-shaped tip surface, fabricated for the purpose of attaching a broad range of target samples to sense with the NV, such as uniform thin films, magnetic nanostructures, or spin-containing biological molecules. (b) Scanning electron micrograph of a completed Si plateau probe in sample SOI1 of diameter 3.5 μm, fabricated in the UCSB nanofab cleanroom. These suspended flat tips are subsequently glued to high-spring-constant tuning fork resonators.

7.2.3 Custom silicon plateau probes

Our goal was to fabricate few-micron-diameter platform with subnanometer surface roughness to serve as a substrate for putting target spins or other nanostructure materials to image, shown schematically in Fig. 7.7(a) and as a finished probe in Fig. 7.7(b). This plateau would be situated on a cantilever so that it could be glued onto a tuning fork and severed from the probe substrate. The process steps to make the silicon probes are schematically shown in Figure 7.8. Here we highlight the main features of the process.

We begin with a 2" silicon-on-insulator (SOI) wafer with buried SiO_2 (BOX) layer of 1 μm and device layer of 10 μm. First, the front and back sides are covered with a few-hundred nanometers of low-stress PECVD SiN. The device side is patterned with resist to outline the probe body and cantilever, and the nitride is dry etched. Using backside lithography alignment, the non-device side is also patterned with the probe body excluding the cantilever shape. Next, a thick photoresist dot of size ~ 27 μm was patterned near apex of the cantilever. A dry etch of silicon transfers the SiN pattern

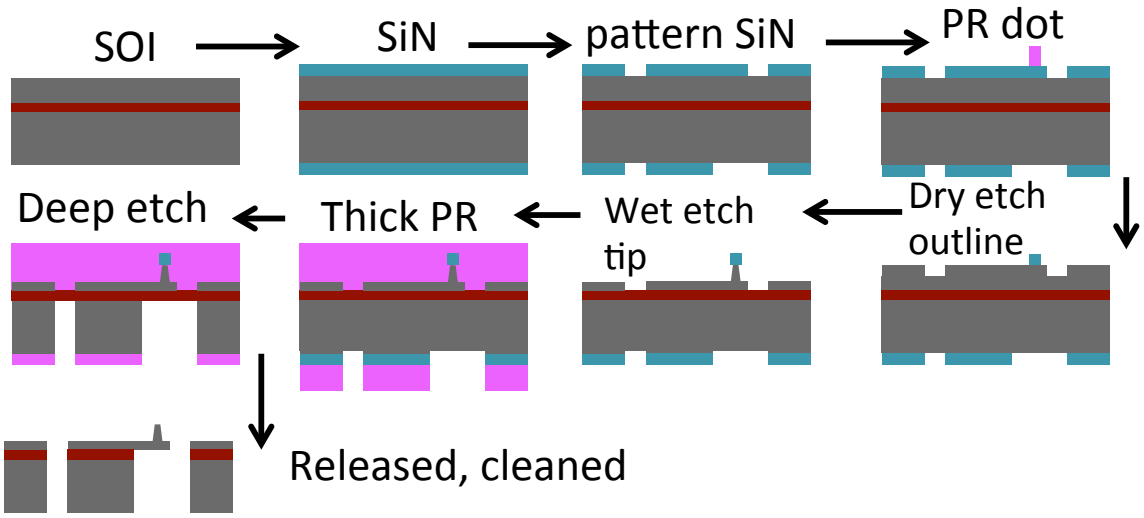

Figure 7.8: Fabrication process steps for released Si microcantilevers containing plateau-shaped tips with diameters of 1-5 μm. Silicon is gray, BOX is red, SiN is blue, and photoresist is magenta.

of the cantilever and leaves the SiN under the PR dot intact. The silicon pillar itself is etched in KOH solution, where the probe tip and backside patterns are protected by the nitride. The PR dot size of 27 μm was determined by prior KOH etch tests to obtain a few-micron-diameter plateau top and tip height of 7-10 μm above the etched cantilever. There was generally variation across the wafer in final diameter from 0 μm (unuseable) at some edges to 5-6 μm. SEM and top-down optical inspection was done for iterative etching steps.

A sloped probe tip via wet etch, instead of a dry-etched cylindrical tip, was chosen for mechanical robustness in subsequent cleaning and functionalization steps and in the AFM scanning. Once a reasonable yield of acceptable probe diameters is found the top and bottom sides are twice spin-coated in thick positive and negative resists, respectively, to prepare for the final etch and release of cantilevers. The top side in particular must have a thick enough resist to cover the 10-micron-tall plateau tips, which are still covered by a suspended nitride mask. The backside is etched with the Bosch deep RIE [259] until

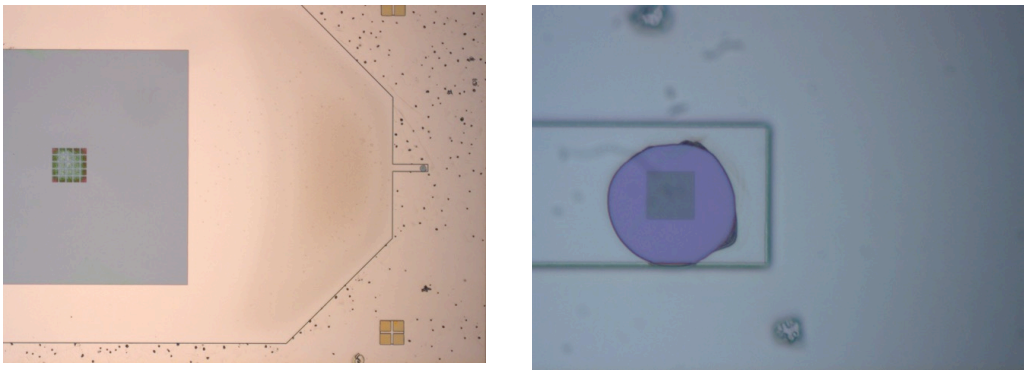

Figure 7.9: Micrographs of Si plateau probe fab process at the step before wet etching of the tip. (a) One silicon probe viewed from the device-layer side of the SOI wafer. The body has been dry etched a few-100 nanometers to transfer the pattern for subsequent lithography and deep-etch steps. (b) Close-up of the cantilever apex, showing a SiN dot of diameter 27 μm to serve as the mask to form the few-micron-wide plateau tip with a KOH wet etch. The purple dot is aligned to a faint square, which is a 10-μm-square grid of 70-nm-diameter holes defined with E-beam lithography and etched into silicon prior to SOI probe processing steps. In this example, the two features are slightly misaligned, but the nanopattern grid extent is large enough to ensure a pattern on the final plateau of diameter 2-3 μm.

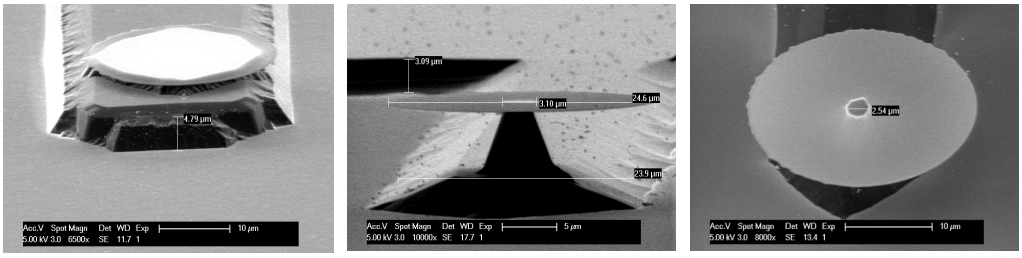

Figure 7.10: SEM images of successive KOH wet etching steps, masked by a 27-um-wide SiN disk, to form silicon plateau probes. 40% KOH heated to 60° was used with mild agitation. The etching was checked with the SEM at few-minute intervals; shown here are (a) 6 min, (b) 21 min (steeper viewing angle), and (c) 23 min. The final plateau diameter is 2.5 μm.

the BOX layer is exposed. Next, the structure is released in buffered HF, which also generally removes the nitride mask. An image of typical results for the released plateau probe cantilevers is shown in Fig. 7.7(b).

The plateau probes with the original silicon surface at the tip are useful for patterning target spins with chemical functionalization and for applying thin films for distance-dependent sensing and imaging with the shallow NV spin (Fig. 7.7(a)). Most of the SOI wafers we processed included an additional step at the beginning in order to nanostructure the silicon surface. Electron beam lithography with PMMA resist was used to pattern line and dot features at the eventual locations of the probe plateaus, with a field size large enough at each site to mitigate photolithography alignment imperfections. After inspection, trenches of 200-300 nm depth are etched by standard RIE. The subsequent steps were identical to the previous process for planar tips. Examples of the completed patterns on plateaus of sample SOI5 are shown in Figure 7.11. We coated these nanopatterned probes with a variety of materials for imaging experiments with the NV, including gadolinium-DOTA, nickel, and silver.

Because the size of the SOI probe tips is several microns and the NV diamond pillar is 260-400 nm, a primary challenge was to control the tilt of the two surfaces such that the NV could be placed as close as possible to the target sample on Si. Figure 7.6 shows a schematic of this challenge. Our approach to overcome tilt was varied for each experiment. However, the main points include: 1) optimizing the cantilever-to-tuning-fork gluing mounting and procedure so that the angle is the same as that in the scanning magnetometer setp; 2) estimating tip-on-tuning-fork tilt in SEM imaging; 3) characterizing both diamond and silicon tip tilt with AFM topographic scans and confocal optical methods; 4) for the most recent experiments, installing inclinometer electronics and a two-axis tilt stage on the probe-holder of the magnetometer to read out and adjust tilt. Figures 7.13 and 7.14 show SEM images of tilt characterization, which we refer to

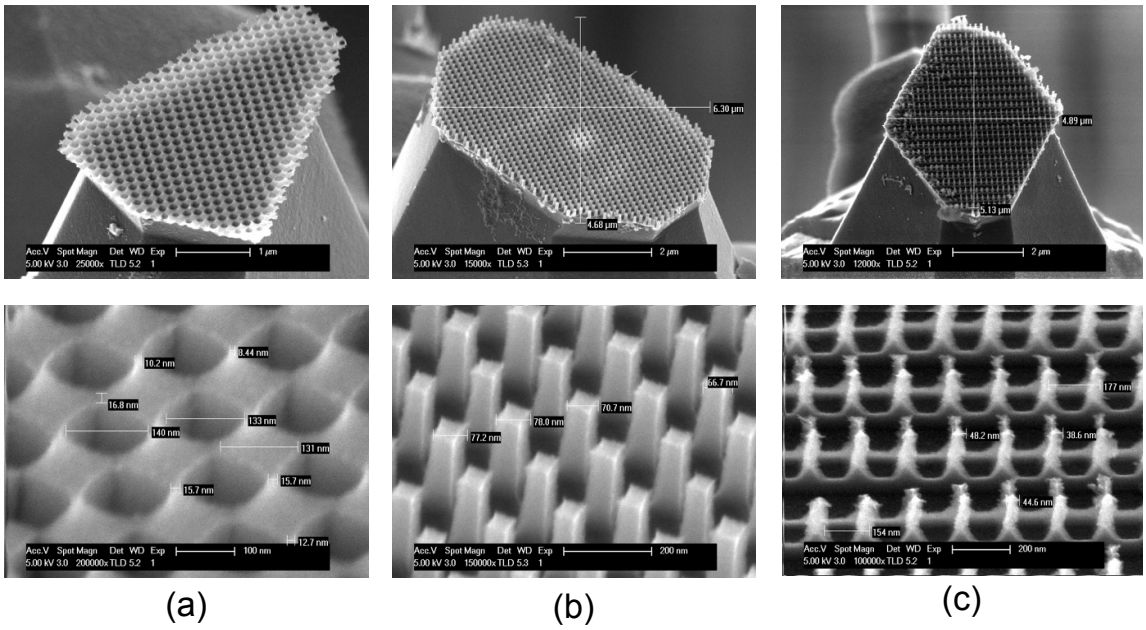

Figure 7.11: SEM images of etched nanopatterns on Si plateau probes etched on cantilevers in sample SOI5. Original E-beam patterns were (a) 70-nm disks in square grid of columns and rows, (b) 90-nm disks in square grid of columns and rows, and (c) alternating pattern of etched lines and etched lines with disks inside. Gd-spin–containing molecules of low concentration can be attached to the nanosized islands towards imaging of single spins with relaxometry. The ability to image the wide field of view of these structures with the PL of a diamond nanopillar is also an indication of precise sample-diamond tilt control.

by "pitch" and "roll" as referenced to the cantilever axis.

Photographs of the micromanipulator setup for gluing the tuning forks is shown in Figure 7.12. The tuning fork glued to a sapphire substrate is first clamped to a block with a 5-degree incline matched to the magnetometer mount. This Al block is placed on a manual (x, y)-rotation stage under a high-magnification microscope. Two cameras are sometimes used to observe the attachment, one in the top-down microscope (x, y plane) and one USB scope facing the user (x, z plane). First a pulled glass fiber or sharp metal tip in the manipulator arm was used to apply a tiny volume of UV-curing glue to the tuning fork tine apex, as shown in Fig. 7.12. In some trials, multiple glue drops were applied and UV-cured before attaching the tip in order to form a tall platform for the tip to lie above the tuning fork, as in Fig. 7.14.

Next, the top face of a fabricated silicon probe body is taped to a silicon chip that is then clipped to the manipulator arm. Rotation of the arm is done for leveling the cantilever parallel to the tuning fork, which is aided especially by the YZ camera view. Once leveling is done, the cantilever is lowered onto the glue blob until it just touches so as not to submerge the tip. A UV-LED lamp is used to cure the glue. The micromanipulator is then stepped down and wiggled until the lever breaks free of the probe body. This procedure yields a cantilever of roll $\sim 5^{\cdot}$ and pitch near $0^{\cdot}$.

Further details about tip preparation and alignment in Magnetometer B are in Appendix B.

7.3 Two-dimensional imaging of nanostructures

The nanostructured AFM plateau probe serves as a testbed for determining how close the plateau tip surface can be brought to the NV center because it provides a spatially varying signal that can only be imaged at close separations. Close separations can only

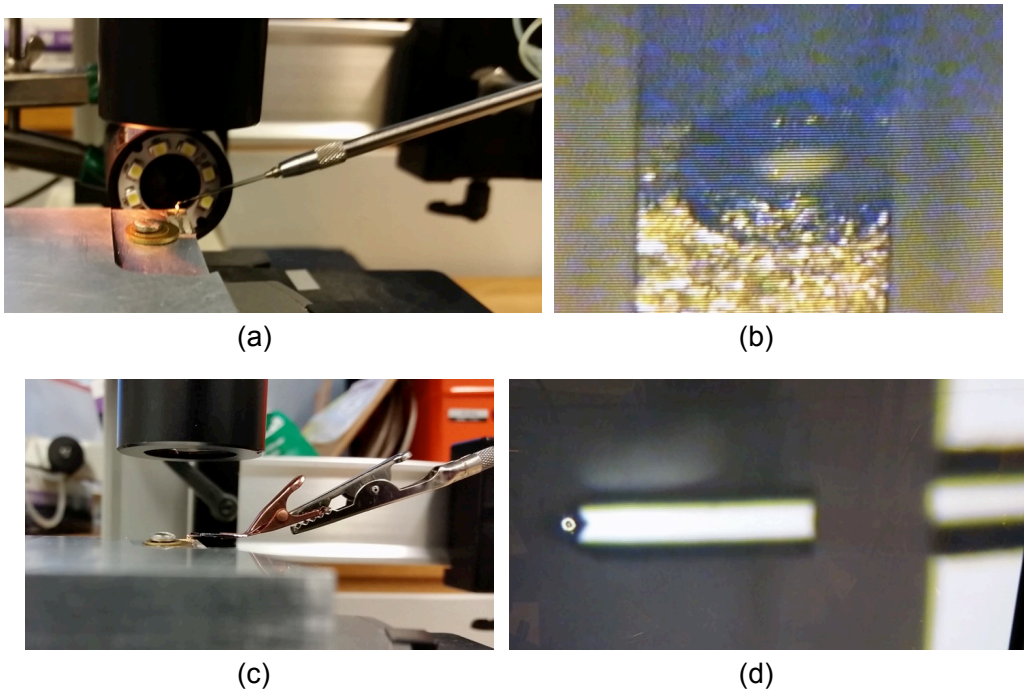

Figure 7.12: Photographs of procedure for attaching a Si tip to a tuning fork. (a) UV-curable glue is added to the end of the tuning-fork tine with a tapered glass fiber positioned by a micromanipulator. (b) Top-down micrograph of the glue blob with a specular reflection spot in the middle highest point where the cantilever should be placed. (c) The custom plateau AFM probe, with the substrate taped to a larger silicon chip, is held in an alligator clip for tilt adjustment and then positioning onto the glue. (d) Cantilever on the glue after curing by UV light and breaking from the silicon substrate. The microscope is defocused onto the plateau, showing it is the highest point while the cantilever and glue are out of focus.

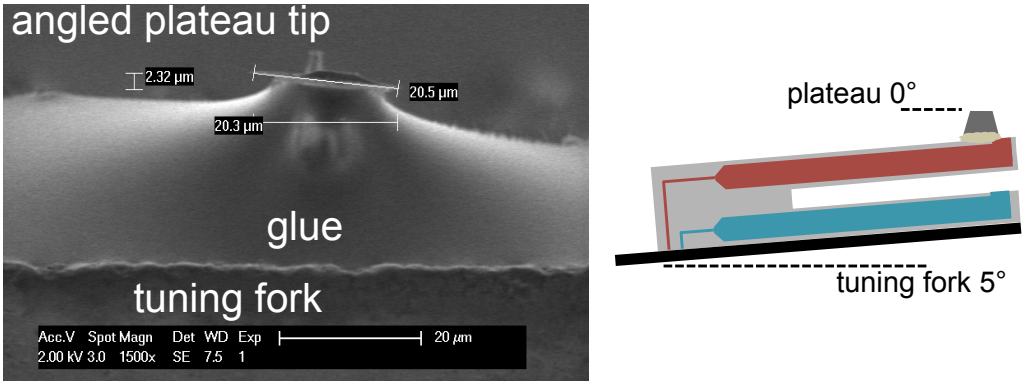

Figure 7.13: Controlling plateau-tip "roll" tilt by angled gluing procedure. (a) SEM of the glued plateau Si probe on a tuning fork where the tine runs left to right, as in the schematic in (b). The tip is glued at roughly $\tan^{-1}(2.32/20.3) = 6.5°$, close to the ideal 5° goal. (b) Schematic (not to scale) of the tuning fork as angled at a fixed 5°, the angle used in both the stage for gluing and the stage in the Magnetometer B setup. The ideal plateau is 0° relative to the horizontal scan axis. The angled mounting in the magnetometer, as photographed in Fig. 2.23(b), is used to ensure the $\sim$ 7-μm-tall tip is the highest point to contact the diamond first.

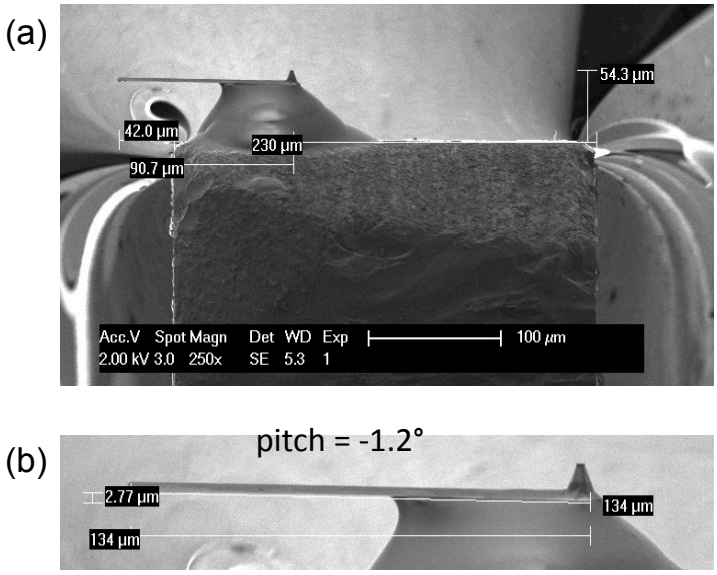

Figure 7.14: (a) SEM image of plateau attachment with increased effective tip height for clearance. Three successive layers of glue are applied via the micromanipulator, with UV illumination applied between each application. The final plateau height of 54 μm above the tuning fork is effective in ensuring the tip contacts the sample first. (b) Pitch angle measurement of $\sim 1.2°$ by SEM. We note this angle offset and attempt to adjust using shimming or a custom tilt stage in the Magnetometer B setup.

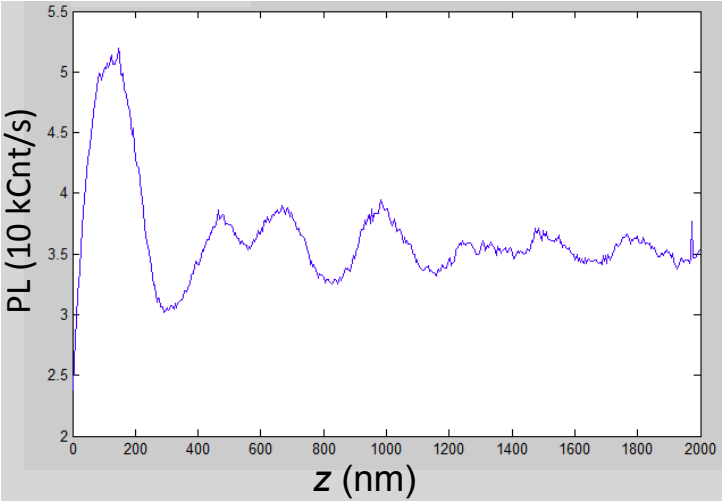

Figure 7.15: Photoluminescence versus AFM plateau probe lift height z for NV in a nanopillar. The likely mechanisms responsible for causing each of the features are discussed in the text.

be achieved with relative tilt of the plateau and pillar that is nearly parallel. Moreover, the nanostructure islands on such a probe can be used to isolate a small number of spins, such as Gd^{3+} in molecules, in a specific pattern, making interpretation of relaxometry imaging more feasible.

7.3.1 PL and ODMR imaging

We first describe an imaging signal that can be acquired rapidly to form an image but is still sensitive to NV-sample distance for characterizing tilt. This signal is the change in NV PL emission as a material is scanned near the NV in the diamond nanopillar. Fig. 7.15 shows a scan of PL versus z for a plateau tip approaching an NV in a diamond nanopillar. z is determined by tapping at an oscillation amplitude of about 2 nm peak-to-peak reduced to an amplitude setpoint of 92% and then moving the scanner z stage by a pre-calibrated amount in nanometers. We find that the PL oscillates at the far z values and finally increases to a maximum around $z \approx 100$ nm, followed by a reduction to as low as $\sim 50\%$ when the tip is in feedback tapping on the diamond surface.

There exist several possible contributions to the PL changes we observe as a function of z [260, 261, 66, 179, 79, 262]. These may include 1) altering the emission pattern of the dipole through the dielectric environment above the pillar, 2) interference of the NV emission with the retarded emission reflected from a surface, 3) the Purcell effect, and 4) changes to the fluorescence lifetime.

We simulated the collection of NV electric dipole emission for an emitter 5-10 nm from the surface of a diamond nanopillar that is approached by a dielectric surface at offset z. We find that (1) plays an important role in monotonic reduction of PL at distances $z < 100$ nm from the diamond surface, which we attribute to a larger fraction of dipole emission going into the dielectric rather than the diamond nanopillar. We find that (2) causes oscillations in collected PL are farther distances of $z > 100$ nm to $z \sim 4$ μm. The Purcell effect also plays a role that we are investigating further. However, in summary, we are interested in reducing z as close to zero as possible, so the main effect we look for in experiments is the reduction of PL, typically $\gtrsim\sim 50\%$ of the PL level when the tip is retracted.

We next investigated the PL signal as a function of position of a nanostructured plateau tip. The probe plateau has nine etched nanolines with a pitch of 100 nm, as shown in SEM images of Figs. 7.16(a,b). Nickel was evaporated on this structure, though the NV imaging signal is primarily due to the presence of a non-air dielectric close to the diamond as bar Si gives a similar image. Figure 7.16(c) and (d) show a two-dimensional NV PL image and a line cut of the entire plateau while the probe is in feedback with the diamond pillar. Details are discussed in the figure caption. In summary, the spatial resolution of this all-optical technique is better than 50 nm and shows that the NV can get close to every point on the wide target sample.

To more precisely investigate the dependence of NV-target separation on the ability to resolve these nanostructures, we performed a two-dimensional x, z scan with the same

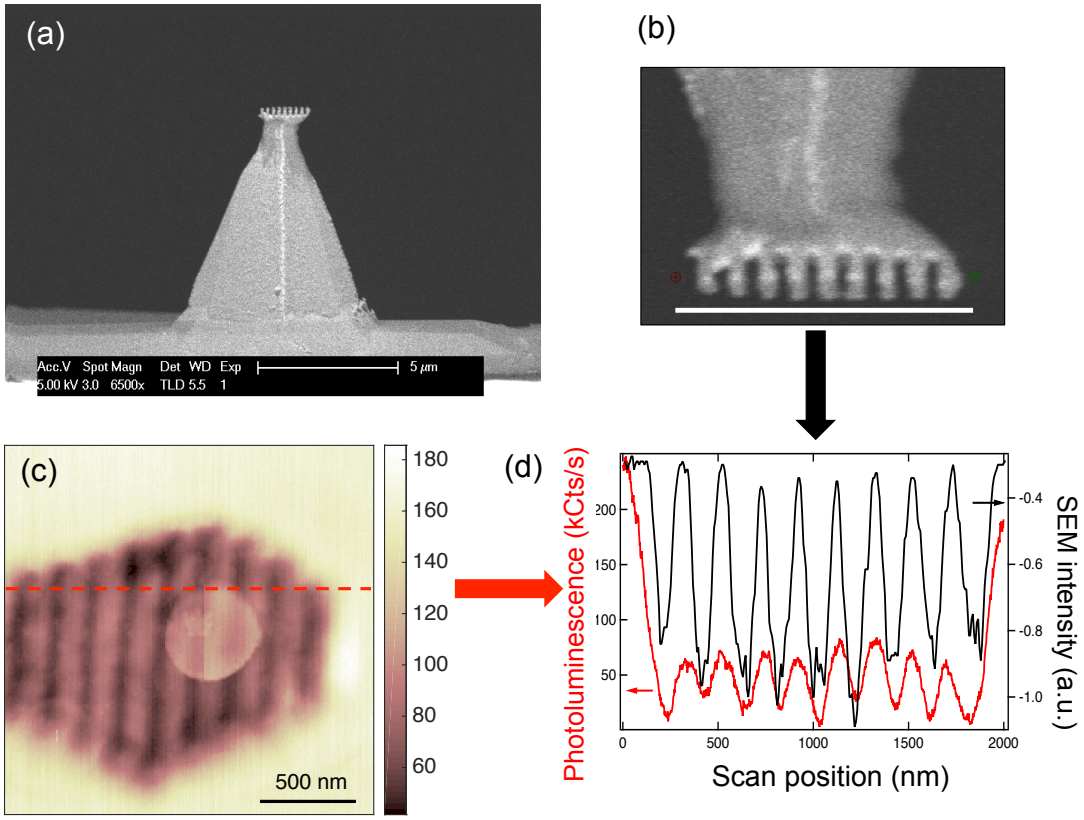

Figure 7.16: Two-dimensional NV-photoluminescence imaging of a nanostructured Ni film. (a) SEM image of a fabricated Si plateau tip with etched 200-nm-pitch nanolines and Ni deposited on top. (b) Close-up SEM image showing nine comb teeth. The white scale bar is 2 μm. (c) Photoluminescence quenching image (2 μm$\times$2 μm) of the this nanolines probe using a NV-containing diamond nanopillar in the scanning magnetometer. The $\sim$ 500-nm-diameter disk feature near the center is caused by a small piece of debris on the nanolines that causes the diamond-to-nickel separation to increase a few nanometers, thereby reducing the quenching effect in the convolved region. This feature illustrates the topographic challenges of scanning diamond nanopillars. (d) Line cut of the SEM lines (black) and quenching image (red), showing good correspondence of comb teeth with darker PL. The all-optical technique's spatial resolution here is approximately 50 nm if defined as the closest that two PL peaks can be placed together before becoming a single peak. This resolution is probably not limited by Ni on the sidewalls and bottom of the trench because we acquired similar quenching images with bare silicon nanolines. The silicon sidewalls may limit resolution depending on the distance dependence of the quenching interaction.

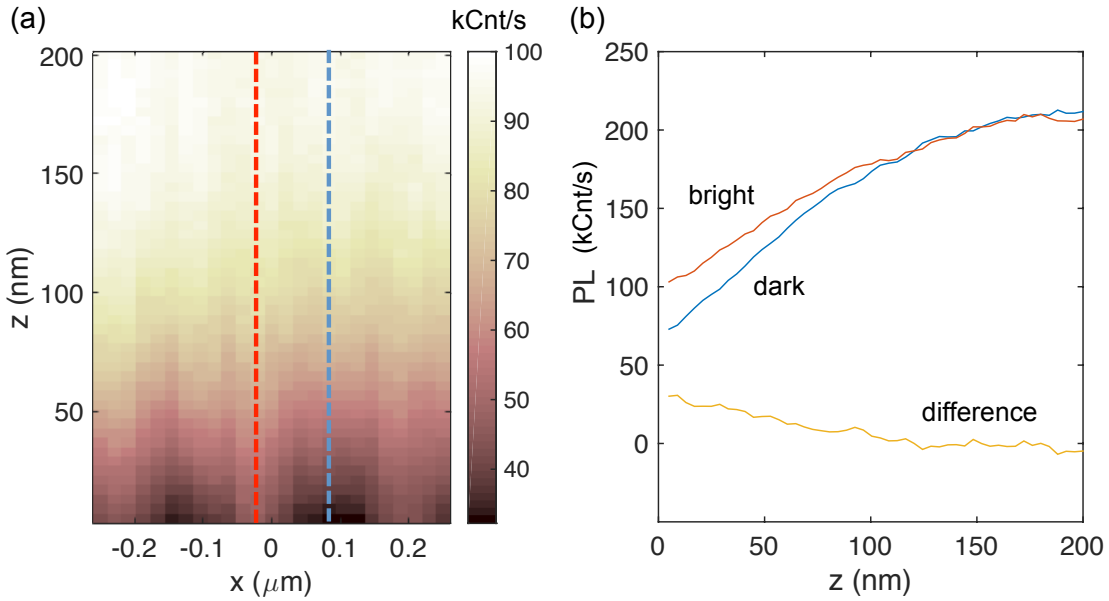

Figure 7.17: (a) Scanning NV photoluminescence image of a plateau probe structued with Ni nanolines (see Fig. 7.16) in lateral (x) and height (z) directions. The nanoline pitch is 100 nm. (b) Line cuts of the image at bright (red) and dark (blue) PL x positions. At a lift height above about 100 nm, the difference curve (yellow) has decayed to zero, showing how close the diamond nanopillar must be to the structure to spatially resolve the line and trench features with the high-SNR continuous PL measurement.

PL imaging signal. The result is shown in Fig. 7.17(a) as a two-dimensioanl image up to a lift height of 200 nm and accross a x-axis cut of two nanolines of the structure. Figure 7.17(b) is a plot of PL in line cuts of the z-axis over a nanoline and over a trench between lines. The PL features become unresolveable above the noise at a lift height of approximately 100 nm or greater. This result demonstrates that our previous x, y image likely kept the NV at a roughly constant separation from the features, since the entire two-dimensional area appears to have excellent contrast.

As a last experiment with the Ni nanolines tip, we demonstrate simultaneous dc magnetic resonance imaging and PL imaging, which together give different and complementary information about the magnetic nanostructure. The details of this measurement are given in Fig. 7.18(a) for the experimental data and Fig. 7.18(b) for a simulation of the

ODMR signal based on the seven-level NV model discussed in [121], which captures also the effects of PL quenching due to $B_\perp$-induced mixing of the pure bright ($|0\rangle$) and dark ($|1\rangle$) eigenstates. The main points are 1) the PL quenching features from the vertical-running nanolines are primarily not due to magnetic-induced spin mixing because they are not replicated in the simulation. Rather, most of this PL variation is due to the changing dielectric environment of the NV in the nanopillar as the tip scans by. 2) A simple model of parallel bar magnets can replicate features of the resonance lines observed in the experiment. 3) The PL reduced further at the ends of the AFM structure can be reproduced by higher $B_\perp$ at the ends of the "bar magnets." 4) Spatial resolution, as defined by widths of resonance lines, at the points of high field gradient is about 3 nanometers, which is shown in the next section.

In summary, we have shown experimentally with simple NV PL and ODMR imaging that the custom Si plateau AFM probes can in principle be useful for more intricate measurements of small fluctuating magnetic signals. For example, small patches of the nanostructures can be used to isolate target Gd spins from one another for more straightforward imaging of few spins by the sensing NV pillar. The shapes resolved by the PL images can also be readily used for more precise image registration to actively correct for AFM drift. In the next section we discuss the passive techniques used to reduce AFM drift below the levels observed in Chapter 6.

7.3.2 Drift and spatial resolution

Temperature control and drift are of critical importance in AFM techniques in ambient conditions. Most AFM systems can scan rapidly to produce an image, which helps to mitigate long-term drifts. However, for imaging with the NV quantum sensor, especially for slow relaxometry imaging, the scan times can take several to 10s of hours. Here, we

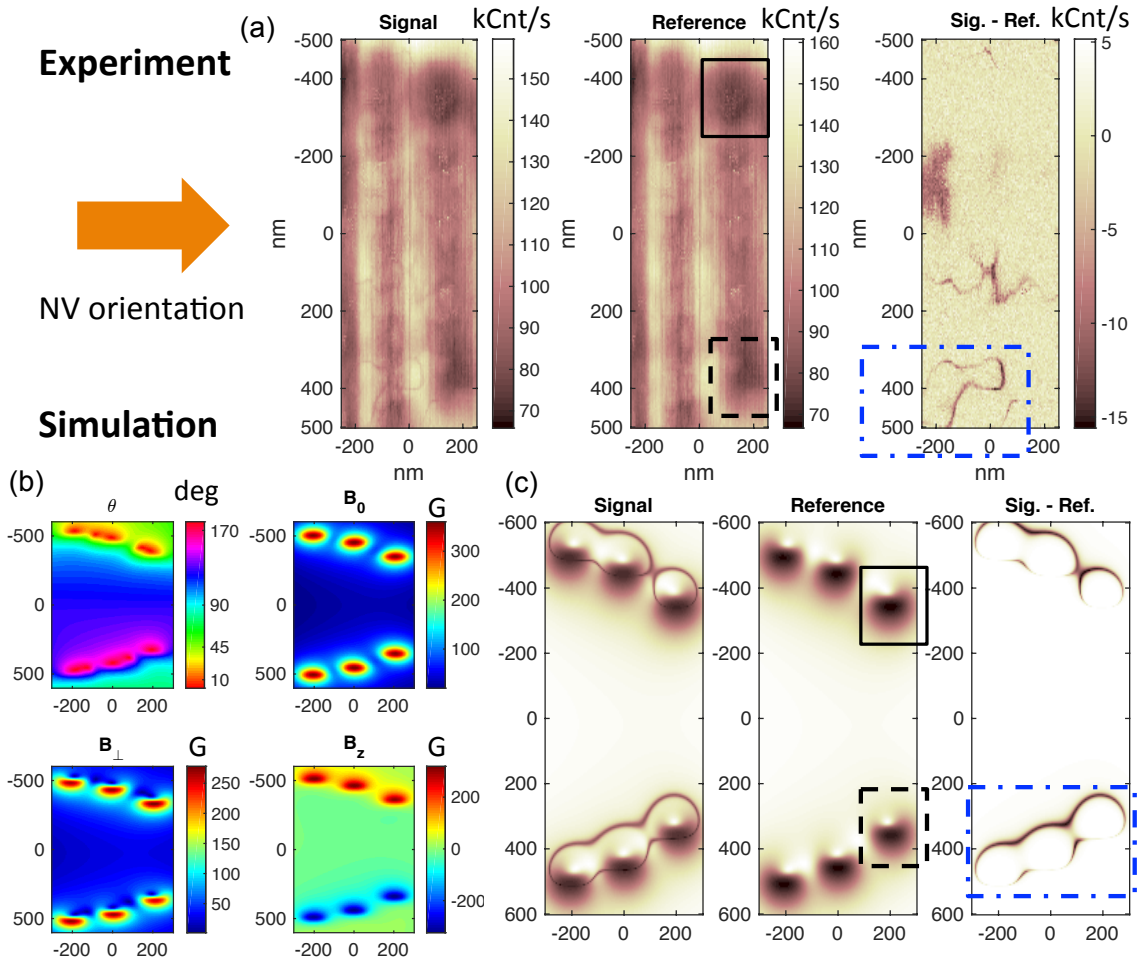

Figure 7.18: Imaging stray dc magnetic fields from Ni nanolines fabricated on plateau AFM tips. (a) Experimental two-dimensional images acquired on a three-line region of the same Ni tip as in Fig. 7.16. The signal (mw on) and reference (mw off) images were taken concurrently and subtracted to obtain the resonance slice image (right). (b) The stray field from the Ni nanolines was modeled with three equally magnetized rectangular bar magnets of thickness 50 nm and pitch 200 nm. The four panels show the magnetic field relative to the NV z axis (orange arrow, right and out of the page), assuming a NV standoff of 30 nm, which accounts for diamond-tip tilt and NV depth. (c) Simulation of NV PL accounting for 1) quenching due to spin mixing from $B_\perp$ fields and 2) reduction in PL when the $m_s = 0, -1$ transition is shifted on resonance with microwaves. The Hamiltonian is solved at each pixel to compute the eigenvalues and spin-mixing from the magnetic field in (b). The black line and dashed line boxes in simulation and experiment show increased quenching at the ends of a "bar magnet" due to large $B_\perp$. The blue dash-dot box qualitatively shows reproduction of a resonance line in the experiment. The overall quenching along the vertical nanolines, not accounted for by simulation, is not due to magnetic effects but by direct emission quenching that occurs from even an Si tip near the NV

highlight a few observations and improvements to the AFM stability.

The mechanical path lengths from AFM tip to diamond mount in the setup of Magnetometer B used in this chapter are shorter than in the magnetometer configuration used in Chapter 6 (picture not shown), where the tip and optics came from the top. We also encased the sample region of the CFM and AFM in a rigid box with walls of plastic, lead, and acoustic damping foam. The optical table was closed off with plastic curtains to eliminate air holes that would transmit temperature fluctuations in the room.[2]

Figure 7.19 shows temperature measurements inside and outside the box after setting up the AFM and diamond samples and closing the box for more than 24 hours. There is no active temperature control inside the box for these measurements. Figure 7.20 shows another set of measurements where drift in the scanner position was measured concurrently. By putting the diamond nanopillar into continuous feedback with the silicon, we found a change in output of the feedback lift height z of about 1 nm per milliKelvin by tracking the temperature concurrently. This estimate indicates that we must control our temperature to much better than within 10 mK per day to limit drift to the level required to image single spins without need for active correction.

Figure 7.21 shows nano-MRI imaging with an NV nanopillar in B033. The sample on the flat probe is a nickel nanostructure that is scanned in a 50×30 nm^2 area, with a total acquisition time of 1 h, 17 min. The 3-nm-wide resonance line here was limited by the DAC voltage resolution, but the main point is that the curved line does not drift, and if it has distorted at all, the distance is less than 5 nm over the total time. Therefore, the lateral drift is less than 0.1 nm per hour, a significant improvement over the 10 nm/min observed without the isolated system for the measurements in Chapter 6.

Further improvements we have recently made include higher-resolution thermometry

[2]We have not yet closed off every air gap, particularly concerning the optics paths, which is to be addressed in the future.

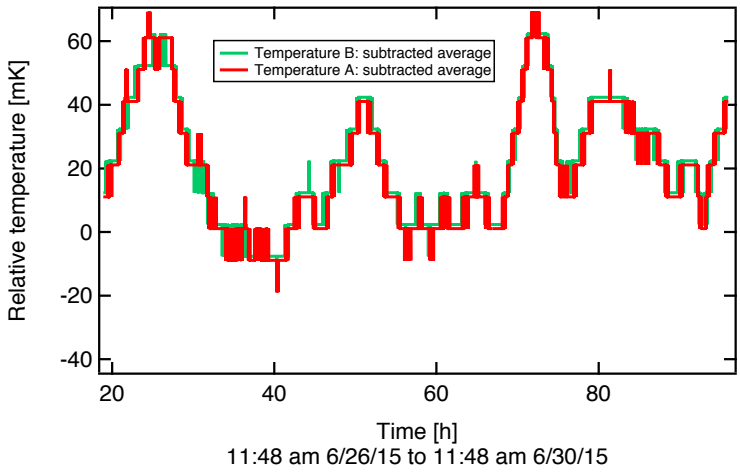

Figure 7.19: Temperature variations in Magnetometer B enclosure in the room-temperature lab measured simultaneously with two identical platinum RTD thermometers read out by a Lakeshore 331 temperature controller. One sensor is positioned on the 3-axis motor stage for diamond mounting (red) and one is positioned on the aluminum platform which mounts both the 3-axis scanner and motor stages (green). The temperatures are shown on a relative scale for clarity, and the precision of this instrument is 10 mK. The largest excursions are of the order 4 mK/h.

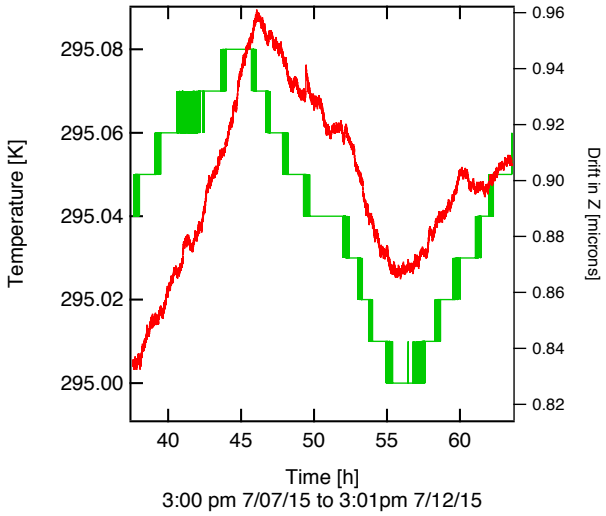

Figure 7.20: Correlation of AFM drift to temperature variations under conditions where the ambient room temperature exhibited oscillations from suboptimal control. The temperature plotted is measured within the enclosed magnetometer box, and fluctuations are generally an order of magnitude smaller than in the ambient room (not shown). The AFM drift is measured as the PI loop output in the z dimension while the tip is in tapping feedback. The slope shown is a drift of 91 nm over an 80-mK change, yielding an approximate drift of 1.1 nm/mK. The timescale was 8.4 mK/h, which implies a drift of 0.1-0.2 nm/min in one primary direction.

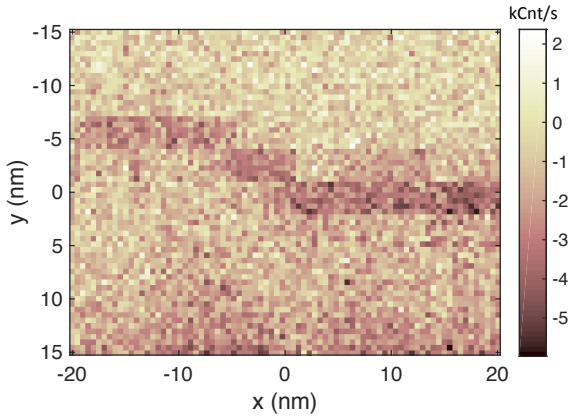

Figure 7.21: Spatial resolution and drift in magnetic resonance imaging of Ni nanostructure. The ODMR imaging technique using the CWESR detection (Chapter 4) is used. The image is 50×30 nm^2 and 4800 pixels with 0.5 nm/pixel. However, in this case the 16-bit DAC resolution limited the scanner x, y displacement to 1.5-nm steps for the 10 V range and 10 μm/V, which could be reduced with a divider. The slow scan direction is y and the tip remains in feedback the entire time.This curved resonance line remains continuous and does not shift over the 1 h, 17 min scan. This scan demonstrates x, y stability better than 5 nm over the hour, or roughly 0.1 nm/min.

read out by a digital multimeter to precision of better than 10 mK, which serves as input to a feedback loop for heater bars inside the enclosure. The advantage we see with this approach is faster temperature stabilization in hours instead of 24 hours. However, not all drifts correspond to apparent temperature changes, and analysis of AFM-diamond drift effects with this active-feedback setup are ongoing.

7.4 Scanning NV relaxometry of noise near metal surfaces

We study the dependence of nitrogen-vacancy (NV) spin relaxation times T_1 on nanometer-scale distance z to metal films at room temperature. In the NV's three-level ground state, we find that single-quantum relaxation rates increase with decreasing z and increasing metal electrical conductivity, consistent with evanescent wave Johnson noise.

In contrast, we find that the double-quantum (DQ) relaxation rate can decrease at small z, which we attribute to metal-induced reduction of electric field noise intrinsic to the diamond surface. The total T_1 is thus a non-trivial combination of these competing effects that depends on the type of metal used, and we show that the relaxation-limited qubit coherence time can be increased for scanning probe imaging using a low-conductivity metal such as Ti.

7.4.1 Introduction

The technique of scanning probe imaging with near-surface nitrogen-vacancy (NV) centers in diamond is firmly positioned to have a broad impact on the understanding of nanoscale phenomena in condensed matter systems, such as domain walls [67] and superconductors [68, 69]. The versatility of the NV sensor is established by its spin polarizability and coherence properties at a range of temperatures [12], in addition to an array of pulsed magnetic resonance techniques to make the NV sensitive to magnetic fields from dc to microwave frequencies [76, 214]. Sensing of dc and ac electric fields with NV centers has also been established using bulk NV centers [29], including the observation of a single-electron charge within diamond [30]. Thus, the scanning probe NV tool is well suited to study the microscopic origins of electromagnetic noise associated with material surfaces. For example, metal gate electrodes, which are incorporated in the control lines of a broad variety of qubits from quantum dots to trapped ions, are known to cause performance-limiting dephasing and dissipation.

Magnetic noise from a metal film has previously been studied via near-surface NV centers in a diamond coated with a ramp of polycrystalline or single-crystalline silver [234]. In that study, measurements of the spin relaxation rates $1/T_1$ of fixed NV centers at a range of nanoscale depths were used to probe GHz-frequency evanescent wave Johnson

noise (EWJN)[234], thereby validating a theoretical model of nonlocal corrections to the dielectric function [263]. These results on magnetic EWJN raise the question of whether the complementary presence of *electric* EWJN may be detected simultaneously with the NV sensor. Moreover, the application of electric field noise imaging has yet to be demonstrated with NVs.

Scanning quantum decoherence microscopy with NV centers [104] has been used for imaging noise from paramagnetic spin labels [71], ferromagnetic nanoparticles [74, 264], and external diamond surfaces [223]. Until now the T_1-based approaches have focused on the single-quantum (SQ, $\Delta m_s = \pm 1$) transitions, which can be measured with simple optical control and are sensitive primarily to magnetic field noise. In Chapter 5, we demonstrated that electric field noise intrinsic to the diamond surface [90] can be probed spectroscopically using double-quantum (DQ, $\Delta m_s = \pm 2$) spin relaxometry [92]. Therefore, the presence of a dielectric or metallic sample approached with the NV-diamond imaging probe is expected to modify the electric field and DQ relaxation rate.

Here, we apply both SQ and DQ relaxometry to a scanning probe NV in a diamond nanopillar to image magnetic and electric field noise as a function of NV distance to metallic surfaces. First, we demonstrate the SQ and DQ relaxometry technique with a scanning NV in a diamond nanopillar. Then, we study the distance dependence of the SQ and DQ relaxation rates for non-magnetic metal films of different electrical conductivities: silver, gold, and titanium. By monitoring the full set of $S = 1$ ground state relaxation rates, we observe non-trivial behavior at close metal-NV proximity, finding that the SQ rate is consistent with magnetic EWJN and the DQ rate actually decreases at nanometer-scale separations. From this result, we show how performing scanning probe imaging with a low-electrical-conductivity tip such as Ti can produce a net increase in T_1, thereby enabling a longer maximum coherence time for NV superpositions in the SQ $\{|0\rangle, |-1\rangle\}$ and especially DQ $\{|+1\rangle, |-1\rangle\}$ bases. This work establishes a method of electrical

conductivity imaging with a single NV spin, and it also raises fundamental and technical considerations for NV scanning probe imaging of condensed matter systems [67, 69, 68], both conductive and non-conductive.

7.4.2 Methods

The experimental setup is composed of a confocal microscope combined with a home-built atomic force microscope (AFM) operating in tapping mode (Figure 7.22(a)). A lithographically patterned on-diamond microwave stripline was used for $|0\rangle \leftrightarrow |\pm 1\rangle$ spin rotations. Tapered diamond nanopillars of 400-nm diameter were patterned to increase the collection efficiency of the NV sensor [78, 171] and for topographic imaging [66, 179]. We fabricated custom silicon AFM cantilever probes from silicon-on-insulator. The tip of the probes was designed to be a $\sim$ 2-μm plateau of the original silicon device layer surface. Once detached from the wafer, the probe was coated with a 100-nm-thick metal film, Ag, Au, or Ti. The plateau-tipped cantilever was glued to a tuning fork and approached via AFM to the diamond nanopillar.

We consider contributions to spin relaxation as described by the Zeeman and Stark terms in the NV ground state Hamiltonian [29, 92]: magnetic field noise $B_\perp$ and electric field noise $E_\perp$ perpendicular to the NV symmetry axis cause SQ spin relaxation and DQ spin relaxation, respectively. We apply a static bias magnetic field B_z aligned along the NV axis so that the spin eigenstates are the $|m_s\rangle$ of the spin-1 S_z operator. We define Ω as the total relaxation rate of each SQ channel $|0\rangle \leftrightarrow |\pm 1\rangle$, and we define γ as the total relaxation rate of the DQ channel $|1\rangle \leftrightarrow |-1\rangle$, as shown in the energy level diagram of Fig. 7.22(a) [92].

The pulse sequences to extract the Ω and γ rates are shown in Figs. 7.22(b) and 7.22(c), respectively[92]. A choice of microwave $\pi_{0,\pm 1}$ pulse, before and after the dark

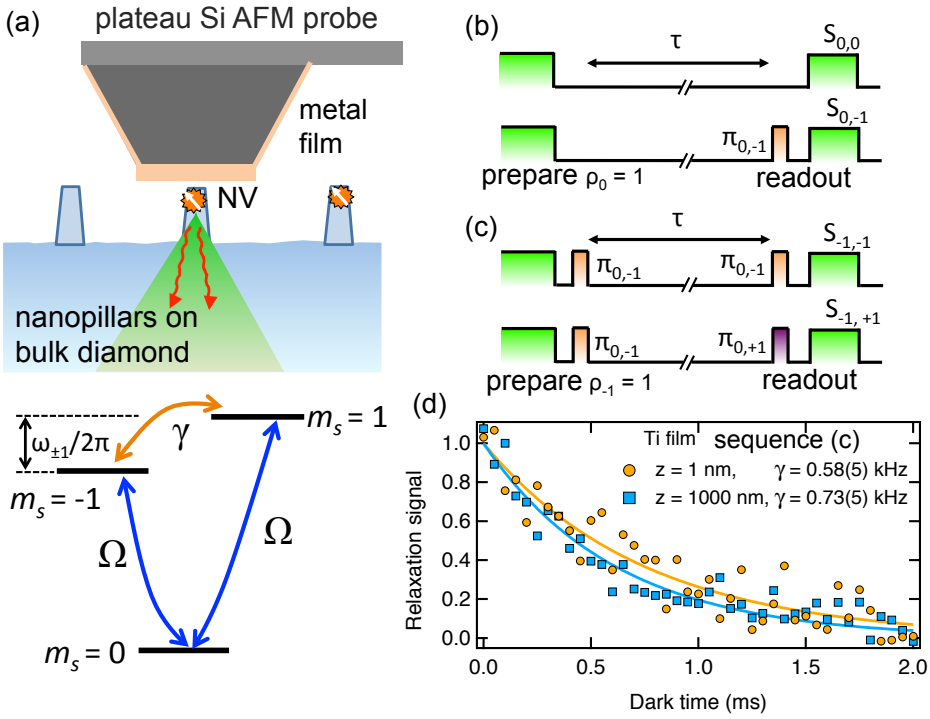

Figure 7.22: Scanning NV relaxometry of metallic surface noise. (a) Schematic of a near-surface NV in a diamond nanopillar used to sense magnetic and electric field noise. A 2-μm-wide plateau tip scans relative to the NV to study the distance dependent effects of the metal on NV spin relaxation. (b) Sequence for measuring single-quantum (SQ) relaxation rate Ω. (c) Sequence for measuring double-quantum (DQ) relaxation rate γ. (d) Example of data at lift heights $z = 1$ nm and $z = 1000$ nm using the DQ sequence in (c), showing that γ can actually increase in proximity to a metal with low electrical conductivity like Ti, which can lead to a net increase the relaxation contribution $2T_1$ to the total T_2 coherence time. The curves in (d) look quite close together because the fits are to Eq. 7.2 $\exp(-(\Omega + 2\gamma)\tau)$, which includes a Ω contribution that is extracted with sequence (b) and slightly increases with decreasing z. The inset shows the fit result: γ relaxation at $z = 1$ nm is about 20% suppressed compared to γ at $z = 1000$ nm.

relaxation period of time τ, enables the initialization and readout of population in any of the three $\{m_s\}$ spin levels. As described in our prior report [92] and Chapter 5, the fit functions for the measurements are

$$F_1(\tau) = S_{0,0}(\tau) - S_{0,-1}(\tau) = re^{-3\Omega\tau} \tag{7.1}$$

$$F_2(\tau) = S_{-1,-1}(\tau) - S_{-1,+1}(\tau) = re^{-(\Omega+2\gamma)\tau}. \tag{7.2}$$

with the signals $S_{i,j}(\tau)$ introduced in Figs. 7.22(b) and 7.22(c), and r is PL contrast.

7.4.3 NV relaxation versus distance to Ag

We first investigated the effect of a highly conductive material on the single-quantum relaxation rate of near-surface NVs. Thermal currents within the metal produce Johnson magnetic field noise with a white noise spectrum. Silver has among the highest electrical conductivities, $\sigma_e \approx 2.9 \times 10^7$ S/m [234], and it is therefore expected to yield large magnetic noise fluctuations. We deposited 100 nm of polycrystalline Ag on a Si tip and controllably approached it to NV-containing diamond nanopillars on the scanning Magnetometer B. A schematic of the experiment is shown in Fig. 7.23(a), defining the distance parameter z as the lift height from AFM tapping feedback on the pillar.

Figure 7.23(b) summarizes the spin relaxation results of the metal-diamond distance z dependence of $T_1^{(0)}$ for two NV nanopillars. The spin is prepared in $|0\rangle$ and the depolarization rate $1/T_1^{(0)}$ is extracted from a fit to single exponential decay $\exp(-\tau/T_1^{(0)})$. The increasing $1/T_1^{(0)}$ for decreasing z data is in good agreement with a magnetic noise model based on evanescent wave Johnson noise (EWJN), as derived in [263]. The model has roughly a $1/z$ dependence without adjusting for finite-thickness effects. Although

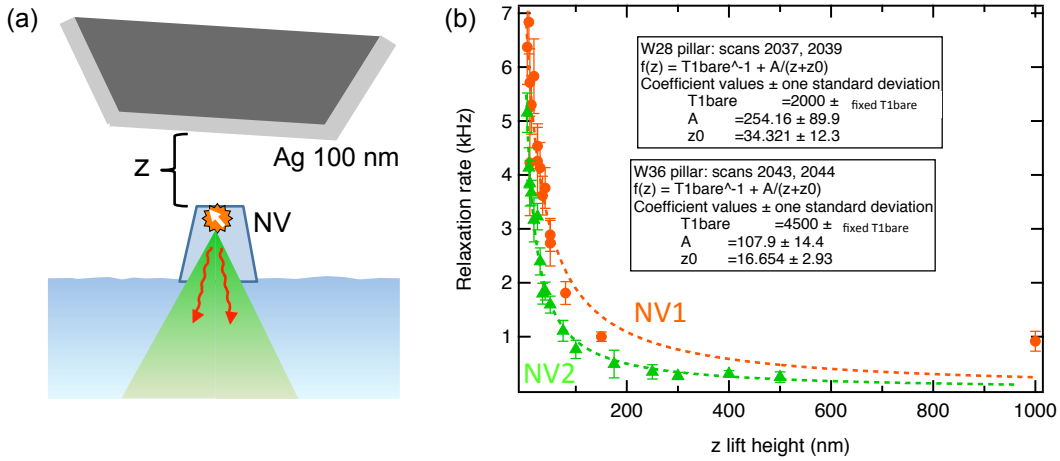

Figure 7.23: Distance dependence of single-quantum relaxation of a shallow NV versus lift height z of a 100-nm-thick Ag film. (a) Schematic of the experiment, where z is defined as the lift height of the tip from the position of tapping feedback. A small tilt of the two surfaces is present in practice. (b) Results of relaxation rate $1/T_1^{(0)}$ for NVs in two different nanopillars. $T_{1,\mathrm{bare}}$ is the relaxation time measured with the tip retracted several microns. The data are fit to the function $1/T_1^{(0)} = 1/T_{1,\mathrm{bare}}^{(0)} + A/(z+z_0)$, which is an approximate model for magnetic evanescent wave Johnson noise (EWJN) from a metal. The electrical conductivity, σ, of the metal film is extracted from parameter A, giving 3.2×10^7 S/m (orange circles) and 1.4×10^7 S/m (green triangles), in good agreement with the accepted value for silver. The $z_0 > 0$ fit parameter accounts for both 1) an unknown distance offset between the two surfaces due to effects like tilt and 2) the NV depth below the diamond. The results here are $z_0 \approx 34$ nm (orange circles) and $z_0 \approx 17$ nm (green triangles).

the distance to the NV is not known precisely due to a finite metal-diamond-tilt-induced offset and the uncertainty in NV depth, we extract a distance offset z_0, which was 17 nm and 34 nm for the two NVs in the measurement. Since the two NVs are expected to be roughly at the same depth of implantation, $d \sim 7 \pm 4$ nm, the difference in z_0 is likely due to different positioning of the plateau tip in each case or lateral position of the NVs in the 400-nm-wide pillars.

The EWJN model also gives an estimate for the electrical conductivity of the metal film. The extracted values of $1.4 - 3.2 \times 10^7$ S/m are in excellent agreement with σ_e, and therefore we can be reasonably confident that EWJN is an appropriate model for the relaxation behavior. This metal EWJN experiment for NVs was recently demonstrated

for a static film of Ag deposited directly on to diamond [234]. Our approach adds the flexibility afforded by a scanning probe, which allows many different z distances to be attempted for the same NV center. Furthermore, the technique can potentially be extended to nanoscale electrical conductivity imaging via monitoring of changes in the single-quantum relaxation rate of the scanned NV center over more interesting conductive samples.

7.4.4 Evidence for electric screening with Ag, Au, Ti

Magnetic EWJN should occur in tandem with the electrical analog [263], which raises the question of whether electric field noise emanating from the metal can also be detected with the near-surface NV. In Chapter 5, we have introduced double-quantum relaxation relaxometry pulse sequences to probe the presence of electric field noise at the diamond surface, and we apply these same techniques here to the scanning metal plateau.

To demonstrate the plausibility of electric field EWJN that could cause the increase of the gamma relaxation rate, we use a theory of qubit relaxation in the presence of a metal [263]. The effect on two-level relaxation for the electric EWJN from a conducting half-space applied to our "qubit" subspace of the NV $|\pm 1\rangle$ states:

$$\gamma_E = \frac{d_\perp^2}{\hbar^2} \chi_{ii}^E \left(\mathbf{r}, \omega_{\pm 1}\right) \coth\left(\frac{\hbar\omega_{\pm 1}}{2k_b T}\right) \tag{7.3}$$

where the NV is at a position $\mathbf{r}$ relative to the metal, $d_\perp$ and $\omega_{\pm 1}$ are as defined in Chapter 5, T is temperature, and $\chi_{ii}^E\left(z, z, \omega_{\pm 1}\right)$ is the electric spectral density at frequency $\omega_{\pm 1}$.

The relevant silver skin depth δ for the $\omega_{\pm 1}/2\pi$ range we use of 30 MHz - 1 GHz is 2 μm or larger for the metals we use. Therefore, we make the quasistatic approximation since $z \ll \delta$ to simplify the electric spectral noise density $\chi_{zz}^E\left(z, z, \omega_{\pm 1}\right)$ given in Eq. 7.3.

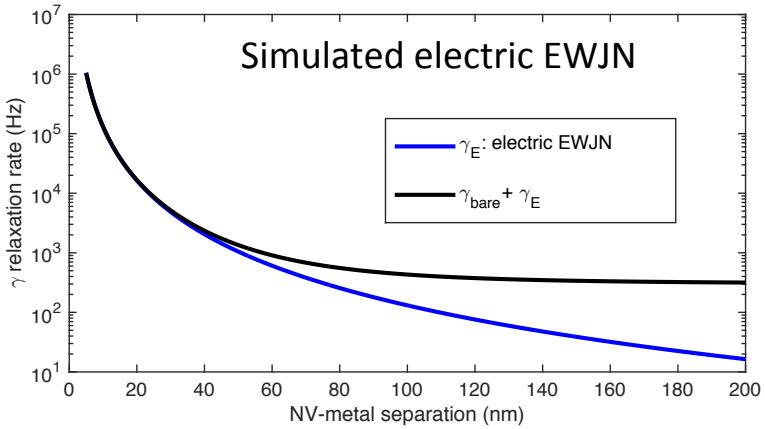

Figure 7.24: Calculated estimate of electric evanescent wave Johnson noise effect on the DQ relaxation rate of a near-surface NV. The blue curve is based on Eq. 7.4 at $T = 295$ K and $\omega_{\pm1}/2\pi = 160$ MHz. The black curve adds the bare $\gamma \sim 0.3$ kHz rate we typically measure at this $\omega_{\pm1}$ for near-surface NVs.

At room temperature, $\coth\left(\frac{\hbar\omega_{\pm1}}{2k_bT}\right) \approx 2k_bT/\hbar\omega_{\pm1}$, and therefore

$$\gamma_E = \frac{d_\perp^2}{\hbar^2}\frac{2k_bT}{\hbar\omega_{\pm1}}\left[\frac{\hbar}{8\epsilon_0 z^3}\mathrm{Im}\frac{\epsilon-1}{\epsilon+1}\right] \approx (2\pi)^2\left(\frac{d_\perp}{h}\right)^2\frac{1}{8\epsilon_0 z^3}\frac{2k_BT}{\omega_{\pm1}} \tag{7.4}$$

Although $\mathrm{Im}(\epsilon) \approx i\sigma/\epsilon_0\omega$ itself contains frequency-dependence, this dependence effectively drops out because the large conductivity gives $\mathrm{Im}(\epsilon_{Ag}) \approx 4.17 \times 10^8$. The remaining $1/f$-like frequency dependence at room temperature then comes from just the simplified coth[...] factor. Three notable features compared to the magnetic field EWJN effect are that 1) there remains frequency dependence $\gamma_E \propto 1/\omega_{\pm1}$, 2) there is no explicit σ-dependence, and 3) there is a stronger distance dependence of $1/z^3$.

In Fig. 7.24 we plot a calculation of the γ_E from Eq. 7.4 as a function of distance z for $\omega_{\pm1}/2\pi = 160$ MHz, $T = 295$ K, and $d_\perp/h = 0.17$ Hz·m/V. We see that the relaxation rate reaches kHz values at NV-metal separations of 20-60 nm, of which 20 nm is about the minimum we expect given a combination of NV depth of $\sim$ 7 nm and moderate tilt-induced offset between the diamond and plateau.

We perform the experiment of DQ relaxation rate as a function of z and the results are shown for three different metals in Figs. 7.25, 7.26, and 7.27. We observe sometimes conflicting qualitative results we label (1) and (2). In behavior (1), for metal tips Ag, Au, and Ti, of 100 nm thickness we observed the γ to be constant with decreasing z and then actually drop by nearly a factor of 2 at the closest separations near tapping contact. We attribute this observation to screening of the electric field noise at the diamond surface due to the presence of image charges in the approaching metal tip. Assuming that the bare γ_{d} due to the diamond surface is dominated by electric field noise, for example at a small splitting $\omega_{\pm 1}$, then a simplistic electrostatics image-charge analysis would yield an estimate of the screening effect as

$$\gamma_{\mathrm{scr}} = \gamma_{\mathrm{d}} - \frac{\gamma_{\mathrm{d}} d^2}{(d+2z)^2} \tag{7.5}$$

where d is the depth of the NV and z is the lift height so $2z$ is the effective distance of the fluctuating image charges. The γ_{scr} in Eq. 7.5 changes negligibly from γ_{d} until z is of the order of d, which in our case is about 7 nm. This functional behavior is consistent with our observation that the γ reduction only occurs noticeably in feedback and a few nanometers lift height.

For behavior (2), for some prepared metal tips of the same metal and thickness, we actually did not observe the reduction in γ, but rather a slight increase. This observation is actually more in line with the expected increase due to increasing electric EWJN with lower z. However, we do not fit the depth dependence of the γ data as there may be other electric field factors at play, as indicated by the prior screening results.

Of the two observed effects of increasing and decreasing γ with reduced z, the more interesting one is perhaps the screening-like effect because it implies that the maximum decoherence rate can be increased. For example, our measurements of the Ω rate near

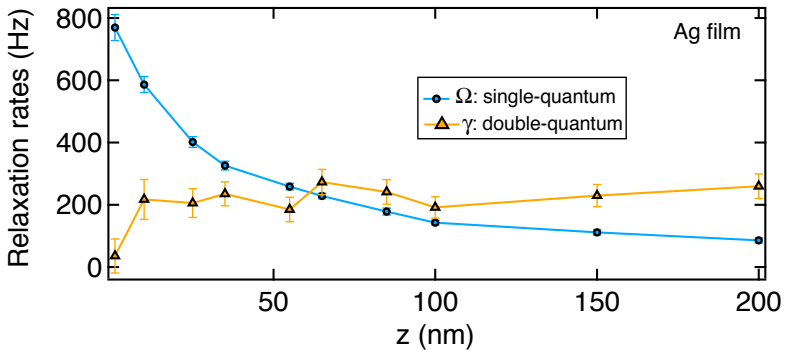

Figure 7.25: NV three-level relaxation versus distance to a 100-nm Ag film. Measurements were done with $\omega_{\pm1}/2\pi = 300$ MHz. The Ω rate increases at smaller z while the γ rate decreases, the latter possibly due to screening of diamond electric noise by the metal. Overall SQ qubit coherence limit $T_1 = (3\Omega + \gamma)^{-1}$ goes down as the film approaches the NV because the magnetic noise effect on Ω dominates.

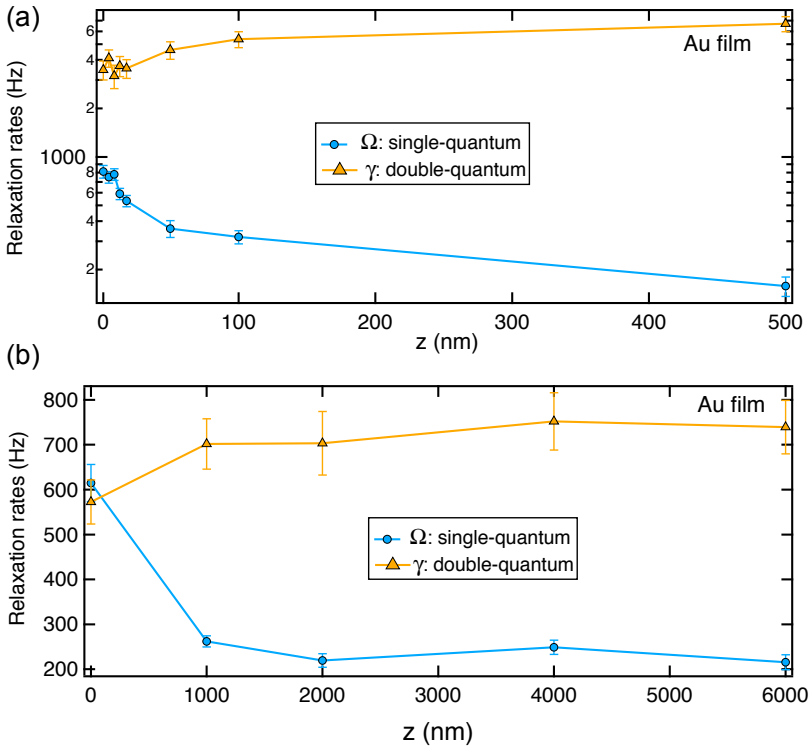

Figure 7.26: NV three-level relaxation versus distance to a 100-nm Au film. Measurements were done with (a) $\omega_{\pm1}/2\pi = 165$ MHz and (b) $\omega_{\pm1}/2\pi = 150$ MHz with two different NVs and two different Au tips. The Ω rate increases at smaller z while the γ rate decreases, the latter possibly due to screening of diamond electric noise by the metal. Overall SQ qubit coherence limit $T_1 = (3\Omega + \gamma)^{-1}$ actually increases slightly at some close separations as the film approaches the NV because the magnetic noise effect on Ω is smaller than in the more-conductive Ag film.

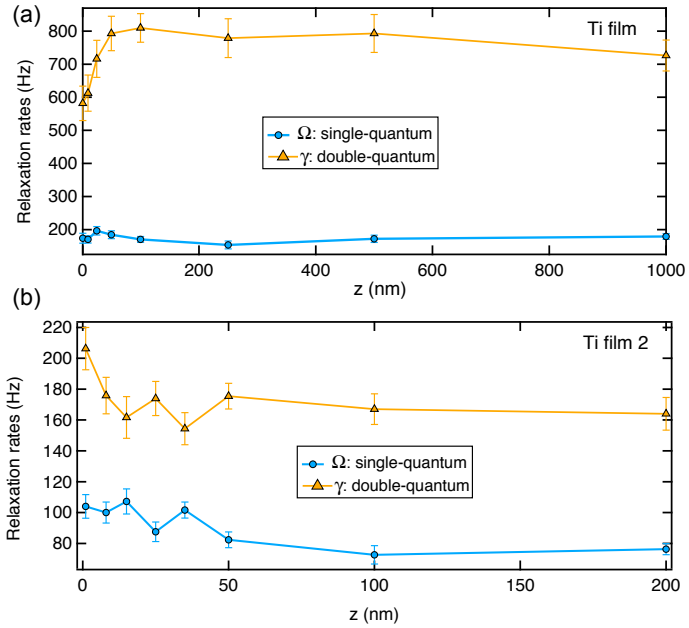

Figure 7.27: NV three-level relaxation versus distance to a 100-nm Ti film, which as about an order of magnitude lower electrical conductivity σ than Ag. Measurements were done with (a) $\omega_{\pm 1}/2\pi = 165$ MHz and (b) $\omega_{\pm 1}/2\pi = 150$ MHz with two different NVs and two different Ti tips. In (a) the Ω rate increases slightly at smaller z while the γ rate decreases, the latter possibly due to screening of diamond electric noise by the metal. Overall SQ qubit coherence limit $T_1 = (3\Omega + \gamma)^{-1}$ actually increases slightly at some close separations as the film approaches the NV because the magnetic noise effect on Ω is smaller for the small σ of Ti. However, for the film use in (b) the γ appears to increase, possibly due to additional electric field noise from the Ti film.

a Ti surface show that magnetic Johnson noise has only a small effect, as we expect from the dependence of the magnetic noise on electrical conductivity σ. Thus, with a decreased γ the T_1 actually increases with the metal nearby, and therefore the maximum possible $T_2 = 2T_1$ also increases. This increase is only a small factor of order 1, however, it indicates that substrates that reduce near-surface NV decoherence could potentially be useful to place target samples on, such as nuclear spins.

Our work on scanning conductive materials near shallow NV centers is ongoing, and there are several knobs that can potentially be turned. We have already shown in Chapter 5 that the γ due to intrinsic diamond noise increases like $1/f^\alpha$ for $\alpha \approx 1.5 - 2$. Similarly, relaxation from electric evanescent wave Johnson noise at room temperature is expected to have a $1/f$ dependence on the qubit frequency. The possible effects of screening also demonstrate that the diamond nanopillar may not be fully non-invasive as a probe to image nanoscale electromagnetism on condensed matter surfaces. Interactions of surface charges and the interfacing dielectric materials, or perhaps even interactions between spins on the two surfaces, may be factors that must be accounted for in quantitative imaging of ac fields in future scanning experiments. The decoherence effects of the surfaces on the NV sensor, here shown through the relaxation channels, must also be considered in maintaining high sensitivity.

7.5 Future directions

7.5.1 Near-surface NV decoherence

This dissertation makes the following contributions to the understanding of decoherence of near-surface NV centers in diamond.

1. Studied coherence decay times T_2 as a function of NV depth, demonstrating clear

evidence of surface-related decoherence in NVs in an isotopically enriched diamond sample. The surface effect is dominant for NVs less than about 25 nm from the surface, depending on bulk intrinsic coherence time.

2. Showed, via dynamical decoupling, that decoupling efficiency is degraded for shallower NVs, which reveals a noise source with shorter correlation time than exists in the bulk of the ultra-pure diamond film. Such a noise source requires more closely spaced π pulses to mitigate dephasing for a given total precession time.

3. The distance dependence of the total noise power of these surface fluctuations is approximately $1/d^4$, which is consistent with a model of fluctuating magnetic fields from a surface spin bath.

4. Showed, by considering the full set of three spin-relaxation rates of near-surface NV centers, that the double-quantum relaxation channel is important to consider to define and understand the T_1 limit of T_2, particularly at applied magnetic fields of less than 100 G.

5. Having fully measured T_1 through the three relaxation rates of the NV qutrit, the qubit coherence time of shallow NVs was enhanced to $T_2 \gtrsim T_1$, which is limited still below $2T_1$ by the finite level of noise causing dephasing at $N > 1000$ pulses.

6. Demonstrated NV double-quantum relaxation spectroscopy, and, by combining the technique with dephasing spectroscopy, a model was developed for electric and magnetic field noise at near-surface NVs . The knowledge of double-quantum relaxation rate allows differentiation of the parts of this noise spectrum due to electric fields. Revised the previous conclusion that the low-frequency part of this surface noise (3) is due to surface spins, finding it is more likely associated with electric field fluctuations that cause both dephasing and spin relaxation.

7. Propose that the selective sensitivity of double-quantum relaxation to electric field noise makes it a valuable measurement to include with the commonly performed T_2 measurements to study the effects of changes to the diamond surface on the spin properties of the NV center. This relaxation rate might also be correlated with parameters that affect the NV's charge state stability and optical properties.

Several broad questions remain about decoherence of near-surface NV centers. Practically, can it be completely mitigated? Fundamentally, what are the sources of the decoherence? How far can decoherence be mitigated with a better understanding? Our simple interpretation of the noise sources with dipoles and charges only accounts for mean-field effects that would create a classical electric field or magnetic field. Decoherence due to electric fields associated with the diamond surface will perhaps depend on a microscopic form of the surface states and band bending that varies with surface termination, as has been studied theoretically [265] and experimentally [194] concerning the charge stability of the NV^-. Some work has been done on single-quantum relaxation rates and bare Hahn echo T_2 with various surface terminations [201, 86], though no strong effect was reported or modeled. The electric-field sensitivity of the double-quantum relaxation NV measurement may yield new information about decoherence effects related to termination.

There also appear to be multiple time scales reported for the correlation times of surface paramagnetic centers. Spins with sub-nanosecond correlation times may limit single-quantum relaxation times of very shallow NVs in single-crystal diamond films [86], though the origin of this $T_1^{(0)}$ reduction is not definitively shown to be due to magnetic noise. On the other end of the spectrum, certain surface-related paramagnetic centers in diamond that have T_{1e} times of a few to 10s of microseconds, as determined by double electron-electron resonance (DEER) [41, 70, 90], can apparently be rearranged or removed

with chemical or annealing treatments of the surface [88, 55, 196]. However, our work [92] and measurements on dynamical decoupling of shallow NVs near a dielectric liquid [90] suggest that the low-frequency ($\sim 10 - 100$ kHz) part of the near-surface-NV dephasing noise spectrum can be dominated by non-magnetic noise. Thus, it is possible that these particular long-T_{1e} surface spins measured by DEER do not contribute as substantially to the low-frequency dephasing noise, at least for some NVs. A challenging technique not yet demonstrated is a type of dephasing spectroscopy based on dynamical decoupling double-quantum swap pulses [224], which should yield a spectrum dependent on only parallel magnetic noise without influence of parallel electric noise. Double-quantum dephasing spectroscopy therefore might be a valuable tool to study surface spin noise further.

We have shown the value of using moderately shallow NVs (7-50 nm) as probes to learn about the magnitude of surface-induced decoherence in a general way. If surface-related noise sources are within 0-2 nanometers of the top atomic layer of diamond, then spin dephasing, relaxation, and overall decoherence rates of near-surface NV centers will probably exhibit a wider variance for very shallow NVs, those that are < 5 nanometers from the surface, precisely due to the NV's local sensitivity. The NV decoherence may be dominated by just a few nearby discrete spins or trapped charges, for example. In such a case, conclusions about an overall depth dependence can not necessarily be drawn from just a small number of NV spin measurements. This sensitivity is the same property that makes the NV a desirable quantum sensor for nanoscale imaging, though. Thus, the flipside is that not every NV is a "useful" candidate sensor, since they cannot yet be deterministically constructed in identically ideal diamond bulk and surface environments.

7.5.2 Decoherence in nanoscale detection of NMR

Our findings about surface-induced decoherence may also have implications for two recent directions in nuclear spin detection and imaging. First, generating coherence between the $m_s = \pm 1$ levels has been shown to enhance the signal-to-noise of nuclear spin detection, since both states acquire phase [224]. Double-quantum spin relaxation of near-surface NVs should theoretically limit these $\{|1\rangle, |-1\rangle\}$ coherence times as much as a factor of two lower than for the single-quantum $\{|0\rangle, |-1\rangle\}$ qubit subspace we have considered in our experiments. This comparison of T_2 limits depends on the degree to which dephasing can be mitigated in the two cases; multipulse decoupling is more challenging to perform without pulse errors for double-quantum coherence.

Second, the NV-based nuclear sensing community has recently moved towards techniques that monitor nuclear free precession [157, 206, 55, 266, 158, 267] because the technique prevents spurious signals observed due to finite-width pulses in dynamical decoupling sequences like XY-8 [156]. Correlation spectroscopy does not rely upon storing NV coherence for a long period because, after a short DD interval, the NV phase acquired from precession in the nuclear field is mapped back to a population while the nuclear spins precess freely. While this property makes the technique's resolution limited by the NV's T_1, superior to T_2 in strict DD, we deduce from our present work on double-quantum relaxation that this T_1 limit can be shorter than expected from an all-optical depolarization measurement of T_1. For example, a phase between the $|m_s = 0\rangle$ and $|m_s = -1\rangle$ states that is mapped onto population necessarily yields some population in both $|0\rangle$ and $|-1\rangle$. Therefore, some population in $|-1\rangle$ can leak to $|1\rangle$ at the rate γ, which still loses the population-encoded phase information, albeit without any direct dephasing. Therefore, one must be careful in specifying what "T_1" is relevant in describing the limits to techniques like correlation spectroscopy, as here it cannot just be the relatively long $T_1^{(0)}$ since

populations in $|1\rangle$ and $|-1\rangle$ are driven out of equilibrium. An advantage here, though, is that large magnetic fields are typically used, which we found reduces the γ rate, but still does not reduce it to a level below the single-quantum relaxation rate.

7.5.3 Scanning decoherence imaging

This dissertation makes the following contributions to scanning probe imaging with single NV centers.

1. Demonstrated nanoscale imaging of high-frequency magnetic noise using changes in the spin-relaxation rate of an NV scanning probe.

2. Reached 20-nm spatial resolution in spin-relaxation imaging of Gd^{3+}. Identified the effect of drift on the sensitivity for projections in imaging a single Gd spin.

3. Demonstrated a hybrid approach to the NV scanning probe configuration, where arrays of diamond nanopillars are fixed to bulk diamond and the target sample is scanned on a flat probe tip. Using this approach, achieved wide-area two-dimensional NV photoluminescence and ODMR imaging of magnetic nanostructures.

4. Measured the distance dependence of NVs' single-quantum spin relaxation rate near metal surfaces with different electrical conductivities. Results are consistent with magnetic evanescent wave Johnson noise.

5. Demonstrated double-quantum spin relaxation as a signal to be used for imaging surfaces that produce or modify electric field noise.

An important and already successful application of single-NV scanning probe imaging is to dc magnetism in condensed matter systems from ambient to cryogenic temperatures,

such as domain walls in thin films [67, 268] and vortices in superconductors [68, 69]. T_1-based relaxometry imaging extends the spectral sensitivity of the NV to noise in the MHz and GHz frequencies, which could be useful for studying thermally activated magnetic or electric processes in materials.

In this work, we have demonstrated the scanning NV spin-relaxation microscope for imaging sources of high-frequency magnetic and electric field noise, such as spins and charges in condensed matters systems. We have first applied the technique to two-dimensional imaging of a few-thousand Gd^{3+} electronic spins with 20-nm spatial resolution. We have taken steps to increase the magnetic sensitivity and spatial resolution of this imaging for the purpose of reaching the level required for imaging individual fluctuating spins in, for example, a patterned array. These improvements have included producing shallower NV centers that maintain millisecond coherence times, using diamond nanostructures for higher light collection efficiency, stabilizing the AFM temperature to mitigate drift, and fabricating a versatile platform for attaching few-micron-area spin samples and magnetic nanostructures.

We have probed the effects of different surfaces on the spin state and properties of shallow NV centers using the scanning probe technique. Our results demonstrate decoherence, particularly spin relaxation, as a signal resource for acquiring an image at nanoscale resolution. For example, electrical conductivity imaging may be feasible through monitoring of the NV's single-quantum relaxation rate. At the same time, our results imply that these T_1 effects will also be a sometimes unwelcome issue to consider for future NV-based imaging experiments on condensed matter samples, which often may contain conductive layers that produce magnetic noise. Furthermore, the presence of the dielectric diamond probe surface near the sample under study could make imaging of electrical phenomena actually invasive and more difficult to model. To our knowledge, no scanning probe NV imaging has yet been demonstrated on ac or dc electric fields, and

it will be a rich area to explore.

The challenges that lie ahead for T_1-based imaging primarily relate to SNR and therefore long data acquisition times. With present collection efficiencies, the experiment might only receive 0.03 photons per readout after a wait time of $\tau \sim T_1 \sim 1$ ms, adding up to seconds or minutes per pixel for acceptable SNR. Long measurements not only have slow turnaround times for learning trials, but also make the measured data more susceptible to setup drift, especially as measurements are done in ambient conditions. The ongoing current work includes improving tilt control and readout procedures of the tilt angle to reduce diamond-target distance, preparing samples with target spins at low concentration, and mitigating and correcting precisely for residual mechanical drift to the 1-nm level over hour to day timescales. We have shown in simulation that a single Gd spin is detectable in less than 1 second given a 3-nm separation, though more practical separations will be of order 10 nm, requiring several minutes for adequate signal to noise.

Another challenge for T_1-based imaging is that the magnetic or electric noise causing a signal is incoherent by nature. Therefore, the origin of a signal is not as straightforward to ascertain as a signal from coherent NV-spin interaction, for example. Coupled with this challenge is that the noise spectrum of the desired target, for example a Gd spin, may not be known precisely, so the magnitude of a signal may be attributed to either NV-Gd separation, Gd concentration, or noise spectral presence at the NV's Larmor filter frequency. Therefore, in ongoing work we seek to reduce the target spin concentration sufficiently so that only magnetic noise from a single molecule is significant. Once the signal from single spins can be well-characterized with the scanning probe technique, the technique could be extended to imaging the positions of spin-labels attached to small molecules.

Appendix A

Diamond samples and processing

A.1 Single-crystal diamond processing

A.1.1 Sample B001a for Chapter 4

We prepared shallow NVs — all within 160 nm of the surface — in three depth-confined layers of isotopically pure ^{15}N ($>$ 98%) within an isotopically purified ^{12}C (99.999%) CVD-grown film, shown schematically in Fig. 4.3(a). We grew the SCD epitaxially using plasma-enhanced CVD. The diamond sample began with a commercially available electronic grade substrate (Element Six) on which we grew a single crystal diamond film of total thickness $>$ 150 nm. The diamond sample was grown in a Seki Technotron AX6300 1.5 kW microwave plasma-enhanced chemical vapor deposition (PE-CVD) system. The sample was thinned to approximately 40 μm from the backside to optically access the NVs from the bottom while the AFM probe approaches the NVs on the untouched film side. Vacancies were formed using electron irradiation (10^{14} cm^{-2} dose at 2 MeV) and the samples were then annealed in H_2/Ar forming gas at 850 °C for 2 hours. In order to stabilize the NV centers in the negatively charged state the diamond

Properties	Sample A (B033)	Sample B (B001a)
substrate	E6 electronic	E6 electronic
thickness	150 μm	30 μm
pre-growth	polished, $ArCl_2$ etch	polished, no etch
CVD growth	50 nm ^{12}C (99.99%)	150 nm ^{12}C (99.999%)
N incorporation	^{14}N implanted 4.0 keV	^{15}N delta doped, multi-layer
vacancies	from N implantation	2-MeV electron irradiation
annealing	850 °C vacuum 2.5 h	850 °C H_2/Ar 2 h
fabrication	on-chip waveguide, nanopillars	on-chip metal coordinates
NV depths	not measured	measured with MRI + NMR

Table A.1: Diamond samples with implanted and delta-doped NVs measured in this work.

surface was oxygen terminated in an acid process (H_2SO_4:HNO_3:HCl_4 = 1:1:1 at 190 °C for 30 min).

Each N-doped layer is nominally 2.1 nm thick based on the a priori growth rate of 8.2 ± 3.2 nm/h determined from secondary ion mass spectrometry (SIMS) on several delta-doped samples grown on the same machine [43]. The grown film side of the sample was lithographically patterned with a coordinate system to identify the locations of specific NVs. This Ti/Au e-beam evaporation process does not employ any etching of the diamond film, and NVs are laterally several microns away from markers.

A.1.2 Sample B033 for Chapter 5

In Chapter 5, B033 is referred to as sample A and B001a as sample B. Table A.1 lists the main features in comparison with a Sample B used for supplemental measurements.

We prepared sample A as a (001) single-crystal diamond film with near-surface NV centers. Sample A started as a polished electronic grade (Element Six) substrate of original dimensions $2 \times 2 \times 0.5$ mm^3. The substrate was sliced into two plates and polished from the cut side down to a measured thickness of 150 μm. AFM measurements indicated a surface roughness of 160 pm with a step flow pattern. The diamond was

etched with $ArCl_2$ plasma (Ar 25 sccm, Cl_2 40 sccm, ICP 500 W, bias 200 W, 0.7 Pa) for 20 minutes to mitigate polishing damage. After cleaning in boiling acid H_2NO_3:H_2SO_4 2:3 for 40 minutes we grew 40-50 nm of ^{12}C-enriched diamond with plasma-enhanced chemical vapor deposition (CVD) at 800 °C, 750 W, 0.1 sccm $^{12}CH_4$ (99.99%), and 400 sccm H_2. The sample was implanted with 4 keV ^{14}N ions of dose 5.2×10^{10}cm^{-2} at a tilt angle of 7°. This was followed by annealing in vacuum ($P < 10^{-9}$ Torr at max temperature) at 850 °C for 2.5 hours with a 40-minute temperature ramp. The sample was cleaned in $HClO_4$:H_2NO_3:H_2SO_4 1:1:1 for 1 hour at 230-240°C.

Standard photolithography and deposition of Ti/Au 6 nm/350 nm was used to pattern a microstrip for microwave control. Diamond nanopillars were patterned on sample A to increase the collection efficiency of the NV PL [78, 171], which significantly reduces the required long averaging time of relaxation measurements. Tapered diamond nanopillars of 400-nm diameter were patterned with e-beam lithography and etched in O_2 plasma to a height of 500 nm. The small height was chosen to limit the amount of time of exposure of sidewalls to the plasma.

The diamond was glued to a thin metal sheet with a hole for optical high-NA access through the backside. The microstrip was wirebonded off-chip to a PCB waveguide to interface with a microwave amplifier circuit. A microwave source was gated by two in-series fast switches for extra isolation during long spin relaxation measurements. Two-tone measurements (Fig. 5.1(c)) for γ were done by combining individually gated $f_{0,-1}$ and $f_{0,+1}$ carrier signals from two microwave sources. The total signal was amplified and delivered to the on-diamond waveguide. The use of the on-diamond waveguide mitigates drift of the Rabi frequency during long large-N dynamical decoupling measurements in comparison to a free wirebond loop or off-chip waveguide.

Measurements on sample B spins NVB1 and NVB2 were carried out on the same shallow NV "k7" and deep NV "k26" discussed in our prior work relating NV depth

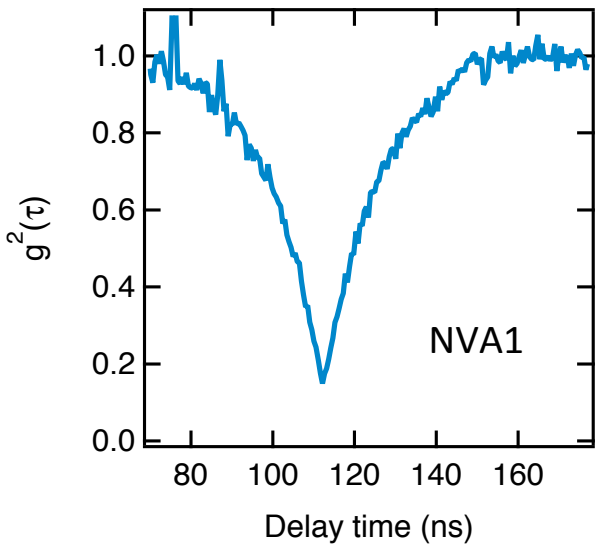

Figure A.1: Correlation photon count measurement of pillar containing NVA1, showing $g^2(\tau = 0) < 0.5$, indicating a single-spin emitter.

and decoherence rates [87]. Details of the diamond preparation are included in the supplementary online material of that work. No diamond nanopillars were fabricated on sample B and NV depths were measured.

Figure A.1 is a normalized $g^2(\tau)$ correlation measurement of emitted photons from the pillar containing NVA1, showing a dip in coincidence counts at zero delay time (offset). The high signal-to-background in the nanopillar causes the dip to be well below the $g^2(\tau = 0) < 0.5$ threshold. A histogram of time-tagged counts was collected from two APDs connected to a fiber beamsplitter.

A.1.3 Sample B001c for Chapter 6

The diamond film used in this work, named B001c, was grown with the nitrogen delta-doping method of Chapter 3, in which nitrogen is incorporated into the diamond sample during epitaxial growth [43, 201]. Growth was followed by electron irradiation and annealing for vacancy creation and diffusion [43]. The thin single-crystal delta-doped

diamond sample described in the Chapter 4, B001, was originally 2x2 mm^2. After growth and all subsequent processing was completed, it was cleaved into three pieces B001a-c, and B001c was used for the Gd-imaging work. Therefore, *a priori* the distribution of NV depths is expected to be similar to that measured in B001a.

Appendix B

Setup procedures for scanning NV magnetometers

Two scanning probe magnetometers, described in Chapter 2, were constructed for the work in this dissertation, both operating in ambient conditions. The primary difference is that Magnetometer A uses an optical based silicon cantilever detection and Magnetometer B uses electrical detection of a quartz cantilever. This section lists a few of the procedures for setting up instrument control, tip fabrication, or NV-tip alignment.

B.1 Magnetometer A

The Bruker Catalyst Bioscope AFM was interfaced with the Matlab confocal microscope program ImageScan via a Distributed Component Object Model (DCOM) connection on the local network. Bruker provides a COM to access several AFM commands and properties, and we used DCOM to keep the PCs separate that controlled the Catalyst and confocal microscopes. The "Nanoman" nanomanipulation functions from Bruker were used to control the tip position, feedback settings, and stage position of the AFM

through DCOM.

B.1.1 Communication between Matlab and Nanoscope: DCOM

This section lists the steps for all the settings that work for our lab network in setting up communication between two computers to control 1) Matlab to Matlab, or 2) Matlab to Nanoscope (or other COM). There are a few extra things that make it general to connections between PCs running different Windows OS, such as Windows 7 and XP. The first example will be to open a Matlab COM server on PC2 through a Matlab client on PC1. The same basic settings would apply for the no. 2 scenario, too.

1. Be sure both computers on the network are running copies of Matlab that use the same license source, such as from the University. It may also help if they are the same version, 7.11 currently.

2. On PC1, assumed Windows 7 here, in the START search prompt type 'dcomcnfg' and right-click on the result dcomcnfg.exe. Select Run as Administrator.

3. Under Component Services → Computers → right-click My Computer and click Properties. On the Default Properties tab make such Enable Distributed COM on this computer is checked. Set Default Authentication to None. Set Default Impersonation Level to Identify.

4. On the COM Security tab open the Edit Limits on Access Permissions and to the list make sure to add Everyone, SYSTEM, NETWORK, user1, user2, INTERACTIVE, and ANONYMOUS. Check Local Access and Remote Access for these.

5. What is meant by user1 and user2 are the login names that will be used on the computer. For example for communicating from the confocal (Alice) to AFM (AFMPC)

the typical user names were lab and nanoscope. Be sure that both computers have a user called lab with the same password and both computers have user nanoscope with the same password. Of course, a single username could be used, but we were using the nanoscope account name for AFMPC.

6. Still on the COM Security tab click Edit Default on Access Permissions. Add the same users as in step 4 with all check box permissions. Repeat the same for the Launch permissions. The Launch permissions govern what users can start a new server (e.g., on PC2) from a client computer (on PC1). The Access Permissions govern who can communicate with the COM server once it is established.

7. Apply these settings. Exit from the My Computer properties and open up the sub directory DCOM Config. Find the COM server that we want to use, here Matlab.Application (Version 7.11). Open its properties.

8. Under the General tab select None in the Authentication Level menu. In the Location tab select Run application on this computer. On the Security tab for Launch and Activation Permissions choose Default, and choose Default as well for Access Permissions. The default refers to those permissions settings we chose in the global properties for My Computer. Under Configuration Permissions, however, add the user permissions as before in step 4. Under the last tab, Identity, select the radio button for The interactive user.

9. Apply these changes. Now, in PC2 also open up the dcomcnfg.exe as administrator and apply the same settings as in steps 2-9.

10. When all that is done, do the following also on both computers. From the classic view in Control Panel open up the Local Security Policy. Under the Local Policies folder open the Security Options folder.

11. First to check is that DCOM: Machine Access Restrictions in Security...' and DCOM: Machine Launch Restrictions in Security... are both set to Not Defined. Next find Network access: let everyone permissions apply to anonymous and set to Enabled. Then find Network security: Sharing and security model for local accounts and set it to Classic - local users authenticate as themselves.

12. Having done this for both computers, there is one more step found to be necessary if a Windows 7 PC is accessing a Windows XP PC. On the XP machine right-click the red shield in the Desktop taskbar for security settings. Click Windows Firewall. Under the Exceptions tab click the Add port... button and type DCOM for Name and 135 for Port number. Click Ok to get out of the windows.

13. It should now be possible to run a copy of Matlab on PC2 from PC1 (or vice versa). Here say PC1 is Alice and PC2 is AFMPC. Open Matlab in PC1 and at the command line type v = actxserver('Matlab.Application.7.11','\\AFMPC'). v is then a handle to the COM server. The second argument tells which machine to run the server on. You can get the correct form, here \\AFMPC for this by opening the network in My Computer, clicking the computer you want to connect to, and getting the path to it. When the actxserver command is entered a Matlab command line should pop up on PC2. The methods that can be used from PC1 to control Matlab in PC2 are given in online Mathworks documentation. Important functions are Execute and feval because they take a string in valid Matlab syntax and execute it on PC2.

14. To do the same for a non-Matlab COM server, such as Nanoscope, apply the DCOM config settings above to the Nanoscope COM. Note that for any COM objects that are not already in Microsoft Windows, you need to first open the command line cmd as Run as administrator. Use the cd <folder> command to navigate to the

folder that contains the .exe for the COM. For example, the one for Nanoscope is in \\Afmpc \d\Program Files \Bruker \Nanoscope \8.10 and is called z.exe. At this folder enter the command z.exe /regserver. Only after this has been done will Nanoscope be visible as a COM object under the Component Services DCOM Config folder.

15. The nanoscope COM interfaces are opened through Matlab commands

    nn = actxserver('NanoScope.zApi','\\AFMPC') and

    nn = actxserver('NanoScope.OpenArchitecture','\\AFMPC').

    These will not work unless the server is being made on a PC authorized to use the real time mode of the software, which is only AFMPC in our lab.

B.1.2 CPW on glass for NV resonance slice imaging

Figure B.1 shows a screenshot of the mask design for a Ti/Au microwave coplanar waveguide (CPW) to be fabricated on 40-mm-round coverglass or even on part of a rectangular 75 mm × 25 mm coverglass. The design contains four CPWs where the wide end can be soldered to a small PCB connector, such as an SMP style, and each CPW is shorted from signal to ground as shown in Fig. B.1(b). The basic procedure for making the device uses either wet etching of Au and Ti or metal liftoff with a single contact lithography step. The advantage of the etching recipe is that the metal deposition can be done before lithography. These procedures differ in the use of resist tone and mask polarity.

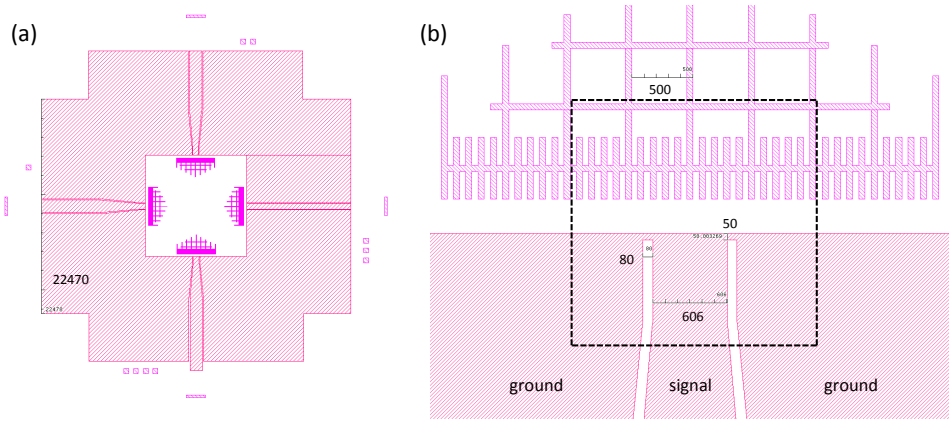

Figure B.1: Mask design for shorted CPW on a 40 mm diameter round cover glass. (a) Full pattern with four CPWs, each with two clear gaps where optical access can address NV centers. A PCB-to-SMP connector is soldered to the free outside edge of the CPW. (b) Close up of one CPW in the region where the thin diamond is placed. The markers (violet) are a ruler for placing the sample reproducibly on the CPW so that the NV centers may be positioned the same way relative to the CPW short. Dimensions on the figure are in microns. A typical diamond chip is (2000 μm)^2, referenced here by a square dashed line.

B.1.3 Improvements to Magnetometer A

The most important change to Magnetometer A (though not used in Chapter 4 experiments) was the replacement of the APON 60XOTIRF objective with a UPLSAPO40X2 air objective with NA = 0.95, the same used in Magnetometer B discussed below. The primary reason for this change from oil to air was to remove contact between the glass waveguide and the objective to eliminate a source of nanometer-scale mechanical vibrations seen with the AFM. Second, the coverslip-corrected air objective is more suitable to image through 150-160-μm-thick diamond samples, which are convenient to handle and process. Third, the back aperture size of the two objectives is nearly identical despite the magnification difference, so the two can be interchanged with little effect on the imaging quality of the laser-scanning CFM and just an adjustment of the μm/V number in calibration of the galvo mirrors.

The configuration of optics in Magnetometer A works well for diffraction-limited

imaging of NVs. Nevertheless, one optical design flaw should be noted that results from a combination of the specific choice of objective and galvo mirror system. The objective $\phi_{\mathrm{BA}} \approx 8.49$ mm is large, so the beam must be on the order of 10 mm to overfill the aperture. However, the galvo mirrors are small, about 5 mm wide, which means the ~ 2 mm beam must be expanded between the scan and tube lenses by about $4\times$ to meet the ϕ_{BA} size. The axial magnification of the scan and tube lens pair is 4^2, meaning that the pivot point for the 1-cm-separated x and y mirrors cannot physically be coincident at the back aperture, rather there is a 16-cm gap. Therefore, a compromise must be made here on the clipping of the scanned beam at the back aperture in the two dimensions. Practically this results in a smaller imaging field and slight lateral shift with focus changes at large scan angles, but the NVs of interest can always be translated near to the center of the scan range. In some later CFMs in the lab we used a single fast steering two-axis mirror and avoid this problem. Similarly, in Magnetometer B larger galvo mirrors were used than in Magnetometer A so that the excitation beam could be expanded before the galvos without clipping, thereby avoiding the $4\times$ expansion that leads to large axial magnification in Magnetometer A.

B.2 Magnetometer B

B.2.1 NV-to-sample alignment for scanning probe measurements

Following are the general steps for setting up the AFM measurement.

I) Preparing the diamond sample

1. A piece of square titanium foil of thickness ~ 50 μm has a 1-mm hole drilled into the center and edge through holes to screw into an aluminum sample plate. Use UV curing glue NBA 107 (white bottle), meant for temporary optical-use adhesion,

to dab dots of glue at 4 points around the 1-mm hole.

2. With sharp tweezers press the 2-mm-square diamond chip with backside into the hole with the glue around it. The diamond can alternatively be pressed onto the bare hole and the painted with a bit of glue around the edges. Then the UV lamp can be shined on the diamond for a few.

3. Inspect the diamond connection under a stereroscope from the side to see if there is any glue gap that tilts the diamond. If so the gluing should be removed with solvents and retried. The reason is two-fold: a) a gap too large will mean the objective working distance may not be able to "see" the top side surface without touching the diamond, bad for AFM vibration, and b) the tilt makes it more difficult to align an AFM plateau tip parallel to the diamond pillars.

4. Wirebond a coplanar waveguide to the on-chip diamond microwave structures. Test the connection with a multimeter. Photos of the diamond sample holder are shown in Chapter 2.

II) Attaching and aligning the AFM tuning fork probe

Turn off the Zurich HF2LI lockin signal output before mounting so that the TF excitation is not applied.

1. Mount the tuning-fork-on-sapphire (TFOS) piece to the top of the 5^{cdot} aluminum mount disconnected from the setup. Put in specific brass shims if needed to tilt the probe to be more parallel to the scan axis. Use nylong screws to tighten the conductive clamps onto the silver leads of the TFOS. Alternatively, a two-dimensional tilt-tip stage is used.

2. Check the resistance between the two MCX connectors (excitation and readout of

the TF) to the silver paint leads. Typical readings are $0.5 - 4\ \Omega$. The two leads also should not be shorted.

3. Attach the MCX connectors lightly to double-side tape or holes on the aluminum mount to secure them in place while transporting the mount into the scanner setup. This is important to keep the wires from dangling and possibly breaking as well as to put them in accessible places once in the setup and connections need to be made.

4. Place the mount on the MCL XYZ scanner stage. Line up the 4-40 mounting holes and use one 4-40 screw to attach the closest hole to the MCL stage. A magnet wire for grounding to other parts of the stage should go under this screw and then the screw must be only lightly tightened to avoid torquing the stage significantly.

5. Connect the MCX excitation and readout connectors to the MCX-BNC cables on the setup. The readout line is the shorter wire connected to the current amplifier.

6. Turn on the lockin signal output. Sweep around 32 kHz to locate the resonance. A Q of a few-hundred to 2000 is typical. If the Q is only a couple-hundred or much less then it is best to take out the mount and try clamping the TFOS differently. The best Qs are generally found when the back tine-connecting end of the TF is on the alminum mount edge and only the tines are protruding off the mount edge. To remove the mount carefully, first shut off the signal output and disconnect the MCX connectors, placing the wires on the tape or holes to secure them. Loosen the 4-40 screw and take the mount out.

7. Once the Q is acceptable, place a narrow strip of lens tissue on top of the MCL stage hole between the Micronix assembly and the tuning fork mount. This serves as a screen for transmitted 532 nm light while doing rough focusing and alignment.

8. Turn off the lights and turn on the APD power and 532 nm laser keyswitch. From Matlab run the AFM "test gui" and "ImageScan." The digital MCL x and y positions should each be set to 25 μm on the scanner digital control window if not there by default. From the Figure 3 scan parameters window first set the "Tip position" to 2.5 V and hit Enter, which is the analog input portion to the x axis. Monitor the total x displacement on the "test gui" to see it increase to 50 μm. Once in the correct position the Figure 3 "Tip position" in volts will also update. Repeat the same for the y axis analog position, and do not change those parameters simultaneously until updates are completed. The idea of this central setting is to have a good buffer of analog voltage "play" to offset the stage and have sufficiently large scan sizes.

9. Manually lower the objective via the micrometer translation stage until the shadow of the tuning fork appears on the tissue screen. A good practice is to remote login or Teamview into the controls and monitor the TF amplitude and the ImageScan window together while approaching the objective. The objective working distance is less than 200 μm so it can be lowered until the tuning fork shadow expands significantly. In practice to be cautious you can repeatedly do piezo z scans of the objective to see if a PL peak appears, and if none appears lower the objective further manually. Alternatively you can do x, y laser scans to see if the tuning fork structure appears in the confocal image.

10. Eventually a cantilever-shaped form will be visible in the confocal images against a brighter background of the glue. Retract the objective by increments of $5 - 10$ μm until the confocal image shows the tip and the cantilever then goes out of focus.

10. Translate the manual x, y stage that the MCL scanner sits on while taking fast continuous confocal images until the tip is centered around the confocal 0, 0 point.

11. Once centered and moving on to the next step, DO NOT translate the manual stage by hand any further, otherwise the tip position will not be known.

III) Aligning the diamond nanopillars and engaging the probe

1. In the Micronix control window of the Matlab $test_gui$, click "Open port" to begin COM port communication to the three-axis positioning stage. It is usually fine to set the x and y axes to smooth open loop but important to set the z axis to closed loop.

2. If the Micronix z stage was not already retracted $\sim$ 4.5 mm above the center position, translate it roughly to the center and click "Zero z." Then retract the stage by increments of 500 μm until its read out position is -4.5 mm.

3. This step must be done carefully since the AFM tip is exposed facing up. The objective should also be fully retracted via the manual stage. Insert a screw into the diamond sample holder and guide the piece horizontally between the objective and micronix stage, placing it down on the mount of the Micronix z stage. Use a small hex key to tighten the screw while supporting the plate with the other hand until tight. The assembly should now look like the photo in Fig. 2.23(a) with the diamond and AFM tip separated by a distance on the order of 1 cm.

4. Plug in the diamond sample holder's MCX connector to the output of the microwave amplifier circuit.

5. Turn off the lights and turn on the laser AOM and APD power. Remote control the Micronix z stage, lowering it by few-hundred-micron steps until it is a few millimeters from the AFM tip. Lower the objective manually until the excitation light projects an image of the diamond sitting on the Ti foil hole. If there is no

image then the Micronix x, y position is probably far off. Translate the x and y of the electronic Micronix control until the green spot appears on the screen directly below the objective and tuning fork. Use the projected shadows to roughly align to the portion of the diamond to look at, typically using the on-chip waveguide features for reference. Again DO NOT move the manual x, y stage to position the diamond sample, otherwise the tip becomes misaligned from the optics.

6. Set the Micronix z step size to a smaller and smaller value while approaching the diamond to the tip by clicking the "+z" button. A typical step size near the end of the manual approach would be 20 μm, and you can look through a handheld magnifying lens to see the remaining gap between the tuning fork apex and diamond surface. Go as far as comfortable with the Micronix steps.

7. Put in a beamsplitter between the galvo mirrors and the dichroic mirror to project the green light reflected from the sample back onto a screen. Lower the objective towards the diamond sample until it passes just through the second focus point. The first is the top surface (where glued to Ti) and the second is the desired nanopillar surface.

8. Perform a z objective piezo scan to find the maximum of PL. Set the z piezo to this position, and then do a confocal scan. Use fine adjustments of the electronic Micronix x, y stages to position the area of interest near the confocal 0, 0 position where the tip will engage.

9. If the diamond is lowered as far to the tip as comfortable by Micronix steps by eye, then close up one panel of the enclosure box and prepare for the automatic engage sequence.

10. The AOM can be turned off during approach. Run the "approach pid" Matlab

script with any adjustments to setpoint or I gain that are needed. Typical values are a drive amplitude of 1-2 mV (depending on Q), PID setpoint of $0.92 - 0.95$, I gain of -45. The approach speed is typically $50 - 100$ nm/sec with minor adjustments to setpoint amplitude and gain. If the script halts in a false engage, it can be restarted. Likewise, if the amplitude changes dramatically (due to various observed non-contact reasons) such that the setpoint is no longer low enough to maintain a reasonable approach speed, then the setpoint can be lowered more.

11. The automatic approach algorithm follows a three-step process. Ramp the PID output by turning on the lockin PID 1 control which moves the height of the MCL z scanner up over a range of about 9 μm. If the PID does not reach a stationary point, then set it back to 0 output and increase the direct DAQ input to the z scanner by some 8.5 μm. Continue these two steps until the MCL z scanner is at $\sim$ 90 μm, which is 90% of the maximum. Quickly set the DAQ output back to the low point of 10 μm. The Micronix then takes a closed loop z step of 60 μm, moving the diamond down towards the tip. The cycle then completes until the tip contacts the diamond, signaled by the lockin PID reaching its setpoint. This fact is relayed to Matlab to stop the PID and retract the scanner some few microns.

12. Approach the objective manually the remaining distance using the same beamsplitter method. Perform a confocal scan to verify that the correct diamond area is near the center of the confocal scan area.

13. Engage the tip by turning on the PID output after verifying a proper setpoint amplitude, usuall 0.9-0.95 of the retracted-tip free amplitude. Taking a confocal scan while the tip is engaged should show some signature that resembles the tip during the alignment step without diamond.

B.2.2 Tip attachment and mounting to the magnetometer

1. Sometimes the remaining cantilever base hanging off the edge of the tuning fork can hit the diamond sample before the tip for even a small pitch angle of a few degrees. A first step is to shorten the cantilever. Break it off by pushing with a glass fiber or metal point in the micromanipulator arm.

2. Many of the fabricated cantilevers were easily submerged in glue, covering the tip. One method to mitigate this is to build up one to two layers of buffer glue cured to make an elevated platform for the final glue. Then a very small amount of glue can be used for the cantilever attachment, where the tip apex does not even need to be placed directly over the glue.

3. Small adjustments to the pitch or roll angle without a tilt stage can be made with narrow metal shims placed under the sapphire probe base. This can also be done, usually for pitch, if a non-tip part of the tuning fork or cantilever is hitting the diamond first. In a more recent iteration, we have implemented a tilt stage on the magnetometer to precisely adjust the AFM probe tilt in two dimensions with angle-readout circuitry.

4. The tuning fork Q is very sensitive to the amount of overhang of the tuning fork base over the aluminum mounting platform. Generally a $Q < 100$ can even be improved to $Q > 1000$ with minor adjustment, placing the base of the fork tines at the overhang edge while only the tines are suspended.

Appendix C

Supporting material for Chapter 4

C.1 NV relative depths

In this section N refers to the number of NVs in the depths measurement set. We extracted the relative depth δ_{ij} between each NV_i with every other of the set of $(N-1)$ NV_j by using a sub-pixel image registration algorithm [255] to determine the image offset in the z axis. The algorithm first computes the 2D Fast Fourier Transform of each image and then retrieves the relative phase, which is then converted to a fractional pixel shift. We multiplied this pixel shift by the measurement pixel size in the z direction, 7.69 nm. Due to image noise, the offsets are not precisely consistent with one another for a given i, j, k. Therefore, to compute one overall depth value (for arbitrarily chosen zero depth point) for NV_i we averaged over the z offsets as summarized in Chapter 4: $d_i = \left(\sum_{j=1}^{N} \delta_{ij}\right)/N$.

To extract an error in mean relative position for NV_i we first set a specific "image reference NV" called NV_n with $n = i$ permitted. We computed the image registration of NV_n with NV_i to obtain their relative offset $\Delta_{i,n}^{n}$, where the superscript indicates the reference NV and the two subscripts are for the two NVs whose depth difference

is indicated. Using this same NV_n we registered its image to all other NVs' images to obtain $\Delta_{i,n}^n$ for $j = 1, 2, 3, ...N$. These $\Delta_{i,n}^n$ for fixed i and n then represent the relative depths of NV_i to each NV_j, as referenced by comparisons to NV_n. Therefore, we take as one value of the mean depth position of NV_i as $\bar{\Delta_i}^n = \left(\sum_{j=1}^{N-1} \Delta_{i,j}^n\right) / (N-1)$, which excludes index $j = i$. There are N total values from cycling through all different NV_n references for the fixed i. The mean from all values is $\bar{\Delta}_i = \left(\sum_{n=1}^{N-1} \bar{\Delta_i}^n\right) /N$, and the sample variance is $\sigma_i^2 = \left(\sum_{n=1}^{N-1} \left(\bar{\Delta_i}^n - \bar{\Delta}_i\right)^2\right) / (N-1)$. The standard error of the mean depth position of NV_i is finally $\mathrm{SE}\Delta_i = \sigma_i/\sqrt{N}$ given the sample size of N. Values of $\mathrm{SE}\Delta_i$ for the different NV_i were in the range $1 - 2$ nm.

We also empirically measured the error in depth that would result from uncertainty in choosing the fixed x position x_f for the (y, z) scans. This is related to the slopes of the resonance slice dZ/dY and dZ/dX. We first performed a (y, z) scan choosing the predicted circle fit center $x_f = x_0$. We then repeated the scan five more times for $x_f = x_0 \pm x_p, x_0 \pm 2x_p, x_0 + 5x_p$, where $x_p = 45$ nm is the approximate lateral pixel size. The results of this measurement for one pixel offset x_p are $\sigma_1 = 2.6$ nm and for offset of two pixels $2x_p$ they are $\sigma_2 = 6$ nm. This is a unidirectional error since a positive or negative offset would shift the resonance slice down in apparent tip height. Even so, since we fit each NVs (x, y) ring with the same method and image resolution, consistency likely diminishes the effect of this potential error source. That is, such a systematic error would be subtracted out when comparing NVs.

Two NVs, named m61 and m62, were excluded from the image registration routine because (m61) its image size was incompatible with the others and (m62) the spot contained another NV that was at a different orientation and therefore had an intersecting resonance slice. We fit a fourth order polynomial $z = p_1y^4 + p_2y^3 + p_3y^2 + p_4y + p_5$ to each image and used p_5 as the depth offset to compare. In m62 this required excluding pixels from the fit that contained optically detected resonance of the intersecting NV. We then

performed polynomial fits of the group of image registered NVs in order to connect m61 and m62 with the other relative depth results. This alternate method accounts for the larger depth error bar estimates in the m62 and m61 data points of Fig. 4.16.

C.2 Coherence data analysis

Here we discuss the data acquisition and error analysis of the coherence measurements, followed by a discussion of the theory for the coherence decay fit functions.

Plots of coherence versus total precession time, as in Figs. 4.9, E.1, and 4.14, were obtained by fixing τ in the pulse sequence and repeating the sequence for 10,000 cycles. One cycle consisted of NV initialization for 1400 μs, 500 ns depopulation time, microwave sequence, signal photon collection for 350 ns, initialization, 500 ns depopulation time, and reference photon collection for 350 ns. The reference readout gives the photon count rate for the NV in the $|0\rangle$ state. The total number of signal and reference counts over the 10,000 cycles are $S_{\tau,i}$ and $R_{\tau,i}$, respectively, where i indicates the current sweep through all τ points. Typically $K = 25$ or more sweeps are used for a total of at least 250,000 measurements per τ point. We determined the means $\bar{S}_\tau = \frac{1}{K}\sum_{i=1}^{K} S_{\tau,i}$ and $\bar{R}_\tau = \frac{1}{K}\sum_{i=1}^{K} R_{\tau,i}$, the sample variances $\sigma^2_{S,\tau} = \frac{1}{K-1}\sum_{i=1}^{K}(S_{\tau,i} - \bar{S}_\tau)^2$ and $\sigma^2_{R,\tau} = \frac{1}{K-1}\sum_{i=1}^{K}(R_{\tau,i} - \bar{R}_\tau)^2$, and the covariance $\mathrm{Cov}(S_\tau, R_\tau) = \frac{1}{K-1}\sum_{i=1}^{K}(S_{\tau,i} - \bar{S}_\tau)(R_{\tau,i} - \bar{R}_\tau)$. The covariance identifies the correlations between the signal and reference readouts as might be caused by laser power fluctuations and slow drifts in power or photon collection. We computed the mean background-subtracted NV signal $\bar{D}_\tau = \bar{S}_\tau - \bar{R}_\tau$ and propagated the errors using the 2×2 covariance matrix, giving $\sigma^2_{D,\tau} = \sigma^2_{S,\tau} + \sigma^2_{R,\tau} - 2\mathrm{Cov}(S_\tau, R_\tau)$. Lastly, for error bars on the final coherence data points $\bar{D}_\tau$, we calculated the standard error of the mean $\mathrm{SEM}_\tau = \sigma_{D,\tau}/\sqrt{K}$. The error bars agree excellently with theoretically computed photon

counting shot noise error computed from the square root of the total photon counts. We verified this shot noise limited uncertainty for each of the NVs coherence measurements shown in Figure 4.9, and thus we plot there the theoretical shot noise errors. For clarity of converting photon counts to a measure of coherence, we plotted the mean of $S_{\tau,i}/R_{\tau,i}$, or the "normalized photoluminescence."

C.3 Semi-infinite bulk nitrogen spin bath

The nitrogen P1 center spin bath is a complicated entity because it contains five groups of spins with different N-C bonds [10], and these spin groups are individually addressable [141]. Even so, the off-resonant NV-bath coupling behaves similarly to a classical noise field at the NV. It is not certain that the Ornstein-Uhlenbeck process would be valid for this bath for NVs within 10s of nm of the diamond surface, since spin diffusion is limited by the geometry, simply depicted in Fig. 4.17(b). One way to examine this effect is to assume that the NV is within interaction distance of a fewer number of nitrogen impurities, due to the semi-infinite nature of the bath, as depth decreases.

Therefore, to describe this feature we tried a model of the coupling parameter $b^2_{\text{bulk}}(d)$ as a function of depth in the same style as in the previous section. The surface bath of σ_{surf} density is now replaced by a bulk bath of density ρ_{bulk}, and the z spin coordinate is integrated over. The integrand becomes a piecewise function because once the NV depth d becomes less than the average spin-spin separation $\delta r = (3/(4\pi\rho_{\text{bulk}}))^{1/3}$ it is no longer valid, on average, to consider spins directly above the NV.

This semi-infinite bath model predicts a slow decay of $b_{\text{bulk}}(d)$, reaching at most a factor of two reduction below a depth related to ρ_{bulk}. This model was found not to be necessary to describe the data of Fig. 4.16, perhaps because the nitrogen concentration is fairly localized in the delta-doped film. Indeed, the deepest NV investigated had the

longest T_2 of 450 μs, suggesting that it was not in the center of the N doped layer but rather on the deep edge of it where nitrogen concentration is then slightly reduced. Examining the spread of coherence times and depths more NVs of a deep delta-doped layer could reveal whether the N concentration is normally distributed around a center depth, as SIMS data suggest [43], or fairly constant near all NVs. Experiments with a semi-infinite or 2D nitrogen spin bath might be possible with nitrogen delta-doping.

Appendix D

Supporting material for Chapter 5

D.1 Pulse sequences and fitting for Ω, γ

The full experimental form of the pulse sequences described in Fig. 5.1 of the main text is shown in Fig. D.1. The data for the F_1 sequence in Fig. D.1(a) is normalized as

$$F_1 = (S_{0,0} - R_0) - (S_{0,-1} - R_0)\,. \tag{D.1}$$

$S_{0,0}$ was then fit to Eq. 5 in the main text to yield parameters r and Ω. The data plotted as a relaxation signal is normalized by r. The F_2 sequence in Fig. D.1(c) was then performed, which accounts for the indistinguishability of PL from the $|\pm 1\rangle$ states by selectively swapping either ρ_{-1} or ρ_{+1} with the distinguishable ρ_0 population before PL readout. The normalization expression is

$$F_2 = (S_{-1,-1} - R_0) - (S_{-1,+1} - R_0)\,. \tag{D.2}$$

An alternative to the F_2 signal to extract γ is the F_3 signal in Fig. D.1(b), giving

$$F_3 = (S_{-1,-1} - R_0) - (S_{0,-1} - R_0)\,. \tag{D.3}$$

F_3 is fit to a sum of main text Eqs. 5 and 6 $(F_1(\tau) + F_2(\tau))/2$ with Ω fixed to the F_1 result to yield parameters r and γ. The data plotted as a relaxation signal is normalized by r. Joint fits of F_1 and F_3 to data gave the same results and uncertainties in Ω and γ as obtaining first Ω from F_1 and then fixing Ω to fit F_3 for γ. F_3 is an alternative to the two-tone measurement F_2 (Fig. D.1(c)) and F_1, however, an advantage of using F_2 are smaller error bars for γ due to a single-exponential fit function rather than a biexponential fit function in F_3. F_2 also demonstrates most clearly how the pulse sequences give direct readout of the different spin populations.

The subtraction $S_{0,0} - R_0$ eliminates some laser and PL common-mode noise within a sequence shot. Two example data sets before final subtraction and fitting to F_1 and F_3 are shown in Fig. D.2, where the biexponential (blue data) indicates a large γ and small Ω.

We use only "symmetrized" pulse sequences (same total shot time for each τ point) that keep the average laser and microwave power relatively constant for stable AOM operation and heating. The microwave signal was gated by two in-series fast switches and IQ modulation to ensure no spin rotations during the long dark times for T_1 measurements. The on-diamond microwave waveguide also enables stable Rabi frequencies over long time periods. Because the timescales of γ and Ω sometimes differ by more than an order of magnitude the time point sampling must be chosen carefully, for example a larger number of time sampling points at small τ helps to resolve the initial fast DQ relaxation.

CPMG measurements (Fig D.1(d)) were normalized on a coherence scale $[0, 1]$ by

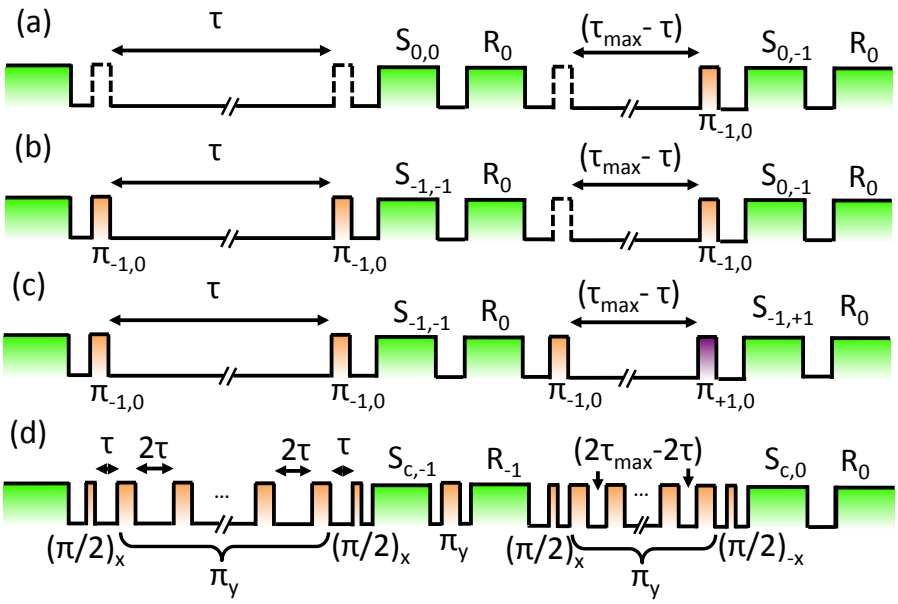

Figure D.1: Full experimental form of the pulse sequences for extracting Ω (a) and γ (b,c) relaxation rates and (d) CPMG-enhanced T_2. Green pulses are for 532-nm initialization and readout, and orange (purple) pulses depict gating the in-series microwave switches with carrier on resonance with the $\omega_{0,-1}/2\pi$ ($\omega_{0,+1}/2\pi$) transition. Dashed-line boxes are blank delays when no pulse is done for $|0\rangle$ preparation or readout. The normalization procedure is described in the supplementary text. For each signal S the first subscript is labeled to 0, -1, or c for the initialized state in $|0\rangle$, $|-1\rangle$, or SQ superposition, and the second subscript refers to the $m_s = 0, -1, +1$ population that is read out, which is effectively a phase readout for the CPMG sequence. The R pulse is for reference of the PL a_0 or a_{-1} of each state $|0\rangle$ or $|\pm1\rangle$. The IQ phases $\pm x, y$ are indicated for the CPMG sequence.

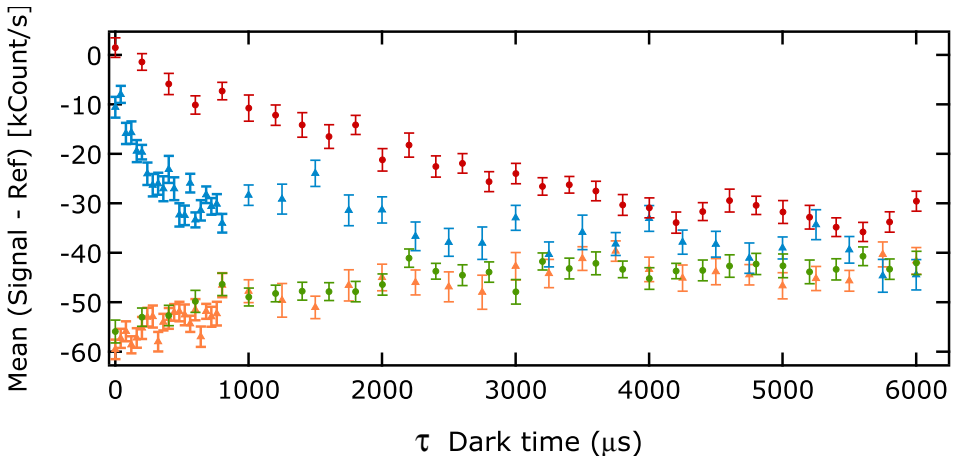

Figure D.2: Four data sets for NVA1 taken at 37.1 MHz using relaxation pulse sequences Fig. D.1(a) (circles) and Fig. D.1(b) (triangles) of Fig. D.1. Red is $(S_{0,0} - R_0)$, green is $(S_{0,-1} - R_0)$, blue is $(S_{-1,-1} - R_0)$, and orange is $(S_{0,-1} - R_0)$. The $\pi - \tau - \pi$ data at short $\tau < 1000$ μs (blue) is sampled at a smaller time spacing to accurately capture the fast γ decay.

measuring the reference PL in the $|0\rangle$ (R_0) and $|-1\rangle$ (R_{-1}) states during every shot. The two measurements with a $(\pi/2)_{\pm x}$ pulse at the end project the phase into a population of either state and these two coherence curves are subtracted and normalized by the contrast $R_0 - R_{-1}$ to obtain the plotted result. Common mode PL noise is primarily subtracted out by (signal − reference) since the two $(\pi/2)_{\pm x}$ signals at a given τ were acquired at different times (seconds to minutes) due to the symmetrization of the sequence.

Error bars on the data points for relaxation population and CPMG coherence data versus time are standard errors over many repetitions at each individual τ point. Error bars in the extracted parameters γ, Ω, and T_2 are fit standard errors, and uncertainties in T_1 were propagated from the errors in γ and Ω.

D.2 Stationary versus non-stationary electric noise source

In the preceding analysis we have made the common assumption of an Ornstein-Uhlenbeck process, which is the unique first-order stationary Gauss-Markov process [211]. The correlation time τ_e of the electric fluctuations affecting γ have been assumed to be much shorter than the single-shot measurement time (milliseconds) as well as the full measurement time (hours). However, we also observed two long-lived "anomalous" data points for γ both shown in the data of Fig. 5.4: one being that $\gamma = 2.4(6)$ kHz at $\omega_{\pm1}/2\pi = 37.1$ MHz deviated more than a factor of two larger than the $\gamma = 0.63(16)$ at $\omega_{\pm1}/2\pi = 39.2$ MHz for NVA1, and the other anomalous point being for a relatively low value of γ at $\omega_{\pm1}/2\pi = 104$ MHz for NVA7. It is possible that a long-lived noise source (minutes or hours) was present at the time of the anomalous point, for example if an electric-dipole-containing molecule had adsorbed in a surface position very close to the NV for some time. Another possibility is the change of charge states of surrounding vacancy defects. It has been shown that the charge state of the NV center (NV^- or NV^0) can be switched for example optically [269] or electrically [270]. However, this particular NV is verified to be a single NV within the diffraction-limited spot size of ~ 500 nm, so it is likely not electric noise from another NV in this case. Note that these $\gamma(\omega_{\pm1})$ measurements were not taken in a monotonically increasing or decreasing $\omega_{\pm1}$, rather we took them out of order pseudo-randomly, and so γ is not for example slowly increasing in time but is quite stable.

Another interesting route of further research in DQ spin relaxation would involve looking at changes in γ with manipulation of the charge state of a small ensemble of NV centers or as a function of laser illumination or static electric fields on surface electrodes. We used constant low-power 532-nm illumination for all measurements in this work of 60

μW into the back of the objective, which still yields high PL counts due to the enhanced collection efficiency of the diamond nanopillars.

D.3 Rabi driving at low B_0

Several of the low-field measurements are performed with $|\pm 1\rangle$ splittings of $\omega_{\pm 1}/2\pi \approx$ 37.1 MHz. Choosing a $|0\rangle \leftrightarrow |-1\rangle$ Rabi frequency is a trade-off between covering the hyperfine bandwidth and avoiding population transfer to the $|1\rangle$ state. For a resonant $\pi_{0,-1}$-pulse, the detuning of the $\omega_{1,0}$ transition is $\omega_{\pm 1}$, which gives an "unintentional" maximum Rabi contrast of $\epsilon_{+1,\max} = \Omega_R^2/\left(\Omega_R^2 + \omega_{\pm 1}^2\right) \approx 5\%$ for $\Omega_R = 8.33$ MHz (60-ns π-pulse). Over the duration of the π-pulse the final population leaked into $|1\rangle$ is then

$$\epsilon_{+1} = \frac{\Omega_R^2}{\Omega_R^2 + \omega_{\pm 1}^2} \sin^2\left(\pi t \sqrt{\Omega_R^2 + \omega_{\pm 1}^2}\right) \approx 0.029 \tag{D.4}$$

This 3% is a relatively low population compared to our PL signal noise, which is about 10%. In general this population leak in the F_3 or F_2 measurement will alter the initial conditions after the first π_{-1}-pulse to $\rho_{-1} = 1 - \epsilon_{+1}$ and $\rho_1 = \epsilon_{+1}$. Likewise, at the end of the dark time τ, there will be an imperfect population transfer between $|-1\rangle$ and $|0\rangle$. Longer π pulse durations can be used to reduce the bandwidth and prevent significant population transfer. These considerations do not affect the fundamental decay rates γ and Ω between the levels, and low-B_z effects are an interesting avenue for future relaxation studies on both SQ and DQ qubit coherence.

D.4 Effects of static $B_\perp$ and magnetic field noise on γ

The component of the applied static magnetic field transverse to the NV axis will change the eigenvectors $|0\rangle$, $|\pm1\rangle$ into a general mixed form. For relatively small $B_z < 200$ G the spin mixing is not severe. However, for a misalignment angle θ approaching $80-90°$ most of the total field is $B_\perp$, and the mixing will be more significant even at small $B_0 = \sqrt{B_\perp^2 + B_z^2}$. The implication is that there will be a modified set of spin relaxation transition rates that differ from the pure Ω_+, Ω_-, and γ.

In the presence of a weak transverse magnetic field compared to $D_{\rm gs}$ and $B_z = 0$ ($\theta = 90°$) the eigenstates are approximately [29, 271]

$$|\psi_z^{(0)}\rangle \approx |0\rangle \tag{D.5}$$

$$|\psi_x^{(0)}\rangle \approx \frac{1}{\sqrt{2}}\left(|-1\rangle - |1\rangle\right) \tag{D.6}$$

$$|\psi_y^{(0)}\rangle \approx \frac{i}{\sqrt{2}}\left(|-1\rangle + |1\rangle\right) \tag{D.7}$$

The measurements of NVA2 were taken in a non-zero small B_z and transverse magnetic field of $B_\perp = 44.8$ G and $\theta \approx 83°$, which results it a splitting of the resonance lines $\omega_{xy} = 30.6$ MHz. Since $B_z = 5.4$ G in this case, diagonalizing $H = hDS_z^2 + g\mu_B \mathbf{B}\cdot\mathbf{S}$ shows that the mixing between all three $|m_s\rangle$ states is very weak (populations better than 99% pure), meaning that we can still consider to good approximation that it is the as-defined γ that we are measuring with the F_1 and F_3 or F_2 methods. For all other NVs the $B_z \gg B_\perp$ condition was fulfilled even more strongly, so the $|m_s\rangle$ eigenstates are

always valid.

In the hypothetical case that $\theta = 90°$ ($B_z \approx 0$), there is still very little mixing of $|1\rangle$ and $|-1\rangle$ with $|0\rangle$ as shown by Eqs. D.5-D.7. This means that the DQ relaxation channel will act between $|\psi_x^{(0)}\rangle$ and $|\psi_y^{(0)}\rangle$, although the splitting $\omega_{x,y}$ will be much smaller and subject to other factors like static strain and static electric field in comparison to the $\omega_{\pm 1}$ values considered in the present work [29, 235]. This may be an interesting versatility to the DQ relaxation method for spectroscopy. When **B** is perfectly aligned to the NV center axis one can probe solely electric field and strain noise, and but tuning θ to the other extreme one can also become sensitive to magnetic noise using the same pulse sequence.

Finite $B_\perp$ can also make the DQ transition of a $S = 1$ defect system susceptible to coherent driving by magnetic fields, though it is a second-order effect that requires significantly more power [33, 216]. We consider for our experiment the effect of incoherent magnetic noise on γ to further check whether the observed frequency dependence can really be attributed to electric field noise. Our measurements were performed with misalignment angles $\theta = 0 - 8°$ so there is a small contribution of $B_\perp$ to the total field.

As an experimental check of the potential for magnetic driving, we tuned the applied magnetic field such that $\omega_{\pm 1}/2\pi = 1376$ MHz with $\theta \approx 8.7°$ and γ of NVA8 was mostly saturated at $\gamma = \gamma_\infty$. The corresponding SQ transition is at $\omega_{0,-1}/2\pi = 2188.65$ MHz. We set up a second microwave source to output a tone at $f_2 = 1376$ MHz with its phase modulated by a noise source. We combined this non-gated microwave channel with the double-gated coherent drive at $f_1 = 2188.65$ MHz. We coherently drove the $\omega_{0,-1}$ transition in order to perform the F_3 measurement while the noisy f_2 tone was continuously applied. We used the Rabi frequency due to f_1 for calibration to estimate that we could increase the measured γ to 1.9 kHz using a magnetic-field amplitude of $B_{1x} = 1$ G at f_2. A noise spectrum amplitude of 1 G/Hz$^{1/2}$ is many orders of magnitude

larger than the amplitude of the magnetic (b_m) Lorentzian with parameters in Table 5.2 at frequencies of $\omega = \omega_{\pm 1} = 20 - 1375$ MHz and accounting for linewidth. Therefore, this magnetic noise from the surface is far too small to have an effect on γ comparable to the applied test 1-G noisy driving field. We conclude that magnetic noise in the diamond or at the surface is not responsible for the observations of γ in this work.

In a related argument, from second-order perturbation theory, with perturbation as a small $g\mu_B B_\perp$, the ratio of the DQ to SQ magnetic Rabi frequencies is approximately given by [33]

$$R = \frac{\Omega_{R,\pm 1}}{\Omega_{R,-10}} = \frac{\sqrt{2}\,(g\mu_B/\hbar)\,B_\perp D_{\rm gs}}{D_{\rm gs}^2 - (g\mu_B/\hbar)^2\,B_\parallel^2} \tag{D.8}$$

For the numbers $D_{\rm gs} = 2870.5$ MHz, $B_\perp = 37.7$ G, and $B_\parallel = 246.0$ G we get $R_\Omega = 0.052$. We can also think of this ratio R as relating the bare coupling of the NV magnetic fields $\gamma_{\rm NV} = 2\pi \times 2.8$ MHz/G to an effective reduced coupling $\gamma_{\rm NV}^{\rm (eff)} = R\gamma_{\rm NV}$. In this way the determination of the effect of magnetic noise on the DQ relaxation is in mathematical analogy to the disparate couplings to transverse and parallel electric fields $d_\parallel$ and $d_\perp$ shown in Eq. 5.29. That is, when the effective $|\pm 1\rangle$ coupling to magnetic fields $\gamma_{\rm NV}^{\rm (eff)}$ comes into the noise spectral density it must be squared, meaning that the DQ relaxation rate γ actually depends on the even smaller factor $R^2 = 0.0027$ in relation to $\langle B^2 \rangle$ noise. For sufficiently misaligned magnetic fields then the inequality $B_\parallel \gg B_\perp$ does not hold and Eq. D.8 is not correct. We performed noise-spectroscopy measurements only under the conditions of $B_\parallel \gg B_\perp$, so we do not consider the other cases here.

Appendix E

^{15}NV electron spin echo envelope modulation

The experiments in this study were done on NVs consisting of a host nitrogen-15 atom. When the applied external magnetic field is not perfectly aligned to the NV axis, then the Hahn echo and XY4 pulsed measurements reveal the electron spin echo envelope modulation (ESEEM) due to interaction with the nitrogen-15 nuclear spin of I = 1/2. Contrary to what happens in NVs consisting of a host nitrogen-14 atom, the nuclear spin is here free to precess.

One non-classical model for ESEEM was proposed in [272]. After a brief discussion of the theory and assumptions, the detailed derivation of the fit functions used in this paper will be presented.

E.1 Model Hamiltonian

The model proposed in [272] was first developed to explain signals observed in electron spin resonance experiments in $CaWO_4$ doped with Ce^{3+}. This crystal has a tetragonal

symmetry similar to the trigonal symmetry of the NV center. The resulting hypothesis for the form of the Hamiltonian can also be applied to the NV center.

The electron system generates a magnetic field at the location of the nuclear spin. If the electronic spin is flipped in a time much shorter than the Larmor period of the nuclear spin, the spin experiences a non-adiabatic change in the local magnetic field it is sensitive to. That change will cause the nuclear spin to precess around a new axis of quantization. If an external magnetic field is applied, non-collinear to the dipolar field of the electron at the location of the nuclear spin, then, after flipping the electronic spin with a π pulse, the axis of quantization is tilted with respect to the previous axis orientation. The actual modulation of the Hahn echo signal will result from the interferences between the beatings induced by the nuclear spin at its two Larmor frequencies (one for each axis). The strength of the modulation will be linked to the angle between the two axes of quantization.

The more general Hamiltonian describing the interaction between the electronic spin of the NV center and the nuclear spin of the nitrogen-15 takes the following form:

$$H/\hbar = \underbrace{DS_z^2}_{\text{ZFS}} + \underbrace{\mathbf{S}\overset{\leftrightarrow}{A}\mathbf{I}}_{\text{Hyperfine interaction}} + \underbrace{\mu_e \mathbf{B}\cdot\mathbf{S}}_{\text{Zeeman electron}} - \underbrace{g_n\mu_n\mathbf{B}\cdot\mathbf{I}}_{\text{Zeeman nuclear}} \tag{E.1}$$

where $\mathbf{S}$ is the electronic spin-1 operator, D is the zero-field splitting in the ground state, $\mathbf{I}$ is the nuclear spin-1/2 operator, $\mathbf{B}$ is the applied static magnetic field, μ_e is the Bohr magneton with electron g-factor absorbed for simplicity, $\overset{\leftrightarrow}{A}$ is the nuclear-electron hyperfine tensor, g_n is the nuclear g-factor, and μ_n is the nuclear magneton.

The C_{3v} symmetry of the NV constrains the g-tensor of the hyperfine interaction

to be diagonal and to have only two independent components: one lying on the axis of symmetry ($A_\parallel$) and one orthogonal to it ($A_\perp$). Because the nitrogen nuclear spin lies on the z-axis, the anisotropic hyperfine interaction (described using a dipole-dipole approximation) does not generate off-diagonal terms in the tensor, such as A_{xy} and A_{xz}. We can describe the whole hyperfine interaction using one diagonal tensor (see [272] for the last two points). As the system is invariant by rotation around z, we choose z and x so that the magnetic field lies in the xz plane with positive projections on both axes. We can further simplify the Hamiltonian by moving into a frame rotating at D, which is the largest energy scale in our problem. The resulting Hamiltonian is

$$\mathcal{H}/\hbar = S_z A_\parallel I_z + \mu_e B_z S_z - g_n \mu_n \left(B_z I_z + B_x I_x\right) \tag{E.2}$$

It has been demonstrated in [22] that in the presence of an external field, the non-secular terms of the hyperfine interaction can drive virtual transitions, resulting in a magnification of the transverse field experienced by the nuclear spin. A perturbative calculation of the impact of the non-secular term, to second order in $1/D$, leads to a corrected expression of the nuclear spin g-tensor.

$$g_n = \begin{pmatrix} 1 & 0 & 0 \\ 0 & 1 & 0 \\ 0 & 0 & 1 \end{pmatrix} - \frac{\mu_e}{\mu_n D}\left(2 - 3\left|m_s\right|\right) \begin{pmatrix} A_\perp & 0 & 0 \\ 0 & A_\perp & 0 \\ 0 & 0 & 0 \end{pmatrix} \tag{E.3}$$

If we take this correction into account, our calculated Hamiltonian becomes

$$\mathcal{H}/\hbar = \left(A_\parallel I_z + 3\frac{\mu_e}{\mu_n D} A_\perp B_x\right) S_z + \mu_e B_z S_z$$

$$-\mu_n \left(B_z I_z + \left(B_x - 2\frac{\mu_e}{\mu_n D} A_\perp B_x\right) I_x\right) \tag{E.4}$$

We can use a rotation generated by I_y to put the Hamiltonian into the form used in [272]:

$$\mathcal{H}/\hbar = \mu_e B_z S_z + S_z \left(\Upsilon I_x + \Lambda I_z\right) - \omega_n I_z \tag{E.5}$$

$$\text{with } \omega_n = \mu_n \sqrt{\left(B_x - 2\frac{\mu_e}{\mu_n D} A_\perp B_x\right)^2 + \left(B_z\right)^2}$$

$$\Upsilon = \mu_n \frac{\left(-3\frac{\mu_e}{D} A_\perp B_x\right) B_z - A_\parallel \left(B_x - 2\frac{\mu_e}{\mu_n D} A_\perp B_x\right)}{\omega_n}$$

$$\Lambda = \mu_n \frac{A_\parallel B_z + \left(-3\frac{\mu_e}{D} A_\perp B_x\right) \left(B_x - 2\frac{\mu_e}{\mu_n D} A_\perp B_x\right)}{\omega_n}$$

Taking into account the impact of the non-secular terms does not change the form of the Hamiltonian and could have been ignored for the purpose of deriving fit function in terms of the phenomenological quantities Υ and Λ. Nonetheless, the explicit forms of Υ and Λ explain why it is possible in practice to eliminate modulation by reducing $B_x \to 0$. We use this magnetic field alignment for the dynamical decoupling measurements in Chapter 4 that extend to a large number of π pulses. This dependence of modulation depth on $B_\perp$ can itself be used for magnetic field alignment, as we discuss in the Appendix XXX.

The Hamiltonian of Eq. E.5 can be diagonalized by performing a rotation generated by I_y of angle ϕ defined by $\tan\phi\left(m_s\right) = \pm\frac{\Upsilon}{m_s\Lambda - \omega_n}$. The eigenvalues are

$$K_{m_s} = \sqrt{(\Lambda m_s - \omega_n)^2 + \Upsilon^2 m_s^2}, \tag{E.6}$$

where m_s again refers to the z projection of the electronic spin. In the case of $m_s = 0$ when $B_x \ll B_z$, the NV spin has little effect on the precession of the nuclear spin and $K_0 \approx \mu_n B_z$. For the $m_s = \pm 1$ case, however, even when $B_x \ll B_z$ the Λ term retains

$A_\parallel B_z$, and the result is to roughest approximation $K_1 \approx (A_\parallel + \mu_n B_z)$. $A_\parallel = -3.1$ MHz [181], which accounts for the field-independent $f_1 \sim 3$-MHz oscillations observed in the Hahn echo signal of a ^{15}NV, as shown in Fig. 3.6(c). The slower envelope modulation is actually dependent on B_x, and oscillates with roughly a 14-fold enhancement over the bare ^{15}N gyromagnetic ratio of $\gamma_{15\mathrm{N}}/2\pi = -4.316$ MHz/T [273]. Specifically, from Eq. E.3 $2(g\mu_B/h)/[(\gamma_{15\mathrm{N}}/2\pi)D] \approx 14$ and $f_0 \approx 14(\gamma_{15\mathrm{N}}/2\pi)B_\perp$. From these simplifications we have the following conceptual picture when $B_x \ll B_z$ but non-zero: the NV spin in $|m_s = 0\rangle$ results in a ^{15}N nuclear spin precession at f_0 that is enhanced by the presence of the perpendicular component of magnetic (hyperfine) field from the NV, while the NV spin in $|m_s = 1\rangle$ results in a strong parallel hyperfine field that dominates the ^{15}N precession at a fixed value $f_1 \approx 3.1$ MHz. Since the NV is in a superposition for the Hahn echo precession period, these effects are simultaneous and cause interferences in the NV phase accumulation.

From the full form of Eq. E.6, the ESEEM signal can be computed using the formalism of density matrices, as explained in the next section.

E.2 Computation of ESEEM fit functions

The computation of the fit functions relies on the following hypotheses:

1. Each pulse is supposed to be perfect and of negligible duration and is therefore represented as a rotation operator

2. Any kind of decoherence is neglected, so the free evolution intervals are described by the Hamiltonian introduced in the previous section.

3. The only states of the electronic spin considered are $m_s = 0$ and $+1$; we choose $\phi\,(m_s = 1)$ so that it is the angle between the two axes of quantization (for $m_s = 0$

no rotation is needed)

The relative photoluminescence (PL) of the NV center measures the difference of the population between the two states, which is equal to $\mathrm{Tr}\left(Z\rho\left(t\right)\right)$ with $Z=\sigma_z/2$.

To evaluate the trace we just need to know the initial density and the evolution operators. The electronic spin is initialized in its $|0\rangle$ state via laser pumping, and the nuclear spin is in a statistical mixture of states described by the diagonal matrix $(p,1-p)$ for some $p<1$. The evolution operator is given by the product of the rotation operators, which describe the pulses, and the evolution operators $e^{-i\mathcal{H}t/\hbar}$ associated with each free evolution period; the Hamiltonian is constant.

The evaluation of the electronic spin expectation value begins with the trace over the electronic state as the Hamiltonian is already diagonal with respect to it. We assume that the microwave is perfectly tuned to the frequency of the transition. The result of that calculation can be expressed under the following form:

$$\mathrm{Tr_e}\left(\mathrm{Re}\left(\prod_{k=1}^{N+1}e^{-i\mathcal{H}\left(m_s=\left(1+(-1)^k\right)/2\right)t/\hbar}\rho\left(0\right)\prod_{k=1}^{N+1}e^{i\mathcal{H}\left(m_s=\left(1-(-1)^k\right)/2\right)t/\hbar}\right)\right) \tag{E.7}$$

with N the number of π pulses. If we do not assume perfect matching of the microwave and transition frequencies then we must include $e^{i\delta t}$, where δ is the detuning, tacked on to Eq. E.7.

The evaluation of the trace over the nuclear spin state is then straightforward. The fit function for the Hahn echo and CP-like XY4 sequences, respectively, are presented below (P_0 is the probability for the system to be found in $m_s=0$, and $c=\cos\left(\phi\right)$ and

$s = \sin(\phi)$):

$$P_{0,\text{echo}} = 1 - \sin^2(\phi)\sin^2\left(\frac{K_0 t}{2}\right)\sin^2\left(\frac{K_1 t}{2}\right) \tag{E.8}$$

and

$$P_{0,\text{XY4}} =$$

$$(1 - (\Big(\Big(\big(4-3s^2\big)\Big(\sin(K_0t)^2 + \cos(K_0t)\Big) + 3s^2 - 5\Big)\sin(K_0t)^2 - \cos(K_0t) + 1\Big)4s^2\sin(K_1t)^4$$

$$+(\Big(\big(\big(s^2-4\big)\cos(K_0t) - s^2 + 4\big)\sin(K_0t)^3 + (3\cos(K_0t) - 3)\sin(K_0t)\Big)\cos(K_1t)$$

$$+\big(\big(4-s^2\big)\cos(K_0t) + s^2 - 2\big)\sin(K_0t)^3 + (1-\cos(K_0t))\sin(K_0t))4cs^2\sin(K_1t)^3$$

$$+(\Big(\big(4-3s^2\big)\sin(K_0t)^4 + \big(\big(2-2s^2\big)\cos(K_0t) + 2s^2 - 3\big)\sin(K_0t)^2\Big)\cos(K_1t)$$

$$+\big(3s^2-5\big)\sin(K_0t)^4 + \big(\big(2s^2-3\big)\cos(K_0t) - 2s^2 + 5\big)\sin(K_0t)^2 + \cos(K_0t) - 1)4s^2\sin(K_1t)^2$$

$$+(\Big((3\cos(K_0t) - 1)\sin(K_0t)^3 + (1-\cos(K_0t))\sin(K_0t)\Big)\cos(K_1t)$$

$$+(1 - 3\cos(K_0t))\sin(K_0t)^3 + (\cos(K_0t) - 1)\sin(K_0t))4cs^2\sin(K_1t)$$

$$+4s^2\Big(\sin(K_0t)^2 - \sin(K_0t)^4\Big)\cos(K_1t) + 4s^2\sin(K_0t)^4 - 4s^2\sin(K_0t)^2 + 1))/2$$

We confirmed the validity of these two functions by performing stochastic numerical simulations of the electron-nuclear system and plotting both analytical and numerical results, which coincide. An example of the model fit $P_{0,\text{XY4}}$ to the XY4 ESEEM data of an intermediate-depth NV, k30, is shown in Fig. E.1. To measure coherence decay envelopes for Figure 4.21, we aligned the field within 1 degree of the NV symmetry axis to suppress the ESEEM below the measurement noise level.

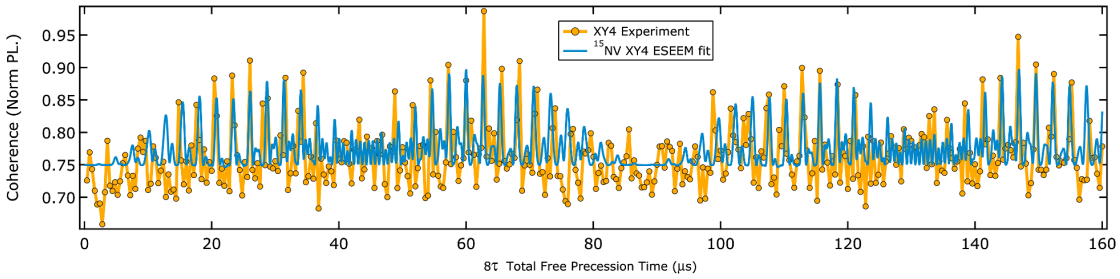

Figure E.1: XY4 ESEEM measurement (orange circles) and fit function (blue line) for a NV at depth 29 nm. For NVs with long T_2 of several 100 μs we choose to measure the coherence decay at the nodes determined by the enhanced Larmor precession frequency, K_0, of the ^{15}N nucleus. The modulations persist even for an external field within a few degrees of the NV axis, but will disappear for perfect alignment. The coherence decay was not included in the fit here.

Appendix F

Static magnetic field alignment

Alignment of the externally applied magnetic field **B** to the NV center symmetry axis is important for a number of reasons that vary by experimental goals. These reasons include optimal NV ODMR contrast through preservation of S_z eigenstates [120, 121], mitigation of ^{13}C bath-induced NV decoherence [137, 136], increasing the PL rate [120], and investigation of dynamics at the ground state level avoided crossing (GSLAC) [274]. For ^{15}NV centers it can also be advantageous to remove effects of ESEEM in dynamical decoupling measurements to simplify the analysis of coherence decay envelopes and analysis of detecting external nuclear spins [87]. Outside of axial alignment, precise control of field angle is useful, for example, in studying hyperfine couplings [54] or reducing the ambient magnetic field to near zero [29, 235].

For many applications, the azimuthal angle ϕ of **B** does not matter, meaning that we parametrize alignment by one angle θ to the z axis and a magnitude $B_0 = \sqrt{B_z^2 + B_\perp^2}$. A number of the θ-dependent phenemonea listed above can be used as feedback for the degree of alignment.

F.1 CWESR method

The first method of alignment to the z axis is by the Zeeman spectrum of a single or multiple NV centers measured with optically detected CWESR. Ideally the two m_s transitions $|0\rangle \leftrightarrow |\pm 1\rangle$ are measured at low optical and microwave fields to resolve the hyperfine structure for best peak fitting. We obtain left and right frequencies relative to the zero field splitting $D \equiv D_{\text{gs}} \approx 2.87$ GHz: $f_L \equiv f_{0,-1}$ and $f_R \equiv f_{0,+1}$ from the fitted centers of the hyperfine-split spectra. These are differences of the three eigenvalues of the basic Hamiltonian containing only zero-field splitting and Zeeman terms. We invert the eigenvalue equations to find the magnetic field magnitude B_0 and angle θ as [136]

$$\begin{aligned} P &= f_L^2 + f_R^2 - f_L f_R \\ Q &= (f_L + f_R)(2f_L^2 + 2f_R^2 - 5f_L f_R) \\ B_0 &= \sqrt{(P - D^2)/3} \\ \cos^2\theta &= (Q + 9DB_0^2 + 2D^3)/(27DB_0^2). \end{aligned} \tag{F.1}$$

Because θ in Eq. F.1 depends on D, the result is highly sensitive to an accurate measure of the zero-field splitting. This measurement can be done to reasonable absolute precision of about 10-100 kHz with CWESR at zero applied field, however, for small B_z the θ extracted is most sensitive to D and the simple CWESR method here may be better applied for alignment of large B_z (several 10s to 100s of Gauss). If D or the frequencies f_L and f_R are not accurately measured, then the result for θ and B_0 can become an imaginary number, which is a helpful indicator. A more precise alignment using CWESR at low field may be performed by monitoring the hyperfine splitting near zero applied magnetic field. We do not require this condition for our measurements, and details can be found in supporting information of references [29, 30].

F.2 ^{15}NV ESEEM method

We primarily use the CWESR followed by more-precise ESEEM-related methods for the work in this dissertation because the alignment feedback result (ESEEM depth) is directly applicable to the dynamical decoupling signal. For alignment of $\mathbf{B}$ to $\theta < 1°$ we monitored the Hahn echo ESEEM signal of a ^{15}NV delta doped or implanted NV center. In Appendix E we give the full expression for the depth and rate of ESEEM modulations. The locations of the troughs of the fast f_1 oscillations, such as shown in Fig. 3.6, are very nearly unchanged with small adjustments in the magnetic field orientation because $f_1 \gg f_0$. Echo measurements can be time consuming, taking several minutes for each round of adjustment if a fully sampled data set is taken. Therefore, to perform a rapid adjustment of the magnetic field, we set our Hahn echo measurement to take data at τ points corresponding to these local minima for a few f_0-modulation periods. This measurement is done with two channels with the final $\pi/2$ pulse having either a $+x$ or $-x$ phase, and these signals are subtracted at the end. Thus, for a large θ the two channel signals will cross. As the θ is made small (reduced $B_\perp$), the depth of the modulations goes to zero, and therefore the separation of the two signals gets larger, that is the differential signal tends away from any zero crossing. The ESEEM method has the advantage of working well at any magnetic field value, in principle, so the alignment can be tested at a specific B_z.

At a few 100 Gauss fields an alignment of $\theta = 0 - 3°$ provides a measurable polarization of the ^{15}N nuclear spin as well [131], such as shown in Fig. 1.11. Therefore, this polarization can be measured in a few-minute CWESR measurement and fit to a model [131] for a second confirmation of the field alignment angle.

F.3 ESLAC optical method

At magnetic fields near the excited state level avoided crossing (ESLAC) of $B_0 \sim 500$ G, the PL emission rate of the NV center is significantly reduced when θ is nonzero [120, 131]. This effect can be used as a rapid method of feedback for alignment, as only the PL needs to be measured. In principle it is limited more by how fast the magnetic field can be changed, and whether the setup remains stable in doing so. A detailed example of this procedure is given in supporting information of [218]. In practice, one challenge of this method is that it must be performed near 500 G, so the alignment position of the permanent magnet for other B_z values must be exprapolated. Another challenge for rapid scanning of the magnet to produce this PL image is that other effects like drift or magnetic forces on the sample mount can change the alignment of the laser spot on the NV, and there is no normalization measurement at each specific magnetic field. Therefore, the mechanical stability of the setup must be robust to these changes, or the NV must be tracked at several points, which simply increases the time required for the measurement.

Appendix G

Description of software control

G.1 Outline of pulsed ODMR control software

The pulsed ODMR experiments run from a global Matlab GUI called ImageScan. ImageScan itself is directly used for all aspects of confocal microscope control: sending analog voltages to scan mirrors and objective focus piezo, timing fluorescence collection in 2D or 3D confocal scans, 3D tracking the laser to an NV, labelling NVs to address, and controlling electronic filter wheels.

ESRControl is the main GUI for performing any microwave and pulsed experiments. It is divided into two sections to modify parameters for either CWESR or pulsed ESR experiments. ESRControl also contains automation code to program a user-defined list of measurements at each NV position labelled in the ImageScan scan window. The pulse timing and ODMR program is described here.

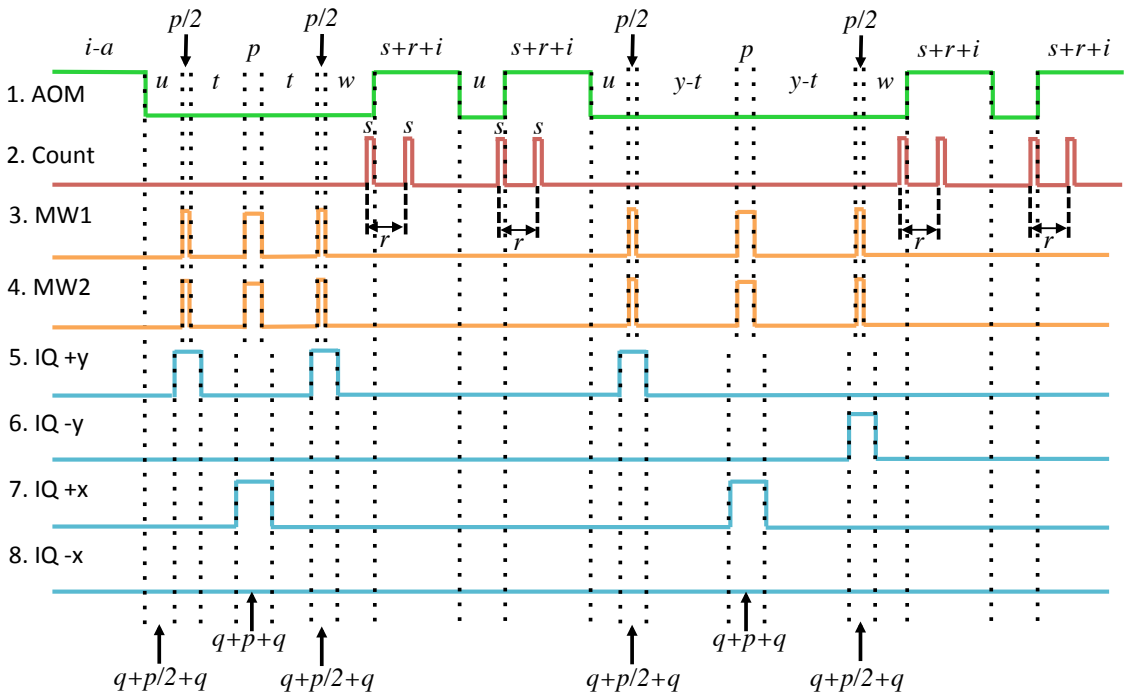

Figure G.1: Technical form of a symmetrized differential YXY-phase Hahn echo pulse sequence with delays specified by input parameters described in Table G.1. Pulseblaster bit numbers are listed on the left. For clarity, an AOM delay $a = 0$ is drawn here, but is in practice 800 to 1300 ns. For $t_{\text{start}} \neq 0$, the y is replaced in runtime by $y \rightarrow y + t_{\text{start}}$ to ensure the two channels have the same list of τ time delays. The bit2 channel turns on 50 ns earlier than the readout laser pulse to ensure counting during the initial period of highest PL contrast. bit3 and bit4 here control microwave switches in series for high isolation, though in general IQ bits off also provide isolation and the microwave switches can gate different frequencies, such as in Chapter 5.

G.2 Pulse sequences and photon binning

The program interface to run CWESR and pulse sequences is called ESRControl, which runs functions from classes EsrPulsedSweep, EsrCWSweep, and EsrGlobalMethods. The equipment controlled by functions in ESRControl are the National Instruments DAQ 6363, SRS SG384 signal generator with externally triggered IQ modulation, and the SpinCore Pulseblaster ESR-PRO 500 MHz.

Figure G.1 shows a typical microwave pulse sequence to illustrate the time delays variables ('t','a','u', etc) that are entered at runtime. A CPMG sequence is similar

in structure but has an even number of π_x pulses and a loop around this period of the sequence. Table G.1 gives a short description of the most common use of each parameter. The pulse sequences are written in a tab-delimited text file with five columns. There is one text file per bit, and one *.esr* file of the same base filename that simply has the same number of column headings as bit files. Any number of bits are permissible by the Matlab parsing algorithm as the number of columns in the *.esr* file contains this information, but we use only up to eight bits for dynamical decoupling.

- Col 1: line number 0 to ascending.
- Col 2: bits on or off, in decimal form. Least significant bit1 is AOM, bit2 is readout trigger, bit3 is microwave switch 1, bit4 is microwave switch 2, and bit5-8 control the IQ modulation for $+y$,$-y$,$+x$,$-x$ phases. The first three most significant bits are always equal to 1 for enabling long delays.
- Col 3: command type as indicated in Pulseblaster documentation. We use 0 for a regular delay, 2 and 3 for loops, and 1 for STOP at the final line. In runtime, the STOP is changed to a 7 for branching to the beginning of the sequence, and the regular delays with longer than 500 ns are refactored into long delay commands.
- Col 4: Data for each command. For example, we use n for the number of repeats in a loop command for dynamical decoupling and the first line number to close a loop, same as the Pulseblaster documentation.
- Col 5: How long to delay on each instruction line in nanoseconds. We specify this as an expression of summed variables and numbers that can be evaluated at runtime by Matlab and loaded in to the Pulseblaster once the variables are replaced by user-inputted numbers. For example $(i - a)$ gives an AOM initialization time that is turned on early by the AOM delay time a.

For each pulse sequence shot – the full cycle of the written sequence up through the branch command – the number of DAQ counter samples is a multiple of 4. The typical number is 8 for a sequence that will have long delay times, which is usually anything other than a Rabi sequence: Hahn echo, CPMG dynamical decoupling, spin relaxation, and variants of these. The APD is not itself gated and is always sending photon-count pulses to the DAQ counter. As shown in Fig. G.2, these samples alternate between "garbage" counts when the non-readout parts of the sequence are running and the desired readout counts during the r periods. The measurements are typically "symmetrized" with two pairs of signal and readout for 4 total useful count samples per pulse shot. Symmetrization refers to the first channel increasing in delay time t at subsequent τ points while the second channel decreases in duration between the microwave pulses with an expression such as $y - t$ or $2 * y - t$. The reason for symmetrization is to keep each pulse shot of equal time length as t is incremented though the list of τ points, which keeps the AOM duty cycle quasi-constant to avoid changes in average laser power or heating that can lead to artifacts in the PL data.

The pulse sequence at each τ point is run for a *repsPerTau* number of times before the methods in EsrPulsedSweep loads the next sequence to the pulseBlaster to advance the τ point. *repsPerTau* is typically 2000-10^5, on the shorter end when millisecond-long pulse shots like T_1 measurements are done. The probability of collecting a photon during the r = 350-ns window is (*photonEmissionRate*)(*collectionEfficiency*)(350 ns), on the order of 0.03 for our practical detection collected count rates of $\sim$ 100kPhoton/s. The number of count samples (or bins) collected by the DAQ during each shot is (*repsPerTau*)(*numSamp*)+1 with *numSamp* typically 4 or 8 for one-channel or two-channel measurements, respectively. The DAQ records a cumulative count per bin, so subtracting each (j+1)th bin by the jth bin with a **diff** command gives the incremented counts during each time bin. For a one-channel (two-channel) measurement, we sum the counts from

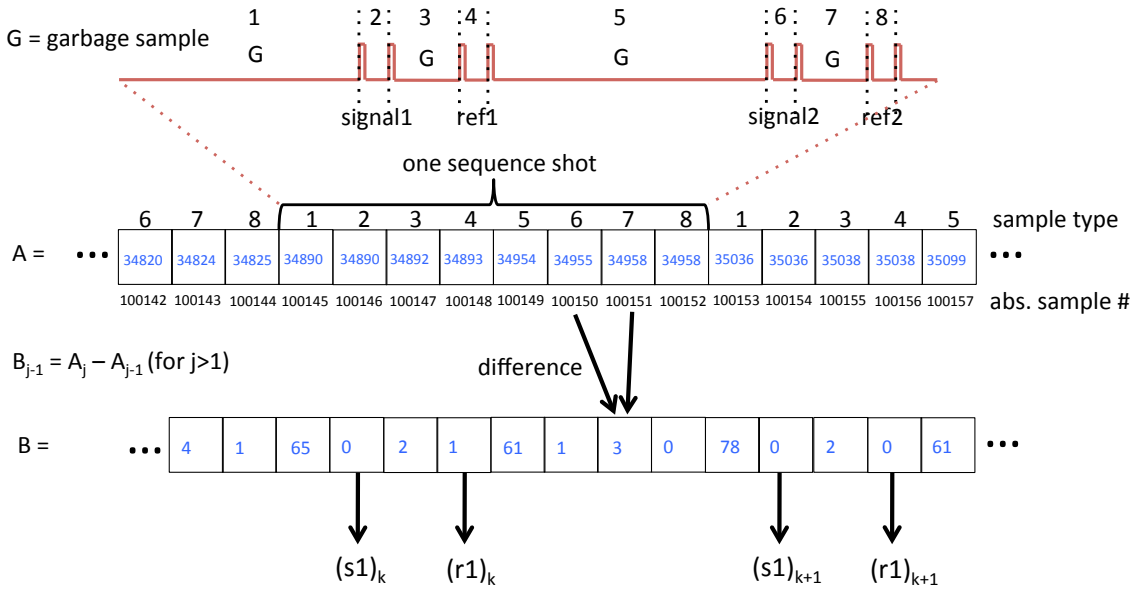

Figure G.2: Photon count sampling and generation of signal and reference. The top red sequence is the readout bit2 (see Fig. G.1) for a single shot of a sequence that has two channels of signal and reference, a total of 8 counting samples per shot. The up-edges of the bit2 pulses trigger the DAQ to advance to counting in the next sample. The middle row is a schematic of the samples collected by the DAQ, row vector A, where the blue number in each box is the cumulative count that starts at an arbitrary number. "Garbage" samples (1,3,5,7) are during long non-readout periods like microwave manipulation and free spin precession, so they will always have more incremented counts on average. The absolute sample number indicates the index, for example there are $N_s = 800,001$ total samples for the case of 10^5 pulse sequence shots. The next step (bottom row) is to take the difference $B_{j-1} = A_j - A_{j-1}$ for $j > 1$, leaving $N_s - 1$ samples that now contain the number of actual photon counts per time sample. The final step is to obtain the total signals and references, for example signal1 $S1 = \sum_{j=1}^{(N_s-1)} B_{8j-7}$ and reference1 $R1 = \sum_{j=1}^{(N_s-1)} B_{8j-5}$, and similarly for $S2$ and $R2$. The garbage samples can also be monitored, which is useful for error checking: if a garbage photon count, which is always orders of magnitude larger, becomes significantly smaller at some τ point then something went wrong. For example the samples would get mixed up between signal (low counts) and garbage (high counts) due to a missing trigger pulse. This issue does not occur so much with the Pulseblaster, but rather other pulse generation instruments employed in the lab.

each 4th (8th) sample for the total signal or reference counts for each channel. These sums are the raw data that are normalized, plotted, and analyzed further. We cycle through each of the τ points multiple times, on the order of $(repsPerTau)(numSweeps) = 10^5$ total pulse shots, to compute standard errors of the PL at each τ point.

G.2.1 Pulse sequence processing

The Pulseblaster expects one array of fully numerical input of five columns with the number of rows being the total number of instructions where bits are switched as in column 2 and some number of clock cycles passes specified by column 5. We write our pulse sequence files, however, as individual bit files, so these must all be combined into a single instruction set. The reason for writing different bits in separate files is because the user does not have to think about when certain on/off pulses will intersect with those from other bits due to general delays that are specified as variables. This combining is instead done at runtime once the variables are replaced with numbers. All of the bit files in a sequence must have the same total duration, or algebraic sum of column 5 entries, otherwise unpredictable sequences may result. Also, the use of minus signs in the duration expressions must be done with care to be sure no negative durations are possible. For example, if the initialization time were set to a short value 1000 ns and the AOM delay were 1200 ns, then the time expression $i - a$ will not work as expected.

The two different methods of writing a bitX file are, for example, 1) put a new line for each time the bitX flips between 0 and 1, or 2) make an equal number of lines in each bit file, so that each line of the individual bit file may not necessarily change the bit value. Both methods are compressible into a single sequence. Method 1 is more common for simpler sequences without loops and has an advantage of readability per each bit since there are not as many total lines. Method 2 is useful for larger sequences with loops,

such as XY-8, because the whole structure of the sequence is seen in each bit file, and the duration expressions of delays do not get too long if a particular bit is not changed often; rather each line ends up containing only 2-3 timing variables. Therefore, method 2 may be easier to debug for a large sequence.

Once the list of M number of τ points are specified in ESRControl and the sequence is run, the EsrPulsedSweep program precomputes all M sequences. The most critical step here is that the duration expressions containing variables in column 5 are evaluated and replaced with single numbers in nanoseconds. The channel on/off column 2 in the bit files are also stored as a shorter decimal form when written by hand, and these numbers are automatically translated to bit string form. Again, the last line of the bit files are each written with a STOP command. The bit files in one τ point sequence are combined automatically by first translating the Δt durations to a global time within the sequence. Then, these steps can be sorted and interleaved from the various bit files.

One challenge in computation is the presence of loops in a sequence. Since n is a variable that has been specified now at runtime, for example in CPMG-N with $N = 256$, the procedure is to first unwind these loops into a series of non-loop instructions. Once the bit file instructions are all interleaved into a single sequence, then the program compresses this very long instruction list by locating repeating sequences of lines and implementing the loop command. The output of the total sequence to the Pulseblaster, and user for debugging, then ends up being approximately the same number of lines as the starting bit files. For example, a CPMG that was written with $n = 100$ loops on some part of its instructions rows typically is output in final form with a section having the same number of loops. The M sequences as are all stored as numerical matrices a cell array for loading to the Pulseblaster during the measurement as the τ points are incremented.

Parameter	Name	Description
t	Tau time t_{start} is input	Used between microwave pulses as a delay for Rabi driving, precession, etc. Plotted on x axis.
y	Tau end time	Largest time for swept parameter t.
u	Depopulation time	Delay after green laser polarization to allow spin population in the metastable state to decay to $m_s = 0$. A reference PL read out after u also gives a more accurate comparison to the signal for normalization: e.g., $S/R = 1$ or $S - R = 0$ for unrotated spin or full coherence.
w	Pre-readout wait time	Technical delay to ensure microwave pulses are not overlapped with optical readout. Doesn't interfere with most measurements as population decay time T_1 is much longer.
p	Pi pulse time	Calibrated microwave pulse width for a π rotation on the Bloch sphere.
v	User variable	General purpose
s	Sample trigger width	Short pulse width for triggering the DAQ's counter to advance to the next sample. Triggering set to occur on the up-edges only.
a	AOM delay	Calibrated time delay that the AOM must be turned on earlier than the readout pulses. This value will depend on the beam width and position on the AOM crystal aperture.
i	Initialization time	Period that the AOM is on to polarize the NV into the $m_s = 0$ state.
r	Readout time	Period between up-edges of the sample trigger pulses going to the DAQ counter. Total time that PL is read from the NV.
q	IQ time	Buffer time for the external IQ triggers of the signal generator to switch phase before and after a microwave pulse period.
n	Number of loops	For a loop within the sequence, the total number of times to execute the instruction block, e.g., for dynamical decoupling.

Table G.1: Pulse parameters for sequence run in ESRControl, each specified in nanoseconds except for n.

Bibliography

[1] N. H. Bonadeo, J. Erland, D. Gammon, D. Park, D. S. Katzer, and D. G. Steel. Coherent optical control of the quantum state of a single quantum dot. *Science*, 282(5393):1473–1476, 11 1998.

[2] D. J. Wineland, C. Monroe, D. M. Meekhof, B. E. King, D. Leibfried, W. M. Itano, J. C. Bergquist, D. Berkeland, J. J. Bollinger, J. Miller, and P.-O. Löwdin. Coherent quantum state manipulation of trapped atomic ions. *Advances in Quantum Chemistry*, Volume 30:41–64, 1998.

[3] A. Gruber, A. Dräbenstedt, C. Tietz, L. Fleury, J. Wrachtrup, and C. von Borczyskowski. Scanning confocal optical microscopy and magnetic resonance on single defect centers. *Science*, 276(5321):2012–2014, 06 1997.

[4] C. L. Degen. Scanning magnetic field microscope with a diamond single-spin sensor. *Applied Physics Letters*, 92(24):–, 2008.

[5] J. M. Taylor, P. Cappellaro, L. Childress, L. Jiang, D. Budker, P. R. Hemmer, A. Yacoby, R. Walsworth, and M. D. Lukin. High-sensitivity diamond magnetometer with nanoscale resolution. *Nat Phys*, 4(10):810–816, 10 2008.

[6] F. Dolde, I. Jakobi, B. Naydenov, N. Zhao, S. Pezzagna, C. Trautmann, J. Meijer, P. Neumann, F. Jelezko, and J. Wrachtrup. Room-temperature entanglement between single defect spins in diamond. *Nat Phys*, 9(3):139–143, 03 2013.

[7] D. Rugar, H. J. Mamin, P. Guethner, S. E. Lambert, J. E. Stern, I. McFadyen, and T. Yogi. Magnetic force microscopy: General principles and application to longitudinal recording media. *Applied Physics Letters*, 68(1169), 1990.

[8] J. Cai, F. Jelezko, M. B. Plenio, and A. Retzker. Diamond-based single-molecule magnetic resonance spectroscopy. *New Journal of Physics*, 15(1):013020, 2013.

[9] D. Loss and D. P. DiVincenzo. Quantum computation with quantum dots. *Phys. Rev. A*, 57:120–126, Jan 1998.

[10] J. H. N. Loubser and J. A. van Wyk. Electron spin resonance in the study of diamond. *Reports on Progress in Physics*, 41(8):1201, 1978.

[11] E. van Oort, N. B. Manson, and M. Glasbeek. Optically detected spin coherence of the diamond N-V centre in its triplet ground state. *Journal of Physics C: Solid State Physics*, 21(23):4385, 1988.

[12] D. M. Toyli, D. J. Christle, A. Alkauskas, B. B. Buckley, C. G. Van de Walle, and D. D. Awschalom. Measurement and control of single nitrogen-vacancy center spins above 600 k. *Phys. Rev. X*, 2:031001, Jul 2012.

[13] N. Bar-Gill, L. M. Pham, C. Belthangady, D. Le Sage, P. Cappellaro, J. R. Maze, M. D. Lukin, A. Yacoby, and R. Walsworth. Suppression of spin-bath dynamics for improved coherence of multi-spin-qubit systems. *Nat Commun*, 3:858, 05 2012.

[14] C. G. Yale, B. B Buckley, D. J. Christle, G. Burkard, F. J. Heremans, L. C Bassett, and D. D. Awschalom. All-optical control of a solid-state spin using coherent dark states. *Proceedings of the National Academy of Sciences of the United States of America*, 110(19):7595–7600, 05 2013.

[15] R. T. Harley, M. J. Henderson, and R. M. Macfarlane. Persistent spectral hole burning of colour centres in diamond. *Journal of Physics C: Solid State Physics*, 17(8):L233, 1984.

[16] E. van Oort and M. Glasbeek. Cross-relaxation dynamics of optically excited N-V centers in diamond. *Phys. Rev. B*, 40:6509–6517, Oct 1989.

[17] E. van Oort and M. Glasbeek. Electric-field-induced modulation of spin echoes of N-V centers in diamond. *Chemical Physics Letters*, 168(6):529 – 532, 1990.

[18] M. W. Doherty, N. B. Manson, P. Delaney, F. Jelezko, J. Wrachtrup, and L. C.L. Hollenberg. The nitrogen-vacancy colour centre in diamond. *Physics Reports*, 528(1):1 – 45, 2013.

[19] F. Jelezko, T. Gaebel, I. Popa, A. Gruber, and J. Wrachtrup. Observation of coherent oscillations in a single electron spin. *Phys. Rev. Lett.*, 92:076401, Feb 2004.

[20] R. Hanson, O. Gywat, and D. D. Awschalom. Room-temperature manipulation and decoherence of a single spin in diamond. *Phys. Rev. B*, 74:161203, Oct 2006.

[21] R. Hanson, F. M. Mendoza, R. J. Epstein, and D. D. Awschalom. Polarization and readout of coupled single spins in diamond. *Phys. Rev. Lett.*, 97:087601, Aug 2006.

[22] L. Childress, M. V. Gurudev Dutt, J. M. Taylor, A. S. Zibrov, F. Jelezko, J. Wrachtrup, P. R. Hemmer, and M. D. Lukin. Coherent dynamics of coupled electron and nuclear spin qubits in diamond. *Science*, 314(5797):281–285, 10 2006.

[23] J. Wrachtrup and F. Jelezko. Processing quantum information in diamond. *Journal of Physics: Condensed Matter*, 18(21):S807, 2006.

[24] B. M. Chernobrod and G. P. Berman. Spin microscope based on optically detected magnetic resonance. *Journal of Applied Physics*, 97(1), 2005.

[25] G. Balasubramanian, I. Y. Chan, R. Kolesov, M. Al-Hmoud, J. Tisler, C. Shin, C. Kim, A. Wojcik, P. R. Hemmer, A. Krueger, T. Hanke, A. Leitenstorfer, R. Bratschitsch, F. Jelezko, and J. Wrachtrup. Nanoscale imaging magnetometry with diamond spins under ambient conditions. *Nature*, 455(7213):648–651, 10 2008.

[26] J. R. Maze, P. L. Stanwix, J. S. Hodges, S. Hong, J. M. Taylor, P. Cappellaro, L. Jiang, M. V. Gurudev Dutt, E. Togan, A. S. Zibrov, A. Yacoby, R. L. Walsworth, and M. D. Lukin. Nanoscale magnetic sensing with an individual electronic spin in diamond. *Nature*, 455(7213):644–647, 10 2008.

[27] S. Steinert, F. Dolde, P. Neumann, A. Aird, B. Naydenov, G. Balasubramanian, F. Jelezko, and J. Wrachtrup. High sensitivity magnetic imaging using an array of spins in diamond. *Review of Scientific Instruments*, 81(4), 2010.

[28] B. J. Maertz, A. P. Wijnheijmer, G. D. Fuchs, M. E. Nowakowski, and D. D. Awschalom. Vector magnetic field microscopy using nitrogen vacancy centers in diamond. *Applied Physics Letters*, 96(9), 2010.

[29] F. Dolde, H. Fedder, M. W. Doherty, T. Nobauer, F. Rempp, G. Balasubramanian, T. Wolf, F. Reinhard, L. C. L. Hollenberg, F. Jelezko, and J. Wrachtrup. Electric-field sensing using single diamond spins. *Nat Phys*, 7(6):459–463, 06 2011.

[30] F. Dolde, M. W. Doherty, J. Michl, I. Jakobi, B. Naydenov, S. Pezzagna, J. Meijer, P. Neumann, F. Jelezko, N. B. Manson, and J. Wrachtrup. Nanoscale detection of a single fundamental charge in ambient conditions using the NV^- center in diamond. *Phys. Rev. Lett.*, 112:097603, Mar 2014.

[31] V. M. Acosta, E. Bauch, M. P. Ledbetter, A. Waxman, L.-S. Bouchard, and D. Budker. Temperature dependence of the nitrogen-vacancy magnetic resonance in diamond. *Phys. Rev. Lett.*, 104:070801, 2010.

[32] M. W. Doherty, F. Dolde, H. Fedder, F. Jelezko, J. Wrachtrup, N. B. Manson, and L. C. L. Hollenberg. Theory of the ground-state spin of the NV^- center in diamond. *Phys. Rev. B*, 85:205203, May 2012.

[33] E. R. MacQuarrie, T. A. Gosavi, N. R. Jungwirth, S. A. Bhave, and G. D. Fuchs. Mechanical spin control of nitrogen-vacancy centers in diamond. *Phys. Rev. Lett.*, 111:227602, Nov 2013.

[34] P. Ovartchaiyapong, K. W. Lee, B. A. Myers, and A. C. Bleszynski Jayich. Dynamic strain-mediated coupling of a single diamond spin to a mechanical resonator. *Nat Commun*, 5:4429, 07 2014.

[35] J. Tisler, G. Balasubramanian, B. Naydenov, R. Kolesov, B. Grotz, R. Reuter, J.-P. Boudou, P. A. Curmi, M. Sennour, A. Thorel, M. Börsch, K. Aulenbacher, R. Erdmann, P. R. Hemmer, F. Jelezko, and J. Wrachtrup. Fluorescence and spin properties of defects in single digit nanodiamonds. *ACS Nano*, 3(7):1959–1965, 2009. PMID: 21452865.

[36] L. Rondin, J.-P. Tetienne, P. Spinicelli, C. Dal Savio, K. Karrai, G. Dantelle, A. Thiaville, S. Rohart, J.-F. Roch, and V. Jacques. Nanoscale magnetic field mapping with a single spin scanning probe magnetometer. *Applied Physics Letters*, 100(15):–, 2012.

[37] A. Laraoui, J. S. Hodges, and C. A. Meriles. Nitrogen-vacancy-assisted magnetometry of paramagnetic centers in an individual diamond nanocrystal. *Nano Letters*, 12(7):3477–3482, 07 2012.

[38] M. S. Grinolds, P. Maletinsky, S. Hong, M. D. Lukin, R. L. Walsworth, and A. Yacoby. Quantum control of proximal spins using nanoscale magnetic resonance imaging. *Nat Phys*, 7(9):687–692, 09 2011.

[39] B. Grotz, J. Beck, P. Neumann, B. Naydenov, R. Reuter, F. Reinhard, F. Jelezko, J. Wrachtrup, D. Schweinfurth, B. Sarkar, and P. Hemmer. Sensing external spins with nitrogen-vacancy diamond. *New Journal of Physics*, 13(5):055004, 2011.

[40] B. K. Ofori-Okai, S. Pezzagna, K. Chang, M. Loretz, R. Schirhagl, Y. Tao, B. A. Moores, K. Groot-Berning, J. Meijer, and C. L. Degen. Spin properties of very shallow nitrogen vacancy defects in diamond. *Phys. Rev. B*, 86:081406, Aug 2012.

[41] H. J. Mamin, M. H. Sherwood, and D. Rugar. Detecting external electron spins using nitrogen-vacancy centers. *Phys. Rev. B*, 86:195422, Nov 2012.

[42] T. Ishikawa, K.-M. C. Fu, C. Santori, V. M. Acosta, R. G. Beausoleil, H. Watanabe, S. Shikata, and K. M. Itoh. Optical and spin coherence properties of nitrogen-vacancy centers placed in a 100 nm thick isotopically purified diamond layer. *Nano Letters*, 12(4):2083–2087, 04 2012.

[43] K. Ohno, F. J. Heremans, L. C. Bassett, B. A. Myers, D. M. Toyli, A. C. Bleszynski Jayich, C. J. Palmstrøm, and D. D. Awschalom. Engineering shallow spins in diamond with nitrogen delta-doping. *Applied Physics Letters*, 101(8), 2012.

[44] D. Budker and M. Romalis. Optical magnetometry. *Nat Phys*, 3(4):227–234, 04 2007.

[45] A. Abragam and B. Bleaney. *Electron paramagnetic resonance of transition ions*. Clarendon, Oxford, U.K., 1970.

[46] C.P. Slichter. *Principles of Magnetic Resonance*. Springer-Verlag Berlin Heidelberg, 3 edition, 1990.

[47] Excelitas Technolgies. *SPCM-AQRH Single Photon Counting Module*, rev 2016-02 edition, 2016.

[48] J. A. van Wyk, E. C. Reynhardt, G. L. High, and I. Kiflawi. The dependences of esr line widths and spin - spin relaxation times of single nitrogen defects on the concentration of nitrogen defects in diamond. *Journal of Physics D: Applied Physics*, 30(12):1790, 1997.

[49] C. J. Jones and C. K. Larive. Could smaller really be better? Current and future trends in high-resolution microcoil NMR spectroscopy. *Analytical and Bioanalytical Chemistry*, 402(1):61–68, 2012.

[50] E. Bouleau, P. Saint-Bonnet, F. Mentink-Vigier, H. Takahashi, J.-F. Jacquot, M. Bardet, F. Aussenac, A. Purea, F. Engelke, S. Hediger, D. Lee, and G. De Paepe. Pushing NMR sensitivity limits using dynamic nuclear polarization with closed-loop cryogenic helium sample spinning. *Chem. Sci.*, 6:6806–6812, 2015.

[51] P. Glover and P. Mansfield. Limits to magnetic resonance microscopy. *Reports on Progress in Physics*, 65(10):1489, 2002.

[52] P. W. Stroman, C. Wheeler-Kingshott, M. Bacon, J. M. Schwab, R. Bosma, J. Brooks, D. Cadotte, T. Carlstedt, O. Ciccarelli, J. Cohen-Adad, A. Curt, N. Evangelou, M. G. Fehlings, M. Filippi, B. J. Kelley, S. Kollias, A. Mackay, C. A. Porro, S. Smith, S. M. Strittmatter, P. Summers, and I. Tracey. The current state-of-the-art of spinal cord imaging: Methods. *NeuroImage*, 84:1070–1081, 01 2014.

[53] T. H. Taminiau, J. J. T. Wagenaar, T. van der Sar, F. Jelezko, V. V. Dobrovitski, and R. Hanson. Detection and control of individual nuclear spins using a weakly coupled electron spin. *Phys. Rev. Lett.*, 109:137602, Sep 2012.

[54] S. Kolkowitz, Q. P. Unterreithmeier, S. D. Bennett, and M. D. Lukin. Sensing distant nuclear spins with a single electron spin. *Phys. Rev. Lett.*, 109:137601, Sep 2012.

[55] A. O. Sushkov, I. Lovchinsky, N. Chisholm, R. L. Walsworth, H. Park, and M. D. Lukin. Magnetic resonance detection of individual proton spins using quantum reporters. *Phys. Rev. Lett.*, 113:197601, Nov 2014.

[56] F. Shi, X. Kong, R. Wang, F. Kong, N. Zhao, R.-B. Liu, and J. Du. Sensing and atomic-scale structure analysis of single nuclear-spin clusters in diamond. *Nat Phys*, 10(1):21–25, 01 2014.

[57] G. Binnig, H. Rohrer, Ch. Gerber, and E. Weibel. Surface studies by scanning tunneling microscopy. *Phys. Rev. Lett.*, 49:57–61, Jul 1982.

[58] G. Binnig, C. F. Quate, and Ch. Gerber. Atomic force microscope. *Phys. Rev. Lett.*, 56:930–933, Mar 1986.

[59] D. M. Eigler and E. K. Schweizer. Positioning single atoms with a scanning tunnelling microscope. *Nature*, 344(6266):524–526, 1990.

[60] F. J. Giessibl. Atomic resolution on Si (111)-(7x7) by noncontact atomic force microscopy with a force sensor based on a quartz tuning fork. *Applied Physics Letters*, 76(1470), 2000.

[61] S. Morita, F. J. Giessibl, and Wiesendanger R., editors. *Noncontact atomic force microscopy*. Springer-Verlag Berlin Heidelberg, 2009.

[62] Y. Gan. Atomic and subnanometer resolution in ambient conditions by atomic force microscopy. *Surface Science Reports*, 64(3):99–121, 3 2009.

[63] D. G. de Oteyza, P. Gorman, S. Chen, Y.-C.and Wickenburg, A. Riss, D. J. Mowbray, G. Etkin, Z. Pedramrazi, A. Tsai, H.-Z.and Rubio, M. F. Crommie, and F. R. Fischer. Direct imaging of covalent bond structure in single-molecule chemical reactions. *Science*, 05 2013.

[64] R. Wiesendanger. Spin mapping at the nanoscale and atomic scale. *Rev. Mod. Phys.*, 81:1495–1550, Nov 2009.

[65] A. Spinelli, B. Bryant, F. Delgado, J. Fernández-Rossier, and A. F. Otte. Imaging of spin waves in atomically designed nanomagnets. *Nat Mater*, 13(8):782–785, 08 2014.

[66] P. Maletinsky, S. Hong, M. S. Grinolds, B. Hausmann, M. D. Lukin, R. L. Walsworth, M. Loncar, and A. Yacoby. A robust scanning diamond sensor for nanoscale imaging with single nitrogen-vacancy centres. *Nat Nano*, 7(5):320–324, 05 2012.

[67] J.-P. Tetienne, T. Hingant, J. V. Kim, L. Herrera Diez, J. P. Adam, K. Garcia, J. F. Roch, S. Rohart, A. Thiaville, D. Ravelosona, and V. Jacques. Nanoscale imaging and control of domain-wall hopping with a nitrogen-vacancy center microscope. *Science*, 344(6190):1366–1369, 2014.

[68] M. Pelliccione, A. Jenkins, P. Ovartchaiyapong, C. Reetz, E. Emmanouilidou, N. Ni, and A. C. Bleszynski Jayich. Scanned probe imaging of nanoscale magnetism at cryogenic temperatures with a single-spin quantum sensor. *Nat Nano*, pages –, 05 2016.

[69] L. Thiel, D. Rohner, M. Ganzhorn, P. Appel, E. Neu, B. Müller, R. Kleiner, D. Koelle, and P. Maletinsky. Quantitative nanoscale vortex imaging using a cryogenic quantum magnetometer. *Nat Nano*, advance online publication:–, 05 2016.

[70] M. S. Grinolds, M. Warner, K. De Greve, Y. Dovzhenko, L. Thiel, R. L. Walsworth, S. Hong, P. Maletinsky, and A. Yacoby. Subnanometre resolution in three-dimensional magnetic resonance imaging of individual dark spins. *Nat Nano*, 9(4):279–284, 2014.

[71] M. Pelliccione, B. A. Myers, L. M. A. Pascal, A. Das, and A. C. Bleszynski Jayich. Two-dimensional nanoscale imaging of gadolinium spins via scanning probe relaxometry with a single spin in diamond. *Phys. Rev. Applied*, 2:054014, Nov 2014.

[72] D. Rugar, H. J. Mamin, M. H. Sherwood, M. Kim, C. T. Rettner, K. Ohno, and D. D. Awschalom. Proton magnetic resonance imaging using a nitrogen–vacancy spin sensor. *Nat Nano*, 10(2):120–124, 02 2015.

[73] T. Häberle, D. Schmid-Lorch, F. Reinhard, and J. Wrachtrup. Nanoscale nuclear magnetic imaging with chemical contrast. *Nat Nano*, 10(2):125–128, 02 2015.

[74] D. Schmid-Lorch, T. Häberle, F. Reinhard, A. Zappe, M. Slota, L. Bogani, A. Finkler, and J. Wrachtrup. Relaxometry and dephasing imaging of superparamagnetic magnetite nanoparticles using a single qubit. *Nano Letters*, 15(8):4942–4947, 2015.

[75] A. Laraoui, H. Aycock-Rizzo, Y. Gao, X. Lu, E. Riedo, and C. A. Meriles. Imaging thermal conductivity with nanoscale resolution using a scanning spin probe. *Nature Communications*, 6:8954 EP –, 11 2015.

[76] E. Schäfer-Nolte, L. Schlipf, M. Ternes, F. Reinhard, K. Kern, and J. Wrachtrup. Tracking temperature-dependent relaxation times of ferritin nanomagnets with a wideband quantum spectrometer. *Phys. Rev. Lett.*, 113:217204, Nov 2014.

[77] P. Appel, M. Ganzhorn, E. Neu, and P. Maletinsky. Nanoscale microwave imaging with a single electron spin in diamond. *New Journal of Physics*, 17(11):112001, 2015.

[78] B. J. M. Hausmann, T. M. Babinec, J. T. Choy, J. S. Hodges, S. Hong, I. Bulu, A. Yacoby, M. D. Lukin, and M. Lončar. Single-color centers implanted in diamond nanostructures. *New Journal of Physics*, 13(4):045004, 2011.

[79] A. W. Schell, P. Engel, J. F. M. Werra, C. Wolff, K. Busch, and O. Benson. Scanning single quantum emitter fluorescence lifetime imaging: Quantitative analysis of the local density of photonic states. *Nano Letters*, 14(5):2623–2627, 05 2014.

[80] S. J. DeVience, L. M. Pham, I. Lovchinsky, A. O. Sushkov, N. Bar-Gill, C. Belthangady, F. Casola, M. Corbett, H. Zhang, M. Lukin, H. Park, A. Yacoby, and R. L. Walsworth. Nanoscale nmr spectroscopy and imaging of multiple nuclear species. *Nat Nano*, 10(2):129–134, 02 2015.

[81] C. Müller, X. Kong, J. M. Cai, K. Melentijević, A. Stacey, M. Markham, D. Twitchen, J. Isoya, S. Pezzagna, J. Meijer, J. F. Du, M. B. Plenio, B. Naydenov, L. P. McGuinness, and F. Jelezko. Nuclear magnetic resonance spectroscopy with single spin sensitivity. *Nat Commun*, 5:4703, 08 2014.

[82] P. London, J. Scheuer, J.-M. Cai, I. Schwarz, A. Retzker, M. B. Plenio, M. Katagiri, T. Teraji, S. Koizumi, J. Isoya, R. Fischer, L. P. McGuinness, B. Naydenov, and F. Jelezko. Detecting and polarizing nuclear spins with double resonance on a single electron spin. *Phys. Rev. Lett.*, 111:067601, Aug 2013.

[83] R. Schirhagl, K. Chang, M. Loretz, and C. L. Degen. Nitrogen-vacancy centers in diamond: Nanoscale sensors for physics and biology. *Annual Review of Physical Chemistry*, 65(1):83–105, 2016/08/31 2014.

[84] L. P. McGuinness, L. T. Hall, A. Stacey, D. A. Simpson, C. D. Hill, J. H. Cole, K. Ganesan, B. C. Gibson, S. Prawer, P. Mulvaney, F. Jelezko, J. Wrachtrup, R. E. Scholten, and L. C. L. Hollenberg. Ambient nanoscale sensing with single spins using quantum decoherence. *New Journal of Physics*, 15(7):073042, 2013.

[85] J.-P. Tetienne, T. Hingant, L. Rondin, A. Cavaillès, L. Mayer, G. Dantelle, T. Gacoin, J. Wrachtrup, J.-F. Roch, and V. Jacques. Spin relaxometry of single nitrogen-vacancy defects in diamond nanocrystals for magnetic noise sensing. *Phys. Rev. B*, 87:235436, Jun 2013.

[86] T. Rosskopf, A. Dussaux, K. Ohashi, M. Loretz, R. Schirhagl, H. Watanabe, S. Shikata, K. M. Itoh, and C. L. Degen. Investigation of surface magnetic noise by shallow spins in diamond. *Phys. Rev. Lett.*, 112:147602, Apr 2014.

[87] B. A. Myers, A. Das, M. C. Dartiailh, K. Ohno, D. D. Awschalom, and A. C. Bleszynski Jayich. Probing surface noise with depth-calibrated spins in diamond. *Phys. Rev. Lett.*, 113:027602, Jul 2014.

[88] M. Kim, H. J. Mamin, M. H. Sherwood, C. T. Rettner, J. Frommer, and D. Rugar. Effect of oxygen plasma and thermal oxidation on shallow nitrogen-vacancy centers in diamond. *Applied Physics Letters*, 105(4), 2014.

[89] Y. Romach, C. Müller, T. Unden, L. J. Rogers, T. Isoda, K. M. Itoh, M. Markham, A. Stacey, J. Meijer, S. Pezzagna, B. Naydenov, L. P. McGuinness, N. Bar-Gill, and F. Jelezko. Spectroscopy of surface-induced noise using shallow spins in diamond. *Phys. Rev. Lett.*, 114:017601, Jan 2015.

[90] M. Kim, H. J. Mamin, M. H. Sherwood, K. Ohno, D. D. Awschalom, and D. Rugar. Decoherence of near-surface nitrogen-vacancy centers due to electric field noise. *Phys. Rev. Lett.*, 115:087602, Aug 2015.

[91] J. Wang, W. Zhang, J. Zhang, J. You, Y. Li, G. Guo, F. Feng, X. Song, L. Lou, W. Zhu, and G. Wang. Coherence times of precise depth controlled NV centers in diamond. *Nanoscale*, 8:5780–5785, 2016.

[92] B. A. Myers, A. Ariyaratne, and A. C. Bleszynski Jayich. Double-quantum spin-relaxation limits to coherence of near-surface nitrogen-vacancy centers. *arXiv*, arXiv:1607.02553, 2016.

[93] A. Safavi-Naini, P. Rabl, P. F. Weck, and H. R. Sadeghpour. Microscopic model of electric-field-noise heating in ion traps. *Phys. Rev. A*, 84:023412, Aug 2011.

[94] D.A. Hite, Y. Colombe, A.C. Wilson, D.T.C. Allcock, D. Leibfried, D.J. Wineland, and D.P. Pappas. Surface science for improved ion traps. *MRS Bulletin*, 38(10):826–833, 10 2013.

[95] B. C. Stipe, H. J. Mamin, T. D. Stowe, T. W. Kenny, and D. Rugar. Noncontact friction and force fluctuations between closely spaced bodies. *Phys. Rev. Lett.*, 87:096801, Aug 2001.

[96] F. C. Wellstood, C. Urbina, and J. Clarke. Low–frequency noise in dc superconducting quantum interference devices below 1 K. *Applied Physics Letters*, 50(12):772–774, 1987.

[97] R. de Sousa. Dangling-bond spin relaxation and magnetic $1/f$ noise from the amorphous-semiconductor/oxide interface: Theory. *Phys. Rev. B*, 76:245306, Dec 2007.

[98] L. Cywiński, R. M. Lutchyn, C. P. Nave, and S. Das Sarma. How to enhance dephasing time in superconducting qubits. *Phys. Rev. B*, 77:174509, May 2008.

[99] R. de Sousa. Electron spin as a spectrometer of nuclear-spin noise and other fluctuations. In M. Fanciulli, editor, *Electron Spin Resonance and Related Phenomena in Low-Dimensional Structures Topics in Applied Physics*, volume 115, page 183. Top. Appl. Phys., 2009.

[100] G. de Lange, Z. H. Wang, D. Ristè, V. V. Dobrovitski, and R. Hanson. Universal dynamical decoupling of a single solid-state spin from a spin bath. *Science*, 330(6000):60–63, 10 2010.

[101] J. Bylander, S. Gustavsson, F. Yan, F. Yoshihara, K. Harrabi, G. Fitch, D. G. Cory, Y. Nakamura, J.-S. Tsai, and W. D. Oliver. Noise spectroscopy through dynamical decoupling with a superconducting flux qubit. *Nat Phys*, 7(7):565–570, 07 2011.

[102] T. Staudacher, F. Shi, S. Pezzagna, J. Meijer, J. Du, C. A. Meriles, F. Reinhard, and J. Wrachtrup. Nuclear magnetic resonance spectroscopy on a (5-nanometer)^3 sample volume. *Science*, 339(6119):561–563, 02 2013.

[103] S. Kaufmann, D. A. Simpson, L. T. Hall, V. Perunicic, P. Senn, S. Steinert, L. P. McGuinness, B. C. Johnson, T. Ohshima, F. Caruso, J. Wrachtrup, R. E. Scholten, P. Mulvaney, and L. C. L. Hollenberg. Detection of atomic spin labels in a lipid bilayer using a single-spin nanodiamond probe. *Proceedings of the National Academy of Sciences*, 110(27):10894–10898, 07 2013.

[104] J. H. Cole and L. C. L. Hollenberg. Scanning quantum decoherence microscopy. *Nanotechnology*, 20(49):495401, 2009.

[105] J. R. Maze, A. Gali, E. Togan, Y. Chu, A. Trifonov, E. Kaxiras, and M. D. Lukin. Properties of nitrogen-vacancy centers in diamond: the group theoretic approach. *New Journal of Physics*, 13(2):025025, 2011.

[106] T. Plakhotnik, M. W. Doherty, J. H. Cole, R. Chapman, and N. B. Manson. All-optical thermometry and thermal properties of the optically detected spin resonances of the NV–center in nanodiamond. *Nano Letters*, 14(9):4989–4996, 09 2014.

[107] K. W. Lee, D. Lee, P. Ovartchaiyapong, J. Minguzzi, J. R. Maze, and A. C. Bleszynski Jayich. Strain coupling of a mechanical resonator to a single quantum emitter. *arXiv*, arXiv:1603.07680, 2016.

[108] B. B. Buckley, G. D. Fuchs, L. C. Bassett, and D. D. Awschalom. Spin-light coherence for single-spin measurement and control in diamond. *Science*, 330(6008):1212–1215, 11 2010.

[109] E. Togan, Y. Chu, A. S. Trifonov, L. Jiang, J. Maze, L. Childress, M. V. G. Dutt, A. S. Sorensen, P. R. Hemmer, A. S. Zibrov, and M. D. Lukin. Quantum entanglement between an optical photon and a solid-state spin qubit. *Nature*, 466(7307):730–734, 08 2010.

[110] K. V. Kepesidis, S. D. Bennett, S. Portolan, M. D. Lukin, and P. Rabl. Phonon cooling and lasing with nitrogen-vacancy centers in diamond. *Phys. Rev. B*, 88:064105, Aug 2013.

[111] F. Hilser and G. Burkard. All-optical control of the spin state in the NV$^-$ center in diamond. *Phys. Rev. B*, 86:125204, Sep 2012.

[112] A. Alkauskas, B. B. Buckley, D. D. Awschalom, and C. G. Van de Walle. First-principles theory of the luminescence lineshape for the triplet transition in diamond NV centres. *New Journal of Physics*, 16(7):073026, 2014.

[113] F. Jelezko, C. Tietz, A. Gruber, I. Popa, A. Nizovtsev, S. Kilin, and J. Wrachtrup. Spectroscopy of single N-V centers in diamond. *Single Molecules*, 2(4):255–260, 2001.

[114] N. Aslam, G. Waldherr, P. Neumann, F. Jelezko, and J. Wrachtrup. Photo-induced ionization dynamics of the nitrogen vacancy defect in diamond investigated by single-shot charge state detection. *New Journal of Physics*, 15(1):013064, 2013.

[115] A. Batalov, C. Zierl, T. Gaebel, P. Neumann, I.-Y. Chan, G. Balasubramanian, P. R. Hemmer, F. Jelezko, and J. Wrachtrup. Temporal coherence of photons emitted by single nitrogen-vacancy defect centers in diamond using optical rabi-oscillations. *Phys. Rev. Lett.*, 100:077401, Feb 2008.

[116] M. L. Goldman, M. W. Doherty, A. Sipahigil, N. Y. Yao, S. D. Bennett, N. B. Manson, A. Kubanek, and M. D. Lukin. State-selective intersystem crossing in nitrogen-vacancy centers. *Phys. Rev. B*, 91:165201, Apr 2015.

[117] L. Robledo, H. Bernien, T. van der Sar, and R. Hanson. Spin dynamics in the optical cycle of single nitrogen-vacancy centres in diamond. *New Journal of Physics*, 13(2):025013, 2011.

[118] G. D. Fuchs, A. L. Falk, V. V. Dobrovitski, and D. D. Awschalom. Spin coherence during optical excitation of a single nitrogen-vacancy center in diamond. *Phys. Rev. Lett.*, 108:157602, Apr 2012.

[119] A. Jarmola, V. M. Acosta, K. Jensen, S. Chemerisov, and D. Budker. Temperature- and magnetic-field-dependent longitudinal spin relaxation in nitrogen-vacancy ensembles in diamond. *Phys. Rev. Lett.*, 108:197601, May 2012.

[120] R. J. Epstein, F. M. Mendoza, Y. K. Kato, and D. D. Awschalom. Anisotropic interactions of a single spin and dark-spin spectroscopy in diamond. *Nat Phys*, 1(2):94–98, 11 2005.

[121] J. P. Tetienne, L. Rondin, P. Spinicelli, M. Chipaux, T. Debuisschert, J. F. Roch, and V. Jacques. Magnetic-field-dependent photodynamics of single NV defects in diamond: an application to qualitative all-optical magnetic imaging. *New Journal of Physics*, 14(10):103033, 2012.

[122] S. G. Schirmer and A. I. Solomon. Constraints on relaxation rates for N-level quantum systems. *Phys. Rev. A*, 70:022107, Aug 2004.

[123] M. Hirose and P. Cappellaro. Coherent feedback control of a single qubit in diamond. *Nature*, 532(7597):77–80, 04 2016.

[124] R. de Sousa and S. Das Sarma. Theory of nuclear-induced spectral diffusion: Spin decoherence of phosphorus donors in si and gaas quantum dots. *Phys. Rev. B*, 68:115322, Sep 2003.

[125] J. R. Maze, A. Dréau, V. Waselowski, H. Duarte, J.-F. Roch, and V. Jacques. Free induction decay of single spins in diamond. *New Journal of Physics*, 14(10):103041, 2012.

[126] J. Zhang, P. Chen, B. Yuan, W. Ji, Z. Cheng, and X. Qiu. Real-space identification of intermolecular bonding with atomic force microscopy. *Science*, 342(6158):611–614, 2013.

[127] T. Yamamoto, T. Umeda, K. Watanabe, S. Onoda, M. L. Markham, D. J. Twitchen, B. Naydenov, L. P. McGuinness, T. Teraji, S. Koizumi, F. Dolde, H. Fedder, J. Honert, J. Wrachtrup, T. Ohshima, F. Jelezko, and J. Isoya. Extending spin coherence times of diamond qubits by high-temperature annealing. *Phys. Rev. B*, 88:075206, Aug 2013.

[128] A. Dréau, M. Lesik, L. Rondin, P. Spinicelli, O. Arcizet, J.-F. Roch, and V. Jacques. Avoiding power broadening in optically detected magnetic resonance of single NV defects for enhanced dc magnetic field sensitivity. *Phys. Rev. B*, 84:195204, Nov 2011.

[129] A. Dréau, J.-R. Maze, M. Lesik, J.-F. Roch, and V. Jacques. High-resolution spectroscopy of single NV defects coupled with nearby ^{13}C nuclear spins in diamond. *Phys. Rev. B*, 85:134107, Apr 2012.

[130] P. Huang, X. Kong, N. Zhao, F. Shi, P. Wang, X. Rong, R.-B. Liu, and J. Du. Observation of an anomalous decoherence effect in a quantum bath at room temperature. *Nat Commun*, 2:570, 12 2011.

[131] V. Jacques, P. Neumann, J. Beck, M. Markham, D. Twitchen, J. Meijer, F. Kaiser, G. Balasubramanian, F. Jelezko, and J. Wrachtrup. Dynamic polarization of single nuclear spins by optical pumping of nitrogen-vacancy color centers in diamond at room temperature. *Phys. Rev. Lett.*, 102:057403, Feb 2009.

[132] G. Balasubramanian, P. Neumann, D. Twitchen, M. Markham, R. Kolesov, N. Mizuochi, J. Isoya, J. Achard, J. Beck, J. Tissler, V. Jacques, P. R. Hemmer, F. Jelezko, and J. Wrachtrup. Ultralong spin coherence time in isotopically engineered diamond. *Nat Mater*, 8(5):383–387, 05 2009.

[133] K. Fang, V. M. Acosta, C. Santori, Z. Huang, K. M. Itoh, H. Watanabe, S. Shikata, and R. G. Beausoleil. High-sensitivity magnetometry based on quantum beats in diamond nitrogen-vacancy centers. *Phys. Rev. Lett.*, 110:130802, Mar 2013.

[134] D. M. Toyli, C. F. de las Casas, D. J. Christle, V. V. Dobrovitski, and D. D. Awschalom. Fluorescence thermometry enhanced by the quantum coherence of single spins in diamond. *Proceedings of the National Academy of Sciences*, 110(21):8417–8421, 05 2013.

[135] B. Smeltzer, L. Childress, and A. Gali. ^{13}C hyperfine interactions in the nitrogen-vacancy centre in diamond. *New Journal of Physics*, 13(2):025021, 2011.

[136] P. L. Stanwix, L. M. Pham, J. R. Maze, D. Le Sage, T. K. Yeung, P. Cappellaro, P. R. Hemmer, A. Yacoby, M. D. Lukin, and R. L. Walsworth. Coherence of nitrogen-vacancy electronic spin ensembles in diamond. *Phys. Rev. B*, 82:201201, Nov 2010.

[137] J. R. Maze, J. M. Taylor, and M. D. Lukin. Electron spin decoherence of single nitrogen-vacancy defects in diamond. *Phys. Rev. B*, 78:094303, Sep 2008.

[138] L. Childress. *Coherent manipulation of single quantum systems in the solid state*. PhD thesis, Harvard University, 2007.

[139] N. Mizuochi, P. Neumann, F. Rempp, J. Beck, V. Jacques, P. Siyushev, K. Nakamura, D. J. Twitchen, H. Watanabe, S. Yamasaki, F. Jelezko, and J. Wrachtrup. Coherence of single spins coupled to a nuclear spin bath of varying density. *Phys. Rev. B*, 80:041201, Jul 2009.

[140] Z.-H. Wang and S. Takahashi. Spin decoherence and electron spin bath noise of a nitrogen-vacancy center in diamond. *Phys. Rev. B*, 87:115122, Mar 2013.

[141] G. de Lange, T. van der Sar, M. Blok, Z.-H. Wang, V. V. Dobrovitski, and R. Hanson. Controlling the quantum dynamics of a mesoscopic spin bath in diamond. *Sci. Rep.*, 2, 04 2012.

[142] T. H. Taminiau, J. Cramer, T. van der Sar, V. V. Dobrovitski, and R. Hanson. Universal control and error correction in multi-qubit spin registers in diamond. *Nat Nano*, 9(3):171–176, 03 2014.

[143] D. A. Redman, S. Brown, R. H. Sands, and S. C. Rand. Spin dynamics and electronic states of n- V centers in diamond by epr and four-wave-mixing spectroscopy. *Phys. Rev. Lett.*, 67:3420–3423, Dec 1991.

[144] Hall L. T., P. Keyhayias, D. A. Simpson, A. Jarmola, A. Stacey, D. Budker, and L. C. L. Hollenberg. Electron spin resonance spectroscopy via relaxaiton of solid-state spin probes at the nanoscale. *Arxiv*, arXiv:1503.00830, 2015.

[145] L. T. Hall, P. Kehayias, D. A. Simpson, A. Jarmola, A. Stacey, D. Budker, and L. C. L. Hollenberg. Detection of nanoscale electron spin resonance spectra demonstrated using nitrogen-vacancy centre probes in diamond. *Nat Commun*, 7:10211, 01 2016.

[146] H. Y. Carr and E. M. Purcell. Effects of diffusion on free precession in nuclear magnetic resonance experiments. *Phys. Rev.*, 94:630–638, May 1954.

[147] S. Meiboom and D. Gill. Modified spin echo method for measuring nuclear relaxation times. *Review of Scientific Instruments*, 29(8):688–691, 1958.

[148] Z.-H. Wang, G. de Lange, D. Ristè, R. Hanson, and V. V. Dobrovitski. Comparison of dynamical decoupling protocols for a nitrogen-vacancy center in diamond. *Phys. Rev. B*, 85:155204, Apr 2012.

[149] N. Bar-Gill, L. M. Pham, A. Jarmola, D. Budker, and R. L. Walsworth. Solid-state electronic spin coherence time approaching one second. *Nat Commun*, 4:1743, 04 2013.

[150] C. A. Ryan, J. S. Hodges, and D. G. Cory. Robust decoupling techniques to extend quantum coherence in diamond. *Phys. Rev. Lett.*, 105:200402, Nov 2010.

[151] S. Wimperis. Broadband, narrowband, and passband composite pulses for use in advanced nmr experiments. *Journal of Magnetic Resonance, Series A*, 109(2):221–231, 1994.

[152] N. Khaneja, T. Reiss, C. Kehlet, T. Schulte-Herbrüggen, and S. J. Glaser. Optimal control of coupled spin dynamics: design of nmr pulse sequences by gradient ascent algorithms. *Journal of Magnetic Resonance*, 172(2):296–305, 2 2005.

[153] G. S. Uhrig. Exact results on dynamical decoupling by pulses in quantum information processes. *New Journal of Physics*, 10(8):083024, 2008.

[154] V. V. Dobrovitski, G. de Lange, D. Ristè, and R. Hanson. Bootstrap tomography of the pulses for quantum control. *Phys. Rev. Lett.*, 105:077601, Aug 2010.

[155] M. Loretz, S. Pezzagna, J. Meijer, and C. L. Degen. Nanoscale nuclear magnetic resonance with a 1.9-nm-deep nitrogen-vacancy sensor. *Applied Physics Letters*, 104(3):–, 2014.

[156] M. Loretz, J. M. Boss, T. Rosskopf, H. J. Mamin, D. Rugar, and C. L. Degen. Spurious harmonic response of multipulse quantum sensing sequences. *Phys. Rev. X*, 5:021009, Apr 2015.

[157] A. Laraoui, F. Dolde, C. Burk, F. Reinhard, J. Wrachtrup, and C. A. Meriles. High-resolution correlation spectroscopy of 13c spins near a nitrogen-vacancy centre in diamond. *Nat Commun*, 4:1651, 04 2013.

[158] T. Staudacher, N. Raatz, S. Pezzagna, J. Meijer, F. Reinhard, C. A. Meriles, and J. Wrachtrup. Probing molecular dynamics at the nanoscale via an individual paramagnetic centre. *Nat Commun*, 6, 10 2015.

[159] A. Kuzmich, N. P. Bigelow, and L. Mandel. Atomic quantum non-demolition measurements and squeezing. *EPL (Europhysics Letters)*, 42(5):481, 1998.

[160] J. Pawley, editor. *Handbook of Biological Confocal Microscopy*, chapter 1. Springer US, 3 edition, 2006.

[161] S. Wilhelm, B. Gröbler, M. Gluch, and H. Heinz. *Confocal laser scanning microscope principles*. Carl Zeiss Jena.

[162] S. Hell, G. Reiner, Cremer C., and E. H. K. Steltzer. Aberrations in confocal fluorescence microscopy induced by mismatch in refractive index. *Journal of Microscopy*, 169:391–405, 3 1993.

[163] K. Ohno, F. J. Heremans, C. F. de las Casas, B. A. Myers, B. J. Alemán, A. C. Bleszynski Jayich, and D. D. Awschalom. Three-dimensional localization of spins in diamond using ^{12}C implantation. *Applied Physics Letters*, 105(5), 2014.

[164] C. A. McLellan, B. A. Myers, S. Kraemer, K. Ohno, D. D. Awschalom, and A. C. Bleszynski Jayich. Patterned formation of highly coherent nitrogen-vacancy centers using a focused electron irradiation technique. *Nano Letters*, 16(4):2450–2454, 2016.

[165] V. M. Acosta, E. Bauch, M. P. Ledbetter, C. Santori, K.-M. C. Fu, P. E. Barclay, R. G. Beausoleil, H. Linget, J. F. Roch, F. Treussart, S. Chemerisov, W. Gawlik, and D. Budker. Diamonds with a high density of nitrogen-vacancy centers for magnetometry applications. *Phys. Rev. B*, 80:115202, Sep 2009.

[166] P. Török, P. Varga, Z. Laczik, and G. R. Booker. Electromagnetic diffraction of light focused through a planar interface between materials of mismatched refractive indices: an integral representation. *J. Opt. Soc. Am. A*, 12(2):325–332, Feb 1995.

[167] P. Török and P. P. Varga. Electromagnetic diffraction of light focused through a stratified medium. *Appl. Opt.*, 36(11):2305–2312, Apr 1997.

[168] P. Török. Focusing of electromagnetic waves through a dielectric interface by lenses of finite Fresnel number. *J. Opt. Soc. Am. A*, 15(12):3009–3015, Dec 1998.

[169] V. N. Mahajan. Line of sight of an aberrated optical system. *J. Opt. Soc. Am. A*, 2(6):833–846, Jun 1985.

[170] V. N. Mahajan. Uniform versus Gaussian beams: a comparison of the effects of diffraction, obscuration, and aberrations. *J. Opt. Soc. Am. A*, 3(4):470–485, Apr 1986.

[171] S. A. Momenzadeh, R. J. Stöhr, F. F. de Oliveira, A. Brunner, A. Denisenko, S. Yang, F. Reinhard, and J. Wrachtrup. Nanoengineered diamond waveguide as a robust bright platform for nanomagnetometry using shallow nitrogen vacancy centers. *Nano Letters*, 15(1):165–169, 2015.

[172] W. Christian and M. Lee. OpticsApplet v4.1.

[173] J. P. Hadden, J. P. Harrison, A. C. Stanley-Clarke, L. Marseglia, Y.-L. D. Ho, B. R. Patton, J. L. O'Brien, and J. G. Rarity. Strongly enhanced photon collection from diamond defect centers under microfabricated integrated solid immersion lenses. *Applied Physics Letters*, 97(24), 2010.

[174] D. Riedel, D. Rohner, M. Ganzhorn, T. Kaldewey, P. Appel, E. Neu, R. J. Warburton, and P. Maletinsky. Low-loss broadband antenna for efficient photon collection from a coherent spin in diamond. *Phys. Rev. Applied*, 2:064011, Dec 2014.

[175] L. Li, E. H. Chen, J. Zheng, S. L. Mouradian, F. Dolde, T. Schröder, S. Karaveli, M. L. Markham, D. J. Twitchen, and D. Englund. Efficient photon collection from a nitrogen vacancy center in a circular bullseye grating. *Nano Letters*, 15(3):1493–1497, 03 2015.

[176] R. Garca and R. Pérez. Dynamic atomic force microscopy methods. *Surface Science Reports*, 47(6–8):197–301, 2002.

[177] K. Karrai and R. D. Grober. Piezoelectric tip-sample distance control for near field optical microscopes. *Applied Physics Letters*, 66(1842), 1995.

[178] K. Karrai and I. Tiemann. Interfacial shear force microscopy. *Phys. Rev. B*, 62:13174–13181, Nov 2000.

[179] M. S. Grinolds, S. Hong, P. Maletinsky, L. Luan, M. D. Lukin, R. L. Walsworth, and A. Yacoby. Nanoscale magnetic imaging of a single electron spin under ambient conditions. *Nat Phys*, 9(4):215–219, 04 2013.

[180] J. Liu, A. Callegari, M. Stark, and M. Chergui. A simple and accurate method for calibrating the oscillation amplitude of tuning-fork based AFM sensors. *Ultramicroscopy*, 109(1):81–84, 2008.

[181] J. R. Rabeau, P. Reichart, G. Tamanyan, D. N. Jamieson, S. Prawer, F. Jelezko, T. Gaebel, I. Popa, M. Domhan, and J. Wrachtrup. Implantation of labelled single nitrogen vacancy centers in diamond using ^{15}N. *Applied Physics Letters*, 88(2), 2006.

[182] D. M. Toyli, C. D. Weis, G. D. Fuchs, T. Schenkel, and D. D. Awschalom. Chip-scale nanofabrication of single spins and spin arrays in diamond. *Nano Letters*, 10(8):3168–3172, 2010.

[183] B. Naydenov, F. Reinhard, A. Lämmle, V. Richter, R. Kalish, U. F. S. D'Haenens-Johansson, M. Newton, F. Jelezko, and J. Wrachtrup. Increasing the coherence time of single electron spins in diamond by high temperature annealing. *Applied Physics Letters*, 97(24):–, 2010.

[184] K. Cho, W.R. Allen, T.G. Finstad, W.K. Chu, J. Liu, and J.J. Wortman. Channeling effect for low energy ion implantation in si. *Nuclear Instruments and Methods in Physics Research Section B: Beam Interactions with Materials and Atoms*, 7:265 – 272, 1985.

[185] S. Koizumi, C. E. Nebel, and M. Nesladek. *Physics and applications of CVD diamond*. Wiley-VCH, 2008.

[186] K. D. Jahnke, B. Naydenov, T. Teraji, S. Koizumi, T. Umeda, J. Isoya, and F. Jelezko. Long coherence time of spin qubits in ^{12}C enriched polycrystalline chemical vapor deposition diamond. *Applied Physics Letters*, 101(1), 2012.

[187] H. S. Knowles, D. M. Kara, and M. Atatüre. Observing bulk diamond spin coherence in high-purity nanodiamonds. *Nat Mater*, 13(1):21–25, 01 2014.

[188] K. Kobashi. *Diamond films: chamical vapor deposition for oriented and heteroepitaxial growth*. Elsevier, Ltd., 2005.

[189] K. Hayashi, S. Yamanaka, H. Okushi, and K. Kajimura. Stepped growth and etching of (001) diamond. *Diamond and Related Materials*, 5(9):1002 – 1005, 1996.

[190] K. Ohno. *Nanometer-scale engineering of shallow spins in diamond*. PhD thesis, University of California, Santa Barbara, 2014.

[191] H. Okushi, H. Watanabe, S. Ri, S. Yamanaka, and D. Takeuchi. Device-grade homoepitaxial diamond film growth. *Journal of Crystal Growth*, 237–239, Part 2:1269 – 1276, 2002.

[192] P. John, N. Polwart, C. E. Troupe, and J. I. B. Wilson. The oxidation of (100) textured diamond. *Diamond and Related Materials*, 11(3–6):861–866, 2002.

[193] K.-M. C. Fu, C. Santori, P. E. Barclay, and R. G. Beausoleil. Conversion of neutral nitrogen-vacancy centers to negatively charged nitrogen-vacancy centers through selective oxidation. *Applied Physics Letters*, 96(12), 2010.

[194] M. V. Hauf, B. Grotz, B. Naydenov, M. Dankerl, S. Pezzagna, J. Meijer, F. Jelezko, J. Wrachtrup, M. Stutzmann, F. Reinhard, and J. A. Garrido. Chemical control of the charge state of nitrogen-vacancy centers in diamond. *Phys. Rev. B*, 83:081304, Feb 2011.

[195] A. O. Sushkov, N. Chisholm, I. Lovchinsky, M. Kubo, P. K. Lo, S. D. Bennett, D. Hunger, A. Akimov, R. L. Walsworth, H. Park, and M. D. Lukin. All-optical sensing of a single-molecule electron spin. *Nano Letters*, 14(11):6443–6448, 11 2014.

[196] I. Lovchinsky, A. O. Sushkov, E. Urbach, N. P. de Leon, S. Choi, K. De Greve, R. Evans, R. Gertner, E. Bersin, C. Müller, L. McGuinness, F. Jelezko, R. L. Walsworth, H. Park, and M. D. Lukin. Nuclear magnetic resonance detection and spectroscopy of single proteins using quantum logic. *Science*, 351(6275):836–841, 2016.

[197] Z. Huang, W.-D. Li, C. Santori, V. M. Acosta, A. Faraon, T. Ishikawa, W. Wu, D. Winston, R. S. Williams, and R. G. Beausoleil. Diamond nitrogen-vacancy centers created by scanning focused helium ion beam and annealing. *Applied Physics Letters*, 103(8), 2013.

[198] F. F. de Oliveira, S. A. Momenzadeh, D. Antonov, J. Scharpf, C. Osterkamp, B. Naydenov, F. Jelezko, A. Denisenko, and J. Wrachtrup. Toward optimized surface -profiles of nitrogen-vacancy centers activated by helium irradiation in diamond. *Nano Letters*, 16(4):2228–2233, 2016.

[199] S. Cui, A. S. Greenspon, K. Ohno, B. A. Myers, A. C. Bleszynski Jayich, D. D. Awschalom, and E. L. Hu. Reduced plasma-induced damage to near-surface nitrogen-vacancy centers in diamond. *Nano Letters*, 15(5):2887–2891, 2015.

[200] F. F. de Oliveira, S. A. Momenzadeh, Y. Wang, M. Konuma, M. Markham, A. M. Edmonds, A. Denisenko, and J. Wrachtrup. Effect of low-damage inductively coupled plasma on shallow nitrogen-vacancy centers in diamond. *Applied Physics Letters*, 107(7):073107, 2015.

[201] K. Ohashi, T. Rosskopf, H. Watanabe, M. Loretz, Y. Tao, R. Hauert, S. Tomizawa, T. Ishikawa, J. Ishi-Hayase, S. Shikata, C. L. Degen, and K. M. Itoh. Negatively charged nitrogen-vacancy centers in a 5 nm thin ^{12}C diamond film. *Nano Letters*, 13(10):4733–4738, 10 2013.

[202] A. Tallaire, M. Lesik, V. Jacques, S. Pezzagna, V. Mille, O. Brinza, J. Meijer, B. Abel, J.F. Roch, A. Gicquel, and J. Achard. Temperature dependent creation of nitrogen-vacancy centers in single crystal CVD diamond layers. *Diamond and Related Materials*, 51:55 – 60, 2015.

[203] C. Osterkamp, J. Lang, J. Scharpf, C. Müller, L. P. McGuinness, T. Diemant, R. J. Behm, B. Naydenov, and F. Jelezko. Stabilizing shallow color centers in diamond created by nitrogen delta-doping using SF_6 plasma treatment. *Applied Physics Letters*, 106:113109, 2015.

[204] J. Schwartz, S. Aloni, D. F. Ogletree, and T. Schenkel. Effects of low-energy electron irradiation on formation of nitrogen–vacancy centers in single-crystal diamond. *New Journal of Physics*, 14(4):043024, 2012.

[205] C. A. Meriles, L. Jiang, G. Goldstein, J. S. Hodges, J. R. Maze, M. D. Lukin, and P. Cappellaro. Imaging mesoscopic nuclear spin noise with a diamond magnetometer. *The Journal of Chemical Physics*, 133(12):–, 2010.

[206] H. J. Mamin, M. Kim, M. H. Sherwood, C. T. Rettner, K. Ohno, D. D. Awschalom, and D. Rugar. Nanoscale nuclear magnetic resonance with a nitrogen-vacancy spin sensor. *Science*, 339(6119):557–560, 02 2013.

[207] H. Bluhm, J. A. Bert, N. C. Koshnick, M. E. Huber, and K. A. Moler. Spinlike susceptibility of metallic and insulating thin films at low temperature. *Phys. Rev. Lett.*, 103:026805, Jul 2009.

[208] R. H. Koch, D. P. DiVincenzo, and J. Clarke. Model for $1/f$ flux noise in SQUIDs and qubits. *Phys. Rev. Lett.*, 98:267003, Jun 2007.

[209] T. Schenkel, J. A. Liddle, A. Persaud, A. M. Tyryshkin, S. A. Lyon, R. de Sousa, K. B. Whaley, J. Bokor, J. Shangkuan, and I. Chakarov. Electrical activation and electron spin coherence of ultralow dose antimony implants in silicon. *Applied Physics Letters*, 88(11):–, 2006.

[210] G. de Lange, D. Ristè, V. V. Dobrovitski, and R. Hanson. Single-spin magnetometry with multipulse sensing sequences. *Phys. Rev. Lett.*, 106:080802, Feb 2011.

[211] G. E. Uhlenbeck and L. S. Ornstein. On the theory of the Brownian motion. *Phys. Rev.*, 36:823–841, Sep 1930.

[212] L M. Pham, S. J. DeVience, F. Casola, I. Lovchinsky, A. O. Sushkov, E. Bersin, J. Lee, E. Urbach, P. Cappellaro, H. Park, A. Yacoby, M. D. Lukin, and R. L. Walsworth. NMR technique for determining the depth of shallow nitrogen-vacancy centers in diamond. *Phys. Rev. B*, 93:045425, Jan 2016.

[213] J. Cai, A. Retzker, F. Jelezko, and M. B. Plenio. A large-scale quantum simulator on a diamond surface at room temperature. *Nat Phys*, 9(3):168–173, 03 2013.

[214] L. Rondin, J.-P. Tetienne, T. Hingant, J.-F. Roch, P. Maletinsky, and V. Jacques. Magnetometry with nitrogen-vacancy defects in diamond. *Reports on Progress in Physics*, 77(5):056503, 2014.

[215] N. B. Manson, X.-F. He, and P. T. H. Fisk. Raman heterodyne detected electron-nuclear-double-resonance measurements of the nitrogen-vacancy center in diamond. *Opt. Lett.*, 15(19):1094–1096, Oct 1990.

[216] P. V. Klimov, A. L. Falk, B. B. Buckley, and D. D. Awschalom. Electrically driven spin resonance in silicon carbide color centers. *Phys. Rev. Lett.*, 112:087601, Feb 2014.

[217] A. Barfuss, J. Teissier, E. Neu, A. Nunnenkamp, and P. Maletinsky. Strong mechanical driving of a single electron spin. *Nat Phys*, 11(10):820–824, 10 2015.

[218] T. van der Sar, F. Casola, R. L. Walsworth, and A. Yacoby. Nanometre-scale probing of spin waves using single electron spins. *Nat Commun*, 6:7886, 08 2015.

[219] R. J. Schoelkopf, A. A. Clerk, S. M. Girvin, K. W. Lehnert, and M. H. Devoret. *Quantum Noise in Mesoscopic Physics*, chapter Qubits as Spectrometers of Quantum Noise, pages 175–203. Springer Netherlands, Dordrecht, 2003.

[220] S. Steinert, F. Ziem, L. T. Hall, A. Zappe, M. Schweikert, N. Götz, A. Aird, G. Balasubramanian, L. Hollenberg, and J. Wrachtrup. Magnetic spin imaging under ambient conditions with sub-cellular resolution. *Nat Commun*, 4:1607, 03 2013.

[221] A. L. McWhorter. $1/f$ noise and related surface effects in germanium. Univ Penn Press, 1957.

[222] J. Labaziewicz, Y. Ge, D. R. Leibrandt, S. X. Wang, R. Shewmon, and I. L. Chuang. Temperature dependence of electric field noise above gold surfaces. *Phys. Rev. Lett.*, 101:180602, Oct 2008.

[223] L. Luan, M. S. Grinolds, S. Hong, P. Maletinsky, R. L. Walsworth, and A. Yacoby. Decoherence imaging of spin ensembles using a scanning single-electron spin in diamond. *Scientific Reports*, 5:8119 EP –, 01 2015.

[224] H. J. Mamin, M. H. Sherwood, M. Kim, C. T. Rettner, K. Ohno, D. D. Awschalom, and D. Rugar. Multipulse double-quantum magnetometry with near-surface nitrogen-vacancy centers. *Phys. Rev. Lett.*, 113:030803, Jul 2014.

[225] I. Talukdar, D. J. Gorman, N. Daniilidis, P. Schindler, S. Ebadi, H. Kaufmann, T. Zhang, and H. Häffner. Implications of surface noise for the motional coherence of trapped ions. *Phys. Rev. A*, 93:043415, Apr 2016.

[226] R. J. Epstein, S. Seidelin, D. Leibfried, J. H. Wesenberg, J. J. Bollinger, J. M. Amini, R. B. Blakestad, J. Britton, J. P. Home, W. M. Itano, J. D. Jost, E. Knill, C. Langer, R. Ozeri, N. Shiga, and D. J. Wineland. Simplified motional heating rate measurements of trapped ions. *Phys. Rev. A*, 76:033411, Sep 2007.

[227] D. A. Hite, Y. Colombe, A. C. Wilson, K. R. Brown, U. Warring, R. Jördens, J. D. Jost, K. S. McKay, D. P. Pappas, D. Leibfried, and D. J. Wineland. 100-fold reduction of electric-field noise in an ion trap cleaned with *in situ* argon-ion-beam bombardment. *Phys. Rev. Lett.*, 109:103001, Sep 2012.

[228] H. Lüth. *Space-Charge Layers at Semiconductor Inferfaces*, pages 323–376. Springer Berlin Heidelberg, Berlin, Heidelberg, 2010.

[229] D. R. Alfonso, D. A. Drabold, and S. E. Ulloa. Phonon modes of diamond (100) surfaces from *ab initio* calculations. *Phys. Rev. B*, 51:1989–1992, Jan 1995.

[230] A. O. Sushkov, I. Lovchinsky, N. Chisholm, R. L. Walsworth, H. Park, and M. D. Lukin. Magnetic resonance detection of individual proton spins using quantum reporters. *Phys. Rev. Lett.*, 113:197601, Nov 2014.

[231] S. Cui and E. L. Hu. Increased negatively charged nitrogen-vacancy centers in fluorinated diamond. *Applied Physics Letters*, 103(5):051603, 2013.

[232] L. C. Bassett, F. J. Heremans, C. G. Yale, B. B. Buckley, and D. D. Awschalom. Electrical tuning of single nitrogen-vacancy center optical transitions enhanced by photoinduced fields. *Phys. Rev. Lett.*, 107:266403, Dec 2011.

[233] C. I. Pakes, D. Hoxley, J. R. Rabeau, M. T. Edmonds, R. Kalish, and S. Prawer. Scanning Kelvin-probe study of the hydrogen-terminated diamond surface in ultrahigh vacuum. *Applied Physics Letters*, 95(12), 2009.

[234] S. Kolkowitz, A. Safira, A. A. High, R. C. Devlin, S. Choi, Q. P. Unterreithmeier, D. Patterson, A. S. Zibrov, V. E. Manucharyan, H. Park, and M. D. Lukin. Probing Johnson noise and ballistic transport in normal metals with a single-spin qubit. *Science*, 347(6226):1129–1132, 2015.

[235] P. Jamonneau, M. Lesik, J. P. Tetienne, I. Alvizu, L. Mayer, A. Dréau, S. Kosen, J.-F. Roch, S. Pezzagna, J. Meijer, T. Teraji, Y. Kubo, P. Bertet, J. R. Maze, and V. Jacques. Competition between electric field and magnetic field noise in the decoherence of a single spin in diamond. *Phys. Rev. B*, 93:024305, Jan 2016.

[236] E. R. MacQuarrie, T. A. Gosavi, S. A. Bhave, and G. D. Fuchs. Continuous dynamical decoupling of a single diamond nitrogen-vacancy center spin with a mechanical resonator. *Phys. Rev. B*, 92:224419, Dec 2015.

[237] H. Hegyi and M. Gerstein. The relationship between protein structure and function: a comprehensive survey with application to the yeast genome 1. *Journal of Molecular Biology*, 288(1):147–164, 4 1999.

[238] P. C. Lauterbur, M. H. Mendonca-Dias, and A. M. Rudin. Augmentation of tissue water proton spin-lattice relaxation rates by in vivo addition of paramagnetic ions. In P.L. Dutton, J.S. Leigh, and A. Scarpa, editors, *Frontiers of Biological Energetics, 3rd ed.*, volume 1, page 752. Academic Press, New York, 1978.

[239] D. H. Carr and D. G. Gadian. Contrast agents in magnetic resonance imaging. *Clinical Radiology*, 36(6):561–568, 11 1985.

[240] H. J. Weinmann, R. C. Brasch, W. R. Press, and G. E. Wesbey. Characteristics of gadolinium-dtpa complex: a potential nmr contrast agent. *American Journal of Roentgenology*, 142(3):619–624, 1984.

[241] C.-H. Huang and A. Tsourkas. Gd-based macromolecules and nanoparticles as magnetic resonance contrast agents for molecular imaging. In *Current Topics in Medicinal Chemistry*, volume 13, pages 411–421. Bentham Science, 2013.

[242] R. Di Corato, F. Gazeau, C. Le Visage, D. Fayol, P. Levitz, F. Lux, D. Letourneur, N. Luciani, O. Tillement, and C. Wilhelm. High-resolution cellular MRI: Gadolinium and iron oxide nanoparticles for in-depth dual-cell imaging of engineered tissue constructs. *ACS Nano*, 7(9):7500–7512, 09 2013.

[243] M. F. Kircher, A. de la Zerda, J. V Jokerst, C. L Zavaleta, P. J Kempen, E. Mittra, K. Pitter, R. Huang, C. Campos, F. Habte, R. Sinclair, C. W. Brennan, I. K. Mellinghoff, E. C. Holland, and S. S. Gambhir. A brain tumor molecular imaging strategy using a new triple-modality MRI-photoacoustic-raman nanoparticle. *Nat Med*, 18(5):829–834, 05 2012.

[244] S. Serres, M. S. Soto, A. Hamilton, M. A. McAteer, W. S. Carbonell, M. D. Robson, O. Ansorge, A. Khrapitchev, C. Bristow, L. Balathasan, T. Weissensteiner, D. C. Anthony, R. P. Choudhury, R. J. Muschel, and N. R. Sibson. Molecular MRI enables early and sensitive detection of brain metastases. *Proceedings of the National Academy of Sciences*, 109(17):6674–6679, 04 2012.

[245] A. Potapov, H. Yagi, T. Huber, S. Jergic, N. E. Dixon, G. Otting, and D. Goldfarb. Nanometer-scale distance measurements in proteins using Gd^{3+} spin labeling. *Journal of the American Chemical Society*, 132(26):9040–9048, 07 2010.

[246] D. T. Edwards, Z. Ma, T. J. Meade, D. Goldfarb, S. Han, and M. S. Sherwin. Extending the distance range accessed with continuous wave EPR with Gd^{3+} spin probes at high magnetic fields. *Phys. Chem. Chem. Phys.*, 15:11313–11326, 2013.

[247] V. V. Dobrovitski, G. D. Fuchs, A. L. Falk, C. Santori, and D. D. Awschalom. Quantum control over single spins in diamond. *Annual Review of Condensed Matter Physics*, 4(1):23–50, 2015/07/17 2013.

[248] G. Kucsko, P. C. Maurer, N. Y. Yao, M. Kubo, H. J. Noh, P. K. Lo, H. Park, and M. D. Lukin. Nanometre-scale thermometry in a living cell. *Nature*, 500(7460):54–58, 08 2013.

[249] E. Schäfer-Nolte, L. Schlipf, M. Ternes, F. Reinhard, K. Kern, and J. Wrachtrup. Tracking temperature-dependent relaxation times of ferritin nanomagnets with a wideband quantum spectrometer. *Phys. Rev. Lett.*, 113:217204, Nov 2014.

[250] D. H. Carr, J. Brown, G. M. Bydder, R. E. Steiner, H. J. Weinmann, U. Speck, A. S. Hall, and I. R. Young. Gadolinium-DTPA as a contrast agent in MRI: initial clinical experience in 20 patients. *American Journal of Roentgenology*, 143(2):215–224, 1984.

[251] F. C. Ziem, N. S. Götz, A. Zappe, S. Steinert, and J. Wrachtrup. Highly sensitive detection of physiological spins in a microfluidic device. *Nano Letters*, 13(9):4093–4098, 09 2013.

[252] A. Ermakova, G. Pramanik, J. M. Cai, G. Algara-Siller, U. Kaiser, T. Weil, Y. K. Tzeng, H. C. Chang, L. P. McGuinness, M. B. Plenio, B. Naydenov, and F. Jelezko. Detection of a few metallo-protein molecules using color centers in nanodiamonds. *Nano Letters*, 13(7):3305–3309, 07 2013.

[253] L. Rondin, J. P. Tetienne, S. Rohart, A. Thiaville, T. Hingant, P. Spinicelli, J. F. Roch, and V. Jacques. Stray-field imaging of magnetic vortices with a single diamond spin. *Nat Commun*, 4, 07 2013.

[254] T. Häberle, D. Schmid-Lorch, K. Karrai, F. Reinhard, and J. Wrachtrup. High-dynamic-range imaging of nanoscale magnetic fields using optimal control of a single qubit. *Phys. Rev. Lett.*, 111:170801, Oct 2013.

[255] M. Guizar-Sicairos, S. T. Thurman, and J. R. Fienup. Efficient subpixel image registration algorithms. *Optics Letters*, 33(2):156–158, 2008.

[256] H.-K. Kim, T.-J. Lee, G.-H. an Kim, and Y. Chang. Determination of correlation times of new paramagnetic gadolinium MR contrast agents by EPR and ^{17}O NMR. *Bulletin of the Korean Chemical Society*, 30(4):849–852, 2009.

[257] G. M. King, A. R. Carter, A. B. Churnside, L. S. Eberle, and T. T. Perkins. Ultrastable atomic force microscopy: Atomic-scale stability and registration in ambient conditions. *Nano Letters*, 9(4):1451–1456, 04 2009.

[258] D. Rugar. Private communication.

[259] F. Laermer and A. Schilp. Method of anisotropically etching silicon. Patent 5501893, March 1996.

[260] B. C. Buchler, T. Kalkbrenner, C. Hettich, and V. Sandoghdar. Measuring the quantum efficiency of the optical emission of single radiating dipoles using a scanning mirror. *Phys. Rev. Lett.*, 95:063003, Aug 2005.

[261] J. T. Choy, B. J. M. Hausmann, T. M. Babinec, I. Bulu, M. Khan, P. Maletinsky, A. Yacoby, and M. Loncar. Enhanced single-photon emission from a diamond-silver aperture. *Nat Photon*, 5(12):738–743, 12 2011.

[262] S. Johnson, P. R. Dolan, T. Grange, A. A. P. Trichet, G. Hornecker, Y. C. Chen, L. Weng, G. M. Hughes, A. A. R. Watt, A. Auffèves, and J. M. Smith. Tunable cavity coupling of the zero phonon line of a nitrogen-vacancy defect in diamond. *New Journal of Physics*, 17(12):122003, 2015.

[263] L. S. Langsjoen, A. Poudel, M. G. Vavilov, and R. Joynt. Qubit relaxation from evanescent-wave Johnson noise. *Phys. Rev. A*, 86:010301, 2012.

[264] J.-P. Tetienne, A. Lombard, D. A. Simpson, C. Ritchie, J. Lu, P. Mulvaney, and L. C. L. Hollenberg. Scanning nanospin ensemble microscope for nanoscale magnetic and thermal imaging. *Nano Letters*, 16(1):326–333, 01 2016.

[265] M. Kaviani, P. Deák, B. Aradi, T. Frauenheim, J.-P. Chou, and A. Gali. Proper surface termination for luminescent near-surface nv centers in diamond. *Nano Letters*, 14(8):4772–4777, 08 2014.

[266] Xi Kong, Alexander Stark, Jiangfeng Du, Liam P. McGuinness, and Fedor Jelezko. Towards chemical structure resolution with nanoscale nuclear magnetic resonance spectroscopy. *Phys. Rev. Applied*, 4:024004, Aug 2015.

[267] J. M. Boss, K. Chang, J. Armijo, K. Cujia, T. Rosskopf, J. R. Maze, and C. L. Degen. One- and two-dimensional nuclear magnetic resonance spectroscopy with a diamond quantum sensor. *Phys. Rev. Lett.*, 116:197601, May 2016.

[268] J. P. Tetienne, T. Hingant, L. J. Martínez, S. Rohart, A. Thiaville, L. Herrera Diez, K Garcia, J. P. Adam, J. V. Kim, J. F. Roch, I. M. Miron, G. Gaudin, L. Vila, B. Ocker, D. Ravelosona, and V. Jacques. The nature of domain walls in ultrathin ferromagnets revealed by scanning nanomagnetometry. *Nature Communications*, 6:6733 EP –, 04 2015.

[269] N.B. Manson and J.P. Harrison. Photo-ionization of the nitrogen-vacancy center in diamond. *Diamond and Related Materials*, 14(10):1705 – 1710, 2005.

[270] B. Grotz, M. V. Hauf, M. Dankerl, B. Naydenov, S. Pezzagna, J. Meijer, F. Jelezko, J. Wrachtrup, M. Stutzmann, F. Reinhard, and J. A. Garrido. Charge state manipulation of qubits in diamond. *Nat Commun*, 3:729, 03 2012.

[271] C. S. Shin, M. C. Butler, H.-J. Wang, C. E. Avalos, S. J. Seltzer, R.-B. Liu, A. Pines, and V. S. Bajaj. Optically detected nuclear quadrupolar interaction of ^{14}N in nitrogen-vacancy centers in diamond. *Phys. Rev. B*, 89:205202, May 2014.

[272] L. G. Rowan, E. L. Hahn, and W. B. Mims. Electron-spin-echo envelope modulation. *Phys. Rev.*, 137:A61–A71, Jan 1965.

[273] P. C. Maurer, J. R. Maze, P. L. Stanwix, L. Jiang, A. V. Gorshkov, A. A. Zibrov, B. Harke, J. S. Hodges, A. S. Zibrov, A. Yacoby, D. Twitchen, S. W. Hell, R. L. Walsworth, and M. D. Lukin. Far-field optical imaging and manipulation of individual spins with nanoscale resolution. *Nat Phys*, 6(11):912–918, 11 2010.

[274] S. Sangtawesin, C. A. McLellan, B. A. Myers, A. C. Bleszynski Jayich, D. D. Awschalom, and J. R. Petta. Hyperfine-enhanced gyromagnetic ratio of a nuclear spin in diamond. *New Journal of Physics*, 18(8):083016, 2016.